Volume I

Atmospheric processes

FINAL REPORTS

SCIENTIFIC SUPPORT PLAN FOR A SUSTAINABLE DEVELOPMENT POLICY SPSD 1

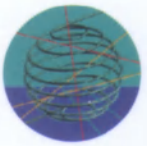

This booklet is realised in the framework of the Scientific Support Plan for a Sustainable Development Policy (SPSD I).

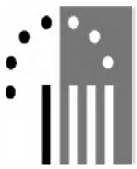

D/2002/47
Published in 2004 by the
Belgian Science Policy
Rue de la Science 8
Wetenschapsstraat 8
B-1000 Brussels
Belgium
Tel : 32/2/238.34.11 – Fax : 32/2/230.59.12
http://www.belspo.be (FEDRA)

Contact person:
Mrs Martine Vanderstraeten (vdst@belspo.be)
Secr : 32/2/238.36.13

CONTENTS

Volume 1: Reducing uncertainties - Atmospheric processes

- Experimental studies of atmospheric changes (ESAC) I
- Anthropogenic and biogenic influences on the oxidising capacity of the atmosphere II
- Sources, physico-chemical characteristics, and climate forcing of atmospheric aerosols III

Supporting actions IV

- BelEUROS: Implementation and extension of the EUROS (EURopean Operational Smog) model for policy support in Belgium V
- Development of a specific interpolation method for air pollutants measured in automatic networks (SMOGSTOP) VI

CG/DD/01

EXPERIMENTAL STUDIES OF ATMOSPHERIC CHANGES (ESAC)

BELGISCH INSTITUUT VOOR RUIMTE AERONOMIE
Ringlaan 3
B-1180 BRUSSEL
M. DE MAZIÈRE (coordinator CG/DD/01A)

UNIVERSITÉ LIBRE DE BRUXELLES
LABO. DE CHIMIE PHYSIQUE MOLÉCULAIRE
Avenue F.D. Roosevelt 50 CP 160/09
B-1050 BRUXELLES
R. COLIN (promoter CG/DD/01B)

KONINKLIJK METEOROLOGISCH INSTITUUT VAN BELGIË
Ringlaan 3
B-1180 BRUSSEL
D. DE MUER (promoter CG/DD/01C)

UNIVERSITÉ DE LIÈGE
INSTITUT D'ASTROPHYSIQUE ET DE GÉOPHYSIQUE
Avenue de Cointe 5
B-4000 LIEGE
R. ZANDER (promoter CG/DD/01D)

TABLE OF CONTENTS

ABSTRACT 1

1. OVERALL CONTEXT AND GENERAL OBJECTIVES OF ESAC 3

2. METHODOLOGY: STATE OF THE ART TECHNIQUES 4

2.1 Remote sensing by optical spectrometry 5
2.1.1 V-visible differential optical absorption spectrometry (DOAS) 5
2.1.2 Fourier transform spectrometry 6
2.2 In situ Ozone soundings 7
2.3 UV-visible spectral radiometry 7
2.4 Laboratory experiments 7
2.5 Numerical modelling 7

3. METHODOLOGY: NEW DEVELOPMENTS AND IMPROVEMENTS AS TO INSTRUMENTS, ALGORITHMS AND DATA ANALYSIS TOOLS 8

3.1 DOAS Off-axis instruments 8
3.2 WinDOAS 11
3.3 PSCBOX, a coupled photochemical box-/radiative transfer model 12
3.3.1 Model package description 12
3.3.2 Model package validation 13
3.4 Altitude-Differential column measurements 18
3.5 Advanced FTIR spectral analysis algorithms 18
3.5.1 O_3 vertical column abundance retrieval including a daily, tropopause dependent climatological model 19
3.5.2 Vertical inversion algorithms for FTIR spectra: SFSP upgraded to SFSP2, and SFIT2 21
3.5.2.1 The Optimal Estimation Method and its application for inversion of FTIR spectra 21
3.5.2.2 Preliminary results for O_3, HCl and HF vertical profiles retrieved from ISSJ FTIR spectra 23
Ozone profiles 24
Ozone total columns: improved consistency between various data sets 24
HF profile inversion and comparison with HALOE 30
Comparison of stratospheric O_3, HF and HCl with the 3D CTM SLIMCAT for the 1999-2000 winter 30

3.6 Wspectra and bFit **34**
3.7 New correction procedures for the pump efficiency of Ozone sondes **35**

4. RESULTS OF GEOPHYSICAL RELEVANCE **36**

4.1 Evaluation of long-term atmospheric chemistry data. Variability and global changes of the atmospheric composition **36**
4.1.1 Long-term data at the Jungfraujoch 37
4.1.1.1 Evolution of the budget of inorganic chlorine (Cly) above ISSJ *41*
4.1.1.2 Evolution of the budget of inorganic fluorine (F_y) above ISSJ *46*
4.1.1.3 The evolution of HCl/HF *48*
4.1.1.4 Evolution of the budget of NO_y above ISSJ, and the impact of Mt. Pinatubo on the NO_2 abundance *50*
Impact of the eruption of Mt. Pinatubo on the NO_2 abundance above the Jungfraujoch *53*
4.1.1.5 Kyoto Protocol-related investigations *55*
4.1.1.6 Findings related to other species *57*
Ozone (O_3) *57*
Carbon monoxide (CO), ethane (C_2H_6) and hydrogen cyanide (HCN) *58*
Formaldehyde (H_2CO) *59*
Carbonyl Sulfide (OCS) *59*
4.1.2 Long-term data at Harestua and OHP 61
4.1.2.1 Introduction 61
4.1.2.2 Instrument updates *61*
4.1.2.3 Stratospheric BrO *62*
4.1.2.4 Tropospheric BrO *63*
4.1.2.5 OClO observations and model simulations *65*
4.1.2.6 Simulations of NO2 DSCDs at Harestua and OHP with PSCBOX *69*
4.1.3 Long-term ozone data at Ukkel 69
4.1.3.1 Data homogenisation *71*
4.1.3.2 Ozone trends *74*
4.1.4 Synergy with satellite data 78
4.1.4.1 Satellite validation *78*
TOMS and ADEOS O_3 data *78*
Geophysical consistency of stratospheric NO_2 measurements *80*
4.1.4.2 Development of an NO_2 vertical profile climatology *83*
4.1.4.3 ATMOS-related research *88*
The ATMOS "Version 3" geophysical data *88*
Auxiliary data *92*

4.2 Evaluation of long-term spectral UV irradiance and UV Index data at Ukkel. Variability, global changes, and UV Index forecasting 93
4.2.1 Introduction 93
4.2.2 Time series of effective UV irradiances 94
4.2.3 Factors of influence 95
4.2.3.1 Ozone 95
4.2.3.2 Clouds 97
4.2.4 Trends in UV effective irradiance 98
4.2.5 UV Index forecasting 99
4.2.5.1 Development of an operational UV Index forecasting procedure 99
4.2.6 UV Index forecasting 100
4.2.6.1 Development of an operational UV Index forecasting procedure 100
4.2.6.2 Comparison of UV models and UV Index forecasts 103
4.3 Atmospheric process studies 104
4.3.1 Tropospheric O3 in Ukkel 104
4.3.2 Urban pollution in Brussels 108
4.3.2.1 Methodology 108
4.3.2.2 Discussion of the results 110
ULB97 campaign 110
Models results 112
Conclusions 113
4.3.3 Planetary boundary layer investigations in the Jungfraujoch area 114
4.4 Laboratory measurements of spectroscopic parameters of atmospheric relevance 116
4.4.1 Experimental conditions 116
4.4.2 Results 118
4.4.2.1 Line parameters and absorption cross-sections in the UV-VIS-NIR 118
NO_2 118
O_2 121
H_2O 126
4.4.2.2 Line parameters and absorption cross-sections in the IR-NIR 130
Stable species (OCS, $^{12}C_2H_2$, HCFC-22 and HFC-152a) 130
Unstable species: HOCl 131

ACRONYMS 133

REFERENCES 135

ESAC PUBLICATIONS 150

ABSTRACT

This document is the final scientific report for the project ESAC, Experimental Studies of Atmospheric Changes, a project contributing to the Global Change and Sustainable Development Programme of the Belgian Prime Minister's Services - Federal Offices for Scientific, Technical and Cultural Affairs. It integrates the achievements obtained during the project (1/12/1996- 31/5/2001) by all four partners collaborating in the project. They are the Belgian Institute for Space Aeronomy (BIRA-IASB), the Laboratoire de Chimie Physique Moléculaire of the Université Libre de Bruxelles (LCPM-ULB), the Royal Meteorological Institute of Belgium (KMI-IRM), and the Institut d'Astrophysique et de Géophysique of the Université de Liège (ULg).

The project aims at a better understanding of the Earth atmospheric composition and chemical processes, from ground level up to the stratosphere, and at an assessment of the atmosphere's actual state and evolution. To achieve this goal, ESAC relies on the acquisition, analysis and geophysical interpretation of atmospheric data. Data are collected at four European stations that belong to the Network for the Detection of Stratospheric Change, and are complemented with *in situ* and satellite data, campaign observations, and model simulations. The four stations are Ukkel (Belgium, 50.5°N, 4.3°E), Jungfraujoch in the Swiss Alps (46.5°N, 8°E), Harestua (Norway, 60.2°N, 10.7°E), and Observatoire de Haute Provence (France, 44°N, 6°E). Studies concerning the consistency between the various data sets have been performed to enable synergistic use of all the data.

Starting from state of the art experimental techniques and numerical models, more performant instruments, advanced data acquisition and analysis methods, and new modelling activities have been developed. Particular progress has been made in tropospheric composition measurements, including the development of vertical inversion algorithms, and in the investigations of fast twilight photochemistry of species like OClO.

Existing time series of atmospheric species concentrations and of UV spectral irradiances have been improved for quality and consistency, and have been updated with four and a half years of data. The actual extent of the time series has allowed to identify and quantify changes in the rates of increase for some gases and families, an issue that is of special importance to assess the effectiveness and further requirements of international regulations like the Montreal Protocol and its successive Amendments, and the Kyoto Protocol. For example for inorganic chlorine above the Jungfraujoch, the turnover time of maximum abundance has been observed around 1998 ; it has been evaluated against the expected evolution when

taking into account the gradual phase out of chlorine-bearing emissions. Height-resolved trends of ozone above Ukkel have been updated, based on a homogenized and validated time series of soundings since 1969.

Particular events have been investigated, such as the impact of the Mt. Pinatubo eruption of summer 1991 on the evolution of the NO_2 abundance above the Jungfraujoch. Tropospheric process studies have been made, including an evaluation of the boundary layer O_3 budget and measurements of pollution in Brussels.

A reanalysis of all occultations performed with the Atmospheric Trace Molecule Spectroscopy (ATMOS) instrument during 4 shuttle-based space missions has allowed to produce an improved "Version 3" set of geophysical data for over 30 atmospheric species. This has resulted in volume mixing ratio profiles now extending throughout the entire stratosphere and further down into the free troposphere, thus demonstrating that infrared remote sensing from space can be used to consistently investigate the exchanges between the upper troposphere and lower stratosphere

The field measurements are supported by high-quality laboratory experiments. New and/or improved spectroscopic parameters for a number of atmospherically relevant species (NO_2, O_2, H_2O, some HCFC, ...) have been obtained and provided to the community.

The achievements made in ESAC have been valorised on a national and international level, through many communications, publications, participations to symposia, working groups and assessment efforts, through contributions to European research projects and international programmes, and through the dissemination of results and the submission of data to international databases. The public has been informed through participation to colloquia and expositions for a large audience, and the distribution of brochures. During ESAC, the procedure for UV index forecasting has been established and implemented, and the daily publication of the UV index has been initiated.

This report provides an extensive overview of the achievements made by the ESAC consortium during the project. It reviews and completes the previously submitted yearly reports, at the end of 1997, 1998 and 1999.

1. OVERALL CONTEXT AND GENERAL OBJECTIVES OF ESAC

The composition of the Earth's atmosphere is changing as the concentrations of a number of radiatively and chemically active atmospheric constituents emitted at the surface are rapidly increasing, mainly due to man-made activities. These increased emissions influence atmospheric ozone, the Earth's radiative balance, hence climate, and modify the oxidising capacity of the atmosphere. It has become clear also that the upper troposphere / lower stratosphere is a region of high interest, because it controls the exchange of gases between the troposphere, where the sources are, and the stratosphere, and it controls to a great extent the radiative balance of the atmosphere.

A better knowledge of atmospheric composition and chemical processes, from ground level up to the stratosphere, is fundamental to assess the present state and changes and predict the future evolution of the Earth's environment, so that regulatory decisions about mankind practices can be identified on the basis of firm scientific grounds. This can only be achieved by a comprehensive series of complementary measurements including ground-based observations, aeroplane and balloon-borne campaigns, and global satellite missions, by improving the probing capabilities in the troposphere, and by comparing and integrating the observational data with numerical models.

In the field of atmospheric chemistry three main objectives can be identified:

- Long-term global monitoring of key stratospheric and tropospheric species such as ozone, halogen and nitrogen compounds, and the radiatively active gases or so-called 'greenhouse' gases[#]
- Advance knowledge of processes that control the chemical behaviour of the stratosphere and the troposphere, as determined from the observed spatial and temporal variability of trace species. The UV spectral irradiance is an important parameter in these processes.
- Identification of sources and sinks of primary species, and of their spatial and temporal variability.

ESAC contributes to the objectives of investigating the behaviour of ozone and many key stratospheric and tropospheric species at four stations in Europe, complemented by global satellite observations. This investigation includes long-term monitoring and the evaluation of radiative, dynamical, and chemical mechanisms underlying the observed variabilities and changes. The four stations are Ukkel (Belgium, 50.5°N, 4.3°E), Jungfraujoch (ISSJ) in the Swiss Alps (46.5°N, 8°E), Harestua (Norway, 60.2°N, 10.7°E), and Observatoire de Haute Provence (OHP, France, 44°N, 6°E);

they are part of the international Network for Detection of Stratospheric Change (NDSC). Additionally it was tasked to improve the acquisition of tropospheric data, and in particular, to pursue the analysis of earlier ATMOS/Shuttle observations to assess the possibilities to study the upper troposphere by infrared remote sensing from space. Long-term monitoring of the spectral UV irradiance is performed at Ukkel, in compliance with the international quality standards. The atmospheric observations are supported by numerical modelling of the atmosphere and by laboratory experiments that provide the fundamental spectroscopic and radiative data needed in the models and in the spectral data analyses.

ESAC is linked to international research activities, in particular to projects funded within the EC Environment Programme and EUROTRAC. Its results contribute to international research programmes like SPARC/WCRP (Stratospheric Processes and Their Role on Climate/ World Climate Research Programme) and NDSC/GAW/WMO (Network for Detection of Stratospheric Change / Global Atmosphere Watch / World Meteorological Organisation), and to international assessment studies, in support of environmental policies and the Montreal and Kyoto Protocols, aiming at preserving the Earth's environment from threats resulting from mankind's activities. Resulting data are archived for further exploitation in local and international databases.

2. METHODOLOGY: STATE OF THE ART TECHNIQUES

The research carried out in ESAC relies on the acquisition, analysis and geophysical interpretation of atmospheric data. The acquisition is performed with a suite of state of the art spectrometric instruments, and the spectral analysis is done with appropriate retrieval algorithms. Performant numerical models of the atmosphere are used for comparison and integration with observational data, to support the geophysical interpretation of the experimental data. Once validated, they can be used to make predictions of the future evolution of the atmosphere.

Both for the analysis of spectral observations of the atmosphere as well as in chemical-dynamical-radiative modelling of the atmosphere, one needs the spectroscopic and radiative parameters of the atmospheric absorbers and scatterers with high accuracy: they are obtained in laboratory experiments tailored to these needs.

It must be emphasized that the remote sensing measurements carried out in ESAC are part of the NDSC. They are complementary to atmospheric composition measurements from space and balloons. Therefore, part of the activities in ESAC concerns satellite data validation using NDSC ground-based data, and the

geophysical interpretation of the data is mostly done making synergistic use of the network, satellite and model data.

Although attention is paid to particular stratospheric and tropospheric process studies (see, chapters 4.1 and 4.3), mainly in the context of campaign measurements, the continuity of the measurements is of utmost importance for addressing the global change issues. Instrument maintenance and calibration, data verification and validation, and homogenisation of long-term time series represent major efforts in this field of research. Examples are given throughout Chapter 4.

Qualified data series are stored locally and in international databases, in particular HITRAN/GEISA for spectroscopic data, and NADIR (NILU's Interactive Database for Atmospheric Retrieval) at NILU (Norway) and the NDSC database at NOAA for the geophysical data. The Ukkel soundings are transmitted to WMO and ECMWF (European Centre for Meteorology and Weather Forecasting).

More details about the instruments and techniques used in ESAC are given in the following subsections (2.1 to 2.5).

2.1 Remote sensing by optical spectrometry

2.1.1 UV-visible differential optical absorption spectrometry (DOAS)

The DOAS instruments operated in ESAC at the Jungfraujoch, Harestua and OHP observatories are spectrographs with linear photodiode arrays or CCD arrays; they are operated automatically. The Jungfraujoch instrument is a commercial SAOZ (Système d'Analyse par Observations Zénithales), the other ones have been built at BIRA-IASB. The DOAS method is based on spectral measurements of the solar light in the UV and/or visible range (300-600 nm) of the spectrum that is diffused by the atmosphere at the zenith or at another angle with respect to the zenith ('off-axis' measurement). The spectrum is analysed for its high frequency structures (resolution $\cong$ 0.5 nm) that are representative of the atmospheric molecular absorptions. Measurements can be performed irrespective of the weather conditions. The technique is capable of detecting and quantifying the total column abundances of O_3, NO_2, OClO, BrO, H_2CO (O_4 and H_2O).

2.1.2 Fourier transform spectrometry

High resolution Fourier transform spectrometry (FTS) is based on the principle of Michelson interferometry. In ESAC, FTS are used in the UV-visible and infrared spectral range. The technique allows the recording of absorption spectra over a large spectral range, carrying many absorption signatures simultaneously; mostly the individual absorption lines can be resolved.

Currently the Fourier transform infrared (FTIR) measurements are performed at the Jungfraujoch, in the 2 to 15 μm region, with a maximum resolution of order 0.003 cm^{-1}. Two FTIR instruments have been operational: a commercial Bruker 120 HR and a home-made spectrometer built at the University of Liège. An important list of atmospheric species can be detected and their total column abundances determined: CO_2, CH_4, N_2O, CO, O_3, NO, NO_2, HNO_3, HNO_4, $CFCl_3$, CF_2Cl_2, CHF_2Cl, HCl, HF, $ClONO_2$, COF_2, SF_6, C_2H_2, C_2H_6, OCS, HCN, H_2CO. The measurements require clear-sky conditions and are not automatic. Table I illustrates the species currently monitored at the Jungfraujoch, including (between parentheses) an estimate of the precisions of the retrieved total column abundances.

A mobile Bruker 120 M FTS, with a maximum resolution of 0.008 cm^{-1}, has been operated in the UV-visible for horizontal long-path measurements of atmospheric pollutants (O_3, NO_2, SO_2, C_2H_6, H_2CO,...) at the ULB campus in Brussels, and in the infrared range for field experiments in the Jungfraujoch area (see chapter 4.3).

Table I: *List of Molecules Studied in FTIR Solar Observations at the Jungfraujoch. The relative precisions, in percentage, with which the total column abundances can be derived routinely from typical individual observations are given between parentheses for each species. Species that are primarily stratospheric are listed in italic, the other ones are primarily tropospheric; species under evaluation are put between square brackets.*

Reference gas:	N_2(≈1%)
Minor constituents:	CO_2(<2%), N_2O(≤2%), CH_4(≈2%), CO(≤4%), O_3(≤5%), [H_2O]
Trace constituents:	
Halogenated species:	*HCl*(≤4%), *$ClONO_2$*(≈ 20%), CCl_2F_2(≤4%), $CHClF_2$(≤6%), *HF*(≤3%), *COF_2*(≤20%), SF_6(≈30%)
Nitrogenated species:	*NO*(≤6%), *NO_2*(≤10%), *HNO_3*(≈5%), *HNO_4* (monthly avg.)
Others:	C_2H_2(≈20%), C_2H_6(≤6%), HCN(≤8%), OCS(≤8%), H_2CO(≥monthly avg.), [H_2CO_2, CH_3Cl, CCl_4, CCl_3F,...];
Various isotopes	

2.2 In situ Ozone soundings

Ozone soundings are based on a reduction reaction in an electro-chemical cell, carried by a small balloon to about 35 km altitude. Currently at Ukkel (since 1997) they are performed with Z-ECC type sondes; before Brewer-Mast type cells were used. Vertical profiles of ozone concentrations can be measured with a very high vertical resolution, of order 100 m, from ground to the burst altitude of the balloon.

2.3 UV-visible spectral radiometry

Spectral monitoring of the solar irradiance in the UV and visible is performed with radiometrically calibrated instruments of different types. The core instruments at Ukkel are a Brewer Mk II spectrophotometer (280-325 nm) at KMI-IRM, and a double modified HD10 Jobin-Yvon monochromator at BIRA-IASB. Additional instruments are 3 filter radiometers and 4 pyranometers. Together, they allow measurements of the total and direct and diffuse components of the solar irradiance; complementary information on the ozone total column and aerosol optical depth can be extracted. The spectral range of the core instruments covers the UVA to UVC (280 nm - 600 nm).

2.4 Laboratory experiments

Laboratory experiments are performed with similar Fourier transform instruments as the ones mentioned above, coupled to long path absorption cells with known gas concentrations inside. The cells are temperature and pressure controlled. The gas pressure, temperature and concentration in the cell must be varied, to mimic the atmospheric conditions. In ESAC, laboratory experiments are performed in collaboration with the Laboratoire de Spectrométrie Moléculaire et Atmosphérique (GSMA) of the Université de Reims, where cells with optical path lengths up to 2 km and temperature cooling down to 220 K are available.

2.5 Numerical modelling

In the ESAC project, we have used various radiative transfer (RT) and UV models, 1-dimensional chemical box models, and 3-dimensional chemistry-transport models (3D CTM). Most of them were developed in the consortium. Moreover several statistical models and empirical regression models have been developed for analysis of experimental data and time series.

3. METHODOLOGY: NEW DEVELOPMENTS AND IMPROVEMENTS AS TO INSTRUMENTS, ALGORITHMS AND DATA ANALYSIS TOOLS

3.1 DOAS Off-axis instruments

The DOAS technique is configured commonly for observations of the solar light scattered at zenith, the so-called zenith-sky viewing geometry. However, one can also apply the technique to the off-axis viewing geometry, i.e., the collected light comes from a scattering point at a large angle with respect to the zenith). A combination of measurements successively performed in zenith-sky and off-axis geometries allows to derive the tropospheric content of the measured species, in a relatively thin layer (2-3 km) above the earth surface. The principle of the method is schematically outlined in Figure 1, where typical ray-paths corresponding to both viewing geometries are represented. Off-axis and zenith-sky rays being scattered at approximately the same altitude, their difference is mainly sensitive to the region below the scattering altitude (which roughly corresponds to the location of the planetary boundary layer PBL).

The zenith-sky UV-visible spectrometer in operation at Observatoire de Haute Provence has been modified in December 2000 to include an off-axis mode where the scattered light is measured in a quasi-horizontal direction (see Figure 2). Located a few meters above the ground, the spectrometer benefits from an unobstructed field of view down to the horizon in all directions. The similar transformation of the Harestua instrument (off-axis measurement mode) is planned for late 2001.

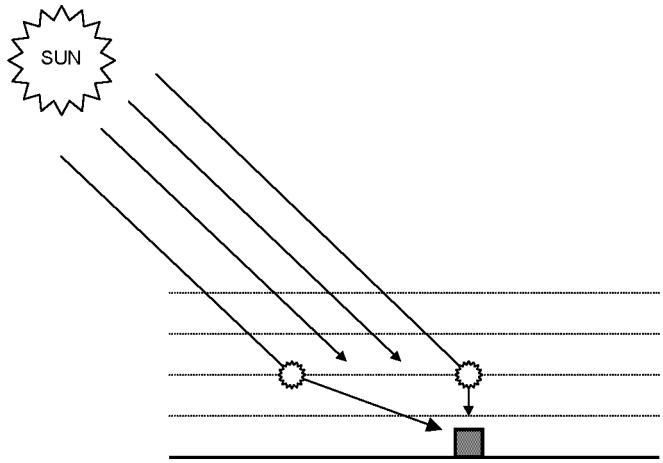

Figure 1: *Schematic drawing comparing typical ray-paths for zenith-sky and off-axis viewing geometries. Paths before the scattering altitude are similar in both geometries.*

Figure 2: *BIRA-IASB UV-visible spectrometer operated at OHP. Alternate observations of the zenith-sky and of the "off-axis" scattered light (10° above horizon) are obtained by means of a rotating mirror installed in a quartz dome on top of the box.*

Figure 3 displays preliminary results obtained using the OHP instruments on January 16, 2001. The spectral analysis of zenith-sky and off-axis observations performed around noon within a few minutes of interval reveals significant differences in the absorption of O_3, NO_2, BrO and formaldehyde (HCHO), thus providing evidence for the presence of these species in the troposphere. These promising results confirm the potential of off-axis measurements for tropospheric investigations. Quantitative interpretation will be the subject of algorithm developments planned in the near future.

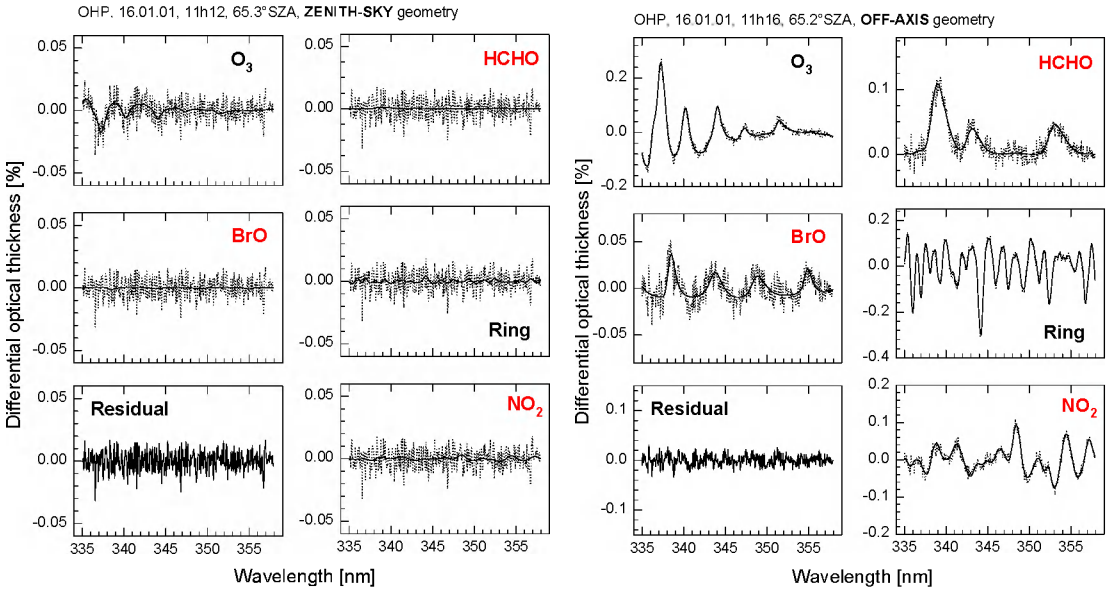

Figure 3: *Results of DOAS fitting procedures applied to zenith-sky and off-axis spectra measured quasi-simultaneously at noon with the OHP spectrometer on 16 January 2001. The increased absorption of O_3, HCHO, BrO and NO_2 in the off-axis geometry compared to the zenith-sky geometry is a signature of the presence of these species in the troposphere. Further developments of the analysis algorithms are still needed for a quantitative interpretation.*

In addition to the modification of the OHP spectrometer, a new instrument was built to enable combined measurements under different viewing geometries. The instrument consists of a commercial ARC Spectra-Pro 150-S spectrometer equipped with a grating of 1200 l/mm and a cooled CCD from Princeton Instrument. The whole spectrometer is mounted on a BRUSAG solar tracker allowing for precise pointing in any direction, including towards the sun and the moon. The spectral range covered by the instrument extends from 300 nm to 650 nm (in 3 independent spectral windows), with a resolution of about 0.7 nm full width half maximum (FWHM).

A preliminary version of this instrument was used for the first time during a campaign at the University of Reims during the solar eclipse of 11 August 1999, inside the zone of total occultation. The total eclipse was observed at 12h25 local time during 2 minutes, while the complete phase of occultation lasted 2h40m. The instrument was set up to allow measurements of O_3 and NO_2 stratospheric and tropospheric columnar abundances from the observation of the scattered skylight in the UV-visible spectral region.

The large differences between the NO_2 slant columns observed in both observation geometries were a clear indication for the presence of large amounts of NO_2 in the

planetary boundary layer (PBL) in the few hours that followed the eclipse. The data showed a large increase in the NO_2 content just after the eclipse, and later again around 14 UT.
This instrument will be used in the future for campaign observations in the context of the Network for the Detection of Stratospheric Change (NDSC).

3.2 WinDOAS

The SAOZ and DOAS data processing have been improved in the course of the ESAC project duration (see section 4.1). Moreover, the spectral analysis tools have been extended to include the analysis of DOAS spectra taken in zenith and off-axis geometries, from balloon (e. g., the SAOZ balloon spectra from Service d'Aéronomie du CNRS) and space (e.g., GOME). An operational version of the data processing algorithm has been implemented under Windows '98, called WinDOAS (Van Roozendael et al., 1999), that integrates all algorithm improvements and various analysis options, with a user-friendly graphical interface as illustrated in Figure 4. WinDOAS is already used by about 11 research groups in- and outside Europe, and still broader distribution is expected in the near future.

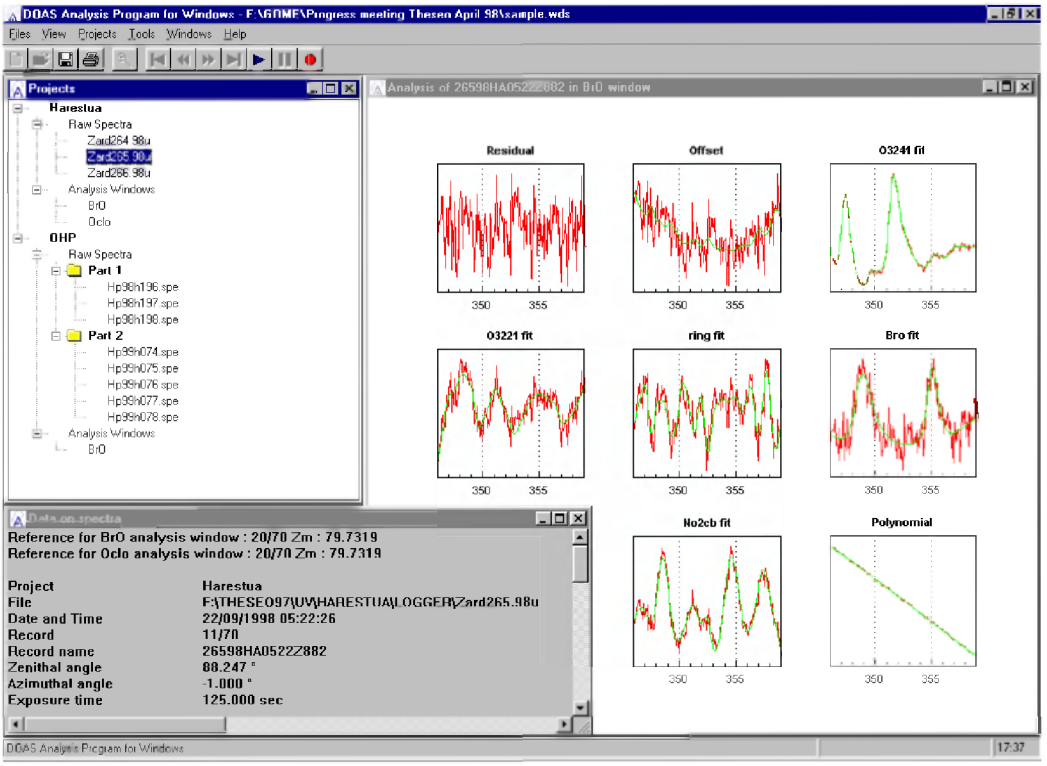

Figure 4: *The graphical user interface of the BIRA-IASB DOAS analysis software package (Windoas).*

3.3 PSCBOX, a coupled photochemical box-/radiative transfer model

Model packages based on coupled 1D photochemical box-/radiative transfer models and initialised by chemical fields from 3D chemical transport models (3D CTM) enable the simulation with full diurnal cycle of slant column densities (SCDs) of stratospheric constituents. A model package of this kind called PSCBOX has been developed at BIRA-IASB primarily for modelling SCDs of fast diurnally varying species such as BrO, OClO or NO_2, for both nadir and zenith observation geometries. These simulations are being used to interpret SCDs measured by the DOAS instruments at the three ground-based stations Harestua, OHP, and Jungfraujoch.

3.3.1 Model package description

The model package PSCBOX consists of the stacked version of the trajectory box-model PSCBOX (Fonteyn et al., 2000) coupled to a radiative transfer (RT) model. PSCBOX includes 48 variable species, 104 gas-phase and 27 photolysis reactions. Treatment of heterogeneous chemistry reactions on liquid sulfuric acid aerosols and on PSC particles is included also; more details about this can be found in Fonteyn et al. (2000). The model makes neither family nor photochemical equilibrium assumptions. Updated kinetic and photochemical data are taken from the JPL 2000 compilation (Sander et al., 2000). Photolysis rates are computed off-line by using the RT scheme developed by Toon et al. (1989). This scheme includes multiple scattering and a pseudo-spherical geometry approximation. PSCBOX is initialised with 12h UT pressure, temperature, and chemical species fields from the 3D CTM SLIMCAT (Chipperfield, 1999). Pressure and temperature fields used in SLIMCAT are taken from UKMO (UK Meteorological Office) meteorological analyses.

Two kinds of RT models have been used to generate slant columns from the box-model outputs: (1) a single scattering ray tracing model (Van Roozendael et al., 1998) and (2) the model S-DISORT/UVspec (Kylling, 1995). (1) calculates the rays in a full spherical geometry using the appropriate local concentration of the absorbing species along the light path. O_3 absorption, Mie scattering (stratospheric background conditions), and refraction can also be included. (2) solves the RT equation by the discrete ordinate method and includes full treatment of multiple scattering in pseudo-spherical geometry (direct beam only), Mie scattering, ground albedo, and refraction. The program has been modified in order to take into account the variation of the concentration of the absorbing species along the light path with varying solar zenith angle (direct beam only).

3.3.2 Model package validation

PSCBOX has been validated through an intercomparison exercise with two other similar packages including a stacked 1D photochemical box-model and a single scattering ray tracing model (Hendrick et al., 2000): SLACO (IFE Bremen) and SLIMCAT1D (University of Leeds). During the intercomparison the consistency between the three packages has been verified through comparison of model results obtained using common initialisation data. Calculated BrO differential slant column densities (DSCDs) have been also compared to ground-based zenith-sky DOAS measurements for the following locations and days: Bremen (53°N, 8.8°E), 4/3/97 (outside polar vortex scenario) and Ny-Ålesund (79°N, 11.9°E), 19/3/97 (inside polar vortex scenario). The adopted approach included three comparison tests:

Test 1 ("blind test"): Initialisation of the photochemical models with common SLIMCAT 12h UT profiles for the above-mentioned locations and days. The photochemical models keep their own reaction schemes and kinetic and photochemical data (also for the heterogeneous chemistry processes). The settings of the RT models are let free.

Test 2: Similar reactions scheme and rate constants based on the JPL97 compilation (DeMore et al., 1997) are now implemented in the three photochemical models and the settings of the RT models are imposed (except the BrO fields which are provided by each box-model).

Test 3: Verification of the consistency between the three RT models through their initialisation with identical parameters including the BrO fields (from SLIMCAT1D).

Modelled BrO DSCDs resulting from Test 1 are compared to measurements in Figure 5. Considering the quite large uncertainties of the measurements, the three models capture reasonably well the observations for Ny-Ålesund and Bremen. However, for both scenarios, discrepancies are observed between modelled BrO DSCDs, especially at large SZAs. SLIMCAT1D values are generally larger than PSCBOX and SLACO ones. These discrepancies could be due to differences in the photochemical models outputs but also in the settings of the ray tracing models.

Results from Test 2 as well as from sensitivity tests to the inclusion of Mie scattering, O_3 absorption, and refraction in the RT calculations show that a large part of the discrepancies obtained in the blind test is due to differences in the conditions of initialisation of the ray tracing models. This highlights the importance of defining appropriate settings for the radiative transfer part of the slant column interface.

A detailed comparison of the photochemical models outputs from Test 2 also reveals significant discrepancies which points to differences in the calculations of photolysis rates and in the treatment of heterogeneous chemistry processes (the only parameters not set up in a common way in this test). This is illustrated in Figures 6 and 7 where the volume mixing ratio of BrO, HOBr, $BrONO_2$, BrCl, OClO, and NO_2 calculated at 20 km for the Bremen scenario are plotted as a function of the SZA respectively for both cases with and without heterogeneous chemistry processes taken into account. Note the severe discrepancies observed above 80° SZA for HOBr, $BrONO_2$ and BrCl, when the heterogeneous chemistry processes are switched on. As to be expected, a significant improvement of the agreement between the model outputs is obtained when switching off the heterogeneous chemistry processes (Figure 7). Remaining discrepancies are likely to be due to differences in the calculation of photolysis rates that was not constrained in this comparison test.

Finally, Test 3 has revealed that significant discrepancies between modelled BrO DSCDs are still observed when the ray tracing models are identically initialised. Differences found are in the range 5-10 %, which is larger than reported in previous intercomparison exercises (e.g. Sarkissian et al., 1995) and is probably related to differences in the way the 2-dimensional BrO concentration matrices are handled in each model.

To summarize, this intercomparison exercise shows that the three model packages reproduce reasonably well the measurements for the selected days and locations. However, comparisons for more than two days are needed to conclude on the agreement between measurements and models. Discrepancies have been observed between modelled BrO DSCDs and can be attributed to differences between the ray tracing models and especially to their conditions of initialisation. The comparison of photochemical model outputs also reveals significant differences in the treatment of heterogeneous chemistry processes and in the calculation of the photolysis rates. These differences will be further investigated.

An example of the exploitation of PSCBOX for comparison with observational data is given in section 4.1.2.

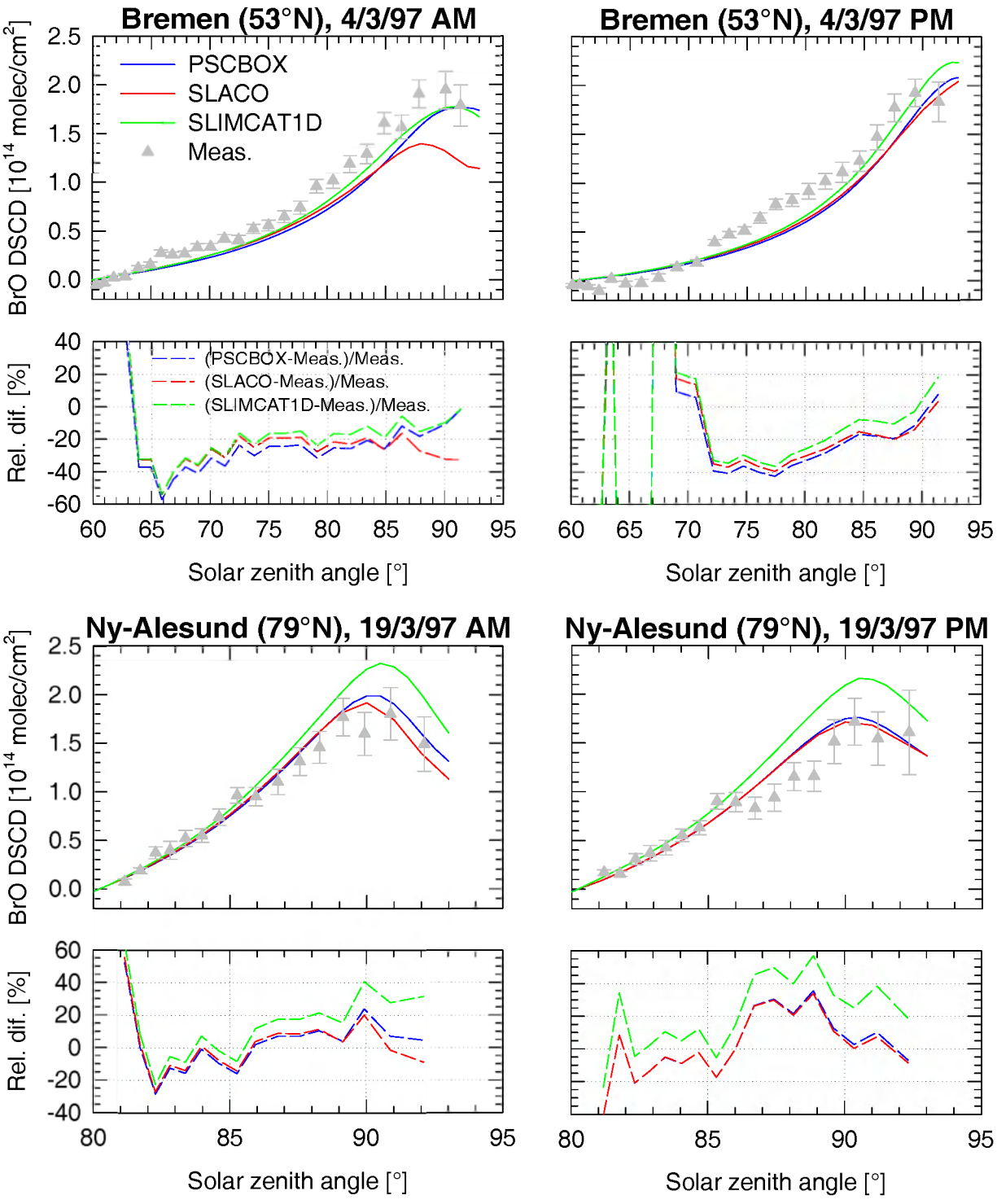

Figure 5: *Comparison between measured and modeled BrO DSCDs resulting from Test 1. The DSCDs are relative to the local noon.*

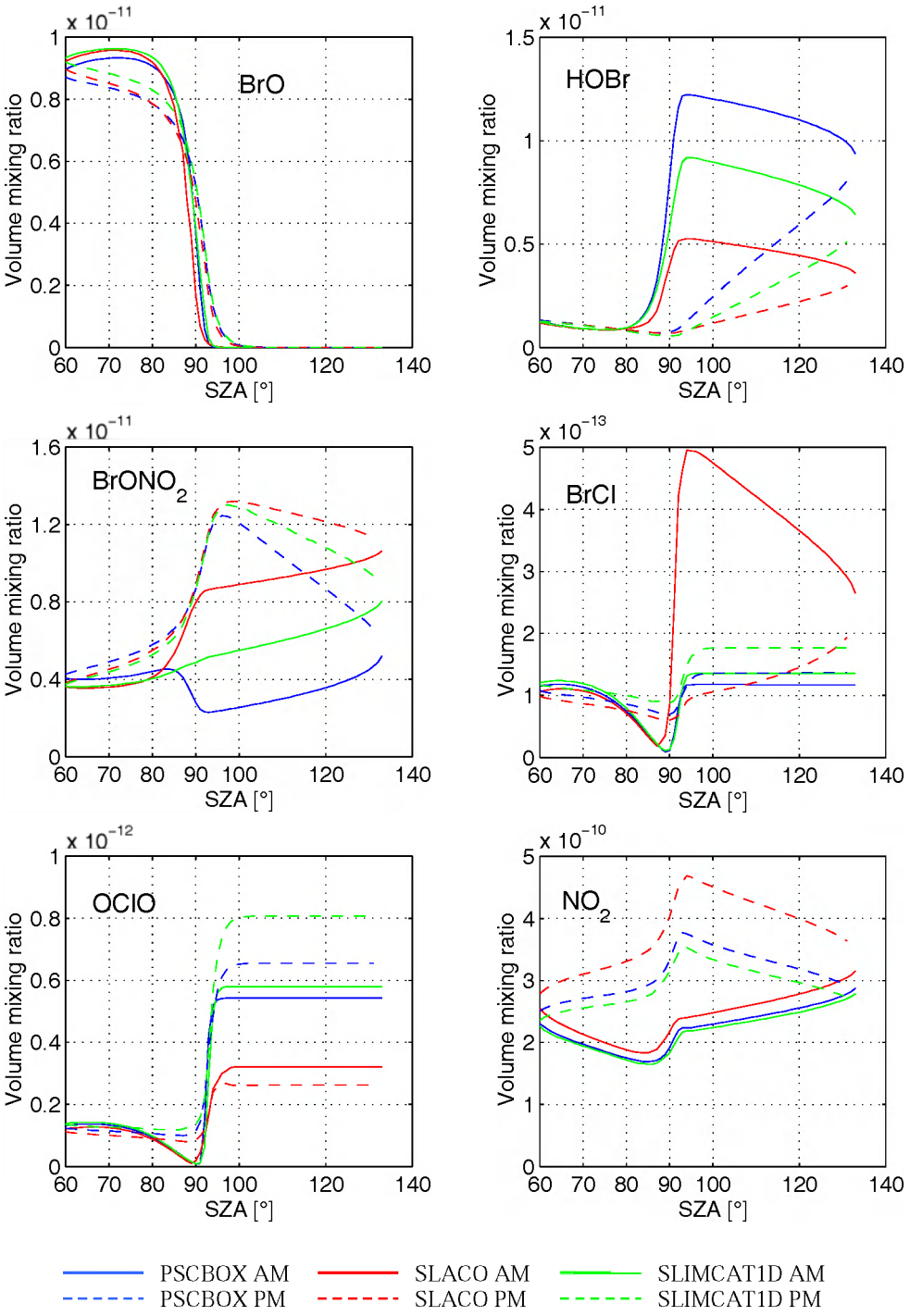

Figure 6: *Comparison between photochemical models outputs for BrO, HOBr, $BrONO_2$, BrCl, OClO, and NO_2 at 20km of altitude for the Bremen scenario resulting from Test 2. Heterogeneous chemistry processes are switched ON.*

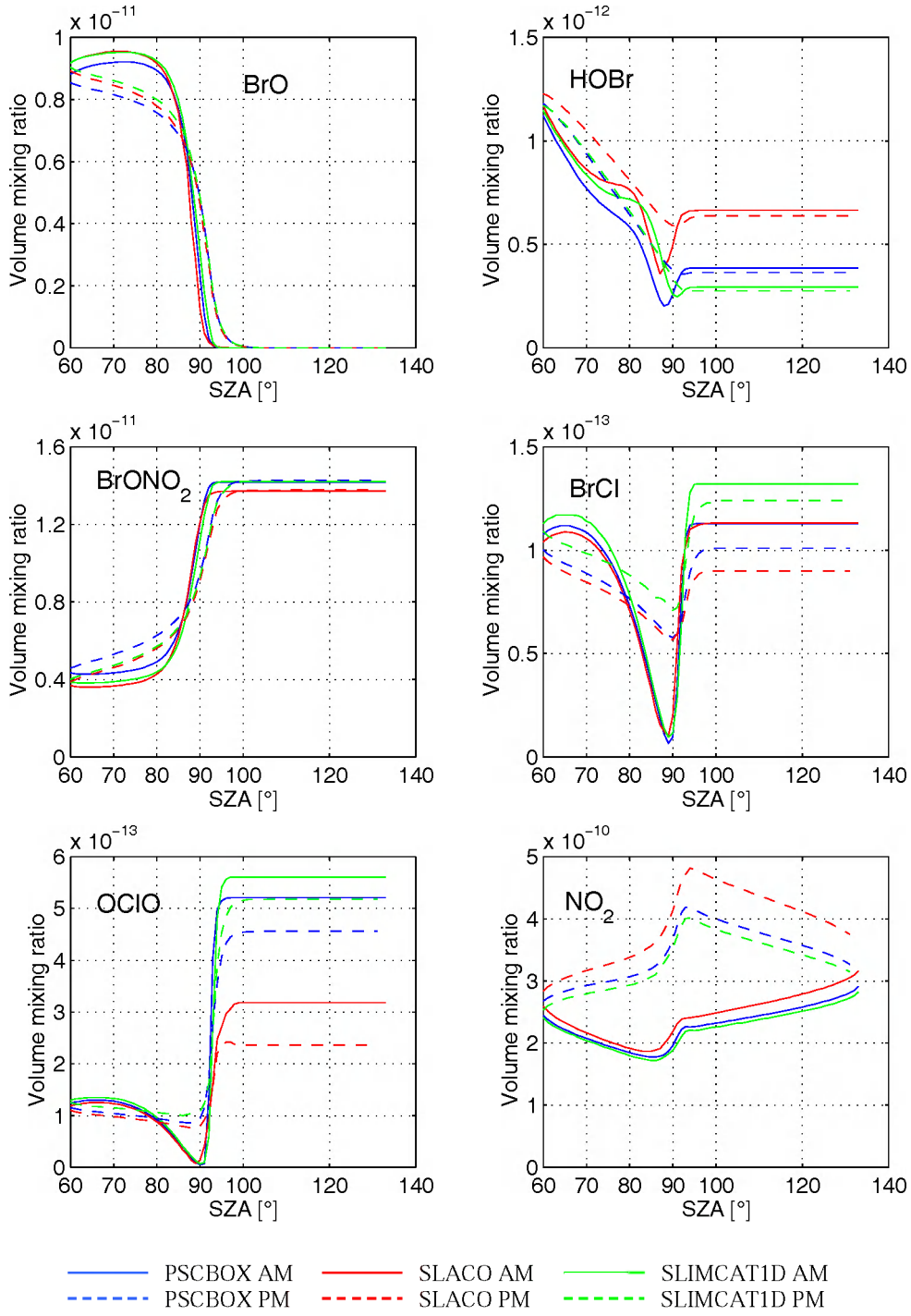

Figure 7: *Comparison between photochemical models outputs for BrO, HOBr, $BrONO_2$, BrCl, OClO, and NO_2 at 20km of altitude for the Bremen scenario resulting from Test 2. Heterogeneous chemistry processes are switched OFF.*

3.4 Altitude-Differential column measurements

In a search for distinguishing contributions from different altitude ranges in the atmosphere from ground-based FTIR measurements, an original method of altitude-differential measurements was tested during a campaign in summer 1998 in the Jungfraujoch area. The idea is as follows: two similar FTIR instruments are operated simultaneously at two different altitudes, making observations of the same species. The differences between the column abundances measured at both sites represent the amount of the species that is present in the height range between the two observation altitudes. To validate the technique, both instruments were operated initially side-by-side at one location (on top of the Jungfraujoch), to verify that they made consistent measurements. After that initial period, one instrument (the Bruker 120M) was moved down to the valley, in Grindelwald, at an altitude of 1070 m asl., while the other one (the Bruker 120 HR) continued its measurements at the Jungfraujoch observatory, at an altitude of 3580 m asl. The geophysical results of the campaign are discussed briefly in Chaper 4.

The method has proven valid and worth for the measurements of column measurements in the lower troposphere and planetary boundary layer of species like CO, CH_4, N_2O, C_2H_6 ... for which the distribution with altitude in the troposphere is badly known. It may be repeated on the purpose of validation of tropospheric satellite measurements like MOPITT.

3.5 Advanced FTIR spectral analysis algorithms

In the consortium, two state of the art algorithms are used for retrieval of vertical column abundances of atmospheric absorbers from high resolution FTIR solar absorption spectra, namely SFIT (Rinsland et al., 1984) and SFSP (Synthspec & Fitspec, a home-made code from BIRA-IASB). In both codes an a priori profile shape of the target species is adopted; a scaling factor of the profile is adjusted by least squares minimisation of the difference between the observed spectrum and the corresponding synthetic one, using a Levenberg-Marquardt procedure. Part of the uncertainty in the resulting column abundance therefore originates in the choice of the a priori profile.

In a first step (section 3.5.1), the a priori profile was replaced by a 'model' of profiles to better represent the actual state of the atmosphere: this has been developed and implemented for the retrieval of ozone. In a second step (section 3.5.2), profile retrieval has been implemented.

3.5.1 O_3 vertical column abundance retrieval including a daily, tropopause dependent climatological model

The geophysical model that was developed for the O_3 vertical distribution model is based on local meteorological/dynamical parameters, namely the local tropopause height, and on a climatology for the seasonal variation of O_3.
The model is meant to replace the single standard a priori profile in spectral data analyses, in particular of FTIR spectra, with the purpose of optimizing the retrieved ozone column abundance. At the same time, in the FTIR spectral fit procedure, it attempts to eliminate or reduce the importance of the effective apodization parameter (EAP). The effective apodisation is an ad hoc fit parameter to compensate for any discrepancies of instrumental or geophysical origin between reality and its parametrized representation in the retrieval process.

The model is based on the following known facts: (i) the ozone column abundance is correlated positively with the local tropopause pressure, (ii) there exists some correlation between the ozone vertical profile and the tropopause parameters at least in the lowest stratosphere, up to about 22 to 25 km, and (iii), the tropopause changes capture only part of the observed ozone total column changes that are also influenced by longer-lasting perturbations such as the annual cycle, planetary waves, etc. Trials with a model which introduces a seasonal variation only in the upper part of the O_3 profile, above 25 km, have shown that hereby the seasonal O_3 variation is not adequately represented. Therefore, a climatology as to ozone vertical profiles has been constructed as follows: the ozone sonde data at Uccle (Belgium) since 1969 from the Royal Meteorological Institute have been sorted according to 4 seasons and 9 tropopause height classes, from (7.0 $\pm$ 0.5) km to (15.0 $\pm$ 0.5) km. Above 25 km the profiles have been extended with the CIRA '86 ozone seasonal model data for the 40°-50° latitude band. Figure 8 is an example set, showing some model profiles for the most frequently occurring tropopause heights, for each season. The most important model characteristics are the following. The altitude of the ozone concentration maximum (AOCM) increases when the tropopause rises, and the value of the ozone concentration at AOCM concurrently decreases. The increase of AOCM with rising tropopause is most evident in winter and spring. The less systematic relationship observed in summer and fall originates in the fact that for these seasons the peak in the ozone profile is wider along the vertical, and therefore the location of the ozone maximum is less precise. There is a remarkable difference of about 20% between the higher values of the ozone concentration maximum in winter and spring on the one hand, and the lower ones in summer and fall on the other hand. The appearance of a secondary maximum in the ozone concentration vertical profiles

between 10 and 15 km altitude becomes more pronounced as the tropopause altitude goes down, and is most evident in summer and spring.

It has been demonstrated that the above O_3 vertical profile climatology based on Uccle data is representative of the Jungfraujoch as well, from comparisons with sonde and microwave observations at Payerne and Bern, respectively, which are both within 100 km of the Jungfraujoch.

For evaluation of the appropriateness of the model, the model has been implemented for the selection of the a priori profile in SFIT and SFSP. ISSJ Bruker IR O_3 spectra for 1995 to 1997 have been analysed with the SFIT algorithm, once using a standard O_3 profile, and a second time using the new O_3 vertical profile model as the a priori, keeping all other parameters identical. It has been demonstrated that the use of the O_3 a priori vertical profile model significantly improves the agreement between the FTIR and SAOZ time series at the Jungfraujoch: the agreement gets as close as the one between O_3 data obtained with different UV/visible DOAS spectrometers and well calibrated Dobson and Brewer spectrophotometers - see also section 3.5.2.2. and Figures 12 and 13. It has been demonstrated also that the model addresses most of the atmospheric changes that are otherwise dissimulated by an ad hoc adjustment of the EAP. Nevertheless, even with this new profile model, an additional adjustment of the EAP in the fit procedure is still beneficial to improve the accuracy of the retrieved ozone column amounts, by accounting for some systematic discrepancies between observed and calculated spectra.

More details can be found in De Mazière et al. (1999).

The development and evaluation of the O_3 vertical distribution model have been conducted for the FTIR ozone measurements at Jungfraujoch, but the concept holds at all midlatitude locations, and it can be applied probably also to space-borne nadir looking observations (thermal infrared emission). It has also been implemented in the analysis of the Jungfraujoch SAOZ data as a test case in validation exercises (see section 3.5.2.2).

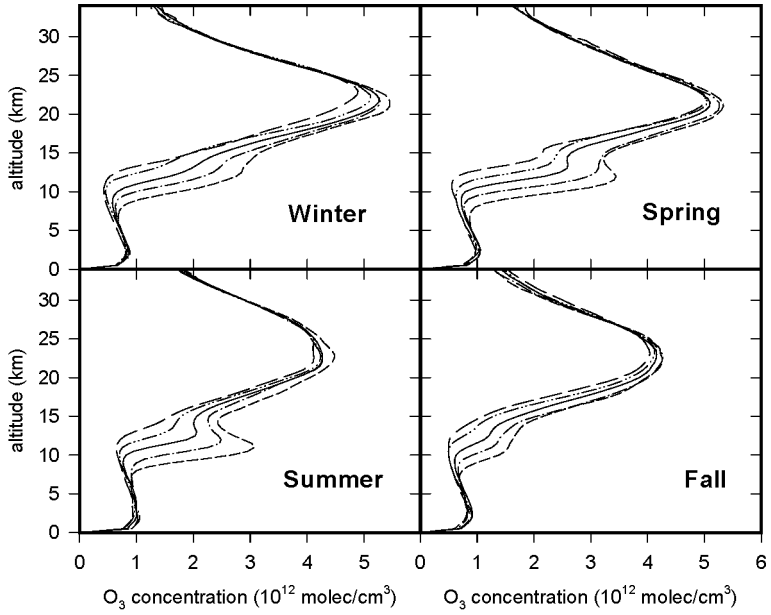

Figure 8: *Example profiles from the climatological O_3 a priori profile model for each season, for tropopause heights of 9 km (short-dashed line), 10 km (dash-dotted line), 11 km (solid line), 12 km (dash-double-dotted line), and 13 km (long-dashed line).*

3.5.2 Vertical inversion algorithms for FTIR spectra: SFSP upgraded to SFSP2, and SFIT2

3.5.2.1 The Optimal Estimation Method and its application for inversion of FTIR spectra

In the spectral analysis retrieval algorithms, a forward model F describes how the measurement vector I_m (measured spectrum) depends on the state vector x (molecular profiles, additional parameters to be fitted) and on a model parameters vector b (spectral line data...) :

$$\mathbf{I}_m = \mathbf{F}(\mathbf{x},\mathbf{b}) + \varepsilon_I$$

where ε_I is the vector of direct measurement errors (noise).

In order to obtain information about the height profiles, the optimal estimation method (OEM) (Rodgers 1976) has been implemented in the retrieval algorithm. This method is based on a statistical approach in which the solution is a weighted average of the measurements and the a priori information. The a priori information consists of a virtual measurement of the height profile x_a together with its covariance matrix S_a that

is supposed to reproduce the variability of the profile. The measurements consist of a measured spectrum I_m together with a covariance matrix S_I. This matrix is diagonal with the inverse of the squared signal-to-noise ratio (S/N) on the diagonal.

OEM requires the linearisation of the forward model about the a priori state vector

$$\mathbf{I_m} = \mathbf{F}(\mathbf{x_a}, \mathbf{b}) + \frac{\partial \mathbf{F}}{\partial \mathbf{x}}(\mathbf{x} - \mathbf{x_a}) = \mathbf{F}(\mathbf{x_a}, \mathbf{b}) + \mathbf{K}(\mathbf{x} - \mathbf{x_a})$$

The measured spectrum can be converted into a measured profile $K^{-1}I_m$ with covariance matrix $K^T S_I^{-1} K$.

In a linear case the weighted profile average is given by :

$$\bar{\mathbf{x}} = (\mathbf{S_a^{-1}} + \mathbf{K}^T \mathbf{S_I^{-1}} \mathbf{K})^{-1} (\mathbf{S_a^{-1}} \mathbf{x_a} + \mathbf{K}^T \mathbf{S_I^{-1}} \mathbf{I_m})$$

while in a non-linear case the estimation is made iteratively with the (n+1)st iterate given by :

$$\mathbf{x_{n+1}} = \mathbf{x_a} + (\mathbf{S_a^{-1}} + \mathbf{K_n^T S_I^{-1} K_n})^{-1} \mathbf{K_n^T S_I^{-1}} \left[(\mathbf{I_m} - \mathbf{I_n}) - \mathbf{K_n} (\mathbf{x_a} - \mathbf{x_n}) \right]$$

This method also provides the uncertainty covariance matrix of the result profile

$$\bar{\mathbf{S}} = (\mathbf{S_a^{-1}} + \mathbf{K}^T \mathbf{S_I^{-1}} \mathbf{K})^{-1}$$

We have implemented OEM in SFSP, and we call this new upgraded version SFSP2. Analogously, SFIT2 is a version of SFIT in which OEM was implemented in a collaboration between NIWA and LaRC. We verified that SFSP2 and SFIT2 produce similar results if used in common conditions.

An example of some O_3 profiles retrieved from spectra in the 3039 cm^{-1} microwindow recorded at ISSJ in March 1996 is shown in Figure 9. The profile of March 29 represents a situation where the polar vortex moved close to the Jungfraujoch.

Preliminary analyses of various FTIR time series recorded at the Jungfraujoch are discussed hereinafter.

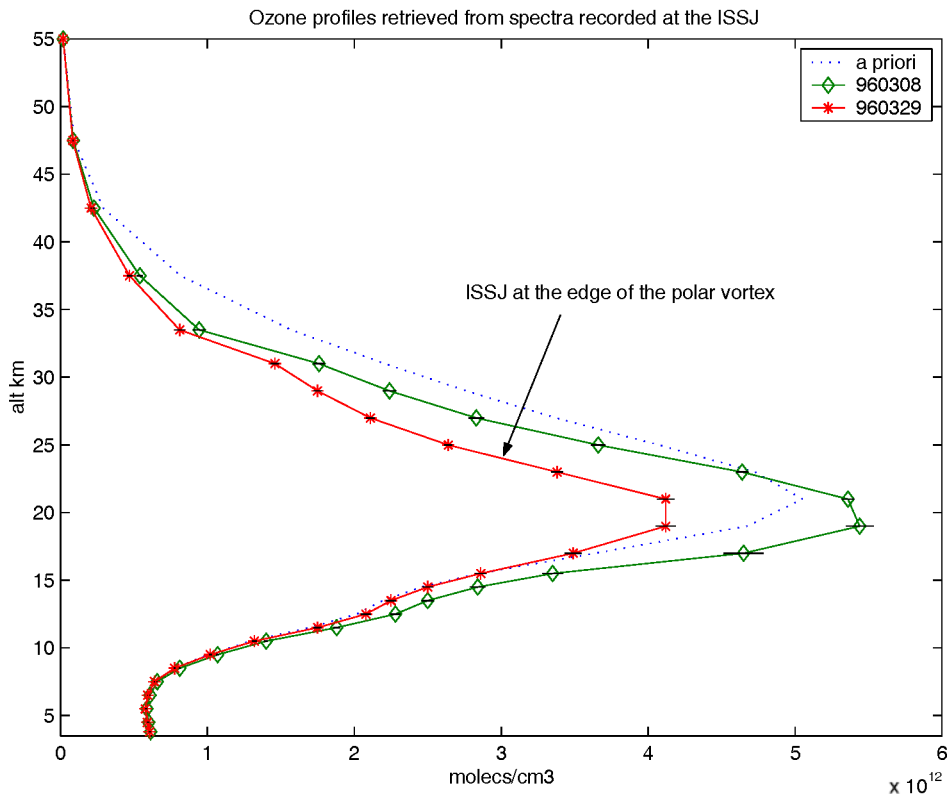

Figure 9: *O_3 profiles on March 8 and 29, 1996 (solid green and red lines, respectively), retrieved from FTIR spectra recorded at ISSJ. The profiles are daily means; error bars represent the standard deviation throughout the day. The dotted line represents the a priori profile used in the retrieval procedure.*

3.5.2.2 Preliminary results for O_3, HCl and HF vertical profiles retrieved from ISSJ FTIR spectra

The vertical distributions of O_3, HCl and HF have been retrieved using SFIT2 from high resolution FTIR solar spectra recorded at the Jungfraujoch. When available, the results have been compared to correlative measurements. The HF vertical distributions retrieved from the spectra recorded between November 1995 and January 1997 have been compared to correlative measurements from the HALOE instrument on board the UARS satellite. The ozone profiles retrieved from FTIR spectra recorded from June 1997 to June 2000 have been compared to correlative profiles measured by the ozone soundings from Payerne. For the three molecules, the stratospheric columns have been compared to correlative results of the SLIMCAT Chemistry Transport Model for the winter 1999-2000.

Ozone profiles

To enhance the sensitivity to the troposphere, vertical inversions for ozone have been performed in the 1003 cm^{-1} window (1002.6 – 1003.2 cm^{-1}), a window which was already chosen by Pougatchev et al. (1995, 1996) for that reason. The tropospheric sensitivity is indeed apparent in the averaging kernel for this window shown in Figure 10, calculated for conditions that are characteristic of the Jungfraujoch FTIR spectra. The kernels indicate a vertical resolution of order 10km FWHM for the retrieved profiles. Figure 11 shows retrieved daily mean partial column abundances in 3 distinct layers, up to 30km altitude (the mean altitude range of the sondes), in comparison with sonde data, for coincident measurement days, integrated over the same altitude range. The plots include also running averages over 15 days of the sonde data. A very good agreement is observed between the individual sonde and FTIR observations, in all layers. We also checked the derived total column abundances in comparison with Arosa Dobson data for the same period. The agreement is excellent, with a bias of –1.6%, and a dispersion (1 sigma standard deviation) of 2.3%. An interesting point to note is that particular ozone sonde profiles are well captured by the FTIR data. For example, on February 12, 1999, the vortex came over the Jungfraujoch, the tropopause lowered to 9 km, and the integrated ozone amount was particularly high, well above the associated running average. The FTIR data are still in very good agreement with coincident sonde data. For each layer the mean and standard deviation of the differences between both data sets have been calculated (see plot). One sees some underestimation by FTIR in the troposphere (3.58-14 km layer) and some overestimation by FTIR in the next layer, just above the tropopause (14-24 km layer). Both compensate each other in the integrated amount, where a mean difference of 2.5% ($\pm$2.9%) between both datasets is obtained. In a subsequent step, a better quantification of the associated error budget will be attempted.

Ozone total columns: improved consistency between various data sets

The successive advances in the ozone retrieval procedures from FTIR spectra have resulted in significant improvements in the agreement of the FTIR total column ozone data with correlative data, in particular with the co-located SAOZ data, TOMS overpass data and Dobson data from Arosa. Figures 12 and 13 show the intercomparisons between successive versions of the FTIR and SAOZ daily mean ozone data (see also section 4.1.1) and the TOMS and Dobson data. The successive versions of the FTIR data are: (i) the common SFIT retrieved data, using a fixed a priori profile, annotated 'FTIR-noclim', (ii) the SFIT retrieved data using the climatological tropopause dependent model for the a priori profiles, annotated 'FTIR-

clim' (cf. section 3.5.1), and (iii), the FTIR total column data obtained from a vertical inversion with SFIT2 as discussed above, annotated 'FTIR-SFIT2'. As to the SAOZ data, successive versions are : (i) the SAOZ vertical column data based on a climatological sine-like air mass factor, annotated SAOZ-sine, (ii) the SAOZ vertical column data based on an air mass factor that is calculated using the above mentioned climatological model for the ozone profiles, annotated 'SAOZ-clim', and (iii), the actual new SAOZ homogenised time series as described in section 4.1.1 that uses again the sine-like air mass factor, annotated as 'new SAOZ-sine'. Figures 12 and 13 plot relative differences (in percentage) between the various data sets, and indicate the mean and standard deviation (between parentheses) over the respective time series. The period before April 1992 is eliminated from the evaluation of the mean and standard deviation, because of known biases in the data caused by the Pinatubo aerosol loading in the atmosphere. Also the SAOZ-sine and SAOZ-clim data beyond 1998 shouldn't be considered because they are obtained with the upgraded instrument, before revision and homogenisation of the whole time series (see section 4.1.1). It must be noticed that Dobson and TOMS data have not been corrected for the differential ozone column between the altitude of the Jungfraujoch and that of Arosa and ground-level, respectively, which explains part of the observed biases.

It clearly appears in the various graphs that there is a seasonal variation in the relative differences with FTIR-noclim data, and that the amplitude of this sine-like variation decreases upon use of the climatological model for the a priori profiles (FTIR-clim). This decrease is most significant in the intercomparison between FTIR-clim and SAOZ-clim data. If however the vertical profiles are really retrieved (FTIR-SFIT2), then the consistency with the TOMS and Dobson data becomes very good : the standard deviation of the difference, which is a measure of the scatter, decreases to about 2%, to be compared with 3 and 5% in the former cases for the comparison with TOMS and Dobson, respectively. There appears a change in behaviour in the FTIR-SFIT2 versus TOMS and Dobson intercomparison around mid-1997 : this is explained by a realignment of the FTIR instrument at the Jungfraujoch, making the retrievals before the realignment less reliable. We also see that the scatter of the newSAOZ-sine data with respect to TOMS and Dobson data (of order 4.5%) is larger than that observed for the FTIR-SFIT2 data with respect to these data (of order 2%), proving that the reduction of uncertainties in the vertical distribution obtained with the FTIR inversion is worth the effort even for total column determinations. This is illustrated very clearly in early 1999, when exceptionally high ozone columns were observed : FTIR-SFIT2 catches the high values and therefore the high discrepancies observed in this period in the intercomparisons with other FTIR data sets (Figure 13, upper 2 plots) disappear. Climatological approaches, like the one adopted for the

SAOZ air mass factors, cannot compensate sufficiently for day-to-day variations. This latter point is confirmed by the fact that the scatter of the FTIR-SFIT2 data is higher with respect to the new SAOZ-sine data than with respect to the TOMS and Dobson data, despite the fact that the SAOZ data should better correlate because of the closer co-location of the sampled airmasses. Overall the agreement between the latest versions of all ozone data sets is within 3% (±5%).

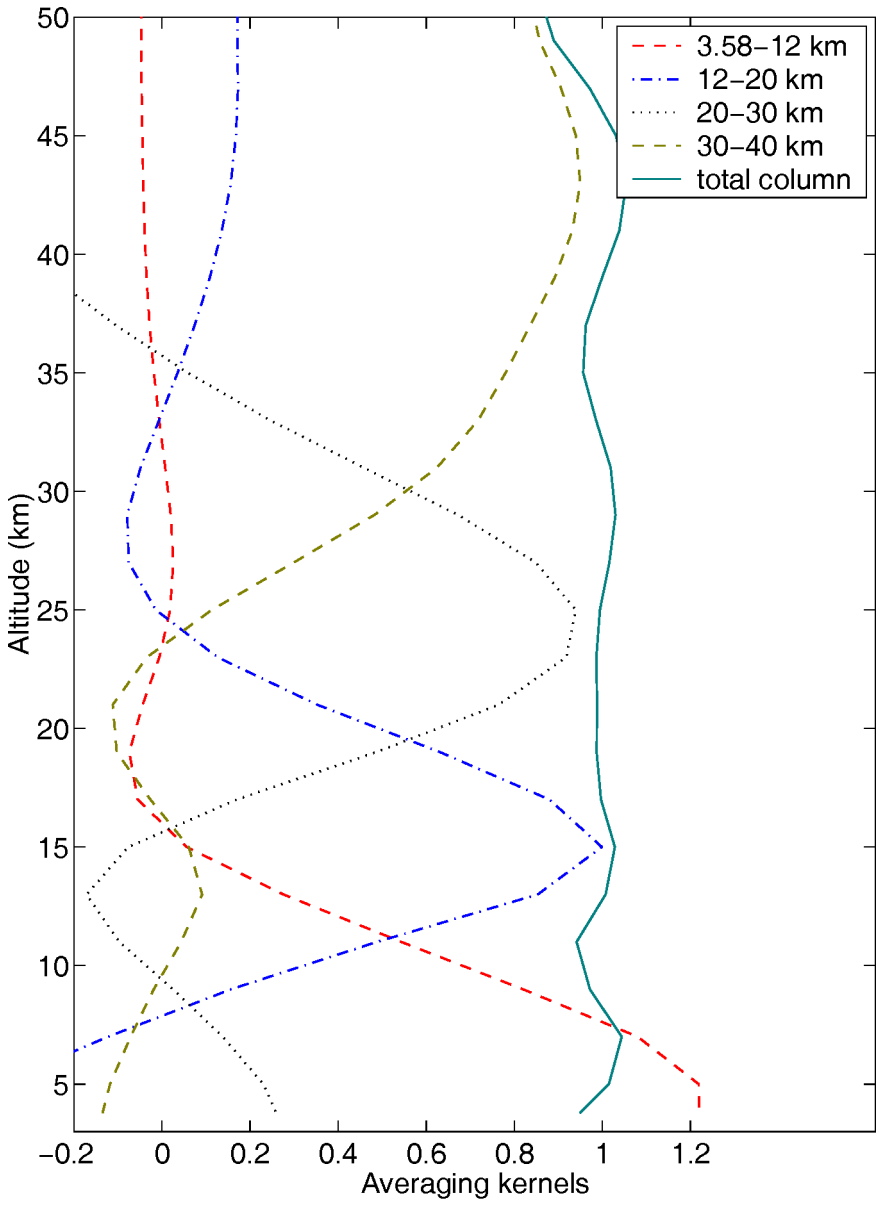

Figure 10: *Averaging kernels for ozone profile retrieval in the 1002.6-1003.3 cm^{-1} for spectral characteristics typical of the Jungfraujoch FTIR solar spectra. Layer averaging kernels are represented corresponding to the 4 independent information elements (see legend on top), as well as the averaging kernel for the total column (solid line).*

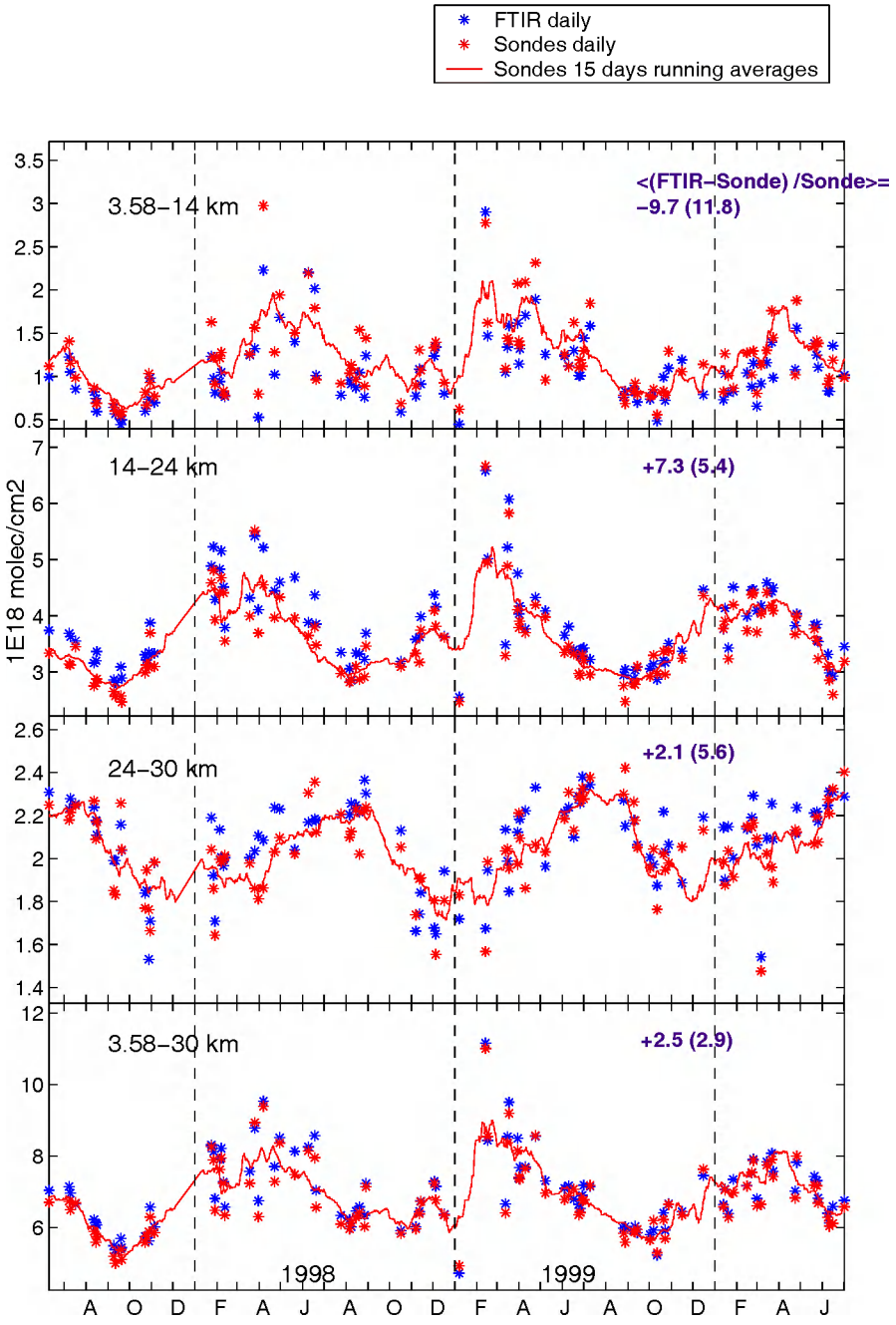

Figure 11: *Comparison between ozone partial column abundances retrieved from FTIR spectra at the Jungfraujoch (black asterisks) and from ozone soundings at Payerne (daily values: grey asterisks; 15-days running means: solid line). The layers are, from top to bottom, 3.58-14 km, 14-24 km, 24-30 km, and the total range covered by the soundings (above the Jungfraujoch altitude) 3.58-30 km. In the upper right corner of each plot is given the mean relative difference (in percentage) between FTIR and sonde data and its corresponding standard deviation (in parentheses).*

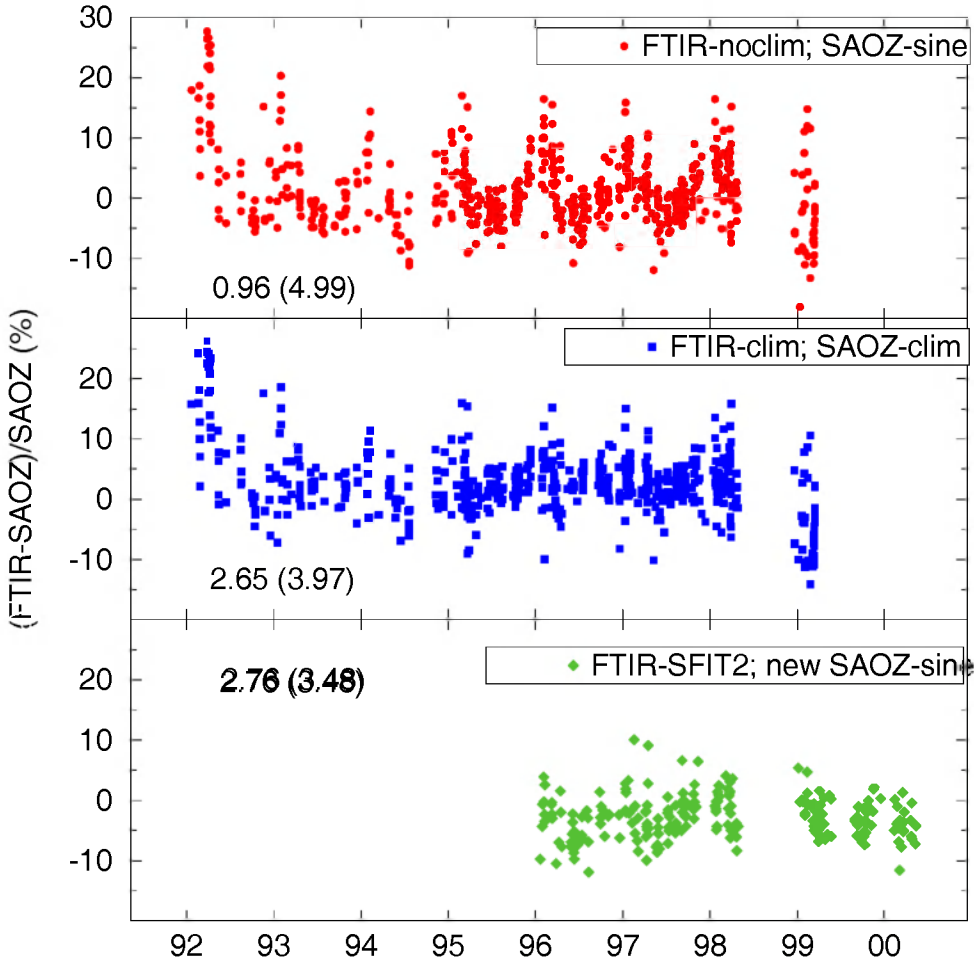

Figure 12: *Relative differences, in percentage, between different sets of correlative data for total ozone measured above the Jungfraujoch. For identification of the various data sets: see text.*

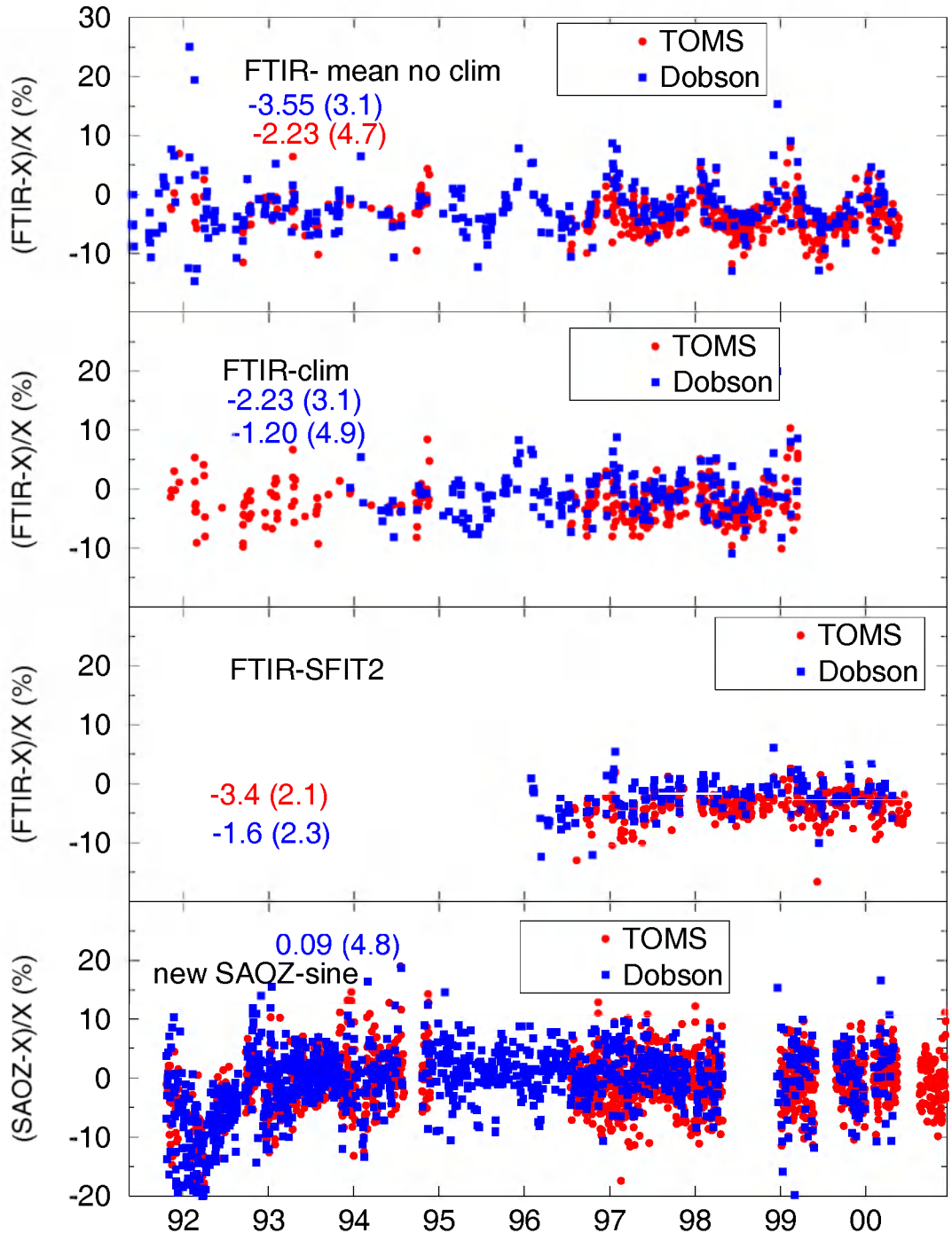

Figure 13: *Similar to Figure 12, but for other total ozone data sets.*

HF profile inversion and comparison with HALOE

HF profiles were retrieved from the spectral microwindow from 4037.8 to 4039.1 cm^{-1} for a 14 months record between November 1995 and January 1997. Comparisons with HALOE overpass profiles were performed in 2 layers from 20 to 28 km and from 28 to 40 km (Figure 14). In the bottom layer, the FTIR results are higher than HALOE (<HALOE-FTIR> = -11.1±10.1%) while they are lower in the top layer (11.6 ± 9.0%). Both layer biases compensating each other, the agreement is very good in the total layer (-2.4 ± 6%). Two reasons can explain this lack of height resolution. The averaging kernels for the two layers are not well separated and the ILS could not be retrieved in this spectral domain. During the intrusion of HF-rich polar air masses in mid April 1996 (PV at 475K of 38 PVU on April the 18th 1996) a very good agreement was found between the space-based and ground-based instruments in the 20 to 28 km layer.

These results were presented at the Quadrennial Ozone Symposium - Sapporo 2000.

Comparison of stratospheric O_3, HF and HCl with the 3D CTM SLIMCAT for the 1999-2000 winter

The vertical distributions of O_3, HF and HCl were retrieved from the Jungfraujoch FTIR spectra for the winter 1999-2000. For O_3 and HF, the same microwindows as above were used, while the spectral interval 2925.69 to 2926.21 cm-1 was used for the retrieval of the HCl vertical distribution. The results of the retrievals were compared to the results of a run of the 3D CTM model SLIMCAT for the location of the Jungfraujoch. For O_3 (Figure 16, lower plot) and HCl (Figure 15, lower plot), the modelled integrated stratospheric columns (from 12 to 55 km) are in very good agreement with the FTIR measurements. For HF, the measured stratospheric columns are systematically 30% lower than the modelled ones (Figure 15, upper plot). This effect is due to a tuning of the CFC and HFC´s emissions in the model, which does not reproduce the absolute stratospheric HF quantity. Concerning the vertical profiles, except for O_3, the discrepancies are high between the model and the measurements. For HCl and HF, the profiles retrieved from the FTIR spectra have systematically lower values than the modelled profiles in the lower stratosphere (below 20 to 24 km) and higher ones in the middle to upper stratosphere. The explanations for these discrepancies have not yet been studied in detail and require a better characterisation of the retrievals. The situation is better for ozone, for which one does not observe systematic oscillations between the measured and the modelled profiles. The O_3 partial columns between 12 and 28 km (Figure 16, upper

plot) observed by both the ozone sondes and the FTIR spectrometer are in good agreement with the model except in March and April 2000 with both techniques measuring values lower than the modelled ones suggesting a problem in the modelisation of midlatitudinal ozone for this period. Also for HCl, discrepancies between FTIR and model data seem to be larger in April than in the earlier part of the winter.

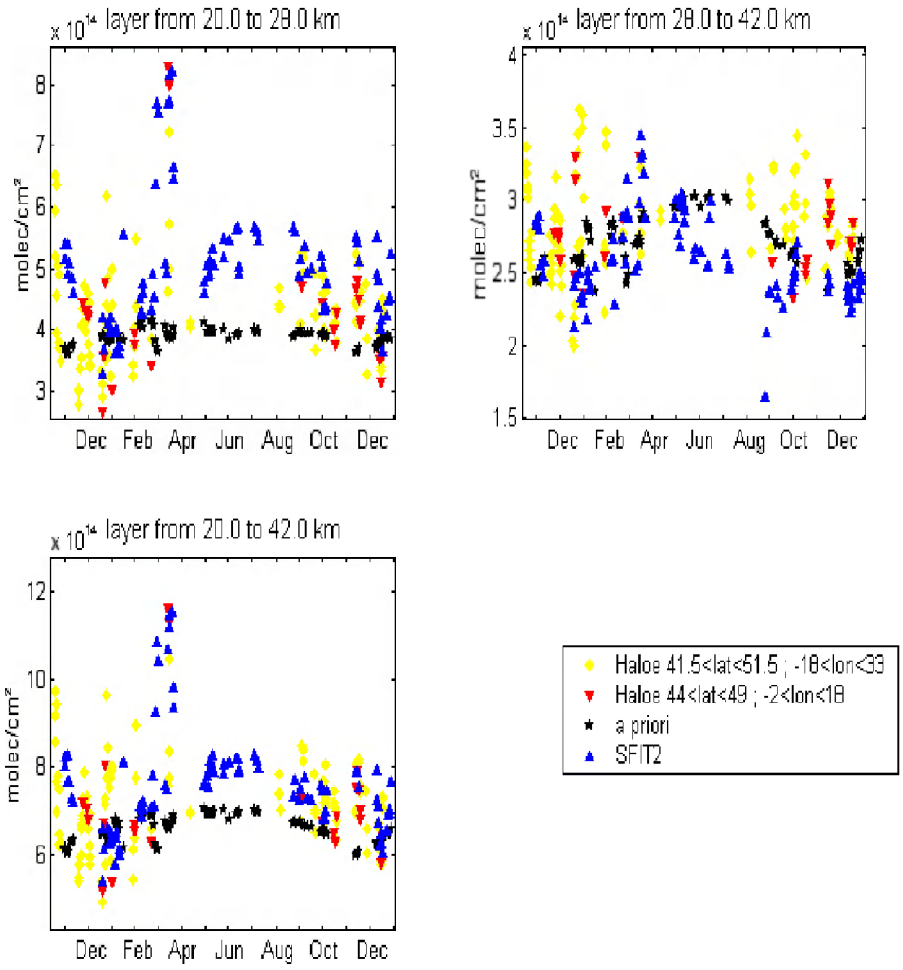

Figure 14: *Comparison between HF partial column abundances from FTIR measurements at ISSJ (SFIT2, blue upward triangles) and correlative HALOE observations (yellow diamonds and red downward triangles, for more or less restricted spatial coincidence, respectively), in 2 stratospheric layers (upper left: 20-28 km, and upper right: 28-42 km) and for the total layer between 20 and 42 km (lower left).*

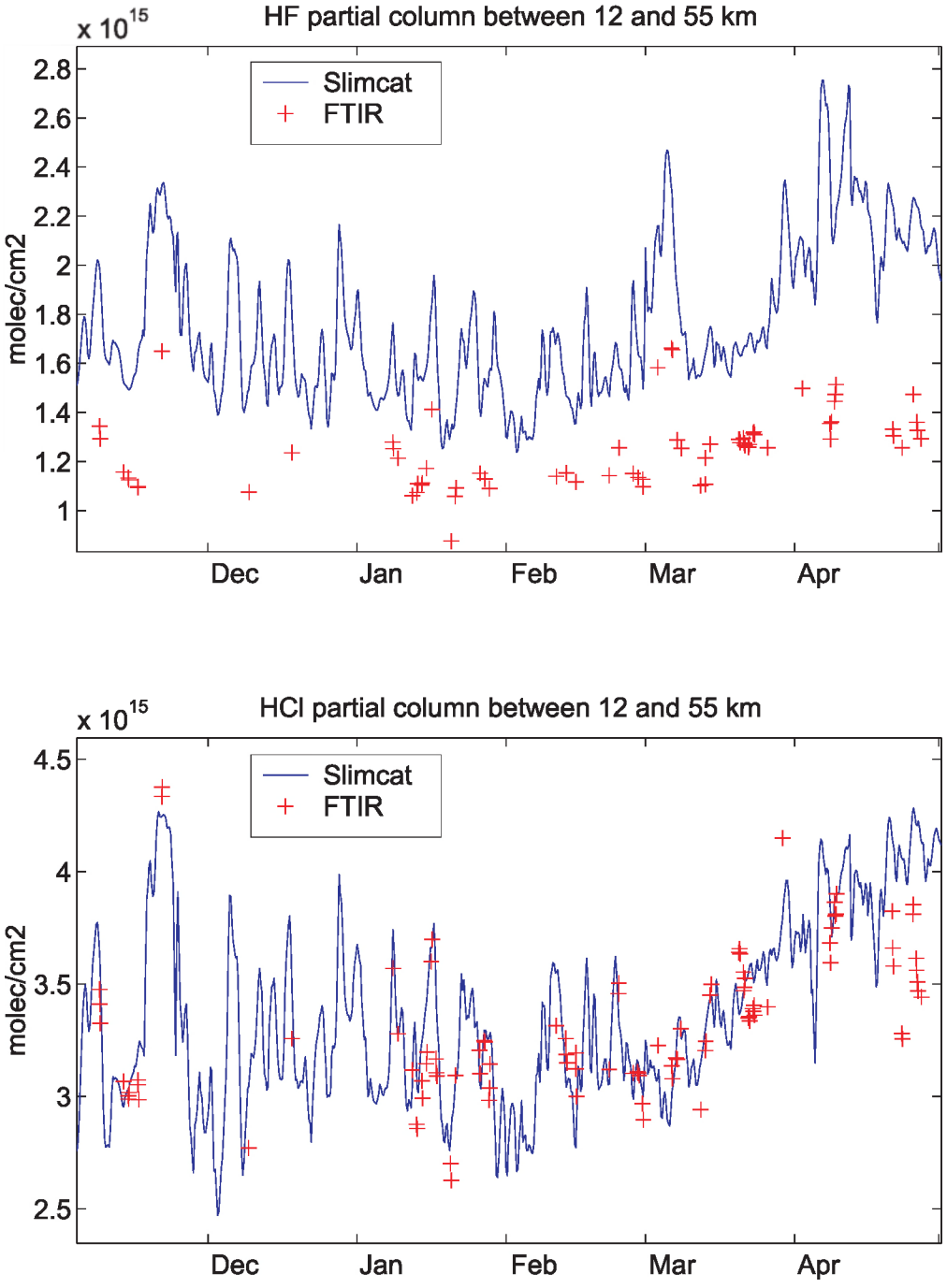

Figure 15: *Comparison between HF (top) and HCl (bottom) stratospheric column (12-55 km) data retrieved from FTIR spectra at the Jungfraujoch (+) and corresponding data from the 3D CTM SLIMCAT model (solid lines).*

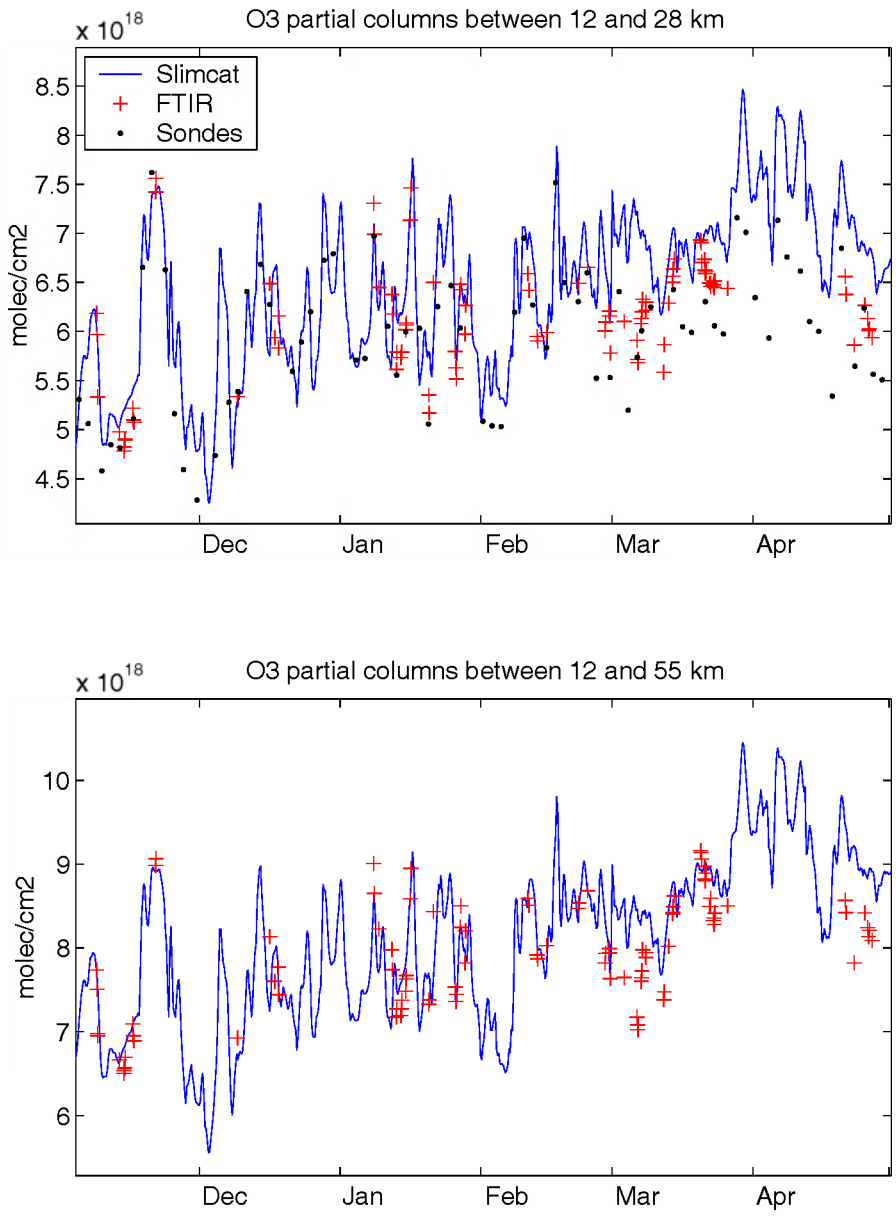

Figure 16: *Similar to Figure 15 but for ozone. Upper plot: partial columns between 12 and 28 km, with in addition sonde data from Payerne (•); lower plot: stratospheric columns (12-55 km).*

3.6 Wspectra and bFit

The analysis of reference spectra recorded in the laboratory under strictly controlled conditions must be of the best possible precision. Therefore analysis programs that are capable of retrieving highly accurate intensity and profile parameters of the absorption or emission lines of the atmospherically relevant molecules are required. Two computer programs – WSpectra and bFit – have been developed to satisfy this requirement.

WSpectra is a Windows 32 bit program developed to view, find, manipulate and, most importantly, measure the line parameters of high-resolution FT spectra. Measuring spectral lines parameters consists in a process done in two consecutive steps.

The first step consists of automatically finding all the lines in a spectrum. It is done by determining the zero-crossing points of the first and second derivatives of the spectrum. The finding procedure is followed by a second step in which each found line is, in turn, fitted by least squares to a theoretical line profile that provides the searched parameters. In Wspectra, the theoretical line profile can be a simple Voigt profile taking into account the temperature and pressure effects, or the more sophisticated Rautian-Sobelman and Galatry profiles that refine the profile by modelling the effect of molecular collisions. Wspectra is capable of measuring isolated absorption lines with a precision on the line position as good as 5 10^{-6} cm^{-1}, and a precision on the absorbed light intensity better than 0.5%.

bFit, also running under the Microsoft Windows operating system, measures absorption line parameters by adjustment of a synthetic spectrum to an observed spectrum, using a Levenberg-Marquardt least squares fitting procedure. The synthetic spectrum is calculated by convolution of a monochromatic Voigt transmission spectrum with an instrument line shape function, which includes the effects of the finite maximum optical path difference and the finite entrance aperture in the interferometer (Birk et al., 1996). Any number of lines (limited by available memory) can be fitted simultaneously. Adjustable parameters include the position, the intensity, the Gaussian width, the pressure self- and air-broadening parameters of each line, the diameter of the entrance aperture of the interferometer and the background level (modelled by a second order polynomial expansion).

The user has full control on the choice of parameters to fit.

3.7 New correction procedures for the pump efficiency of Ozone sondes

The vertical distribution of ozone is measured at RMI since 1969 with the Brewer-Mast (BM) ozonesondes. For various reasons it was decided to change to the Z-ECC type of ozonesonde in 1997. To assure the homogeneity of the long-term data series it was necessary to have good information on possible systematic differences between data obtained with both types of ozone sensors. Results of international intercomparisons found in the literature were not conclusive, and not applicable to our station. Therefore a campaign of double soundings, carrying both types of sonde on the same balloon was started in October 1996. By the end of 1997, 23 successful pairs were available for intercomparison.

Figure 17 shows that with the standard operational procedures there is a systematic, altitude dependent difference between both types of profiles. Near the ground the BM sondes measure on average up to 15% more ozone than the Z-ECC sondes. Around the 40 hPa level (which is near the mean level of the ozone maximum at 22 km) the agreement is excellent, but at higher levels the BM sondes underestimate the ozone amounts, ending by about -5 % at the highest level of the soundings. The differences are statistically significant in the whole troposphere and above the ozone maximum. An earlier intercomparison of the Brewer-Mast ozone profiles in Uccle with ECC profiles measured in De Bilt (NI) showed similar deviations. From those results, it was suspected that an underestimation of the decrease of the pump efficiency with decreasing pressure of the BM sondes causes these discrepancies.

In addition to the double soundings the efficiency of the pumps of both types of sondes was tested in a vacuum chamber at different pressures and temperatures before launch. From the results of these extensive measurements, a new altitude dependent correction profile was proposed. When it is applied the two types of ozonesondes agree to within 3 % (see thick line in Figure 17), while the differences are statistically insignificant over nearly the whole altitude range (0-32 km). The standard deviation of the differences is also lower, suggesting that part of the instrumental noise in the differences has been removed.

Detailed results of this study are reported in De Backer et al. (1998).

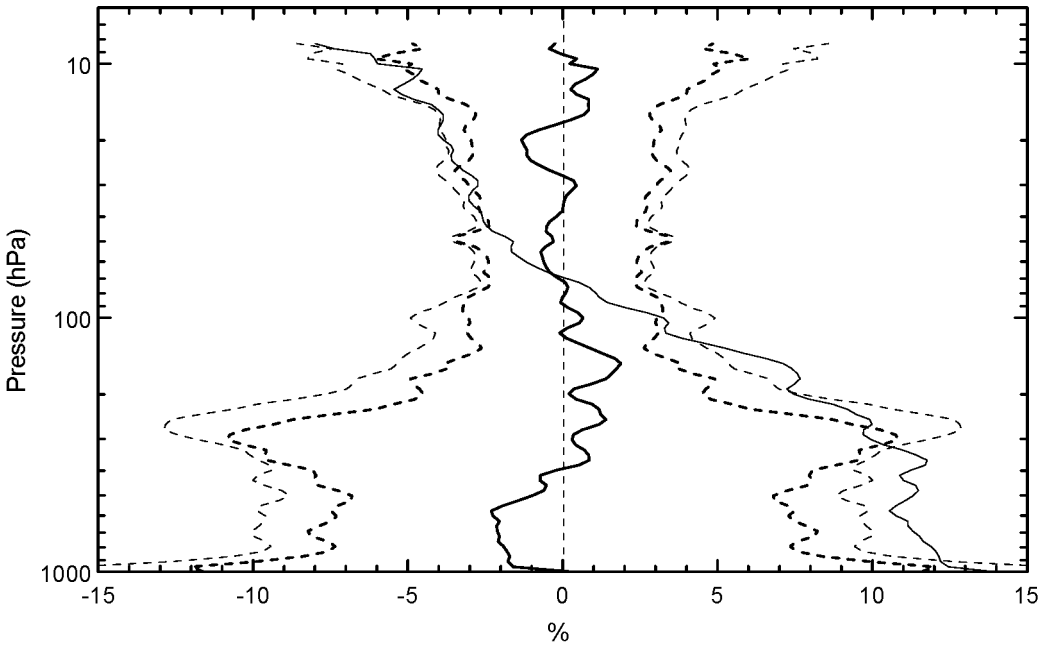

Figure 17: *Mean percentage differences between ozone profiles obtained from simultaneous measurements with Brewer-Mast and Z-ECC sondes with the standard (thin solid line) and the newly proposed (thick solid line) correction procedures in Uccle. The thin and thick dashed lines give the standard deviation of the differences, with the standard and new correction procedures respectively.*

4. RESULTS OF GEOPHYSICAL RELEVANCE

4.1 Evaluation of long-term atmospheric chemistry data. Variability and global changes of the atmospheric composition

The long-term monitoring performed at the four stations of the Jungfraujch, Harestua, OHP and Uccle contributes to the NDSC programme (Uccle has been recognised officially as a secondary NDSC station by the end of 2000). The NDSC was incepted in the mid-1980s, in response to the need for the scientific community to identify, document and understand atmospheric composition and climate changes. The NDSC dual goal of observation and understanding, as well as its task of establishing the links between stratospheric changes, ultraviolet radiation at the ground, and tropospheric chemistry and climate, requires the investigation of key stratospheric species resulting from manmade source gas emissions at the ground and affecting the stability of the ozone layer. They include HCl, OClO, $ClONO_2$, HNO_3, NO_2, and NO, which along with O_3 allow to investigate the relative impact of chlorine- and nitrogen-bearing species upon the ozone erosion via the Cl_x and NO_x catalytic cycles, and additional constituents among which species such as BrO, HF and COF_2, as well as source gases and tracers of atmospheric circulation and dynamics (e.g., N_2O).

The data obtained during the ESAC project have been merged with previous results, in order to build long-term data bases and draw conclusions concerning the long-term behaviour of stratospheric and tropospheric constituents and to distinguish it from short-term (daily, seasonal and interannual) variabilities. Attention has been paid to the long-term homogenisation of the various time series, by internal consistency checks and verifications with respect to correlative data. Validated time series have been submitted to international databases, in particular NADIR/NILU (http://www.nilu.no/projects/nadir) and the NDSC database at NOAA (http://www.ndsc.ws).

4.1.1 Long-term data at the Jungfraujoch

Already in 1989 (Kurylo and Solomon, 1989), the NDSC selected the Jungfraujoch as part of its northern hemisphere mid-latitude "Primary Alpine Station", on the basis of infrared solar observations and related monitoring activities performed successfully by the "Groupe Infra-Rouge de Physique Atmosphérique et Solaire" (GIRPAS) of the University of Liège (ULg) during previous years. BIRA-IASB has added a SAOZ UVVis instrument at the Jungfraujoch in 1990. At present, the responsibilities for the long-term data at the Jungfraujoch lie with GIRPAS (ULg) for the FTIR data, in collaboration with KSB-ORB and BIRA-IASB, and with BIRA-IASB for the SAOZ UV-Vis data.

During the period covered by this contract (1/12/1996 to 5/31/2001), solar FTIR observations have been performed on 555 clear sky days which are reported by month in Table II; this required the presence at the site of observers from ULg, IASB/BIRA and ORB/KSB during more than 1100 days. Overall, the FTIR monitoring activities conducted consistently at ISSJ primarily cover the period from 1985 to present, with some investigations reaching back to the mid-1970s, even to 1950 (e.g., Zander et al., 1994).

Since 1991, climatological observations of NO_2 and O_3 total columns at morning and evening twilight have been performed at the Jungfraujoch station using the SAOZ instrument. In early 1998 the original instrument has been irreversibly damaged; it has been replaced by a new version in late 1998. During this project, the homogeneity of the complete time-series of observations has been verified. The whole data set has been reprocessed using the latest version of the data analysis programme including most recent updates on laboratory data and corrections for seasonal drifts in instrumental slit functions previously identified. O_3 columns were

retrieved using climatological air mass factors as described in Van Roozendael et al. (1998). The complete time-series has been submitted to the NDSC data base.

Table II: *Number of days per month with FTIR observations at the Jungfraujoch.*

Month	1996	1997	1998	1999	2000	2001	TOTAL
JANUARY	9	17	13	9	15	10	**73**
FEBRUARY	6	8	17	6	8	1	**46**
MARCH	15	6	14	14	14	7	**70**
APRIL	9	12	9	13	9	8	**60**
MAY	7	16	12	5	10	15	**65**
JUNE	15	10	13	18	7		**63**
JULY	12	10	13	10	8		**53**
AUGUST	6	8	16	12	9		**51**
SEPTEMBER	10	20	9	9	12		**60**
OCTOBER	8	10	5	15	10		**48**
NOVEMBER	7	13	8	7	12		**47**
DECEMBER	4	2	12	4	1		**23**
TOTAL	**108**	**132**	**141**	**122**	**115**	**41**	**659**

The consistency of the O_3 time-series has been checked by comparison with TOMS and Dobson measurements as well as co-located FTIR measurements (see section 3.5.2.2). The systematic differences between these data sets are found to be smaller than 3%. Similarly the NO_2 time-series has been compared with HALOE and FTIR measurements (see Figure 18). This comparison reveals a systematic bias between the data sets. The FTIR instrument measures NO_2 columns in average 15% larger than the SAOZ, while HALOE measurements are approximately 10% smaller than SAOZ ones. Part of the discrepancy between SAOZ and HALOE can be explained by the tropospheric part of the NO_2 column not measured by the satellite. More work planned in the near future is needed to understand the origin of the differences between FTIR and SAOZ results.

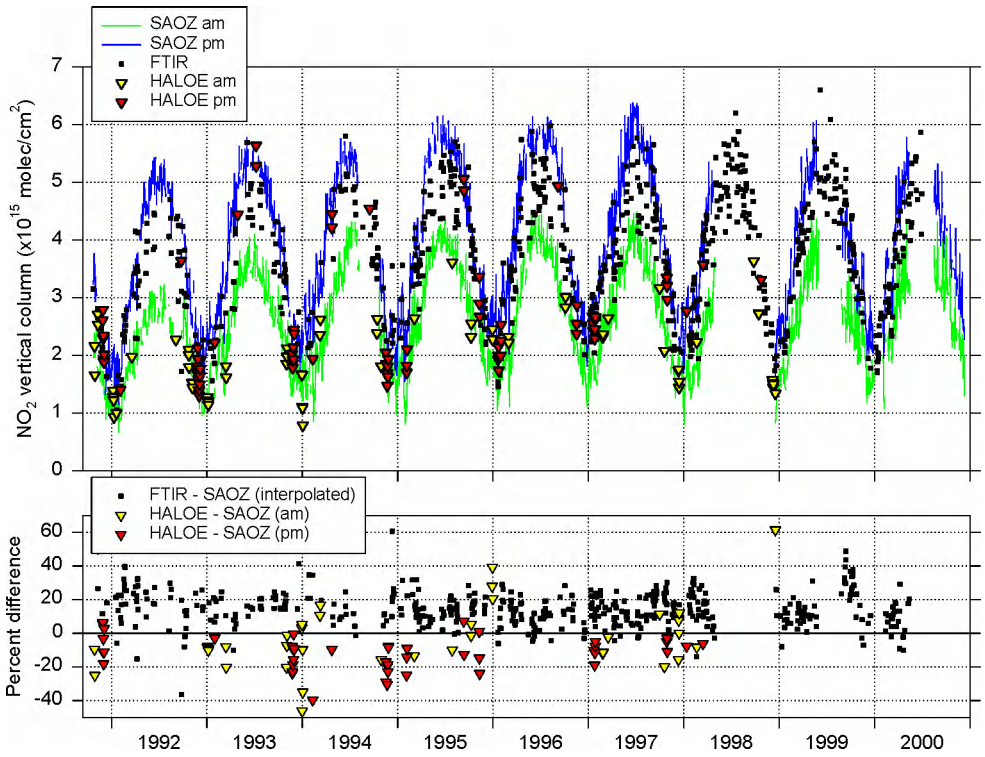

Figure 18: *NO_2 total column measurements by SAOZ, FTIR and HALOE instruments above the Jungfraujoch between November 1991 and December 2000 (upper plot). The relative differences between the various data sets and SAOZ measurements are displayed in the lower plot.*

Figure 19 reproduces the FTIR 1990-2001 daily mean vertical column abundance data sets of the key stratospheric species mentioned in the previous paragraph, as well as the long-lived N_2O and HF tracers. They all show noticeable seasonal variations (primarily resulting from the annual change in solar irradiance which affects photo-chemistry, temperature gradients and the tropopause height) as well as strong short-term variability during the winter-spring seasons (which is associated to enhanced meridional circulation and local dynamics), often superimposed on long-term rates of change (which essentially reflect the secular evolution of related source gas emissions at the ground). Consequently, mean secular trend characteristics can only be derived when the time bases are sufficiently long, so that short-term changes can be properly identified and be dealt with in a quantified way. Further noticeable in Figure 19 is the fact that short-term variability occurs primarily during the winter-spring months (December to May), so that secular trend determinations often are better defined by considering only summer-fall (June to November) measurements. In addition, monthly mean columns are often considered in trend evaluations, in order to attenuate the impact of months with different observation densities. With these considerations in mind (which may slightly affect mass loadings, but not trends), the following sections will deal with specific investigations involving various data sets of Figure 19 as well as additional ones of relevance within the ESAC context.

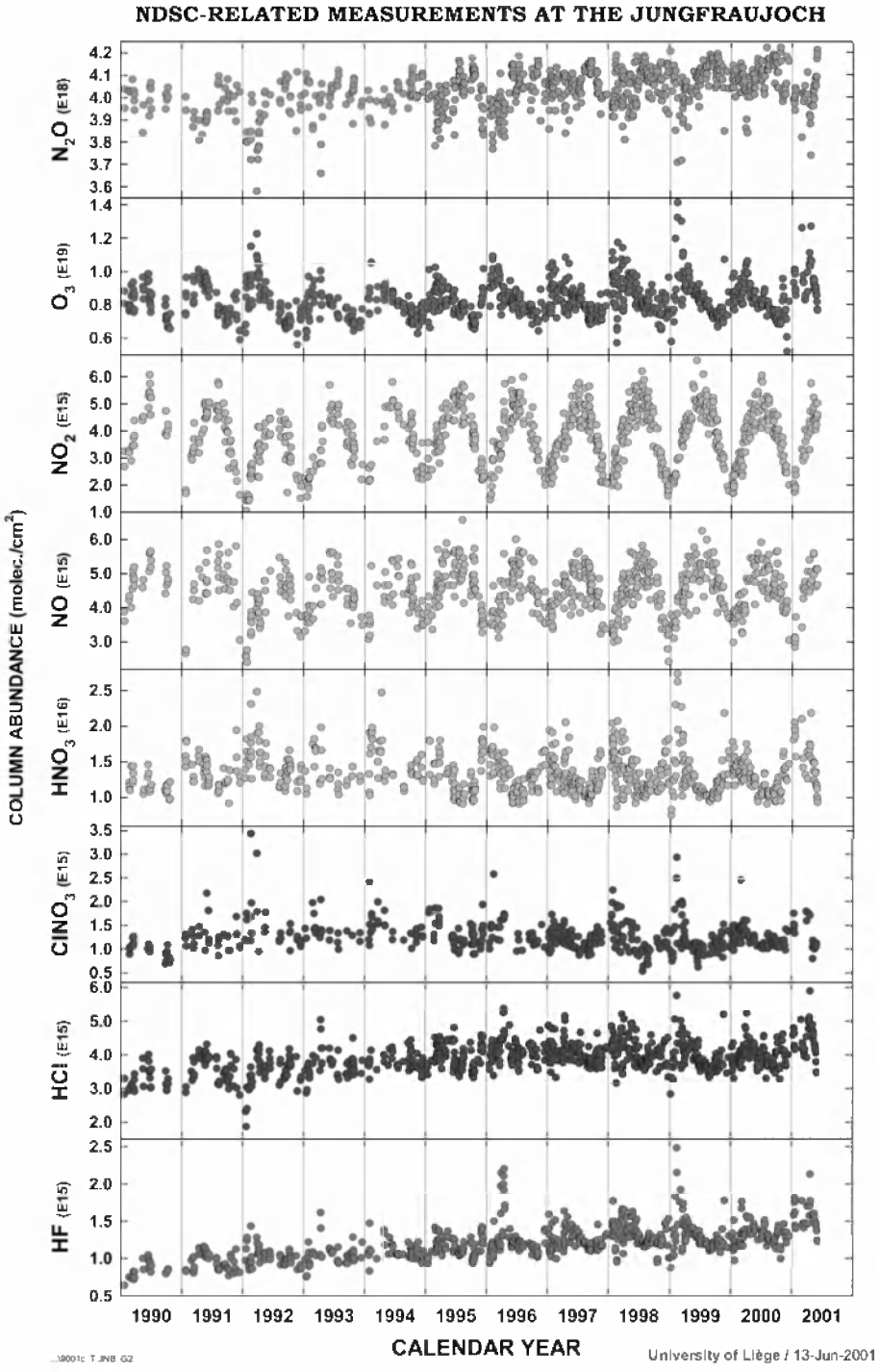

Figure 19: *An excerpt of daily mean vertical column abundances derived consistently from Jungfraujoch FTIR solar observations since the mid-1980s. The 8 molecules shown here are key species allowing to study the chemistry and dynamics of the stratosphere within the frame of the ULg commitment towards the international Network for the Detection of Stratospheric Change (NDSC).*

The following sections deal with specific research activities and findings related to these data sets.

4.1.1.1 Evolution of the budget of inorganic chlorine (Cly) above ISSJ

Inorganic chlorine primarily results from organic chlorine-bearing source gases released at the ground and sufficiently long-lived that they can be transported into the stratosphere and be broken apart by photolysis and reactions with OH and $O(^1D)$. Based on our current knowledge of inorganic chlorine partitioning in the stratosphere, total Cl_y is defined as follows:

$$Cl_y = [HCl] + [ClONO_2] + [ClO] + [OClO] + 2[ClOOCl] + [HOCl] + [ClONO] + [COClF] + [Cl] + 2[Cl_2] + [BrCl] \quad (1)$$

where the brackets indicate the vertical column abundances of each reported compound. In this evaluation, the dominant species present under normal background conditions at mid-latitudes are the two reservoirs HCl and $ClONO_2$ which can be measured and monitored in FTIR remote observations. They account, indeed, for over 92% of the total inorganic Cl_y loading (Zander et al., 1992) and their sum can be considered as a good Cl_y surrogate.

Figure 20 reproduces the monthly mean vertical column abundance measurements above the Jungfraujoch of HCl (circles) between 1977 and present, and of $ClONO_2$ (triangles) from 1986 to present. The full symbols correspond to the months of June to November, whereas the open symbols refer to the winter-spring months of December to May. Summing on the polynomial curves fitted to the summer-fall data points (full symbols; to avoid significant variability during the winter-spring time) gives the upper thick black curve labeled Cl_y which extends over the common time interval of 1986 to present. Inspection of the latter indicates that the growth rate of inorganic chlorine loading at northern mid-latitudes has progressively slowed down during the 1990s: it was equal to (4.4 ± 0.3) %/yr. between 1986-90, reaching zero sometimes during 1997-1998.

Discrete column changes (expressed in molec./cm^2/yr and in % of total column) for HCl, $ClONO_2$ and Cl_y are given in Table III.

When accounting for a mixing time of 3 to 5 years for long-lived chlorine-bearing source gases to reach mid-latitude stratospheric altitudes and decompose into inorganic compounds, the timely occurrence of this maximum Cl_y loading is in line

with the peaking of total organic chlorine (CCl_y) in the lower troposphere that occurred between mid-1992 and mid-1994 as found by two *in situ* global measurement networks, namely AGAGE (Advanced Global Atmospheric Gases Experiment) and NOAA/CMDL (National Oceanic and Atmospheric Administration/Climate Monitoring and Diagnostics Laboratory) (Montzka et al., 1999). As can be seen in Figure 20, the timely evolution of CCl_y resulting from AGAGE measurements (orange curve referred to the right hand volume mixing ratio scale) had to be shifted by +4.0 years for its peak to best match the maximum occurrence of the Cl_y loading above the Jungfraujoch. This result further agrees satisfactorily with model calculations (e.g., +3.7 years found by D. Considine at NASA-Goddard Space Center, Greenbelt, MD, USA; private communication, 2000) based on the scenario of chlorine-bearing source gas emissions controlled by the Montreal Protocol and its subsequent Amendments and Adjustments (WMO Report Nr.44, 1999).

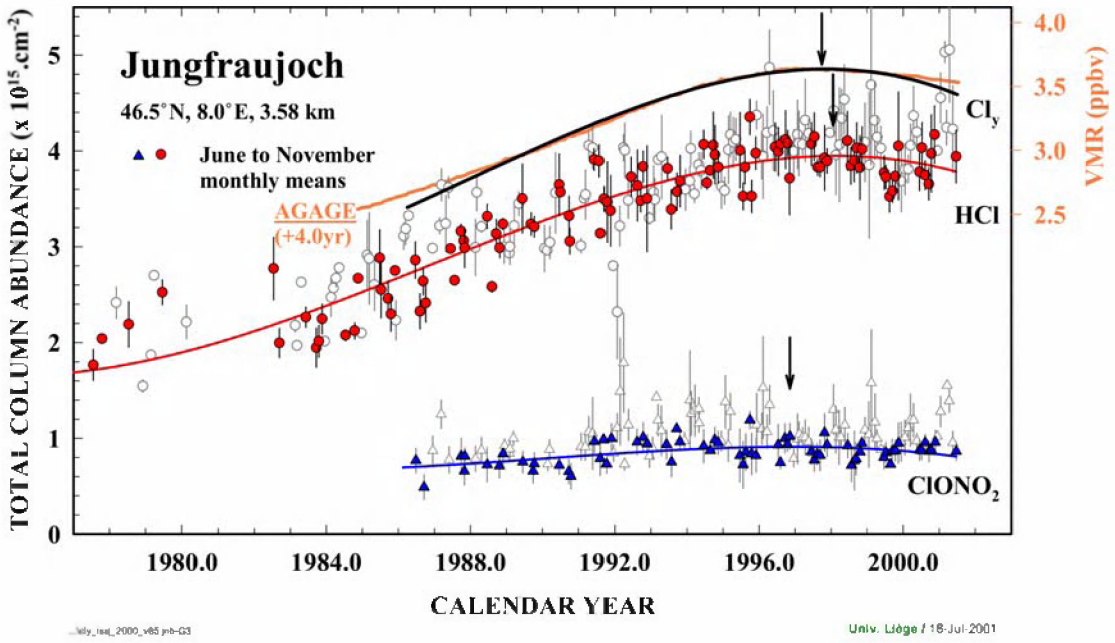

Figure 20: *The timely evolution of inorganic chlorine (Cl_y) above the Jungfraujoch based on monthly mean vertical column abundances of HCl and $ClONO_2$. The maximum Cl_y loading is found here to have occurred near the end of 1997, about 4 years after the load of organic chlorine peaked in the troposphere.*

Table III: *Typical column changes per year for species of relevance to Cl_y and F_y*

Species	**1987**	**1992**	**1997**	**2000**
HCl (x10^{14} molec/cm^2/yr)	1.50 (5.20%)	1.14 (3.20%)	0.17 (0.44%)	-0.7 (-1.8%)
$ClONO_2$ (x10^{14} - - -)	0.23 (3.10%)	0.23 (2.74%)	-0.05 (-0.55%)	-0.36 (- 4.24%)
Cl_y (x10^{14} - - -)	1.73 (4.80%)	1.37 (3.10%)	0.12 (0.25%)	-1.07 (-2.3%)
HF (x10^{13} - - -)	3.84 (5.12%)	5.51 (5.54%)	4.52 (3.60%)	2.61 (1.91%)
COF_2 (x10^{13} - - -)	0.41 (2.05%)	1.06 (4.40%)	0.47 (1.66%)	-0.50 (-1.75%)
F_y (x10^{13} - - -)	5.38 (4.68%)	7.26 (4.90%)	5.55 (3.06%)	2.75 (1.41%)
CFC-12 (x10^{14} - - -)	2.06 (3.70%)	1.33 (2.06%)	0.59 (0.85%)	0.15 (0.21%)
HCFC-22 (x10^{13} - - -)	0.73 (7.10%)	0.82 (5.80%)	0.91 (4.93%)	0.96 (4.53%)

The vertical arrows in Figure 20 correspond to the turnover times of the various curves, i.e., 1996.9 for $ClONO_2$, 1998.1 for HCl, and 1997.8 for the resulting Cl_y curve. The difference of over one year between the $ClONO_2$ and the HCl peak occurrences is definitely within the uncertainty of the peak determinations which have been estimated at ± 1.5 years for the former and ± 1.0 year for the latter at the 90% confidence level; these large uncertainties are due to the very slow rates of change observed in both the HCl and $ClONO_2$ columns, as well as their associated variabilities and measurement precisions. It should be further noted here that the interannual variations observed recently (e.g., the minimum during 1999 and the enhanced columns during winter-spring of 2000-2001 in the HCl data base) render the peak determinations uncertain. This has been raised by Anderson et al. (2000) and by Waugh et al. (2001) who have critically discussed the evolution of the HCl concentration near 55 km altitude as measured since October 1991 to present by the HALOE experiment aboard the UARS satellite. In particular, the latter concluded that the turnover time of HCl in the lower mesosphere, found by the former to occur as early as at the start of 1997 could not be explained by any model hypotheses that rather predicted late 1999. In our present research, it ought to be stressed that we are dealing with the integrated Cl_y columns and that its maximum occurrence in late

1997 is in much better agreement with the Waugh et al (2001) model calculations (D. Considine, private communication, 2000). To statistically improve the moment of the Cl_y peak occurrence, it is important to continue measurements during the next years and to combine a multi-station approach; this latter task has been initiated during the past months and involves 7 NDSC sites equipped with FTIR instruments and located in both hemispheres. Beside the Jungfraujoch, however, only two of these have sufficiently long observational time bases (Kitt Peak, USA and Lauder, New-Zealand) to contribute to improving the Cl_y issue as reported above; the other sites (Ny Ålesund, Spitzbergen; Zugspitze, Germany; Mauna Loa, Hawaii; Wollongong, Australia) have shorter data sets only allowing to assess the post-maximum evolution. Related findings will be presented by C.P. Rinsland (from NASA-Langley Research Center, Hampton, VA, USA) at the September 2001 NDSC Symposium to be held in Arcachon, France.

It should be noted here that we have tested and adopted an improved set of spectroscopic line parameters for $ClONO_2$ (Birk and Wagner, 2000), which leads to lower column abundances by about 10-15 % with respect to those reported earlier using the Bell et al. (1992) linelist. This partly accounts for discrepancies generally noted between observations and model calculations.

Once the Cl_y column decrease has been observed unambiguously, it will be important to correlate its rate of decrease with any subsequent change in the ozone layer, and estimate the time of full ozone recovery.

During the past three decades, the predominant chlorine-bearing source gases responsible for the increase of Cl_y in the stratosphere have been the anthropogenic CFCs and HCFCs. The Montreal Protocol (1987) was enacted and subsequently amended and adjusted in order to progressively and efficiently reduce the production and release to the atmosphere of those source gases with large ozone depletion potentials (ODP; see WMO Report No. 44 (1999)) thus causing significant threat to the stratospheric ozone layer.

While all source gase concentrations with noticeable ODPs are being monitored at the ground by *in situ* techniques and related to industrial production inventories and to protocol restrictions, it was thought useful to monitor the total column abundances above the Jungfraujoch of a couple of them, in order to have a quantitative link between Cl_y and CCl_y. CFC-12 (CCl_2F_2) and HCFC-22 ($CHClF_2$) were chosen, because of their clear and well defined absorption signatures in infrared solar spectra.

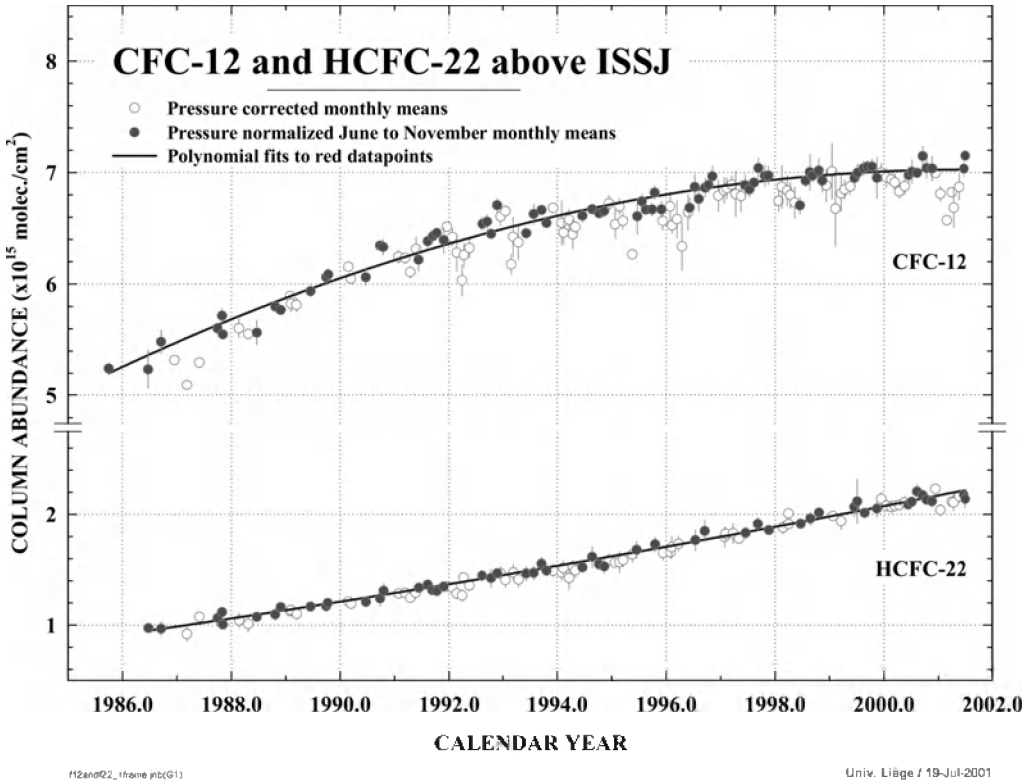

Figure 21: *The timely evolution above the Jungfraujoch of the column abundances of CFC-12 (CCl_2F_2) and HCFC-22 ($CHClF_2$) which are two important source gases contributing to the budget of Cl_y in the stratosphere. The former has been progressively phased out by the Montreal Protocol and subsequent Amendments, while the latter is not yet regulated.*

Figure 21 displays the monthly mean column abundances of CFC-12 and HCFC-22 as determined above ISSJ from the mid-1980s to present. Only the data points corresponding to the quietest June to November months have been considered in the polynomial curve fitting process for reasons already evoked before. While the rate of increase of the regulated CFC-12 has definitely slowed during the 1990s, it has not yet reached its maximum loading despite its production and consumption having been phased out to 100% in the developed countries in 1996 (WMO Nr. 44, 1999); this behaviour mirrors the evolution of CFC-12 observed at the ground (S. Montzka, NOAA, Boulder,CO, USA; private communication, 2001) and is indicative of the CFC-12 long lifetime (~ 100 years), applications with time-delayed releases (e.g., refrigeration, cellular foam blowing) and small consumption in developing countries.
On the other hand, the columns of $CHClF_2$ (HCFC-22; which is not yet regulated), have increased steadily; this increase is the consequence of this compound being used in various applications as a substitute for the banned CFC-11 and –12. Notice that HCFC-22 has a lifetime of 12 years and thus will be removed from the atmosphere much faster than CFC-12 after its phase out has begun in 2004.

Discrete column increases for CFC-12 and HCFC-22 are reported in Table 3; they have been compared with increases measured at the ground by *in situ* techniques and found in excellent agreement (WMO Report Nr 44, 1999).

4.1.1.2 Evolution of the budget of inorganic fluorine (F_y) above ISSJ

Inorganic fluorine does not contribute to stratospheric ozone depletion (Stolarski and Rundel, 1975). However, the evaluation of its loading provides an independent check regarding the anthropogenic contribution to chlorine loading by CFCs and HCFCs because, thus far, the latter have also been the predominant sources of inorganic fluorine-bearing compounds in the stratosphere. Total inorganic fluorine, F_y, can be defined as:

$$F_y = [HF] + 2[COF_2] + [COClF] \quad (2)$$

Based on earlier fluorine budget evaluations from ATMOS measurements (Zander et al., 1992) and by MarkIV-balloon observations (Sen et al., 1996), HF and COF_2 account for some 98% of the total F_y column. Therefore, the combination as per equation (2) of the HF and COF_2 vertical column abundances measured above the Jungfraujoch is an excellent surrogate of the total inorganic F_y loading and its timely evolution.

The lower part of Figure 22 displays the monthly mean vertical column abundances of HF and COF_2 observed above ISSJ between 1985 and present. Their mean timely evolution is reproduced by polynomial curves fitted to all data points (all months were included here, as HF is a good tracer of meridional transport and dynamics/subsidence). Until the mid-1990s, both species showed relatively monotonous column increases which were in agreement with the continued emission increases of their principal parent source gases CFC-11, CFC-12 and HCFC-22 (Mahieu et al., 1998; Mélen et al., 1998). Subsequently, the fitted curves reveal a weak slowing down in the rate of increase of HF after about 1996, as well as a levelling off for COF_2 around 1997 and a subsequent slight decrease which, however, is not yet significant at the 90% confidence level. Further noticeable are the low columns observed for both species during 1999-2000 as well as enhanced columns measured during the first months of 2001. Whether this 2-year minimum is related to some special atmospheric circulation behaviour or special chemistry will have to await near future observations (it needs to be investigated in parallel with the 1999-2001 behaviour of HCl mentioned in Section 4.1.1.1.

The upper curve of Figure 22 reproduces the inorganic F_y atom total vertical column abundance evolution above ISSJ resulting from the combined contributions of HF and COF_2 as per equation (2). Here, data points have been displayed for months during which both HF and COF_2 measurements were available; the continuous curve corresponds to the best polynomial fit to all these points. Rates of column abundance changes for HF, COF_2 and F_y are also provided in Table III. The F_y rates of change are consistent with those found for the organic fluorine (CF_y) loading in the troposphere by the *in situ* networks AGAGE and NOAA/CMDL (WMO Report Nr. 44, 1999).

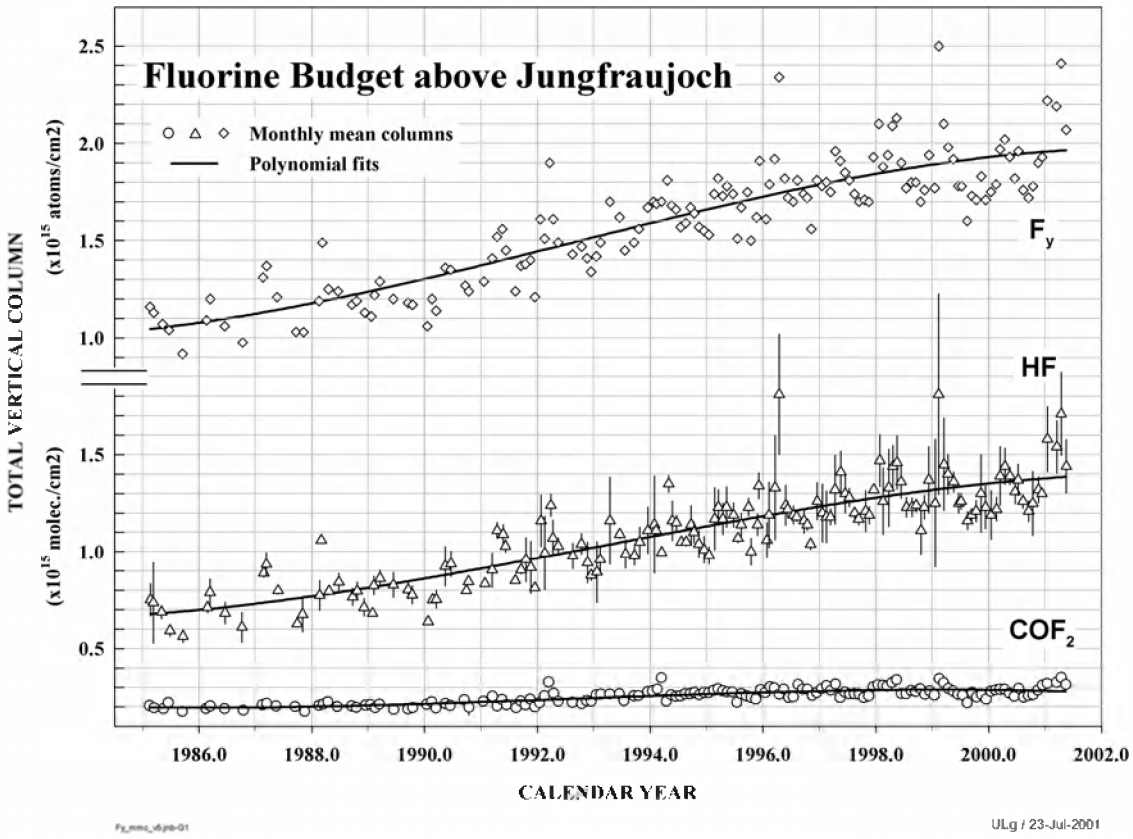

Figure 22: *The timely evolution of inorganic fluorine (F_y) above the Jungfraujoch obtained by combining the column abundances of HF and COF_2. The slowing down of the F_y rate of increase observed since the late 1990s results from the mixed use of regulated CFCs and substituted HFCs and FCs (WMO Report Nr. 44, 1999).*

The evolution of F_y observed here contrasts with that of the Cl-atom loading mentioned in the previous paragraph. It is further in disagreement with findings by Considine et al. (1997) who report a slowing in the rate of increase of HF above 55 km altitude, in a manner consistent with the tropospheric loadings and trends of CCl_3F and CCl_2F_2 in the early 1990s (Montzka et al., 1996); these findings were based on HALOE observations of HF volume mixing ratio profiles over the 50°N to

50°S latitude band. Contacts with modelers have been initiated to understand and quantify the above problem and with colleagues involved in *in situ* measurements to relate the observed F_y changes with CF_y loadings in the troposphere.

4.1.1.3 The evolution of HCl/HF

Beside long-term background column evolutions described in this report, related effects of atmospheric transport have also been investigated and identified, generally involving correlations with long lived tracers. Here, as HF is chemically stable in the stratosphere, any change in its column abundance will reflect some special circulation that brings masses of air above the Jungfraujoch having different latitudinal origins. Figure 23 displays the ratios of the HCl over the HF daily mean column abundances observed above the site on same days since 1991 (all circles).

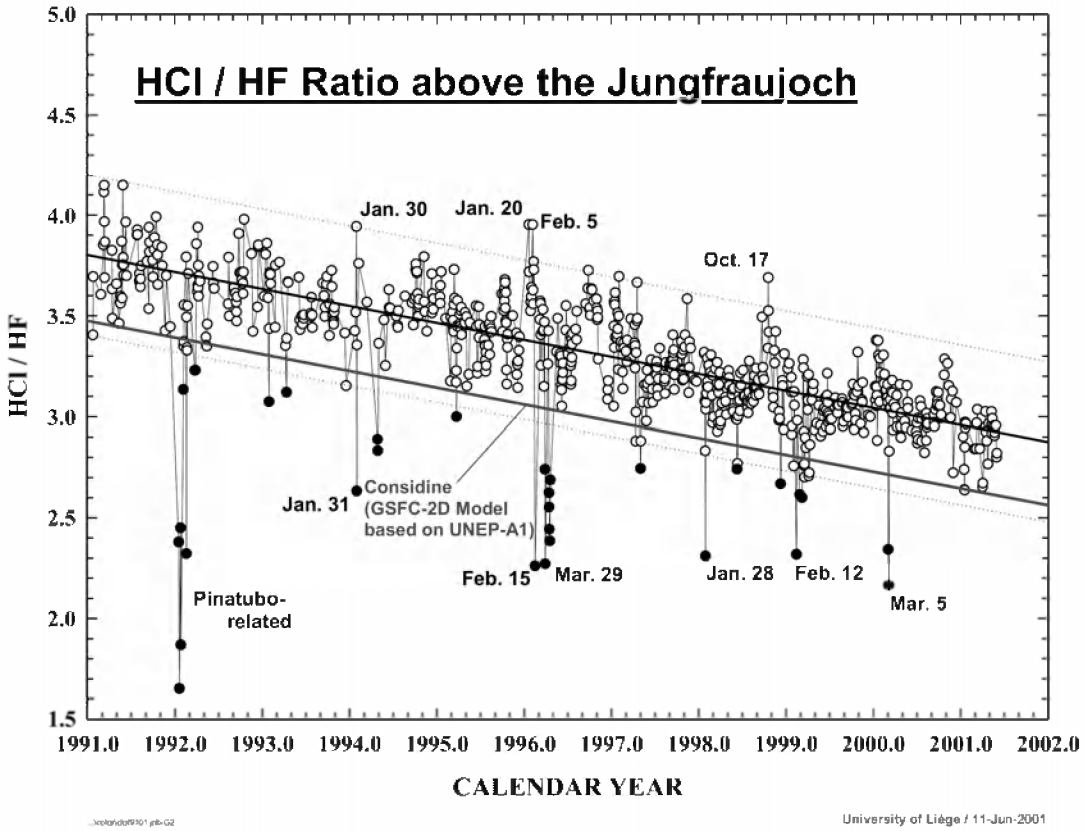

Figure 23: *Timely evolution of the columns ratio HCl/HF above the Jungfraujoch. The overall decrease results from the progressive phase-out by the Montréal Protocol and subsequent Amendments of Chlorine-bearing source gases with large ozone depletion potentials. This evolution is consistent with model predictions. The filled circles indicate days when masses of stratospheric polar air had been transported over central Europe and having eventually undergone heterogeneous chemistry processing in the presence of heavy aerosol loading and polar stratospheric clouds (e.g. low Pinatubo-related values).*

The overall tendency is given by a two-iterations linear fit to the data points; its regular decrease results from the relative background evolution of the HCl and HF loadings, which reflect changes in CFC-, HCFC- and HFC emissions mix; the 99% confidence range is delineated by the thin dotted lines. All HCl/HF ratios falling below this lower range are reproduced by filled circles. These latter, as well as a few ones observed above the high limit of the range are considered to result from unusual atmospheric circulation situations. The extremely low ratios observed during the winter 1991-92 primarily result from polar air transported to mid-latitudes after HCl had undergone heterogeneous conversion in the presence of polar stratospheric clouds at high aerosol loading resulting from the Mt. Pinatubo volcanic eruption in June 1991; this was further confirmed by the record high columns of $ClONO_2$ observed during this period (see Figure 19). Other special pre-1997 features in Figure 23 have been discussed by Mahieu et al. (1998).

During the more recent years, only isolated, less pronounced cases than those of early 1992 and early 1996, have been recorded, but all could be associated with high to low latitudes meridional transport. Confirmation of this latter relation could generally be obtained from the analysis of air circulation back trajectories and potential vorticity maps produced by the ECMWF and made available via NILU.

Worth being mentioned here is that the simultaneous analysis of HCl versus HF (correlation plot) allows to characterise the atmospheric loading of HCl at zero HF loading. The result already reported in 1996 (Zander et al., 1996) was confirmed on the basis of additional measurements performed during this ESAC project, indicating a pre-CFC background loading of HCl above the Jungfraujoch equal to (0.75 ± 0.1) x 10^{15} molec./cm^2. Additionally, series of analyses performed with the retrieval code SFIT2 (which allows to retrieve profile information versus altitude (e.g., Connor et al., 1996) have returned tropospheric columns equal to about (0.3 ± 0.1) x 10^{15} molec./cm^2. From these two estimates one can evaluate the stratospheric background burden of HCl to have been equal to (0.45 ± 0.2) x 10^{15} molec./cm^2 during the pre-CFC time. The weakest point in this evaluation results from the poor knowledge of the *a priori* profile of HCl in the troposphere.

4.1.1.4 *Evolution of the budget of NO_y above ISSJ, and the impact of Mt. Pinatubo on the NO_2 abundance*

The main contributors to the stratospheric budget of reactive nitrogen, NO_y, are NO, NO_2, NO_3, HNO_3, N_2O_5, HNO_4, $ClONO_2$ and $BrONO_2$. This budget is obtained by summing the individual columns of each compound, with N_2O_5 being counted twice. As NO_3, N_2O_5, HNO_4 and $BrONO_2$, which can not be measured from the ground (because, either they are masked by strong water vapour interferences, or their concentrations are too weak to be detected in infrared solar spectra), contribute at most for 5% of the total NO_y under typical daytime background conditions prevailing at mid-latitudes (WMO Report Nr. 44, 1999), the commensurate NO_y daytime column above ISSJ can be defined as:

$$[NO_y] = [NO] + [NO_2] + [HNO_3] + [ClONO_2] \qquad (3)$$

Since last reported (Demoulin et al., 1998; Mahieu et al., 2000) and as shown in Figure 19, the daytime daily mean burdens of these main reactive nitrogen species monitored above ISSJ have continued to show their characteristic seasonal modulation and large short-term and inter-annual variabilities. For reasons evoked before, the upper frames of Figure 24 reproduce the data points of Figure 19 (and their extensions back in time) converted into monthly means for the four contributing species, while the resulting NO_y values calculated as per equation (3) are shown next. It is worth noting the different ordinate scales for the various compounds, with mean contributions to NO_y equal to about 58 % for HNO_3, 20 % for NO, 17 % for NO_2 and 5 % for $ClONO_2$. Consequently, NO_y is heavily "biased" towards the characteristic variations of HNO_3 as well as its variability which is quite large during winter and spring. In this Fig. 6, all data sets have been fitted by a simple sinusoidal function (to visualise the seasonal variations) superimposed on a mean linear background trend. The mean linear rates of change so derived over the displayed time frame are found equal to: (+0.1 ± 0.1)%/yr for NO, (+0.6 ± 0.2)%/yr for NO_2, (-0.2 ± 0.2)%/yr for HNO_3, and (+0.8 ± 0.4)%/yr for $ClONO_2$ (a more detailed rate of change for this latter has been provided in Section 4.1.1.1 with discrete changes in Table 3). The monthly mean NO_y data points return a mean trend equal to (-0.1 ± 0.2)%/yr, which is statistically insignificant, despite the long measurement timeframe. The same remark holds for HNO_3 with its (-0.2 ± 0.2)%/yr rate of change, although this value has significantly improved as compared to the value of (-0.1 ± 0.4)%/yr derived earlier from the 1985-96 time base (Demoulin et al., 1998). It appears that the data bases for the individual species are best behaved as their sum, which likely results from the fact that NO_y data points are fewer than those making up the individual data sets (due to occasional missing monthly mean columns for one or

more of the contributing gases). As a consequence, an approach combining the different best fits to the latter sets (similar to that adopted for the Cl_y evaluation) is being envisaged.

At this time, NO_2 reveals a rate of change that is statistically significant. Its trend of (+0.6 ± 0.2)%/yr observed above the Jungfraujoch has been confirmed recently by Liley et al. (2000) who reported a rate of increase equal to (5 ± 2)% per decade, based on NO_2 UV-Vis measurements at Lauder (New Zealand) from 1984 to 1999. These findings at the two mid-latitude NDSC sites in both hemispheres are important results which modellers need to reproduce and help to understand.

Additionally, the post-Pinatubo HNO_3 column time base from 1992 to present has undergone a statistically significant rate of change equal to (-0.8 ± 0.4)%/yr when including all months of the year, and as high as (-1.4 ± 0.4)%/yr when only considering the more quiet periods from June to November. This negative rate of change for HNO_3 has been confirmed based on observations at Kitt Peak (Arizona, USA) between 1992 to present, with a decrease of nearly 2%/yr during this post Mt. Pinatubo volcanic eruption (C.P. Rinsland, private communication, 2001). As for NO_2, these HNO_3 rates of change will have to be simulated by model calculations and explained (groups at the Universities of Oslo and Leeds are working on this problem); we believe that the stratospheric aerosol loading is a key compound influencing these findings.

The bottom frame of Figure 24 displays the mean trend of N_2O which is the main source gas feeding the NO_y family of compounds in the stratosphere; its long-term rate of increase of (0.30 ± 0.01) %/yr, is quite different from the statistically significant trends observed for NO_2 and HNO_3, but the chemistry and photo-chemistry of the latter is sufficiently complex for a linear source-sink relation not to prevail.

With respect to the growth rates of N_2O volume mixing ratios at the ground derived globally by the *in situ* networks mentioned before (typically 0.25 %/yr), the Jungfraujoch increase in the N_2O vertical column has consistently been higher. We have shown that the difference can be explained by a heightening of the tropopause by some 100 to 150 m over the period 1985 to present, which can result from some warming of the troposphere or/and cooling of the stratosphere. This suggestion is in line with findings in the long-term ozone and temperature data bases gathered at Hohenpeissenberg, Germany (Steinbrecht et al., 1998).

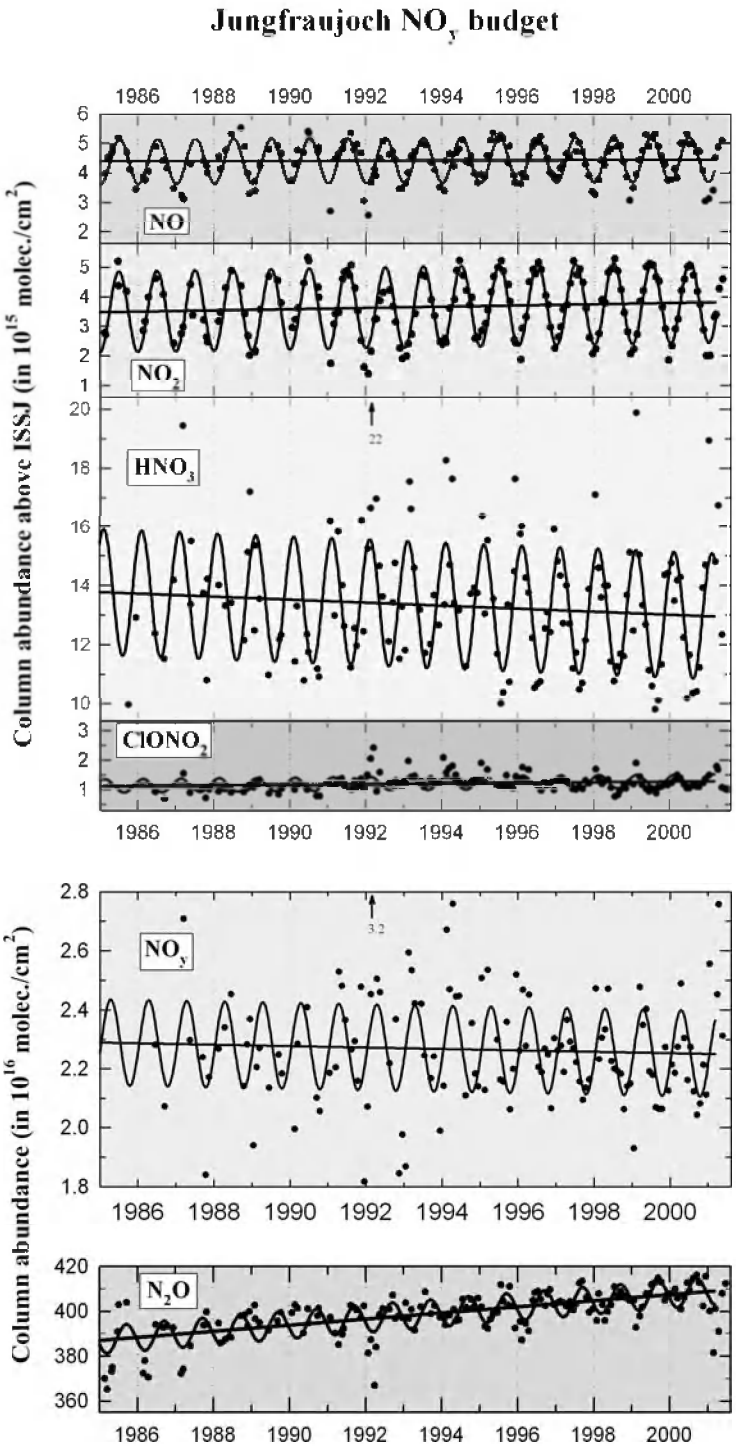

Figure 24: *The 4 upper frames reproduce the evolution of the column abundances of the most important constituents contributing to the stratospheric NO_y loading above the Jungfraujoch, that is shown below. Among all these compounds, only NO_2 shows a long-term statistically significant rate of change equal to (+0.6 ± 0.2) %/yr. The evolution of N_2O, which is the main source of NO_y, is displayed in the bottom frame.*

Due to its long lifetime (120 years), N_2O is an excellent tracer of atmospheric transport and dynamics, and we monitor its variability to identify unusual meridional circulation patterns, primarily polar air intrusions and related "equivalent" subsidence. In Figure 19, the "opposite" variations in the columns of the ground-based long-lived source gas N_2O and the stratospheric long-lived HF are striking and their simultaneous monitoring add confidence in the way latitudinal circulation and subsidence influence the mean atmospheric state at mid-latitude.

Impact of the eruption of Mt. Pinatubo on the NO_2 abundance above the Jungfraujoch

As a consequence of the eruption of Mount Pinatubo in June 1991 in the Philippines (15°N, 120°E) and the corresponding globally enhanced aerosol load in the stratosphere, a reduction of the NO_2 amount was observed at ISSJ. Part of this was attributed to enhanced conversion of N_2O_5 to HNO_3 due to heterogeneous processing on the aerosol particles surfaces (e.g., Hofmann and Solomon, 1989; Brasseur and Granier, 1992; Rinsland et al., 1994). A precise quantification of the reduction required the establishment of a reliable pre-Pinatubo NO_2 climatology. To this end the FTIR time series of NO_2 columns at the Jungfraujoch observatory, which starts as early as 1985, has been combined with the SAOZ series which only starts in mid-1990, but which has the advantage of providing morning and evening twilight data each day. To use the combined data set, they have been corrected first for mutual biases. Still, because of the NO_2 diurnal variation and the different sampling times of the FTIR and SAOZ instruments, a direct intercomparison and/or combination with the SAOZ data is impossible. Therefore, a photochemical model (Nevison et al., 1996) was used for evaluating the morning and evening twilight values corresponding to FTIR measurements which are spread throughout the day. The model uses actual temperature data, locally measured ozone column values and a mean monthly NO_2 vertical profiles at midlatitude derived from SAGE II observations. The resulting combined time series of the NO_2 abundance at Jungfraujoch and its evolution during the last decade, in terms of monthly mean percentage differences relative to the pre-Mount Pinatubo climatology established over the 1988 to mid-1991 period, are displayed in Figure 25.

The figure also shows the reduction of the NO_2 amount: it peaks at the turnover between 1991 and 1992 and amounts to 45% with respect to the pre-Mount Pinatubo 1988 to mid-1991 mean level; no distinct behaviour between morning and evening columns is observed. The recovery can be modeled reasonably well by a sum of two exponentials, an initial fast one with an *e*-folding time of 2.7 months, followed by a slower one with an *e*-folding time of 35 months (solid line in Figure 25). If we limit the

fit to the 24-month period following the maximum impact for comparison with the decay of the aerosol load measured above the closest lidar station of Garmisch-Partenkirchen (Jäger et al., 1995), we find approximately the same 10-month *e*-folding time, as represented by the dashed line in Figure 25. By mid-1994, both the aerosol load and the NO_2 reduction had decreased to about 10% of their maximum value. The NO_2 amount came to complete recovery only by January/February 1995. The NO_2 abundance observed at the end of 1996 appears to be higher by about 7% than the reference level, which might be related to the fact that the actual aerosol load came down approximately to the 1978/1979 background level, at least below the 1988/1991 one (H. Jäger, private communication, 1997), or to the actual rate of increase of NO_2 derived from the FTIR time series as discussed above.

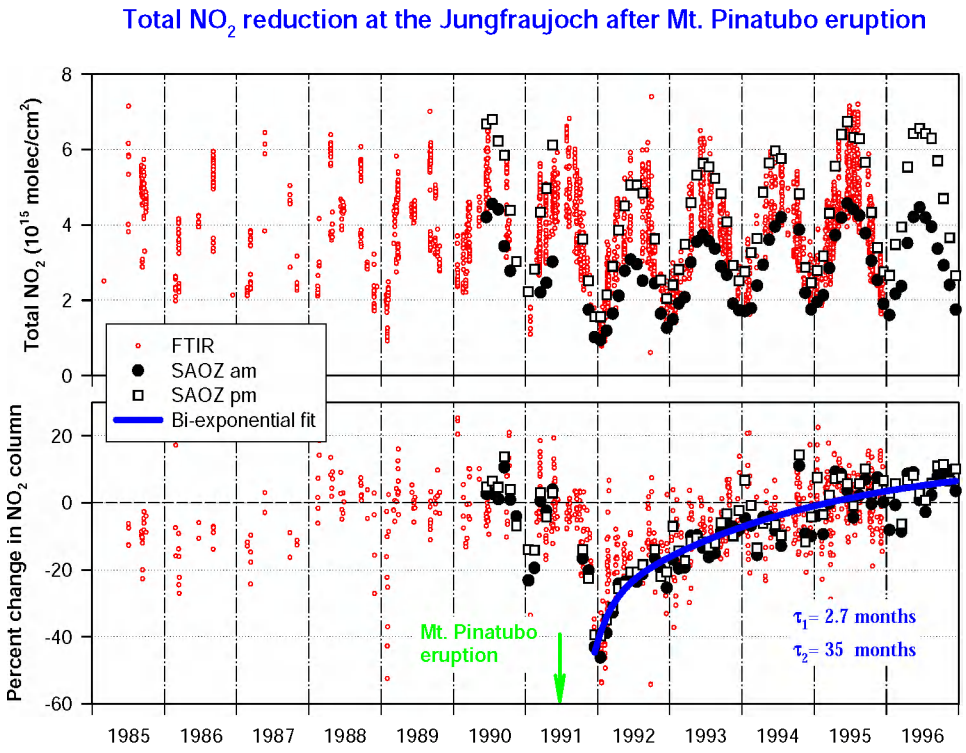

Figure 25: *Top: Superposition of FTIR (small open circles) and SAOZ (solid circles and open squares) time series of NO_2 columns at the Jungfraujoch. Bottom: Percentage monthly mean NO_2 vertical column reductions observed at the Jungfraujoch by the SAOZ and FTIR instruments. Reductions are evaluated relative to the 1988 to mid-1991 monthly mean reference values derived from the FTIR observations. SAOZ data are monthly means for morning and evening vertical column amounts; FTIR data are daily values.*

It is our intention in the near future to re-examine the combined FTIR and SAOZ NO_2 time series at the Jungfraujoch, using the latest homogenised and revised SAOZ data up to present (cf. section 4.1.1); the latter data were not available yet for the analysis discussed here above (De Mazière et al., 1998).

4.1.1.5 Kyoto Protocol-related investigations

The "Kyoto Protocol on Climate Change" (1997) has set initial recommendations and quota to achieve stabilization of the atmospheric loading of strong greenhouse gases at levels acceptable for durable development. These initial measures aim at a first "modest" reduction in emissions referred to 1990 levels, to be reached during the first commitment period ending in 2010. The reduction levels are expressed as "aggregate anthropogenic carbon dioxide equivalent emissions" of the following greenhouse compounds: CO_2, CH_4, N_2O, SF_6, HFCs (hydrofluorocarbons) and PFCs (perfluorocarbons). The amended and adjusted Montreal Protocol is assumed to remain in effect, as ozone depletion and climate change interact through common physical and chemical processes.

While CO_2, CH_4 and N_2O have been recognised for long time as important contributors to the greenhouse characteristics of the atmosphere, SF_6 was included in the Kyoto list, because of being the strongest absorber of infrared radiation on a per-molecule basis (e.g., Rinsland et al., 1990), and once released, it persists in the atmosphere for millennia (Ravishankara et al., 1993; Mahieu et al., 1996). Its presence in the atmosphere is believed to be entirely of anthropogenic origin.

Within that context, the monitoring effort undertaken by GIRPAS since the mid-1980s includes the four gases specifically cited above (see also Zander et al., 2000). Related measurements performed at ISSJ during the recent years are displayed in Figure 26 and confirm the persistence of positive rates of change for all these gases, as already evoked partially in the final SMAC Report (Simon, 1996). However, noteworthy features emerging from the timely extended data bases are briefly pointed out here below.

1. As visualised in the top left frame of Figure 26, the $\underline{CO_2}$ vertical column abundance has continued to increase by a mean 2.16×10^{19} molec./cm^2/yr, which corresponds to a rate of change equal to (0.41 ± 0.01) %/yr, when referenced to year 2000. Its seasonal modulation is primarily the result of CO_2 uptake during the vegetation photosynthesis period. A slight "anomaly" observed in 1997 has also been noticed in the Mauna Loa reference data base accessible at the Carbon Dioxide Information Analysis center (CEDIAC), Oak Ridge, TE, USA; no

explanation has been found for this feature, as additional measurements during a few more years are needed to better quantify it.

2. After H_2O and CO_2, *methane (CH_4)* is the most abundant greenhouse gas in the troposphere and its transformation in the stratosphere leads primarily to water vapour. As can be seen from the top right frame of Figure 26, the rate of growth of the CH_4 column has continued to slow down: during the years 1987, 1992, 1997 and 2000, the rates of increase have been found equal to 1.59×10^{17}, 1.07×10^{17}, 0.55×10^{17}, and 0.23×10^{17} molec./cm^2/yr, or 0.74%, 0.48%, 0.24%, and 0.10%, respectively; this corresponds to a growth rate slowing down by nearly a factor 7 during the past 15 years. The post 1996 rates of change are the slowest observed since the 1940s (Etheridge et al., 1998). Overall, the reported rates of change are consistent with those derived from ground-level *in situ* monitoring networks (WMO Report No.44, 1999).

3. The data set of the *nitrous oxide (N_2O)* column abundances displayed in the bottom left part of Figure 26 also reveals a slight rate of decrease during the recent years, but this remains statistically uncertain, so that we report trends based on a linear rate of increase throughout the 1986 to present period; consequently, the mean rate of increase is found equal to 0.30%/yr, or 1.17×10^{16}, 1.19×10^{16}, 1.22×10^{16} and 1.23×10^{16} molec./cm^2/yr in 1987,1992, 1997 and 2000.

4. The *sulfur hexafluoride (SF_6)* column abundance above ISSJ has reached a value of 7.2×10^{13} molec./cm^2 at the end of year 2000, over 3 times its mean 1986 value (see bottom right frame of Figure 26). The average column increase above ISSJ has been 3.55×10^{12} molec./cm^2/yr, which corresponds to percentage increases equal to 14% in 1987, 8.3% in 1992, 5.86% in 1997, and 4.98% in 2000.

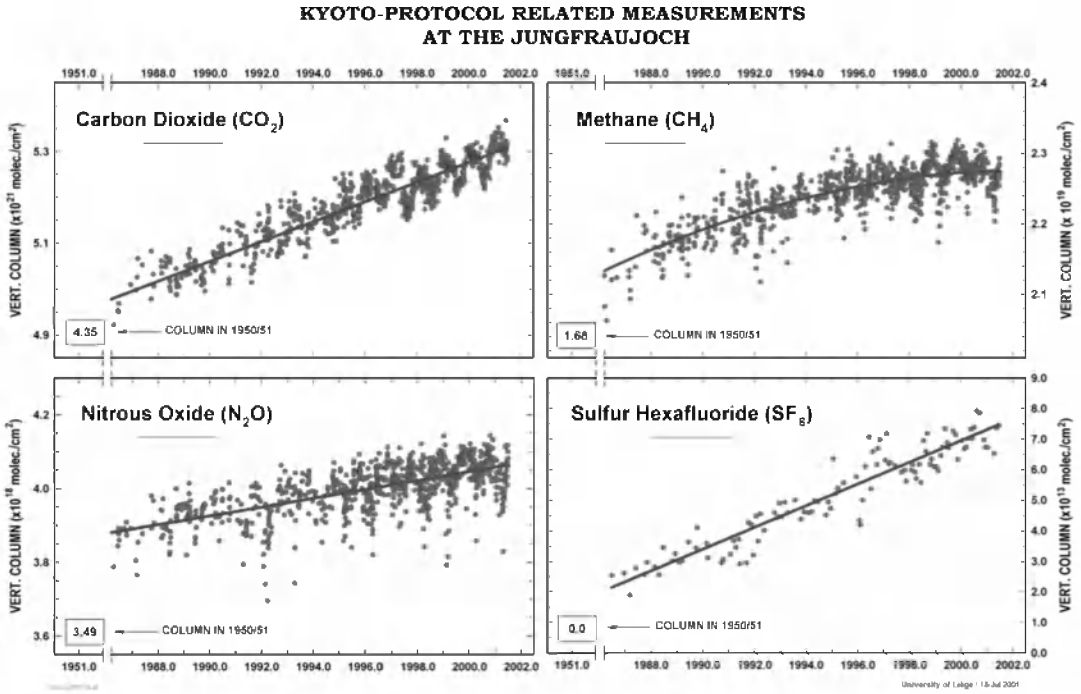

Figure 26: *The timely evolution of the vertical column abundances of 4 important greenhouse gases listed for regulation in the Kyoto Protocol. With the exception of CH_4 whose rate of increase has significantly slowed down during the 1990s, all other species have continued to accumulate in the atmosphere at relatively constant rates. For details, see text.*

4.1.1.6 Findings related to other species

Ozone (O_3)

The entire Jungfraujoch database of O_3 is being re-analyzed using the improved retrieval approach developed by De Mazière et al. (1999), as discussed in section 3.5.1. Advantage will be taken of this reprocessing effort to further implement spectroscopic parameter changes to minimise otherwise systematic residual features in the fittings. Two conclusions which are worth being mentioned here are that (1) the long-term rates of change (trends) in the O_3 columns are not significantly affected by the new approach, and (2) the seasonal differences, otherwise noticeable, disappear in the comparison between the SAOZ and FTIR column retrievals (cf. Figures 12 and 13 and associated discussions). Over the period 1985 to present, the mean rate of change determined for the total O_3 column abundance above ISSJ is equal to (-0.25 ± 0.15)%/yr. Since 1994, the observations indicate that total ozone has started to recover but whether this is a recovery from the minimum observed after the Mt. Pinatubo volcanic eruption or resulting from some change in atmospheric background transport/circulation remains to be assessed through additional

measurements and correlative investigations. It has been shown by De Mazière et al. (1999b) that heightening of the tropopause above the Jungfraujoch in the 80s and early 90s contributes to the observed O_3 decrease. This is in agreement with similar findings by Steinbrecht et al. (1998) at Hohenpeissenberg. Since the mid 90s; the tropopause above ISSJ seems to lower again, which may be correlated with the apparent increase of the ozone abundance, and maybe with the above mentioned decrease of N_2O. This must be confirmed during the next years.

To be noted here are the extreme column abundances observed during the period covered by this project: record high on February 13 (14.1×10^{18} molec./cm^2, or 526 DU), and record low on November 2000 (5.17×10^{18} molec./cm^2, or 192 DU). All high columns are associated with intrusions of unprocessed air masses that originate from higher latitudes, as evidenced from back-trajectories supplied by ECMWF through NILU.

Carbon monoxide (CO), ethane (C_2H_6) and hydrogen cyanide (HCN)

Figure 27 displays the monthly mean vertical column abundances of CO and C_2H_6 observed above the Jungfraujoch between 1984 and present. The mean rates of change over that entire period are equal to (-0.35 ± 0.15)%/yr for CO and (-1.9 ± 0.2)%/yr for C_2H_6; they are the only statistically significant negative rates among all source gases under investigation (see Table I).

Their seasonal modulations are well defined, with mean peak-to-peak modulations of 35% for the former and 45% for the latter. Noticeable in Figure 27 are the high columns observed during 1998 for both species; consequently, a detailed investigation of CO, C_2H_6 and HCN (which was also high in 1998) in the free troposphere above the Jungfraujoch from 1995 to 1999 was undertaken in collaboration with C.P. Rinsland and colleagues from the Swiss federal Laboratories for Materials Testing and Research (EMPA, Dübendorf). Extensive details about that work can be found in Rinsland et al. (2000).

The increased ISSJ 1998 tropospheric columns of all 3 species coincided with the period of widespread wildfires during the strong El Niño warm phase of 1997-1998 which resulted in abnormal emissions of CO, C_2H_6 and HCN, and they peaked after the increases measured above Mauna Loa (Hawaii), suggesting that these south Asia wildfires were responsible for the observed 1998 increases at both Mauna Loa and Jungfraujoch.

Comparisons between the tropospheric columns and local concentrations at the Jungfraujoch by EMPA, confirms that the CO free tropospheric vertical volume mixing ratio profile generally decreases with altitude throughout the year.

Formaldehyde (H_2CO)

Formaldehyde (as well as other aldehydes) is presumed to have a catalyzing effect on the production of chemical smog and of ozone in polluted urban areas, but its background concentrations as well as production sources and destruction processes are poorly known. Column abundance measurements of H_2CO have been derived from investigations of characteristic absorption features showing up very weakly in solar spectra recorded at ISSJ since 1988 (Demoulin et al., 1999). The columns had to be averaged over two-months time intervals to become reasonably reliable.

Beside of the retrieval difficulty, it also appears that the relative quality of the spectroscopic parameters available for various transitions, and missing parameters for weak interfering features need to be further studied in the laboratory. Because of the large variability observed in the columns and the uncertainty in their retrievals, no statistically significant trend emerges from the current 1988-2000 data base and the mean loading above ISSJ is likely to lie between 2 and 4 x 10^{14} molec./cm^2. A seasonal modulation with lower columns in winter is also suggested.

Carbonyl Sulfide (OCS)

OCS (carbonyl sulfide) has maintained an averaged rate of column decrease of –0.35%/yr, with large interannual variability. During the 1998 winter-spring time such variability was abnormally large. OCS is believed to be the main source responsible for the persistence of the sulphur layer in the stratosphere. Its main identified sources are natural, i.e., 30% oceans, 20% microbial processes in soils, 30% conversion of natural CS_2, and 20% anthropogenic.

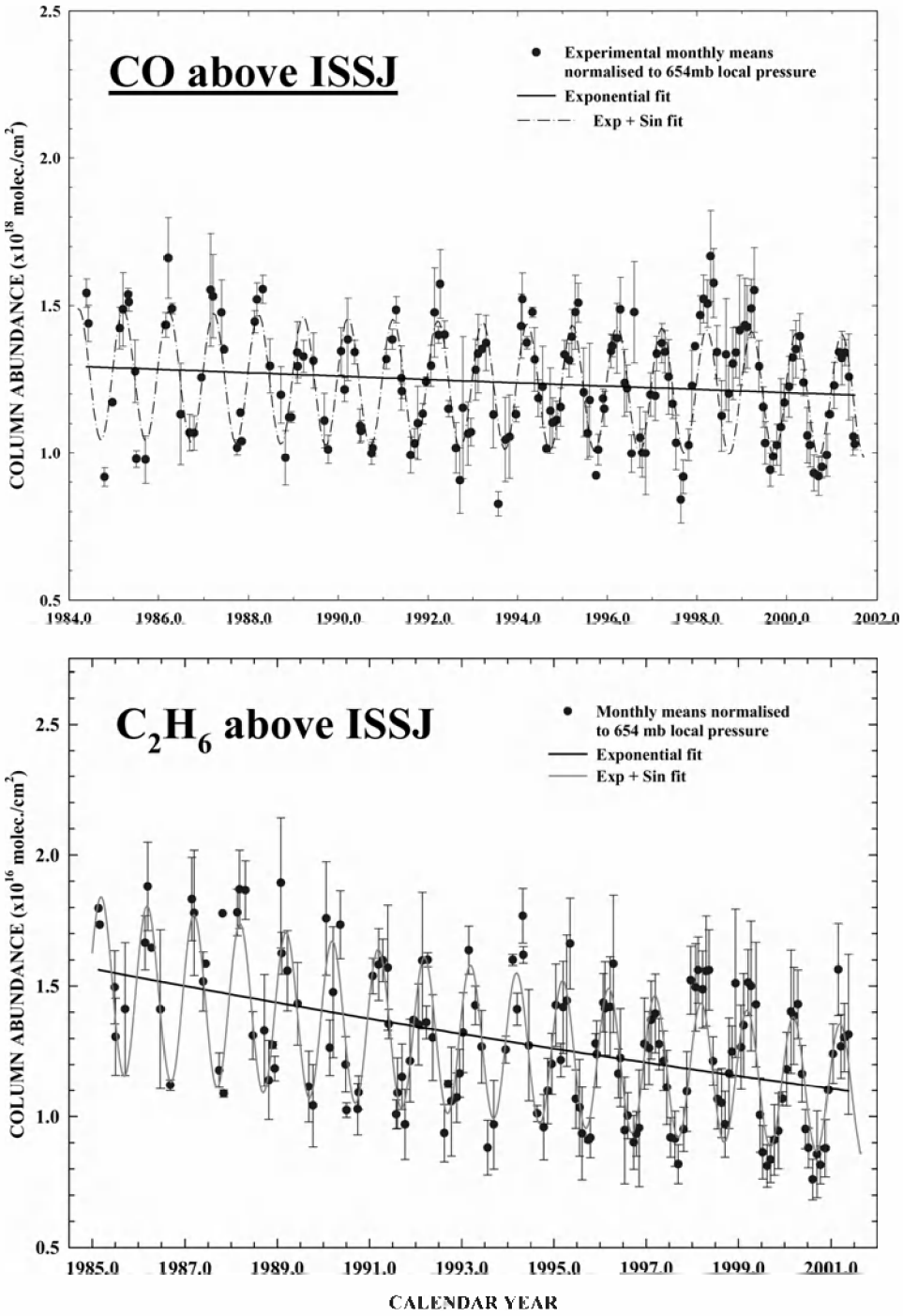

Figure 27: *Graphical representation of the column abundance evolution of CO and C_2H_6, both showing clear seasonal variations as well as rates of decrease, equal to (-0.35 ± 0.15) %/yr for the former and (-1.91 ± 0.18) %/yr for the latter. The monitoring of such species is indirectly of relevance to the Kyoto Protocol, as they affect the oxidizing capacity of the troposphere which influences lifetimes of greenhouse gases, e.g., CH_4.*

4.1.2 Long-term data at Harestua and OHP

4.1.2.1 Introduction

Since 1994, UV-visible zenith-sky observations have been performed by BIRA-IASB at the complementary NDSC site of Harestua (60°N, 10°E). In summer 1998, an additional instrument has been installed in the NDSC Alpine station at the Observatoire de Haute Provence (OHP, 44°N, 6°E). These instruments allow monitoring of O_3, NO_2, BrO and OClO column abundances. Results reported here focus on BrO observations performed in both stations, and on OClO measurements performed in Harestua. As described in section 3.3, a slant column model based on the BIRA-IASB photochemical box-model (PSCBOX) was set up and validated by comparison with similar models developed in other European Institutes. This model was used to interpret the BrO and OClO slant columns simultaneously measured in Harestua, confirming the ability of the model to quantitatively capture the behaviour of both species in conditions of large chlorine activation but also revealing some possible deficiencies of the model in conditions of weak activation.

4.1.2.2 Instrument updates

In early 1998 the UV-visible instrument was modified in order to optimise its performance in the UV region. A new grating and a cooled diode-array detector from Hamamatsu / Princeton Instruments were installed. The BrO spectrometer covers the region from 320 to 390 nm with a spectral resolution of 0.6 nm and a sampling ratio of 8 pixels/FWHM. A depolarising fiber optic bundle is used as entrance slit (200 microns wide).

At OHP a new home-made spectrometer with a design optimised for BrO observation was installed at OHP. This instrument consists of a thermally regulated Czerny-Turner spectrometer (J-Y TRIAX-180) equipped with a 1024 pixels Hammamatsu diode array detector cooled to -40°C. Spectra are recorded over the interval 330-390 nm with a resolution of 0.7 nm and a sampling ratio of 10 pixels/FWHM. In contrast to the instrument operated in Harestua, the OHP spectrometer has a linear polariser mounted at the entrance slit and is attached to a computer-driven rotating plate that follows the direction of polarisation of the zenith-sky. The advantages of this design are (1) to eliminate possible artefacts due to polarisation sensitive parts in the instrument (mainly the diffraction grating) and (2) to reduce the contribution of the Ring effect in twilight observations.

4.1.2.3 Stratospheric BrO

Figure 28 displays the time-series of BrO differential slant columns (DSCDs) measured from January 1998 until July 2000 at the two stations. This analysis uses daily twilight reference spectra taken at 80° of solar zenith angle (SZA), except during the months of December and January where the minimum SZA of the day (larger than 80°) is used instead. Analysis parameters were set according to the recommendations described in Aliwell et al. (2000).

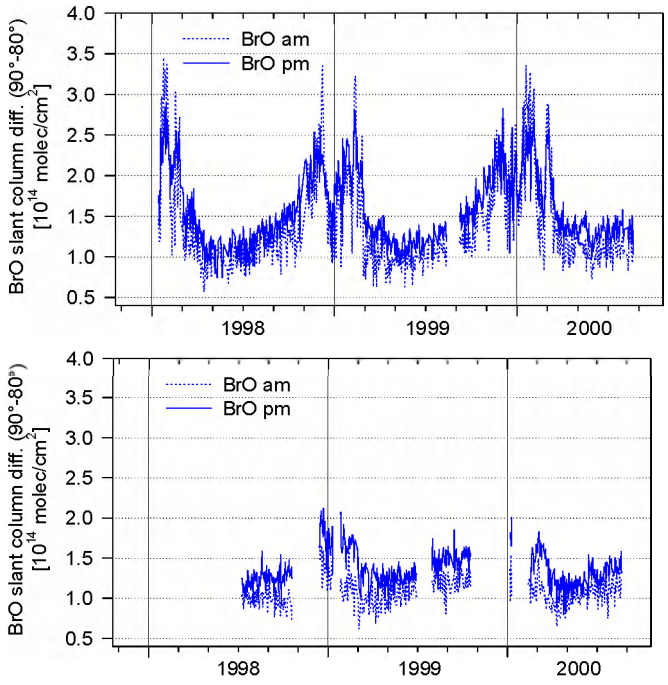

Figure 28: *Daily AM and PM BrO differential slant columns measured in Harestua (upper plot) and in OHP (lower plot) between January 1998 and July 2000.*

BrO differential slant columns are the natural product of the zenith-sky DOAS observations. The choice of the 90-80° SZA range, generally reported in previous studies (e.g., Fish et al., 1995), is done primarily to optimise the signal to noise ratio of the differential BrO absorption. This choice also presents the advantage of maximising the sensitivity of the observation to the stratospheric part of the BrO profile, due to the strong geometrical enhancement of the optical path in the stratosphere at twilight (Solomon et al., 1987) and the comparatively small variation of the tropospheric air mass factor.

A large part of the observed seasonal variation of the BrO DSCD is related to the seasonality of stratospheric NO_2 through the reaction BrO + NO_2 → $BrONO_2$, which

controls the efficiency of conversion of BrO into its nighttime reservoirs. Largest BrO DSCDs are therefore obtained in winter under denoxified conditions. It has been shown that these results are in good quantitative agreement with model simulations (Sinnhuber et al., 2000; Van Roozendael et al., 2000a).

4.1.2.4 Tropospheric BrO

It has been known for some time, that in polar spring episodes of strongly reduced boundary layer ozone occur at many locations. With the ERS-2 Global Ozone Monitoring Experiment (GOME), global BrO measurements have been made possible for the first time, and the extent of the bromine activation in polar spring has become evident. Recent comparisons of GOME BrO columns with 3D model results and with integrated stratospheric BrO profiles measured from balloons also show GOME columns systematically exceeding amounts expected for stratospheric BrO, at all latitudes and seasons. These results suggest the presence of a global background of tropospheric BrO. During this project, ground-based BrO measurements have been used to search for further evidence of BrO in the troposphere and to test for consistency with GOME observations.

One major difference between ground-based and GOME measurements is the time of the measurements: while GOME observes most locations around local noon (10h30 local time), zenith-sky measurements are usually performed during twilight when the sensitivity towards stratospheric absorbers is highest. For this reason, a direct comparison of ground-based DSCDs with GOME measurements is not possible. Two different approaches have been used to allow quantitative comparison with GOME BrO measurements, one using the Langley plot technique and the other one introducing an assumption on the tropospheric BrO column.

For an absorber without diurnal variation, the vertical column can be retrieved from zenith-sky measurements by plotting the measured slant columns as a function of air mass factor, and determining the slope of the resulting straight line. This technique is often called a Langley plot. If, however, the absorber is not constant with time, or if the air mass factor used is not appropriate, then the Langley plot will not be a straight line, but rather have a curvature. By applying the Langley plot to different solar zenith angle ranges, different vertical columns are retrieved as shown in Figure 28. In the case of BrO, the agreement between the GOME measurement and the vertical column from the Langley plot is much improved, if only small solar zenith angles are taken into account. This result can be explained in two ways: either, there is a strong diurnal variation of stratospheric BrO with a maximum at noon, or there is a substantial amount of BrO located in the troposphere. As the first possibility is in

sharp contrast to model results and independent measurements, it is assumed, that the latter explanation is correct.

A second, independent method relies on using a single background spectrum for a complete time series, in contrast to the standard evaluation, where daily background spectra are used. This technique can only be applied if the instrument is very stable. In the analysis, there is one free parameter, namely the amount of BrO in the single background spectrum. By varying this amount, systematic changes can be introduced in the seasonal variation of the BrO time series as an effect of the changing air mass factor. As demonstrated in Figure 29, assuming a tropospheric amount in the background spectrum leads to good agreement between ground-based and GOME BrO columns, whereas the assumption of a purely stratospheric BrO profile leads to unrealistic BrO columns for the ground-based instruments at both stations.

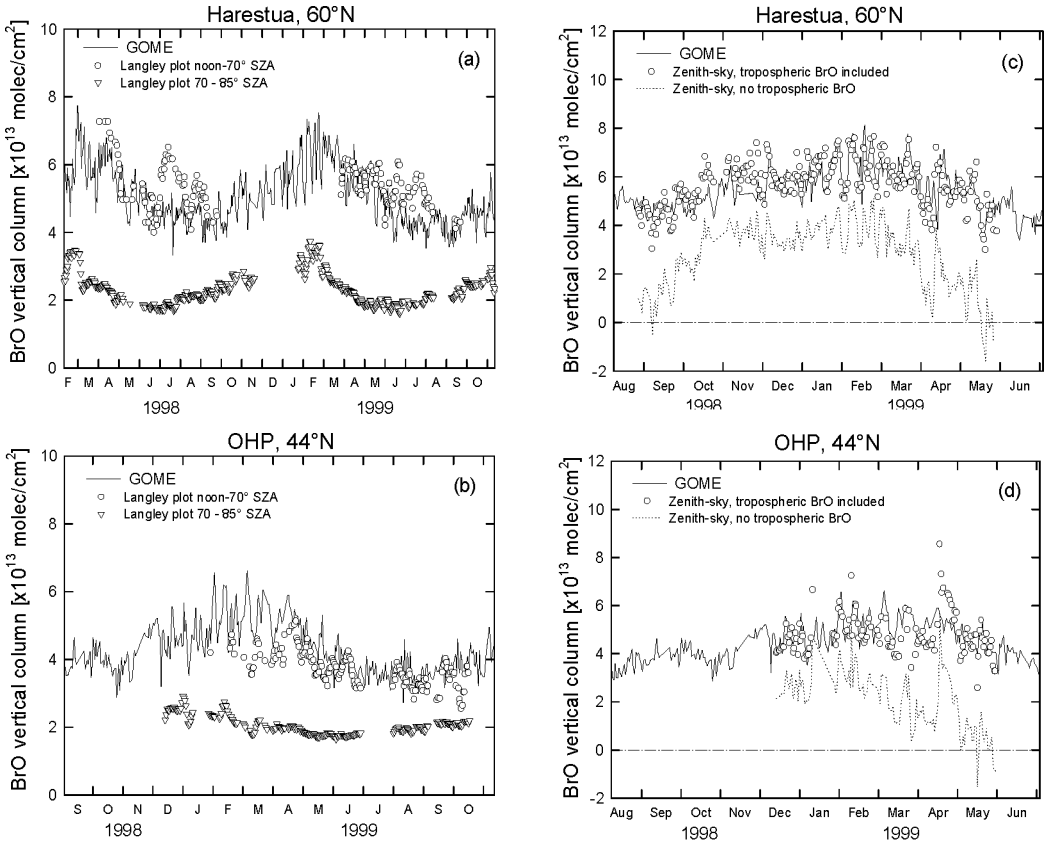

Figure 29: *GOME BrO vertical columns calculated in 500 km radius around indicated ground-based stations, compared to vertical columns derived from zenith-sky data by a Langley plot method (left panel) or from noon "GOME overpass" analyses using a seasonal reference spectrum (right panel).*

Summarising these results, good agreement is found between ground-based and GOME measurements of BrO for both the seasonal and the day to day variation, but only if a tropospheric background is assumed. The sources of this tropospheric BrO are still to be established. Although a significant contribution probably comes from to the transport of BrO plumes produced in the PBL of both polar hemispheres in spring (Wagner and Platt, 1998), it is unlikely that this mechanism can sustain large amounts of BrO over mid-latitudes in all seasons. Alternatively a production mechanism involving the inorganic bromine existing in the free-troposphere could be searched as proposed by Fitzenberger et al. (2000). Further work is needed to address this subject.

4.1.2.5 OClO observations and model simulations

OClO measurements have been performed at Harestua between January 1998 and June 2000. Important efforts have been devoted to the optimisation of the data analysis in order to lower down the detection limit. Figure 30 shows an example of optimised OClO fit obtained in the 358-380.5 nm region. During the project, the OClO (and BrO) observations performed in Harestua have been probed for consistency with current chlorine and bromine chemistry through comparison to calculations from the 3D chemical transport model SLIMCAT (Chipperfield, 1999). OClO DSCDs have been simulated using the model package PSCBOX, daily initialised with noon UT pressure, temperature, and chemical species profiles from SLIMCAT. Validation of the BIRA-IASB slant model was obtained through comparison with two other models, as described in section 3.3.2

Figure 31 shows the time-series of measured and modelled OClO DSCDs between January 1998 and June 2000. DSCDs are calculated between 92 and 80° of SZA (or 92-minimum SZA of the day if 80° is not reached). Note that events of large OClO column enhancements, observed during the winter when activated polar air masses are advected above the station, are generally well captured by the model both in time and amplitude. The comparison suggests an overestimation of modelled OClO during the winter 1998/99, possibly resulting from a dynamical effect. The time-series also clearly show the contrast between the exceptionally cold 1999/2000 winter during which numerous chlorine activation events occurred and the two previous warmer ones.

Although OClO measurements alone do not provide strong constraints on chlorine partitioning, some test on chlorine chemistry can be obtained by investigating the evolution of OClO as a function of the solar zenith angle. Figure 32 shows a comparison between observed and modeled OClO DSCDs as a function of the SZA,

for condition of large chlorine activation. As can be seen, the average agreement between the model and the measurements is excellent up to 92° SZA suggesting that chemical reactions controlling the change in OClO concentration during morning and evening twilight are well understood.

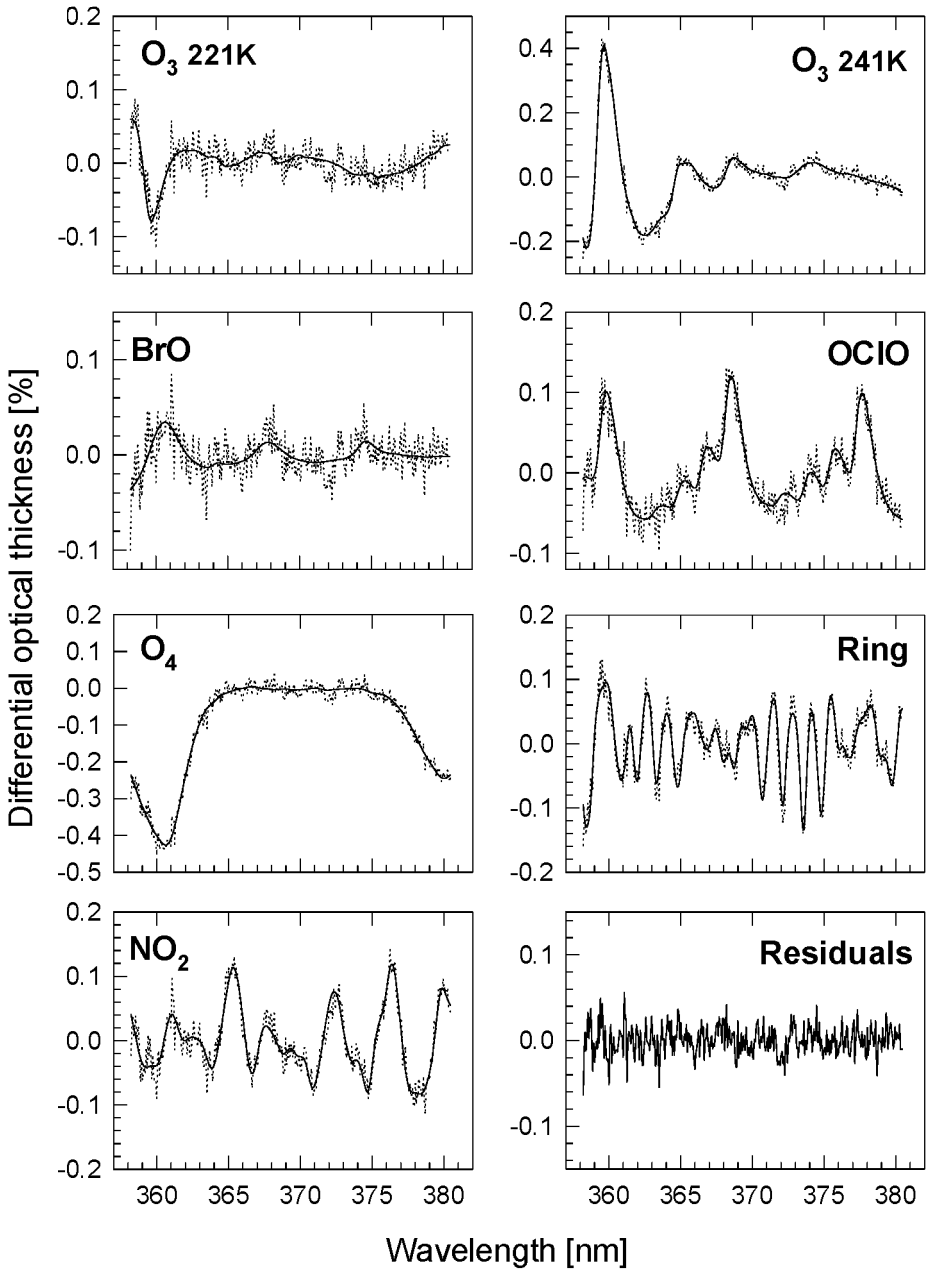

Figure 30: *Example of OClO DOAS spectral fit obtained in Harestua on 27 Jan. 2000, 90.2° SZA, PM. Calculated and measured spectra are represented by solid and dotted lines respectively.*

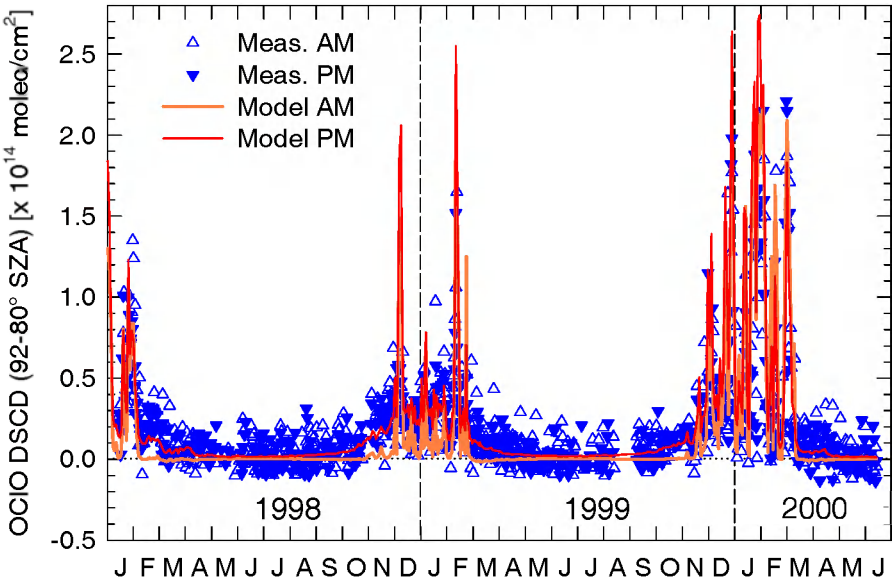

Figure 31: *Time-series of measured and modelled OClO 92-80° SZA DSCDs in Harestua for the period from January 1998 to June 2000.*

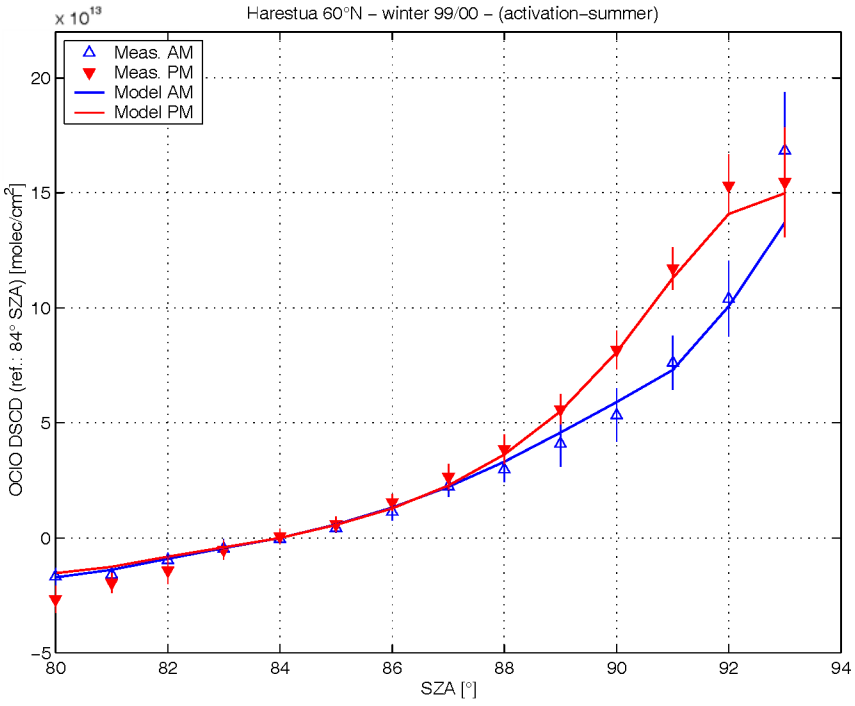

Figure 32: *Measurements and model simulations of the solar zenith angle evolution of the OClO slant columns, for conditions of large chlorine activation above Harestua (60°N).*

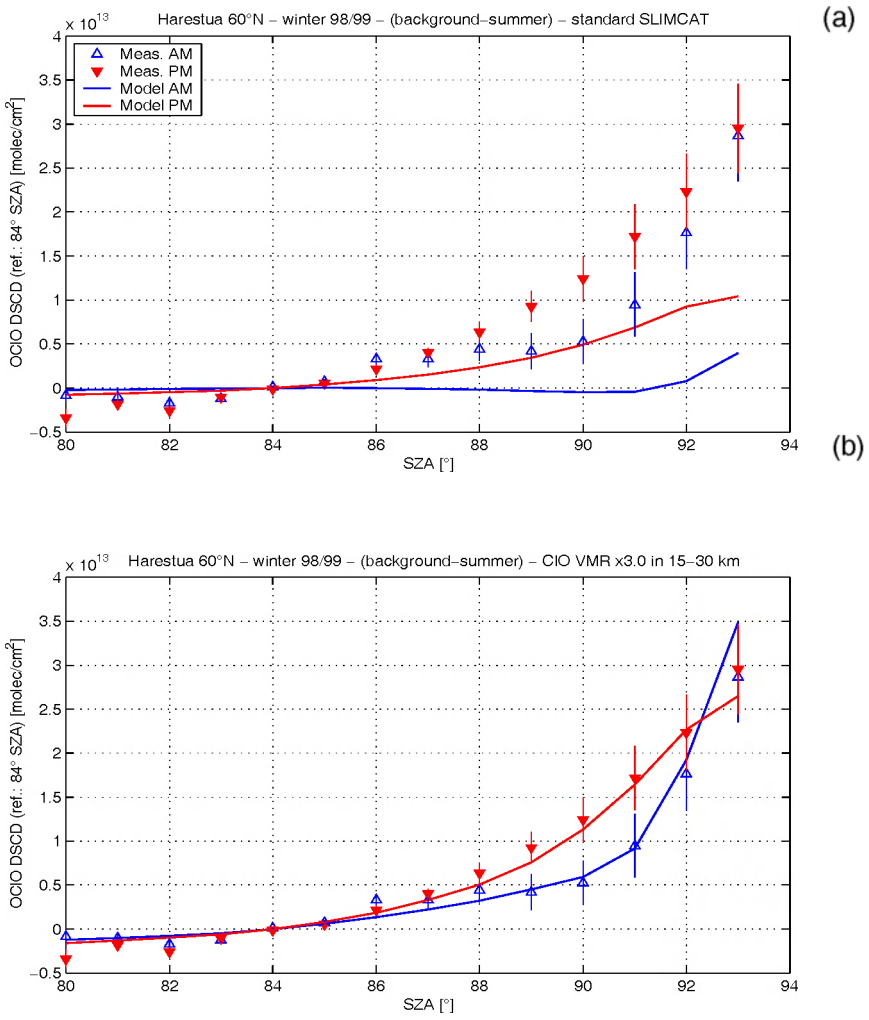

Figure 33: *Measurements and model simulations of the solar zenith angle evolution of the OClO slant columns, for conditions of weak chlorine activation above Harestua. In the upper plot, the PSC-BOX model is initialised with concentration profiles from the SLIMCAT 3D CTM model. In the lower plot, the concentration of ClO used to initialise PSC-BOX has been increased by a factor 3.*

Figure 33(a) displays a similar comparison obtained in conditions of weak activation outside of the vortex. In these conditions, the model definitely tends to underestimate the observations. Increasing the amount of ClO available to react with BrO allows to reconcile model results and measurements as shown in Figure 33(b). Work is in progress to test whether the needed ClO amounts would be consistent with in-situ measurements of ClO performed in comparable conditions during the SOLVE/THESEO 2000 campaign.

4.1.2.6 Simulations of NO_2 DSCDs at Harestua and OHP with PSCBOX

Ground-based UV-visible zenith-sky observations of NO_2 slant column densities have been performed from January 1998 through June 2000 at Harestua (60°N) and OHP (44°N). The observed time-series of 90-80° SZA NO_2 differential slant column densities (DSCDs) - which are the direct product of the DOAS analysis – have been compared to time-series calculated using the model package PSCBOX. The RT model S-DISORT in multiple scattering mode and including Mie scattering (stratospheric background conditions) has been used for these calculations. The results of this comparison are shown in Figure 34.

A good agreement between measured and calculated NO_2 DSCDs is obtained at both stations until August 1998. However, comparisons at other SZAs – which are currently under progress - are needed to conclude on the ability of the model to well reproduce the observations for this period. From September 1998 onwards, the model underestimates the observations by 20% in average. This behaviour results from a decrease of NO_2 concentrations in the SLIMCAT 12h UT profiles in this period, especially between 12 and 30 km of altitude. This feature – which is currently being investigated – seems to be related to the UKMO meteorological analyses (B.-M. Sinnhuber and M. P. Chipperfield, personal communication).

4.1.3 Long-term ozone data at Ukkel

The routine ozone measurements at KMI-IRM were continued as planned during the whole period of ESAC. These measurements comprised:

- daily measurements of the total ozone amounts with a Dobson and a Brewer spectrophotometer;
- ozone soundings three times per week (on Monday, Wednesday and Friday) by means of Vaisala radiosondes and ECC ozonesondes.

Figure 35 shows the daily variation of the total ozone amount at Uccle in 2000.

The 2000 annual mean total ozone amount was slightly higher than the long term mean.

Very low values were measured during a 2-days period, on 28 November and 29 November. These low values were mainly caused by the fact that in the altitude region between 11 and 17 km there was an intermediate layer comprising air masses with low ozone concentrations that originated from the subtropical tropopause.

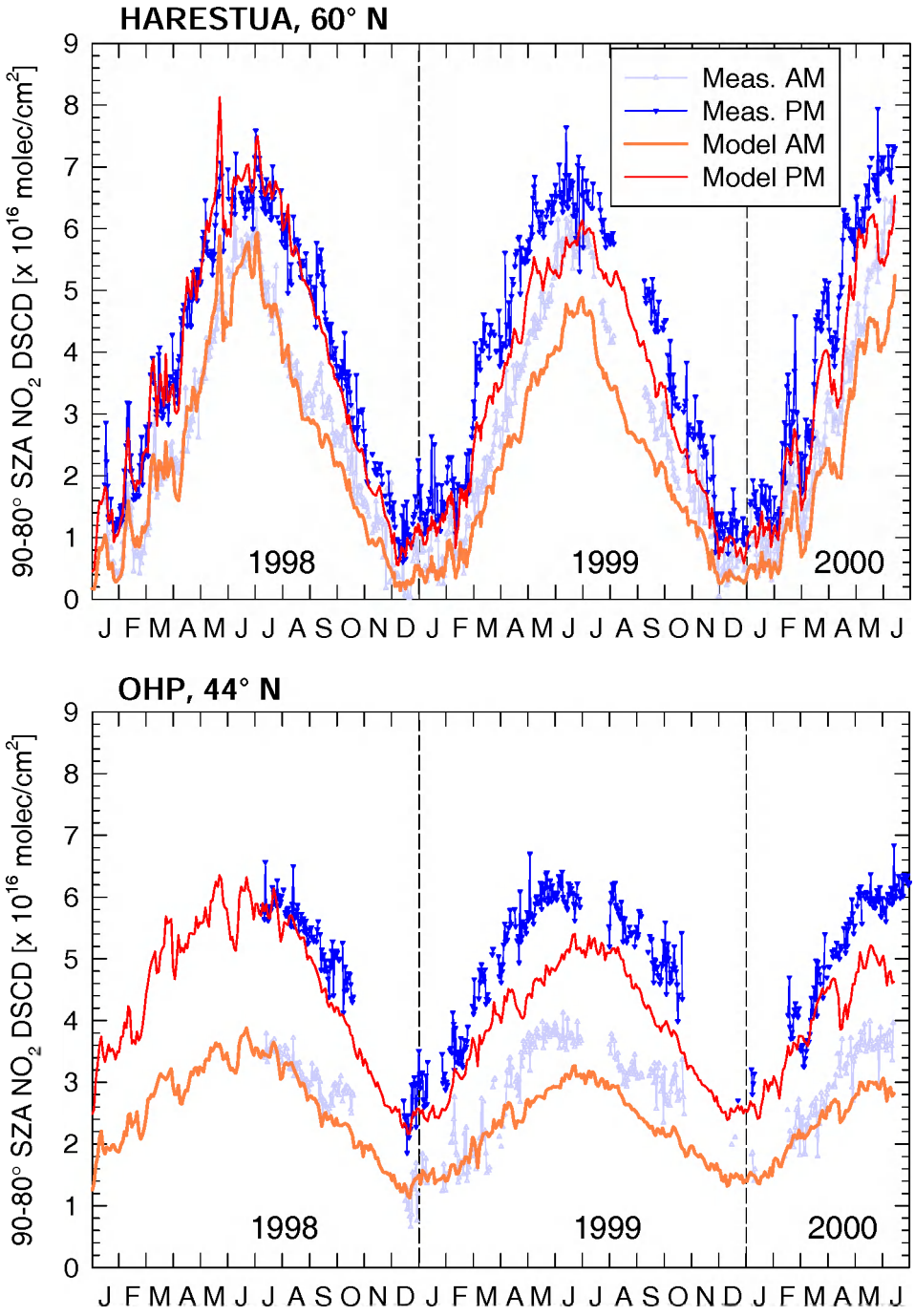

Figure 34: *Time-series of measured and calculated 90-80° SZA NO_2 DSCDs at Harestua (60°N) and OHP (44°N) for the period from January 1998 through June 2000.*

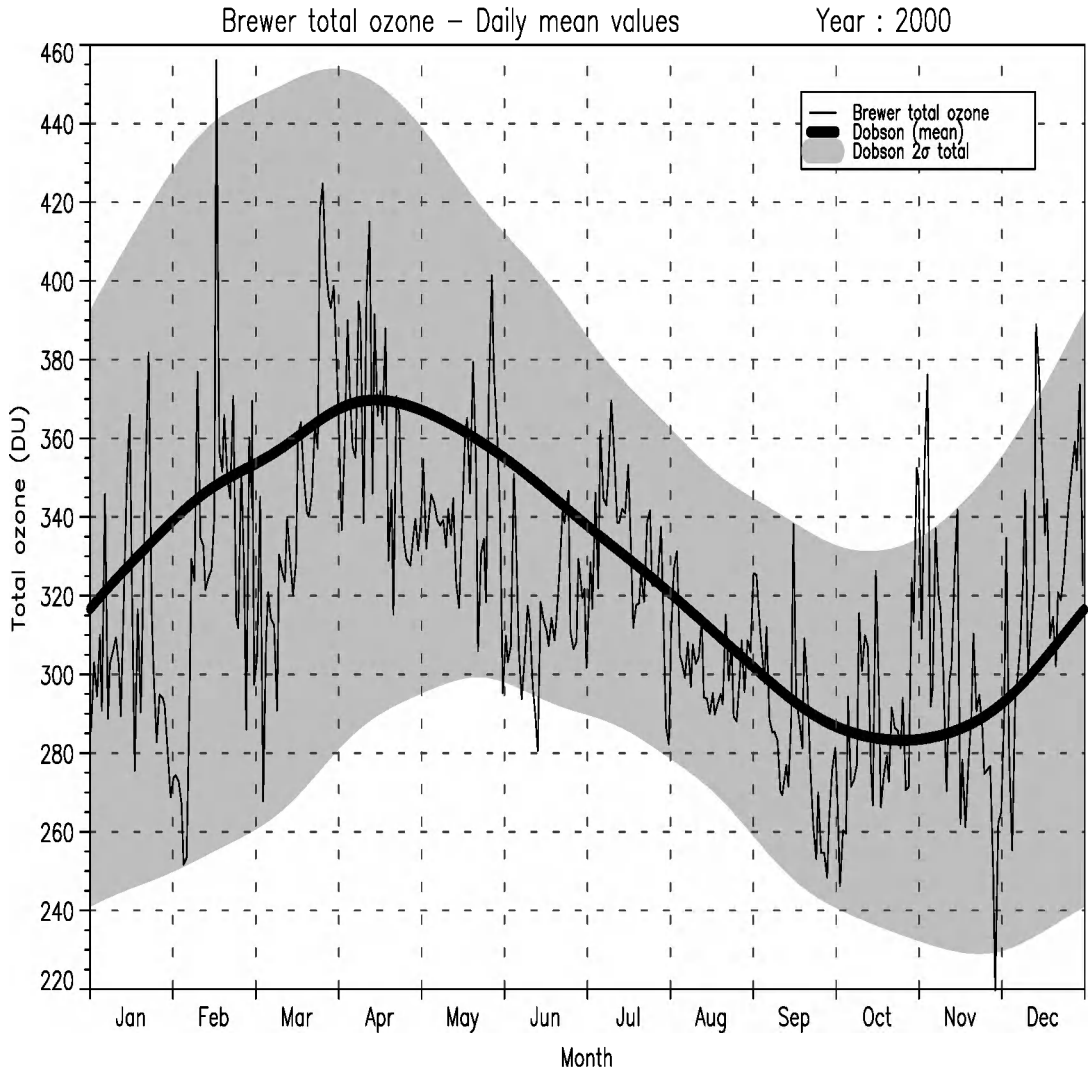

Figure 35: *Daily means of total ozone amounts measured at KMI-IRM with a Brewer spectrophotometer in 2000. The thick line shows the mean seasonal variation since the start of the total ozone observations (in 1971); the shaded area shows the 2-sigma variability over the same period.*

4.1.3.1 Data homogenisation

The homogenisation of the Uccle ozone sounding data set was finished in 1999. The corrections worked out in this study are all based on physical evidences such as changes in the equipment and changes in the operational procedures. The results were published by De Backer (1999).

In a continuous effort to improve the accuracy of the ozone measurements with the ozone sondes, the homogeneity of the time series may be lost. Post-flight processing

of the data is introduced to correct as much as possible the deficiencies of the historic observations. The main corrections applied are described below.

1. Box temperature. To convert the electronic signal of the sensor to ozone partial pressure, the temperature of the air passing through the pump is needed. This is only measured since 1990. Before that time a fixed temperature of 300K was assumed. Now the mean temperature of one year of observations is used, which reduces the ozone by about 8% at the top of the sounding (10hPa).
2. Altitude measurement. Changes in the errors in the altitude measurements cause a corresponding error in the ozone profile by shifting it up- or downward. The known altitude errors are now corrected.
3. SO_2 correction. If SO_2 is present in the air this causes an opposite signal in the ozone sensor. With the aid of measurements of a ground-based network an estimate is made of the profile of SO_2 on days of ozone soundings. This is especially important for the profiles obtained at the beginning of the time series, since at that time the concentration of SO_2 was high, and the corrections may amount to 50% and more in the lower troposphere. Since there was a spectacular downward trend in SO_2, not correcting for this effect would yield erroneous trend analyses.
4. Background current. A better preconditioning of the sondes caused a change in the background current. Again a post-flight procedure was introduced to remove this effect from the time series.
5. Pump efficiency. The standard procedure provides a mean pump efficiency profile to be used. De Backer et al. (1998) found that this procedure is not adequate for Brewer-Mast sondes and proposed a new correction profile (see chapter 3.7). This algorithm is now applied to all the ozone profiles. Also some changes in the performance of the pumps during the years have been taken into account.

A comparative study of the re-evaluated ozone sounding data with co-located ozone profiles obtained from space by the SAGE II instrument was initiated. Initial results confirm the homogeneity of the post-processed Uccle ozone sonde data. An example of results is shown in Figure 36.

The calibration level of the Brewer instrument for UV measurements was adjusted to the results obtained with new certified 50W lamps. This calibration level turned out to be consistent with a re-calibration of some of the old UV lamps during a Brewer workshop in Halkidiki in September 1998.

In May-June 2000 the calibration of the Dobson instrument nr 40 was verified during an intercomparison campaign in Hohenpeißenberg (Germany). It turned out that there was only a slight shift in the calibration level of 0.5%. This was taken into

account and this resulted in a very good agreement between the time series of total ozone obtained with the Dobson and the Brewer spectrophotometers at Uccle (Figure 37).

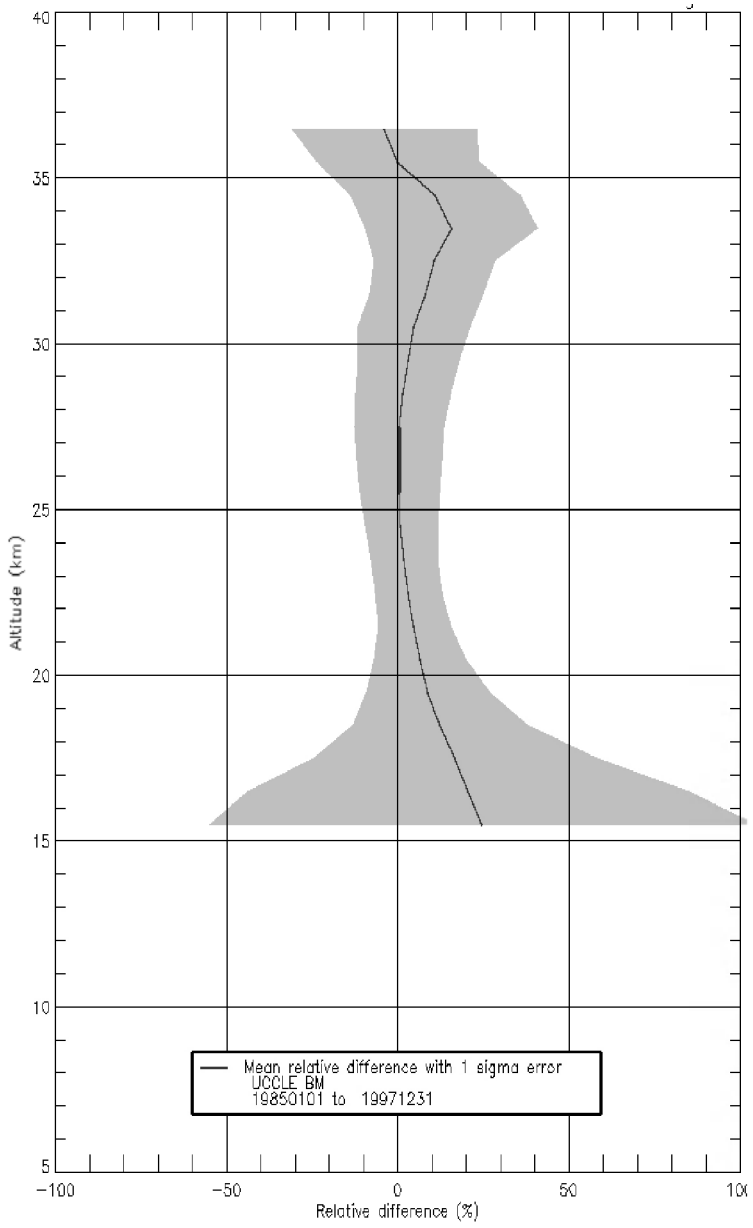

Figure 36: *Mean relative difference between colocated ozone profiles from SAGE II and from Brewer-Mast ozone sonde launches at Uccle.*

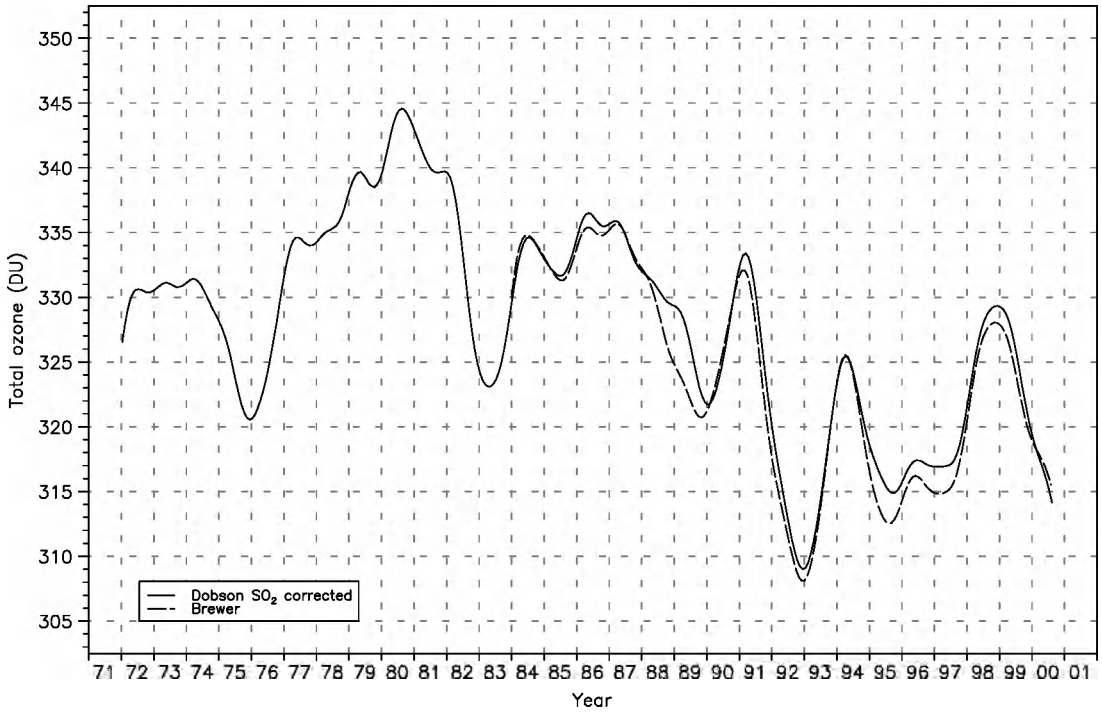

Figure 37: *Smoothed total ozone time series measured with Dobson nr 40 (full line) since 1971 and with Brewer nr 16 (dashed line) since 1983.*

4.1.3.2 Ozone trends

The re-evaluated data set of ozone soundings at Uccle from 1969 to 1996 was used for a sensitivity study of instrumental effects on calculated ozone trends. The results are shown in Figure 38. All the calculated trends are based on a least squares analysis of deseasonalized data. Results of this analysis have been presented at the EUROTRAC symposium (De Backer, 2001)

With the standard algorithm and corrections for calculation of ozone profiles from soundings with sondes of the Brewer type, the ozone trends in the middle troposphere amount to 1.2 to 1.4 %/yr; in the boundary layer the calculated trends are even larger than 2.5 %/yr (dashed line in Figure 38). In the middle stratosphere the magnitude of the negative trends shows a pronounced increase with altitude, to values of about -1.4% near mean burst level.

The SO_2 levels in the lower troposphere above the urban area of Brussels decreased rapidly in the 1970s and to a lesser extend in the 1980s. After applying a correction for the SO_2 interference on the ozone soundings at Uccle, as described by De Muer et al. (1995), the calculated ozone trends in the boundary layer are reduced by about half of the value without SO_2 correction; in the lower free troposphere trends of about

1%/yr are found (see curve with solid triangles in Figure 38). Upper tropospheric and stratospheric trends are hardly affected by this additional correction.

Before re-evaluation of the Uccle time series of ozone soundings, a jump was observed in 1989, resulting in too high ozone values in the troposphere and too low values above the ozone maximum. After application of the pump efficiency profile that was measured in the lab (and that shows much higher pump corrections than adopted in the standard profile), this jump was largely removed. This new pump correction had also a pronounced effect on the calculated ozone trends, the magnitude of the calculated negative trends in the middle stratosphere being considerably reduced. As a consequence of the normalization of the ozone profiles, the calculated ozone trends below the ozone maximum are also affected: the ozone trend profile below the ozone maximum (which is at about 22 km) is lowered, resulting in more pronounced year-round negative trends up to about -0.5%/yr in the lower stratosphere. With all corrections applied, the positive trend in the troposphere is considerably reduced and varies between 0.35 and 0.85%/yr (see solid line in Figure 38).

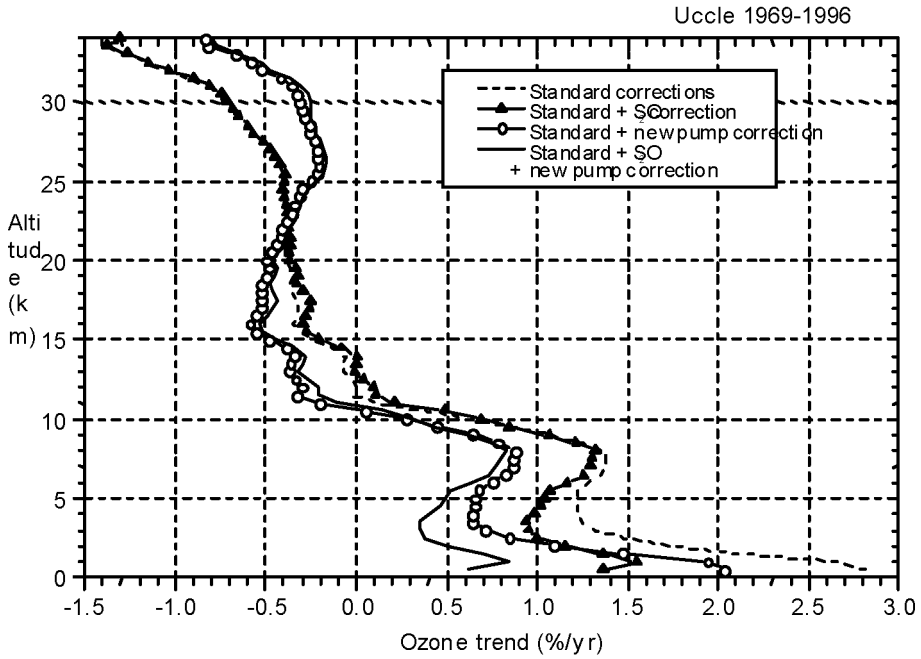

Figure 38: *Profiles of calculated ozone trends at Uccle for the period 1969-1996. The different curves are obtained with different combinations of corrections applied to the sounding data.*

The homogenised data set of ozone soundings at Uccle was subjected to a trend analysis (a least squares analysis of deseasonalized monthly means). The result is shown in Figure 39.

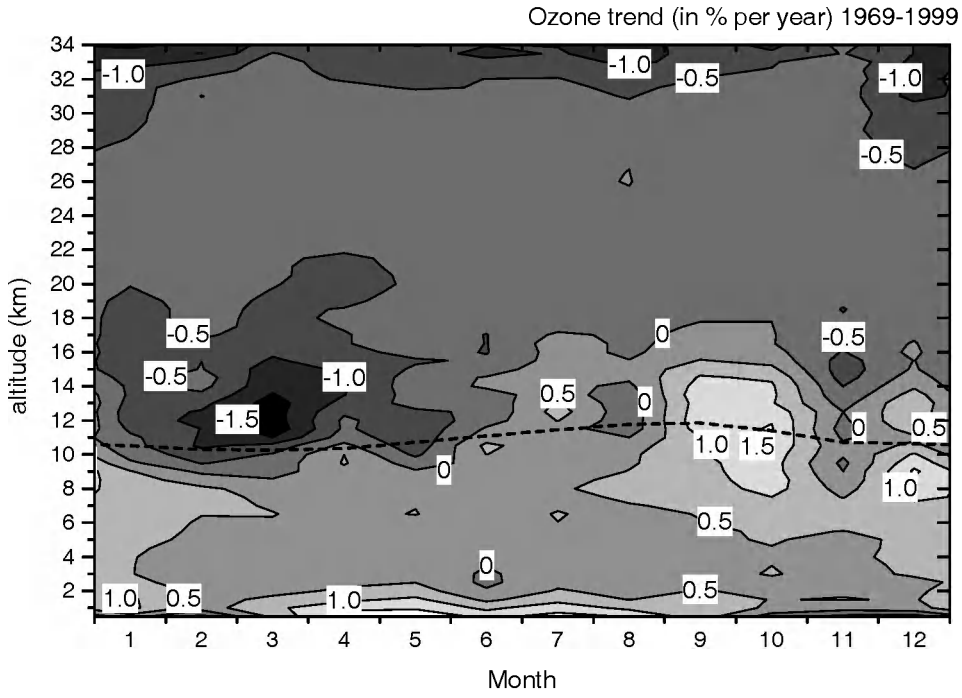

Figure 39: *Season – altitude cross section of ozone trends (in % per year) at Uccle over the period 1969-1999. Dashed line: mean tropopause level.*

The main feature is a pronounced long-term decrease of ozone in winter and spring at lower stratospheric levels.

The ozone in the free troposphere increases at nearly all levels and seasons. The ozone in the boundary layer shows a strong seasonal variation: a strong increase from March to September and a decrease during the other months.

From Figure 40 we see that at the 5 km altitude level, which is in the free troposphere, the highest ozone increases occurred in the 70s and the early 80s. Over the last 15 years there is no noticeable trend at that level.

At an altitude of 1 km, which is in the boundary layer, the situation is completely different: at that level the ozone increase is discernible at any sub-period, with the highest trends in recent years. There is no doubt that this trend (that is mainly imposed by an ozone increase in the summer months as is shown in Figure 40) is

induced by an increase of photochemical ozone production in the boundary layer. Therefore it may be a local effect that is not necessarily representative for other areas.

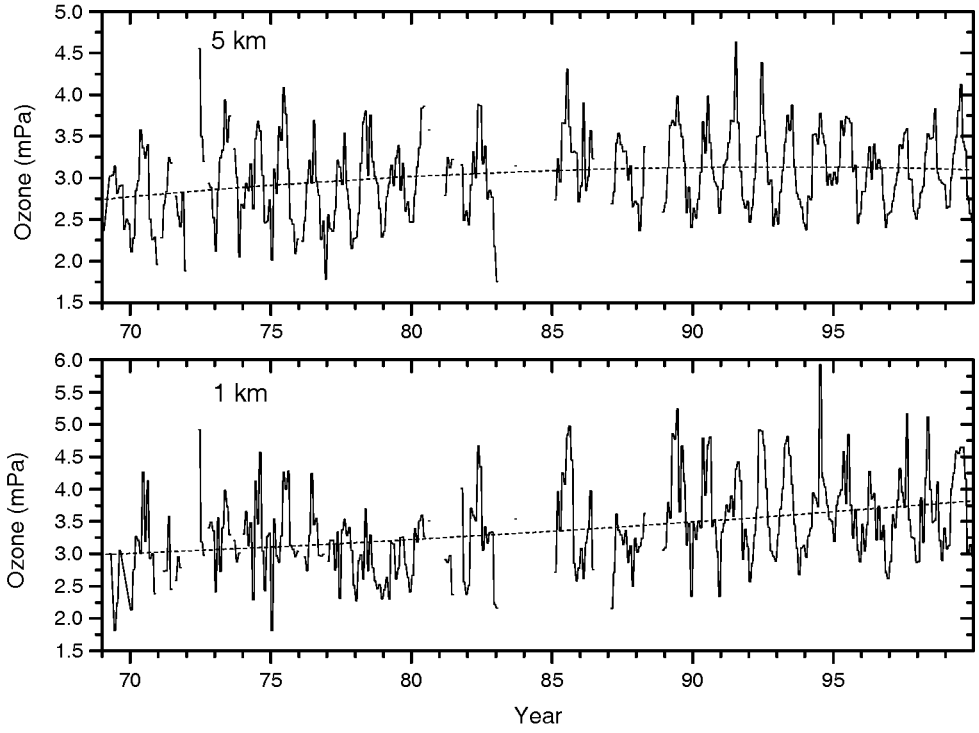

Figure 40: *Monthly means of ozone partial pressures at two tropospheric levels over Uccle. Dashed lines: 2nd order polynomial fit.*

The aim of ozone trend analyses is to examine whether there exists a systematic change in the ozone concentration throughout the atmosphere. However, these trends, if present, are small compared to the short-term weather-related fluctuations and the seasonal variation caused by the sun. Therefore, the key issue in trend analysis is to find a suitable technique to disentangle the potential long-term trend from the data. A literature study of existing techniques revealed the high effectiveness of the Kolmogorov-Zurbenko (adaptive) filter technique. We therefore started programming this filter technique which will enable us in the future to carry out a more in-depth trend analysis of the Uccle ozone sounding time series. First results are shown in Figure 41. This picture shows some anomalies around 1984.

This is probably caused by the lack of data in this period and it must be further investigated how to handle this period with missing data.

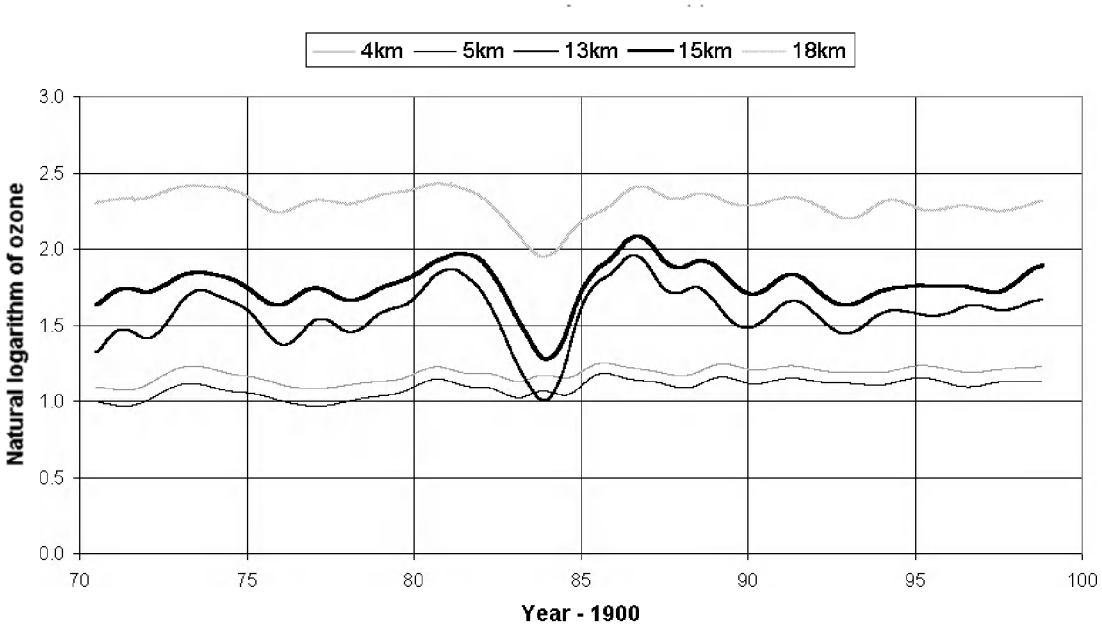

Figure 41: *Low frequency signal of the logaritm of ozone concentrations (in mPa) at Uccle, obtained with a Kolmogorov-Zurbenko filter.*

4.1.4 Synergy with satellite data

4.1.4.1 Satellite validation

TOMS and ADEOS O_3 data

Several years of total ozone measured from space by the Earth Probe TOMS (since July 1996), the ADEOS TOMS (September 1996-June 1997), and the ERS-2 GOME (since June 1995), have been compared with high-quality ground-based observations associated with the NDSC, over an extended latitude range and a variety of geophysical conditions. The comparisons with each spaceborne sensor have been combined altogether for investigating their respective solar zenith angle (SZA) dependence, dispersion, and difference of sensitivity. From the qualitative analysis of global ozone maps derived from TOMS-EP, TOMS-AD and ERS-2 GOME data, one concludes that the three spaceborne sensors capture similarly the spatial structure of the total ozone field. The comparison of the space- and ground-based time-series leads to similar conclusions for the day-to-day variability of the ozone column, under normal conditions as well as during springtime polar ozone depletion. The

quantitative comparison of time-series does not reveal any significant long-term drift. Although mutually consistent within a few percent, systematic differences are observed between TOMS-AD and TOMS-EP total ozone. They might be attributed partly to air mass differences in time (the orbits of ADEOS and Earth Probe are different) and in space (the lines of sight and resulting ground pixels are different), and partly to calibration uncertainties. No significant difference is observed between TOMS-AD data prior to and after the recent re-calibration performed at NASA/GSFC.

After properly taking into account the known biases of the ground-based total ozone time-series (e.g., seasonal/latitudinal variation in real-time SAOZ data, or temperature dependence of the ozone absorption coefficients for the Dobson and Brewer instruments), comparisons between satellite and different ground-based observations generally are consistent within the accuracy level of the ground-based data. A consistency by latitude belt is also noticed. The average agreement between the TOMS and ground-based total ozone is better than ±2-3% at northern middle latitudes. The agreement at higher latitudes depends on the SZA. At low and moderate SZA, the TOMS instruments report in the Arctic larger total ozone values by 3-5% on average in summer-fall, while the agreement is better in wintertime. Beyond 80° SZA, the TOMS columns are smaller by 5-10% on average. A SZA dependence similar in shape and amplitude is observed in Antarctica, but there the mean relative difference is dominated by the systematic bias described in the next paragraph. The shape of the SZA dependence does not vary with the season. The most striking feature of both TOMS-EP and TOMS-AD total ozone data is the pseudo interhemispheric difference of their agreement with ground-based observations as well as with ERS-2 GOME data. At the southern Tropics, a small difference of sensitivity appears compared to the SAOZ.

The pole-to-pole comparison confirms the clear north/south difference already reported in the agreement between the TOMS and ground-based data. While the agreement is reasonable in the northern hemisphere, both TOMS-EP and TOMS-AD are reporting larger ozone columns in the southern hemisphere. At low and middle latitudes, the overestimation of ground-based data by TOMS is about 4-8% on average. At the three stations around the Antarctic polar circle, the agreement is better in winter likely because of the SZA dependence as observed in the Arctic, however, a systematic bias of 6-10% appears after September as the SZA decreases. The bias does not vanish in summer, that is, when both Dobson and SAOZ data are expected to be the most accurate. At the high Antarctic site of Halley, a permanent offset of 8-12% is observed from early spring through late fall. The recent re-calibration and subsequent reprocessing of the entire TOMS-AD data record does not yield much improvement. GOME data exhibit cyclic signatures

compared to ground-based data, but show no evidence of a year-round systematic offset as that reported with TOMS data. It must be pointed out that, although representative of a variety of relevant geophysical conditions, the distribution of ground-based stations used in the present study does not allow to determine whether the difference is really interhemispheric, or changing with the latitude in a more complex way, e.g., with the latitude belts defined in the TOMS V7 algorithm.

Possible causes have already been proposed, but further research is still required. An interhemispheric difference might arise from the climatology of ozone and temperature profiles used in the TOMS V7 algorithm, possibly biased towards the northern hemisphere, and poorly represented at polar latitudes. The interhemispheric consistency of the comparison with GOME seems to indicate a separate treatment of each hemisphere. At Antarctic stations, both the cloud cover fraction derived from GOME and the reflectivity derived from TOMS indicate an almost permanent overcast. The tropospheric contribution to the satellite measurement is partly masked and a climatological ozone profile below clouds must be used, which can also introduce an offset in the satellite data. Errors of the TOMS calibration in the southern hemisphere can not be excluded, however, as already mentioned, the recent re-calibration of TOMS-AD data does not modify the results.

To conclude, the global picture of total ozone provided by the three spaceborne sensors studied in this work is globally consistent with high-quality ground-based observations associated with the NDSC. No long-term drift can be detected after several years of operation. However, various discrepancies are identified or confirmed, that could impact the scientific interpretation of satellite data: (i) a SZA dependence with TOMS beyond 80° SZA; (ii) a north/south difference of TOMS with the ground-based observations; (iii) and a difference of sensitivity to low total ozone values between satellite and SAOZ sensors around the southern tropics. The recent re-calibration of the whole TOMS-AD data record does not attenuate its interhemispheric bias. Further investigations are required to understand the discrepancies.

Geophysical consistency of stratospheric NO_2 measurements

Several sensors operating from space, balloon and the ground monitor the column abundance and vertical distribution of stratospheric NO_2. Within the framework of the international Network for the Detection of Stratospheric Change (NDSC), the vertical column abundance of sunrise and sunset NO_2 is monitored from pole to pole by a network of ground-based UV-visible spectrometers, including several BIRA-IASB instruments. The HALogen Occultation Experiment (HALOE) aboard NASA's UARS

satellite measures stratospheric NO_2 profiles at sunrise and sunset, extending ground-based results to the global domain. The nadir-viewing ESA's ERS-2 Global Ozone Monitoring Experiment (GOME) monitors the vertical column amount of mid-morning NO_2.

In the present study, the geophysical consistency of those three complementary components of the multi-platform observing system for atmospheric NO_2 have been examined at a number of NDSC stations, including Jungfraujoch and Harestua as illustrated in Figure 42 as well as stations at other latitudes (see e.g. Figure 43). The investigation relies on correlative studies of measurement data records under a variety of geophysical conditions. Results have been interpreted in the light of information provided by the chemical transport model of the troposphere IMAGES. In particular, to derive HALOE vertical columns, HALOE profiles have been integrated over the stratosphere and extended towards the ground using a tropospheric content estimated by IMAGES, also depicted in Figure 42.

The study concludes to a reasonable geophysical consistency of stratospheric measurements. All instruments capture similarly major features such as post-Pinatubo recovery of stratospheric NO_2, annual variation, other low-frequency periodic signals (e.g., Southern Atlantic Oscillation and Quasi-Biennial Oscillation), wintertime polar denoxification, and dawn-to-dusk diurnal variation. In general, ground-based UV-visible spectrometers and HALOE report a similar day-to-day scatter. GOME data are somewhat more scattered. Most of outlying GOME data observed at the Jungfraujoch – where ground-based UV-visible data have been filtered out – are indicative of enhanced tropospheric NO_2 to which the GOME measurement is highly sensitive. Despite the reasonable general agreement, the study also highlights some discrepancies such as those observed between sunset measurements in the subtropics. It also raises some issues such as the possible enhanced NO_2 observed by HALOE under midnight sun.

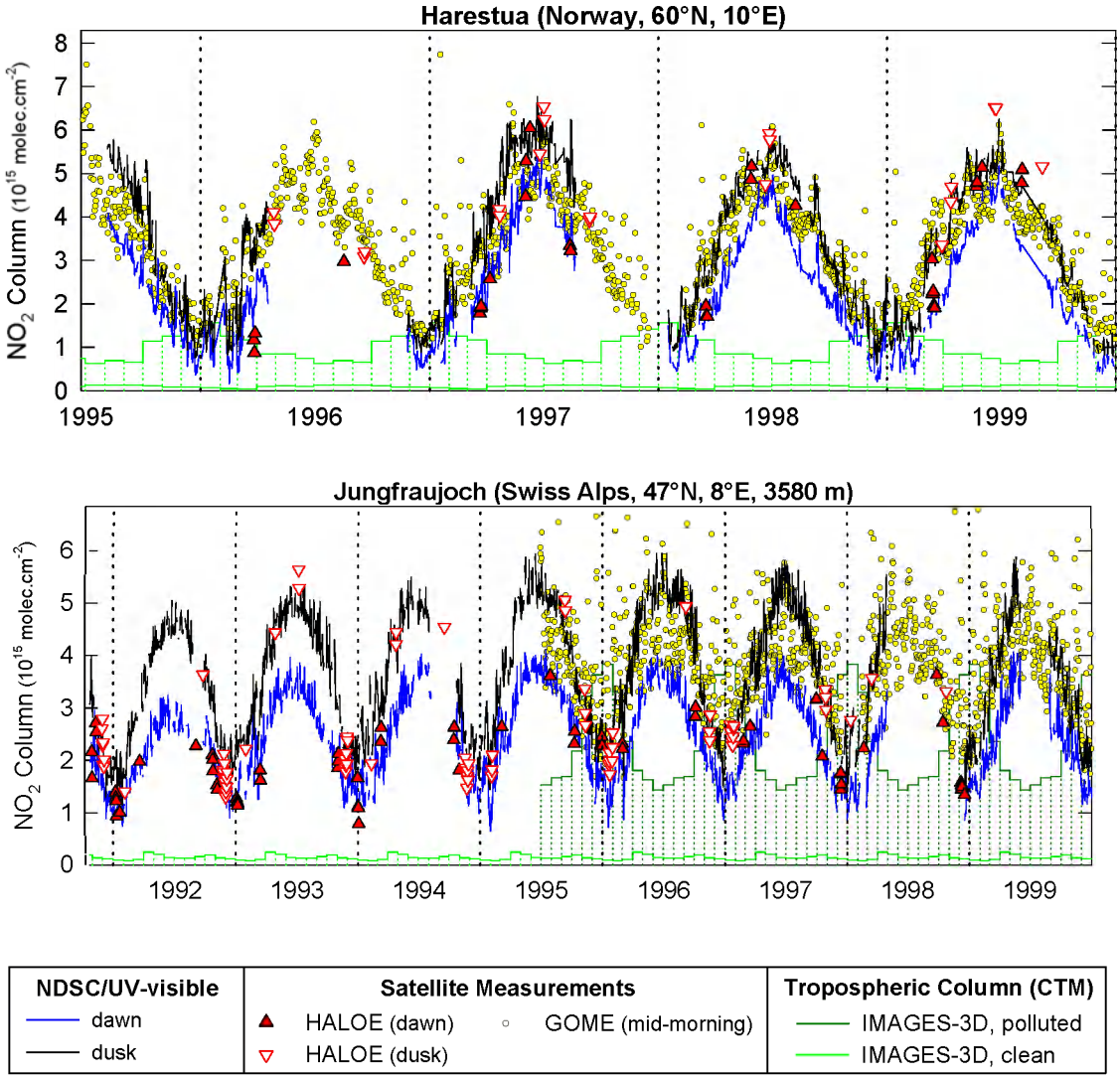

Figure 42: *NO_2 column time-series at Harestua (1995-1999) and Jungfraujoch (1991-1999) as derived from measurements acquired by BIRA-IASB and SAOZ UV-visible spectrometers, HALOE v19, and GOME GDP2.7. Bar plots show modelled tropospheric contents representative of clean and polluted conditions, respectively.*

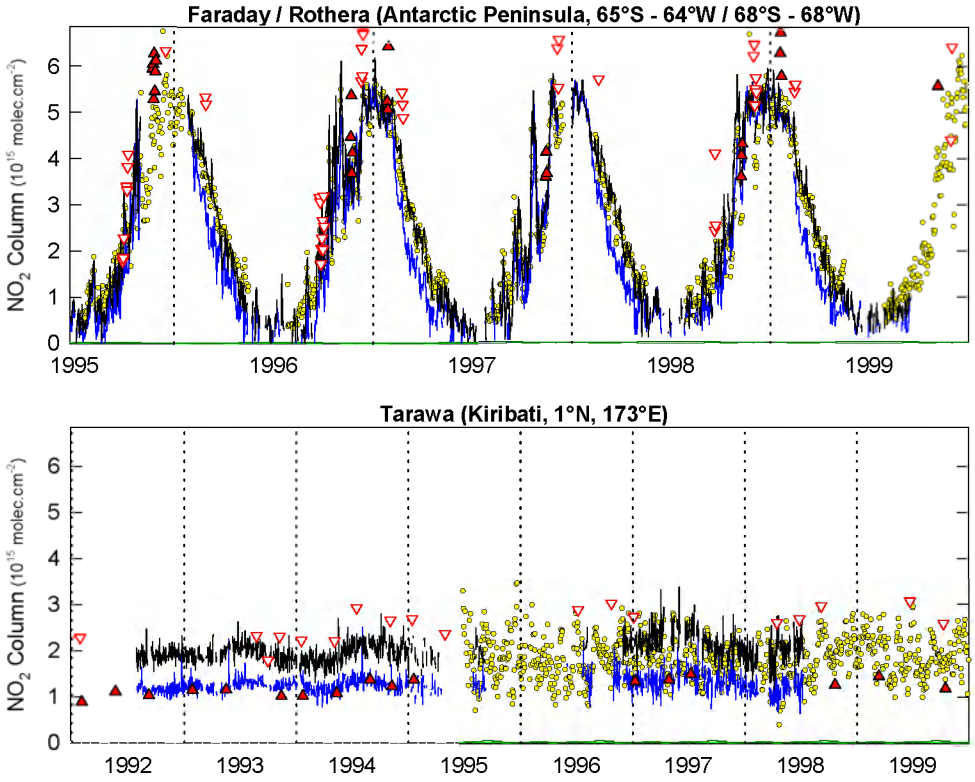

Figure 43: *Same as in Figure 42, but at Rothera in Antarctica (1995-1999) and at Tarawa on the Equator (1992-1999).*

4.1.4.2 Development of an NO_2 vertical profile climatology

Within the framework of the NDSC, the vertical column abundance of sunrise and sunset NO_2 is monitored from pole to pole by a network of ground-based UV-visible spectrometers. Slant column amounts derived from the measurement of the zenith-scattered sunlight at twilight are converted into vertical columns using an optical enhancement factor, or air mass factor (AMF). AMFs are calculated with a radiative transfer model assuming the vertical distributions of NO_2 and of radiatively active atmospheric parameters. Current NO_2 AMFs are based on a basic reference atmosphere. Previous studies have raised the issue of the AMF sensitivity to the profile shape of NO_2 and of other atmospheric parameters. In this study, the sensitivity of NO_2 AMF towards a variety of inputs has been studied in order to identify the critical parameters that have to be improved for better accuracy of the data products.

As a first step, AMF from 4 different radiative transfer models (see Table III) were compared for the case of a pure Rayleigh atmosphere. Carried out in collaboration with three other research institutes involved in UV-visible spectrometry (CNRS, NILU, and U. Bremen), the purpose of this test is to detect discrepancies between the models and problems with synchronising the input. The four NO_2 AMFs are plotted in Figure 44, arbitrarily normalised to the SAOZ standard AMF. The differences between the models are in the order of 1% and even smaller below 90° SZA, showing that no further model tests are necessary at this point.

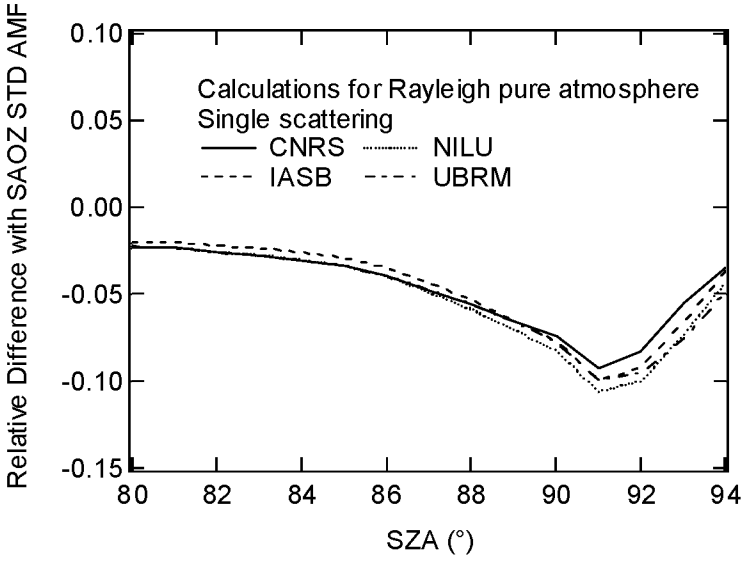

Figure 44: *Normalised NO_2 Air Mass Factors from 4 different radiative transfer models for a pure Rayleigh atmosphere. The differences are small for all SZA and negligible below 90° SZA.*

Table III*: Legend to the plots in Figure 45. The AMF for Haute Provence (OHP) have been added as they have been used for the SCUVS intercomparison campaign at OHP in June 1996 and have to be compared to the improved AMFs computed in this study using vertical profiles appropriate for this time and location.*

SSC	SSA	MSC	MSA	OHP	STD
Single Scattering Calculations	Single Scattering with Aerosol	Multiple Scattering Calculations	Multiple Scattering with Aerosol	AMF used in June 1996 at OHP (SCUVS)	AMF used in the instrument in real time

The sensitivity of the NO_2 AMF has been investigated further towards changes in the assumptions of the radiative transfer. Six different scenarios, of which details are described in Table III, have been analysed with all models. The resulting AMFs are depicted in Figure 45. All models agree very well for all scenarios. Inclusion of multiple scattering increases the AMF at all solar zenith angles (SZA), while accounting for aerosol scattering leads to increases at large SZA only. Changes in surface albedo were found to be negligible for twilight conditions but induce changes of up to 1.5% at high sun. All scenarios are significantly different from the SAOZ standard AMF at 90° SZA, emphasising the need for improvements in NO_2 AMF.

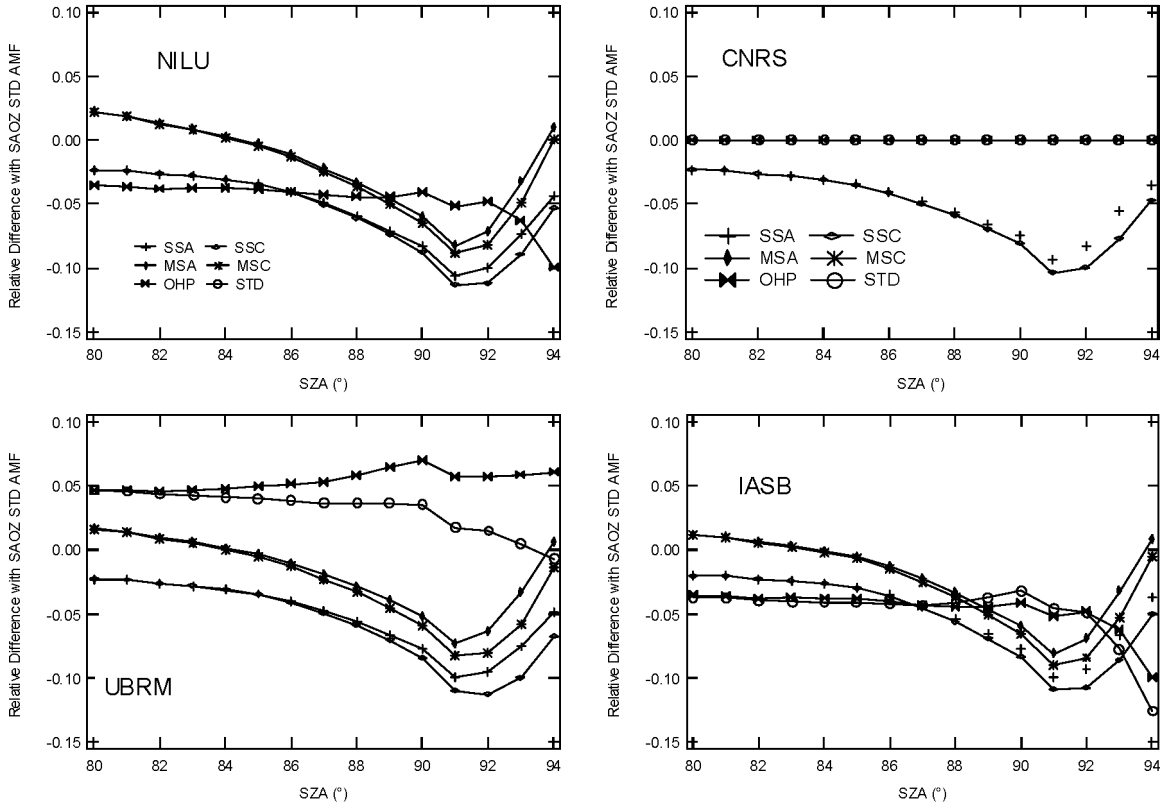

Figure 45: *Influence of multiple scattering, stratospheric aerosols, and profile assumptions on arbitrarily normalised AMF to the SAOZ standard AMF. See Table III for details on the scenarios.*

As a second step, an improved NO_2 reference atmosphere has built up. A perturbation study has revealed that the AMF sensitivity is highest for NO_2 changes in the stratosphere between 20 and 35 km and in the troposphere below 5 km. Accordingly, a climatological model of NO_2 profiles has been derived from measurements from space (UARS HALOE), balloon (SAOZ-balloon) and the ground (NDSC/UV-visible network), and complemented by modelling results (IMAGES). The resulting NO_2 profile climatology covers altitudes from the ground up to 70 km. The

principle of this composite database is illustrated in Figure 46 The mutual consistency of the various databases has been investigated carefully and has led to the validation of NO_2 stratospheric columns as derived from the integration of HALOE profile measurements.

As a third step, the new NO_2 reference atmosphere has been combined with pressure, temperature and ozone climatological databases in order to investigate possible periodic signatures in the AMF related to seasonal, latitudinal, and sunrise/sunset change of the vertical distribution of NO_2, pressure, temperature, and ozone. The study highlights periodic signatures in the AMF which need to be taken into account when retrieving NO_2 vertical columns from ground-based observations of zenith-scattered sunlight. Figure 47 shows that, in general, the AMF based on the US Standard Atmosphere would yield an underestimation of the retrieved vertical columns in the northern hemisphere and an overestimation at southern middle and high latitudes. The bias would exceed 10% in denoxification conditions in polar winter. The US Standard AMF exhibits a seasonal variation, which grows from a few percent in the tropics, up to about 5-6% at middle latitudes and 8-10% at high latitudes. The dawn-to- dusk photochemical variation of stratospheric NO_2 affects the AMF by a few percent, sunset AMFs being generally larger than sunrise AMFs.

In conclusion, sensitivity studies have been performed to identify critical parameters in the NO_2 AMF calculation. A model intercomparison showed excellent agreement between 4 models used in the international NDSC/UV-visible community. Multiple scattering and to a lesser degree aerosol loading increase NO_2 AMFs, tropospheric contributions on the other haFnd decrease it. Changes in the vertical profiles of temperature, pressure, ozone, and NO_2 mixing ratio lead to a seasonal variation of NO_2 AMF, but the magnitude depends on the NO_2 profile shape. All tests show, that the use of current standard AMF for NO_2 is not acceptable, and that more sophisticated approaches have to be used to improve the accuracy of NO_2 columns from zenith-sky measurements.

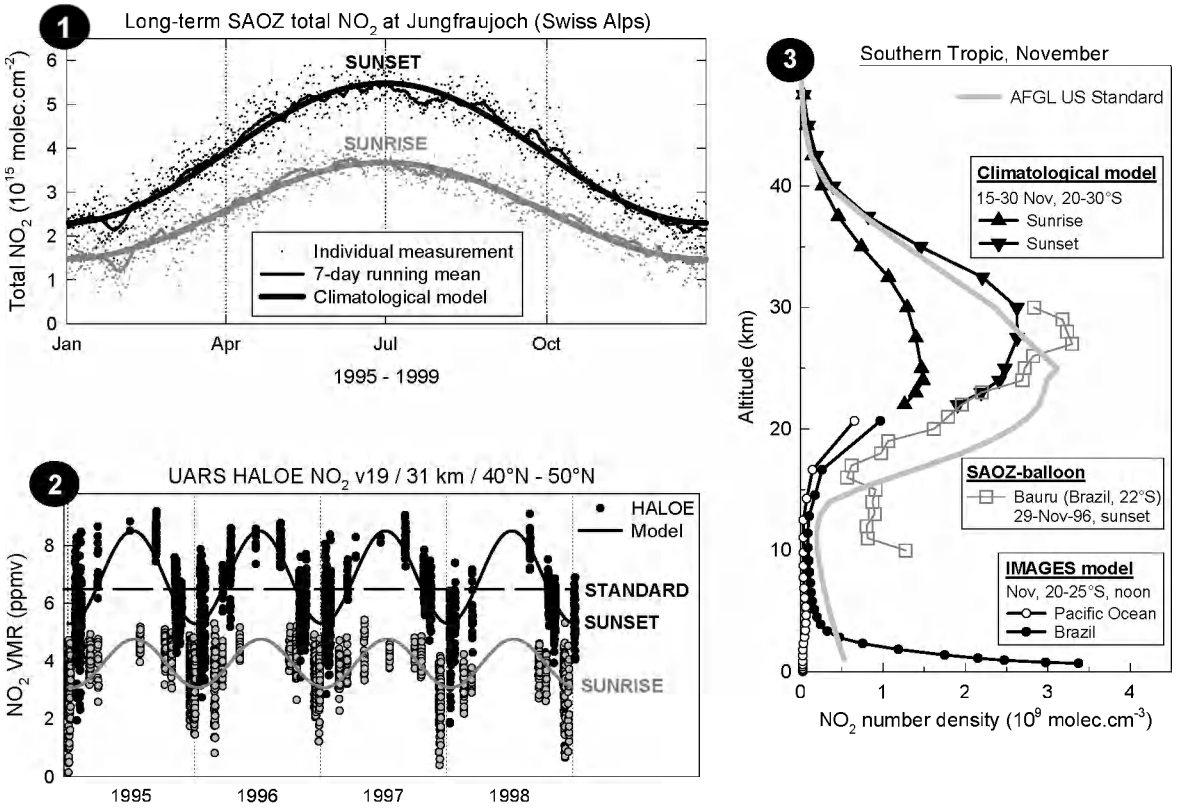

Figure 46: *Construction of the composite NO_2 profile database: (1) ground-based determination of climatological characteristics of stratospheric NO_2; (2) at each altitude, fitting of HALOE data with functions inspired from the ground-based characteristics; (3) use of IMAGES model results and SAOZ-balloon observations to complete the profile down to the ground. US Standard Atmosphere values are depicted for comparison.*

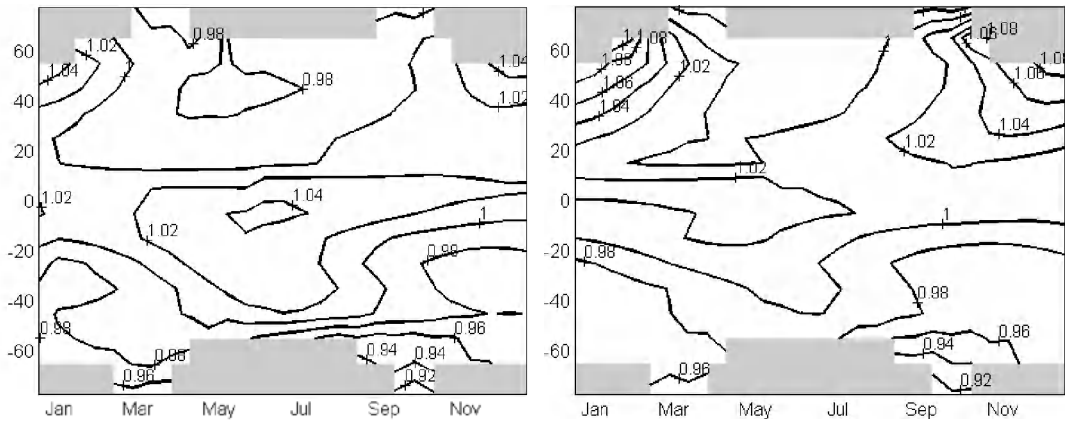

Figure 47: *Seasonal, latitudinal, and sunrise/sunset variation of NO_2 air mass factors: ratio of NO_2 AMFs at 90°SZA calculated with the US Standard and the climatological NO_2 profiles for a sunrise (left) and a sunset (right) stratosphere and a clean troposphere.*

4.1.4.3 ATMOS-related research

The ATMOS (Atmospheric Trace Molecule Spectroscopy) instrument is a fast-scanning, fast-response and high-resolution FTIR spectrometer that operates from space in the solar occultation mode over the 2.1 to 15 □m (4800 to 650 cm^{-1}) infrared domain. As a core experiment of the NASA-Spacelab and ATLAS (ATmospheric Laboratory for Applications and Science) programmes, the ATMOS instrument took part in the Spacelab-3 (SL-3; Challenger shuttle; 29 April- 7 May 1985), ATLAS-1 (AT-1; Atlantis; 24 March-3 April 1992), ATLAS-2 (AT-2; Discovery; 8-16 April 1993) and ATLAS-3 (AT-3; Atlantis; 3-14 November 1994) missions. During these missions, it performed altogether measurements over 480 complete occultations, about half of which were sunrises and the others sunsets, spanning latitudes from about 65°N to 73°S. Until about 1995, the data processing and analysis method adopted for the inversion of the ATMOS solar occultation measurements into geophysical parameters followed the procedure described by Norton and Rinsland (1991), making use of the "ODS" (for Occultation Display Spectra) retrieval code specifically developed for ATMOS and based on the "onion peeling" approach, with the individual spectra being investigated successively for each target gas and each chosen characteristic absorption feature (microwindow), in a top-to-bottom retrieval sequence. The data base resulting from the consistent analysis of all four ATMOS missions with ODS was called "Version 2" (abbreviated hereafter as V2). An important aspect of spectroscopic remote sensing of the atmosphere by the solar occultation method from space is the precision and accuracy with which related measurements can be made (Abrams et al., 1996a). Considering the methodology and input parameters adopted along the data processing and inversion, these have been determined for all individual VMR profiles of the V2 data base (Abrams et al., 1996b) which is publicly available at ftp://remus.jpl.nasa.gov/pub/atmos/version2.

The "ODS" procedure was slow and did not take advantage of simultaneous, multiple microwindows fittings, and its automatic operation in the "spectra after spectra" onion-peeling mode generally failed in the inversion of observation into geophysical parameters below about 16 km (~ 100 mb pressure level; e.g., Zander et al., 1996), although many occultations showed high quality spectra recorded by ATMOS well below that altitude.

The ATMOS "Version 3" geophysical data

Within the ESAC research context reported about here, our main task was to contribute, as ATMOS Science Team partner, to the production of an "ATMOS-Version-3" set of volume mixing ratio profiles that would extend reliably to lower altitudes, down into the free troposphere, and to inter-compare such profiles with

independent measurements from other space- and ground-based instruments. Here below, Version-2 and Version-3 will be abbreviated by V2 and V3, respectively.

Following a Science Team meeting and numerous teleconferences, it was decided to implement the GFIT retrieval code which itself was an adaptation of "ODS" but specifically developed at the Jet Propulsion Laboratory (Pasadena, CA, USA) for the analysis of MkIV-balloon observations (Toon et al., 1999). This batch-automated code allows to fit numerous (target- and interfering-) species simultaneously, using various sets of microwindows, and treating all spectra of an occultation at once. The main benefits resulting from this adaptation include (i) the extension of retrieved concentration profiles to lower altitudes, well into the free troposphere, (ii) the retrieval of a couple of additional species such as CH_2O and HOCl, and (iii) a more reliable evaluation of the statistical uncertainties (precision) affecting the VMR profiles at all altitudes. During 1998-99, the V3 data base has undergone quantitative evaluations with respect to V2 (at least over overlapping altitude ranges) and versus data produced by other space-based instruments such as MAS (Millimeter-wave Atmospheric Sounder), HALOE (Halogen Occultation Experiment) and MLS (Microwave Limb Sounder), also with measurements performed by experiments aboard the NASA ER-2 airplane and the MkIV-balloon FTIR spectrometer (e.g., Toon et al., 1999). The V3 database includes profiles regarding all four ATMOS missions performed between 1985 and 1994.

Typical examples of the V3 profile retrievals with GFIT, to which ULg has contributed significantly are reported hereafter. Figure 48 displays the profiles of the various constituents intervening in the evaluation of the total chlorine loading versus altitude at the time of the ATMOS/ATLAS-3 mission of November 1994, for the northern mid-latitude zone spanning 35 to 49ºN. With the exception of $C_2Cl_3F_3$, CH_3CCl_3, COClF and ClO, all other contributing species are derived from the ATMOS-FTIR solar occultation observations. The important contributors to the organic Cl inventory in the upper troposphere (e.g., CCl_2F_2, CH_3Cl, CCl_3F, $CHClF_2$, CCl_4) appear to be properly retrieved with the GFIT algorithm; these free tropospheric concentrations are in good agreement with related concentrations made independently at the ground by *in situ* networks (see the square symbols on the lower frame of Figure 48) at the time of the AT-3 mission. The horizontal arrow indicates the altitude above which the chlorine budget was evaluated and reported on the basis of the V2 retrieval data (Zander et al., 1996).

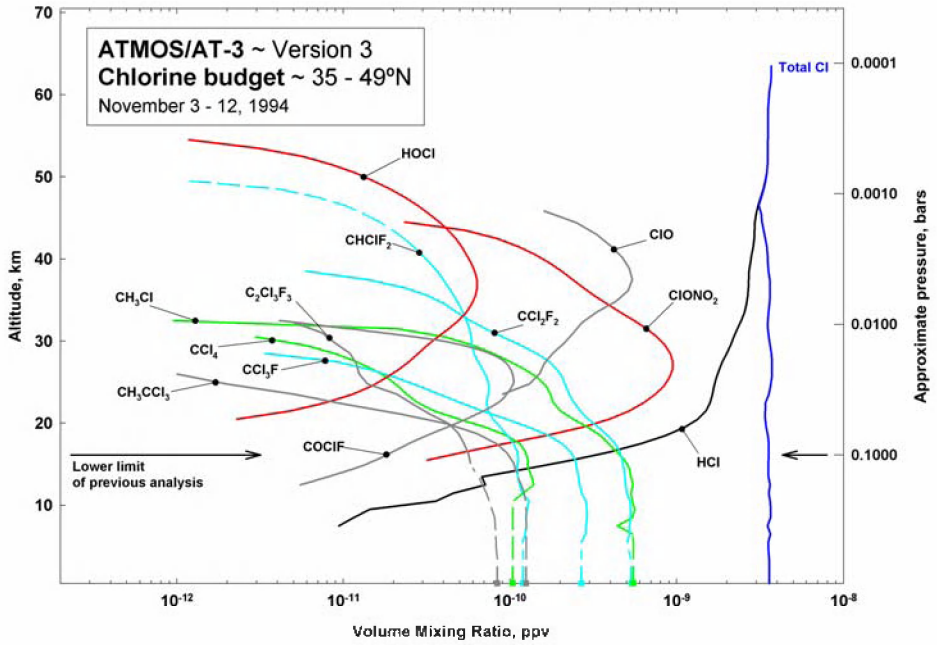

Figure 48: *The chlorine budget of the upper troposphere and stratosphere as derived for northern mid-latitudes in November 1994. It includes all important chlorinated gases (sources, sinks and reservoirs combined) observed by ATMOS during the ATLAS 3 shuttle mission, as well as a few complementary species (grey traces) measured by other techniques. The horizontal arrows indicate the level down to which the Version 2 data were retrieved automatically with the ODS code; the new Version 3 allows to extend the profiles further down, well into the free troposphere. Notice the good agreement (except for CCl_4; see text) between lowermost volume mixing ratios derived from ATMOS spectra and corresponding in situ concentrations measured at the ground (square symbols).*

In a way similar to the confection of total Cl in Figure 48 Figure 49 displays the elements intervening in the production of total fluorine budget throughout the troposphere and stratosphere.

The comparison between the latter 1994 budgets of Cl and F and similar ones produced from the ATMOS SL-3 mission of 1985 (Zander et al., 1992), indicates increases in the stratospheric loading of Cl and F equal to nearly 40% and 70%, respectively. When taking into account the time delay necessary for long-lived source gases to mix into the mid-latitude stratosphere (4 to 6 years), the above increases are consistent with the trends measured in the tropospheric Cl and F loading resulting from increased ground-level emissions, during the 1980s, of anthropogenic Cl- and F-bearing source gases, in particular the CFCs -11 and -12, and the HCFC-22. No volcanic contribution needs to be invoked to explain both the loadings and trends of inorganic Cl and F throughout the stratosphere as observed by ATMOS over the 1985 to 1994 time period. These results and conclusions have been

extremely important in justifying and assessing the merits of international policy decisions such as those defined in the Montreal Protocol (1987) and its successive Amendments and Adjustments (1990, 1992, 1995 and 1997).

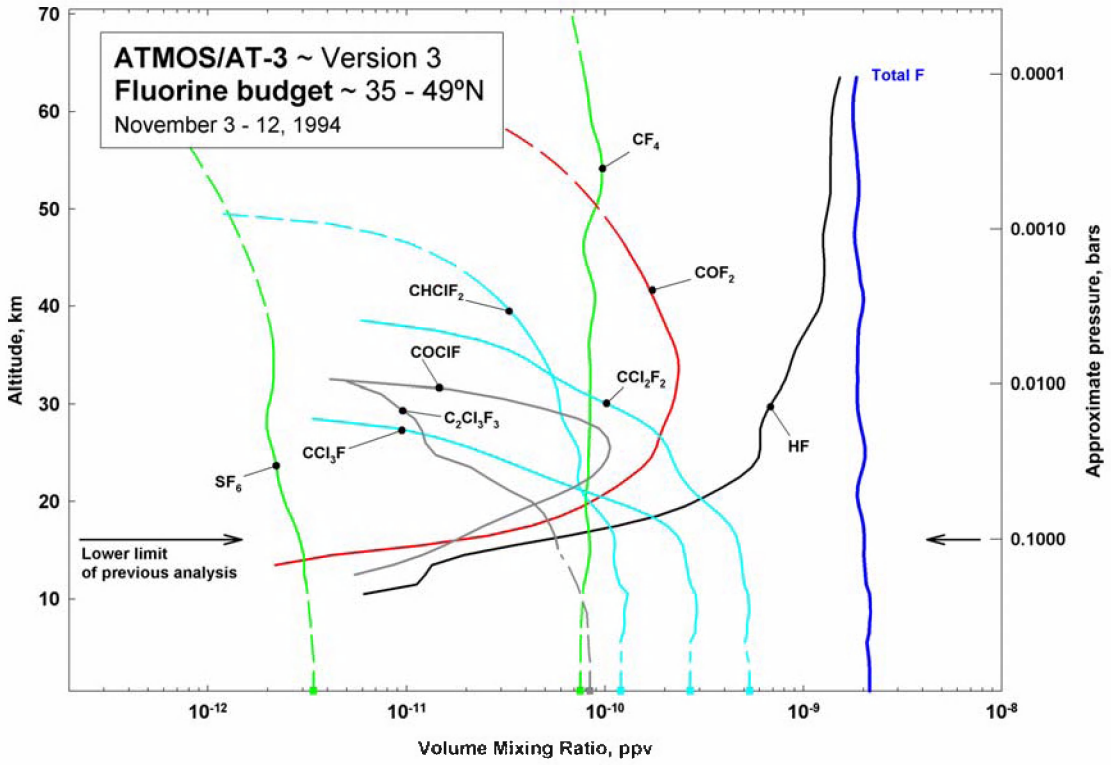

Figure 49: *The fluorine budget of the upper troposphere and stratosphere as derived for northern mid-latitudes in November 1994. It includes all important fluorinated gases (sources, sinks and reservoirs combined) observed by ATMOS during the ATLAS 3 shuttle mission, as well as a few complementary species (grey traces) measured by other techniques. The horizontal arrows indicate the level down to which the Version 2 data were retrieved automatically with the ODS code; the new Version 3 allows to extend the profiles further down, well into the free troposphere. Notice the good agreement between lowermost volume mixing ratios derived from ATMOS spectra and corresponding in situ concentrations measured at the ground (square symbols).*

A concerted activity has also been maintained (via teleconferences) among the ATMOS Science Team regarding the precision and accuracy with which water vapor volume mixing ratio profiles can be derived from the V3 data analysis, especially in the lower stratosphere and upper troposphere (Michelsen et al., 2001). Important conclusions from that investigation indicate that (i) the consistency between V2 and V3 averaged H_2O profiles is very good in the lower and middle stratosphere; (2) in the upper stratosphere and mesosphere, the retrievals are dryer for V3 than for V2; (3) compared to V2, the V3 profiles of H_2O reveal more small-scale variability in the

stratosphere and capture more reliably sharp features such as the hygropause. Improvements have resulted, not only from adopting the "global fit" approach evoked before, but also by adding a number of new microwindows (which can be partly corrupted by interfering gases, because of the multiple-species retrieval possibility of the GFIT algorithm). H_2O-related intercomparisons with measurements by airborne Lyman-α hygrometers from NOAA and from Harvard (Hintsa et al., 1999), by the MkIV balloon FTIR (Toon et al., 1999), by the shuttle-based MAS microwave instrument (Bevilacqua et al., 1996), by the UARS-HALOE (Harries et al., 1996) and –MLS (Pumphrey, 1999) indicate differences ranging from 4 to 30 % in the lower stratosphere, 3 to 15 % in the middle stratosphere, 5 to 15 % in the upper stratosphere, and 0 to 30 % in the mesosphere. The best agreement is with the MkIV balloon FTIR (3 to 5 %) throughout the lower and middle stratosphere.

Another research to be briefly evoked here deals with ATMOS observations inside the November 1994 Antarctic stratospheric vortex and inside the April 1993 remnant Arctic stratospheric vortex. In both regions, a pocket of elevated CO was observed in the midstratospheric vortex, a feature resulting from downward transport of air originating at mesospheric altitudes. In the Antarctic, the CO peak was located about 1 km below a region of elevated NO_y, whereas there was no evidence of such an enhancement in the Arctic observations. The interpretation of these new findings has been reported in Rinsland et al. (1999).

Auxiliary data

During the past year, we have further investigated UARS/HALOE measurements regarding HCl, HF and CH_4, the ultimate aim being to produce series of "most realistic" profiles to be used in the retrieval of vertical column abundances from ISSJ observations. HALOE data have been taken since October 1991, with on average 15 occultations being registered per day. The latest "Version 19" (abbreviation V19) is publicly accessible via Internet. The procedure adopted to derive most realistic profiles for ISSJ from the HALOE archive includes calculations of daily and monthly zonal averaged profiles in the 41.5 to 51.5ºN latitudinal band, i.e ±5º centered on the Jungfraujoch. In this 10º latitude zone, the HALOE occultations are not distributed homogeneously versus time, the April to August months being poorly covered (1 to 3 occultations per month and per year). However, a recurrent seasonal behaviour of the vertical distributions has been derived from the entire 9-year HALOE database and typical monthly profiles have been produced. The latter, regrouped per season, are currently being used as "reference" profiles in conjunction with an approach to derive partial column abundances throughout the year.

On the basis of the most recent ATMOS-V3 and HALOE-V19 data bases, we have compared average HCl profiles derived from spatial and temporal coincidences over the latitudinal zones 63-69ºN and 44-50ºS during the ATMOS-AT2 mission, as well as the 20-35ºN and 35-49ºN zones during AT3. The intercomparisons show that HALOE measurements are systematically lower by about 11% throughout the stratosphere; this value has lowered somewhat with respect to corresponding values (10 to 20%) reported by Russell et al. (1996) on the basis of earlier data versions.

4.2 Evaluation of long-term spectral UV irradiance and UV Index data at Ukkel. Variability, global changes, and UV Index forecasting

4.2.1 Introduction

The penetration of solar UV radiation through the atmosphere depends on the solar zenithal angle (SZA), the ozone overhead column and other atmospheric absorbers and scatters such as clouds and aerosols. In particular, clouds are responsible for a great deal of the observed irradiance variability. The interpretation of observed UV-B time series, and, e.g., the detection of possible trends due to human activity, requires the correct understanding of the effects of these different 'factor of influence' and a detailed study of their evolution with time.

The automated station for UV monitoring at BIRA-IASB is operational since mid-March 1993. At KMI-IRM, spectral UV measurements (280 – 325 nm) are available since 1989; initially, from April 1989 to December 1990, data were taken at noon; since January 1991, they are taken on an hourly base. Auxiliary data (total ozone, ozone, temperature and relative humidity profiles as well as cloud fraction, cloud type and ground meteorological parameters (pressure, temperature, horizontal visibility…) are provided routinely by KMI-IRM. Periodical absolute calibrations of the instruments and instrument intercomparisons are performed: calibration uncertainties can be estimated to be less than ±5% over the whole wavelength range. This estimation was confirmed during the previous European Inter-comparison Campaign (Gardiner et al., 1993).

From the available 11-years period of continuous measurements, it is possible to define the major characteristics of the UV climatology in Belgium and by extension in the 50° - latitude band. Hereinafter, The major results are presented and discussed in terms of correlation between the UV-B irradiance and the main atmospheric parameters like ozone, SO_2, clouds cover, aerosols… Some preliminary results on potential trends are also presented and discussed. The development of a UV Index forecasting model is also discussed.

4.2.2 Time series of effective UV irradiances

Erythemal doses (or effective UV irradiances) at noon in Uccle are evaluated from both sets of spectral UV-Visible measurements, by weighting each spectrum by the CIE action spectrum (McKinlay and Diffey, 1987). The KMI-IRM data set is corrected to take into account the lack of spectral measurements between 325 and 400 nm. The comparison of the two data sets gives a good agreement (within 5%) for most of the cases over the overlap period (1993-1999). Nevertheless, in some occasions, the discrepancy can reach 20-25%. This is probably due to 1) the unperfected synchronism between the measurements and 2) the correction of the Brewer measurements which does not take into account the modification of the cloud cover during one scan duration. Figure 4.33 illustrates the available time series and shows their seasonal variation. The peak values are achieved in June, corresponding to the smallest SZA of the year and relatively low ozone columns. The scatter within the seasonal fluctuation can be ascribed to changes in cloud coverage.

From the daily observations of UV spectra, a climatology of effective UV-irradiance at local noon was extracted. It was checked how this effective irradiance depends on the degree of cloudiness (see Figure 51). From this figure the influence of the mean annual variation of the thickness of the ozone layer may also be noted: at mid April (when the mean total ozone amount is largest) the intensity of the effective UV irradiance is about 20 % smaller than at the end of August (when the elevation of the sun at solar noon is the same as at mid April).

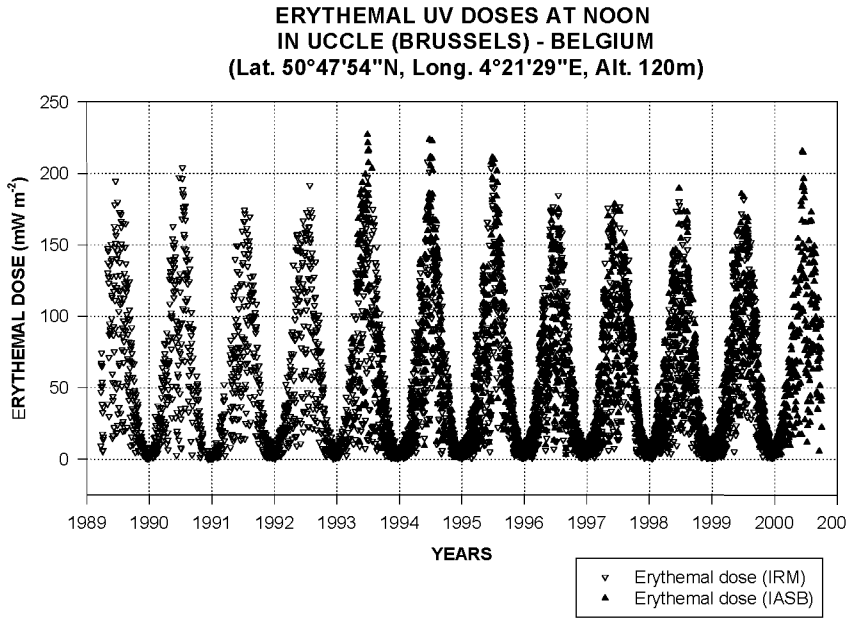

Figure 50: *Time series of the erythemal doses at Uccle*

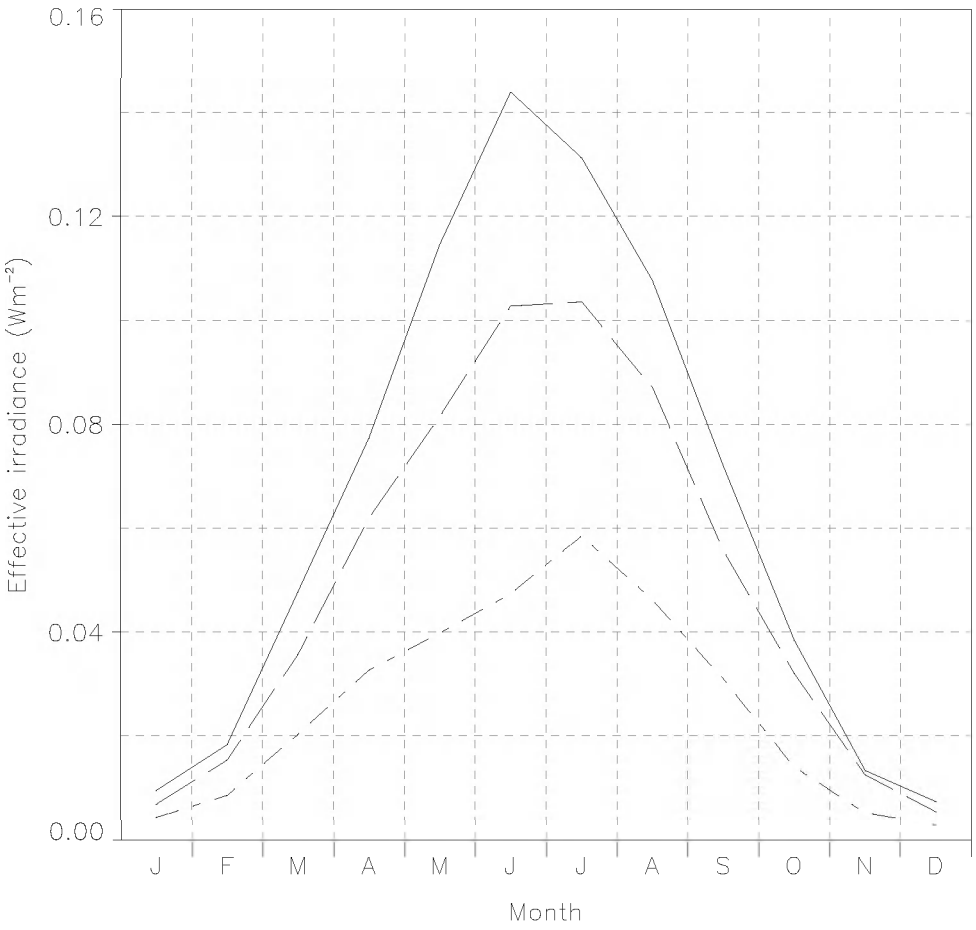

Figure 51: *Influence of cloud cover on effective UV irradiance at solar noon (Uccle, 1989-1997): cloudless sky (solid line), cloud cover between 1/8 and 6/8 (dashed line) and cloud cover > 6/8 (dash-dot line).*

4.2.3 Factors of influence

The two most important factors limiting the penetration and explaining the day to day variations of the UV-B radiation to the Earth's surface are the ozone and the cloud coverage. These two 'factors of influence' will be detailed in the next sections. Other factors like aerosols, which are relatively constant in Brussels, will be neglected.

4.2.3.1 Ozone

Figure 52 illustrates the anti-correlation between ozone total column and UV-B integrated irradiance corrected for the effect of cloud cover. The applied correction is simply the ratio UV-B/UV-A that takes into account, as a first approximation, the effect of clouds as a neutral filter.

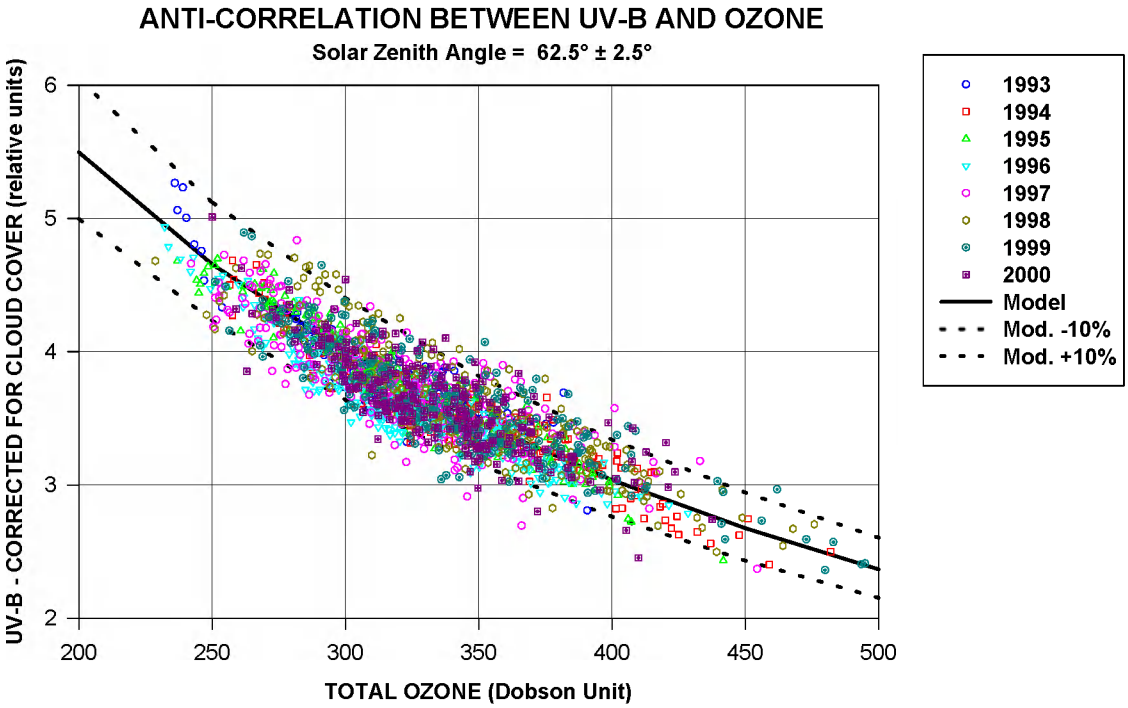

Figure 52: *Anti-correlation between ozone and UV-B.*

A discrete ordinates radiative model (Stamnes et al., 1988) has been used to simulate the experimental data and verify the anti-correlation between ozone and UV-B. The extraterrestrial flux is a combination of the SUSIM spectrum below 350 nm (Van Hoosier et al., 1984) and the Neckel and Labs spectrum (Neckel and Labs, 1984) up to 600 nm. The wavelength dependence of the aerosol optical properties follows the parameterisation of WCP (WCP, 1986) for typical continental mixtures. This choice is motivated by air pollution lower in Uccle than in typical urban centres. The weak dependence of cloud extinction and asymmetry factor is parameterised following (Slingo, 1989, private communication).

A good agreement (better then 5%) between experimental data and the simulation has been established for SZA between 30° and 70° in clear sky condition. The discrepancies between modelled and experimental data increase generally with the SZA and can exceed 10% at high SZA in the visible range. Figure 52 shows clearly that the anti-correlation observed experimentally is well reproduced by modelling and that practically all the experimental conditions are included in ± 10% limit compared to the predicted anti-correlation. This 10 % variation can easily be explained by considering the error in the ozone measurements (5%) and the unsophisticated correction of the cloud layer effects.

4.2.3.2 Clouds

In order to investigate the role of clouds as a function of wavelength, average spectra for well-defined conditions (complete overcast, similar zenith angles) have been derived from the observations, and compared with a corresponding clear sky spectrum. The average cloud transmission ratios for SZA=30 ° are displayed on Figure 53, and compared to a modelled transmission ratio. A 1-km low cloud with an optical depth equal to 50 has been assumed.

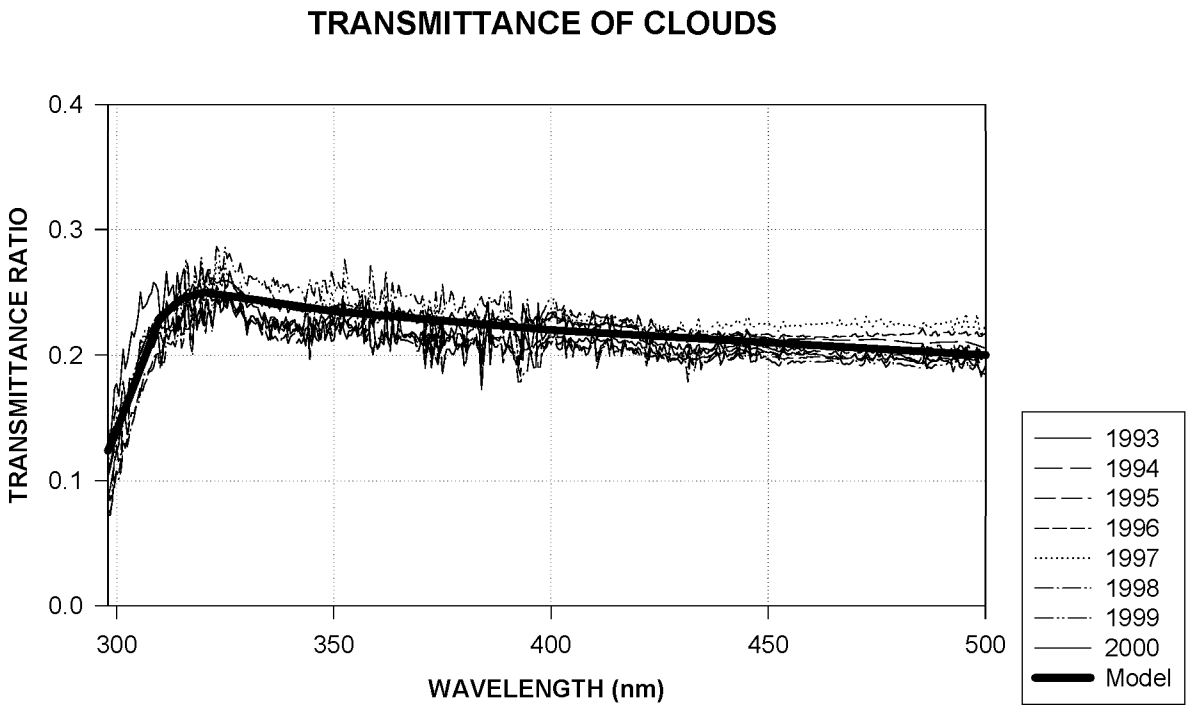

Figure 53: *Ratio of cloudy (8 Octas) to clear sky irradiance.*

Despite the large variability of the cloud impact, a consistent picture is found. The attenuation is lowest in the UV-A, and highest in the ozone absorption bands (UV-B) because of the increased multiple scattering and tropospheric ozone absorption caused by cloud. The attenuation increases to a lesser extent in the visible range, reflecting the smaller importance of Rayleigh diffusion at higher wavelengths. Finally, the average attenuation of sunlight by different type of clouds can also be directly estimated from the pyranometers data. As expected, the attenuation by cirrus clouds (high altitude) is found to be very small. In contrast, low clouds (mainly stratocumulus) reduce solar irradiance by about a factor 5 on average.

This attenuation is found to increase monotonously with the solar zenith angle in the UV-A and UV-B ranges, but not for the total integrated irradiances (300-3000 nm). These last results have to be examined in the more detailed future modelling studies.

4.2.4 Trends in UV effective irradiance

Possible trends of UV-B radiation at the Earth's surface due to human activity is of high interest for the public health medical community as well as for all the scientists interested in the effects of UV-B on biology and material sciences.

The aim of this chapter is just to illustrate what can be deduced from an 11-years period of UV-B monitoring. Figure 54 illustrates the high variability of UV-B effective doses on a monthly base mainly due to the variability of meteorological conditions.

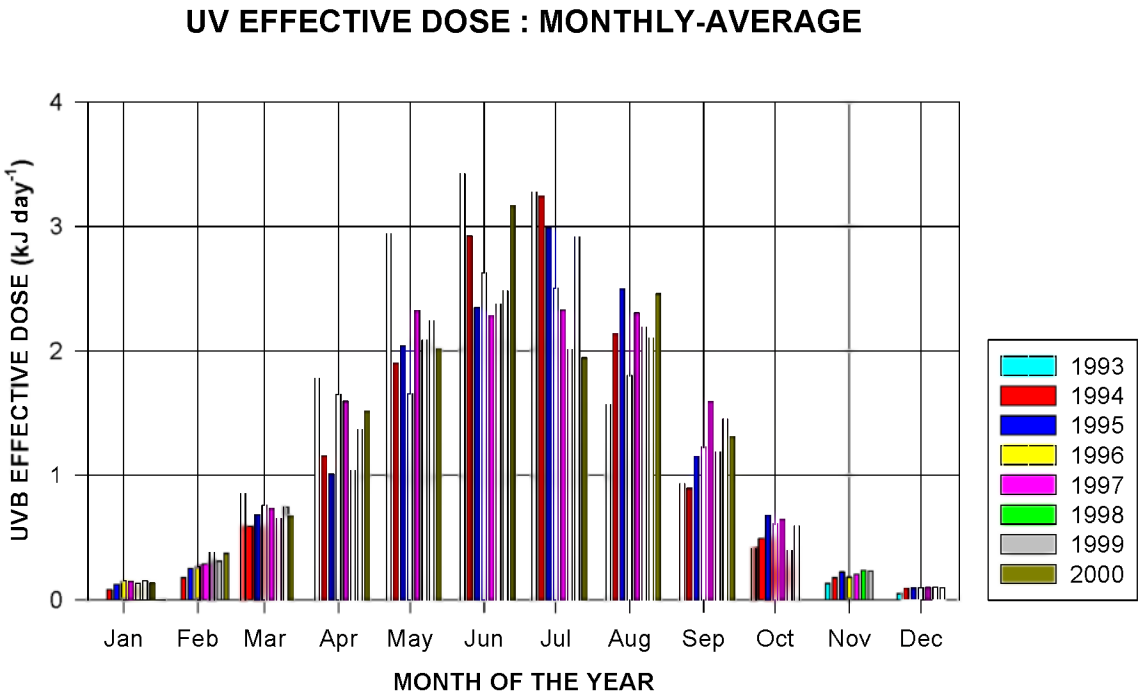

Figure 54: *UV-B effective monthly averaged doses in Uccle (Brussels) Belgium.*

Figure 55 gives a first idea of the potential trend of UV-B in Brussels. UV-B shows an increase of 0.6% per year that looks coherent with observed ozone trends of order -0.3%/year.

4.2.5 UV Index forecasting

4.2.5.1 Development of an operational UV Index forecasting procedure

The UV erythemally weighted irradiances can be converted to the international standardized UV Index, which is an indication for the sunburn risk. A UV Index forecasting algorithm was developed at KMI-IRM, in several steps.
In a first step, the Tropospheric Ultraviolet Visible (TUV) model developed by Madronich (1993) was installed and adapted to the local situation. TUV is a freely distributed FORTRAN coded multiple scattering radiative transfer model. Based on some input parameters, such as solar zenith angle and total ozone column, it calculates the corresponding spectrum. A good agreement with the observed spectra was obtained. Therefore, TUV is a valuable tool for making clear-sky UV Index forecasts, the quality of the forecasts mainly depending on the accuracy of the total ozone forecast.

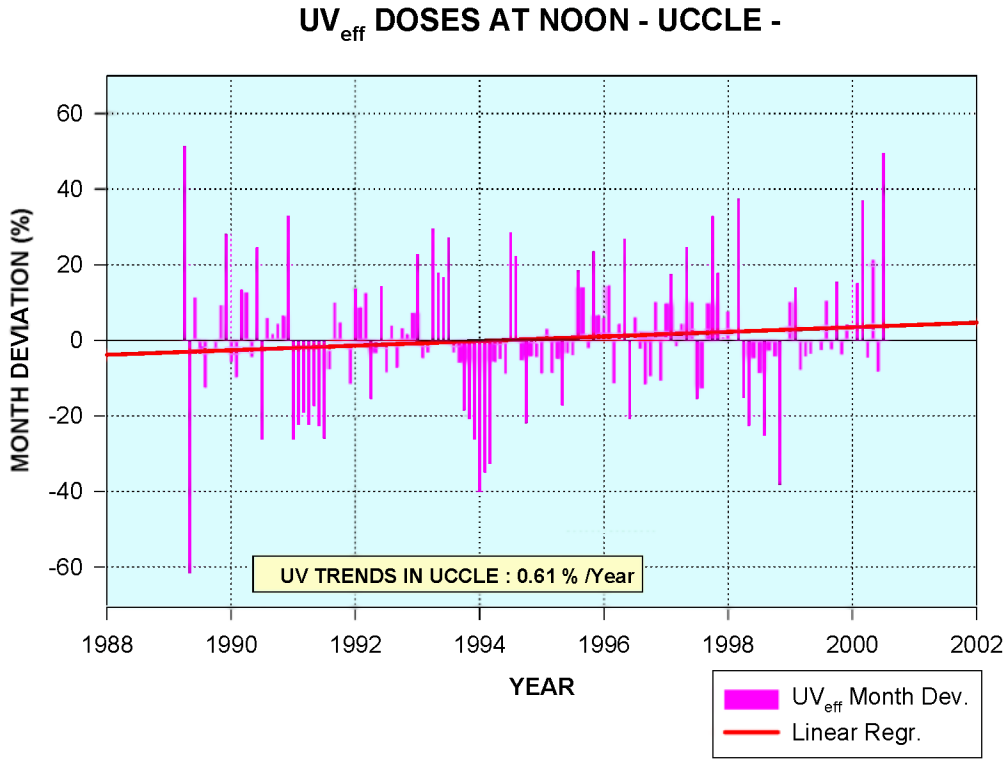

Figure 55: *UV-B trends in Brussels 1989-2000.*

4.2.6 UV Index forecasting

4.2.6.1 Development of an operational UV Index forecasting procedure

The UV erythemally weighted irradiances can be converted to the international standardized UV Index, which is an indication for the sunburn risk. A UV Index forecasting algorithm was developed at KMI-IRM, in several steps.

In a first step, the Tropospheric Ultraviolet Visible (TUV) model developed by Madronich (1993) was installed and adapted to the local situation. TUV is a freely distributed FORTRAN coded multiple scattering radiative transfer model. Based on some input parameters, such as solar zenith angle and total ozone column, it calculates the corresponding spectrum. A good agreement with the observed spectra was obtained. Therefore, TUV is a valuable tool for making clear-sky UV Index forecasts, the quality of the forecasts mainly depending on the accuracy of the total ozone forecast.

Initially, a stepwise multilinear regression of both analyzed and forecasted meteorological parameters together with the last observed total ozone value appeared to be the most adequate ozone forecast method. It resulted in a standard deviation of the difference between forecasted and observed values of the clear-sky UV index in July of the order of 0.5.
In a second step (end of 1997 - early 1998) the UV Index forecasting procedure was further developed. It became operational on April 10, 1998. Since then, each year from April to September, next day's UV Index for Belgium has been disseminated to the press on a daily base. It is broadcasted on TV at noon and in the evening and published in a few newspapers. Twice a week a color map displaying the distribution of the UV Index over Europe is also shown on TV. The meaning of the UV Index has been explained via an Internet site and a leaflet, which was written in collaboration with the 'Belgische Vereniging voor Dermatologie en Venerologie'. A renewed version of an explanatory leaflet for the general public was made in 1999, now in co-operation with Laboratoires Vichy and distributed on a much larger scale. Within the COST action 713 we participated in the edition of a booklet on the UV-index problems which was distributed by the COST secretariat into the participating countries.

Details of the UV Index forecasting procedure can be found in Plets (2000).

As said before, the quality of the UV Index forecast mainly depends on the accuracy of the prediction of the total ozone column. An inventory of existing ozone prediction

models has been made. The best models currently in use are statistical regression models that explain tomorrow's ozone in terms of today's ozone and a set of meteorological parameters. The dynamics of changing weather systems affects the total ozone amount above a given area. This is quantified by correlating the time series of total ozone with the time series of a set of meteorological variables and selecting the ones with the highest correlation. One then usually constructs a multiple linear regression model with this set of meteorological variables. We considered this model as our benchmark model. However, the method of least squares, which is used in linear regression models, requires that there is no serial correlation between the values of the dependent variable and that its variance remains constant. In the case of total ozone column data, both conditions are violated. The serial correlation is high (today's ozone being a better predictor for tomorrow's ozone than the available meteorological variables). The variance changes from relative low values from mid-summer to the beginning of fall to rather elevated values during winter and the beginning of spring. Also the mean ozone value changes with time. The first problem (serial correlation) is usually coped with by adding today's ozone to the pool of predictors. To avoid the second problem (non-stationary mean and variance), all known ozone forecasting regression models use stratified data sets. This means that separate analyses of subsets of the data record which are short enough to be regarded as stationary (usually monthly data sets) are conducted, i.e., an independent regression model is constructed for each month.

However, we felt that this approach was not fully satisfactory. Instead of cutting the time series in monthly subsets, we looked for a transformation on the whole time series to remove the nonstationarity. We developed one global model instead of 12 separate models. We obtained one single regression equation for the whole time series, which yields slightly better results than the common approach. This method was developed in collaboration with Prof. J. Beirlant of the Department of Statistics of the University of Leuven. This approach to deal with the non-stationarity problem allowed us to handle the first problem (serial correlation) by adding a term that deals with the autocorrelative structure of the error term, resulting in a so-called autoregressive (AR) model. We then still had to find a way to correct for the changing variability of the data. This was achieved by incorporating an autoregressive conditional heteroskedasticity (ARCH) model. The ARCH models, widely used in econometric problems, provide a means of estimating the next day's variance of the dependent variable by looking at the previous days' variances. The resulting AR-ARCH model is not only preferable from a theoretical point of view. It reduces the variance of the difference between observed and forecasted values with 8% with respect to the benchmark model. In the period April-September, i.e., the UV forecasting period, the variance was even reduced by 12%.

It can thus be concluded that the effort we took in examining the validity of the regression assumptions exceeds the purely academic interest and can be applied operationally to obtain more accurate UV Index forecasts. The results are published in an international journal (Plets and Vynckier, 2000).

An overview of the UV Index forecasting procedure together with an evaluation of the operational forecasts made so far has been published by Plets (2000).
The UV Index is defined for clear-sky conditions. As can be seen from Figure 56 below, the quality of the predictions is mostly very good for cloudiness less than 4 octas.

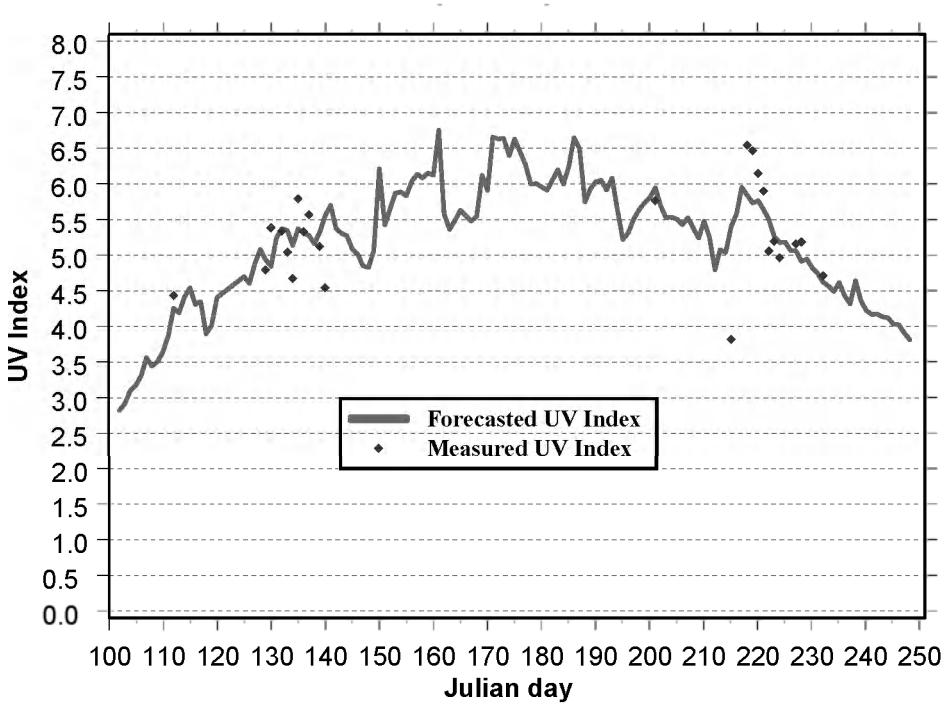

Figure 56: *Evaluation of the UV index forecasts on days with cloudiness < 4/8 at Uccle during April 10 until September 5, 1998.*

Figure 57 shows the difference between the measured and the forecasted UV Index at local noon as a function of cloudiness for the 1998 and 1999 forecasting season. As the UV Index by definition refers to clear-sky conditions, the discrepancy between forecast and measurement will increase with cloudiness. Except for broken clouds, cloudiness always yields a reduction of the intensity of incoming UV radiation. This explains why the differences in Figure 57 are negative in most cases. Typical noontime UV Index values in the forecasting season range from 3.5 in April to 6.5 in the beginning of July, subsequently decreasing again to 3 in September.

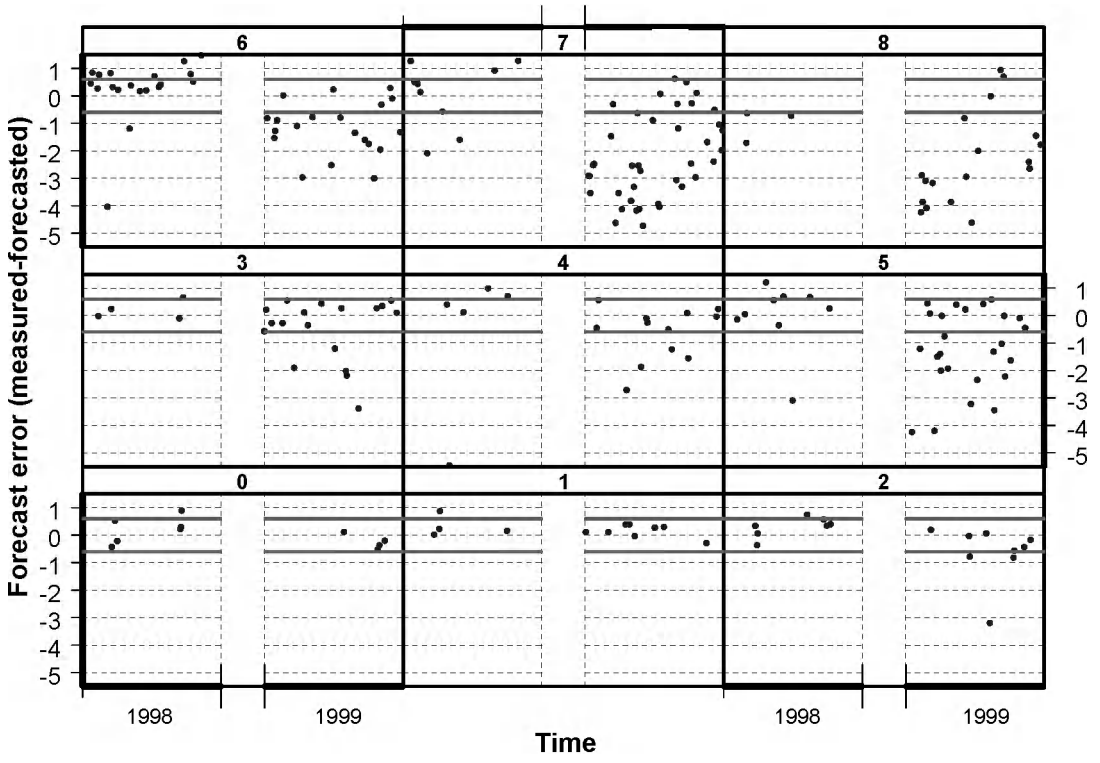

Figure 57: *Evaluation of the UV forecasts (expressed in units of UV Index) as a function of cloudiness (expressed in octas).*

4.2.6.2 Comparison of UV models and UV Index forecasts

Within the framework of the COST action 713 on UVB first a study was performed on the comparison of UV models. The results (Köpke et al, 1998), showed that all radiative transfer models agreed well when the same input parameters are used. Afterwards, a study was initiated to compare UV indices calculated with different models used for UV-Index forecasting and observations at different sites with different instruments. This required the exchange of data between a large number of different UV groups, mainly located in Europe. Finally 13 models were compared with measurements of 5 instruments at 4 locations at very different environments. As an example Figure 58 shows the differences between the measurements and the calculations with three different versions of the Tropospheric Ultraviolet and Visible model (TUV), one of which is in use at RMI. A manuscript on this subject is in press (De Backer et al., 2001). The intermediate results were presented at the EGS assembly in Den Haag (De Backer et al., 1999b). The results were also thoroughly discussed at the Management committee meeting of COST713, held in Antwerp in 1999, and organised by KMI-IRM. UV-Index measurements and forecasts, together with synoptic observations of the summer season of 1999, were transmitted to another COST713 member, for the study of the impact of clouds on the UV-Index.

Also the total ozone forecasts at Uccle were exchanged within the COST713 members. Preliminary results reported during one of the COST713 management committee meetings showed that the total ozone forecasts at Uccle are of good quality.

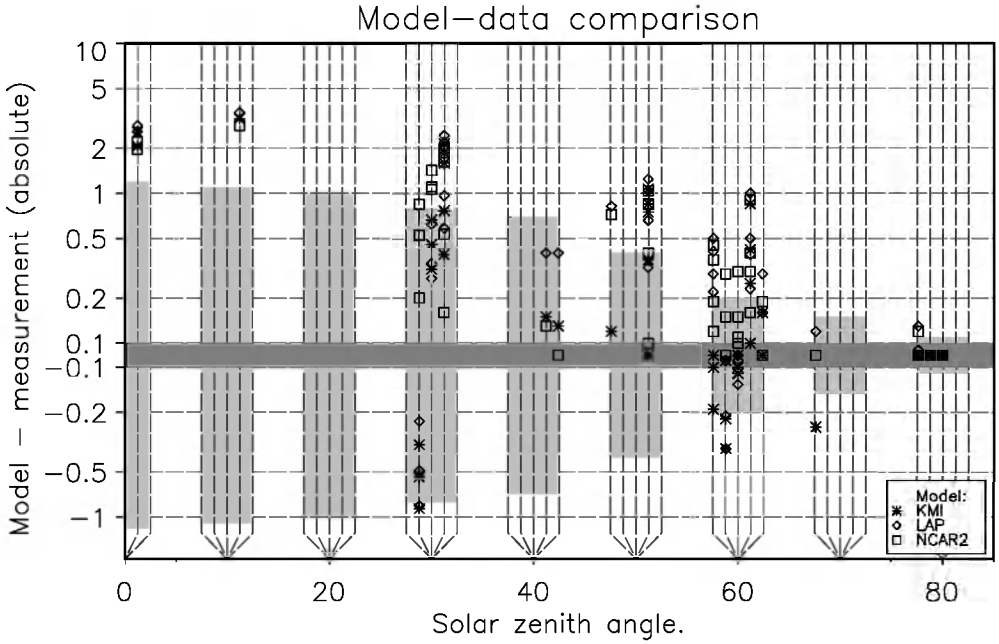

Figure 58: *Absolute differences in UVI units between model and measurement results as a function of solar zenith angle. The different symbols refer to different versions of the TUV model run at different institutes (KMI: Royal Meteorological Institute of Belgium, LAP: Laboratory of Atmospheric Physics of the University of Thessaloniki, NCAR2: National Centre of Atmospheric Research in Boulder). The results are shown for ten degree solar zenith angle intervals, each time from left to right for the stations Sodankylä, Uccle, Thessaloniki, Izaña (Spanish instrument) and Izaña (Finnish instrument). The light grey bars show the estimated uncertainty of the measurements.*

4.3 Atmospheric process studies

4.3.1 Tropospheric O_3 in Ukkel

The Riftoz (Regional Differences in Tropospheric Ozone) project aims at explaining the differences observed in the tropospheric ozone behavior in different European regions. Taking part in this project, the KMI-IRM had to carry out ozone soundings each day during June, July and August 1997 by means of ECC ozonesondes. This resulted in a very valuable time series of ozone soundings that will be used in creating a coherent and complete 3-D tropospheric ozone data set over Europe for the summer of 1997. Additional information such as general meteorological situation,

vertical air mass stability and horizontal extent to which the ozone soundings can be extrapolated, has also been provided.

Figure 59 shows time series of various relevant parameters during June to August 1997. In the time series of the integrated ozone amount in the troposphere we see a very high value on the 1st of June, which is due to a difference between the thermal tropopause (WMO definition) and the ozone tropopause. During the periods from 12 to 13 July and from 6 to 13 August (delimited by dashed lines in Figure 59) there is a clear signature of photochemical ozone production in the boundary layer (sunny weather, high temperatures, and high integrated ozone amounts in the boundary layer).

It is interesting that during the latter period the integrated ozone amount in the free troposphere also shows a cumulative effect, which points to an overflow of ozone from the boundary layer to the free troposphere during ozone episodes. On August 14 the ozone amount in the boundary layer and in the free troposphere dropped by about 60 and 40 percent respectively, due to a change of air mass from a continental to a marine one.

Several cases of stratospheric intrusions were found from the soundings, which could sometimes be followed during some days. A very pronounced intrusion was seen from 14 to 16 July, with signatures of stratospheric air to levels as low as the 700 hPa pressure level.

The first objective of the RIFTOZ (Regional differences in Tropospheric Ozone in Europe) project was to create a coherent hourly averaged tropospheric ozone field covering Europe, through a combination of observations, photochemical dispersion models and data assimilation. The database of daily ozone soundings from KMI-IRM was used to study the ozone budget of the planetary boundary layer (PBL) during ozone episodes. This ozone budget has the following components:

- accumulation in the PBL,
- transfer from the PBL to the free troposphere (FT),
- deposition at the surface,
- horizontal advection.

The ozone accumulation between day [i) and day [i+1) in the layer between z1 and z2 is calculated as follows:

$$A(i)_{z1,z2} = \int_{z1}^{z2} \rho(z, day[i+1])\,dz - \int_{z1}^{z2} \rho(z, day[i])\,dz \qquad (1)$$

where ρ is the ozone density

The terms contributing to the ozone budget in the PBL were calculated as follows:

Accumulation in the PBL: $A(i)_{ground,\ 2km}$ (2)

Transfer: $A(i)_{2km,4km}$ (3)

Deposition:

$$D(i) = \int_{t=noon}^{t=sunset} \rho_g(t, day[i]).q_{day}\ dt + \int_{t=sunset}^{t=midnight} \rho_g(t, day[i]).q_{night}\ dt + \int_{t=midnight}^{t=sunrise} \rho_g(t, day[i+1]).q_{night}\ dt + \int_{t=sunrise}^{t=noon} \rho_g(t, day[i+1]).q_{day}\ dt \quad (4)$$

where ρ_g is the ozone density at the surface;
q is the surface ozone deposition velocity;
z is the altitude.

The top of the PBL of each individual sounding during ozone episodes was determined as the level where the ozone concentration and specific humidity show a sharp decrease with altitude and where the potential temperature steeply increases. In this way a mean PBL height of about 2 km was found.

The mean day-to-day ozone accumulation during ozone episodes with stable air masses above Ukkel was calculated in different layers. In the layers 0 to 2 km, 2 to 3 km, 3 to 4 km and 4 to 5 km, the mean accumulation (in mg m^{-2} day^{-1}) was 45, 10, 5 and –2 respectively. It appears that the accumulation is limited to the lowest 4 km of the troposphere. Therefore, we only take into account the lowest 2 km of the FT for calculation of the transfer of ozone from the PBL to the FT.

The deposition at the ground is calculated assuming a deposition velocity of 1.4 cm s^{-1} at daytime and 0.64 cm s^{-1} at night (De Muer et al., 1997). Hourly mean values of ozone concentration near the ground were kindly provided by the Belgian Interregional Cell for the Environment (IRCEL).

We studied the meteorological synoptic situation and retained only the ozone episodes during which our station was in the same type of air mass. In these cases, the assumption of no horizontal advection is adequate. So the ozone production in the PBL is essentially the sum of the ozone amount deposited at the ground, accumulated in the PBL and transferred to the FT:

$$P(i) = A(i)_{ground,2km} + D(i) + A(i)_{2km,4km} \quad (5)$$

From these calculations the following mean values of the ozone budget during ozone episodes were obtained:

- ozone production in the convective mixed layer: 111 mg m^{-2} day^{-1};
- ozone deposition at the surface: 51 mg m^{-2} day^{-1} (46%);
- accumulation of ozone in the boundary layer: 45 mg m^{-2} day^{-1} (40%);
- overflow of ozone to the free troposphere: 15 mg m^{-2} day^{-1} (14%).

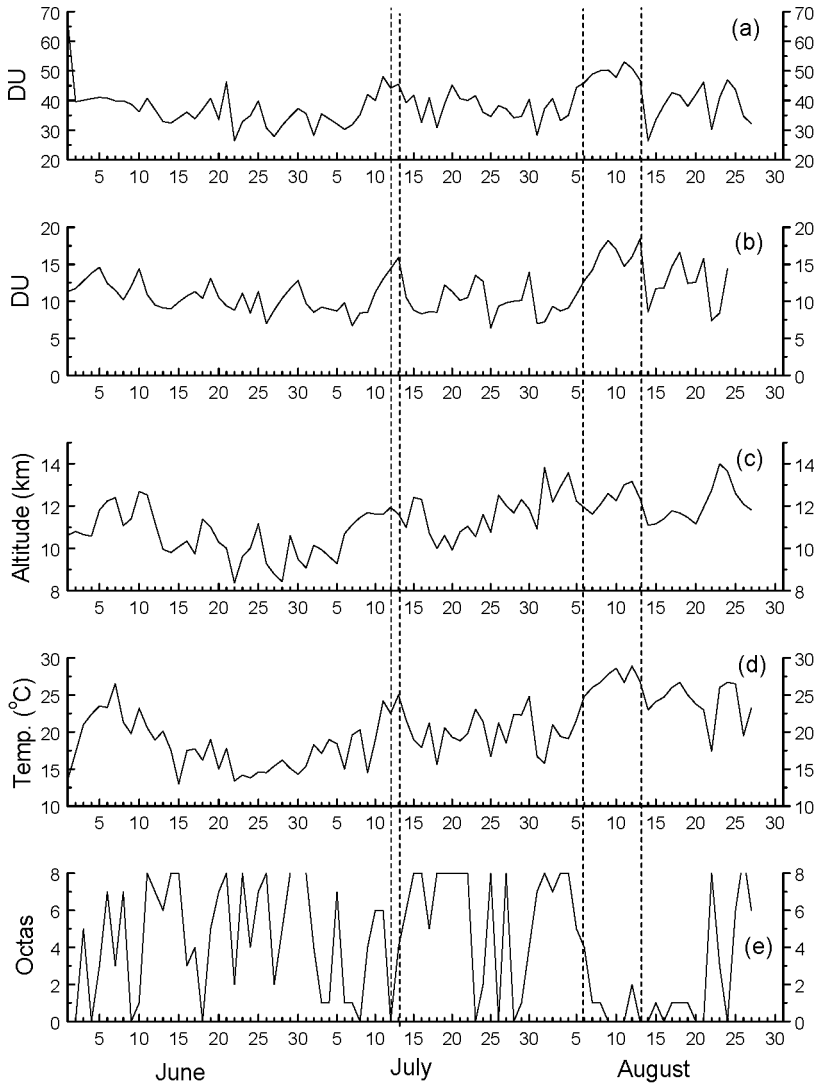

Figure 59: *Day-to-day variation during the period June to August 1997, of the following parameters: integrated ozone amount (expressed in Dobson units (DU)) in (a) the troposphere and in (b) the boundary layer, (c) altitude of the tropopause, (d) surface temperature and (e) cloud cover. integrated ozone amounts in the boundary layer).*

4.3.2 Urban pollution in Brussels

4.3.2.1 Methodology

A 4-months measurement campaign was held at the ULB Campus during 1997. Spectra were obtained with the BRUKER IFS120M Fourier Transform spectrometer in the UV-visible region. Concentrations of O_3, NO_2, SO_2, benzene, toluene, H_2CO, and HONO were routinely measured. Night-time measurements of NO_3 were also performed. O_3 and NO_2 concentrations were also monitored by the Institut Bruxellois pour la Gestion de l'Environnement (IBGE) at the IASB-BIRA location.

The influence of several meteorological parameters on the evolution of the O_3 concentration was investigated. The meteorological parameters were measured by KMI-IRM and by the IBGE. They comprised the wind speed and direction, the irradiance, the temperature, the nebulosity, the thermal inversion height, and the relative humidity. Parameters that were found to be highly correlated with the O_3 values were the wind speed (WS) and direction (WD), the temperature (T), the relative humidity (H), and the irradiance (Ir).

Based on these results two regression models of the O_3 concentration in the city of Brussels have been developed using atmospheric and meteorological measurements: The first one considers only meteorological parameters to explain the O_3 concentrations; the second one makes also use of the NO and NO_2 concentrations. The models are based on the ordinary least square method (OLS). The concentration of ozone $C(O_3)$ is expressed as a function of k chosen explanatory variables X_i (i=1..k), using an exponential relation:

$$C(O_3) = e^{B_0} X_1^{B_1} \cdots X_k^{B_k} \qquad (1)$$

where B_i are the partial regression coefficients which need to be determined. Using natural logarithms, expression (1) can also be written for the j^{th} values of the variables, as:

$$\mathrm{Ln}\left(C(O_3)\right)_j = B_0 + \sum_{i=1}^{k} B_i \mathrm{Ln}\left(X_{ij}\right) + u_j \qquad (2)$$

where u_j are the residuals. Such an exponential relation is believed to be adequate since many of the meteorological parameters have multiplicative effects on the analysed concentration. In the case of the temperature, the adopted form (Table IV) was chosen based on the analysis of several types of relations between O_3 and the

temperature (linear, polynomial, or logarithmic). The function ln([O_3))÷1/T was found to give the best correlation coefficient. The use of the NO and NO_2 concentrations supposes that these values are known in advance. Estimate values, determined either by regression analysis or by photochemical models can be used. In our study we used measured concentrations of the two constituents: NO measured by the IBGE and NO_2 measured with our instrument. The models are summarised in Table IV.

Table IV: *Definition of the regression models.*

Model	Ln($C(O_3)$) =
M1	B_0 + B_1*1400/T + B_2*Ln(WS) + B_3*Ln(WD) + B_4*Ln(H) + B_5*Ln(Ir)
M2	B_0 + B_1*1400/T + B_2*Ln(WS) + B_3*Ln(WD) + B_4*Ln(H) + B_5*Ln(Ir) + B_6*Ln([NO_2)) + B_7*Ln([NO))

The Durbin-Watson test (Draper and Smith, 1980) has been applied to identify the independent variables, which predominate in the model in order to eliminate the ones that are not significant. Moreover a thorough residuals analysis is required to certify the quality of the estimates of the coefficients. Residuals might indeed be highly auto-correlated, in violation with the hypothesis concerning the residual independence (Draper and Smith, 1980). In the case of the presence of a Lag1 correlation, a new model (M1AC) was defined:

$$\mathrm{Ln}\left(C_j\right) = \beta_0 + \sum_{i=1}^{k} \beta_i \mathrm{Ln}\left(X_{ij}\right) + \beta_{k+1} \mathrm{Lag1}_j + e_j \qquad \text{with} \quad j=1..N \qquad (3)$$

where C_j represents the j^{th} value of the independent variable, X_{ij} the j^{th} value of the i^{th} dependent one, and e_j are the residuals (normal distribution with 0 mean value and Σ^2 variance). $Lag1_j$ is a new variable that determines the auto-correlation of the first order of the residuals. It is defined by the following expression:

$$\mathrm{Lag1}_j = \mathrm{Ln}\left(C_{j-1}\right) - B_0 - \sum_{i=1}^{k} B_i \mathrm{Ln}\left(X_{ij-1}\right) \qquad (4)$$

With this formulation, the analytical form of the model M1AC can be rewritten as:

$$\begin{aligned}\mathrm{Ln}[O_3]_j = \; & \beta_0 + \beta_1\left(\frac{1400}{T}\right)_j + \beta_2 \mathrm{Ln}(WD)_j + \beta_3 \mathrm{Ln}(H)_j + \beta_4 \mathrm{Ln}(Ir)_j \\ & + \beta_5\left[\mathrm{Ln}(O_3)_{j-1} - B_0 - B_1\left(\frac{1400}{T}\right)_{j-1} - B_2 \mathrm{Ln}(WD)_{j-1} - B_3 \mathrm{Ln}(H)_{j-1} - B_4 \mathrm{Ln}(Ir)_{j-1}\right] \\ & + e_j \end{aligned} \qquad (5)$$

A similar expression is obtained for the M2AC model, based on the M2 definition.

4.3.2.2 Discussion of the results

ULB97 campaign

The analysis provided almost continuous time series for the three molecules O_3, SO_2, and NO_2. They have been compared to the measurements made by the IBGE during the same period, showing a very good agreement between the two sets of data, as can be seen in Figure 60.

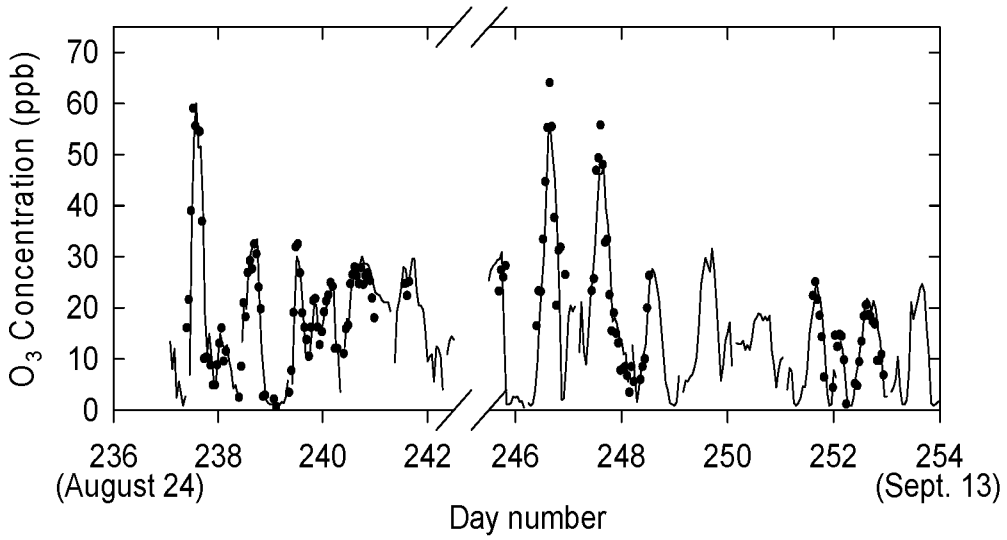

Figure 60: *Comparison of the O_3 concentrations of this work and those of IBGE.*

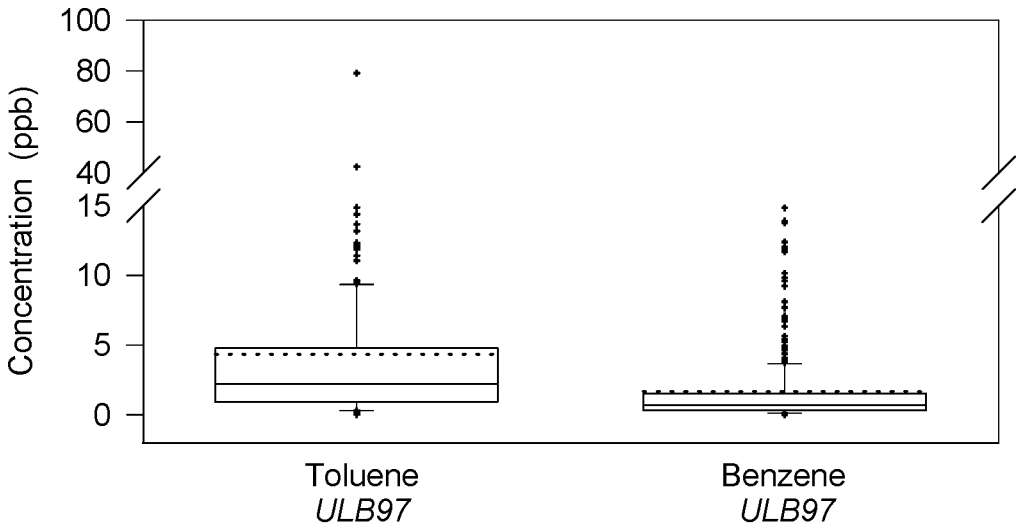

Figure 61: *Distribution of the concentrations of toluene and benzene during the campaign (see text for the description of the symbols).*

Benzene and toluene concentrations up to respectively 19.0 and 80.0 ppb were observed. The mean values are indicated by the broken lines in Figure 61, which gives also some other statistical quantities describing the toluene and benzene fluctuations during the campaign: the median value (plane line), the 25 and 75 percentiles (box limits), and the 10 and 90 percentiles (low and high external lines). The diurnal variation of the toluene concentration reflects the combined effects of the emissions, the transport, the dilution, and the chemical removal. The analysis of the diurnal evolution shows the presence of two peaks centred respectively around 8 am and 6 pm. They correspond to rush hours of the car traffic. This is not surprising as toluene is mainly emitted by car traffic. The first peak is higher than the second one, due to the higher photochemical activity of the atmosphere during the afternoon.

The comparison between the toluene and benzene concentrations shows in general no clear correlation between these two constituents. The toluene concentrations are however always higher than those of benzene by a factor varying between 1.5 and 4. This is not surprising as the toluene content is higher by a factor 3 to 4 in the gasoline and the exhaust gases.

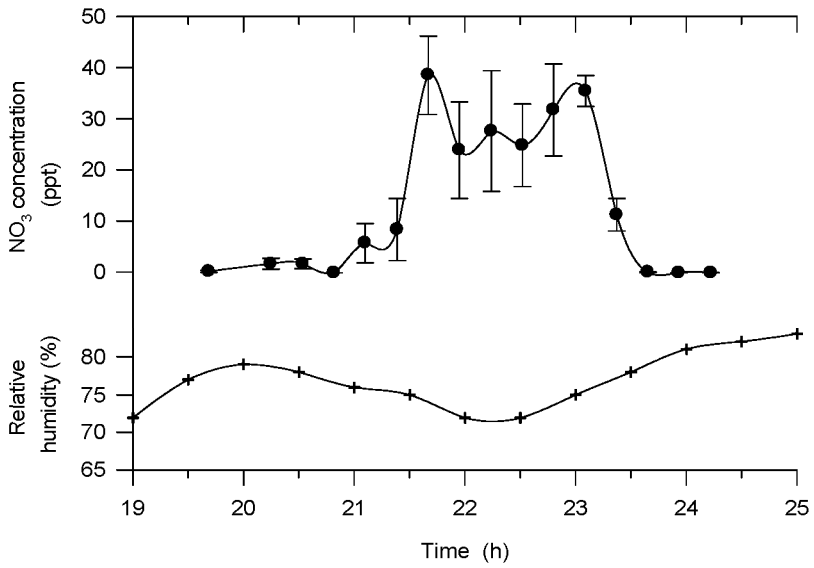

Figure 62: *NO_3 concentration during the night from the 3rd to the 4th of September 1997.*

NO_3 measurements have been performed during the *ULB97* campaign. Concentrations were detected during three nights (3/4, 8/9, and 11/12 September). Figure 62 shows the variation of the NO_3 concentrations during the night from the 3rd to the 4th of September 1997; the evolution of the relative humidity is also shown. The interpretation of these measurements is still under progress.

Models results

The models have been applied to the measurements performed during three measurement campaigns, which were organised by the Laboratoire de Chimie Physique Moléculaire (LCPM) of the ULB and BIRA-IASB. These campaigns have been denoted *ULB95* (May, June and July 1995), *IASB96* (December 6, 1996 – February 2, 1997), and *ULB97* (August - November 1997).

Figure 63 shows the comparison between the measured O_3 values and the predicted ones. The results of the three models M1, M1AC, and M2AC are plotted. The prediction coefficient of the M1AC model is 0.735 for the period from 1st to 18th July, and 0.86 for the 4th to 9th July. The regression coefficient of the M2AC model is 0.938, which is an improvement compared to the M2 value (R=0.85). The prediction coefficient for the 1st to the 18th of July is 0.836, which is quite better than what the M1AC model provided.

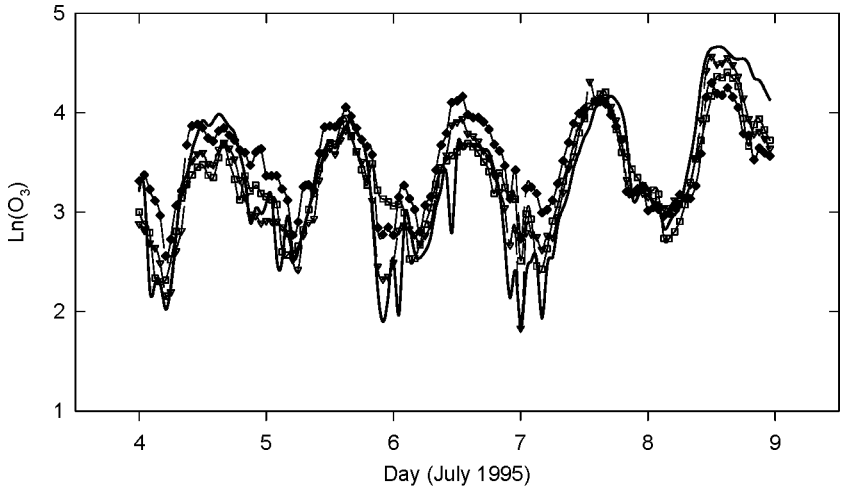

Figure 63: *Comparison of the predicted O_3 concentrations with the IBGE measured ones (—). The predictions of the three models M1 (□), M1AC (♦), and M2AC (▽) are indicated.*

Conclusions

Measurements of several tropospheric species, such as O_3, NO_2, SO_2, benzene, toluene, H_2CO, and HONO, have been performed using a Fourier transform spectrometer operated in the UV-visible region. The feasibility of night-time NO_3 measurements has been demonstrated.

Considering the analysis of the influence of some meteorological parameters, regression models of the O_3 concentration have been developed for the urban area of Brussels. Different meteorological parameters such as the temperature, the wind speed and direction, the relative humidity, and the irradiance have been considered. The models have been tested using the data of three distinct measurement campaigns with different meteorological conditions and with different O_3 levels. They have shown that good estimations of the O_3 concentrations can be performed using only the meteorological parameters ($R_{prediction}$ ~ 0.7), and have pointed out that the use of estimates of the NO and NO_2 concentrations improve the results ($R_{prediction}$ ~ 0.8).

This work contributed to tropospheric process studies by ground-based measurements of several gaseous species, and was part of the PhD thesis of A. Tsouli, presented on the 22 September 2000 (Tsouli, 2000).

4.3.3 Planetary boundary layer investigations in the Jungfraujoch area

To test the method of altitude-differential column measurements presented in section 3.4, a measurement campaign has been organized during the months of May and June 1998 in the Jungfraujoch area. After an initial period of instrument intercomparison at ISSJ, the mobile instrument (Bruker 120M) was moved down in the valley and installed for one month in Grindelwald.

When operated side by side at the Jungfraujoch, measurements made by both instruments showed a very good agreement (maximum bias of 1.5%). Analysis of spectra recorded synchronously at the Jungfraujoch (Bruker 120 HR) and at Grindelwald (mobile Bruker 120 M) gave average boundary layer concentrations for a selected set of tropospheric molecules, i.e., methane, nitrous oxide, carbon monoxide and ethane. We made the assumption of constant volume mixing ratio in the layer between 1070 m and 3580 m asl. Results are shown in Table V. The concentrations presented are the average of all daily means available through the month of June and RSD is the relative standard deviation between all the daily means. With relative standard deviation of less than 3% CH_4 and N_2O are quite constant in the tropospheric boundary layer (TBL) during the month of June while CO and C_2H_6 with RSD of 13 and 18%, respectively, exhibit a strong day to day variability.

Table V: *Average tropospheric boundary layer VMR for CH_4, N_2O, CO and C_2H_6 at Grindelwald (Jungfraujoch area) for the month of June 1998. RSD represents the 1σ standard deviation over all days with observations.*

Molecule	VMR (ppmv)	RSD %
CH_4	1.647	2.03
N_2O	0.298	2.6
CO	0.124	13
C_2H_6	0.001196	18.3

Comparison with other results and with carbon monoxide in-situ measurements made at ISSJ showed a good agreement. In particular, CO is difficult to compare to other data due to its high spatial and temporal variability. The observed CO variations have been compared with in-situ measurements of CO made by EMPA at ISSJ. Hourly means of the FTIR results have been compared with four hour means of the EMPA results: they are shown in Figure 64. A good agreement is observed.

More details about the retrieval technique and results are found in Barret et al. (1999).

It has been verified (for C_2H_6) that the results obtained with the altitude-differential measurements technique agree with the results obtained with SFIT2, the vertical inversion algorithm (taking into account the assumptions made and the limits of uncertainty of both methods).

The results prove that the technique is valuable for making measurements in the free troposphere and tropospheric boundary layer. The probed vertical layer is set by the choice of the (altitudes of) the observation sites, so one can obtain a higher vertical resolution than the one achieved with vertical inversion algorithms like SFIT2 and SFSP2. But the experimental requirements are very stringent, making the technique suitable almost only for campaign measurements, e.g., for satellite validation. Long-term data in the troposphere should be derived better from vertical inversion techniques.

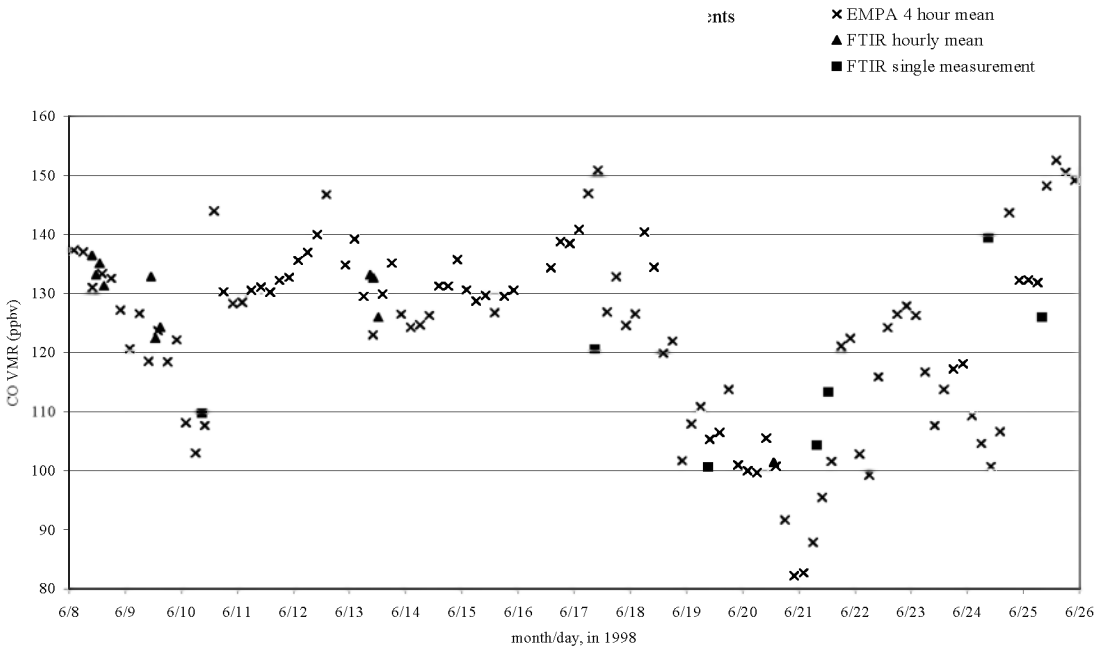

Figure 64: *Comparison between CO VMR values from differential FTIR and in situ measurements at the Jungfraujoch, during the June 1998 campaign. See the legend for the different symbols.*

4.4 Laboratory measurements of spectroscopic parameters of atmospheric relevance

The main objective of this work was to obtain high quality spectroscopic data - essentially absorption cross-sections and line positions and intensities- for atmospherically important molecules in order to improve the existing databases, to lower uncertainties and to resolve discrepancies between data sets. The molecules studied during this work were: O_2 and its collision complex O_2-X (where X can be O_2 itself, N_2 or Ar), NO_2 and its dimer N_2O_4, H_2O and their isotopomers HOD and D_2O, C_2H_2, OCS, HOCl and CFC replacements (HCFC-22 and HFC-152a). They were measured under different conditions of temperature and pressure in the infrared (IR), near infrared (NIR), visible (VIS) and ultraviolet (UV) ranges using Fourier transform spectroscopy. It should be noted that the laboratory work on thirteen CFC's, HCFC's and HFC's performed during the previous Global Change and EUROTRAC programs (1990-1996), has led to new values of the Global Warming Potential (GWP) for these compounds (Clerbaux et al., 1993; Clerbaux and Colin, 1994). Part of this work was published during the period of the present contract (Barry et al., 1997), and these data were incorporated in the GEISA spectroscopic database (Jacquinet-Husson et al., 1999).

4.4.1 Experimental conditions

The species that we have studied in the frame of the ESAC 1996-2000 project are listed in Table VI. Their absorption spectra were recorded using two commercial high-resolution Fourier transform spectrometers (FTS): a portable Bruker IFS120M, having a programmable resolution up to 0.008 cm^{-1} and operating from the IR to the UV and a Bruker IFS120HR, having a programmable resolution up to 0.0018 cm^{-1} and operating from the far infrared (FIR) to the UV. Both instruments are equipped with a variety of absorption sources, beamsplitters, optical filters and detectors, to cover the above-mentioned spectral ranges.

Table VI: *Measurements performed during the 1996-2000 ESAC project.*

	Place Date	Molecules	Resolution (cm^{-1})	Spectral Range	T (K)	P_{tot} (torr)	Ref.
1	Reims 09/95	O_2, O_2+N_2	16, 0.12	10000-42000	290	≤ 760	(a) (c)
2	Reims	NO_2	2	10000-42000	290, 220	0.01-2	(b)
	05-06/96	O_2+N_2	2	25000-42000	290	≤ 760	(a) (c)
3	Reims 04-06/97	O_2,O_2+X#	2, 0.12	25000-42000	290	≤ 760	(a) (c)
		O_2, O_2+N_2	0.02-0.2	7000-18000	290, 220	≤ 760	(c) (d)
4	Reims 03-05/98	H_2O, H_2O+N_2, H_2O+D_2O	0.03, 0.06	10000-26000	290	≤ 760	(e)
5	Reims 11-12/98	NO_2, NO_2+air	0.05-0.1	10000-25000	290, 220, 240	≤ 760	(b)
6	Reims 05-06/99	H_2O, H_2O+HDO	0.03, 0.06	10000-26000	290, 273, 261	≤ 15	(e)
7	ULB	OCS	0.005-0.015	4800 – 8000	294	2 – 76	(f)
8	ULB	C_2H_2	0.003	550 – 1970	296	2 – 8	(g)
9	ULB	HCFC-22 HFC-152a	0.03	600 – 1700	203 – 293	1 – 600	(h)
10	ULB	HOCl	0.007	550 – 1970	295	22	(i)

X= N_2 or Ar. (a) (Bernath et al., 1998) (b) (Vandaele et al., 1998) (c) (Jenouvrier et al., 1999; Fally et al., 2000; Mérienne et al., 2000) (d) (Hermans et al., 1999) (e) (Carleer et al., 1999; Zobov et al., 2000) (f) (Rbaihi et al., 1998); (g) (Vander Auwera, 2000a); (h) (Vander Auwera, 2000b; Ballard et al., 2000); (i) (Vander Auwera et al., 2000).

The measurements performed with the first instrument were carried out at the Université de Reims Champagne-Ardennes (France), in collaboration with the Laboratoire de Spectrométrie Moléculaire et Atmosphérique (GSMA). They involved the coupling of the portable IFS120M with two long path absorption cells, developed by the GSMA. The first one is 50 m long and can cover optical lengths up to 2 km. The second cell, which is 5 m long and can reach paths up to 300 m, is temperature controlled. Experiments no. 1 to 6 in Table VI were carried out in Reims using this

set-up. Experiments no. 7 to 10 were carried out at ULB, using the IFS120HR. This instrument is equipped with two commercial multiple-reflections absorption cells, providing total absorption paths ranging from 60 cm to about 50 m. Home-made thermostatic absorption cells are also available, with nominal path lengths ranging from 1.5 to 25 cm and designed to operate at any temperature between 200 and 300 K. Table VI provides a brief description of the experiments performed for the various target species. Further details can be found in the references mentioned. The treatment of the spectra was performed using a number of programs, most of them home-made and running on personal computers, in particular Wspectra and bFit – see section 3.6.

4.4.2 Results

4.4.2.1 Line parameters and absorption cross-sections in the UV-VIS-NIR

Compared to previous studies, our aim was to work under lower pressures and lower temperatures (when possible) in order to simulate more "atmospheric-like conditions". Another objective was to obtain data at higher resolution, i.e. sufficient for the spectra to be fully resolved.

NO_2

NO_2 plays an important role in the photochemistry of the Earth's atmosphere. It acts as the main ozone source and as a nitric acid precursor in the troposphere. In the stratosphere, it is well known that NO_2 is closely linked to the ozone cycle as well as to the ClO cycle and plays a major role in the coupling of the NO_x and ClO_x families. Atmospheric NO_2 concentrations and their variations, partially due to man-made gaseous emissions, need to be known accurately to help in political decisions concerning the preservation of the stratospheric ozone layer.

The DOAS (Differential Optical Absorption Spectroscopy) technique, widely used for the determination of the NO_2 atmospheric concentrations, often led to inconsistent results (Camy-Peyret et al., 1996). It was first suspected that residual structures appearing in atmospheric spectra after the removal of the NO_2 signature could be due to the temperature dependence of the NO_2 absorption cross-section. Later, discrepancies of the order of 10-20% were found between laboratory absorption cross-sections measured at room temperature (Mérienne et al., 1995; Vandaele et al., 1996). It was therefore urgent to produce accurate absorption cross-sections at (low) temperatures representative of the stratosphere, and to resolve the discrepancies between literature data. The precise knowledge of the temperature

dependence allows moreover the simulation of a spectrum at any temperature, which can be very useful in the determination of the vertical distributions of the concentrations.

Laboratory measurements of NO_2 are very difficult because:

- absorption cross-sections are temperature dependent;
- the NO_2 photodissociation imposes a short time for recording spectra;
- an absorption/desorption phenomena of NO_2 on the cells walls is present;
- the dimer N_2O_4 is present through the reaction $2NO_2 \leftrightarrow N_2O_4$. The equilibrium constant of this reaction is not well defined, particularly at low temperature, and in addition N_2O_4 absorbs light in a region where NO_2 has to be measured (>25000 cm^{-1}).

The first laboratory campaign allowed the determination of NO_2 absorption cross-sections at medium resolution (2 cm^{-1}) in the UV to NIR region (42000-10000 cm^{-1}) and at 2 temperatures (290 and 220 K).

Figure 65 shows as an example the absorption cross-section obtained at 294 K. The temperature effect is confirmed. Its impact on the stratospheric NO_2 calculation was assessed, and the absolute necessity to use cross-sections measured at a temperature as close as possible to that prevailing in the atmospheric layer investigated was emphasized. For the first time, a significant pressure effect was observed in the visible region of the spectrum at both temperatures (Vandaele et al., 1998).

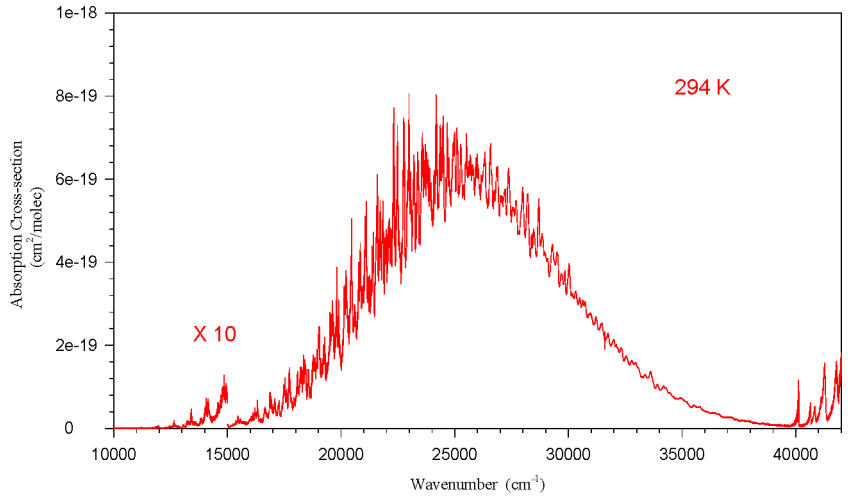

Figure 65: *NO_2 absorption cross-section at 294 K and at a resolution of 2 cm^{-1}.*

During the second laboratory campaign, the pressure effect was investigated through measurements at various pressures (pure NO_2 and NO_2 mixtures with different dilutions) and at 3 different temperatures in the visible to NIR region (25000-10000 cm^{-1}). This campaign has allowed the determination of new absorption cross-sections at higher resolution (0.1 cm^{-1} in the visible and 0.05 cm^{-1} in the NIR instead of 2 cm^{-1}) at 3 temperatures (220, 240, and 290 K). The necessity to work at higher resolution was demonstrated by the fact that the spectra recorded at a resolution of 2 cm^{-1} still showed unresolved absorption features. A linear regression expression was used to quantify the temperature dependence. This expression:δ_{NO2} = :δ_0 + a.T is able to reproduce cross-sections at any temperature with an accuracy better or equal to 10% (Figure 66). The pressure effect has also been investigated by analysing the spectra recorded at different total pressures and at 294 K (Figure 67). The method, which consists of broadening the pure NO_2 spectra with a gaussian function whose width is linearly dependent on the total pressure, is quite satisfactory at room temperature. However, at lower temperature the assumption of a constant width for the gaussian function is not adequate and a more sophisticated model should be developed in the future.

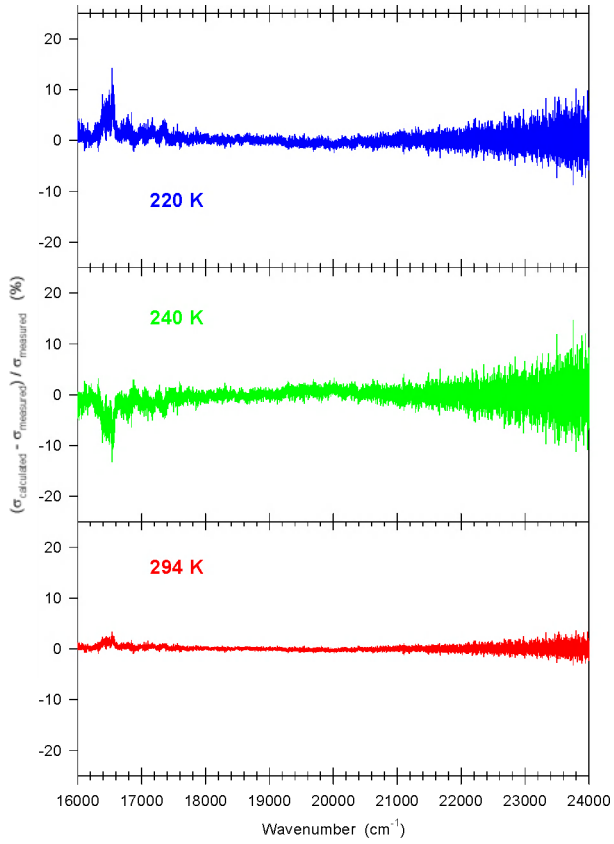

Figure 66: *Temperature effect: Comparison between observed and calculated cross sections using the linear regression parameters.*

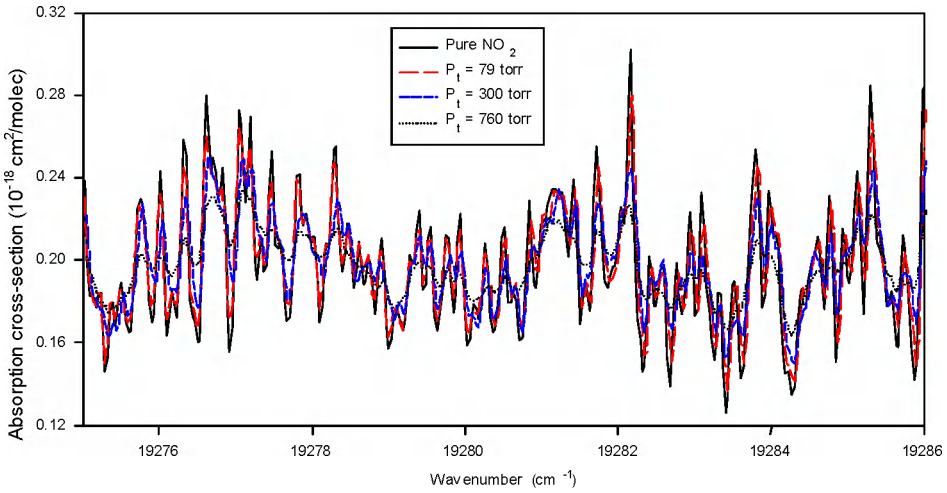

Figure 67: *Pressure effect on a small portion of the NO_2 absorption cross-section obtained at 294 K.*

O_2

In the UV region, the strong ozone Hartley band, which is used to retrieve tropospheric ozone concentrations, overlaps with oxygen bands. Improvements in the spectroscopic analysis of the discrete forbidden Herzberg band systems of oxygen are therefore essential for atmospheric applications. Moreover, the O_2-O_2 diffuse bands, which overlap the discrete forbidden Herzberg bands in this region show similar absorption structures as ozone, as shown in Figure 68.

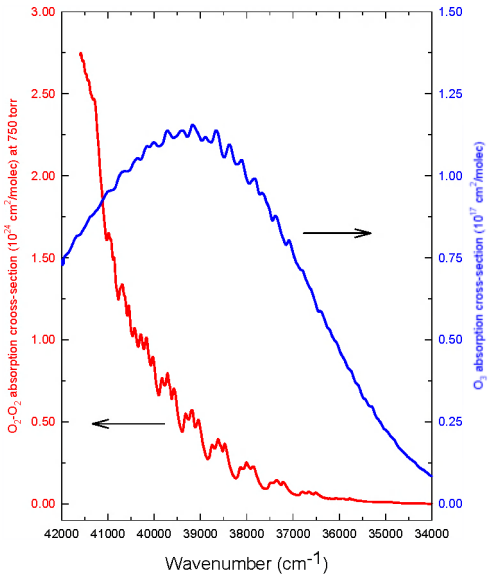

Figure 68: *Overlapping between the ozone Hartley band and the O_2-O_2 absorption bands (=Wulf bands).*

In the visible and NIR regions, the discrete and the diffuse bands of oxygen contribute to the solar absorption and therefore play an important role in the Earth's radiative budget. Up to now, the diffuse bands are not mentioned in the widely used HITRAN and GEISA databases (Rothman et al., 1996; Jaquinet-Husson et al., 1999). The absorption bands of O_2 in this region can also be used to derive various atmospheric properties such as cloud height and coverage parameters, owing to the constant mixing ratio of oxygen in the middle and lower atmosphere. For all these reasons, a complete reinvestigation of the oxygen spectrum from the UV to the NIR (42000-7500 cm^{-1}) was undertaken.

In the UV, a complete spectroscopic high-resolution reinvestigation of the Herzberg I, II and III band systems was carried out (Figure 69). The important parameters deduced from these laboratory measurements are: the line positions, the line intensities, the integrated cross-section values, the band oscillator strengths and the effective transitions moments. The spectroscopic knowledge of the three Herzberg systems was greatly improved: Rotational assignments were extended, molecular constants were improved significantly, interaction between states were better described, and local perturbations near the dissociation limit were reinterpreted. All these parameters constitute an accurate and extensive dataset. Two papers on this subject are published (Jenouvrier et al., 1999; Mérienne et al., 2000), and a complementary note is submitted (Mérienne et al., b). A complete linelist is available on the IASB website (http://www.oma.be/BIRA-ASB/Scientific/Topics/Lower/LaboBase/laboratory. html).

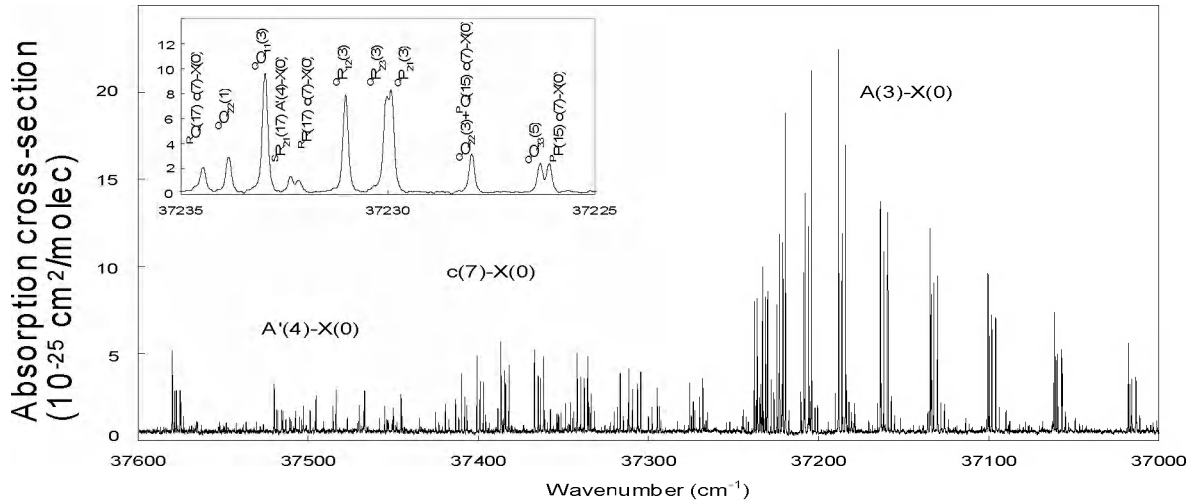

Figure 69: *Portion of a high-resolution O_2 spectrum showing the quality of the data and some rotational assignments.*

In the UV, the medium resolution study of the non-structured absorption, namely the O_2 Herzberg continuum, and the O_2-X collision-induced bands (or Wulf bands) was also completed.

The experimental spectrum (Figure 70a) is composed of the Herzberg I, II, and III systems, the Herzberg continuum, and the broad O_2-O_2 Wulf bands. The Herzberg lines are eliminated by subtracting from an experimental spectrum (Figure 70a) a simulated spectrum at the same pressure and resolution (Figure 70b). The result of the subtraction is shown in Figure 70c, where the three absorption cross-sections are calculated from spectra recorded at several pressures. The separation between the Wulf bands –which are pressure dependent- and the Herzberg continuum –which is pressure independent- is achieved by linear regression. Figure 70a and b show the separated components with their error bars.

The Herzberg continuum absorption cross-section and the collision-induced absorption cross-section have thus been determined, and the Wulf bands characteristics (rotational analysis, pressure effect, foreign gas effect) have been investigated in details. These results are published (Bernath et al., 1998; Fally et al., 2000) and the absorption cross-sections are accessible on the BIRA-IASB website. The originality of these results lies in the removal of the Herzberg bands prior to the determination of the intensity of the Wulf bands.

This enables us to measure the Wulf bands at atmospheric pressures, as opposed to previous studies, which were generally conducted at pressures sufficiently high that the contribution of the Herzberg bands could be neglected.

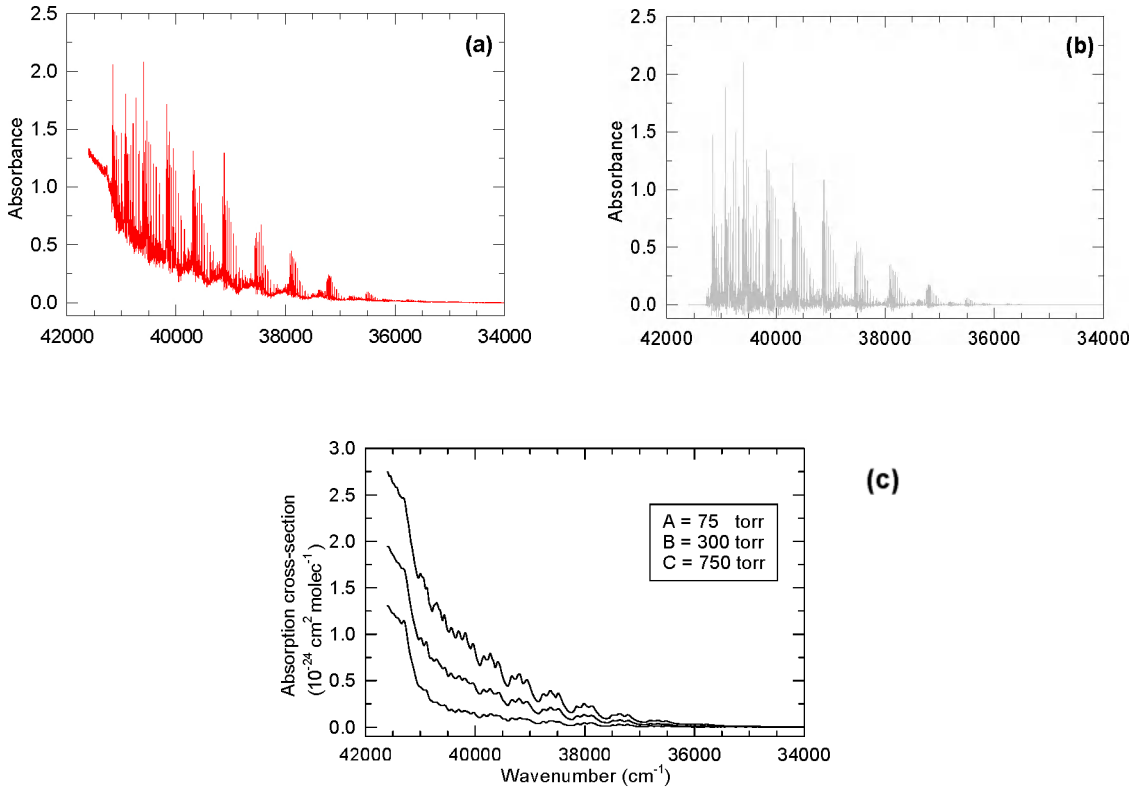

Figure 70: (a) *Experimental spectrum of pure O_2 at 450 torr.* ***(b)*** *Simulated spectrum at the same pressure and resolution.* ***(c)*** *Absorption cross-sections resulting from the subtraction (a)-(b) at 3 pressures*

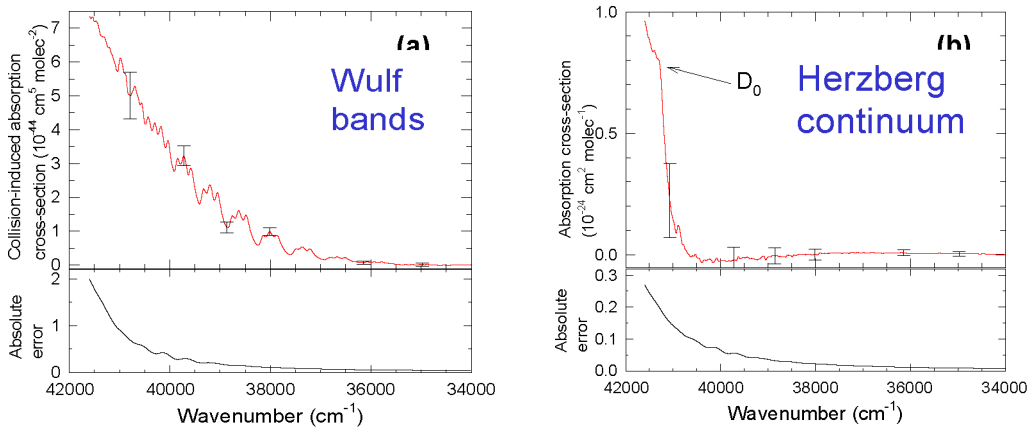

Figure 71: (a) *O_2-O_2 Collision-induced absorption cross-section.* ***(b)*** *Herzberg continuum absorption cross-section.*

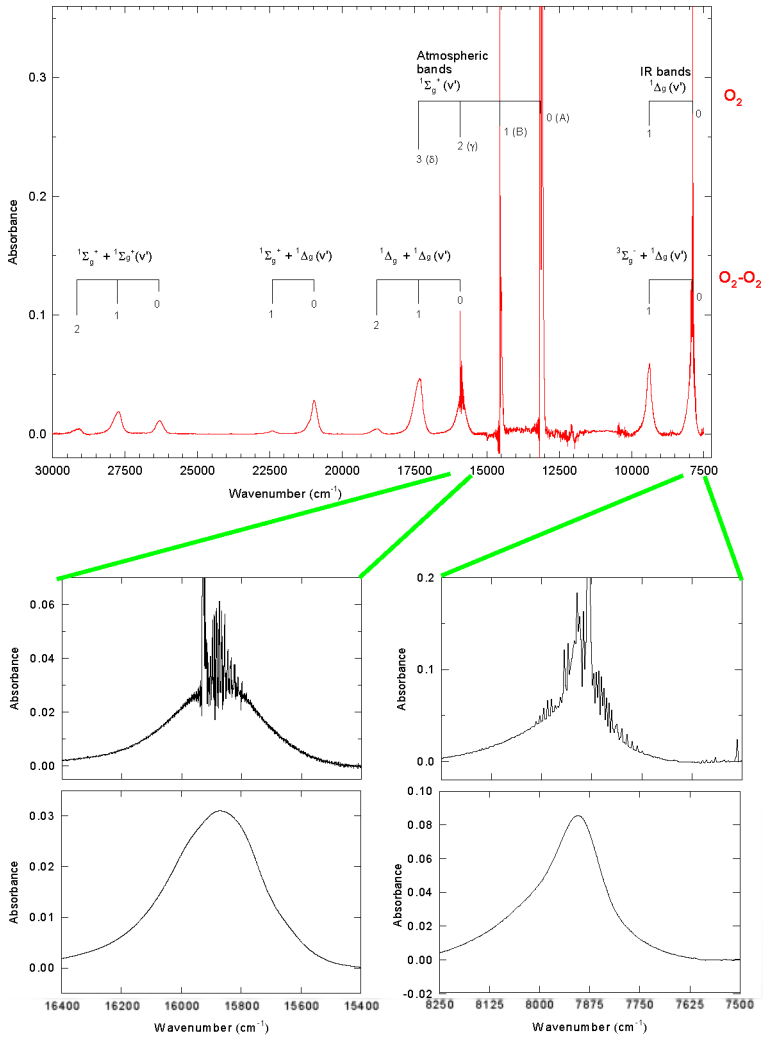

Figure 72: *Visible and NIR experimental spectrum of pure O_2 at 600 torr. Expanded portions show the separation of the O_2 and of the O_2-O_2 contributions.*

In the visible-near infrared region, the oxygen spectrum is composed of the O_2 discrete bands and the overlapping broad O_2-O_2 bands, as shown in the upper part of Figure 72. The spectroscopic study of the A, B, and У atmospheric bands and of the infrared bands allows to determine line positions and intensities. By applying the same procedure as in the UV region, the discrete and diffuse components of the spectrum have been separated. The result of this separation is shown in the bottom part of Figure 72 for two bands. This procedure allows the determination of a new set of O_2-O_2 absorption cross-sections, band centre positions, and bandwidths (Hermans et al., 1999). Pressure and temperature effects have also been described and will appear in a forthcoming paper (Hermans et al.).

H_2O

As the most abundant minor constituent and greenhouse gas of the Earth's troposphere, the water molecule plays a key role in atmospheric studies. The water molecule absorbs strongly in the infrared region, but recently greater interest has been put on the visible and ultraviolet weak absorption lines. The major importance of these weak water vapor lines is their possible contribution to the earth's radiation balance. Up to now, the atmospheric models of the Earth's radiation budget underestimate the observed values (Ramanathan and Vogelman, 1997), and water vapor forms a possible candidate for what is sometimes called the "missing absorber" (Learner et al., 1999). Considering this, it appears essential to improve and extend the spectroscopic data of H_2O by new laboratory measurements, especially in the UV-visible region where the existing data are scarce and mostly inaccurate. However, due to the weakness of the lines in the near-UV and visible regions, this requires very long optical pathlength and very sensitive laboratory techniques. Camy-Peyret et al. (1985) were the first to obtain high-quality laboratory spectra of water vapor between 25000 and 16000 cm^{-1}. They identified 1947 water lines in the 25000 - 16000 cm^{-1} spectral range, measured absolute line intensities for about 35% of them, and assigned about 60 % of them. The spectroscopic measurements and theoretical attributions made by Camy-Peyret et al. (1985) were included in the widely used HITRAN and GEISA databases (Rothman et al., 1996; Jaquinet-Husson et al., 1999). More recently, using a FT solar spectrum, Harder and Brault (1997) identified about 60 % more lines than listed by Camy-Peyret et al. (1985) in the narrow 22721-22230 cm^{-1} spectral range.

By combining the Fourier Transform Spectrometer with the very long multipass cell of the Université de Reims, we have undertaken to improve and extend the existing spectroscopic data. The two measurement campaigns (Table VII) have allowed us to record numerous high resolution spectra at different pressures and temperatures from the near-UV to the NIR (26000-10000 cm^{-1}). Figure 73 presents a raw spectrum of pure H_2O at 16 torr, and expanded portions in the visible and in the UV regions. The line identification by itself is a very time consuming task, because many weak lines are difficult to discriminate from the noise, and also because the high density of lines in most regions causes the overlapping of numerous lines. As the objective is to obtain the best possible line parameters, the fitting procedure is also a long and difficult task. Compared to the HITRAN database, a large number of new lines were identified and assigned in the 26000-13000 cm^{-1} spectral range. The spectral analysis performed in collaboration with the theoretical group at the University College London led to the assignment of about 2500 new lines corresponding to different rovibrational transitions, including transitions to 20 new overtone and

combination bands. Energy levels were successfully calculated (Carleer et al., 1999; Zobov et al., 2000). At present, cross sections and self broadening parameters of about 10000 lines have also been determined. This represents three times more lines than those reported in HITRAN (Table VII). The comparison of our line cross-sections with those listed in HITRAN shows an average discrepancy of about 10% although slight differences appear from band to band, as shown in Figure 74. These smaller values are such that, despite a much larger number of lines, our integrated absorption cross-section over the spectral range investigated is nearly equal to that obtained with the HITRAN data (Table VII).

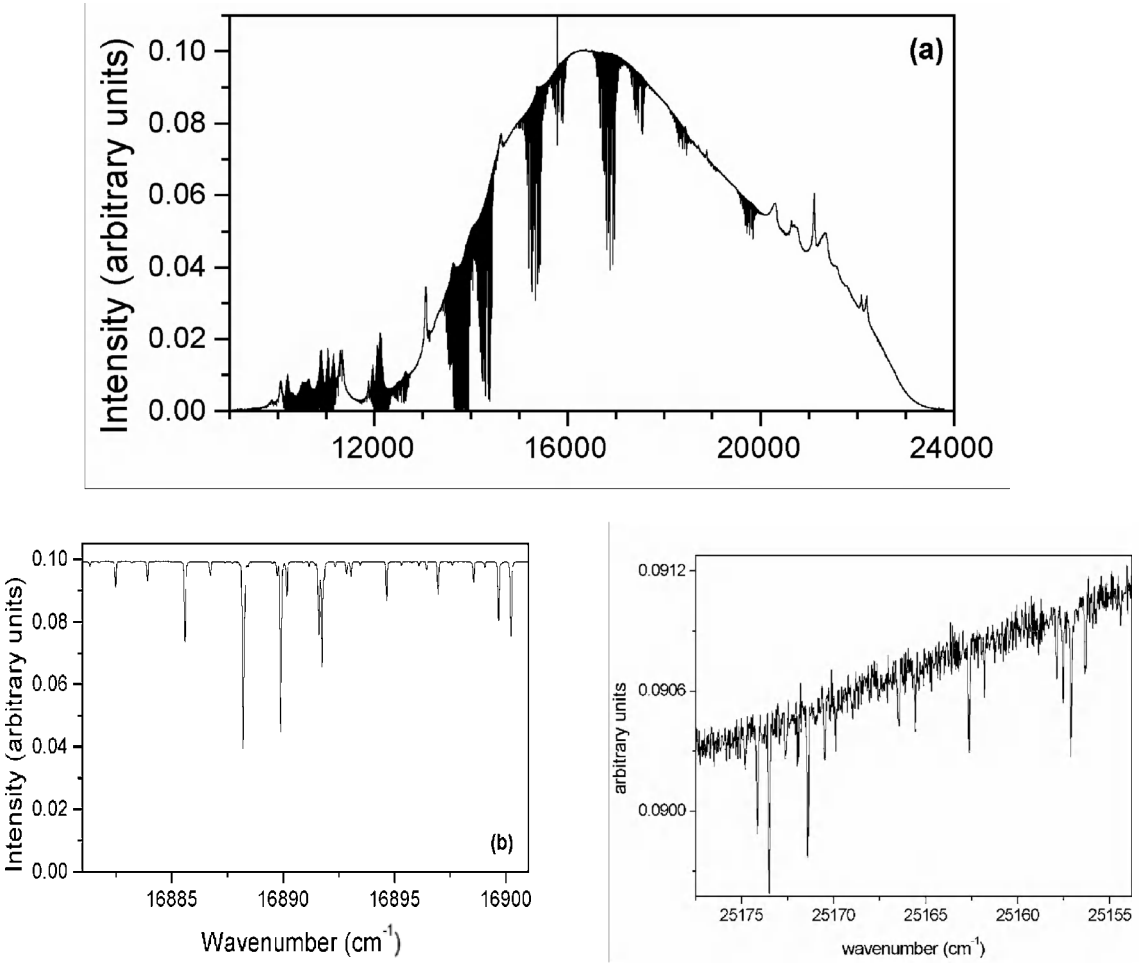

Figure 72: ***(a)*** *Raw water vapor spectrum from the NIR (10000 cm^{-1}) to the near-UV (24000 cm^{-1}). Expanded portions of the spectrum in the visible* ***(b)*** *and in the UV region* ***(c)****.*

By combining the Fourier Transform Spectrometer with the very long multipass cell of the Université de Reims, we have undertaken to improve and extend the existing spectroscopic data. The two measurement campaigns (Table VII) have allowed us to

record numerous high resolution spectra at different pressures and temperatures from the near-UV to the NIR (26000-10000 cm^{-1}). Figure 73 presents a raw spectrum of pure H_2O at 16 torr, and expanded portions in the visible and in the UV regions. The line identification by itself is a very time consuming task, because many weak lines are difficult to discriminate from the noise, and also because the high density of lines in most regions causes the overlapping of numerous lines. As the objective is to obtain the best possible line parameters, the fitting procedure is also a long and difficult task. Compared to the HITRAN database, a large number of new lines were identified and assigned in the 26000-13000 cm^{-1} spectral range. The spectral analysis performed in collaboration with the theoretical group at the University College London led to the assignment of about 2500 new lines corresponding to different rovibrational transitions, including transitions to 20 new overtone and combination bands. Energy levels were successfully calculated (Carleer et al., 1999; Zobov et al., 2000). At present, cross sections and self broadening parameters of about 10000 lines have also been determined. This represents three times more lines than those reported in HITRAN (Table VII). The comparison of our line cross-sections with those listed in HITRAN shows an average discrepancy of about 10% although slight differences appear from band to band, as shown in Figure 74. These smaller values are such that, despite a much larger number of lines, our integrated absorption cross-section over the spectral range investigated is nearly equal to that obtained with the HITRAN data (Table VII).

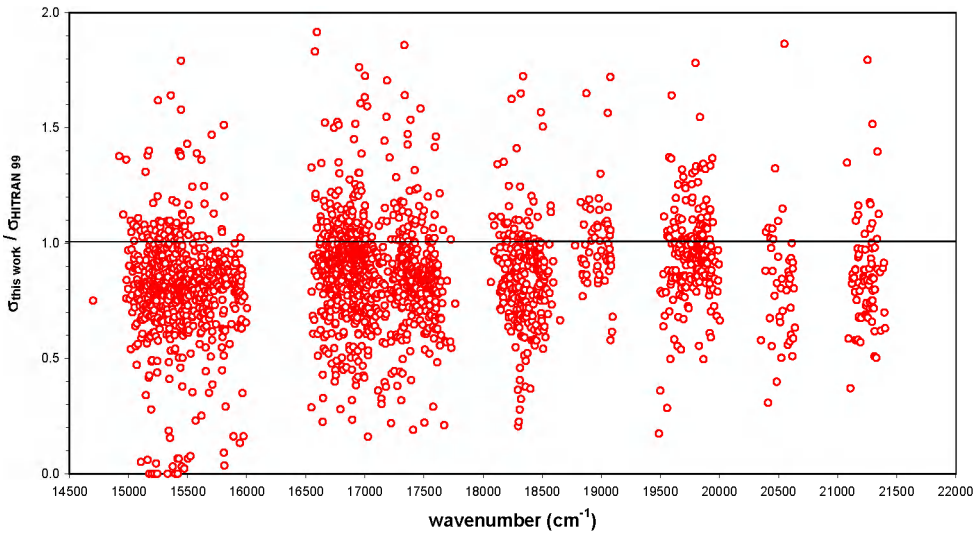

Figure 74: *Comparison of absorption cross-sections obtained in this work ($\sigma_{this\ work}$) and reported in the HITRAN database (σ_{HITRAN}) as a function of wavenumber.*

In the visible-near UV spectral range (26000-20000 cm^{-1}), the number of lines is five times greater than reported in HITRAN and the integrated absorption cross section is twice that reported in HITRAN, as shown in Table VII (sub-total). These results demonstrate the importance of the weak absorption lines of water vapor in the total attenuation of UV light by the atmosphere. This effect can be seen on Figure 75 were preliminary atmospheric simulations performed with a 1D high-resolution radiative transfer model (Clough et al., 1992; Mlawer et al., 1998) using our line list (Figure 4.58a) and the HITRAN line list (Figure 4.58b) as input data are shown. Significant differences between both simulations appear, but the impact of these results on the atmospheric radiative budget has not yet been quantified.

Table VII: *Comparison between the line parameters measured in this work and those reported in the HITRAN database. n refers to the number of lines; σ to the absorption cross-section; and γ_{self} to the self-broadening parameter.*

Spectral Range [cm^{-1}]	**This work**			**HITRAN99**		
	n	σ [cm $molec^{-1}$]	γ_{self} [cm^{-1} atm^{-1}]	n	σ [cm $molec^{-1}$]	γ_{self} [cm^{-1} atm^{-1}]
26000-24000	75	$9.05\ 10^{-25}$	0.68	0		
24000-22000	398	$5.17\ 10^{-24}$	0.52	72	$3.50\ 10^{-24}$	0.45
22000-20000	510	$3.78\ 10^{-24}$	0.45	124	$1.07\ 10^{-24}$	0.46
20000-19300	641	$2.42\ 10^{-23}$	0.59	229	$2.18\ 10^{-23}$	0.45
19300-18700	175	$1.51\ 10^{-24}$	0.53	61	$1.07\ 10^{-24}$	0.46
18700-18000	605	$1.28\ 10^{-23}$	0.55	293	$1.28\ 10^{-23}$	0.45
18000-17200	737	$2.16\ 10^{-23}$	0.54	341	$2.30\ 10^{-23}$	0.44
17200-16400	1295	$1.58\ 10^{-22}$	0.50	678	$1.60\ 10^{-22}$	0.43
16400-15600	810	$1.72\ 10^{-23}$	0.58	197	$1.85\ 10^{-23}$	0.44
15600-14700	1754	$1.07\ 10^{-22}$	0.60	499	$1.07\ 10^{-22}$	0.42
14700-13000	3242	$1.65\ 10^{-21}$	0.44	2052	$1.59\ 10^{-21}$	0.43
Sub-total 26000-20000	983	$9.86\ 10^{-24}$		196	$4.57\ 10^{-24}$	
Total	10242	$2.00\ 10^{-21}$		4546	$1.94\ 10^{-21}$	

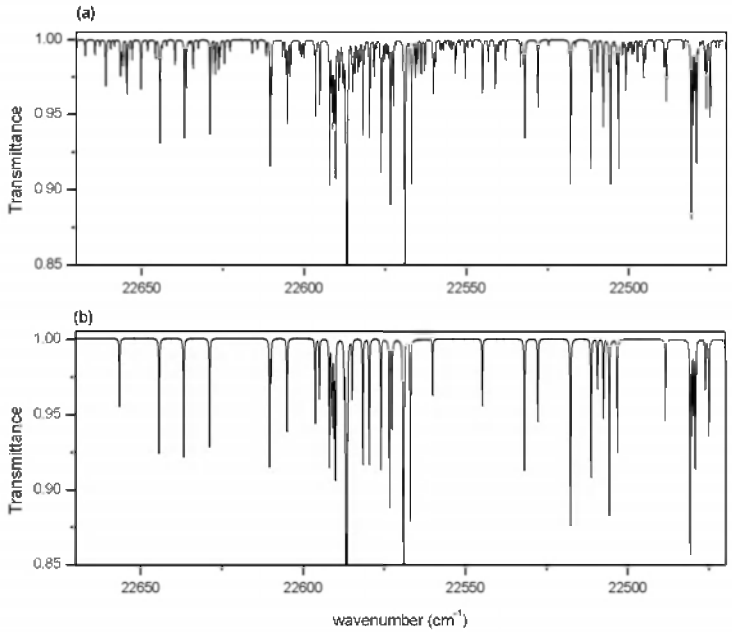

Figure75: *Atmospheric water vapour absorption spectrum, as obtained by a 1D high-resolution radiative transfer simulation in the solar regime using as source data (a) the present line list and (b) the HITRAN line list.*

The analysis of the water vapor spectra recorded under various pressures of nitrogen, which allows the determination of the line broadening and line shifting parameters is in progress. Also, the temperature dependency of all spectral parameters is under investigation. A paper reporting the spectroscopic analysis of the HOD spectrum has been submitted (Mérienne et al, b).

4.4.2.2 Line parameters and absorption cross-sections in the IR-NIR

Stable species (OCS, $^{12}C_2H_2$, HCFC-22 and HFC-152a)

We have studied the absorption spectra of several isotopomers of OCS, of $^{12}C_2H_2$ and two CFC replacements, HCFC-22 and HFC-152a:

- **OCS**: We have recorded the FT spectrum of natural OCS from 4800 to 8000 cm^{-1} with a near Doppler resolution. Vibration-rotation line positions have been measured for a total of 52 absorption bands of 4 isotopomers of the species, with accuracy between 2 and 8×10^{-4} cm^{-1}. Line intensities have also been determined. A global rovibrational analysis of the main isotopomer has been done, leading to a complete description and prediction of its vibration-rotation absorption spectrum (Rbaihi et al., 1998).

- **$^{12}C_2H_2$**: We have measured absolute line intensities in the $\nu_4+\nu_5$ band observed near 7.5 μm (Vander Auwera, 2000a). These measurements have put forward a significant Herman-Wallis dependence, involving an increase of the individual line intensities by as much as 20% from the *P*- to the *R*-branch. The accuracy of the line intensities is estimated to be better than 2%. These intensity data are included in the latest version of the HITRAN database (HITRAN 2000) and will be in the forthcoming version of the GEISA databank.
- **HCFC-22 and HFC-152a**: We have measured absorption cross-sections between 600 and 1700 cm^{-1} for these two species, either as pure gases or in mixtures with dry air at total pressures of 150 torr and 600 torr. Cross-sections have been obtained at several temperatures between 293 and 203K (Vander Auwera, 2000b; Ballard et al., 2000). These experimental conditions aim at reproducing at best the physical conditions encountered in the troposphere and lower stratosphere. Figure 4.59 presents examples of the cross-sections obtained for HFC-152a. These data will also be included in the forthcoming version of the GEISA databank.

Unstable species: HOCl

We have recently extended absolute line intensities measurements to chemically unstable and reactive species, such as acidic compounds found in the troposphere and stratosphere. Such measurements are most challenging because the required concentration of the species is not directly accessible, for instance through the measurement of the total gas pressure. These unstable compounds indeed usually exist only in equilibrium mixtures. Furthermore, their concentration may evolve while their spectra are being recorded, as a result of their reactivity.

In the visible-near UV spectral range (26000-20000 cm^{-1}), the number of lines is five times greater than reported in HITRAN and the integrated absorption cross section is twice that reported in HITRAN, as shown in Table VII (sub-total). These results demonstrate the importance of the weak absorption lines of water vapor in the total attenuation of UV light by the atmosphere. This effect can be seen on Figure 75 were preliminary atmospheric simulations performed with a 1D high-resolution radiative transfer model (Clough et al., 1992; Mlawer et al., 1998) using our line list (Figure 4.58a) and the HITRAN line list (Figure 4.58b) as input data are shown. Significant differences between both simulations appear, but the impact of these results on the atmospheric radiative budget has not yet been quantified.

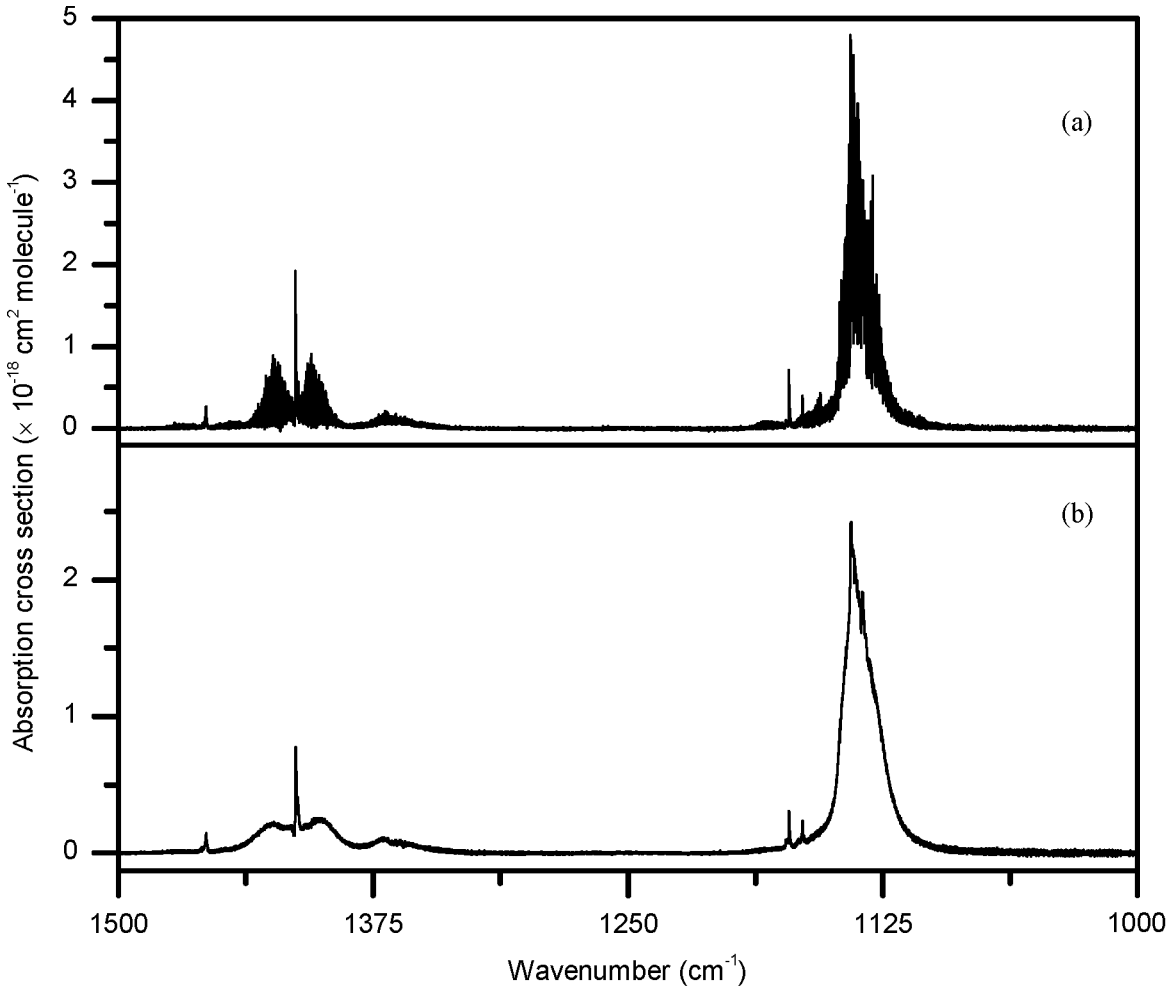

Figure 76: *Absorption cross-sections of HFC-152a: pure sample at 203 K (a) and mixture with dry air at a total pressure of 800 mbar at 293 K (b) (adapted from (Vander Auwera, 2000b).*

ACRONYMS

AMF	Air Mass Factor
BIRA-IASB	Belgisch Instituut voor Ruimte Aeronomie - Institut d'Aéronomie Spatiale de Belgique
CIE	Commission Internationale de l'Eclairage.
CTM	Chemistry Transport Model
DOAS	Differential Optical Absorption Spectroscopy
DSCD	Differential Slant Column Density
EAP	Effective Apodisation Parameter
ECMWF	European Centre for Meteorology and Weather Forecasting
EMPA	Swiss federal Laboratories for Materials Testing and Research
FT	Fourier Transform
FTS	Fourier Transform Spectrometer
FTIR	Fourier Transform Infrared
FWHM	Full width half maximum
GIRPAS	Groupe Infra-Rouge de Physique Atmosphérique et Solaire
GAW	Global Atmosphere Watch
IBGE	Institut Bruxellois pour la Gestion de l'Environnement
IRCEL	Belgian Interregional Cell for the Environment
ISSJ	International Scientific Station of the Jungfraujoch
KMI-IRM	Koninklijk Meteorologisch Instituut van België – Institut Royal Météorologique de Belgique
LCPM	Laboratoire de Chimie Physique Moléculaire
NDSC	Network for the Detection of Stratospheric Change
OEM	Optimal Estimation Method
OHP	Observatoire de Haute Provence
PBL	planetary boundary layer
PSC	Polar Stratospheric Cloud
RT	Radiative Transfer
SAOZ	Système d'Analyse par Observations Zénithales
SCD	Slant Column Density
SPARC	Stratospheric Processes and Their Role in Climate
SZA	Solar Zenith Angle
TBL	Tropospheric Boundary Layer
UKMO	United Kingdom Meteorological Office
ULB	Université Libre de Bruxelles
Ulg	Université de Liège
UV	Ultraviolet
UVI	UV Index
Vis	visible
VMR	volume mixing ratio
WCRP	World Climate Research Programme
WMO	World Meteorological Office

REFERENCES

We use the term greenhouse gases because of its widespread use. However it must be noticed that the term is badly chosen, because the atmospheric warming effect is a different physical process than the one that controls the real greenhouse: the latter is based on the reduction of convective transport, the atmospheric warming is caused by absorption of thermal infrared radiation (Kockarts, 2000).

Abrams, M. C., Gunson, M. R., Lowes, L. L., Rinsland, C. P. and Zander, R. 1996a. Pressure sounding of the middle atmosphere from ATMOS solar occultation measurements of atmospheric CO_2 absorption lines. Appl. Opt. 35: 2,810-2,820.

Abrams, M. C., Chang, A. Y., Gunson, M. R., Abbas, M. M., Goldman, A. G., Irion, F. W., Michelsen, H. A., Newchurch, M. J., Rinsland, C. P., Stiller, G. P. and Zander, R. 1996b. On the assessment and uncertainty of atmospheric trace gas burden measurements with high-resolution infrared solar occultation spectra from space by the ATMOS experiment. Geophys. Res. Lett. 23: 2,337-2,340.

Aliwell, S.R., Van Roozendael, M., Johnston, P.V., Richter, A., Wagner, T., Arlander, D.W., Burrows, J.P., Fish, D.J., Jones, R.L., Tørnkvist, K.K., Lambert, J.-C., Pfeilsticker K. and Pundt, I. (In press 2001). Analysis for BrO in Zenith-Sky Spectra: An Intercomparison Exercise for Analysis Improvement. J. Geophys. Res.

Anderson, J., Russell III, J.M., Solomon, S. and Deaver, L.E. 2000. Halogen Occultation Experiment confirmation of stratospheric chlorine decrease in accordance with the Montreal protocol. J. Geophys. Res. 105: 4,483-4,490.

Ballard, J., Knight, R. J., Vander Auwera, J., Herman, M., Di Leonardo, G., Masciarelli, G., Nicolaisen, F. M., Beukes, J. A., Christensen, L. K., McPheat, R., Duxbury, G., Freckleton, R. and Shine, K. P. 2000. An intercomparison of laboratory measurements of absorption cross-sections and integrated absorption intensities for HCFC-22. J. Quant. Spectrosc. Radiat. Transfer 66: 109-128.

Barret, B., Mahieu, E., Carleer, M., De Mazière, M., Colin, R. and Zander, R. 1999. Tropospheric boundary layer investigations by differential ground-based solar FTIR spectrometry. In: Environmental Sensing and Applications. SPIE Proceedings 3821: 116-123.

Barry J., Locke, G., Scollard, D., Sidebottom, H., Treacy, J., Clerbaux, C., Colin, R. and Franklin, J. 1997. 1,1,1,3,3-pentafluorobutane (HFC-365mfc): atmospheric degradation and contribution to radiative forcing. Int. J. Chem. Kinet. 29: 607-617.

Bell, W., Duxbury, G. and Stuart, D.D. 1992. High-resolution spectra of the v_4 band of chlorine nitrate. J. Mol. Spectrosc. 152: 283-297.

Bernath, P., Carleer, M., Fally, S., Jenouvrier, A., Vandaele, A. C., Hermans, C., Mérienne, M.-F. and Colin, R. 1998. The Wulf bands of oxygen. Chem. Phys. Letters 297: 293-299.

Bevilacqua, R.M., Kriebel, D.L., Pauls, T.A., Aellig, C.P., Siskind, D.E., Daehler, M., Olivero, J.J., Puliafito, S.E., Hartmann, G.K., Kampfer, N., Berg, A. and Croskey, C.L. 1996. MAS measurements of the latitudinal distribution of water vapor and ozone in the mesosphere and lower thermosphere. Geophys. Res. Lett. 23: 2,317-2,320.

Birk, M., Hausamann, D., Wagner, G. and Johns, J. W. C. 1996. Determination of line strenghts by Fourier transform spectroscopy. Appl. Opt. 35: 2,971-2,985.

Birk, M., and Wagner, G. 2000. A new spectroscopic database for chlorine nitrate. In: Poster session 2, Sixth Biennial Hitran Database Conference, Harvard-Smithsonian Center for Astrophysics, Cambridge, MA, 19-21 June 2000.

Brasseur, G., and Granier, C. 1992. Mount Pinatubo aerosols, chlorofluorocarbons, and ozone depletion. Science 257: 1,239-1,242.

Camy-Peyret, C., Flaud, J.-M., Mandin, J.-Y., Chevillard, J.-P., Brault, J., Ramsay, D. A., Vervloet, M. and Chauville, J. 1985. The high-resolution spectrum of water vapor between 16500 and 25250 cm^{-1}. J. Mol. Spec. 113: 208-228.

Camy-Peyret, C., Bergqvist, B., Galle, B., Carleer, M., Clerbaux, C., Colin, R., Fayt, C., Goutail, F., Nunes-Pinharanda, M., Pommereau, J. P., Hausmann, M., Plat,t U., Pundt, I., Rudolph, T., Hermans, C., Simon, P. C., Vandaele, A. C., Plane, J. M. and Smith, N. 1996. Intercomparison of instruments for tropospheric measurements using Differential Optical Absorption Spectroscopy. J. Atm. Chem. 23: 51-80.

Carleer, M., Jenouvrier, A., Vandaele, A. C., Bernath, P. F., Mérienne, M.-F., Colin R., Zobov, N. F., Polyansky, O. L., Tennyson, J. and Savin, S. A. 1999. The near

infrared, visible, and near ultraviolet overtone spectrum of water. J. Chem. Phys. 111 (6): 2,444-2,450.

Chipperfield, M. 1999. Multiannual simulations with a three-dimensional chemical transport. Model. J. Geophys. Res. 104: 1,781-1,805.

Clerbaux, C., Colin, R., Simon, P. C. and Granier, C. 1993. Infrared cross sections and Global Warming Potentials of 10 alternative hydrohalocarbons. J. Geophys. Res. 98 (D6): 10,491-10,497.

Clerbaux, C. and Colin, R. 1994. Determination of the infrared cross sections and Global Warming potentials of 1,1,2-Trifluoroethane (HFC-143). Geophys. Res. Letters 21 (22): 2,377-2,380.

Clough, S. A., Iacono, M. J. and Moncet, J.-L. 1992. Line-by-line calculation of atmospheric fluxes and cooling rates- 1. Application to water vapor. J. Geophys. Res. 97 (D14): 15,761-15,785.

Connor, B.J., Jones, N.B., Wood, S.W., Keys, J.G., Rinsland, C.P. and Murcray F.J. 1996. Retrieval of HCl and HNO_3 profiles from ground-based FTIR data using SFIT2. In: Proceedings of XVIII Quadrennial Ozone Symposium. Bojkov R.J. and Visconti G. (Ed). Parco Sci. e Technol. d'Abruzzo, L'Aquila, Italy : 485-488.

Considine, D.G., Deaver, L.E., Remsberg, E.E. and Russell III, J.M. 1997. HALOE observations of a slowdown in the rate of increase of HF in the lower mesosphere. Geophys. Res. Lett. 24: 3,217-3,220.

De Backer, H., De Muer D. and De Sadelaer, G. 1998. Comparison of ozone profiles obtained with Brewer-Mast and Z-ECC sensors during simultaneous ascents. J. Geophys. Res. 103: 19,641-19,648.

De Backer, H. 1999. Homogenisation of ozone vertical profile measurements at Uccle. Wetenschappelijke en technische publicaties van het K.M.I. 7, ISSN D1999/0224/007, KMI, Ukkel: 26.
(ftp://ftp.kmi-irm.be/dist/meteo/hugo/publ/1999/o3prof.ps)

De Backer, H., Köpke, P., Bais, A., Cuevas, E., Gillotay, D., Haite, C., Heikkilä, A., Koskela, T., Kyrö, E., Lapeta, B., Lorente, J., Mayer, B., Plets, H., Renaud, A., Schmalwieser A.W. and Vanicek, K. 1999. Comparison of measured and modelled UV Indices. 24th General assembly of EGS, Geophysical Research Abstracts. Vol. 1, number 2: 477.

De Backer, H., Koepke, P., Bais, A., de Cabo, X., Frei, T., Gillotay, D., Haite, C., Heikkila, A., Kanzantzidis, A., Koskela, T., Kyrö, E., Lapeta, B., Lorente, J., Masson, K., Mayer, B., Plets, H., Redondas, A., Renaud, A., Schauberger, G., Schmawieser, A., Schwander, H. and Vanicek, K. In press, 2001. Comparison of Measured and Modelled UV Indices. Meteorological Applications.

De Backer, H. In Press. Tropospheric ozone trends in Uccle 1969-1999 after homogenisation of the dataset. In: Proceedings from the EUROTRAC symposium 2000. Midgley, P.M., Reuther, M., Williams M. (Ed). Springer Verlag Berlin, Heidelberg 2001.

De Mazière, M., Van Roozendael, M., Hermans, C., Simon, P.C., Demoulin P. and Roland, G. 1998. Quantitative evaluation of the post-Pinatubo NO_2 reduction and recovery, based on 10 years of FTIR and UV-visible spectroscopic measurements at the Jungfraujoch. J. Geophys. Res. 103: 10,849-10,858.

De Mazière, M., Hennen, O., Van Roozendael, M., Demoulin P. and De Backer, H. 1999. Daily ozone vertical profile model built on geophysical grounds, for column retrieval from atmospheric high-resolution spectra. J. Geophys. Res. 104: 23,855-23,869.

De Mazière, M., Van Roozendael, M., Hennen, O., Demoulin, P. and Mahieu, E. 1999b. Revision of the O3 trend analysis at the Jungfraujoch station. Poster presentation at the Sixth Scientific Conference of the International Global Atmospheric Chemistry Project (IGAC), Bologna, Sept. 13-17, 1999.

De Muer, D., and De Backer, H. 1992. Revision of 20 years of Dobson total ozone data at Uccle (Belgium): Fictitious Dobson total ozone trends induced by sulfur dioxide trends. J. Geophys. Res. 97: 5,921-5,937.

De Muer, D., De Backer, H. and Van Haver, Ph. 1995. Analysis of 25 years of regular ozone soundings at Uccle (Belgium). Atmospheric ozone as a Climate gas. Wang, W. and Isaksen, I. (Ed). Springer-Verlag Berlin: 113-129.

De Muer, D., Heylen, R., Van Loey, M. and De Sadelaer, G. 1997. Photochemical ozone production in the convective mixed layer, studied with a tethered balloon sounding system. J. Geophys. Res. 102: 15,933-15,947.

DeMore, W. B., Sander, S. P., Golden D. M., Hampson, R. F., Kurylo, M. J., Howard, C. J., Ravishankara, A. R., Kolb, C. E., and Molina, M. J. 1997. Chemical Kinetics and Photochemical Data for Use in Stratospheric Modelling. JPL Publication 97-4.

Demoulin, P., Mahieu, E., Zander, R., Roland, G., Delbouille, L., Servais, C., De Mazière, M. and Van Roozendael, M. 1998. The Current Budget of NO_y above the Jungfraujoch as derived from IR Solar Observations. In: Proceedings of the Fourth European Symposium on Polar Stratospheric Ozone Research, Schliersee, Germany, September 22-26, 1997. European Commission, Air pollution research report 66: 427-430.

Demoulin, P., Zander, R., Mélen, F., Mahieu, E. and Servais, C. 1999. Column abundance measurements of formaldehyde above the Jungfraujoch. In: Proceedings of Atmospheric Spectroscopy Applications 1999, Reims, France, September 1-3, 1999: 59-62.

Draper, N. and Smith, H. 1980. Applied regression analysis. J. Wiley & Sons (Ed). New York.

Etheridge, D.M., Steele, L.P., Francey, R.J. and Langenfelds, R.L. 1998. Atmospheric methane between 1000 A.D. and present: Evidence of anthropogenic emissions and climate variability. J. Geophys. Res. 103: 15,979-15,993.

Etheridge, D.M., et al. 2001 (in press). Atmospheric methane between 1000 AD and present: evidence of anthropogenic emissions and climate variability. J. Geophys. Res.

Fally, S., Vandaele, A. C., Carleer, M., Hermans, C., Jenouvrier, A., Mérienne, M.-F., Coquart, B. and Colin, R. 2000. Fourier transform spectroscopy of the O_2 Herzberg bands. III. Absorption cross-sections of the collision-induced bands and of the Herzberg continuum. J. Mol. Spectrosc. 204: 10-20.

Fish, D.J., Jones, R.L. and Strong, E.K. 1995. Midlatitude observations of the diurnal variation of stratospheric BrO. J. Geophys. Res. 100: 18,863-18,871.

Fitzenberger, R., Bösch, H., Camy-Peyret, C., Chipperfield, M.P., Harder, H., Platt, U., Sinnhuber, B.-M., Wagner,T. and Pfeilsticker, K. 2000. First Profile Measurements of Tropospheric BrO. Geophys. Res. Lett. 27: 2921-2924.

Fonteyn, D., Larsen, N. and Remedios, J. J. 2000. Interactive PSC-Chemical Modelling: Lagrangian and Eulerian model case studies. In: Proceedings of the Quadriennial Ozone Symposium, Hokkaido University, Sapporo, Japan, 3-8 July 2000.

Gardiner, B.G., Webb, A.R., Bais, A. F., Blumthaler, M., Dirmhirn, I., Forster, P., Gillotay, D., Henriksen, K., Huber, M., Kirsch, P.J., Simon, P.C., Svenoe, T., Weihs, P. and Zerefos, C.S. 1993. European Intercomparison of ultraviolet spectroradiometers. Environ. Technol. 14: 25-43.

Gillotay D. 1996. UV monitoring in Belgium: Past, present and future. In Measurements and Trends of Terrestrial UVB Radiation in Europe. B. L. Diffey (Ed): 41-53.

Harder, J. W. and Brault, J. W. 1997. Atmospheric measurements of water vapor in the 442-nm region. J. Geophys. Res. 102 (D5): 6,245-6,252.

Harries, J.E., Russell, J.M.,III, Tuck, A.F., Gordley, I.I., Purcell, P.N., Stone, K.A, Bevilacqua, R.M., Gunson, M.R., Nedoluha, G. and Traub, W.A. 1996. Validation of measurements of water vapor from the HALogen Occultation Experiment (HALOE). J. Geophys. Res. 101: 10,205-10,216.

Hendrick, F., Mueller, R., Sinnhuber, B.-M., Bruns, M., Burrows, J. P., Chipperfield, M. P., Fonteyn, D., Richter, A., Van Roozendael, M. and Wittrock, F. 2000. Simulation of BrO Diurnal Variation and BrO Slant Columns: Intercomparison Exercise Between Three Model Packages. In: Proceedings of the 5th European Workshop on Stratospheric Ozone, Saint Jean de Luz, France, 27 Sept.-1 Oct. 1999. Air Pollution Research Report 73, European Commission - DG XII, Brussels, 2000.

Hermans, C., Vandaele, A. C., Carleer, M., Fally, S., Colin, R., Jenouvrier, A., Mérienne, M.-F., and Coquart B. 1999. Absorption cross-sections of atmospheric constituents: NO_2, O_2, and H_2O. Environ. Sci. & Pollut. Res. 6(3): 151-158.

Hermans, C., Jenouvrier, A., Fally, S., Carleer, M., Vandaele, A. C., Mérienne, M.-F., Coquart, B. and Colin, R. In preparation. Absorption cross-sections of oxygen: the IR and visible bands.

Hintsa, E.J., Weinstock, E.M., Anderson, J.G., May, R.D. and Hurst, D.F. 1999. On the accuracy of *in situ* water vapor measurements in the troposphere and lower stratosphere with the Harvard Lyman-α hygrometer. J. Geophys. Res. 104: 8,183-8,189.

Hofmann, D.J., and Solomon, S. 1989. Ozone destruction through heterogeneous chemistry following the eruption of El Chichon. J. Geophys. Res. 94: 5,029-5,041.

Jäger, H., Uchino, O., Nagai, T., Fujimoto, T., Freudenthaler, V. and Homburg, F. 1995. Ground-based remote sensing of the decay of the Pinatubo eruption cloud at three northern hemisphere sites. Geophys. Res. Lett. 22: 607-610.

Jaquinet-Husson, N., Arié, E., Barbe, A., Bjoraker, G., Bonnet, B., Brown, L. R., Camy-Peyret, C., Champion, J.-P., Chédin, Chursin, A. A., Clerbaux, C., Duxbury G., Flaud, J.-M., Fourrié, N., Fayt, A., Graner, G., Gamach, R., Goldman, A., Golovko V., Guelachvilli, G., Hartmann, J. M., Hilico, J. C., Hillman, J., Lefèvre, G., Lellouch, E., Mikhaïlenko S. N., Naumenko, O. V., Nemtchninov, V., Newnham, D. A., Nikitin, A., Orphal, J., Perrin, A., Reuter, D. C., Rinsland, C. P., Rosenmann, L., Rothman, L. S., Scott, N. A., Selby, J., Sinitsa, L. N., Sirota, J. M., Smith, A. M., Smith, K. M., Tyuterev, V. G., Tipping, R. H., Urban, S., Varanasi, P. and Weber, M. 1999. The 1997 spectroscopic GEISA databank. J. Quant. Spectrosc. Radiat. Transfer 61: 4,205-4,254.

Jenouvrier, A., Mérienne, M.-F., Coquart, B., Carleer, M., Fally S., Vandaele, A. C., Hermans, C. and Colin R. 1999. Fourier transform spectroscopy of the O_2 Herzberg bands. I. Rotational Analysis. J. Mol. Spectrosc. 198: 136-162.

Kockarts, G. 2000. Aeronomie: Physique et Chimie de l'atmosphere. De Boeck. (Ed), Bruxelles, 2000.

Köpke, P, Bais, A., Balis, D., Buchwitz, M., De Backer, H., de Cabo, X., Eckert, P., Eriksen, P., Gillotay, D., Koskela, T., Lapeta, B., Litynska, Z., Lorente, J., Mayer, B., Renaud, A., Ruggaber, A., Schauberger, G., Seckmeyer, G., Seifert, P., Schmalwieser, A., Schwander, H., Vanicek K. and Weber, M. (1998) Comparison of models used for UV index -calculations, Photochemistry and Photobiology 67 (6): 657-662.

Kurylo, M. J., and Solomon, S. 1999. The Network for the Detection of Stratospheric Change. A Status and Implementation Report. In : NASA Headquarters – Code EEU, 600 Independent Avenue, S.W., Washington, D.C. 20546, USA, January 1999: 1-70.

Kylling, A. 1995. UVspec: a program package for calculation of diffuse and direct UV and visible intensities and flux. Available by anonymous ftp to kaja.gi.alaska.edu, cd pub/arve.

Learner, R. C. M., Zhong, W., Haigh, J. D., Belmiloud, D. and Clarke J. 1999. The contribution of unknown weak water vapor lines to the absorption of solar radiation. Geophys. Res. Lett. 26 (24): 3,609-3,612.

Liley, J.B., Johnston, P.V., McKenzie, R.L., Thomas, A.J. and Boyd, I.S. 2000. Stratospheric NO_2 variations from a long time series at Lauder, New Zealand. J. Geophys. Res. 105: 11,633-11,640.

Madronich, S. 1993. UV radiation in the natural and perturbed atmosphere. In: Environmental Effects of UV (Ultraviolet) Radiation. M. Tevini, (Ed). Lewis Publisher, Boca Raton: 17-69.

Mahieu, E., Zander, R., Gunson, M.R., Toon, G.C., Rinsland, C.P. and Demoulin, P. 1996. Evaluation of the life-time of SF_6 in the Earth's atmosphere based on ATMOS and Jungfraujoch IR solar observations. In: Proceedings of the Atmospheric spectroscopy Applications Workshop, ASA-Reims 96, Reims 4-6 sept. 1996. Barbe, A., Flaud, J.-M., Jacon, M., Mérienne, M.-F. and Rothman, L. (Ed). UFR Sciences Exactes et Naturelles, BP 1039-51687, Reims: 125-128.

Mahieu, E., Zander, R., Mélen, F., Demoulin, P., Servais, C., Delbouille, L. and Roland, G. 1998. Recent Characteristic Budget of Inorganic Chlorine and Fluorine above the Jungfraujoch Station. In: Proceedings of the Fourth European Symposium on Polar Stratospheric Ozone Research, Schliersee, Germany, September 22-26, 1997. European Commission, Air pollution research report 66: 358-361.

Mahieu, E., Zander, R., Demoulin, P., De Mazière, M., Mélen, F., Servais, C., Roland, G., Delbouille, L., Poels, J. and Blomme, R. 2000. Fifteen years-trend characteristics of key stratospheric constituents monitored by FTIR above the Jungfraujoch. In: Proceedings of the Fifth European Symposium on Stratospheric Ozone, St. Jean de Luz, France, September 27 - October 1, 1999. N. R. P. Harris, M. Guirlet and G. T. Amanatidis (Eds). Air pollution Research Report 73 - EUR 19340: 99-102.

McKinlay, A.F; and Diffey, B.L. 1987. A reference action spectrum for Ultraviolet induced erythema in human shin. CIE J. 6 : 17-22.

Mélen, F., Mahieu, E., Zander, R., Rinsland, C. P., Demoulin, P., Roland, G., Delbouille, L. and Servais, C. 1998. Vertical column abundances of COF_2 above the Jungfraujoch station derived from ground-based infrared solar observations. J. Atmos. Chem. 29: 119-134.

Mérienne, M.-F., Jenouvrier A. and Coquart, B. 1995. The NO_2 absorption spectrum. I: Absorption cross-sections at ambient temperature in the 300-500 nm region. J. Geophys. Res. 20: 281-297.

Mérienne, M.-F., Jenouvrier, A., Coquart, B., Carleer, M., Fally, S., Colin, R., Vandaele, A.C., and Hermans, C. 2000. Fourier transform spectroscopy of the O_2 Herzberg bands. II. Band oscillator strengths and transition moments. J. Mol. Spectrosc. 202 (2): 171-193.

Mérienne, M.-F., Jenouvrier, A., Coquart, B., Carleer, M., Fally, S., Colin, R., Vandaele, A.C., and Hermans C. Submitted[a]. Improved data set for the Herzberg band systems of $^{16}O_2$. J. Mol. Spectrosc.

Mérienne, M.-F., Jenouvrier A., Carleer, M., Colin, R., Vandaele, A. C., Bernath P. F., Polyansky, O. L. and Tennyson, J. Submitted[b]. The visible and near ultraviolet rotation-vibration spectrum of HOD. J. Mol. Spectrosc.

Michelsen, H. A., Manney, G. L., Irion, F. W., Toon, G. C., Gunson, M. R., Rinsland, C. P., Zander, R., Mahieu, E., Newchurch, M. J., Purcell, P. N., Remsberg, E. E., Russell III, J. M., Pumphrey, H. C., Waters, J. W., Bevilacqua, R. M., Kelly, K. K. and Webster, C. R. 2001 (in press). ATMOS Version 3 water vapor measurements: comparisons with ATMOS Version 2 retrievals and observations from NOAA and Harvard Lyman-α hygrometers, MkIV, MAS, HALOE, and MLS. J. Geophys. Res.

Mlawer, E. J., Clough, S. A., Brown, P. P., Stephen, T. S., Landry J. C., Goldman, A. and Murcray, F. J. 1998. Observed atmospheric collision-induced absorption in near-infrared oxygen bands. J. Geophys. Res. 103 (D4): 3,859-3,863.

Montzka, S.A., Butler, J.H., Myers, R.C., Thompson, T.M., Swanson, T.H., Clarke, A.D., Lock, L.T. and Elkins, J.W. 1996. Decline in the tropospheric abundance of halogen from halcarbons: implications for stratospheric ozone depletion. Science 272: 1,318-1,322.

Montzka, S.A., Butler, J.H., Elkins, J.W., Thompson, T.M., Clarke, A.D. and Lock, L.T. 1999. Present and future trends in the atmospheric burden of ozone-depleting halogens. Nature 398: 690-694.

Neckel, H., and Labs, D. 1984. The Solar Radiation Between 3300 and 12500 A. Solar Physics. 90: 205-258.

Nevison, C.D., Solomon, S. and Russell III, J.M. 1996. Nighttime formation of N2O5 inferred from the Halogen Occultation Experiment sunset/sunrise NOx ratios. J. Geophys. Res. 101: 6,741-6,748.

Norton, R.H., and Rinsland, C.P. 1991. ATMOS data processing and science analysis methods. Appl. Opt. 30: 389-400.

Plets, H. and Vynckier, C. (2000) A comparative study of statistical total column ozone forecasting models, J. Geophys. Res. 105: 26,503-26,517.

Pougatchev, N.S., Connor, B.J., Jones, N.B., and Rinsland, C.P. 1995. Infrared measurements of the ozone vertical distribution above Kitt Peak. J. Geophys. Res. 100(D8): 16,689-16,698.

Pougatchev, N.S., Connor, B.J. and Rinsland, C.P. 1996. Validation of ozone profile retrievals from ground-based solar spectra. Geophys. Res. Lett. 23(13): 1,637-1,640.

Pumphrey, H.C. 1999. Validation of a new prototype water vapor retrieval from the UARS Microwave Limb Sounder. J. Geophys. Res. 104: 9,399-9,412.

Ramanathan, V. and Vogelmann, A. M. 1997. Greenhouse effect, atmospheric solar absorption and the Earth's radiation budget: form the Arrhenius-Langley era to the 1990's. Ambio 26 (1): 38-46.

Ravishankara, A.R., Solomon, S., Turnipseed, A.A. and Warren, R.F. 1993. Atmospheric lifetimes of long-lived halogenated species. Science 259: 194-199.

Rbaihi, E., Belafhal, A., Vander Auwera, J., Naim, S. and Fayt, A. 1998. Fourier transform spectroscopy of carbonyl sulfide from 4700 to 8000 cm^{-1} and new global analysis of $^{16}O^{12}C^{32}S$. J. Mol. Spectrosc. 191: 32-44.

Richter, A., Wittrock, F., Ladstätter-Weißenmayer, A., and Burrows, J. P. 2001. GOME measurements of stratospheric and tropospheric BrO. Accepted for publication in Adv. Space Res.

Rinsland, C.P., Boughner, R.E., Larsen, J.C., Stokes, G.M. and Brault, J.W. 1984. Diurnal variations of atmospheric nitric oxide: Ground-based infrared spectroscopic measurements and their interpretation with time-dependent photochemical model calculations. J. Geophys. Res. 89: 9,613-9,622.

Rinsland, C.P., Goldman, A., Murcray, F., Blatherwick, R., Kosters, J., Murcray, D., Sze, N.D. and Massie, S. 1990. Long-term trends in the concentrations of SF_6, $CHClF_2$ and COF_2 in the lower stratosphere from analysis of high-resolution infrared solar occultation spectra. J. Geophys. Res. 95: 16,477-16,490.

Rinsland, C.P., Gunson, M.R., Abrams, M.C., Lowes, L.L., Zander, R., Mahieu, E., Goldman, A., Ko, M.K.W., Rodriguez, J.M. and Sze, N.D. 1994. Heterogeneous conversion of N2O5 to HNO3 in the post-Mount Pinatubo eruption stratosphere. J. Geophys. Res. 99: 8,213-8,219.

Rinsland, C. P., Salawitch, R. J., Gunson, M. R., Solomon, S., Zander, R., Mahieu, E., Goldman, A., Newchurch, M. J., Irion, F. W. and Chang, A. Y. 1999. Polar stratospheric descent of NO_y and CO and Arctic denitrification during winter 1992-1993, J. Geophys. Res. 104: 1,847-1,861.

Rinsland, C. P., Goldman, A., Connor, B. J., Stephen, T. M., Jones, N. B., Wood, S. W., Murcray, F. J., David, S. J., Blatherwick, R. D., Zander, R., Mahieu, E. and Demoulin, P. 2000. Correlation relationships of stratospheric molecular constituents from high spectral resolution, ground-based infrared solar absorption spectra. J. Geophys. Res. 105: 14,637-14,652.

Rodgers, C.D. 1976. Retrieval of atmospheric temperature and composition from remote measurements of thermal radiation. Reviews of Geophysics and Space Physics 14(4): 609-624.

Rothman, L. S., Rinsland, C. P., Goldman, A., Massie, S. T., Edwards, D. P., Flaud, J.-M., Perrin, A., Camy-Peyret C., Dana, V., Mandin, J.-Y., Schroeder, J., McCann, A., Gamache, R. R., Wattson, R. B., Yoshino, K., Chance, K. V., Jucks, K. W., Brown, L. R. , Nemtchinov, V. and Varanasi, P. 1996. The HITRAN molecular spectroscopic database and HAWKS: 1996 edition. J. Quant. Spectrosc. Radiat. Transfer 60 : 665.

Russell, J.M. III, Deaver, L.E., Luo, M., Park, J.H., Gordley, L.L., Tuck, A.F., Toon, G.C., Gunson, M.R., Traub, W.A., Johnson, D.G., Jucks, K.W., Murcray, D.G., Zander, R., Nolt, I.G. and Webster, C.R. 1996. Validation of hydrogen chloride measurements made by HALOE from the UARS platform. J. Geophys. Res. 101: 10,151-10,162.

Sander, S. P., Friedl, R. R., DeMore, W. B., Golden, D. M., Kurylo, M. J., Hampson, R. F., Huie, R. E., Moortgat, G. K., Ravishankara, A. R., Kolb, C. E. and Molina, M. L. 2000. Chemical kinetics and photochemical data for use in stratospheric modelling, supplement to evaluation 12: Update of key reactions, evaluation 13. Nasa JPL Publication 00-3.

Sarkissian, A., Roscoe, H. K., Fish, D., Van Roozendael, M., Gil, M., Dahlback, A., Perliski, L., Pommereau, J.-P. and Lenoble, J. 1995. Ozone and NO_2 air-mass factors for zenith-sky spectrometers: intercomparison of calculations with different radiative transfer models. Geophys. Res. Lett. 22: 1,113-1,116.

Sen, B., Toon, G.C., Blavier, J.-F., Fleming, E.L. and Jackman, C.H. 1996. Balloon-borne observations of mid-latitude fluorine abundance. J. Geophys. Res. 101: 9,045-9,054.

Simon, P.C. 1996. Spectroscopic Measurements of Atmospheric Changes (SMAC) – Final Scientific Report to OSTC, Contracts Nrs. GC/35/002, GC/35/003 and GC/35/004, April 1996: 1-185.

Sinnhuber, B.-M., Chipperfield, M., Enell, C.-F., Friess, U., Hendrick, F., Johnston, P., Kreher, K., Pfeilsticker, K., Platt, U., Richter, A., South, A., Toernkvist, K.K., Van Roozendael, M., Wagner, T. and Wittrock, F. (2000) Comparison of ground-based BrO measurements during THESEO with the SLIMCAT chemical transport model. In: Proceedings of the Fifth European Workshop on Stratospheric ozone, St Jean de Luz, France, 27 Sep-1st Oct 1999. Air Pollution Research Report 73, European Commission - DG XII, Brussels, 2000. EUR 19340: 352-355.

Solomon, S., Schmeltekopf, A.L. and Sander, R.W. 1987. On the interpretation of zenith sky absorption measurements. J. Geophys. Res. 92: 8,311-8,319.

Stamnes, K., Tsay, S. C., Wiscombe, W. J. and Jayaweera, K. 1988. Numerically stable algorithm for discrete-ordinate-method radiative transfer in multiple scattering and emitting layered media. Appl. Opt. 27: 2502-2509.

Steinbrecht, W., Claude, H., Köhler, U. and Hoinka, K.P. 1998. Correlations between tropopause height and total ozone: Implications for long-term changes. J. Geophys. Res. 103: 19,183-19,192.

Stolarski, R.S., and Rundel, R.D. 1975. Fluorine photochemistry in the stratosphere. Geophys. Res. Lett. 2: 443-444.

Toon, O. B., Mckay, C. P., Ackerman, T. P. and Santhanam, K. 1989. Rapid calculation of radiative heating rates and photodissociation rates in inhomogeneous multiple scattering atmospheres. J. Geophys. Res. 94: 16,287-16,301.

Toon, G.C., Blavier, J.-F., Sen, B., Margitan, J.J., Webster, C.R., May, R.D., Fahey, D., Gao, R., Del Negro, L., Proffitt, M., Elkins, J., Romashkin, P.A., Hurst, D.F., Oltmans, S., Atlas, E., Schauffler, S., Flocke, F., Bui, T.P., Stimpfle, R.M., Bonne, G.P., Voss, P.B. and Cohen, R.C. 1999. Comparison of MKIV balloon and ER-2 aircraft measurements of atmospheric trace gases. J. Geophys. Res. 104: 26,779-26,790.

Tsouli A. 2000. Mesures de constituants minoritaires de l'atmosphère en milieu urbain par spectroscopie d'absorption UV-visible et modélisation de la chimie de la troposphère en vue de la prévision des concentrations d'ozone à Bruxelles. PhD thesis, Oct. 2000, ULB.

Van Hoosier, M., Bartoe, J.D., Brueckner, G. and Prinz, D. 1988. Absolute solar spectral irradiance 120 nm - 400 nm (Results from the Solar Ultraviolet Spectral Irradiance Monitor - SUSIM- Experiment on board Spacelab 2). Astro. Lett. and Communications. 27: 163-168.

Van Roozendael, M., Lambert, J.-C. and Roscoe, H.K. Temperature dependent spectral resolution effects in SAOZ UV-visible spectrometers. In: Proceedings of the 7th GOME/SCIAMACHY Workshop, Frascati, Italy, 6-7 April, 1998.

Van Roozendael, M., Peeters, P., Roscoe, H. K., De Backer, H., Jones, A. E., Bartlett, L., Vaughan, G., Goutail, F., Pommereau, J.-P., Kyro, E., Wahlstrom, C., Braathen, G. and Simon, P. C. 1998. Validation of ground-based visible measurements of total ozone by comparison with Dobson and Brewer spectrophotometers. J. Atm. Chem. 29: 55-83.

Van Roozendael, M., Fayt, C., Lambert, J.-C., Pundt, I., Wagner, T., Richter, A. and Chance, K. 1999. Development of a bromine oxide product from GOME. In:

Proceedings of the European Symposium on Atmospheric Measurements from Space (ESAMS), ESA/ESTEC, The Netherlands, 18-21 January 1999. ESA WPP-161, Vol. 2: 543-547.

Van Roozendael M., Fayt, C., Hendrick, F., Hermans, C., Lambert, J.-C., Fonteyn, D., Sinnhuber, B.-M. and Chipperfield, M. P. Seasonal and Diurnal Variation of BrO Column Abundances above Harestua (60°N) and Haute Provence (44°N) during THESEO (2000a). In: Proceedings of the 5th European Symposium on Polar Stratospheric Ozone Research, Saint-Jean-de-Luz, September 27-October 1, 1999. Air Pollution Research Report, European Commission - DG XII, Brussels: 332-335.

Vandaele, A. C., Hermans, C., Simon P. C., Van Roozendael, M., Guilmot, J. M., Carleer, M. and Colin, R. 1996. Fourier transform measurement of NO_2 absorption cross-sections in the visible range at room temperature. J. Atmos. Chem. 25: 289-305.

Vandaele, A. C., Hermans,, C., Simon, P. C., Carleer, M., Colin, R., Fally, S., Mérienne, M.-F., Jenouvrier, A. and Coquart, B. 1998. Measurements of the NO_2 absorption cross-section from 42000 cm^{-1} to 10000 cm^{-1} (238-1000 nm) at 220 K and 294 K. J. Quant. Radiat. Transfer 59 (3-5): 171-184.

Vander Auwera, J., Kleffmann, J., Flaud, J.-M., Pawelke, G., Bürger, H. and Pétrisse, R. 2000. Absolute □$_2$ line intensities of HOCl by simultaneous measurements in the infrared with a tunable diode laser and far-infrared region using a Fourier transofrm spectrometer. J. Mol. Spectrosc. 204: 36-47.

Vander Auwera, J. 2000a. Absolute intensities measurements in the □$_4$+□$_5$ Band of $^{12}C_2H_2$: Analysis of Herman-Wallis effects and forbidden transitions. J. Mol. Spectrosc. 201: 143-150.

Vander Auwera, J. 2000b. Infrared absorption cross-sections of two substituted ethanes: 1,1-difluoroethane (HFC-152a) and 1,2dichloroethane. J. Quant. Spectrosc. Radiat. Transfer 66: 143-151.

Wagner, T., and Platt, U. 1998. Satellite mapping of enhanced BrO concentrations in the troposphere. Nature 395: 486-490.

Wagner, T. 1999. Satellite Observations of Atmospheric Halogen Species. PhD thesis, University of Heidelberg.

Waugh, D.W., Considine, D.B. and Fleming, E.L. 2001. Is upper stratospheric chlorine decreasing? Geophys. Res. Lett. 28: 1,187-1,190.

WMO Report 44. 1999. Scientific Assessment of Ozone Depletion: 1998, World Meteorological Organization – Global Ozone Research and Monitoring Project. WMO, 41, Avenue Guiseppe Motta, P.O. Box 2300, Geneva 2, CH 1211, Switzerland.

World Climate Programme (WCP). 1986. A preliminary cloudless standard atmosphere for radiation computation. WMO Report WMO/TD 24, World Meteorological Organisation.

Zander, R., Gunson, M.R., Farmer, C.B., Rinsland, C.P., Irion, F.W. and Mahieu, E. 1992. The 1985 chlorine and fluorine inventories in the stratosphere based on ATMOS observations at 30° North latitude. J. Atmos. Chem.15: 171-186.

Zander, R., Ehhalt, D.H., Rinsland, C.P., Schmidt, U., Mahieu, E., Rudolph, J., Demoulin, P., Roland, G., Delbouille, L. and Sauval, A. J. 1994. Secular trend and seasonal variability of the column abundance of N_2O above the Jungfraujoch station determined from IR solar spectra. J. Geophys. Res. 99: 16,745-16,756.

Zander, R., Mahieu, E., Gunson, M. R., Abrams, M. C., Chang, A. Y., Abbas, M., Aellig, C., Engel, A., Goldman, A., Irion, F. W., Kämpfer, N., Michelsen, H. A., Newchurch, M. J., Rinsland, C. P., Salawitch, R. J., Stiller, G. P. and Toon, G. C. 1996. The 1994 northern midlatitude budget of stratospheric chlorine derived from ATMOS/ATLAS-3 observations. Geophys. Res. Lett. 23: 2,357-2,360.

Zander, R., Mahieu, E., Demoulin, P., Servais, C. and Mélen, F. 2000. Long-term evolution of the loading of CH_4, N_2O, CO, CCl_2F_2, $CHClF_2$ and SF_6 above Central Europe during the last 15 years. In: Proceedings of the Second International Symposium on Non-CO_2 Greenhouse Gases - Scientific Understanding, Control and Implementation. Noordwijkerhout, The Netherlands, September 8-10, 1999. Sp. Vol. Environmental Monitoring and Assessment, 2000 Kluwer Academic Publishers: 211-216.

Zobov, N. F., Belmiloud, D., Polyansky, O. L., Tennyson, J., Shirin, S. V., Carleer, M., Jenouvrier, A., Vandaele, A. C., Bernath, P. F., Mérienne, M.-F. and Colin, R. 2000. The near ultraviolet rotation-vibration spectrum of water. J. Chem. Phys. 113 (4): 1,546-1,552.

ESAC PUBLICATIONS

Aliwell, S.R., Van Roozendael, M., Johnston, P.V., Richter, A., Wagner, T., Arlander, D.W., Burrows, J.P., Fish, D.J., Jones, R.L., Tørnkvist, K.K., Lambert, J.-C., Pfeilsticker K. and Pundt, I. In press 2001. Analysis for BrO in Zenith-Sky Spectra: An Intercomparison Exercise for Analysis Improvement. J. Geophys. Res.

Arijs, E., Simon, P.C., Nevejans, D., De Mazière, M., Lippens, C., Müller, J.F., Fonteyn, D., Fussen, D., Amelynck, C., Neefs, E., Vanderpoorten, W., Van Roozendael, M., Hermans, C., Gillotay, D., Bolsée, D., Vandaele, A.C. 1996. Atmospheric research related to Global Change at the Belgian Institute for Space Aeronomy. Nouvelles de la Science et des Technologies 14: 43-58.

Ballard, J., Knight, R. J., Vander Auwera, J., Herman, M., Di Leonardo, G., Masciarelli, G., Nicolaisen, F. M., Beukes, J. A., Christensen, L. K., McPheat, R., Duxbury, G., Freckleton, R., Shine, K. P. 2000. An intercomparison of laboratory measurements of absorption cross-sections and integrated absorption intensities for HCFC-22. J. Quant. Spectrosc. Radiat. Transfer 66: 109-128.

Barry, J., Locke, G., Scollard, D., Sidebottom, H., Treacy, J., Clerbaux, C., Colin, R., Franklin, J. 1997. 1,1,1,3,3-pentafluorobutane (HFC-365mfc): atmospheric degradation and contribution to radiative forcing. Int. J. Chem. Kinet. 29: 607-617.

Bernath, P., Carleer, M., Fally, S., Jenouvrier, A., Vandaele, A. C., Hermans, C., Mérienne, M.-F., Colin, R. 1998. The Wulf bands of oxygen. Chem. Phys. Letters 297: 293-299.

Carleer, M., Jenouvrier, A., Vandaele, A. C., Bernath, P. F., Mérienne, M.-F., Colin, R., Zobov, N. F., Polyansky, O. L., Tennyson, J., Savin, V. A. 1999. The near infrared, visible, and near ultraviolet overtone spectrum of water. J. Chem. Phys. 111 (6): 2,444-2,450.

Chipperfield, M. P., Burton, M., Bell, W., Paton Walsh, C., Blumenstock, T., Coffey, M. T., Hanningan, J. W., Mankin, W. G., Galle, B., Mellqvist, J., Mahieu, E., Zander, R., Notholt, J., Sen, B., and Toon, G. C. 1997. On the use of HF as a reference for the comparison of stratospheric observations and models. J. Geophys. Res. 102 : 12,901-12,919.

Clerbaux, C, Colin, R. and Simon, P.C. 1997. Le potentiel de rechauffement global d'hydrohalo-carbures. Physicalia Mag. 19: 51-73.

Colin, R., Mégie, G., and Borrell, P. 2000. Instruments, In: Overview and synthesis of the scientific results from EUROTRAC. Borrell, P. (Ed), vol 1, chap 1.

De Backer, H., De Muer D. and De Sadelaer, G. 1998. Comparison of ozone profiles obtained with Brewer-Mast and Z-ECC sensors during simultaneous ascents. J. Geophys. Res. 103: 19,641-19,648.

De Backer, H., Köpke, P., Bais, A., Frei, T., Gillotay, D., Haite, C., Heikkilä, A., Koskela, T., Kyrö, E., Lapeta, B., Lorente, J., Mayer, B., Plets, H., Redondaz, A., Renaud, A., Schmalwieser A.W. and Vanicek, K. 1999a. Comparison of measured and modelled UV indices, Meteorological applications.

De Backer, H., Koepke, P., Bais, A., de Cabo, X., Frei, T., Gillotay, D., Haite, C., Heikkila, A., Kanzantzidis, A., Koskela, T., Kyrö, E., Lapeta, B., Lorente, J., Masson, K., Mayer, B., Plets, H., Redondas, A., Renaud, A., Schauberger, G., Schmawieser, A., Schwander, H. and Vanicek, K. In press, 2001. Comparison of Measured and Modelled UV Indices. Meteorological Applications.

De Backer, H. In Press, 2001. Tropospheric ozone trends in Uccle 1969-1999 after homogenisation of the dataset. In: Proceedings from the EUROTRAC symposium 2000. Midgley, P.M., Reuther, M., Williams M. (Ed). Springer Verlag Berlin, Heidelberg 2001.

De Mazière, M., Van Roozendael, M., Hermans, C., Simon, P.C., Demoulin P. and Roland, G. 1998. Quantitative evaluation of the post-Pinatubo NO_2 reduction and recovery, based on 10 years of FTIR and UV-visible spectroscopic measurements at the Jungfraujoch. J. Geophys. Res. 103: 10,849-10,858.

De Mazière, M., Hennen, O., Van Roozendael, M., Demoulin P. and De Backer, H. 1999. Daily ozone vertical profile model built on geophysical grounds, for column retrieval from atmospheric high-resolution spectra. J. Geophys. Res.104: 23,855-23,869.

De Muer, D., De Backer, H. and Van Haver, Ph. 1995. Analysis of 25 years of regular ozone soundings at Uccle (Belgium). Atmospheric ozone as a Climate gas. Wang, W. and Isaksen, I. (Ed). Springer-Verlag Berlin: 113-129.

De Muer, D., Heylen, R., Van Loey, M. and De Sadelaer, G. 1997. Photochemical ozone production in the convective mixed layer, studied with a tethered balloon sounding system. J. Geophys. Res. 102: 15,933-15,947.

Fally, S., Vandaele, A. C., Carleer, M., Hermans, C., Jenouvrier, A., Mérienne, M.-F., Coquart, B., Colin, R. 2000. Fourier transform spectroscopy of the O_2 Herzberg bands. III. Absorption cross-sections of the collision-induced bands and of the Herzberg continuum. J. Mol. Spectrosc. 204: 10-20.
Gillotay, D., Walravens, B., Bolsée D. and Simon, P.C. 1999. Comparison of erythemal doses based on solar UV measurements from filter- and spectro-radiometers. Adv. Space Res.

Goldman, A., Schoenfeld, W. G., Goorvitch, D., Chackerian C. Jr., Dothe, H., Mélen, F., Abrams, M. C. and Selby, J. E. A. 1998. Update line parameters for OH $X^2\tilde{I}IX^2II$ (v",v') transitions, J. Quant. Spectrosc. Radiat. Transfer 59: 453-470, 1998.

Hamdouni, A., Barbe, A., Demoulin, P. and Zander, R. 1997. Retrieval of ozone vertical column amounts from ground-based high resolution infrared solar spectra. J. Quant. Spectrosc. Radiat. Transfer 57: 11-22.

Hermans, C., Vandaele, A.C., Carleer, M., Fally, S., Colin, R., Jenouvrier, A., Coquart, B., Mérienne, M.-F. 1999. Absorption cross-sections of atmospheric constituents: NO_2, O_2, and H_2O. Environ. Sci. & Pollut. Res. 6 (3): 151-158.

Hermans, C., Jenouvrier, A., Fally, S., Carleer, M., Vandaele, A. C., Mérienne, M.-F., Coquart, B. and Colin R. In preparation. Absorption cross-sections of oxygen: the IR and visible bands.

Inngold, T., Schmid, B., Mätzler, C., Demoulin P. and Kämpfer, N. 2000. Modeled and empirical approaches for retrieving columnar water vapor from solar transmittance measurements in the 0.72, 0.82 and 0.94 μm absorption bands. J. Geophys. Res. 105: 24,327-24,343.

Jaquinet-Husson, N., Arié, E., Barbe, A., Bjoraker, G., Bonnet, B., Brown, L. R., Camy-Peyret, C., Champion, J.-P., Chédin, Chursin, A. A., Clerbaux, C., Duxbury, G., Flaud, J.-M., Fourrié, N., Fayt, A., Graner, G., Gamache, R., Goldman, A., Golovko, V., Guelachvilli, G., Hartmann, J. M., Hilico, J. C., Hillman, J., Lefèvre, G., Lellouch, E., Mikhaïlenko, S. N., Naumenko, O. V., Nemtchninov, V., Newnham, D. A., Nikitin, A., Orphal, J., Perrin, A., Reuter, D. C., Rinsland, C. P., Rosenmann, L., Rothman, L. S., Scott, N. A., Selby, J., Sinitsa, L. N., Sirota, J. M., Smith, A. M.,

Smith, K. M., Tyuterev, V. G., Tipping, R. H., Urban, S., Varanasi, P., Weber, M. 1999. The 1997 spectroscopic GEISA databank. J. Quant. Spectrosc. Radiat. Transfer 61: 4,205-4,254.

Jenouvrier, A., Mérienne, M.-F., Coquart, B., Carleer, M., Fally, S., Vandaele, A. C., Hermans, C., Colin, R. 1999. Fourier transform spectroscopy of the O_2 Herzberg bands. I. Rotational Analysis. J. Mol. Spectrosc. 198: 136-162.

Köpke, P, Bais, A., Balis, D., Buchwitz, M., De Backer, H., de Cabo, X., Eckert, P., Eriksen, P., Gillotay, D., Koskela, T., Lapeta, B., Litynska, Z., Lorente, J., Mayer, B., Renaud, A., Ruggaber, A., Schauberger, G., Seckmeyer, G., Seifert, P., Schmalwieser, A., Schwander, H., Vanicek K. and Weber, M. 1998. Comparison of models used for UV index -calculations, Photochemistry and Photobiology 67 (6): 657-662.

Lambert, J.-C., Van Roozendael, M., De Mazière, M., Simon, P.C., Pommereau, J.-P., Goutail, F., Sarkissian, A. and Gleason, J.F. 1999. Investigation of pole-to-pole performances of space-borne atmospheric chemistry sensors with the NDSC. J. Atm. Sci. GOMAC Special issue 56: 176-193.

Lambert, J.C., Van Roozendael, M., Simon, P.C., Pommereau, J.P., Goutail, F., Gleason, J.F., Andersen, S.B., Arlander, D.W., Buivan, N.A., Claude, H., De La Noe, J., De Maziere, M., Dorokhov, V., Eriksen, P., Green, A., Karlsen Tornqvist, K., Kastad Hoiskar, B.A., Kyro, E., Leveau, J., Merienne, M.F., Milinevsky, G., Roscoe, H.K., Sarkissian, A., Shanklin, J.D., Staehelin, J., Wahlstrom Tellefsen, C. and Vaughan, G. 2000. Combined characterisation of GOME and TOMS total ozone measurements from space using ground-based observations from the NDSC. Adv. Space Res. 26: 1,931-1,940.

Lambert, J.-C., Van Roozendael, M., Simon, P.C., Pommereau, J.-P., Goutail, F., Andersen, S.B., Arlander, D.W., Bui Van, N.A., Claude, H., de La Noë, J., De Mazière, M., Dorokhov, V., Eriksen, P., Gleason, J.F., Karlsen Tørnkvist, K., Kåstad Høiskar, B.A., Kyrö, E., Leveau, J., Merienne, M.-F., Milinevsky, G., Roscoe, H.K., Sarkissian, A., Shanklin, J.D., Staehelin, J., Tellefsen, C.W. and Vaughan, G. In press 2001. Combined characterisation of GOME and TOMS total ozone using ground-based observations from the NDSC. Adv. Space Res.

Lemoine, René and H. De Backer. 2001. Assessment of the Uccle ozone sounding time series quality using SAGE II data. J. Geophys. Res. 106:14,515-14,523.

Mahieu, E., Zander, R., Delbouille, L., Demoulin, P., Roland, G. and Servais, C. 1997. Observed Trends in Total Vertical Column Abundances of Atmospheric Gases from IR Solar Spectra Recorded at the Jungfraujoch. J. Atmos. Chem. 28: 227-243.

Mélen, F., Mahieu, E., Zander, R., Rinsland, C. P., Demoulin, P., Roland, G., Delbouille, L. and Servais, C. 1998. Vertical column abundances of COF_2 above the Jungfraujoch station derived from ground-based infrared solar observations. J. Atmos. Chem. 29: 119-134.

Mérienne, M.F., Jenouvrie, A., Coquart, B., Carleer, M., Fally, S., Colin, R., Vandaele, A.C. and Hermans, C. 2000. Fourier transform spectroscopy of the O_2 Herzberg bands. II. Band oscillator strengths and transition moments. J. Mol. Spectrosc. 202 (2): 171-193.

Mérienne, M.F., Jenouvrier, A., Coquart, B., Carleer, M., Fally, S., Colin, R., Vandaele A.C., Hermans C. Submitted[a]. Improved data set for the Herzberg band systems of $^{16}O_2$. J. Mol. Spectrosc.

Mérienne, M.-F., Jenouvrie, A., Carleer, M., Colin, R., Vandaele, A. C., Bernath, P. F., Polyansky, O. L., Tennyson, J. Submitted[b]. The visible and near ultraviolet rotation-vibration spectrum of HOD. J. Mol. Spectrosc.

Michelsen, H. A., Manney, G. L., Gunson, M. R. and Zander, R. 1998. Correlations of stratospheric abundances of NO_y, O_3, N_2O and CH_4 derived from ATMOS measurements. J. Geophys. Res. 103: 28,347-28,359.

Michelsen, H. A., Manney, G. L., Gunson, M. R., Rinsland, C. P. and Zander, R. 1998. Correlations of stratospheric abundances of CH_4 and N_2O derived from ATMOS measurements, Geophys. Res. Lett. 25: 2,777-2,780.

Michelsen, H. A., Manney, G. L., Irion, F. W., Toon, G. C., Gunson, M. R., Rinsland, C. P., Zander, R., Mahieu, E., Newchurch, M. J., Purcell, P. N., Remsberg, E. E., Russell III, J. M., Pumphrey, H. C., Waters, J. W., Bevilacqua, R. M., Kelly, K. K. and Webster, C. R. In press 2001. ATMOS Version 3 water vapor measurements: comparisons with ATMOS Version 2 retrievals and observations from NOAA and Harvard Lyman-a hygrometers, MkIV, MAS, HALOE, and MLS. J. Geophys. Res.

Pfeilsticker, K., Arlander, D.W., Burrows, J. P., Erle, F., Gil, M., Goutail, F., Hermans, C., Lambert, J.C., Platt, U., Pommereau, J.P., Richter, A., Sarkissian, A., Van Roozendael, M., Wagner, T. and Winterrath, T. 1999. Intercomparison of the

detected influence of tropospheric clouds on UVvisible absorptions detected during the NDSC intercomparison campaign at OHP in June 1996. Geophys. Res. Lett.,26: 1,169-1,172.

Plets, H. and Vynckier, C. 2000. A comparative study of statistical total column ozone forecasting models, J. Geophys. Res. 105: 26,503-26,517.

Pougatchev, N. S., Jones, N. B., Connor, B. J., Rinsland, C. P., Becker, E., Coffey, M. T., Connors, V. S., Demoulin, P., Dzhola, A. V., Fast, H., Grechko, E. I., Hannigan, J. W., Koike, M., Kondo, Y., Mahieu, E., Mankin, W. G., Mittermeier, R. L., Notholt, J., Reichle H. G. Jr., Steele, L. P., Toon, G. C., Yurganov, L. N., Zander, R. and Zhao, Y. 1998. Ground-based Infrared Solar Spectroscopic Measurements of Carbon Monoxide During 1994 MAPS Flights, J. Geophys. Res. 103: 19,317-19,325.

Rbaihi, E., Belafhal, A., Vander Auwera, J., Naim, S., Fayt, A. 1998. Fourier transform spectroscopy of carbonyl sulfide from 4700 to 8000 cm^{-1} and new global analysis of $^{16}O^{12}C^{32}S$, J. Mol. Spectrosc. 191: 32-44.

Rinsland, C. P., Jones, N. B., Connor, B. J., Logan, J. A., Pougatchev, N. S., Goldman, A., Murcray, F. J., Stephen, T. M., Pine, A. S., Zander, R., Mahieu, E. and Demoulin, P. 1998. Northern and southern hemisphere ground-based infrared spectroscopic measurements of tropospheric carbon monoxide and ethane, J. Geophys. Res.103: 28,197-28,217.

Rinsland, C. P., Gunson, M. R., Wang, P. H., Arduini, R. F., Baum, B. A., Minnis, P., Goldman, A., Abrams, M. C., Zander, R., Mahieu, E., Salawitch, R. J., Michelsen, H. A., Irion, F. W. and Newchurch, M. J. 1998a. ATMOS/ATLAS 3 Infrared Profile Measurements of Trace Gases in the November 1994 Tropical and Subtropical upper Troposphere, J. Quant. Spectrosc. Radiat. Transfer 60: 891-901.

Rinsland, C. P., Gunson, M. R., Wang, P.-H., Arduini, R. F., Baum, B. A., Minnis, P., Goldman, A., Abrams, M. C., Zander, R., Mahieu, E., Salawitch, R. J., Michelsen, H. A., Irion, F. W. and Newchurch, M. J. 1998b. ATMOS/ATLAS 3 Infrared Profile Measurements of Clouds in the Tropical and Subtropical upper Troposphere, J. Quant. Spectrosc. Radiat. Transfer 60: 903-919.

Rinsland, C. P., Salawitch, R. J., Gunson, M. R., Solomon, S., Zander, R., Mahieu, E., Goldman, A., Newchurch, M. J., Irion, F. W. and Chang, A. Y. 1999. Polar stratospheric descent of NO_y and CO and Arctic denitrification during winter 1992-1993, J. Geophys. Res. 104: 1,847-1,861.

Rinsland, C. P., Goldman, A., Connor, B. J., Stephen, T. M., Jones, N. B., Wood, S. W., Murcray, F. J., David, S. J., Blatherwick, R. D., Zander, R., Mahieu, E. and Demoulin, P. 2000. Correlation relationships of stratospheric molecular constituents from high spectral resolution, ground-based infrared solar absorption spectra, J. Geophys. Res. 105: 14,637-14,652.

Rinsland, C. P., Mahieu, E., Zander, R., Demoulin, P., Forrer J. and Buchmann, B. 2000. Free tropospheric CO, C_2H_6 and HCN above central Europe: recent measurements from the Jungfraujoch station including the detection of elevated columns during 1998, J. Geophys. Res. 105: 24,235-24,249.

Rinsland, C. P., Salavitch, R. J., Osterman, G. B., Irion, F. W., Sen, B., Zander, R., Mahieu, E. and Gunson, M. R. 2000. Stratospheric CO at Tropical and Mid-Latitudes : ATMOS Measurements and Photochemical Steady-State Model Calculations, Geophys. Res. Lett. 27: 1,395-1,398.

Rinsland, C. P., Goldman, A., Zander, R. and Mahieu, E. 2001. Enhanced Tropospheric HCN Columns above Kitt Peak during the 1982-1983 and 1997-1998 El Niño Warm Phases. J. Quant. Spectrosc. Radiat. Transfer 69: 3-8.

Roscoe, H.K., Johnston, P.V., Van Roozendael, M., Richter, A., Roscoe, J., Preston, K.E., Lambert, J.-C., Dzienus, S., Winterrath, T., Burrows, J., Sarkissian, A., Goutail, F., Pommereau, J.-P., D'Almeida, E., Hottier, J., Coureul, C., Didier, R., Pundt, I., Bartlett, L.M., McElroy, C.T., Kerr, J.E., Elokhov, A., Giovanelli, G., Ravegnani, F., Premuda, M., Kostadinov, I., Erle, F., Wagner, T., Pfeilsticker, K., Kenntner, M., Marquard, L.C., Gil, M., Puentedura, O., Arlander, W., Kaastad-Hoiskar, B.A., Tellefsen, C.W., Heese, B., Jones, R.L., Aliwell, S.R. and Freshwater, R.E. 1999. Slant column measurements of O_3 and NO_2 during the NDSC intercomparison of zenith-sky UV-visible spectrometers in June 1996, J. Atmos. Chem. 32: 281-314.

Sinnhuber, B.-M., Arlander, D.W., Bovensmann, H., Burrows, J.B., Chipperfield, M.P., Enell, C.F., Friess, U., Hendrick, F., Johnston, P.V., Jones, R.L., Kreher, K., Mohamed-Tahrin, N., Muller, R., Pfeilsticker, K., Platt, U., Pommereau, J.-P., Pundt, I., Richter, A., South, A.M., Tørnkvist, K.K., Van Roozendael, M., Wagner, T. and Wittrock, F. Submitted 2001. The global distribution of stratospheric bromine monoxide: Intercomparison of measured and modeled slant column densities, J. Geophys. Res.

Van Roozendael, M., De Mazière, M., Hermans, C., Simon, P. C., Pommereau, J.-P., Goutail, F., Tie, X.X., Brasseur, G., Granier, C. 1997. Ground-Based Observations of Stratospheric NO_2 at High and Mid-Latitudes in Europe After the Mt. Pinatubo Eruption, J. Geophys. Res. 102: 19,171-19,176.

Van Roozendael, M., Peeters, P., Roscoe, H. K., De Backer, H., Jones, A.E., Vaughan, G., Goutail, F., Pommereau, J.-P., Kyro, E., Wahlstrom, C., Braathen, G. and Simon, P.C. 1998. Validation of Ground-Based Visible Measurements of Total Ozone by Comparison With Dobson and Brewer Spectrophotometers, J. Atm. Chem. 29: 55-83.

Van Roozendael, M., Richter, A., Wagner, T., Pundt, I., Arlander, D. W., Burrows, J. P., Chipperfield, M., Fayt, C., Johnston, P. V., Lambert, J.-C., Kreher, K., Pfeilsticker, K., Platt, U., Pommereau, J.-P., Sinnhuber, B.-M., Tørnkvist, K. K. and Wittrock, F. In press 2001. Intercomparison of BrO Measurements From ERS-2 Gome, Ground-Based and Balloon Platforms, Adv. Space Res.

Vandaele, A. C., Hermans C., Simon, P. C., Van Roozendae,l M., Guilmot, J. M., Carleer, M. and Colin, R. 1996. Fourier transform measurement of NO_2 absorption cross-sections in the visible range at room temperature. J. Atmos. Chem. 25: 289-305.

Vandaele, A.C., Hermans, C., Simon, P.C., Carleer, M., Colin, R., Fally, S., Mérienne, M.F., Jenouvrier, A. and Coquart, B. 1997. Measurements of the NO2 absorption cross-section from 42000 cm-1 to 10000 cm-1 (238-1000 nm) at 220 K and 294 K. J.Q.S.R.T. 59: 171-184.

Vandaele, A. C., Hermans, C., Simon, P. C., Carleer, M., Colin, R., Fally, S., Mérienne, M.-F., Jenouvrier, A. and Coquart, B. 1998. Measurements of the NO_2 absorption cross-section from 42000 cm^{-1} to 10000 cm^{-1} (238-1000 nm) at 220 K and 294 K. J. Quant. Radiat. Transfer 59 (3-5): 171-184.

Vandaele, A. C. and Carleer, M. 1999. Development of Fourier transform spectrometry for UV-visible DOAS measurements of tropospheric minor constituents, Applied Optics 38: 2,630-2,639.

Vander Auwera, J., Kleffmann, J., Flaud, J.-M., Pawelke, G., Bürger, H. and Pétrisse, R. 2000. Absolute □$_2$ line intensities of HOCl by simultaneous measurements in the infrared with a tunable diode laser and far-infrared region using a Fourier transofrm spectrometer. J. Mol. Spectrosc. 204: 36-47.

Vander Auwera J. 2000a. Absolute intensities measurements in the $\nu_4+\nu_5$ Band of $^{12}C_2H_2$: Analysis of Herman-Wallis effects and forbidden transitions. J. Mol. Spectrosc. 201: 143-150.

Vander Auwera J. 2000b. Infrared absorption cross-sections of two substituted ethanes: 1,1-difluoroethane (HFC-152a) and 1,2dichloroethane. J. Quant. Spectrosc. Radiat. Transfer 66: 143-151.

Van Weele, M., Blumthaler, M., Brognier, C., Engelsen, O., Gillotay, D., Lenoble, J., Martin, T., Den Outer, P., Pfister, G., Ruggaber, A., Walravens B. and Wehs, P. 1998. From model intercomparison towards benchmarks UV spectra for real atmospheric cases. ECUV Special Section, J. Geophys. Res.

Vaughan, G., Roscoe, H. K., Bartlett, L. M., O'Connor, F. M., Sarkissian, A., Van Roozendael, M., Lambert, J.-C., Simon, P. C., Karlsen, K., Høiskar, B. A. K, Fish, D. J., Jones, R. L., Freshwater, R., Pommereau, J.-P., Goutail, F., Andersen, S. B., Drew, D. G., Hughes, P. A., Moore, D., Mellqvist, J., Hegels, E., Klupfel, T., Erle, F., Pfeilsticker, K. and Platt, U. 1997. An Intercomparison of ground-based UV-visible sensors of ozone and NO_2, J. Geophys. Res. 102: 1,411-1,422.

Zander, R., Demoulin, P., Mahieu, E., Roland, G., Delbouille, L. and Servais, C. 1997. Total Vertical Column Abundances of Atmospheric Gases Derived from IR Remote Solar Observations made at the Jungfraujoch Station. In: Transport and Chemical Transformation of pollutants in the Troposphere. Vol. 6 - Tropospheric Ozone Research. Østein, H (Ed). Springer-Verlag, Berlin Heidelberg New York: 413-425.

Zerefos, C.S., Balis, D.S., Bais, A.F., Gillotay, D., Simon, P.C., Mayer, B. and Seckmeyer, G. 1997. Variability of UV-B at four stations in Europe, Geophys. Res. Lett. 24: 1,363-1,366.

Zerefos, C.S., Meleti, C., Balis, D.S., Bais, A.F. and Gillotay, D. 1998. On long-term spectral UV-B changes in the 90's in Europe. Adv. Space Res.

Zobov, N. F., Belmiloud, D., Polyansky, O. L., Tennyson, J., Shirin, S. V., Carleer, M., Jenouvrier, A., Vandaele, A. C., Bernath, P. F., Mérienne, M.-F. and Colin, R., 2000. The near ultraviolet rotation-vibration spectrum of water. J. Chem. Phys. 113 (4): 1,546-1,552.

Conference proceedings, abstracts, posters, oral presentations and theses

Adams, F., Brasseur, G., Colin, R., De Muer, D., Gérard, J.-C., Maenhaut, W., Peeters, J., Simon, P. C., Van Cleemput, O., Vander Auwera, J., Vanderstraeten, M., Van Der Werf, A., Van Grieken, R., Vinckier, C. and Zander, R. Belgian Impulse Programme GLOBAL CHANGE 1990-1996: Changes in the chemical Composition of the Atmosphere. Federal Office of Scientific, Technical and Cultural Affairs (OSTC), Brussels, 1997.

Bach, M., Depiesse, C., El Hachtouky, R., El Idrissi, M. I., Herman, M., Herregodts, F., Hurtmans, D., Mellouki, A., Vander Auwera, J. 2000. High resolution laboratory spectroscopy of compounds of atmospheric and astrophysical interest. ATO Advanced Research Workshop Spectroscopy from space, Bratislava, Slovaquie, 31 Oct-4 Nov. 2000.

Bais, A.F., Gardiner, B.G., Slaper, H., Kirsch, P.J., Kazaszis, S., Blumthaler, M., Brognier, C., Eriksen, P., Gillotay, D., Josefsson, W., Kjeldstad, B., Koskela, T., Kuik, F., Leszczynski, K., Mckenzie, R.L., Redondas, A., Reinen, H.A.J.M., Seckmeyer, G., Svenoe, T., Wardle, D.I., Weeb, A.R., Weihs, P., Allabar, W., Bernhard, G., Gay, M., Groebner, J., Huber, M., Johnston, P.V., Karlsson, J.E., Keer, J.B., Kotkamp, M., Manzano, J., Masserot, D., Meleti, C., Pachart, E., Persen, T., Rengarajan, G., Saarinen, E., Schmitt, R., Schreder, J., Thorseth, T.M., Visuri, R., Walravens B. and Wauben, W. 1998. Results from comparisons of global solar UV spectra measured during the SUSPEN intercomparison campaign. Oral presentation at the European Conference on Atmospheric UV Radiation, Helsinki, Finland, June 29 - July 2, 1998.

Barret, B., Mahieu, E., Carleer, M., De Mazière, M., Colin, R. and Zander, R. 1999. Tropospheric boundary layer investigations by differential ground-based solar FTIR spectrometry. In: Environmental Sensing and Applications, SPIE Proceedings 3821: 116-123.

Barret, B., De Mazière, M., Demoulin, P., Mahieu, E., Mélen, F., Connor, B.J. and Jones, N. 2000. Investigation of height-resolved information in ground-based high-resolution infrared solar spectra above the Jungfraujoch. In: Atmospheric Ozone, Proceedings of the Quadrennial Ozone Symposium, Sapporo 2000. 3-8 July 2000, pp; 301-302, 2000.

Bojkov, B.R., De Mazière, M., Krognes, T., Paltiel, R., Walker, S.E. 2000. Metadata guidelines for atmospheric and oceanic sciences: a prototype for NADIR. NILU Report TR-12/2000.

Bojkov, B.R., De Mazière, M., Krognes, T. and Koopman, R. To be published Metadata guidelines for atmospheric and oceanographic sciences: NADIR Index for ESA Envisat Cal/Val HDF files.

Bolsee, D., Gillotay, D. and Walravens, B. Relative spectral response of filter radiometers: an example of calibration facility. 1998. Poster presentation at the European Conference on Atmospheric UV Radiation, Helsinki, Finland, June 29 - July 2, 1998.

Carleer, M., Fally, S., Colin, R., Coquart, B., Jenouvrier, A., Mérienne, M.F., Hermans, C., Vandaele, A.C. and Simon, P.C. O_2 Absorption Cross-sections and Absolute Intensities in the UV-visible using a Fourier Transform Spectrometer. 1996. In: Proceedings of the ASA Symposium 1996, Reims, France, 3-5 September 1996: 87-90.

Carleer M., Jenouvrier, A., Vandaele, A. C., Bernath, P., Colin, R., Mérienne, M.-F., Tennyson, J., Polyansky, L. and Zobov, N. F. 1998. New measurements of the water vapour absorption spectrum in the near-UV to near-IR region. In: Water in the Gas Phase Conference, Paris, France, June 21-24, 1998.

Carleer, M., Colin, R. and Vandaele, A. C. 1998. Using a Fourier transform spectrometer for tropospheric UV-Vis DOAS measurements. In: Spectroscopic Atmospheric Environmental Monitoring Techniques. Proceedings of SPIE, Barcelona, Spain, 21-24 Sept. 1998. Schafer K. (Ed). Europto Series 3493: 11-19.

Carleer, M., Fally, S., Colin, R., Jenouvrier, A., Coquart, B., Mérienne, M.-F., Vandaele, A. C. and Hermans, C. 1998. Fourier transform spectroscopy of atmospheric gases, In: Spectroscopic Atmospheric Environmental Monitoring Techniques. Proceedings of SPIE, Barcelona, Spain, 21-24 Sept. 1998, Schafer K. (Ed). Europto Series 3494: 94-103.

Carleer M. 1999. Tutorial lecture: FTS line shapes and their importance in atmospheric measurements in the UV-VIS and the IR, Europto conference on Environmental Sensing and Applications, Munich, Germany, 14-18 June 1999, SPIE vol. 3821: 70-87.

Carleer M. 2000. A Windows program to measure accurately the line intensities of high resolution Fourier transform spectra. EOS/SPIE symposium on Remote Sensing, Barcelone, 25-29 Sept. 2000.

Chichery, A., Barbe, A., Bourgeois, M. T., Demoulin, P. and Tyuterev, G. 1999. The 3 v_3 bands of isotopic ozone 668 and 686. Proceedings of Atmospheric Spectroscopy Applications 1999, Reims, France, September 1-3, 1999: 147-150.

Coheur, P.-F., Fally, S., Carleer, M., Colin, R., Vandaele, A.C., Hermans, C., Jenouvrie,r A. and Mérienne, M.-F. 2000. Absolute intensities of water vapor lines in the near ultraviolet and visible regions. EOS/SPIE symposium on Remote Sensing, Barcelone, 25-29 Sept. 2000.

Colin R., Carleer, M., Guilmot, J.M., Simon, P.C., Vandaele, A.C., Hermans, C., Dufour, P. and Fayt, C. 1997. The Belgian Contribution to Differential Optical Absorption Studies of the Troposphere between 1990 and 1995. In: Instruments Development for Atmospheric Research and Monitoring. Bösenberg, J., Brassington, D. and Simon, P.C. (Eds). Springer-Verlag, Berlin: 347-354.

Colin R., Carleer, M., Tsouli, A., Simon, P.C., Vandaele, A.C. and Bernath, P. 1998. Ultraviolet spectroscopic measurements of ozone. Journée d'étude "Ozone dans la troposphère", SSTC, Brussels, June 26, 1998.

Coquart, B., Jenouvrier, A., Mérienne, M.F., Hermans, C., Vandaele, A.C., Simon, P.C., Tsouli, A., Carleer M., Fally, S., Rizopoulos, A. and Colin, R. 1997. New Measurements of the NO_2 Absorption Cross-section with a Fourier Transform Spectrometer from 10000 to 42000 cm-1 and its Temperature and Pressure Dependence. In: Proceedings of the ASA Symposium 1996, Reims, France, 3-5 September 1996: 79-82.

De Backer, H. 1999. Homogenisation of ozone vertical profile measurements at Uccle. Wetenschappelijke en technische publicaties van het K.M.I. 7, ISSN D1999/0224/007, KMI, Ukkel: 26.
(ftp://ftp.kmi-irm.be/dist/meteo/hugo/publ/1999/o3prof.ps)

De Backer, H., Köpke, P., Bais, A., Cuevas, E., Gillotay, D., Haite, C., Heikkilä, A., Koskela, T., Kyrö, E., Lapeta, B., Lorente, J., Mayer, B., Plets, H., Renaud, A., Schmalwieser A.W. and Vanicek, K. 1999. Comparison of measured and modelled UV Indices. 24th General assembly of EGS, Geophysical Research Abstracts. Vol. 1, number 2: 477.

De Backer, H. In press, 2001. Tropospheric ozone trends in Uccle 1969-1999 after homogenisation of the dataset. In: Proceedings from the EUROTRAC symposium

2000. Midgley, P.M., Reuther, M., Williams M. (Ed). Springer Verlag Berlin, Heidelberg 2001.

De Mazière, M., Hennen, O., Barbe, A., Mérienne, M.F., Hamdouni, H. and Demoulin, P. 1997. Study of Spectroscopic, Meteorological and Climatological Parameters for the Analysis of O_3 FTIR Spectra: a Case-study for Jungfraujoch Data. In: Proceedings of the ASA Symposium 1996, Reims, France, 3-5 September 1996: 149-152.

De Mazière, M., Hennen, O., Van Roozendael, M., Simon, P. C., Demoulin, P., Roland, G., Zander, R., De Backer, H. and Peter, R. 1998. Towards improved evaluations of total ozone at the Jungfraujoch, using vertical profile estimations based on auxiliary data. In: Proceedings of the XXVIII Quadrennial Ozone Symposium, L'Aquila, Italy, September 12-21, 1996. Bojkov, R. and Visconti G (Eds): 25-28.

De Mazière, M., Van Roozendael, M., Hennen, O., Demoulin, P. and Mahieu, E. 1999. Revision of the O3 trend analysis at the Jungfraujoch station. Poster presentation at the Sixth Scientific Conference of the International Global Atmospheric Chemistry Project (IGAC), Bologna, Sept. 13-17, 1999.

De Mazière, M. 1999. COSE, Compilation of Atmospheric Observations in Support of Satellite Measurements over Europe. In: Proceedings of the European Symposium on Atmospheric Measurements from Space (ESAMS). ESA/ESTEC, The Netherlands, 18-21 January 1999. ESA WPP-161, Vol. 2: 655-659.

De Mazière, M. 1999. Atmospheric observations: synergy between ground, airborne and space-based observations. Invited Lecture at 5ème Colloque ASA, Reims, France, Sept. 1-3, 1999.

De Mazière, M., Mahieu, E., Van Roozendael, M., Lambert, J.C., Peeters, P., Barret, B., Hendrick, F., Hermans, C., Van Daele, A.C., Simon, P.C., Zander, R., Demoulin, P., De Muer, D., De Backer, H., Carleer, M. and Colin, R. 2000. Atmospheric changes at the origin of the environment and climate issue (Atmosfeerveranderingen aan de basis van de milieu- en klimaatproblematiek). Invited speaker op het symposium 'Tussen Onderzoek en beleid', DWTC-SSTC, Congrespaleizen, Brussels, Nov. 24-25, 1999. In: Proceedings, D/2000/1191/23, OSTC: 61-67.

De Mazière, M., Van Roozendael, M., Bojkov, B. R., de la Noë, J., Mahieu, E. and Neuber, R. In press. Archiving of atmospheric data: data formats and database. In:

Proceedings of the International Radiation Symposium 2000, St. Petersburg, July 24-29, 2000.

De Mazière, M. In press 2000. Atmospheric Observations in the perspective of changing climate and environment, and the synergy between ground-based, airborne and space-based measurements. In: Proceedings of the ICTP School on 'Exploring the Atmosphere by Remote Sensing Techniques'. Dirs. Guzzi, R., Furlan, G. and Pfeilsticker K. Trieste, Oct. 18-Nov. 5, 1999. Springer-Verlag.

De Mazière, M. 2001. Trace gas measurements at the Jungfraujoch by Fourier transform infrared and UV-Visible spectrometry. Invited seminar at the Institut für Meteorologie und Klimaforschung, Forschungszentrum Karlsruhe, Jan. 16, 2001.

De Muer, D., and De Backer, H. 1994. Influence of sulfur dioxide trends on Dobson measurements and on electrochemical ozone soundings. In: SPIE proceedings series, Atmospheric ozone conference, Tromsö 28-29 June 1993, Vol. 2047: 18-26.

Demoulin, P., Mahieu, E., Zander, R., Roland, G., Delbouille, L., Servais, C., De Mazière, M. and Van Roozendael, M. 1998. The Current Budget of NO_y above the Jungfraujoch as derived from IR Solar Observations. In: Proceedings of the Fourth European Symposium on Polar Stratospheric Ozone Research, Schliersee, Germany, September 22-26, 1997. European Commission, Air pollution Research Report 66: 427-430.

Demoulin, P., Zander, R., Mélen, F., Mahieu, E. and Servais, C. 1999. Column abundance measurements of formaldehyde above the Jungfraujoch. In: Proceedings of Atmospheric Spectroscopy Applications 1999, Reims, France, September 1-3, 1999: 59-62.

Fally, S., Carleer, M., Hermans, C., Vandaele, A. C., Coquart, B., Jenouvrier, A., Mérienne, M.-F. and Colin, R. 1999. UV and visible absorption cross-sections of O_2. In: Proceedings of the ASA Symposium 1999, Reims, France, September 1-3, 1999. Université de Reims-G.S.M.A. (Eds) : 153-156.

Fally, S., Carleer, M., Hermans, C., Vandaele, A. C., Coquart, B., Jenouvrier, A., Mérienne, M.-F. and Colin, R. Absorption cross-sections of O_2: The Herzberg band systems, the Herzberg continuum, and the collision-induced bands. Inspired by Herberg: Spectroscopy for the year 2000, Cornwall, Ontario, October 30-November 3, 1999.

Fischer, H., Blom, C., Oelhaf, H., Carli, B., Carlotti, M., Delbouille, L., Ehhalt, D., Flaud, J.-M., Isaksen, I., Lopez-Puertas, M., McElroy C. T. and Zander R. 2000. ENVISAT-MIPAS: An Instrument for Atmospheric Chemistry and Climate Research. In: ESA Report SP-1229: 124.

Galle, B., Mellqvist, J., Samuelsson, J., Magnusson, S., Van Roozendael, M., Fayt, C., Hermans, C., Hendrick, F., Chipperfield, M. P. and Bjerke A. 2000. FTIR and UV-Visible Measurements of Stratospheric Trace Species at Harestua, Norway during THESEO and Comparison with a 3-D Model. In: Proceedings of the 5th European Workshop on Stratospheric Ozone, Saint Jean de Luz, France, 27 Sept.-1 Oct. 1999. Air Pollution Research Report 73, European Commission - DG XII, Brussels, 2000.

Gillotay, D., Bolsee, D. and Walravens, B. 1998. UV Effective doses: Comparison of erythemal doses obtained by solar UV measurements with broadband UV meter, filter radiometer and spectro-radiometer. Poster presentation at the European Conference on Atmospheric UV Radiation, Helsinki, Finland, June 29 - July 2, 1998.

Gillotay, D., Müller, J.-F., Walravens, B. and Simon, P.C. 1998. The influence of ozone and clouds on the UV climatology in Uccle, Belgium. Atmospheric Ozone. In Proceedings of the Quadrennial Ozone Symposium at l'Aquila, Italy, 12-21 Sept. 1996. R.J. Bojkov and G. Visconti (Eds): 849-852.

Gillotay, D., Pletz, H., De Backer, H. and Bolsee, D. 1998. Comparison of predicted and measured UV index for the Brussels area Uccle-Belgium (Lat. 50°48'N, Long. 4° 21'E, Alt. 120m asl). Poster presentation at the European Conference on Atmospheric UV Radiation, Helsinki, Finland, June 29 - July 2, 1998.

Gillotay D., Walravens, B. and Simon, P.C. Comparison of erythemal doses based on solar UV measurements from filter- and spectro-radiometers. Oral presentation at the 32nd COSPAR Scientific Assembly, Nagoya, Japan, 12-19 July, 1998.

Hendrick, F., Mueller, R., Sinnhuber, B.-M., Bruns, M., Burrows, J.P., Chipperfield, M. P., Fonteyn, D., Richter, A., Van Roozendael, M. and Wittrock F. 2000. Simulation of BrO Diurnal Variation and BrO Slant Columns : Intercomparison Exercise Between Three Model Packages. In: Proceedings of the 5th European Workshop on Stratospheric Ozone, Saint Jean de Luz, France, 27 Sept.-1 Oct. 1999. Air Pollution Research Report 73, European Commission - DG XII, Brussels, 2000.

Hennen, O., De Mazière, M., Van Roozendael, M., Lambert, J.-C., Mahieu, E., Demoulin, P., Roland, G., Godin, S., De Backer H. 1998. Observations coupled to

the overpasses of the polar vortex over mid-latitude Europe in winter 1995-1996. Polar stratospheric ozone 1997. In: Proceedings of the 4th European Symposium on Stratospheric Ozone Research, Schliersee, Bavaria, Germany, Sept. 22-26, 1997: 451-454.

Hermans C., Vandaele, A.C., Simon, P.C., Carlee, M., Fally, S., Colin, R., Coquart, B., Jenouvrier, A., Mérienne M.F. 1997. NO2 and O2 Absorption Cross-sections for Atmospheric measurements. In: Proceedings of the ASA Symposium 1996, Reims, France, 3-5 September 1996: 83-86.

Hermans C., Vandaele, A. C., Carleer, M., Fally, S., Colin, R., Jenouvrier, A., Coquart, B. and Mérienne, M.-F. 1998. FT Measurements of absorption cross-sections of atmospheric gases. 7th GOME/SCIAMACHY Workshop, Frascati, Italy, 6-7 April 1998.

Hermans C., Vandaele, A. C., Carleer, M., Fally, S., Colin, R., Jenouvrier, A., Coquart, B. and Mérienne, M-F. FT. Measurements of absorption cross-sections of atmospheric gases, SCUVS III Workshop, Paris, France, 28-30 April, 1998.

Hermans, C., Vandaele, A. C., Carleer, M., Fally, S., Colin, R., Jenouvrier, A., Coquart, B. and Mérienne M.-F. FT Measurements of absorption cross-sections of atmospheric gases. In: Proceedings of the 7th GOME/SCIAMACHY Workshop, Frascati, Italy, 6-7 April, 1998.

Hermans, C., Vandaele, A. C., Carleer, M., Fally, S., Colin, R., Bernath P.F., Jenouvrier, A., Coquart, B. and Mérienne, M.-F. FT Absorption Cross-Sections of Atmospheric Constituents: NO2, O2 and H2O. 1998. Poster presentation at the 6th FECS Conference on Chemistry and the Environment, Copenhagen, August 26 to 28, 1998.

Hermans, C., Vandaele, A.C., Coquart, B., Jenouvrier, A., Mérienne M.-F., Fally S., Carleer, M., Colin, R. 2000. Absorption Bands of O_2 and its Collision Induced Bands in the 30000-7700 cm^{-1} wavenumber Region. In: Proceedings of the International Radiation Symposium IRS 2000, St Petersbourg, 24-29 July. 2000.

Jenouvrier, A., Mérienne, M.-F., Coquart, B., Fally, S., Carleer, M., Colin, R., Hermans, C. and Vandaele A. C. 1999. Reinvestigation of the molecular oxygen transitions in the 42000-75000 cm-1 wavenumber region. In: Proceedings of the ASA Symposium 1999, Reims, France, September 1-3, 1999. Université de Reims-G.S.M.A. (Eds): 157-160.

Kelder, H., Platt, U., Simon, P.C., Timmermans, R., Aben, I., Burrows, J.P., Camy-Peyret, C., Hilsenrath, E., Kerridge, B., Künzi, K., Lambert, J.-C., Lelieveld, J., Levelt, P., McKenna, D., Perner, D., Piters, A., Attema, E., Balzer, W., Bruzzi, S., Durville, M. and Friker, A. 1999. SCIAMACHY Validation. In: Proceedings of the European Symposium on Atmospheric Measurements from Space (ESAMS), ESA/ESTEC, The Netherlands, 18-21 January 1999. ESA WPP-161, Vol. 2: 643-647.

Koepke, P., Bais, A.F., Balis, D.S., Buchwitz, M., De Backer, H., De Cabo, X., Eckert, P., Eriksen, P., Gillotay, D., Heikkila, A., Koskela, T., Lapeta, B., Litynska, Z., Lorente, J., Mayer, B., Renaud, A., Ruggaber, A., Schauberger, G., Seckmeyer, G., Schmalwieser, A.W., Schwander, H., Vanicek K. and Weber, M. 1998. UV index calculations: absolute and relative agreement of models with different complexity. Oral presentation at the European Conference on Atmospheric UV Radiation, Helsinki, Finland, June 29-July 2, 1998.

Kurylo, M. J. and Zander, R. J. 2000. The NDSC-Its status after ten years of operation. In: Proceedings of the the International Quadrennial Ozone Symposium, Sapporo, Japan, 3-8 July 2000: 167-168.

Lambert, J.-C., Van Roozendael, M., Simon, P.C., De Mazière, M., Pomereau, J.-P., Goutail, F., Sarkissian, A., Denis, L., Dorokhov, V., Eriksen, P., Kyro, E., Leveau, J., Roscoe, H.K., Tellefsen, C.W., Vaughan, G. Validation of ERS-2 GOME total ozone measurements with the SAOZ ground-based network during the period 28 June-17 August 1996. Atmospheric Ozone. In: Proceedings of the Quadrennial Ozone Symposium at l'Aquila, Italy, 12-21 Sept. 1996. R.J. Bojkov and G. Visconti (Eds): 297-300.

Lambert, J.-C., Van Roozendael, M., Simon, P.C., De Mazière, M., Pomereau, J.-P., Goutail, F., Sarkissian, A., Andersen, S.B., Dorokhov, V., Eriksen, P., Kaastad Hoiskar, B.A. and Kyro, E. 1998. GOME and TOMS total ozone in northern winter 1996-1997: comparison with SAOZ/UV-visible ground-based measurements in the Arctic and at mid-latitude, in Polar stratospheric ozone 1997. In: Proceedings of the 4th European Symposium on Stratospheric Ozone Research, Schliersee, Bavaria, Germany, Sept. 22-26, 1997: 696-699.

Lambert, J.-C., Van Roozendael, M., Granville, J., Gérard, P., Simon, P.C., Claude, H., Staehelin, J. 1998. Comparison of the GOME ozone and NO2 total amounts at mid-latitude with ground-based zenith-sky measurements. Atmospheric Ozone. In: Proceedings of the Quadrennial Ozone Symposium at l'Aquila, Italy, 12-21 Sept. 1996. R.J. Bojkov and G. Visconti (Eds): 301-304.

Lambert, J.-C., Van Roozendael, M., Simon, P.C., Pommereau, J.-P., Goutail, F., Andersen, S.B., Arlander, D.W., Bui Van, N. A., Claude, H., de La Noë, J., De Mazière, M., Dorokhov, V., Eriksen, P., Gleason, J.F., Karlsen Tørnkvist, K., Kåstad Høiskar, B.A., Kyrö, E., Leveau, J., Merienne, M.-F., Milinevsky, G., Roscoe, H.K., Sarkissian, A., Shanklin, J.D., Staehelin, J., Tellefsen, C.W. and Vaughan, G. 1998. Combined characterisation of GOME and TOMS total ozone using ground-based observations from the NDSC. Poster presentation at the 32nd COSPAR Scientific Assembly, Nagoya, Japan, 12-19 July, 1998.

Lambert, J.-C. and De Mazière, M. 1999. Satellite observations of tropospheric ozone-related constituents. In: Proceedings of the 'Ozone in the troposphere: research and policies', Palais des Congrès, Bruxelles, June 26, 1998. DWTC-SSTC publications: 83-90.

Lambert, J.-C., De Mazière, M., Simon, P.C. and Van Roozendael, M. 1999. ESMOS, SCUVS, COSE, and THESEO-BrO: Some EC-sponsored field projects including satellite validation activities. Oral presentation by J.-C. Lambert at the NASA Planning Workshop for Integration of Satellite Cal/Val and Research-Oriented Field Missions in the Next Decade, Snowmass Village, Colorado, USA, 23-27 August 1999.

Lambert, J.-C., Granville, J., Van Roozendael, M., Müller, J.-F., Pommereau, J.-P., Goutail, F. and Sarkissian, A. 1999. A pseudo-global correlative study of ERS-2 GOME NO2 data with ground-, balloon-, and space-based observations. In: Proceedings of the European Symposium on Atmospheric Measurements from Space (ESAMS), ESA/ESTEC, The Netherlands, 18-21 January 1999. ESA WPP-161, Vol. 1: 217-224.

Lambert, J.-C., Granville, J., Van Roozendael, M., Sarkissian, A., Goutail, F., Müller, J.-F., Pommereau, J.-P. and Russell III, J. M. 1999. A climatology of NO2 profile for improved Air Mass Factors for ground-based vertical column measurements. Poster presented at the 5th European Workshop on Stratospheric Ozone, Saint-Jean-de-Luz, France, September 27-October 1, 1999.

Lambert, J.-C., Simon, P.C., De Mazière, M., Van Roozendael, M., Pommereau, J.-P., Goutail, F., Gleason, J.F. and Russell III, J.M. 1999. Integrated use of ground-based network, balloon, satellite and field campaigns data for the validation of ERS-2 GOME. Poster presentation by J.-C. Lambert at the NASA Planning Workshop for Integration of Satellite Cal/Val and Research-Oriented Field Missions in the Next Decade, Snowmass Village, Colorado, USA, 23-27 August 1999.

Lambert, J.-C., Van Roozendael, M., Granville, J., Gerard, P., Simon, P.C., Pommereau, J.-P., Goutail, F. and Sarkissian, A. 1999. Geophysical validation of ERS-2 GOME ozone products by means of correlative observations from the NDSC. In: Proceedings of the European Symposium on Atmospheric Measurements from Space (ESAMS), ESA/ESTEC, The Netherlands, 18-21 January 1999. ESA WPP-161, Vol. 2: 595-601.

Mahieu, E., Zander, R., Mélen, F., Demoulin, P., Servais, C., Delbouille, L. and Roland, G. 1998. Recent Characteristic Budget of Inorganic Chlorine and Fluorine above the Jungfraujoch Station. In: Proceedings of the Fourth European Symposium on Polar Stratospheric Ozone Research, Schliersee, Germany, September 22-26, 1997. European Commission, Air pollution research report 66: 358-361.

Mahieu, E., Zander, R., Demoulin, P., De Mazière, M., Mélen, F., Servais, C., Roland, G., Delbouille, L., Poels, J. and Blomme, R. 2000. Fifteen years-trend characteristics of key stratospheric constituents monitored by FTIR above the Jungfraujoch. In: Proceedings of the Fifth European Symposium on Stratospheric Ozone, St. Jean de Luz, France, September 27 - October 1, 1999. N. R. P. Harris, M. Guirlet and G. T. Amanatidis (Eds). Air pollution Research Report 73 - EUR 19340: 99-102.

Mahieu, E., Zander, R., Mélen, F., Demoulin, P., Rinsland C. P. and Russel III, J. M. 2000. Monitoring the stratospheric chlorine budget during the past decades: the Montreal Protocol at work. In: Proceedings of the International Quadrennial Ozone Symposium, Sapporo, Japan, 3-8 July 2000: 149-150.

Mélen, F., Mahieu, E., Demoulin, Ph., Servais, C. and Zander, R. 1999. Vertical column abundances of COF_2 above the Jungfraujoch Station: update and consolidation of the database with measurements in the ν_4 band region. In: Proceedings of the Atmospheric Spectroscopy Applications 1999, Reims, France, September 1-3, 1999: 77-1 to 77-4.

Paton Walsh, C., Bell, W., Blumenstock, T., Chipperfield, M. P., Galle, B., Mellqvist, J., Notholt, J., Zander, R., Demoulin, P. and Mahieu, E. 1998. Ground-based FTIR Measurements from a Series of European sites during the Winter of 1995/96 and a Comparison with a 3D Chemical Transport Model: Evidence of Chlorine Activation and Ozone Depletion. In: Proceedings of the Fourth European Symposium on Polar Stratospheric Ozone Research, Schliersee, Germany, September 22-26, 1997. European Commission, Air pollution research report 66: 305-308.

Peeters, P., Muller, J.F., Simon, P.C., Gillotay, D., Menklaus, A., Weber, M., Haite, C. and Burrows, J. 1998. Estimation of surface UV dose from satellite data; Comparison with mid-latitude ground measurements. Poster presentation at the European Conference on Atmospheric UV Radiation, Helsinki, Finland, June 29 - July 2, 1998.

Plets, H. 2000. UV index forecasts in Uccle, Wetenschappelijke en technische publicaties van het K.M.I. no 9, ISSN D1999/0224/009, K.M.I., Ukkel: 21.

Prinn, R. G., Zander, R., Elkins, J. W., Fraser, P. J., Ko, M. K. W., Cunnold, D., Engel, A., Gunson, M.R., Mahieu, E., Midgley, P. M., Russell III, J. M. and Weiss, R. F. 1999. Long-lived ozone-related compounds, Scientific Assessment of Ozone Depletion: 1998. In: WMO Report 44: I-1 to I-54. World Meteorological Organization, P.O. Box 2300, Geneva 2, CH 1211, Swizerland, ISBN: 92-807-1722-7.

Pundt, I., T. Wagner, M. Van Roozendael, A. Richter, M.P. Chipperfield, M.P., Burrows, J.P., Fayt, C., Hendrick, F., Pfeilsticker, K., Platt U. and Pommereau J.P. 2000. Simultaneous UV-visible measurements of BrO from balloon, satellite and ground: Implications for tropospheric BrO. In: Proceedings of the fifth European Workshop on Stratospheric Ozone, EUR19340: 316-319.

Richter, A., Van Roozendael, M., Wagner, T., Lambert, J.-C., Arlander, D.W., Burrows, J.P., Fayt, C., Johnston, P.V., Jones, R., Toernkvist, K.K., Kreher, K., Pfeilsticker, K., Platt, U., Pundt, I., South, A., Wittrock, F. 2000. BrO measurements from GOME and from the ground: An intercomparison study. In: Proceedings of the Fifth European Workshop on Stratospheric ozone, St Jean de Luz, France, 27 Sep-1st Oct 1999. EUR 19340: 324-327.

Sarkissian, A., Goutail, F., Pommereau, J.-P., Lambert, J.-C., Van Roozendael, M., Vandenberghe, J.-M., Richter, A., Buchwitz, M., Høiskar, B.A.K., Fløisand, I. and Tørnkvist, K. Improved Air Mass Factors for ground-based total NO2 measurements: A sensitivity study. 5th European.Workshop on Stratospheric Ozone, Saint-Jean-de-Luz, France, 27 September - 1 October 1999.

Schmidt, U., H. K. Roscoe, N. R. P. Harris, K. Künzi, L. Stefanutti, and R. Zander. 1997. Instrument Development and Deployment. In European Research in the Stratosphere - The contribution of EASOE and SESAME to our current understanding of the ozone layer, European Commission - DGXII, Ref. EUR16986/ISBN 92-827-9719-8, 1997: 201-241.

Sinnhuber, B.-M., Chipperfield, M., Enell, C.-F., Friess, U., Hendrick, F., Johnston, P., Kreher, K., Pfeilsticker, K., Platt, U., Richter, A., South, A., Toernkvist, K.K., Van Roozendael, M., Wagner, T. and Wittrock, F. 2000. Comparison of ground-based BrO measurements during THESEO with the SLIMCAT chemical transport model. In: Proceedings of the Fifth European Workshop on Stratospheric ozone, St Jean de Luz, France, 27 Sep-1st Oct 1999. Air Pollution Research Report 73, European Commission - DG XII, Brussels, 2000. EUR 19340: 352-355.

Tsouli A., Vandaele, A.C., Colin, R. and Simon, P.C. 1997. Urban Monitoring during Spring and Summer 1995 in Brussels, Belgium. In: Proceedings of the ASA Symposium 1996, Reims, France, 3-5 September 1996: 143-146.

Tsouli A. 2000. Mesures de constituants minoritaires de l'atmosphère en milieu urbain par spectroscopie d'absorption UV-visible et modélisation de la chimie de la troposphère en vue de la prévision des concentrations d'ozone à Bruxelles, PhD thesis, Oct. 2000, ULB.

Van Roozendael, M., Fayt, C., Hermans, C., Lambert, J.-C. 1998b. Ground-based UV-visible measurements of BrO, NO2, O3 and OClO at Harestua (60°N) since 1994, in Polar stratospheric ozone 1997. In: Proceedings of the 4th European Symposium on Stratospheric Ozone Research, Schliersee, Bavaria, Germany, Sept. 22-26, 1997. Air pollution research report 66, 510-513.

Van Roozendael, M., Lambert, J.-C. and Roscoe, H.K. Temperature dependent spectral resolution effects in SAOZ UV-visible spectrometers. In: Proceedings of the 7th GOME/SCIAMACHY Workshop, Frascati, Italy, 6-7 April, 1998.

Van Roozendael, M., Lambert, J.-C., Simon, P.C., Hansen, G., Dahlback, A., De Muer, D., Schoubs, E., Koopman, R., Vanderwoerd, H., Pieters, A., Barbe, A., Claude, H., de La Noë, J., Merienne, M.-F., Staehelin, J. 1998. Ground-based validation of GOME total ozone measurements by means of Dobson, Brewer and GUV instruments, in Atmospheric Ozone. In: Proceedings of the Quadrennial Ozone Symposium at l'Aquila, Italy, 12-21 Sept. 1996. R.J. Bojkov and G. Visconti (Eds): 665-668.

Van Roozendael, M. et al. THESEO - Stratospheric ozone destruction by bromine: project's overview and first results. Oral communication at the EGS Assembly, Apil 19-23, 1999, Den Hague, The Netherlands.

Van Roozendael, M., Arlander, D. W., De Maziere, M., Fricke, K.H., Goutail, F., Hendrick, F., Klein, U., Oelhaf, H., Pommereau, J.-P., Pundt, I., Richter, A., Sinnhuber, B.M., Toernkvist, K.K. and Wagner, T. 1999. Observations in the high latitude stratosphere during THESEO. Oral presentation at the Fifth European Workshop on Stratospheric ozone, St Jean de Luz, France, 27 Sep.-1st Oct. 1999.

Van Roozendael, M., Fayt, C., Lambert, J.-C., Pundt, I., Wagner, T., Richter, A. and Chance, K. 1999. Development of a bromine oxide product from GOME. In: Proceedings of the European Symposium on Atmospheric Measurements from Space (ESAMS), ESA/ESTEC, The Netherlands, 18-21 January 1999. ESA WPP-161, Vol. 2: 543-547.

Van Roozendael M., Fayt, C., Hendrick, F., Hermans, C., Lambert, J.-C., Fonteyn, D., Sinnhuber, B.-M. and Chipperfield, M. P. Seasonal and Diurnal Variation of BrO Column Abundances above Harestua (60°N) and Haute Provence (44°N) during THESEO (2000a). In: Proceedings of the 5th European Symposium on Polar Stratospheric Ozone Research, Saint-Jean-de-Luz, September 27-October 1, 1999. Air Pollution Research Report, European Commission - DG XII, Brussels: 332-335.

Van Roozendael, M., Arlander, D. W., Burrows, J. P., Chipperfield, M. P., Fayt, C., Hendrick, F., Hermans, C., Johnston, P., Jones, R. L., Kreher, K., Lambert, J.-C., Tahrin, N. M., Newnham, D., Pfeilsticker, K., Platt, U., Pommereau, J.-P., Pundt, I., Richter, A., Sinnhuber, B.-M., South, A., Tørnkvist, K.K. and Wagner, T. 2000b. Lessons learned from 2 years coordinated multi-platform UV-visible observations of atmospheric bromine monoxide. In: Proceedings of the Quadriennal Ozone Symposium, Sapporo, Japan, 3-8 July 2000: 157-158.

Van Weele, M., Blumthaler, M., Brognier, C., Engelsen, O., Gillotay, D., Lenoble, J., Martin, T., Den Outer, P., Pfister, G., Ruggaber, A., Walravens, B. and Wehs, P. 1998. From model intercomparison towards benchmarks UV spectra for real atmospheric cases. Oral presentation at the European Conference on Atmospheric UV Radiation, Helsinki, Finland, June 29 - July 2, 1998.

Vandaele, A.C., Hermans, C., Carleer, M., Tsouli,A. and Colin, R. 1998. Urban Pollution Measurements by UV-Visible DOAS. Poster presentation for the 6th FECS Conference on Chemistry and the Environment, Copenhagen, August 26 - 28, 1998.

Vandaele, A. C., Hermans, C., Fayt, C., Fally, S., Carlee, M., Colin R., Mérienne, M.-F. and Jenouvrier, A. 2000. High resolution Fourier transform measurements of the NO_2 visible absorption cross-section: Temperature and pressure influences on its

atmospheric detection, Proceedings of the International Radiation Symposium IRS 2000, St Petersbourg, 24-29 July 2000.

Zander, R., Demoulin, P., Mahieu, E., Delbouille, L., Roland, G., Mélen, F., Servais, C., De Mazière, M. and Van Roozendael, M. 1998. An overview of NDSC-related activities at the Jungfraujoch through high-resolution infrared solar observations. In: Proceedings of the XXVIII Quadrennial Ozone Symposium, L'Aquila, Italy, September 12-21, 1996. R. Bojkov and G. Visconti (Eds): 1,005-1,008.

Zander, R. 1999. Experimental Studies of Atmospheric Changes and Contribution to the Study of the Earth's Atmosphere from Space (ATMOS). Scientific Report Nr 2 to the OSTC-Research Contract Nr. CG/DD/01D: 1-11.

Zander, R., Mahieu, E., Demoulin, P., Servais, C., Mélen, F., Roland, G. and Delbouille, L. 1999. Spectrometric Solar Observations at the Jungfraujoch for Long-term Atmospheric Monitoring. Actes du Colloque "Ozone dans la Troposphère: la Recherche et la Politique", Bruxelles, 26 juin 1998. SSTC-D/1999/1191/3 : 69-76.

Zander, R., Midgley, P. M. and Kurylo, M. J. 1999. The NDSC in support of satellite data validation and calibration. In: Proceedings of the ESA "European Symposium on Atmospheric Measurements from Space", ESTEC-Nordwijk, The Netherlands, January 18-22, 1999. WPP-161, Vol. 2: 649-654.

Zander, R., Mahieu, E, Mélen, F. and Elkins, J. 2000. An evaluation of the northern mid-latitude tropopause heightening, based on N_2O column abundance measurements above the Jungfraujoch. In: Proceedings of the Fifth European Symposium on Stratospheric Ozone, St. Jean de Luz, France, September 27 - October 1, 1999. N. R. P. Harris, M. Guirlet and G. T. Amanatidis (Eds): 135-138.

Zander, R., Mahieu, E., Demoulin, P., Servais, C., Mélen, F. 2000. Long-term evolution of the loading of CH_4, N_2O, CO, CCl_2F_2, $CHClF_2$ and SF_6 above Central Europe during the last 15 years. In: Proceedings of the Second International Symposium on Non-CO_2 Greenhouse Gases - Scientific Understanding, Control and Implementation, Noordwijkerhout, The Netherlands, September 8-10, 1999. Sp. Vol. Environmental Monitoring and Assessment, 2000. Kluwer Academic Publishers: 211-216.

Zerefos, C.S., Meleti, C., Balis, D.S., Bais, A.F. and Gillotay, D. 1998. On long-term spectral UV-B changes in the 90's in Europe. Oral presentation at the 32nd COSPAR Scientific Assembly, Nagoya, Japan, 12-19 July, 1998

ANTHROPOGENIC AND BIOGENIC INFLUENCES ON THE OXIDISING CAPACITY OF THE ATMOSPHERE

INSTITUT D'AERONOMIE SPATIALE DE BELGIQUE
Avenue Circulaire 3
B-1180 BRUXELLES
J.-F. MÜLLER (coordinator CG/DD/02A)
S. WALLENS
M. CAPOUET

KATHOLIEKE UNIVERSITEIT LEUVEN
FYSISCHE EN ANALYTISCHE CHEMIE
Celestijnenlaan 200 F
B-3000 LEUVEN
Ch. VINCKIER (promoter CG/DD/02B)
V. VAN DEN BERGH
I. VANHEES
F. COMPERNOLLE

TABLE OF CONTENTS

ABSTRACT 1

1. INTRODUCTION 3

2. MATERIALS AND METHODS 6

2.1 Fast-flow reactor 6
2.2 Sampling method 7
2.2.1 LN2 trap coated with DCM 7
2.2.2 LN2 trap coated with a 2,4-DNPH solution 7
2.3 Method of analysis 8
2.3.1 GC-MS 8
2.3.2 HPLC-MS 8
2.4 Synthesis 9
2.5 Reagents 9
2.6 Calibration solutions 10
2.7 The IMAGES model 10
2.8 The MOZART model 11
2.9 Comparisons with observations and with other models 11
2.10 Estimating the source of odd hydrogen and ozone in the upper troposphere 14
2.11 Modelling the emissions of biogenic volatile organic compounds (BVOCs) 15
2.12 Coloring techniques in the IMAGES model 17
2.13 Inverse modelling of surface emissions of ozone precursors 18
2.14 Development of a chemical box model for the oxidation of α-pinene 19

3. RESULTS 20

3.1 On-line mass spectrometric analysis of the volatile oxidation products of the α- pinene/OH reaction 20
3.2 Qualitative determination of the semi-volatile oxidation products for the α/β-pinene-OH reaction 20
3.2.1 α-pinene 20
3.2.2 β-pinene 24
3.3 Quantitative determination of the semi-volatile oxidation products for the α-pinene-OH reaction 28
3.3.1 Product yields at 50 and 100 Torr 28
3.3.2 Influence of NO 30

3.3.3 Influence of the reaction time 31
3.3.4 Influence of the initial H2-concentration 31
3.4 Discussion and interpretation of laboratory results for α-pinene 32
3.5 Discussion and interpretation of laboratory results for β-pinene 36
3.6 Understanding the photo-chemical production of ozone in the upper troposphere: quantification of the sources of HOx and NOx 39
3.7 Modelling the impact of human activities on the global tropospheric composition 40

4. VALORISATION OF RESULTS 42

5. CONCLUSIONS: RECOMMENDATIONS 42

6. REFERENCES 43

ABSTRACT

The oxidizing capacity of the atmosphere determines the fate and lifetime of a large number of pollutants and greenhouse gases. It is affected by biogenic and anthropogenic emissions of chemical compounds, including hydrocarbons, carbon monoxide and the nitrogen oxides. In this project, the impact of these emissions on the formation of tropospheric ozone and other oxidants (including the hydroxyl radical OH) has been investigated through a combination of modeling activities and laboratory studies.

A first achievement of this project is the reduction of uncertainties in the chemical processes that determine the global distributions of tropospheric constituents. A number of chemical mechanisms, which have been identified to be potentially important, have been studied in the laboratory. More specifically, the products formed in the reaction of selected monoterpenes, in particular α-pinene and β-pinene, with hydroxyl radicals in the presence of an excess of oxygen have been identified and quantified. In order to achieve this goal, new analytical methods have been developed for the determination of both the volatile and semi-volatile reaction products. The study was carried out in a fast-flow reactor where hydroxyl radicals were generated from the reaction of hydrogen atoms with nitrogen dioxide. The reactor was equipped with a specially designed microwave cavity designed to operate at pressures up to 100 Torr. The volatile compounds were determined via on-line mass spectrometric analysis. In the case of the α-pinene, carbon dioxide, carbon monoxide, nitrogen dioxide and acetone were identified. The product yields were found to be pressure dependent, indicating that the fate of the initially formed α-pinene-OH adduct is determined by its stabilization rate. At low pressure of a few Torr, this adduct undergoes isomerization and decomposition reactions, while at a high pressure, it reacts mainly with molecular oxygen as is the case under atmospheric conditions. The semi-volatile products were collected on a liquid nitrogen trap and subsequently analyzed by GC-MS and HPLC-MS. When experiments were carried out at a total pressure of 50 Torr, GC-MS analysis showed that campholenealdehyde and pinonaldehyde were formed as oxidation products of the α-pinene/OH reaction, with pinonaldehyde being the main product. In the case of the β-pinene, nopinone is found to be the main oxidation product.

In addition, a new sampling method has been developed based on the conversion of aldehydes and ketones to 2,4-dinitrophenylhydrazone derivatives followed by HPLC-MS analysis. In this way formaldehyde, acetaldehyde and acetone could be determined. The quantification of the semi-volatile compounds was performed using two internal standards, benzaldehyde- and tolualdehyde-2,4-DNPH. Relative molar

yields for th α-pinene/OH reaction products have been determined at 50 and 100 Torr, respectively: 9.7 ± 0.7 and 6 ± 5 for formaldehyde; 1.1 ± 0.1 and 0.9 ± 0.5 for acetaldehyde; 16 ± 1 and 6 ± 2 for acetone; 11 ± 2 and 5.5 ± 0.7 for campholenealdehyde; 63 ± 3 and 82 ± 7 for pinonaldehyde. For the reaction of β-pinene with hydroxyl radicals, the following products have been identified: nopinone, acetone, acetaldehyde, formaldehyde, trans-3-hydroxynopinone, perillaldehyde, perilla alcohol and myrtanal.

A second achievement of this project is a better understanding of the processes controlling the abundance of tropospheric OH and a better quantification of the global budget of ozone and its precursors in the troposphere. Advances have been made towards a better quantification of ozone precursor emissions as well as a better quantification of their role in the global troposphere. For this latter purpose, two distinct chemical/transport models have been used. IMAGES, which provides global climatological distributions of chemical constituents, has been used to quantify the importance of many relevant processes (emissions, chemical reactions, etc.) on the global distribution and budget of tropospheric compounds. MOZART, which accounts for detailed meteorological variability, is most appropriate for the analysis of field observations. Note that, in spite of their different scopes, these models have similar formulations for chemical processes and emissions. In the framework of this project, these models have been intensively compared with chemical observations as well as with many other models. Numerical techniques have been developed to predict the impact of different sources on the distribution of ozone precursors (CO and NO_x). By this way, the pollutant emissions can be optimized in order to achieve a better agreement between the atmospheric model and the observations. The development of these inverse modelling techniques is an important step towards a better utilization of global measurements of pollutants such as the increasingly important satellite observations.

Among the ozone precursors, Biogenic Volatile Organic Compounds (BVOCs) have been given a special attention. Both their emissions by foliage and their subsequent fate in atmospheric conditions have been the subject of our investigations. A detailed BVOC emission model has been developed and tested against field measurements, in order to check the existing parameterizations. A chemical “box” model has been developed in order to integrate the existing knowledge on the oxidation of α-pinene (an important BVOC) by ozone, its largest oxidant. A gas/particle partitioning model has been included to allow the calculation of organic aerosol production from BVOC oxidation. Finally, the IMAGES model has been used in order to quantify the impact of hydrocarbons on the production of odd hydrogen (HO_x) and ozone in the upper troposphere. For example, the respective contributions of the photo-oxidation of

acetone, aldehydes and hydroperoxides have been quantified and compared with the HO_x source due to ozone photolysis.

A third achievement of this project is the determination of the influence of human activities on the chemical composition and the oxidizing capacity of the atmosphere. IMAGES has been used to evaluate the impact of biomass burning and technological emissions, including aircraft emissions. Both past and possible future changes in the composition of the global troposphere have been the subject of our attention. In our estimations of the possible future (2050/2100) changes, the role of both the anthropogenic emissions increases (estimated from standard scenarios of economic and technological development) and water vapor and temperature changes (estimated from a Global Circulation Model) were considered. Part of this work is a contribution to the recent 3rd IPCC Assessment Report.

1. INTRODUCTION

Several important threats for the global environment are currently being considered by the scientific community and by decision-makers. The depletion of stratospheric ozone has received much attention in the past and has triggered worldwide political action. A second global problem is the potential climate changes resulting from increasing emissions of greenhouse gases to the atmosphere. Although many uncertainties remain in the magnitude of these effects, climate conventions have been established calling for a reduction in the emissions. A third threat is the potential change in the global oxidizing capacity of the atmosphere. The importance of this question arises from the fact that pollution, which was regarded in the past as a local or regional problem, appears to affect the global atmosphere and could produce serious impacts on the Earth's biosphere (including humans) and on the climate system. The magnitude (and sometimes even the sign) of the effects remain uncertain and deserve detailed studies. An example of these problems is provided by the large increase recorded in the concentration of ozone in the atmospheric boundary layer over populated areas, and possibly also in remote areas. Changes may have occurred also in the free troposphere, but these are less documented. Ozone is an oxidant that can harm the productivity of crops and other plants and the health of humans. Ozone is also a greenhouse gas and, according to recent model calculations, could have contributed to 20% of the increase in the greenhouse forcing in the Northern Hemisphere since the pre-industrial era.

Another example is provided by the potentially important but unknown changes in the abundance of the hydroxyl radical (OH) in the troposphere. OH acts as a "detergent" of the atmosphere and, as such, determines the atmospheric lifetime of most

chemical pollutants and of several greenhouse gases. Its concentration depends on the production of other gases including the nitrogen oxides (NO_x), CO, and hydrocarbons. Since no global measurement of OH is available, a study of OH and its past and future evolutions must involve a combination of experimental results and modelling studies.

Humans are perturbing the "chemical balance" of the atmosphere through changes in land-use, industrialisation and domestic activities. In certain cases, anthropogenic emissions have become larger than natural sources. Therefore, large impacts on the atmosphere are expected. Three-dimensional chemical-transport models (CTMs) of the atmosphere are thought to be the best tools in order to quantify the magnitude of these effects. *The determination of the influence of human activities on the chemical composition of the troposphere and on its oxidizing capacity is a major objective of this project.*

These impacts are difficult to estimate, though, due to the complexity of the chemical system, and also to the large uncertainties in several important processes. Among others: (a) the estimation of the global emissions of ozone precursors, in particular, CO, NO_x and non-methane hydrocarbons; (b) the chemistry of non-methane hydrocarbons; (c) the role of spatial and temporal variability; etc. It is therefore of critical importance (1) to perform extensive and detailed comparison of the model results with available observations of atmospheric chemical compounds, as well as with other models, in order to identify the areas where the uncertainties are largest (this is best realised by the means of sensitivity studies); (2) to propose improved, more realistic parameterizations of the processes involved (emissions, chemical mechanism, sub-grid scale transport, numerical solving, etc.), based on the most recent and most advanced experimental and numerical studies. *The reduction of the uncertainties in the processes that determine the global distribution of chemical constituents (including oxidants) in the troposphere is a major objective of the present project.* This goal has been achieved by a combination of laboratory experiments and sensitivity studies using advanced models for the emissions, transport and chemical transformations of the ozone precursors.

Ozone precursors (hydrocarbons, CO and NO_x), which also influence OH, are partly produced by natural processes. For example, the largest source of volatile non-methane organic compounds (NMOCs) on the global scale is provided by the biogenic emissions of isoprene, terpenes and other species [Zimmermann et al. (1978), Müller (1992), Guenther et al. (1995)]. The emissions and photochemical degradation of these Biogenic Volatile Organic Compounds (BVOCs) in the atmosphere are a primary focus of the present project. Indeed, the uncertainty in the

estimation of the global source of BVOC is thought to be a factor of 3. Isoprene being the single most important BVOC in terms of surface emissions, the verification of the isoprene emission algorithms by the means of comparisons with field observations is of particular importance and constitutes a specific focus of our project. The photochemical degradation of isoprene in the atmosphere, though, is believed to be well-known and is currently taken into account in many tropospheric CTMs. In contrast, the photooxidation of monoterpenes ($C_{10}H_{16}$) is much more complex and not well understood.

The monoterpenes can react with O_3 and radicals like OH and NO_3. Due to these reactions, these hydrocarbons have an influence on the concentrations of a number of trace gases in the atmosphere on a global scale [Warneck (1988)]. These trace gases include volatile compounds such as carbon monoxide and carbon dioxide [Hanst and Spence, (1980), Hatakeyama et al. (1991), Vinckier et al. (1998)], formaldehyde and acetone [Grosjean et al. (1992), Nozière et al. (1999)] and semi-volatile compounds like pinonaldehyde and nopinone [Hatakeyama et al. (1991), Nozière et al. (1999), Arey et al. (1990), Hakola et al. (1994)]. In addition, biogenic hydrocarbons are known to be involved in the production of atmospheric aerosols [Hatakeyama et al. (1991), Went (1960), Zhang et al. (1992), Hoffmann et al. (1997)].

Since the overall chemistry of BVOCs in the atmosphere is far too complex to study in situ, experiments have to be performed on a laboratory scale. To establish the degradation paths and to determine the product yields of the α/β-pinene/OH reactions, laboratory measurements can be carried out in smog chambers and fast-flow reactors. The disadvantage of smog chambers is the simultaneous occurrence of OH and O_3 reactions, whereas the fast-flow reactor technique has a clean OH-radical source. In this way the reaction with hydroxyl radicals can be separated from other primary reactions with ozone or nitrate radicals.

Only rather recently, laboratory experiments have started to identify and quantify the reaction products of the terpene reactions. *A major objective of this project is to determine the products and the yields of the α-pinene and β-pinene reactions with hydroxyl radicals in the presence of an excess of molecular oxygen.* First, a sampling technique has been developed based on the capture and determination of these products on a liquid nitrogen trap. In the second part of the project, the reaction yields of the products have been determined quantitatively [Vanhees et al. (2001)].

2. MATERIALS AND METHODS

2.1 Fast-flow reactor

The fast-flow reactor technique with its clean OH-radical source was selected in order to simplify the reaction chemistry. Details of the experimental technique are given in references [Vinckier and Van Hoof, (1993), (1994)]. The fast-flow reactor consists of a quartz reactor with an internal diameter of 2.8 cm and a length of 70 cm. By means of an oil rotary pump with a nominal pump capacity of about 12 $m^3\ h^{-1}$, a flow velocity of 3.81 m s^{-1} was obtained with helium as carrier gas. The time scale t_r of the reaction was determined by the position z of the axial inlet probe which is movable along the reactor axis and by the flow velocity v of the reagents: $t_r = z/v$. In these experiments z was set equal to 16 cm corresponding to a reaction time t_r of 42 ms.

The OH-radicals were generated by the titration reaction $H + NO_2 \rightarrow OH + NO$. The H-atoms needed for this reaction were produced by a microwave discharge in a H_2/He mixture. In all experiments the H_2-concentration was 1.37×10^{13} molecules cm^{-3} and the power of the discharge was 100 Watt (except for the blank where the discharge was turned off). In the past the microwave discharge technique, used to produce hydrogen atoms as precursors for the hydroxyl radicals, could only operate in a pressure range from 0.5 to 12 Torr (1 Torr = 133.322 Pa). This limitation was a major drawback of the fast-flow reactor technique since the results had to be extrapolated too much higher pressures to be relevant for atmospheric conditions. This problem has now been solved by installing a specially designed microwave cavity (type Surfatron) which allows to operate at pressures up to 100 Torr. The experiments were carried out at a total pressure of 50 or 100 Torr helium containing 20 % oxygen.

Hydroxyl radicals were produced in an upstream zone in the fast-flow reactor by allowing an excess of hydrogen atoms to react with NO_2 in a concentration of 3.62×10^{12} molecules cm^{-3}. In the downstream zone, addition of α/β-pinene is carried out by allowing a fraction of the carrier gas helium to flow through a vessel containing the α/β-pinene, resulting in a concentration of α/β-pinene in the reactor in the range from 10^{12} to 10^{13} molecules cm^{-3}. The amount of α/β-pinene consumed was determined by the weight difference before and after the experiments. At the downstream end, the quartz reactor was coupled directly to a mass spectrometer VG/MS/8-80 for qualitative and quantitative analysis of the volatile oxidation products.

2.2 Sampling method

The semi-volatile products were collected over a period of 5 to 6 hours on a liquid nitrogen (LN_2) trap and the batch samples were subsequently analyzed by GC-MS and HPLC-MS. Two coating methods were used to collect these products: the LN_2 trap was coated with a frozen layer of dichloromethane (DCM) or with a layer of a 2,4-dinitrophenylhydrazine solution. The LN_2 trap is installed at the downstream end of the reactor.

2.2.1 LN_2 trap coated with DCM

The LN_2 trap can be coated with a layer of frozen DCM in the case of a qualitative analysis. At the end of a collection experiment, the trap is rinsed with about 50 ml DCM. After removal of the condensed water, the solution is concentrated by rotary evaporation at room temperature to about 1 ml. This remaining solution is further analyzed by GC-MS.

2.2.2 LN_2 trap coated with a 2,4-DNPH solution

In the second collection method used in the quantitative analysis, the trap was coated with a solution containing 2,4-dinitrophenylhydrazine (2,4-DNPH). The collection is based on the *in situ* conversion of aldehyde/ketone compounds to their 2,4-dinitrophenylhydrazone derivatives (see figure 1). This is the most frequently used method for the determination of carbonyls in ambient air [Grosjean et al, (1999), Yacoub (1999), Vairavamurthy (1992), Pötter and Karst, (1996), Grosjean and Grosjean, (1995), Grosjean (1983), Kölliker et al. (1998)]. Therefore, the stainless steel cold trap filled with liquid nitrogen was coated with a solution consisting of 2,4-dinitrophenylhydrazine (2,4-DNPH). The 2,4-DNPH solution was made by mixing 0.1 g of 2,4-DNPH with 0.7 ml diluted H_2SO_4.

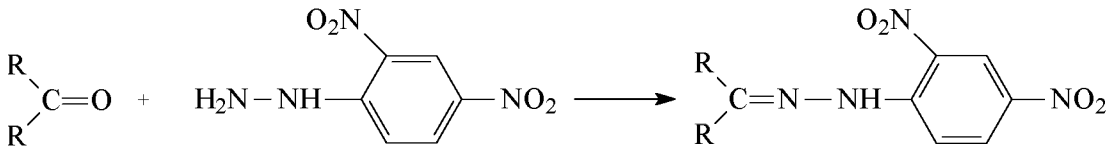

Aldehyde/ketone 2,4-dinitrophenylhydrazine 2,4-dinitrophenylhydrazone derivative

Figure 1: *Reaction mechanism for the derivatization of aldehydes and ketones with 2,4-dinitrophenylhydrazine (in the presence of an acid) to form 2,4-dinitrophenylhydrazone derivatives.*

The solution contains two internal standards: benzaldehyde-2,4-DNPH and tolualdehyde-2,4-DNPH. These two internal standards were needed because treating the trap could result in loss of the coating material. Benzaldehyde-2,4-DNPH was added to the coating solution prior to the coating of the LN_2 trap, whereas tolualdehyde-2,4-DNPH was added to the solution obtained after dissolving the collected residues from the LN_2 trap. Adding these two internal standards in the same concentration allows a correction for possible losses of the first internal standard benzaldehyde-2,4-DNPH. A solution containing benzaldehyde-2,4-DNPH and tolualdehyde-2,4-DNPH both in equal concentrations was analyzed by HPLC in order to derive the ratio of the two peak areas. The resulting value of 0.99 was used to check whether losses of benzaldehyde-2,4-DNPH and the coating occurred during collection experiments or not. Based on this value the loss of the first internal standard benzaldehyde-2,4-DNPH could be calculated. In case the loss of benzaldehyde-2,4-DNPH occurred *after* the collection procedure, it was assumed that the products formed in the α/β-pinene/OH reaction were lost to the same extent. However, if during the coating of the LN_2 trap (*before* the collection experiment) some benzaldehyde-2,4-DNPH would be lost an "over" correction is performed.

2.3 Method of analysis

2.3.1 GC-MS

When the liquid nitrogen trap was coated with DCM, the evaporated solution was analyzed by GC-MS. The GC instrument Carlo-Erba (type Vega GC 6000) was equipped with a Chrompack CP-Sil 5 CB capillary column (25 m length x 0.33 mm inside diameter, df = 2.5 μm) and an on-column injection system. The flow of the helium carrier gas was ca. 1.5 ml min^{-1}. A quantity of 1-2 µl was injected on-column at an oven temperature of 60 °C. After elution of the solvent the oven temperature was raised at a rate of 8 °C min^{-1} to 200 °C. For all experiments electron impact (EI) spectra were recorded on a HP-5989A quadrupole mass spectrometer using an ion source temperature of 250 °C and an electron energy of 70 eV. The temperature of the interface between the GC and the MS was 180°C. The collected compounds were identified by comparing the GC-MS results with published GC-MS [Jay and Stieglitz, (1989)] and mass spectral data [Stenhagen and Abrahamsson, (1968)].

2.3.2 HPLC-MS

When the collection was based on the conversion of carbonyl compounds to their 2,4-dinitrophenylhydrazones, the carbonyl 2,4-DNPH-derivatives were analyzed using a HPLC-MS system equipped with Atmospheric Pressure Chemical Ionization (APCI; Micromass Quattro II). The negative ion mode was selected for the

measurements [Kölliker et al. (1998)]. The scan range of the MS was from 150 to 600 for the determination of m/z values. The APCI probe temperature and the source temperature were 300°C and 80°C, respectively. The cone was set at 22 V. The 2,4-DNPH solutions were separated on a cc Nucleosil 100 C18 column (250 mm length x 3 mm inside diameter, 5 µm particles) using the Hewlett-Packard 1100 HPLC instrument. Separations were carried out at 35 °C using the following mobile phase gradient: from 5 % ACN / 95 % H_2O to 84 % ACN / 16% H_2O in 50 minutes followed by 10 min isocratic elution. The eluent flow rate was 0.6 ml/min and the sample volume injected was 10 µl using a Rheodyne injector. Both a diode array detector (DAD) and a mass spectrometer (MS) for Total Ion Current (TIC) were available as detector. The DAD was set at a wavelength of 360 nm. The mass spectrum corresponding to each peak in the TIC-chromatogram was compared with spectra of reference materials which were obtained from commercial sources or by synthesis.

2.4 Synthesis

2,4-DNPH derivatives of myrtanal, trans-3-hydroxynopinone, perillaldehyde, nopinone, campholenealdehyde and pinonaldehyde were synthesized according to the method described by Behforouz et al. (1985). From these products, only perillaldehyde and nopinone were commercially available. The other products were synthesized. Pinonaldehyde is synthesized by ozonolysis of α-pinene [Vinckier et al. (1997)]. Myrtanal is formed by a Swern oxidation on myrtanol [Peterson and Grant, (1991)]. Trans-3-hydroxynopinone is synthesized through ozonolysis of trans-pinocarveol which is formed by the reaction of α-pinene oxide with lithium diisopropylamide [Lavallée and Bouthillier, (1986)]. Reaction of α-pinene oxide with $ZnCl_2$ yielded campholenealdehyde [Vinckier et al. (1997)].

2.5 Reagents

The following reagents were supplied as gas mixtures: NO_2 (0.1 %) in helium (Oxhydrique), H_2 (0.1 %) in helium (Praxair), O_2 with a purity of 99.998 % (L'Air Liquide), He with a purity of 99.995 % (L'Air Liquide). The liquid reagents α- and β-pinene (Aldrich) had a purity of respectively 98 and 99 %. The solvents used were acetonitrile HPLC grade (Biosolve) and dichloromethane p.a. (Merck). 2,4-DNPH was recrystallized from ethanol, rinsed with ethanol and dried in a dessicator and analyzed by HPLC for possible carbonyl impurities. Formaldehyde-, acetaldehyde-, acetone-, benzaldehyde- and tolualdehyde-2,4-DNPH with a purity of 99 % were obtained from Supelco. Myrtanol (97 %, Aldrich), nopinone (98 %, Aldrich), perillaldehyde (99 %, Aldrich) and α-pineneoxide (97 %, Fluka) were commerically available.

2.6 Calibration solutions

For the quantitative measurements, calibration curves were constructed using the DAD as detector for the following components: formaldehyde-, acetaldehyde-, acetone-, campholenealdehyde-, and pinonaldehyde-di-2,4-DNPH. Benzaldehyde-2,4-DNPH was used as an internal standard.

2.7 The IMAGES model

IMAGES is a global, three-dimensional chemical transport model of the troposphere (Müller and Brasseur, 1995). It calculates the distribution of about 60 species, including ozone, odd hydrogen and odd nitrogen species, sulfur oxides (Pham et al. 1995; 1996), methane, non-methane hydrocarbons (ethane, propane, ethylene, propylene, acetone, isoprene, α-pinene, and n-butane as a surrogate for the other higher hydrocarbons) and their degradation products. Its horizontal resolution is 5° in latitude and in longitude. In the vertical the model includes 25 σ layers from the Earth's surface to the lower stratosphere (50 mbar). Large-scale transport is driven by monthly averaged winds (averaged over the period 1985-1989) taken from an analysis of the European Centre for Medium-Range Weather Forecasts (ECMWF). The impact of wind variability at timescales smaller than one month is taken into account as a diffusion process, with diffusion coefficients estimated from the ECMWF wind variances, following the parameterization of Murgatroyd (1969). The water vapor distribution is also provided by the ECMWF analysis. Note that the use of the ECMWF analysis implies that the model should be considered as climatological, i.e., the modeled distributions do not represent any specific year, and inter-annual variations are ignored. Furthermore, the use of diffusion coefficients to represent temporal variability at short time scales implies that this model isn't appropriate to reproduce the chemical composition of the troposphere during particular episodes at short time scales. Therefore, the model results can't match the short-term variability in the chemical compounds as observed during field campaigns. Instead, the IMAGES model calculates "climatological" distributions of the most important tropospheric trace gases, i.e. multi-year averages in the 1980s and 1990s.

Vertical mixing in the planetary boundary layer is also represented as diffusion. The effect of deep convection on vertical transport is parameterized following Costen et al. (1988). The distribution of cloud updrafts is parameterized using the Cumulonimbus distribution estimated by the International Satellite Cloud Climatology Project (ISCPP) ("D2" climatology). In the latest versions of the model (Müller and Brasseur, 1999), convection and wet deposition schemes are modified to take rainout into account in the convective updrafts.

The trace gas emissions used in the model are those of Müller (1992) and Müller and Brasseur (1995), except that the GEIA (Global Emissions Inventory Activity) inventories are used in the latest versions for the fossil fuel emissions of NO_x and SO_x as well as for the biogenic emissions of BVOCs and NO_x.

2.8 The MOZART model

MOZART is a new three-dimensional global model based in part on the IMAGES model. Both models use the same chemical mechanism, photolysis rates, surface emissions, and dry deposition velocities. In contrast, the spatial resolution (T42 grid, i.e. about 2.8° in latitude and in longitude), the temporal resolution (time step of 20 minutes) and the representation of transport (semi-lagrangian transport from Rasch and Williamson (1990), convection and boundary layer transport parameterization taken from the NCAR Community Climate Model (CCM), a Global Circulation Model (GCM)) represent considerable improvements compared to IMAGES. The major drawback of these changes is the large computer costs they imply.

Dynamical variables (winds, convective fluxes, etc.) are updated every 3 hours. In a first version of the model (Brasseur et al., 1998; Hauglustaine et al., 1998), these fields were calculated off-line by the GCM. In a subsequent version of MOZART, meteorological fields are obtained from an analysis of observed (assimilated) winds taken from the European Centre for Medium-Range Weather Forecasts (ECMWF). In this case, the model calculates distributions of chemical species that are suitable for comparison with chemical data from measurement campaigns over specific periods of time. In both cases, and in contrast with the IMAGES model, MOZART takes fully into account the temporal variability of dynamical fields as well as of photolysis frequencies (since the solar diurnal cycle and the time dependent impact of clouds are explicitly represented).

2.9 Comparisons with observations and with other models

By essence, models are oversimplified representations of reality. Furthermore, a large number of critical model parameters (e.g., chemical rate constants, pollutants emission fluxes, etc.) are poorly quantified. It is therefore of primary importance to evaluate the model performance by the means of extensive comparisons with observations of chemical species. Note that these measurements are generally also tainted with errors. And in some cases, data that are too sparse or too specific might lack representativity for model validation. The troposphere is indeed an extremely variable environment where some species mixing ratios might vary by orders of magnitude within short distances or short periods of time. The interpretation of model-data comparisons therefore requires caution.

The most convenient type of data traditionally used for model evaluation is represented by monthly averaged mixing ratios (averaged over several years) of slowly-varying compounds (O3, CO, CH4,...) at remote places. The year-to-year variations as well as the short-term high-frequency variations are filtered in these averages which can therefore be considered "climatological". Both IMAGES and MOZART have been extensively confronted with such data. These are represented by either surface mixing ratios or vertical profiles obtained by sondes on balloons (for ozone only) (Müller and Brasseur, 1995; Pham et al. 1995; Hauglustaine et al. 1998; Kanakidou et al. 1999a,b).

More recently, aircraft data have proved to be increasingly useful. For example, the routine ozone measurements performed by european commercial airliners in the framework of the MOZAIC program have provided an unprecedented climatology of upper tropospheric/lower stratospheric ozone concentrations over industrialized countries, the North Atlantic, and other regions (Law et al. 2000). Even more significant for model evaluation, dedicated aircraft campaigns (such as the NASA GTE missions and the european STRATOZ/TROPOZ campaigns) are of special interest. In these intensive campaigns, many different chemical compounds and meteorological parameters are measured simultaneously by a collection of sophisticated instruments onboard of aircraft flying in a specific region of particular interest for atmospheric scientists. Although the chemical distributions deduced from these campaigns cannot generally be considered as climatological, they provide unique insights on the role played by shorter-lived compounds such as the nitrogen oxides, oxygenated hydrocarbons, and even radicals. A broad compilation of observations taken from a majority of existing campaigns has been presented by Emmons et al. (2000), with detailed comparisons with the IMAGES and MOZART model distributions. An illustration is provided by the comparison of the measured and calculated vertical profiles of chemical species presented in Fig. 2. The observations reported here are those obtained during the american TRACE-A mission. The IMAGES and MOZART model results shown on the figure were averaged over the mission area (here, Southern Africa). Differences between the two models are often important. They are due to differences in the transport scheme. In general, however, the models are seen to agree reasonably well with the observations. But IMAGES often predicts the existence of an unrealistic minimum in the concentrations of different compounds at around 4 km. This is directly related to the convection parameterization used in the model, which will be improved in future studies. Other comparisons with campaign data have been presented in Thakur et al. (1999), focusing on nitrogen compounds, and in Müller and Brasseur (1999), focusing on upper tropospheric precursors of odd hydrogen radicals.

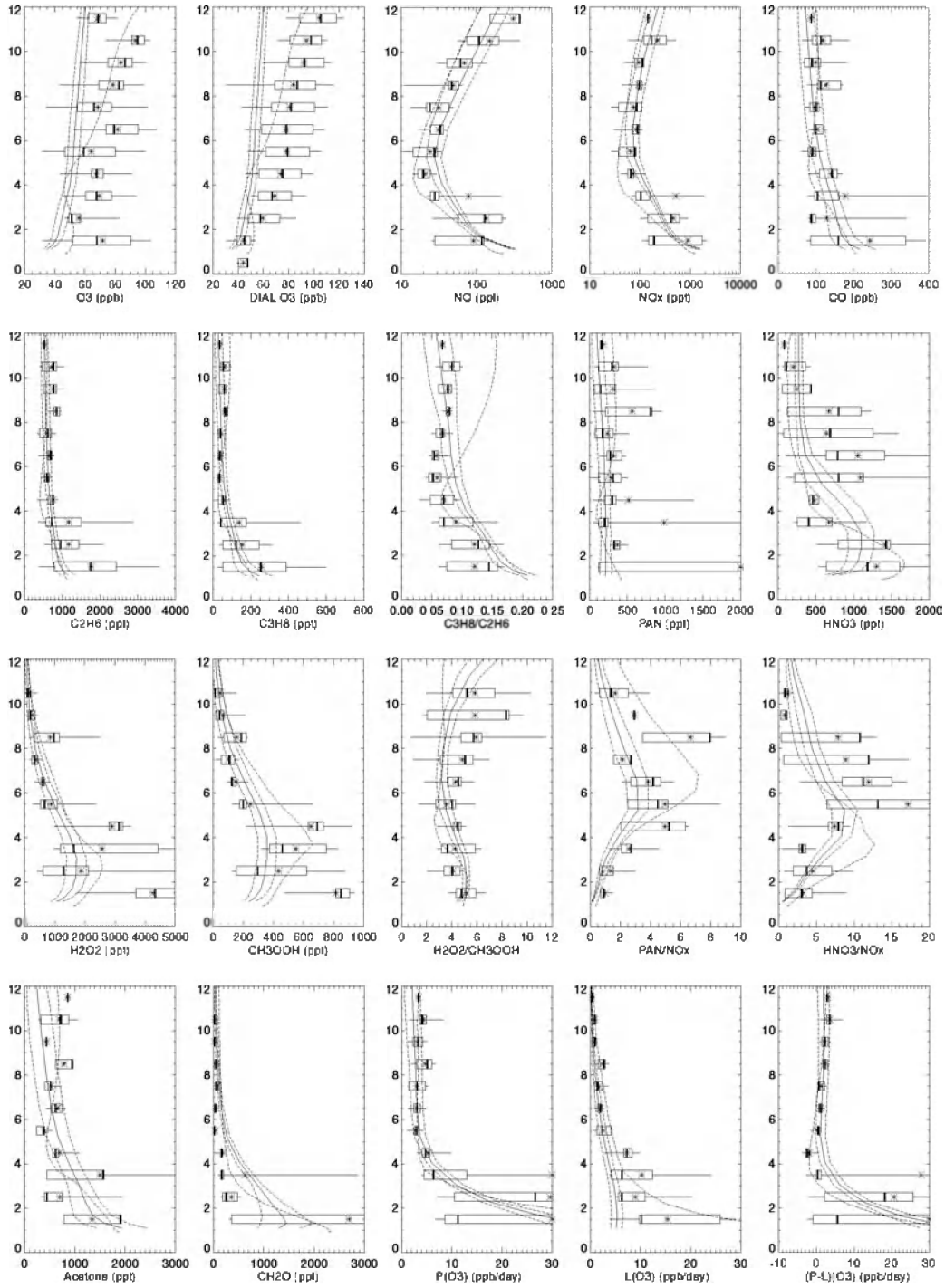

Figure 2: *Vertical profiles of aircraft observations and IMAGES and MOZART results over Southern Africa during the TRACE-A campaign. Solid and dotted lines: MOZART mean and standard deviation in time; dashed lines: IMAGES. Boxes and whiskers indicate the central 50% and 90% of the observations, with a vertical bar at the median, a star at the mean. NO_x (=NO+NO_2) mixing ratio, as well as ozone production ($P(O_3)$), loss ($L(O_3)$) and net loss ($P-L)(O_3$) are estimated from a box model. Adapted from Emmons et al. (2000).*

In the future, remote sensing from space should provide an increasingly reliable and comprehensive set of chemical observations suitable for model validation and for scientific studies. In a preparative step towards this capability, the IMAGES model results have been used in order to optimize a CO/CH_4 retrieval algorithm for a satellite-based interferometer, IMG-ADEOS (Clerbaux et al., 1998). The modeled distribution of NO_2 have also been used to estimate the so-called air mass factors necessary to retrieve this compound by using satellite instruments like GOME (Lambert et al., 1999). The estimation of the tropospheric column of NO_2 by GOME onboard ERS2 (Lambert et al., 2000) and SCIAMACHY onboard ENVISAT will certainly prove to be of considerable help in order to understand the budget and distribution of nitrogen oxides in the troposphere.

In addition, the model outputs have also been compared with other models, in the framework of international intercomparison exercises (Friedl, 1997; Kanakidou et al. 1999a,b).

2.10 Estimating the source of odd hydrogen and ozone in the upper troposphere

The possibility that the subsonic aircraft fleet might enhance the levels of ozone in the upper troposphere/ lower stratosphere (UT/LS) has received considerable attention in the last years. Indeed, aircraft engines are known to release nitrogen oxides in the air, which are essential ingredients in the photochemical make-up of ozone in the troposphere. However, it is important to realize that this production of ozone is also strongly dependent on the levels of odd hydrogen, HO_x ($=OH+HO_2$). The main source of HO_x on the troposphere is the reaction sequence

$$O_3 + h\nu \rightarrow O_2 + O(^1D)$$
$$O(^1D) + H_2O \rightarrow 2\ OH$$

In the UT/LS, though, this production is impeded by the very low relative humidities particular to this region of the atmosphere. Other photochemical sources might therefore become important. We used the IMAGES model in order to calculate the relative contributions of the known photochemical sources to the total HO_x production in the UT/LS. It is believed that the an important source is represented by the convective transport of hydrogen peroxides, organic peroxides, and aldehydes from the Planetary Boundary Layer (PBL) to the UT/LS, followed by their photolysis or oxidation by OH. Therefore a tagging technique has been designed and used in the model in order to determine the role of convective transport on the UT/LS

concentrations of these HOx precursors. Also, the precise yield of HO_x per (oxygenated) hydrocarbon oxidized or photolyzed has been calculated and shown to be a function of other compounds (NO_x in particular). In addition, the IMAGES model has been used in order to estimate the importance of these photochemical processes in the context of the perturbation represented by aircraft.

2.11 Modeling the emissions of biogenic volatile organic compounds (BVOCs)

As noted earlier, the emission of isoprene by terrestrial vegetation is known to provide the dominant input of reactive non-methane hydrocarbons to the atmosphere. Isoprene oxidation influences OH and ozone concentrations, has a significant role in CO production, the formation of organic acids, and photochemical conversion of NO_y species. Since isoprene can influence concentrations of ozone and gases that are removed by OH, including methane, isoprene emissions may indirectly impact climate.

The emissions of isoprene and other BVOCs, however, are still poorly quantified. A global inventory has been developed by Guenther et al. (1995) and is used by most tropospheric CTMs. This inventory relies on algorithms relating the emission rates to environmental factors and vegetation characteristics. BVOC emissions have been shown to depend on light intensity (Photosynthetically Active Radiation or PAR) and/or leaf temperature (Guenther et al., 1993, 1995):

$$F_1 = \varepsilon\, C_L\, C_{T1} \qquad (1) \qquad \text{(ex: isoprene, MBO)}$$

$$F_2 = \varepsilon\, C_{T2} \qquad (2) \qquad \text{(ex: monoterpenes)}$$

Here, ε is a standard emission rate (emission rate at PAR=1000 µmol m^{-2} s^{-1}, and leaf temperature=30°C). This parameter depends on the compound being emitted and on the plant species. The factors C_L and C_{T1}, C_{T2} account for the dependence on PAR intensity and leaf temperature, respectively.

The validation of these algorithms by confrontation with field observations is necessary in order to quantify the possible biases and uncertainties in the global inventory, and also in order to check the impact of proposed model refinements. In that perspective, a detailed vegetation canopy microclimate model has been developed, in collaboration with the team of A. Guenther at NCAR. The fluxes of visible and infrared radiation inside the canopy are calculated from a multi-level (n=8 or 16) radiative transfer model. Leaf temperature in each layer is determined from the energy balance equation at the leaf level:

$$R_{sw} + R_{lw} + SH + LH = 0 \qquad (3)$$

where R_{sw}, R_{lw}, SH and LH are the solar radiation component, the thermal radiation component, the sensible heat flux and the latent heat flux, respectively. To solve this equation requires the determination of physical parameters such as boundary layer resistance to heat and water vapor, stomatal resistance, local wind speed, air temperature, relative humidity, etc. These parameters are related to leaf characteristics such as leaf dimension, leaf reflection coefficient, leaf emissivity, and canopy characteristics such as canopy height, LAI (Leaf Area Index), leaf biomass density, etc.

Figure 3 displays the comparison of isoprene fluxes measured and calculated by this model using the meteorological data (PAR, air temperature at canopy top) determined from the measurements. The site is located in a forest in Massachusetts. The isoprene fluxes were calculated with our model using either the leaf temperature or air temperature in equation (1). Modelled isoprene fluxes are found to be systematically underestimated compared with measurements when ε (eq. (1)) is deduced from vegetation composition and standard emission factors from the literature. We attribute this difference to an underestimation of either the standard emission factors used for oaks or the proportion of oaks (or other high-isoprene emitters) in the surrounding vegetation. It is also calculated that using air temperature (instead of leaf temperature) in equation (1) results in ~ 5 % higher emission estimates (average over the growing period). Sensitivity tests were performed showing that the isoprene emission estimates are not much influenced by possible errors in physical parameters such as the extinction coefficient, the leaf scattering coefficient, and the fraction of diffuse PAR.

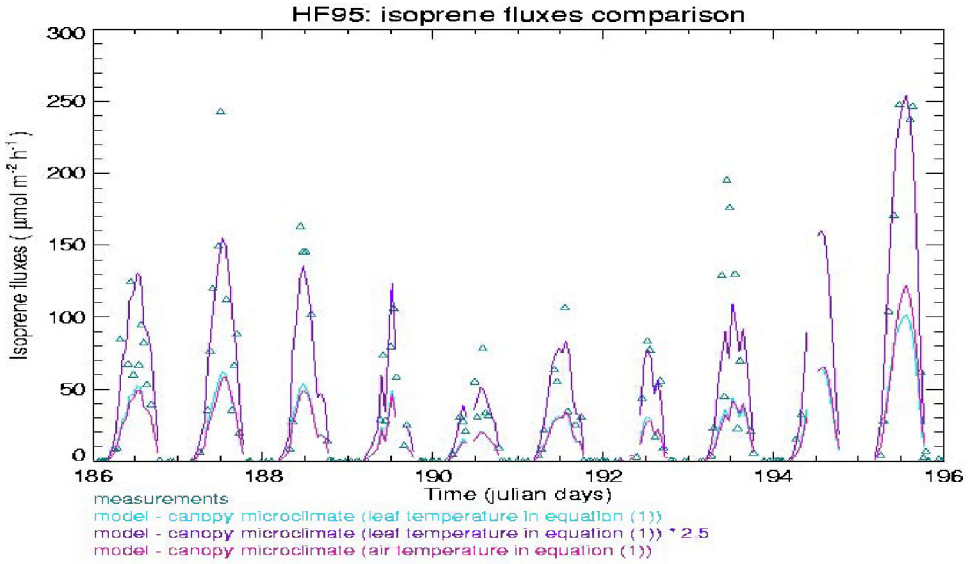

Figure 3: *Isoprene emission fluxes measured and calculated at the Harvard forest site (see text for details).*

2.12 Coloring techniques in the IMAGES model

The role played by the different emission sources (e.g., biomass burning, lightning, soils, etc.) on the distribution and budget of tropospheric pollutants can be investigated by variety of ways. The simplest method consists in varying the emission figures used in a chemical transport model (like IMAGES) and then comparing the results obtained in the different cases. It should be noted, however, that this is not equivalent to estimating the real relative contributions of the different sources on the tropospheric composition. Indeed, the residence time of a given tropospheric chemical species is generally a complex function of the geographical location, the time of the year, and the concentrations of many trace gases, including the compound of interest. This is especially true for carbon monoxide (CO) and nitrogen oxides (NO_x), since these important ozone precursors have a strong influence on the hydroxyl radical (OH) levels. The emissions of these gases are partly biogenic, and partly anthropogenic. In addition, CO is also one of the major end products in the atmospheric oxidation of methane and other hydrocarbons. This explains why it is so difficult to quantify the anthropogenic perturbation to the budget of important species.

In order to overcome these difficulties, innovative modeling techniques must be implemented. The "coloring" or "tagging" technique consists in assigning distinct "colors" or "flavors" to pollutant molecules emitted from different sources in an atmospheric CTM. This method allows to follow the evolution of any pollutant from any source without affecting the overall chemical state of the atmosphere. This technique has been first applied in IMAGES to study the relative contribution of different NO_x sources in the troposphere (Lamarque et al., 1996). In this study, nitrogen originally emitted as one species (e.g., NO) is tagged so that it can be followed during all subsequent chemical transformations (e.g., to NO_2 and other products). If, for example, we consider only two sources, the total NO mixing ratio is written as NO=xNO + yNO, where xNO and yNO refer to the mixing ratio of NO associated with sources x and y, respectively. Six different sources were considered: aircraft, biomass burning, lightning, fossil fuel emissions, soils, and transport from the stratosphere.

In another study, the role of CO sources was investigated (Granier et al., 1999, 2000). This case is more complex because, in addition to surface emissions, the atmospheric oxidation of methane and non-methane hydrocarbons (NMHC) represents important sources of carbon monoxide. In order to distinguish between the contribution of methane, isoprene, terpenes and other hydrocarbons, a large number of oxygenated intermediates (e.g., CH_3O_2, CH_2O, PAN, etc.) involved in the oxidation mechanisms of these hydrocarbons must be "tagged" in order to follow the complete sequence of reactions between the initial hydrocarbon attack by OH, O_3, or

$O(^1D)$ and leading eventually to CO. The surface emissions of carbon monoxide considered in our study include: technological sources, vegetation and ocean, biomass burning.

2.13 Inverse modelling of surface emissions of ozone precursors

The scientific exploitation of satellite-derived tropospheric columns of e.g. CO and NO_2 (two important ozone precursors in the troposphere) requires the development of new modelling techniques. Indeed, global distribution maps for these compounds are expected to provide useful insights on the distribution and strength of the emissions for these compounds. The pollutants emissions used in atmospheric models are based on various global emissions inventories (e.g. Müller, 1992) which are known to be very uncertain because of the major difficulty to extrapolate emissions estimates from local measurements to the global scale. In this perspective, the satellites should help to constrain the repartition of the total emissions into the different sources (e.g. anthropogenic, vegetation, ocean, etc.) and/or into different regions of the world. For that purpose, the pollutants emissions used in atmospheric models should be varied (roughly speaking, within their error bars) in order to minimize the biases between the modeled concentrations and the measurements. This general technique is commonly named inverse modeling.

In an exploratory study (Pétron et al., 2001), we restricted our objectives to the optimization of the surface emissions of CO on a monthly timescale, using monthly means of CO mixing ratio observations from the flask sampling network (CMDL) and the IMAGES model. The inversion scheme attempts to minimize the discrepancies between observed and modeled mixing ratios at the stations by optimizing the direct surface emissions of CO. In this approach, the transport model and the modeled chemical production of CO are assumed to have smaller uncertainties than CO surface emissions. It is also assumed that the relationship between the surface emissions and the concentrations at the measurement sites is linear. This assumption is shown to hold sufficiently well in this case, and a simple iterative procedure is used in order to take the non-linearity into account to a good approximation. The numerical method adopted to perform the inversion (described in detail in Pétron et al. (2001)) is based on the tagging technique described in the previous section. In this study, 5 oceanic regions and 7 continental regions are considered. The continental surface emissions are due to technological activities, biomass burning (2 sub-categories: forest and savanna burning, agricultural waste burning and fuel wood use) and vegetation/microorganisms in soils. This brings a total of 33 tagged CO sources.

2.14 Development of a chemical box model for the oxidation mechanism of α-pinene

The oxidation of terpenes (α-pinene in particular) has received an increasing attention in the last years with a large number of laboratory and theoretical studies being conducted to identify the products and quantify the yields in various conditions. The laboratory investigation conducted in this project is an example of these studies. The extraordinary complexity of the terpene oxidation mechanism, however, makes the interpretation of experimental results extremely difficult. The laboratory conditions used (e.g., initial terpene concentration, NO_x levels, etc.) are most often very unrealistic and, even more significantly, they are generally not well controlled and understood. The partitioning of low-volatility products between the gas- and aerosol-phases represents an additional difficulty of crucial importance. This partitioning is thought to occur both in laboratory and atmospheric conditions, for compounds like the $C_{>9}$ acids and diacids, most (hydroxy) carbonyls, and most probably, for non-measured compounds like hydroperoxides and organic nitrates. The currently accepted gas/particle partitioning theory appears unable to account for the observations of the partitioning ratios for an important α-pinene degradation product, pinonaldehyde. Furthermore, the chemical pathways leading to the formation of highly condensable species like pinic acid (believed to play a crucial role in the aerosol formation process) are probably not understood. Much additional laboratory and theoretical investigations will be necessary in order to provide the kinetic data urgently needed by atmospheric models to estimate the role of terpenes in atmospheric chemistry.

For these reasons, we started the development of a chemical "box" model for the oxidation of α-pinene. The objective is to allow for a better interpretation of the existing laboratory data. Gas-phase chemical kinetic data on the α-pinene oxidation mechanism were provided by the team of J. Peeters at KULeuven on the basis of literature data and theoretical considerations. The resulting gas-phase chemical mechanism remains uncertain and is far from being complete, however. This work is in progress and will be continued in the framework of the OSTC's PADD2 (PODO2) program.

In addition to gas-phase chemical reaction, the partitioning of condensable species on aerosols is also considered, although nucleation of new particles and other microphysical processes are not described in detail. The partitioning coefficients of the condensables are estimated from the literature. This model has already been used to simulate a couple of published laboratory results for α-pinene ozonolysis. Our objective for the future will be the implementation of a complete chemical

mechanism and its validation and fine-tuning by the confrontation with a large number of existing laboratory data.

3. RESULTS

3.1 On-line mass spectrometric analysis of the volatile oxidation products of the α-pinene/OH reaction

The volatile products formed in the reaction between α-pinene and OH were determined quantitatively by measuring the signals of α-pinene, NO_2, CO_2, CO and acetone on-line by means of mass spectrometric detection [Vinckier et al. (1998)].

The product yield R is defined as the ratio of the concentration of the product formed to the amount of α-pinene reacted. The quantitative determination of the volatile products (CO_2, CO, acetone and NO_2) was carried out at different total pressures with 20 % of the total pressure consisting of oxygen. The yields for CO_2, CO and acetone decreased when the pressure was increased, whereas the yield for NO_2 increased with pressure. The relation between pressure and the yields for the volatile components can be explained by considering the α-pinene-OH-adduct. This product is formed by addition of OH to the double bond in α-pinene. The adduct contains a large amount of internal energy and at low pressures it will isomerize or decompose to form several products including CO_2, CO and acetone. At higher pressures the excited adduct is stabilized by collisions with a bath gas. Therefore, the amount of energy left will not be sufficient for decomposition to occur. There is not only the pressure effect of the higher helium concentration, but also the increase of the O_2 concentration at higher pressure, which is more efficient for the stabilization of the activated components [Vereecken and Peeters, (2000)].

3.2 Qualitative determination of the semi-volatile oxidation products for the α/β-pinene-OH reaction

3.2.1 α-pinene

As described in section 2.2.1, a first collection method consists of sampling the products on a LN_2 trap coated with dichloromethane. The reaction products collected on the cold wall were dissolved in DCM and then analysed by GC-MS. For each signal in the GC-MS chromatogram, the EI spectrum can be constructed and compared with reference data. When the experiments were carried out at pressures of 50 and 100 Torr, unreacted α-pinene, campholenealdehyde and pinonaldehyde were identified, with pinonaldehyde being the most important oxidation product. This is illustrated in Figure 4, where a GC-MS chromatogram is shown of the products

found at 50 Torr. Similar results were obtained at 100 Torr (Van den Bergh et al. (2000)).

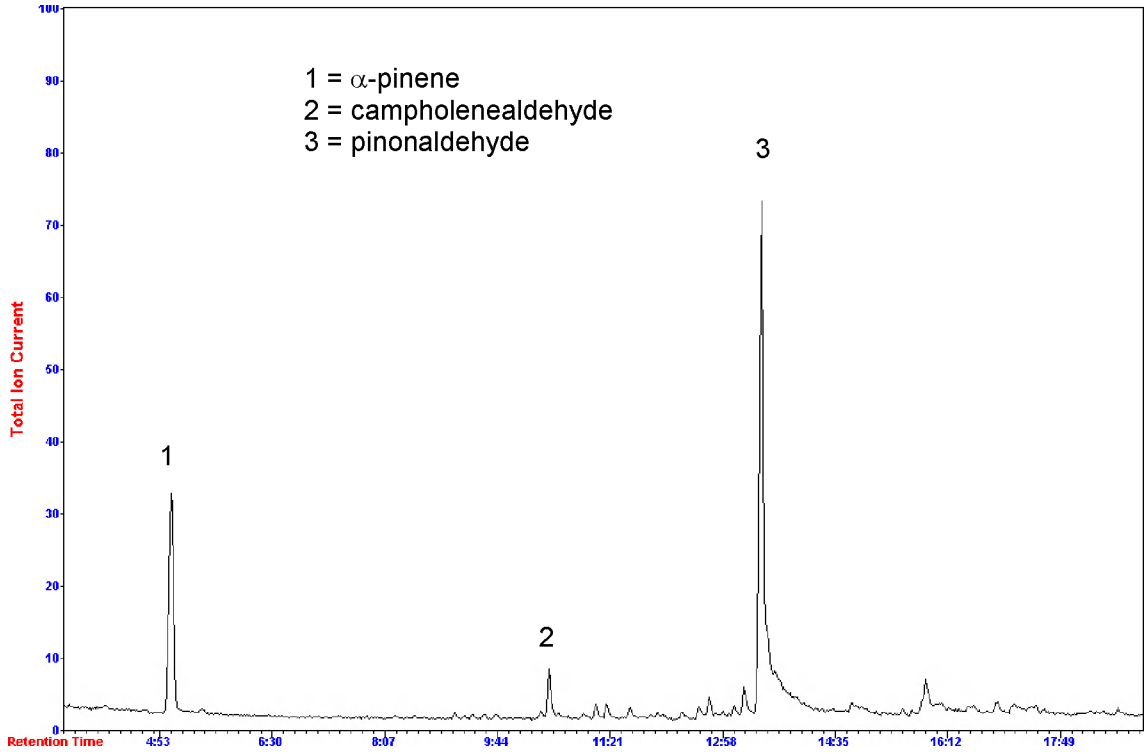

***Figure 4**: GC-MS chromatogram of a collection experiment at a total pressure of 50 Torr. Initial concentrations: [α-$C_{10}H_{16}$] = 3.83x10^{12}, [H_2] = 1.37x10^{13}, [NO_2] = 3.63x10^{12}, [O_2] = 3.24x10^{17} each expressed in molec cm^{-3}. The reaction time t_r = 42 ms, collection time t_c = 381 min. Collection method: LN_2 trap coated with DCM.*

A fundamental problem with this technique is to have a good method for collecting semi-volatile components from a high velocity gas stream passing through a LN_2 trap at low pressure. The semi-volatile products like formaldehyde, acetaldehyde and acetone are not detected when DCM is used as collection agent. Although these products can be captured on the LN_2 trap they are lost while evaporating the solvent. This rotary evaporation was required to reduce the solution from approximately 50 ml to 2-3 ml prior to GC injection. Therefore another coating procedure is developed.

The new method is based on the conversion of the aldehydes/ketones to 2,4-dinitrophenylhydrazone derivatives. The aldehydes and ketones formed in the oxidation reaction of α-pinene were collected on the LN_2 trap coated with a solution of 2,4-DNPH in ACN-DCM containing benzaldehyde-2,4-DNPH as the first internal standard. A quantitative transfer to the cold LN_2 trap was facilitated by instantaneous freezing out of consecutive layers of the ACN-DCM solution applied to the inner wall of the trap. At the end of the collection experiment, the reaction products collected on

the cold wall were recovered by rinsing the frozen solution with further portions of ACN-DCM solvent mixture, followed by addition of tolualdehyde-2,4-DNPH. This solution containing the two internal standards was further analyzed by HPLC-MS. First a blank experiment was run in the absence of α-pinene and OH radicals. The resulting HPLC chromatogram in figure 5 shows that besides 2,4-DNPH, only the signals of the two internal standard were observed.

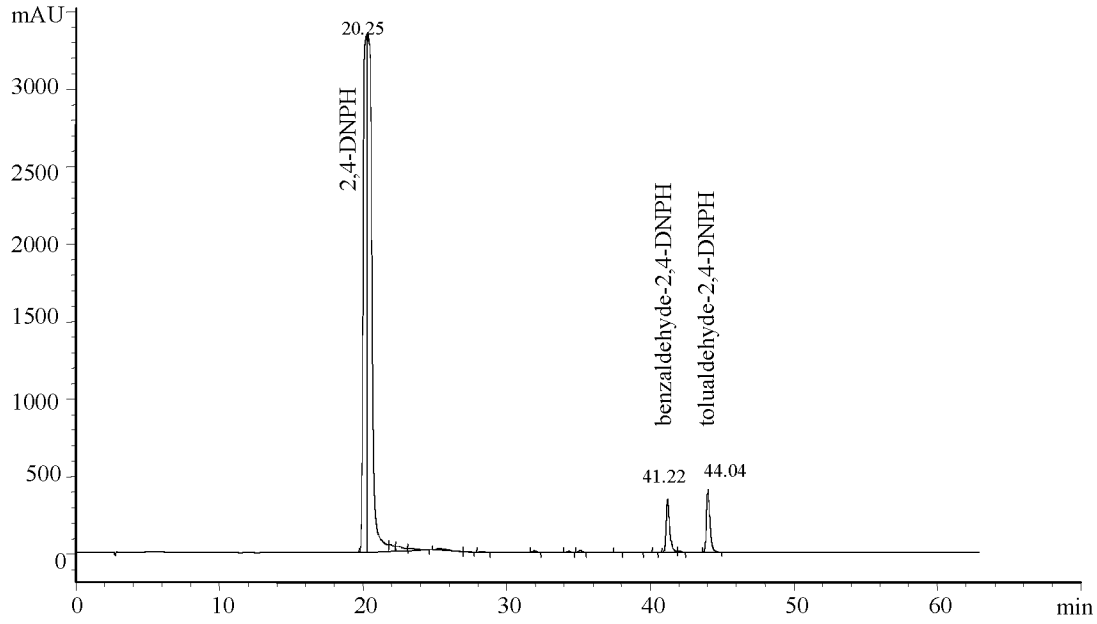

Figure 5: *HPLC (DAD, 360 nm) chromatogram (blank collection experiment) at a total pressure of 50 Torr. Initial concentrations: [α-$C_{10}H_{16}$] = 0, [H_2] = 1.37x10^{13}, [NO_2] = 0, [O_2] = 3.24x10^{17} each expressed in molec cm^{-3}. Microwave discharge turned off. The reaction time t_r = 42 ms, collection time t_c = 170 min.*

When α-pinene was reacting with OH radicals at 50 Torr pinonaldehyde-di-2,4-DNPH (t_R= 51.1 min, M_r = 528) was identified as the main product. Other identified products shown in figure 6 are campholenealdehyde-2,4-DNPH (t_R = 49.4 min, M_r = 332), formaldehyde-2,4-DNPH (t_R = 28.7 min, M_r = 210), acetaldehyde-2,4-DNPH (t_R = 32.2. min, M_r = 224) and acetone-2,4-DNPH (t_R = 35.4 min, M_r = 238). Besides these oxidation products, the chromatogram shown in figure 6 contains three other peaks: dinitroaniline (t_R = 22.5 min) and two unidentified products with t_R = 25.1 min and t_R = 27.0 min. Because the same peaks are detected in a blank experiment with OH radicals but in the absence of α-pinene, it is clear that these products do not result from the α-pinene/OH reaction.

The oxidation products could be identified according to their retention times observed in the Total Ion Chromatogram (TIC) (not shown here). The mass spectrum of each peak can be constructed from the TIC and compared with mass spectral data of reference compounds. The mass spectra of the reference compounds obtained from commercial sources or by synthesis are shown in figure 7. A summary of the retention times, identified products, $(M-H)^-$ values and molecular masses is presented in Table I.

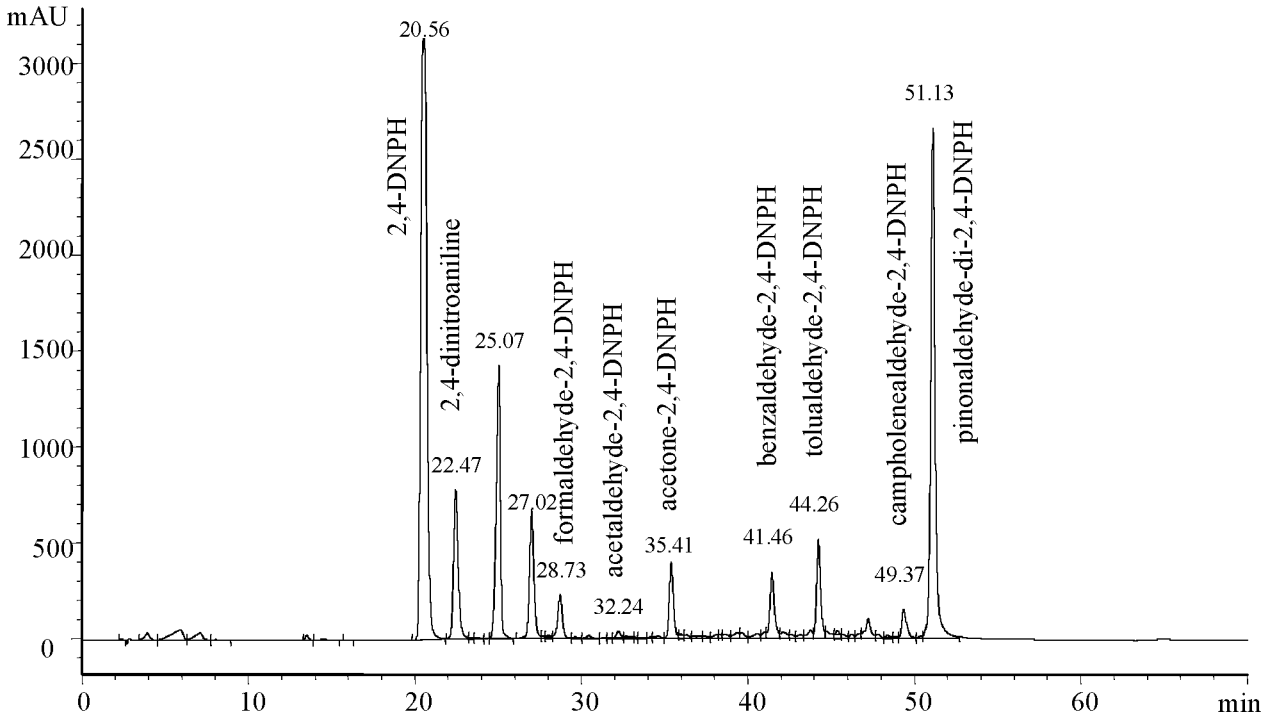

***Figure 6**: HPLC (DAD, 360 nm) chromatogram at a total pressure of 50 Torr. Initial concentrations: [α-$C_{10}H_{16}$] = 5.08x10^{12}, [H_2] = 1.37x10^{13}, [NO_2] = 3.62x10^{12}, [O_2] = 3.24x10^{17} each expressed in molec cm^{-3}. The reaction time t_r = 42 ms, collection time t_c = 306 min. Collection method: LN_2 trap coated with 2,4-DNPH solution.*

Table I: *Retention times t_R, $(M-H)^-$ values and molecular masses M_r of the identified products.*

t_R (min)	product	$(M-H)^-$	M_r
19.3	2,4-DNPH	197	198
27.2	formaldehyde-2,4-DNPH	209	210
30.9	acetaldehyde-2,4-DNPH	223	224
33.9	acetone-2,4-DNPH	237	238
38.2	pinonaldehyde-mono-2,4-DNPH	347	348
48.8	campholenealdehyde-2,4-DNPH	331	332
50.0	pinonaldehyde-di-2,4-DNPH	527	528

3.2.2 β-*pinene*

An analogous study has been performed on the β-pinene/OH reaction. The resulting GC-MS chromatogram for a collection experiment performed at a total pressure of 50 Torr and with the trap coated with DCM, is shown in figure 8. Nopinone is the main oxidation product. Besides nopinone, small signals can be observed which were attributed to myrtanal, trans-3-hydroxynopinone, perillaldehyde and perilla alcohol. Similar results have been obtained for experiments performed at 100 Torr [Van den Bergh et al. (2001)].

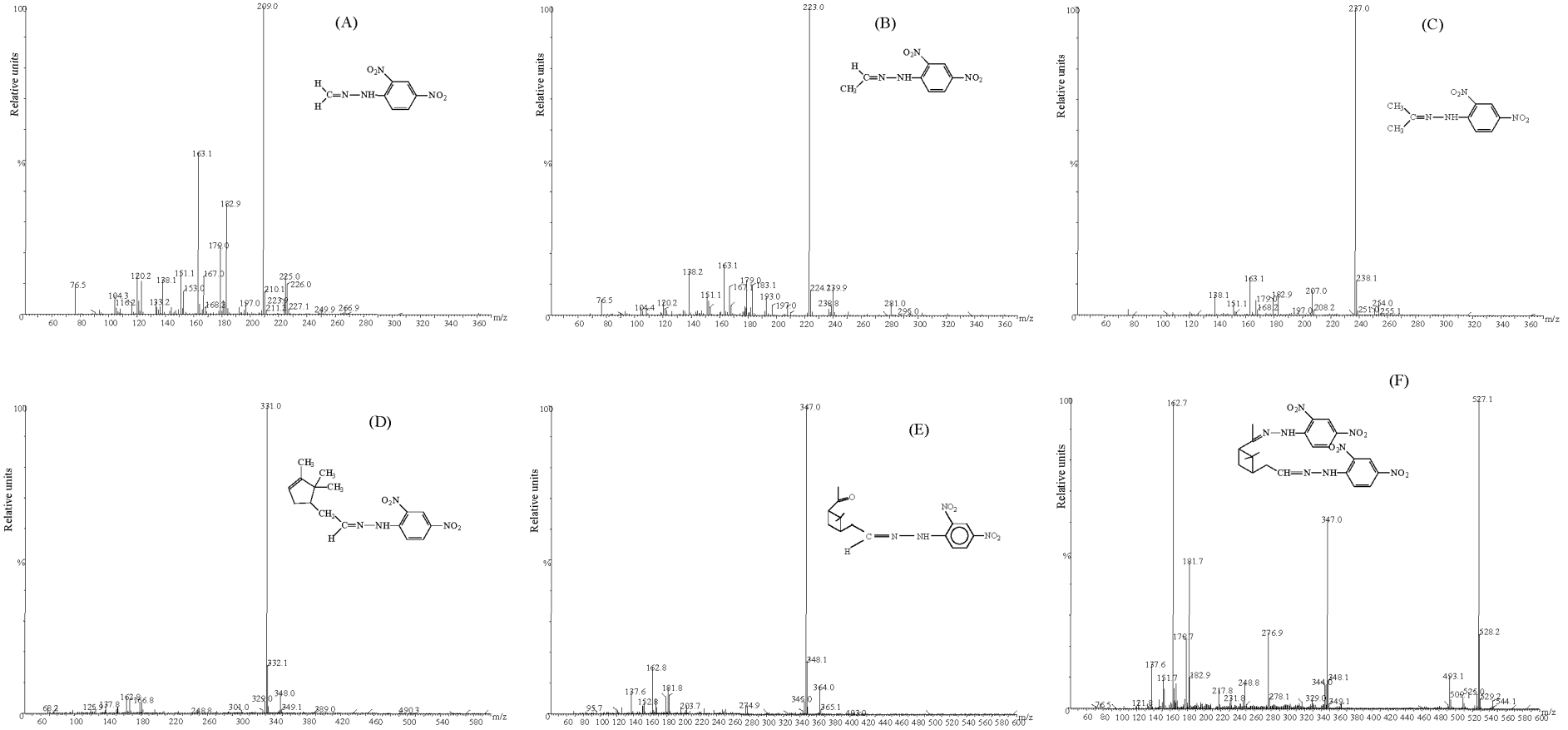

***Figure 7**: APCI(-) generated mass spectra of reference materials obtained from commercial sources [(A) formaldehyde-2,4-DNPH, (B) acetaldehyde-2,4-DNPH, (C) acetone-2,4-DNPH] or by synthesis [(D) campholenealdehyde-2,4-DNPH, (E) pinonaldehyde-mono-2,4-DNPH and (F) pinonaldehyde-di-2,4-DNPH)].*

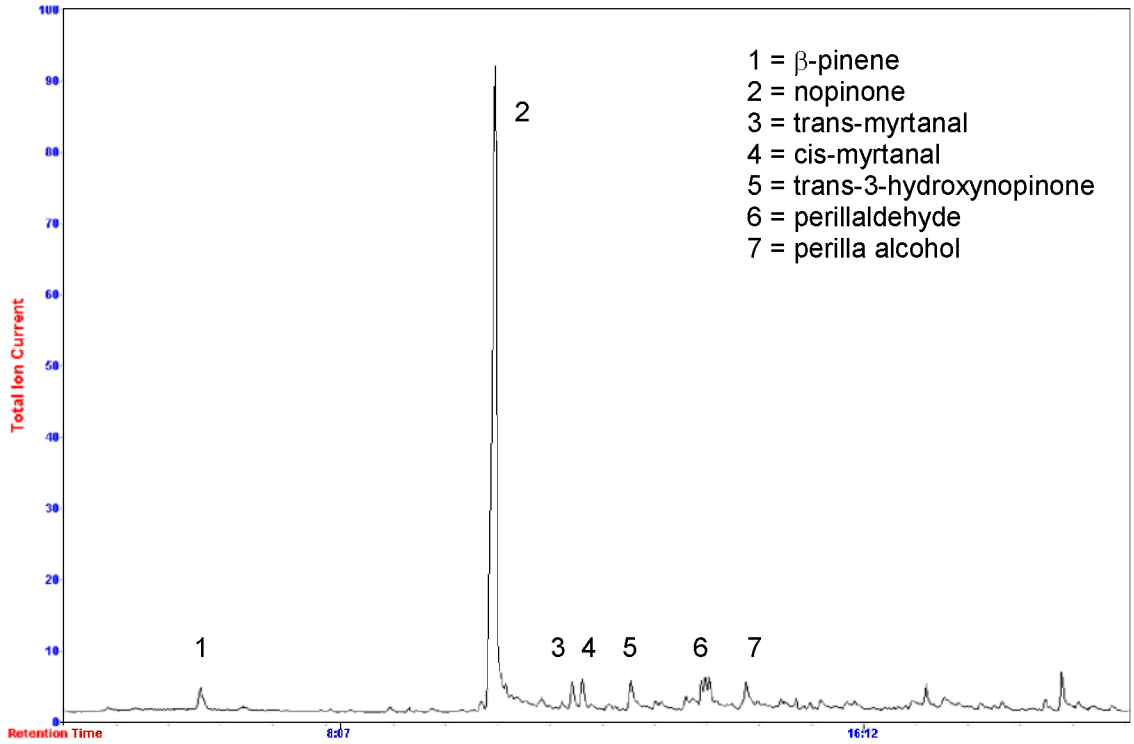

***Figure 8**: GC-MS chromatogram of a collection experiment at a total pressure of 50 Torr. Initial concentrations: [β-$C_{10}H_{16}$] = 4.81x10^{12}, [H_2] = 1.37x10^{13}, [NO_2] = 3.63x10^{12}, [O_2] = 3.24x10^{17} each expressed in molec cm^{-3}. The reaction time t_r = 42 ms, collection time t_c = 437 min. Collection method: LN_2 trap coated with DCM.*

Using the collection method, where the LN_2 trap is coated with a 2,4-DNPH solution the products shown in figure 9 were identified. The identified oxidation products, retention times, ($M-H^-$) values and molecular masses are summarized in table II. The mass spectral data of the reference compounds nopinone-, trans-3-hydroxynopinone-, perillaldehyde- and myrtanal-2,4-DNPH are shown in figure 10.

Table II: *Retention times t_R, $(M-H)^-$ values and molecular masses M_r of the identified products for the β-pinene/OH reaction.*

t_R (min)	product	$(M-H)^-$	M_r
20.1	2,4-DNPH	197	198
28.3	formaldehyde-2,4-DNPH	209	210
31.8	acetaldehyde-2,4-DNPH	223	224
34.9	acetone-2,4-DNPH	237	238
38.7	trans-3-hydroxynopinone-2,4-DNPH	333	334
46.4	nopinone-2,4-DNPH	317	318
49.6	perillaldehyde-2,4-DNPH	329	330
49.9	myrtanal-2,4-DNPH	331	332

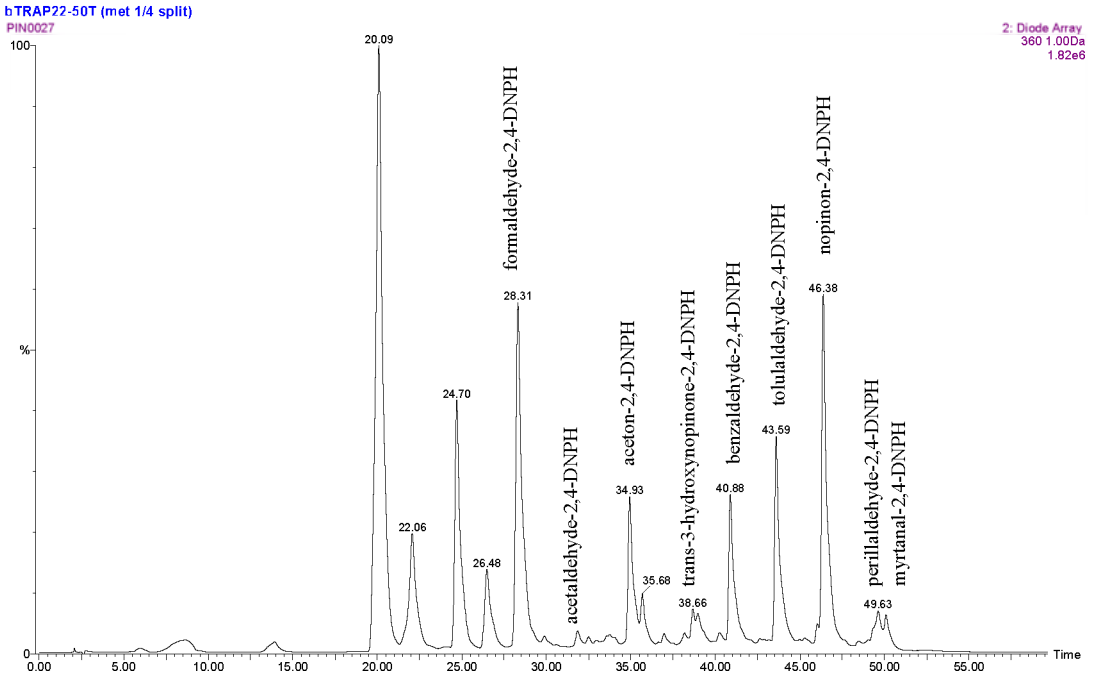

Figure 9*: HPLC (DAD, 360 nm) chromatogram at a total pressure of 50 Torr. Initial concentrations: [α-$C_{10}H_{16}$] = 5.08x10^{12}, [H_2] = 1.37x10^{13}, [NO_2] = 3.62x10^{12}, [O_2] = 3.24x10^{17} each expressed in molec cm^{-3}. The reaction time t_r = 42 ms, collection time t_c = 306 min. Collection method: LN_2 trap coated with 2,4-DNPH solution.*

3.3 Quantitative determination of the semi-volatile oxidation products for the α-pinene-OH reaction

3.3.1 Product yields at 50 and 100 Torr

For quantitative measurements the LN_2 trap is coated with a 2,4-DNPH according to the procedure described in section 2.2.2. The standard solutions described in section 2.6. were used to construct calibration curves for formaldehyde-, acetaldehyde-, acetone-, campholenealdehyde- and pinonaldehyde-di-2,4-DNPH with benzaldehyde-2,4-DNPH as an internal standard. A detailed description of the quantitative determination of the product yields is given in Vanhees et al. (2001). The mean value of the product yields for the five oxidation products at 50 and 100 Torr are shown in table III. Assuming the same collection efficiency on the LN_2 trap, one can conclude that pinonaldehyde is the most abundant semi-volatile oxidation product, present for 63 mol % at 50 Torr and about 82 mol % at 100 Torr.

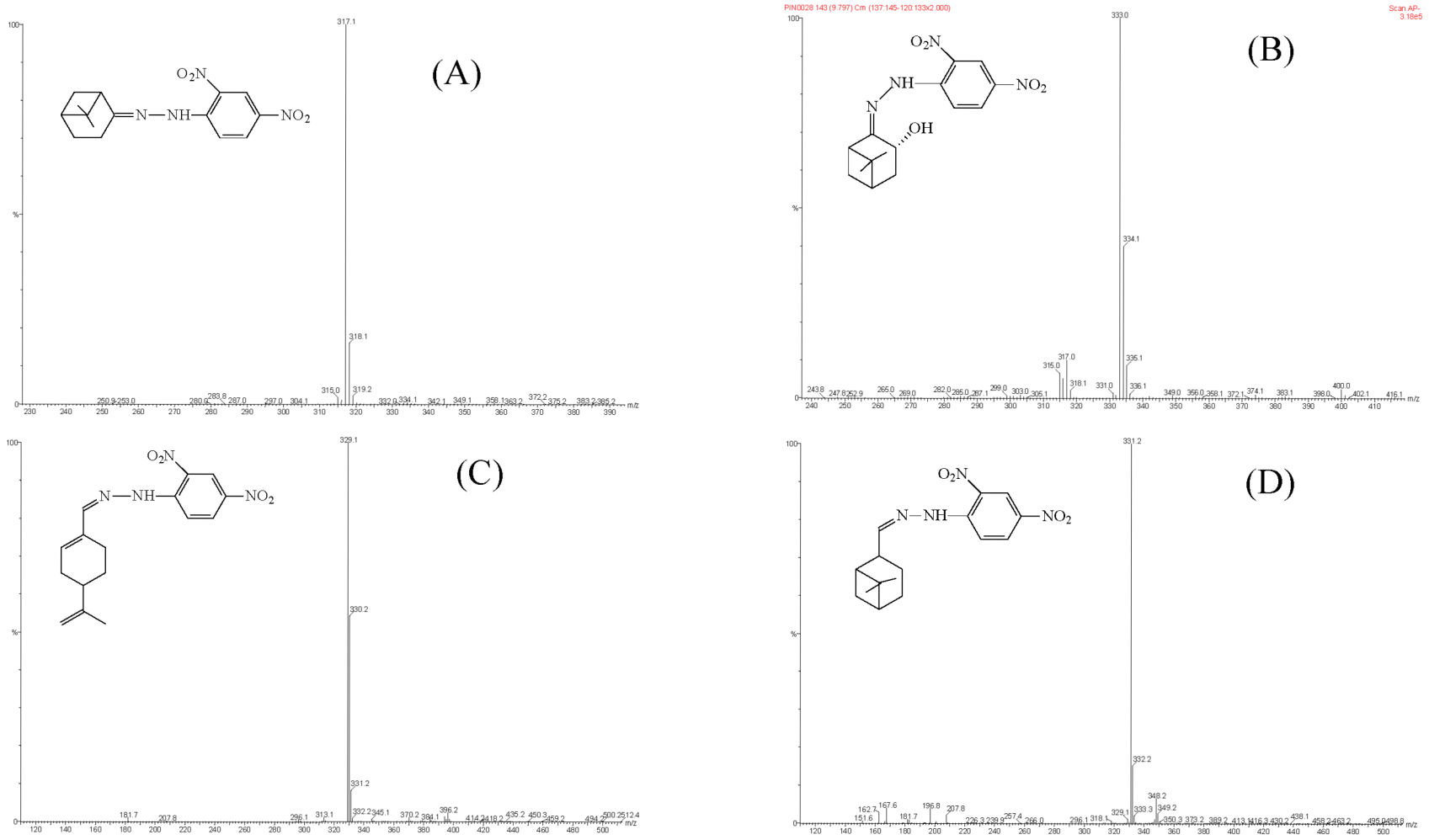

***Figure 10**: APCI(-) generated mass spectra of reference materials obtained by synthesis [(A) nopinone-2,4-DNPH, (B) trans-3-hydroxynopinone-2,4-DNPH, (C) perillaldehyde-2,4-DNPH] and (D) myrtanal-2,4-DNPH].*

Table III: *Product yields expressed in relative units of the five oxidation products at 50 and 100 Torr. Experimental conditions: [α-$C_{10}H_{16}$] ~ $5x10^{12}$, [H_2] = $1.37x10^{13}$, [NO_2] = $3.62x10^{12}$, [O_2] = $3.24x10^{17}$ (50 Torr), [O_2] = $6.48x10^{17}$ (100 Torr) each expressed in molec cm^{-3}. The reaction time t_r = 42 ms.*

	Relative amount (mol %)	
	50 Torr	**100 Torr**
formaldehyde	9.7 ± 0.7	6 ± 5
acetaldehyde	1.1 ± 0.1	0.9 ± 0.5
acetone	16 ± 1	6 ± 2
campholenealdehyde	11 ± 2	5.5 ± 0.7
pinonaldehyde	63 ± 3	82 ± 8

3.3.2 Influence of NO

The relative product yields shown in table IV for an extra added NO concentration of $1.67x10^{13}$ molec cm^{-3} are maximum values for formaldehyde, acetaldehyde, acetone and campholenealdehyde and minimum values for pinonaldehyde. This is due to the fact that also pinonaldehyde-mono-2,4-DNPH was detected. Taking this information into account, it can be concluded that adding extra NO to the system has no pronounced effect on the relative product yields. The yields of acetaldehyde and campholenealdehyde slightly decrease.

Table IV: *Product yields of the five oxidation products in relative units. Experimental conditions: [O_2] = $3.24x10^{17}$ (50 Torr), [H_2] = $1.37x10^{13}$, [NO_2] = $3.62x10^{12}$, [α-pinene] ~ $5x10^{12}$ (expressed in molec. cm^{-3}), t_r = 42 ms.*

$[NO]_{extra}$ (molec cm^{-3})	0	$1.67x10^{13}$
formaldehyde	9.7 ± 0.7	14.4
acetaldehyde	1.1 ± 0.1	0.8
acetone	16 ± 1	20.8
campholenealdehyde	11 ± 2	8.3
pinonaldehyde	63 ± 3	55.7

3.3.3 *Influence of the reaction time*

The results in table V show that the axial distance z and the reaction time t_r have no systematic effect on the relative product yields at reaction times longer than 42 ms. This indicates that subsequent reactions of the carbonyl compounds are unimportant in our experimental conditions.

Table V: *Product yields for the five oxidation products in relative units at different reaction times t_r. Experimental conditions: $[O_2] = 3.24x10^{17}$ (50 Torr), $[H_2] = 1.37x10^{13}$, $[NO_2] = 3.62x10^{12}$, [α-pinene] ~ $5x10^{12}$ (expressed in molec cm^{-3}).*

z (cm)	16	26	31	36	41
$\mathbf{t_r}$ (ms)	42	68	81	94	108
formaldehyde	9.7 ± 0.7	8.7	10.9	11.0	13.5
acetaldehyde	1.1 ± 0.1	0.7	1.3	1.1	1.7
acetone	16 ± 1	19.2	17.4	16.8	19.9
campholenealdehyde	11 ± 2	6.9	9.8	7.5	8.5
pinonaldehyde	63 ± 3	64.5	60.6	63.6	56.3

3.3.4 *Influence of the initial* H_2*-concentration*

The results shown in table VI indicate that doubling of the initial H_2-concentration has no systematic effect on the relative product yields.

Table VI: *Product yields for the five oxidation products in relative units at different initial [H]. Experimental conditions: $[O_2] = 3.24x10^{17}$ (50 Torr), $[NO_2] = 3.62x10^{12}$, [α-pinene] ~ $5x10^{12}$ (expressed in molec cm^{-3}), t_r = 42 ms.*

$[NO_2]$ (molec cm^{-3})	$3.62x10^{12}$	
$[H_2]$ (molec cm^{-3})	$1.38x10^{13}$	$6.91x10^{12}$
formaldehyde	9.7 ± 0.7	8 ± 2
acetaldehyde	1.1 ± 0.1	0.8 ± 0.5
acetone	16 ± 1	13 ± 3
campholenealdehyde	11 ± 2	9.8 ± 0.4
pinonaldehyde	63 ± 3	68 ± 6

3.4 Discussion and interpretation of laboratory results for α-pinene

From the qualitative and quantitative analysis described above, the following products were formed in the α-pinene/OH reaction in the presence of oxygen and nitric oxide: formaldehyde, acetaldehyde, acetone, campholenealdehyde and pinonaldehyde.

A reaction mechanism leading to the formation of formaldehyde, acetone, campholenealdehyde and pinonaldehyde is illustrated in figure 11. In a first step an OH-radical is added to α-pinene. The α-pinene/OH-adduct can either react directly with O_2 (**A**) or isomerize (**B**, **C**). The reaction with O_2 (**A**), followed by O-abstraction with NO, results in a α-pinene/OH/O-adduct. Next, one pathway (**D**) leads to the formation of formaldehyde and another one (**E**) including an H-abstraction with molecular oxygen, leads to the formation of pinonaldehyde. The isomers of the α-pinene/OH-adduct can either lead to the formation of campholenealdehyde (**B**) or react with O_2 and NO, resulting in the formation of acetone (**C**).

For acetaldehyde, which has not been identified before as an oxidation product, the mechanisms shown in Figure 12 are proposed. First, acetaldehyde can be formed by tautomerisation of vinylalcohol in an acidic solution. Vinylalcohol could arise as the initial gas-phase product via decomposition of radical X or Y **(A)**. Because this tautomerisation reaction occurs in solution it is not possible to conclude whether or not acetaldehyde is formed as an oxidation product of the α-pinene/OH reaction in the gas phase. However, if acetaldehyde were to be a real gas phase oxidation product, scheme **B** in Figure 12 is a possible pathway. Formaldehyde and acetone were also identified in a smog chamber study by Grosjean et al. (1992), who used cartridges impregnated with 2,4-DNPH followed by HPLC-MS (CI) detection. Nozière et al. (1999) also detected these products but here Fourier Transform InfraRed (FTIR) was used. The presence of pinonaldehyde was demonstrated by several techniques: GC-MS and GC-FTIR [Hakola et al. (1994)], GC-MS and GC-FID [Arey et al. (1990)], and FTIR [Hatakeyama et al. (1991), Nozière et al. (1999)]. Up till now acetaldehyde and campholenealdehyde have not been identified as products of the α-pinene/OH reaction under atmospheric conditions.
Several mechanisms were proposed in the literature [Nozière et al. (1999), Pilling et al. (1999), Atkinson and Arey, (1998), Fantechi (1999)]. One of the first publications in which reaction schemes were elaborated explaining the formation of the majority of the semi-volatile compounds is given in Vinckier et al. (1997). The reaction pathways for formaldehyde and pinonaldehyde are similar to the mechanisms proposed by Nozière et al. (1999). It should be pointed out though that the reaction schemes don't take into account initial hydrogen abstraction reactions by the OH-radical from α-

pinene [Atkinson and Arey, (1998), Fantechi (1999)]. If that path would be important, other reaction channels may open up leading to the formation of the observed products.

At 50 Torr, the product yields of the five oxidation products in relative units (mole %) are: formaldehyde (9.7 ± 0.7), acetaldehyde (1.1 ± 0.1), acetone (16 ± 1), campholenealdehyde (11 ± 2) and pinonaldehyde (63 ± 3). The yields at 100 Torr are (in mole %): formaldehyde (6 ± 5), acetaldehyde (0.9 ± 0.5), acetone (6 ± 2), campholenealdehyde (5.5 ± 0.7) and pinonaldehyde (82 ± 7). The results clearly indicate that at 50 and 100 Torr pinonaldehyde is the main reaction product. In comparison with the results at 50 Torr, the yield of pinonaldehyde is higher at 100 Torr, while the yields of the other products, especially acetone and campholenealdehyde, decrease. A possible explanation for this pressure dependence can be derived from the reaction mechanism proposed in figure 11. Assuming that the initially formed α-pinene-OH adduct is more readily stabilized at higher pressure, less isomerization occurs leading to a lower formation rate of acetone and campholenealdehyde.

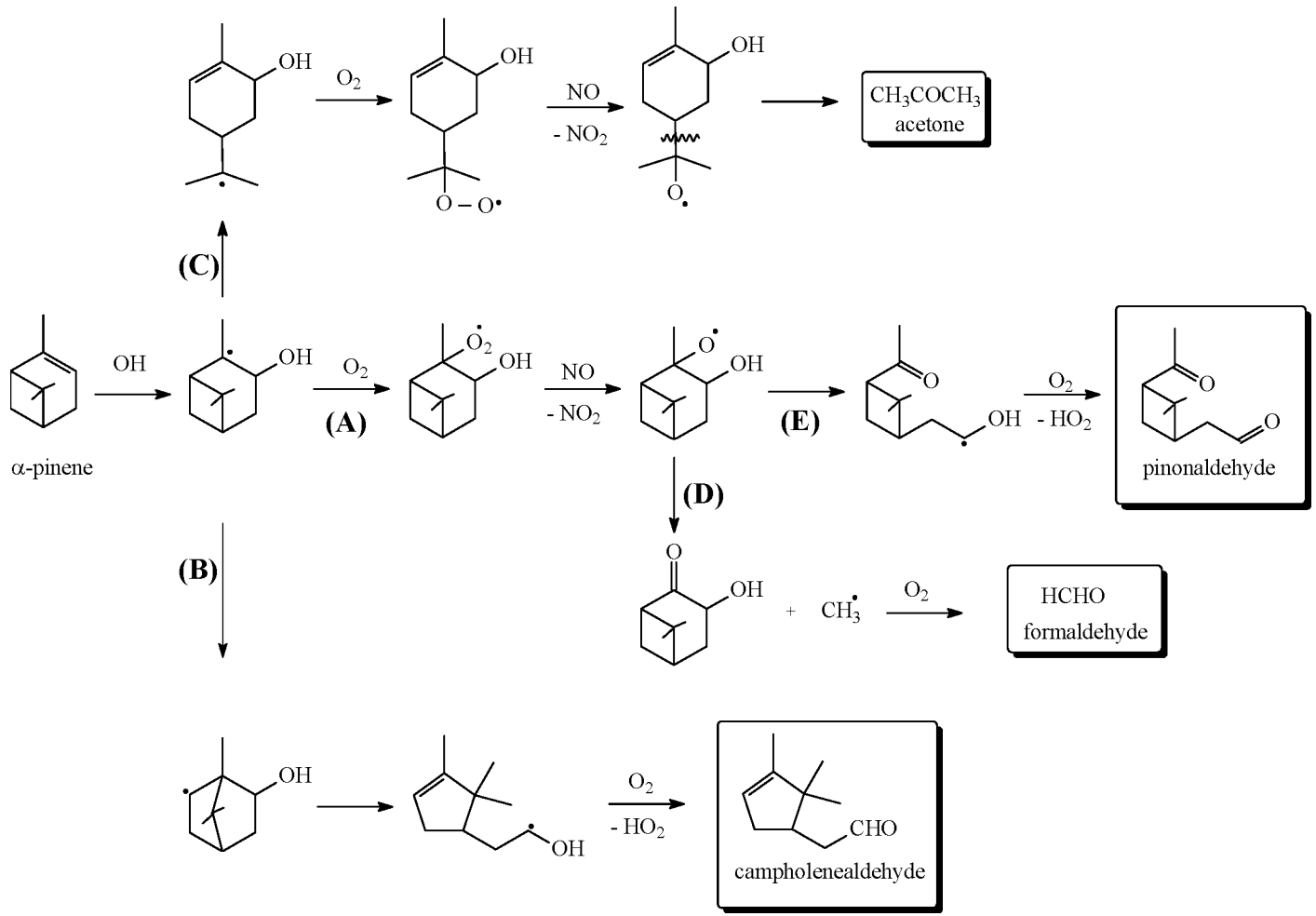

***Figure 11**: Mechanism for the reaction between α-pinene and OH: formation of formaldehyde, acetone, campholenealdehyde and pinonaldehyde.*

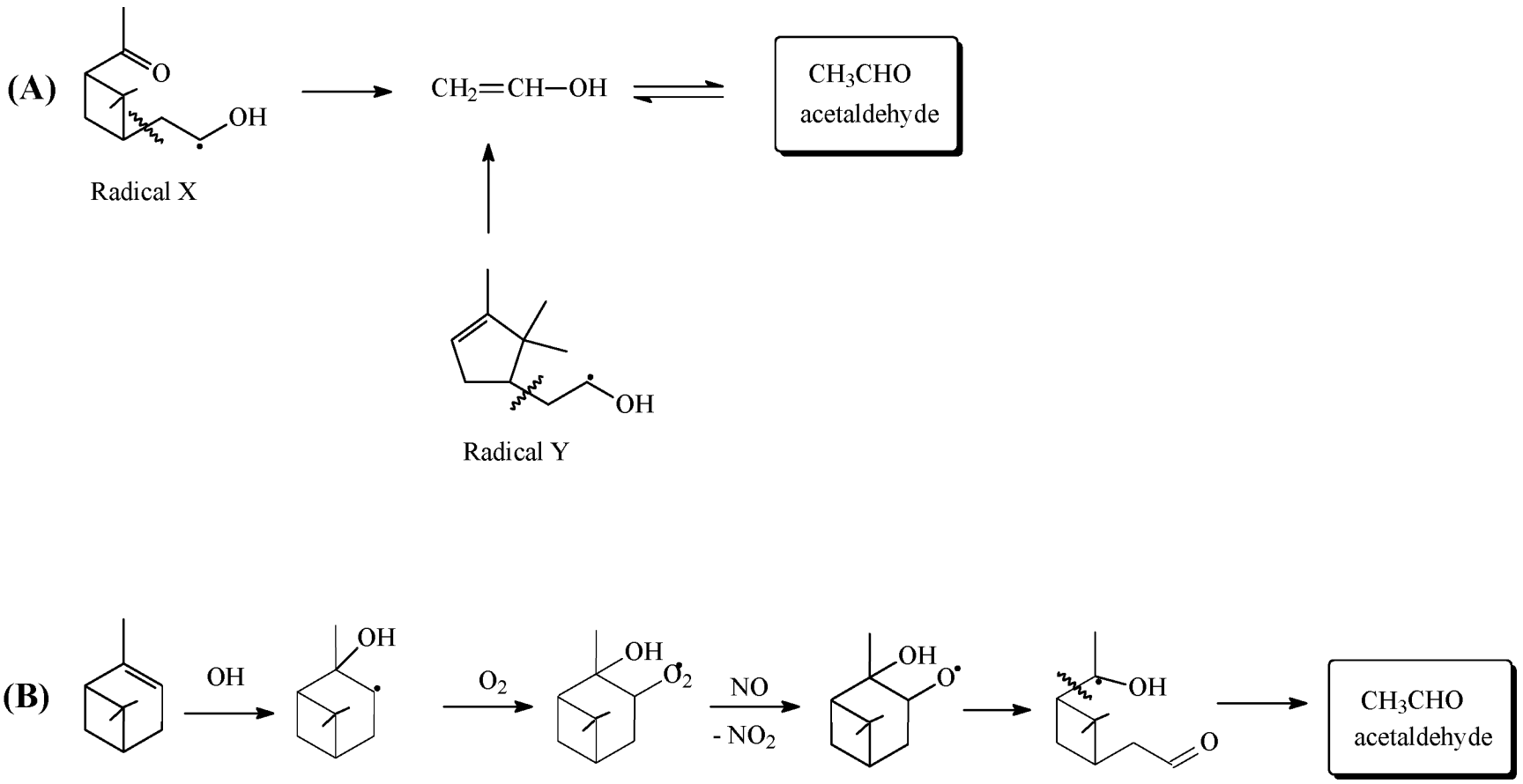

***Figure 12**: Mechanism for the reaction between α-pinene and OH: proposed pathways for the formation of acetaldehyde.*

The presence of pinonaldehyde has been quantified by several research groups [Hatakeyama et al. (1991), Nozière et al. (1999), Arey et al. (1990), Hakola et al. (1994), Pilling et al. (1997)]. It should be pointed out that Nozière et al. (1999) reported a yield for pinonaldehyde of 87 ± 20 %, which is in fairly good agreement with our measurements. The yields of acetone measured in this study (16 ± 1 mole % at 50 Torr and 6 ± 2 mole % at 100 Torr) are of the same order of magnitude as the values found in other studies: 11 ± 2.7 % [Aschmann et al. (1998)], 9 ± 6 % [Nozière et al. (1999)]. The yields of formaldehyde (9.7 ± 0.7 mole % at 50 Torr and 6 ± 5 mole % at 100 Torr) are somewhat smaller than the value (23 ± 9 %) reported by Nozière et al. (1999).

3.5 Discussion and interpretation of laboratory results for β-pinene

From the GC-MS and HPLC-MS analysis, the following oxidation products were identified for the β-pinene/OH reaction: formaldehyde, acetaldehyde, acetone, trans-3-hydroxynopinone, nopinone, perilla alcohol, perillaldehyde and myrtanal. Formaldehyde and nopinone are the most important oxidation products. Plausible reaction paths leading to the formation of formaldehyde, nopinone, perilla alcohol, perillaldehyde, acetone and myrtanal are given in figure 13 to 17. For the other oxidation products a reaction mechanism has still to be designed. In the mechanism for perillaldehyde (figure 17), product A is unstable and in acid medium, this compound will decompose leading to the formation of perillaldehyde.

Up till now only formaldehyde and nopinone have been identified in other studies as oxidation products of the β-pinene/OH reaction. Formaldehyde was also identified by Orlando et al. (2000) and Hatakeyama et al. (1991) but here FT-IR was used. The presence of nopinone was demonstrated by several techniques: GC-MS and GC-FT-IR [Hakola et al. (1994)], GC-MS and GC-flame ionisation detection [Arey et al. (1990)] and FT-IR [Hatakeyama et al. (1991)].

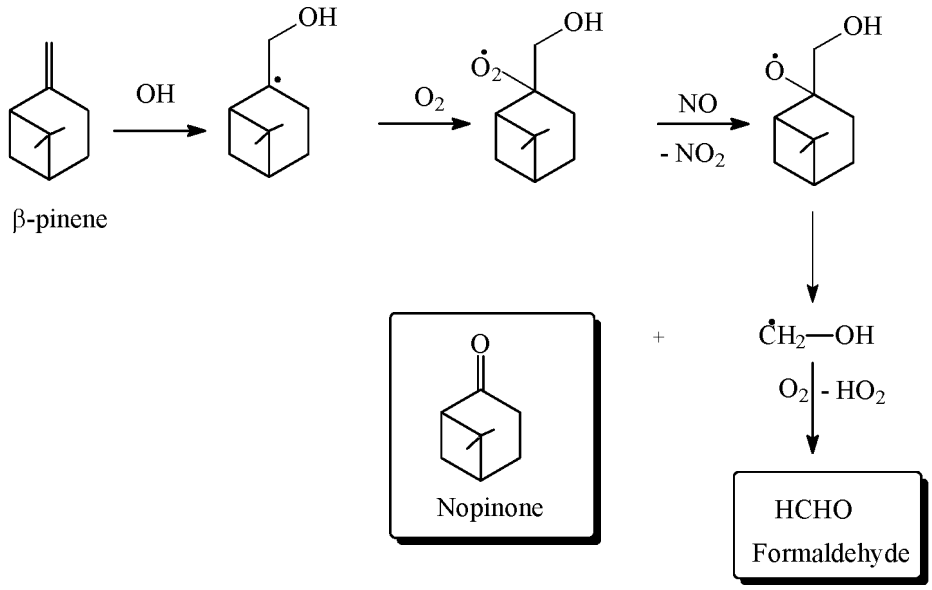

Figure 13: *Mechanism for the reaction between β-pinene and OH: formation of formaldehyde and nopinone.*

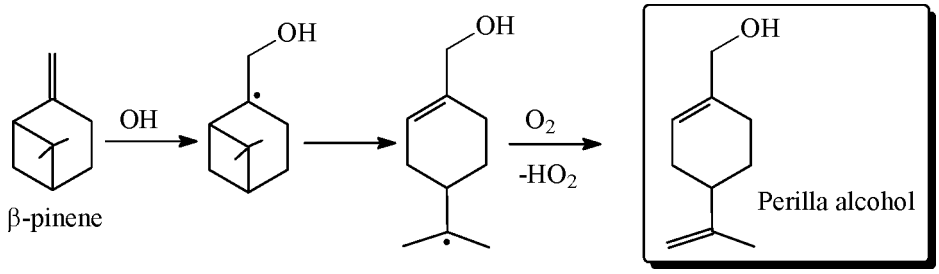

Figure 14: *Mechanism for the reaction between β-pinene and OH: formation of perilla alcohol.*

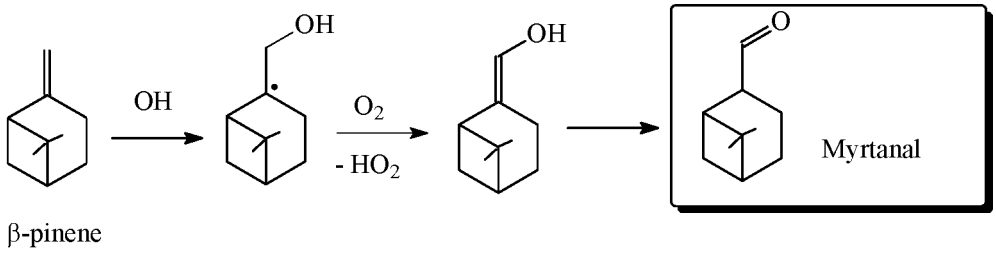

Figure 15: *Mechanism for the reaction between β-pinene and OH: formation of myrtanal.*

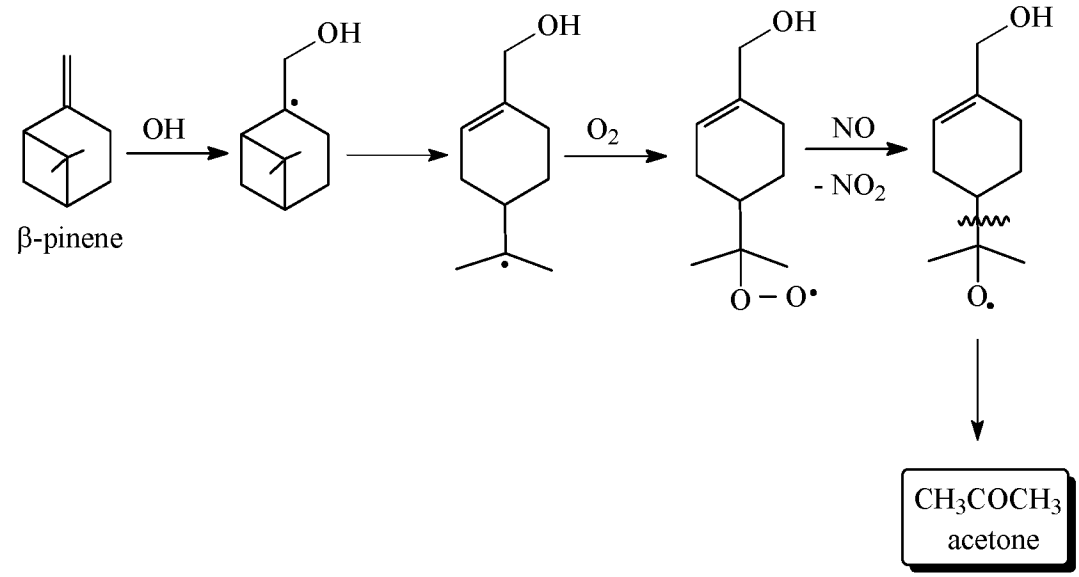

Figure 16: *Mechanism for the reaction between β-pinene and OH: formation of acetone.*

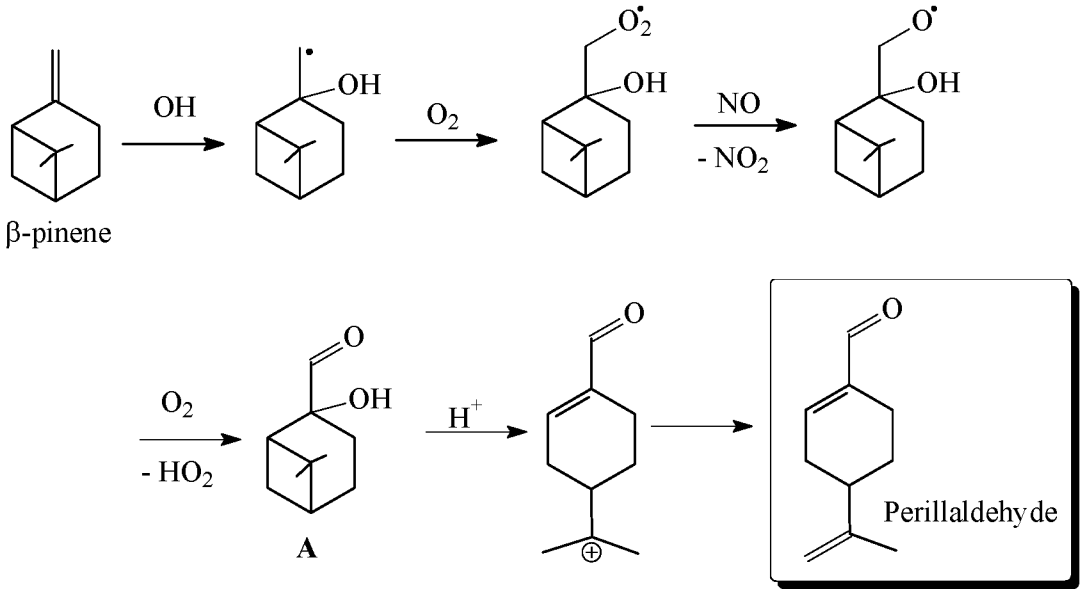

Figure 17: *Mechanism for the reaction between β-pinene and OH: formation of perillaldehyde.*

3.6 Understanding the photochemical production of ozone in the upper troposphere: quantification of the sources of HO_x and NO_x

As described in section 2.10, the IMAGES model has been used to identify and quantify the sources of HO_x in the upper troposphere (Müller and Brasseur, 1999). Figure 18 displays the relative contribution (in %) of different chemical processes to the total production of HO_x in the UT/LS. As expected, ozone photolysis is found to be dominant in the lower and middle troposphere. The photo-oxidation of acetone is shown to be a large and ubiquitous source of HO_x in the UT/LS, especially in the tropopause region (up to 40%). The other sources are found to be important as well: in particular the photolysis of hydroperoxides over oceanic regions, and the photo-oxidation of aldehydes over continental regions, where anthropogenic as well as biogenic emissions lead to high concentration of such compounds in the PBL. The role of these different sources of HO_x on the production of ozone has also been investigated. For example, we demonstrated that the inclusion of acetone in the model calculations increases by about 20% the calculated impact of subsonic aircraft NO_x emissions on UT/LS ozone.

The "tagging" technique described in section 2.12 allowed the quantification of the contributions of different sources on the NO_x concentrations in this region. For instance, the current aircraft fleet is found to contribute to about 20% of the NO_x levels at the mid-latitude tropopause (Lamarque et al., 1996). This estimate is uncertain, however, because the lightning source is poorly quantified (2-20 Tg (N)/year globally according to recent estimates). We also demonstrated the importance of prescribing realistic vertical profiles of NO production by lightning in tropospheric CTMs, since this profile is found to impact UT/LS NO_x levels by up to 35% (Pickering et al., 1998).

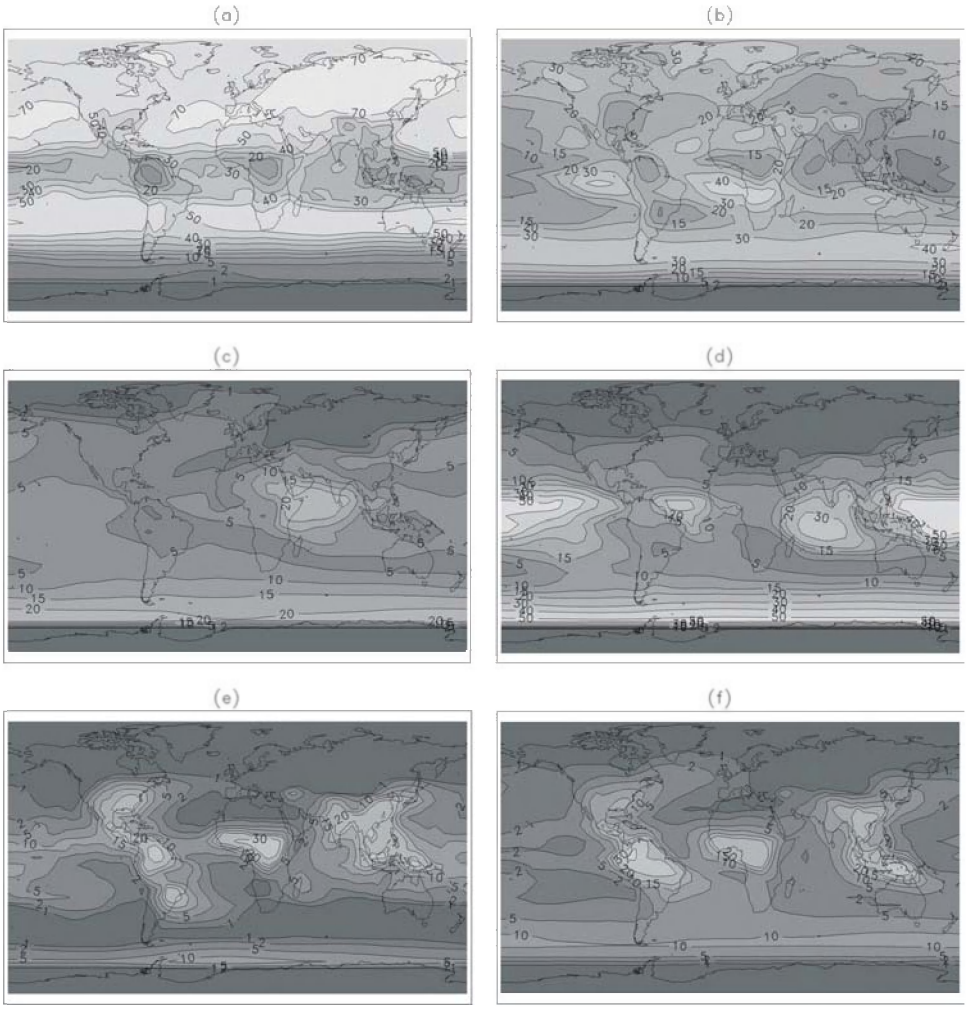

Figure 18: *Relative contributions (in %) of different processes to the primary production of HO_x in the upper troposphere (approx. the 240 mb level): (a) ozone photolysis; (b) acetone photooxidation; (c) photolysis of lower tropospheric H_2O_2; (d) photooxidation of lower tropospheric CH_3OOH; (e) photolysis of lower tropospheric CH_2O; (f) photooxidation of C_2 aldehydes. Adapted from Müller and Brasseur (1999).*

3.7 Modelling the impact of human activities on the global tropospheric composition

The IMAGES model has been used to estimate the past and future changes in the composition of the troposphere resulting from human activities.

The pre-industrial (ca. 1850) composition has been simulated. The results demonstrate that anthropogenic emissions of chemical compounds caused by industrial activities at mid-latitudes in the Northern hemisphere and by biomass

burning in the tropics have produced a large increase in the abundance of tropospheric ozone (about a factor of 2 at the surface in the Northern mid-latitudes on zonal average). Industrialization is also found to lead to a reduction in the oxidizing capacity of the atmosphere (globally averaged OH concentration reduced by 17% and methane lifetime enhanced by 1.5 years) (Brasseur et al., 1998). These perturbations in tropospheric ozone result in a change in annually averaged radiative forcing of 0.37 W m^{-2}. The model calculation also show a large increase in the concentrations of sulfur oxides and sulfates since pre-industrial times, amounting to a factor 2-3 on global average, and reaching more than two orders of magnitude at the surface at some locations (Pham et al., 1996).

The calculated wet and dry deposition fields for nitrogen oxides (the NO_y family) predicted by IMAGES and four other global CTMs were used to drive a model for terrestrial carbon uptake (Holland et al., 1997). From this study it is found that global air pollution might have a significant influence on the global carbon cycle. If nitrogen fertilization of the terrestrial biosphere accounts for a substantial portion of the terrestrial "missing" carbon sink, we expect important reductions in its magnitude over the next century as ecosystems become nitrogen saturated and ozone pollution expands.

Future changes in tropospheric ozone associated with a population increase and economic development (primarily in developing countries) are expected to be largest in the tropics, specifically in South and Southeast Asia. Further changes in the oxidizing capacity of the atmosphere could be small if the abundance of tropospheric water vapor increases as a result of anticipated climate change. In the framework of an international cooperation effort (the 3rd IPCC Report), IMAGES and many other models were used to simulate the expected changes in ozone and other compounds in the 21st century.

The possible impact of the current (1992) and future (2015-2050) aircraft fleet has been also evaluated using IMAGES (Brasseur et al., 1996), in part in the framework of the special IPCC assessment on Aviation and the Global Atmosphere.

4. VALORISATION OF RESULTS

- Our results have been made available by communications in international conferences and publications in international journals, as well as e.g. via a EUROTRAC programme website.

- The laboratory results of our project have been incorporated in the European Environmental Research Programme EUROTRAC 2, within the project "Chemical Mechanism Development" (CMD).

- The model results on the future impact of aviation and industrialisation on the tropospheric composition are contribution to two assessment reports of the Intergovernmental Panel for Climate Change (IPCC).

5. CONCLUSIONS: RECOMMENDATIONS

- Given the widely accepted importance of tropospheric chemistry in outstanding issues such as climate change and air quality, and because of the large remaining uncertainties in the processes involved, we strongly recommend that the Belgian and European research efforts be sustained and possibly enhanced in this area.

- More specifically, noting the importance of the biosphere in the climate system as well as the very large remaining uncertainties in the quantification of biospheric emissions and impacts, we recommend that research efforts be sustained in this area.

- The emissions of non-greenhouse gases like carbon monoxide, nitrogen oxides, and non-methane hydrocarbons are known to enhance the abundance of ozone (a greenhouse gas) in the troposphere. These emissions should be considered in future efforts to mitigate climate change.

- Tropospheric ozone levels are expected to increase to very high values in many heavily populated areas of the world, thereby representing a considerable threat to human health and agricultural yields in these areas. We recommend that strategies be elaborated in order to reduce the emissions of ozone precursors (carbon monoxide, nitrogen oxides and hydrocarbons), not only in our countries, but also in the rest of the world.

6. REFERENCES

Arey, J., Atkinson, R. and Aschmann, S. 1990. Product study of the gas-phase reactions of monoterpenes with the OH radical in the presence of NO_x. J. Geophys. Res. 95 : 18539-18546.

Aschmann, S.M., Reissell, A., Atkinson, R. A. and Arey, J. 1998. Products of the gas-phase reactions of the OH radical with alpha and beta-pinene in the presence of NO, J. Geophys. Res. 103 : 25553-25561.

Atkinson, R. and Arey, J. 1998. Atmospheric chemistry of biogenic compounds. Acc. Chem. Res. 31 : 574-583.

Behforouz, M., Bolan, J. L. and Flyn, M. S. 1985. 2,4-Dinitrophenylhydrazones : A modified method for the preparation of these derivatives and an explanation of previous conflicting results. J. Org. Chem. 50 : 1180-1189.

Brasseur G., J.-F. Müller, C. Granier, Atmospheric impact of NO_x emissions by subsonic aircraft: A three-dimensional model study, J. Geophys. Res., 101, 1423-1428, 1996.

Brasseur, G., J. Kiehl, J.-F. Müller, T. Schneider, C. Granier, X.X. Tie, D. Hauglustaine 1998a. Past and future changes in global tropospheric ozone: Impact on radiative forcing. Geophys. Res. Lett. 25 : 3807-3810.

Brasseur G., D. Hauglustaine, S. Walters, P. Rasch, J.-F. Müller, C. Granier, X. X. Tie 1998b. MOZART: A global chemical transport model for ozone and related chemical tracers, Part1. Model description. J. Geophys. Res. 103 : 28,265-28290.

Brocheton F., J.-F. Müller, B. Aumont, G. Toupance 2001. On the importance of a detailed chemistry of NMHC in 3D global models. In preparation.

Carter, W. P. L. and Atkinson, R. 1996. Development and evaluation of a detailled mechanism for the atmospheric reactions of isoprene and NO_x. Int. J. Chem. Kin. 28 : 497-530.

Chin, M., R. Rood, S.-J. Lin, J.-F. Müller, and A. Thompson 2000. Atmospheric sulfurcycle simulated in the global model GOCART: Model circulation and global properties. J. Geophys. Res. 105 : 24671-24687.

Clerbaux, C., P. Chazette, J. Hadji-Lazaro, G. Mégie, J.-F. Müller, S. A. Clough 1998. Remote sensing of CO, CH4, and O3 using a space-borne nadir-viewing interferometer, J. Geophys. Res. 103 : 18,999-19,013.

Emmons, L., D. Hauglustaine, J.-F. Müller, M. A. Carroll, G. Brasseur, D. Brunner, J. Staehelin, V. Thouret, and A. Marenco 2000. J. Geophys. Res. 105 : 20497-20538.

Fantechi, G. 1999. PH.D thesis, Faculty of Sciences, KULeuven.

Friedl F., editor, 1997. Atmospheric effects of subsonic aircraft: Interim assessment report of the Advanced Subsonic Technology Program. NASA Reference Publ. 1400, Washington, D.C., 143 pp.

Granier, C., J.-F. Müller, S. Madronich, and G. Brasseur 1996. Possible causes for the 1990-1993 decrease in the global tropospheric CO abundance: A three-dimensional sensitivity study. Atmos. Environ. 30 : 1673-1682.

Granier, C., G. Pétron, J.-F. Müller, G. Brasseur 1999. A three-dimensional study of the global CO budget. Chemosphere: Global change science 1 : 255-261.

Granier, C., G. Pétron, J.-F. Müller, G. Brasseur 2000. The impact of natural and anthropogenic hydrocarbons on the tropospheric budget of carbon monoxide. Atmos. Environ. 34 : 5255-5270.

Grosjean, D. 1983. Chemical ionization mass spectra of 2,4-dinitrophenylhydrazones of carbonyl and hydroxycarbonyl atmospheric pollutants. Anal. Chem. 55 : 2436-2439.

Grosjean, D., Williams, E. and Seinfeld, J. 1992. Atmospheric oxidation of selected terpenes and related carbonyls : gas-phase carbonyl products. Env. Sci. Technol. 26 : 1526-1533.

Grosjean, E. and Grosjean, D. 1995. Liquid chromatographic analysis of C1-C10 carbonyls. Intern. J. Environ. Anal. Chem. 61 : 47-64.

Grosjean, E., Green, P.G. and Grosjean, D. 1999. Liquid chromatography analysis of carbonyl (2,4-dinitrophenyl)hydrazones with detection by diode array ultraviolet spectroscopy and by atmospheric pressure negative chemical ionization mass spectrometry. Anal. Chem. 71 : 1851-1861.

Guenther A., Zimmerman P., and Harley P. 1993. Isoprene and Monoterpene emission rate variability: Model evaluations and sensitivity analyses. J. Geophys. Res., 98, 12609-12617.

Guenther, A., Hewith, C.N., Erickson, D., Fall, R., Geron, C., Graedel, T., Harley, P., Klinger, L., Lerdau, M., McKay, W.A., Pierce, T., Scholes, B., Steinbrecher, R., Tallamraju, R., Taylor, J. and Zimmerman, P. 1995. A global model of natural volatile organic compound emissions. J. Geophys. Res. 100 : 8873-8892.

Hakola, H., Arey, J., Aschmann, S.M. and Atkinson, R. 1994. Product formation from the gas-phase reactions of OH radicals and O_3 with a series of monoterpenes. J. Atmos. Chem. 18 : 75-102.

Hanst, P.L., Spence, J.W. and Edney, E.D. 1980. Carbon monoxide production in photooxidation of organic molecules in the air. Atmos. Env. 14 : 1077-1088.

Hatakeyama, S., Izumi, K., Fukuyama, T., Akimoto, H.1991. Reactions of OH with α-pinene and β-pinene in air : estimate of global CO production from the atmospheric oxidation of terpenes. J. Geophys. Res. 96 : 947-958.

Hauglustaine D., G. Brasseur, S. Walters, P. J. Rasch, J.-F. Müller, L. K. Emmons, M. A. Carroll 1998. MOZART: A global chemical transport model for ozone and related chemical tracers, Part 2. Model results and evaluation. J. Geophys. Res. 103 : 28,291.

Hoffmann, T., Odum, J.R., Bowman, F., Collins, D., Klockow, D., Flagan, R.C. and Seinfeld, J. 1997. Formation of organic aerosols form the oxidation of biogenic hyrodcarbons. J. Atmos. Chem. 26 : 189-222.

Holland E., B. Braswell, J.-F. Lamarque, A. Townsend, J. Sulzman, J.-F. Müller, F. Dentener, G. Brasseur, H. Levy II, J. Penner, G.-J. Roelofs 1997. Variations in the predicted spatial distribution of atmospheric nitrogen deposition and their impact on carbon uptake by terrestrial ecosystems. J. Geophys. Res. 102 : 15849-15866.

Jay, K. and Stieglitz , L. 1989. Identifizierung chemischer-photochemischer Umsetzungsprodukte van Biogenen Kohlenwasserstoffen mit Antroppgenen Luftschadstoffen. Report KFK-PEF 53, Karlsruhe, 177.

Kanakidou M., F. J. Dentener, G. Brasseur, T. K. Berntsen, W. Collins, D. Hauglustaine, S. Houweling, I. Isaksen, M. Krol, M. Lawrence, J.-F. Müller, N.

Poisson, G. J. Roelofs, Y. Wang, W. Wauben 1999a. 3-D global simulation of tropospheric CO distributions - results of the GIM/IGAC intercomparison 1997 exercise. Chemosphere: Global Change Science 1 : 263-282.

Kanakidou, M., F. Dentener, G. Brasseur, W. Collins, T. Berntsen, D. Hauglustaine, S. Houweling, I. Isaksen, M. Krol, K. Law, M. Lawrence, J.-F. Müller, P. Plantevin, N. Poisson, G.-J. Roelofs, Y. Wang, W. Wauben 1999b. 3-D global simulations of tropospheric chemistry with focus on ozone distributions, Report EUR 18842 to the European Union, European Communities.

Kölliker, S., Oehme, M. and Dye, C. 1998. Structure elucidation of 2,4-dinitrophenylhydrazone derivatives of carbonyl compunds in ambient air by HPLC/MS and multiple MS/MS using Atmospheric Chemical Ionization in the negative ion mode. Anal. Chem. 70 : 1979- 1985.

Lamarque, J.-F., G. Brasseur, P. Hess, J.-F. Müller 1996. Three-dimensional study of the relative contributions of the different nitrogen sources in the troposphere. J. Geophys. Res. 101 : 22955-22968.

Lambert, J.-C., J. Granville, M. Van Roozendael, J.-F. Müller, J.-P. Pommereau, F. Goutail, A. Sarkissian 1999. A pseudo-global correlative study of ERS-2 GOME NO2 data with ground-, balloon-, and space-based observations. Proceedings of ESAMS (European Symposium on Atmospheric Measurements from Space '99, ESTEC, Noordwijk, WPP-161, Vol. I : 217-224.

Lavallée, P. and Bouthillier, G. 1986. Efficient conversion of (1R,5R)-(+)-α-pinene to (1S,5R)-(-)- nopinone. J. Org. Chem. 51 : 1362-1365.

Law, K., P-H. Plantevin, V. Thouret, A. Marenco, W.A.H. Asman, M. Lawrence, P. Crutzen, J-F. Müller, D. Hauglustaine and M. Kanakidou 2000. Comparison between Global Chemistry Transport Model Results and Measurement of Ozone and Water Vapor by Airbus In-Service Aircraft (MOZAIC) Data. J. Geophys. Res. 105 : 1503-1525.

Lee, J., S.C. Doney, G. Brasseur, J.-F. Müller 1998. A global 3-D coupled atmospheric-oceanic model of methyl bromide, J. Geophys. Res. 103 : 16,039-16,057.

Müller, J. F. 1992. Geographical distribution and seasonal variation of surface emissions and deposition velocities of atmospheric trace gasses. J. Geophys. Res. 97 : 3787-3804.

Müller, J. F. and Brasseur, G. 1995. Images – A 3-dimensional chemical transport model of the global troposphere. J. Geophys. Res. 100 : 16445-16490.

Müller, J. F. and Brasseur, G. 1999. Sources of upper tropospheric HOx: A three-dimensional study. J. Geophys. Res. 104 : 1705-1715.

Nozière, B., Barnes, I. and Becker, K.H. 1999. Product study and mechanisms of the reactions of α-pinene and pinonaldehyde with OH radicals. J. Geophys. Res. 104 : 23645-23656.

Peterson, P.E. and Grant, G. 1991. Preparation of chiral inducers having the bicyclo [3.1.1.] heptane framework. Assignement of diastereomer configuration by NMR and comparison of calculated and observed coupling constants. J. Org. Chem. 56 : 16-20.

Pétron, G., Granier C., Khattatov B., Lamarque J.-F., Yudin V., Müller J.-F., Gille J. 2001. Inverse modeling of carbon monoxide surface emissions using NOAA-CMDL network observations. Submitted to J. Geophys. Res.

Pham, M., J.-F. Müller, G. Brasseur, C. Granier, and G. Mégie 1995. A three-dimensional study of the tropospheric sulfur cycle. J. Geophys. Res. 100 : 26061-26092.

Pham, M., J.-F. Müller, G. Brasseur, C. Granier, and G. Mégie 1996. A 3D model study of the global sulphur cycle: contributions of anthropogenic and biogenic sources. Atmos. Environ. 30 : 1815-1822.

Pickering, K. E., Y. Wang, W.-K. Tao, C. Price, J.-F. Müller, Vertical distributions of lightning NOx for use in regional and global chemical transport models 1999. Atmos. Environ. 33 : 1403-1422.

Pilling, M., Saunders, S., Carslaw, N., Pascoe, S., Jenkin, M. and Derwent, D. 1999. http://cast.nerc.ac.uk/LIBRARY/MCM2/html/main.html

Pötter, W. and Karst, U. 1996. Identification of chemical interferences in aldehyde and ketone determination using dual-wavelength detection. Anal. Chem. 68 : 3354-3358.

Orlando, J. J., Nozière, B., Tyndall, G. S. Orzechowska, G. E., Paulson, S. E. and Rudich, Y. 2000. Product studies of the OH- and ozone-initiated oxidation of some monoterpenes. J. of Geophys. Res. 105 : 11561-11572.

Stenhagen, E. and Abrahamsson, S. 1968. Registry of Mass Spectral Data. F.W. McLafferty, Wiley, New York.

Thakur, A., H. Singh, P. Mariani, Y. Chen, Y. Wang, D. Jacob, G. Brasseur, J.-F. Müller, M. Lawrence 1999. Distribution of reactive nitrogen species in the remote free troposphere: Data and model comparisons, Atmos. Environ 33 : 1403-1422.

Vairavamurthy, A., Roberts, J.M. and Newman, L. 1992. Methods for the determination of low molecular weight carbonyl compounds in the atmosphere : a review. Atmos. Environ. 26A : 1965-1993.

Van den Bergh, V., Vanhees, I., De Boer, R., Compernolle, F. and Vinckier, C. 2000. Identification of the oxidation products of the reaction between α-pinene and hydroxyl radicals by gas and high-performance liquid chromatography with mass spectrometric detection. J. of Chromat. A. 896: 135-148.

Van den Bergh, V. Coeckelberghs, H., Vanhees, I., De Boer, R., Compernolle, F. and Vinckier, C. 2001. Determination of the oxidation products of the reaction between α,β-pinene and OH-radicals by HPLC-MS. Analytical and Bioanalytical Chemistry, in preparation.

Vanhees, I., Van den Bergh, V., Schildermans, R., De Boer, R., Compernolle F. and C. Vinckier. 2001. Determination of the oxidation products of the reaction between α-pinene and hydroxyl radicals by high-performance liquid chromatography. J. Chromat. A. 915: 75-83.

Vereecken, L. and Peeters, J. 2000. Theoretical study of the formation of acetone in the OH-initiated atmospheric oxidation of α-pinene. J. Phys. Chem. A. 104 : 11140-11146.

Vinckier, C. and Van Hoof, N. 1993. Determination of the sticking coefficient of α-pinene on quartz. Proceedings Eurotrac Symposium, SPB Academic Publ., The Hague, The Netherlands, 652-654.

Vinckier, C. and Van Hoof, N. 1994. Rate constant of the α-pinene + atomic hydrogen reaction at 295 K. Int. J. Chem. Kin. 26 : 527-534.

Vinckier, C., Compernolle, F. and Saleh, A.M. 1997. Qualitative determination of the non-volatile reaction products of the α-pinene reaction with hydroxyl radicals. Bull. Soc. Chim. Belg. 106 : 501 – 513.

Vinckier, C., Compernolle, F., Saleh, A.M., Van Hoof, N. and Vanhees I. 1998. Product yields of the α-pinene reaction with hydroxyl radicals and the implication on the global emission of trace compounds in the atmosphere. Fresenius Environ. Bull. 7: 361-368.

Warneck, P. 1988. Chemistry of the Natural Atmosphere, Academic Press, San Diego, 158-170.

Went, F.W. 1960. Blue haze in the atmosphere. Nature 167 : 641-643.

Yacoub, Y. 1999. Method procedures for sampling aldehyde and ketone using 2,4-dinitrophenylhydrazine – a review. Proc Instn Mech Engrs 213 : 503-517.

Zhang, S.H., Shaw, M., Seinfeld, J. and Flagan, C. 1992. Photochemical aerosol formation from α-pinene and β-pinene. J. Geophys. Res. 97 : 20717-20729.

Zimmerman, P.R., Chatfield, R.B., Fishman, J., Crutzen, P. and Hanst, P.L. 1978. Estimates on production of CO and H2 from oxidation of hydrocarbons on emision from vegetation. Geophys. Res. Lett. 5 : 679-682.

CG/DD/03

SOURCES, PHYSICO-CHEMICAL CHARACTERISTICS, AND CLIMATE FORCING OF ATMOSPHERIC AEROSOLS

UNIVERSITEIT GENT (RUG)
DEPARTMENT OF ANALYTICAL CHEMISTRY
INSTITUTE FOR NUCLEAR SCIENCES
RESEARCH GROUP TROPOSPHERIC AEROSOL RESEARCH AND NUCLEAR MICROANALYSIS
Proeftuinstraat 86
B-9000 GENT
W. MAENHAUT (coordinator CG/DD/03A)

UNIVERSITEIT ANTWERPEN (UIA)
MICRO AND TRACE ANALYSIS CENTRE (MITAC)
Universiteitsplein 1
B-2610 ANTWERPEN
F. ADAMS (promoter CG/DD/03B)

UNIVERSITEIT ANTWERPEN (UIA)
DEPARTMENT OF PHARMACEUTICAL SCIENCES
RESEARCH GROUP BIO-ORGANIC MASS SPECTROMETRY
Universiteitsplein 1
B-2610 ANTWERPEN
M. CLAEYS (promoter CG/DD/03C)

TABLE OF CONTENTS

ABSTRACT 1

1. CONTEXT AND OBJECTIVES 7

2. METHODS AND TECHNIQUES 12

2.1 Aerosol collections for subsequent "bulk" chemical analysis or investigation by individual particle techniques 12
2.2 Measurement of in-situ optical and physical aerosol characteristics and of vertical column integrated parameters 13
2.3 Bulk chemical analyses 13
2.4 Microscopical (individual particle) analyses 14
2.5 Chemical mass closure calculations. Identification and apportionment of the major aerosol types and/or source categories and assessment of the dominant source regions and transport pathways. Determination of the relative contributions from natural and anthropogenic sources 14
2.6 Interrelation of the radiative and physicochemical characteristics for in situ aerosols. Calculation of the direct radiative forcing of aerosols 15

3. DEVELOPMENT AND IMPLEMENTATION OF NOVEL TECHNIQUES AND METHODS FOR COLLECTION AND BULK AND MICROSCOPICAL (INDIVIDUAL PARTICLE) ANALYSIS OF ATMOSPHERIC AEROSOLS 15

3.1 Development of analytical methods for organic and elemental carbon 15
3.2 Development of analytical methods for organic compounds in aerosols 17
3.3 Analytical-methodological development on individual particle analysis 20

4. AEROSOL RESEARCH IN ARCTIC AND SUB-ARCTIC AREAS 22

5. RESEARCH WITHIN THE FRAMEWORK OF THE EUROTRAC-2 AEROSOL SUBPROJECT 27

6. COMPREHENSIVE STUDIES ON CHEMICAL, PHYSICAL, AND OPTICAL AEROSOL PROPERTIES IN THE MEDITERRANEAN AND ASSESSMENT OF THE DIRECT RADIATIVE FORCING BY AEROSOL 35

7. AEROSOL RESEARCH IN TROPICAL AND SUBTROPICAL REGIONS 46

8. OTHER AEROSOL-RELATED STUDIES 51

9. VALORISATION POTENTIAL OF THE RESULTS 52

10. CONCLUSIONS 53

ACKNOWLEDGEMENTS 56

REFERENCES 59

ABSTRACT

The overall goal of the project was to contribute to the reduction of the uncertainties in our knowledge of the sources, spatial distribution, and characteristics of the tropospheric aerosols that are of importance for climate. This was accomplished by performing studies at sites which are representative for large regions or are situated within (or downwind of) areas where it is expected that the radiative forcing by anthropogenic aerosols is very substantial. The studies were done (a) at selected sites in Europe within the framework of the EUROTRAC-2 AEROSOL subproject, (b) at sites in the eastern Mediterranean and in the Arctic, which are receptor areas of the European pollution plume, and (c) in tropical and subtropical regions.

The specific objectives of the project were: (1) to provide a comprehensive physico-chemical characterisation of the fine (submicrometer-sized) aerosol in the areas of study; (2) for some study areas, to complement this with purely physical aerosol measurements, with the determination of in-situ optical aerosol parameters and of vertical-column aerosol characteristics, and with measurements of atmospheric trace gases; (3) to determine the relative contributions of the three aerosol types (fine sulphate, organic aerosols, and mineral dust), which are mainly responsible for the aerosol forcing on climate; to differentiate between the natural and anthropogenic contributions to the fine sulphate and the organic aerosols; and to assess the sources, source processes, source areas, and transport mechanisms for the three important radiatively active aerosol types; (4) to investigate to which extent the fine aerosol mass can be reconstituted on the basis of the measured aerosol types, and thus aerosol chemical mass closure can be obtained; (5) to interrelate the various aerosol data sets and to utilise them for model calculations of optical aerosol characteristics or radiative forcing.

The project involved the development and implementation of novel methods and approaches for aerosol collection, for “bulk” and individual particle analysis, and for data interpretation and interrelation.

With regard to methodology, we implemented and evaluated a thermal-optical transmission technique for the determination of organic carbon (OC) and elemental carbon (EC) in aerosols. We participated in the EUROTRAC-2 AEROSOL Carbon Shootout Stages I and II and in other round-robins, which were organised to compare the methods of the various participants and to arrive at improved methods for the determination of and differentiation between OC and EC. We improved and evaluated methods for extracting organic compounds from aerosols for subsequent detailed analysis by capillary gas chromatography - flame ionisation detection (GC-FID) and gas chromatography/mass spectrometry (GC/MS). We started developing a

method for the quantitative determination of levoglucosan (which is a general marker for wood combustion) and related monosaccharide anhydrides in aerosol samples, and we implemented various types of derivatisations and solid-phase extraction in combination with GC/MS for the characterisation and structure elucidation of unknown compounds that were present in notable concentrations in urban and tropical aerosol samples. Methodological development work was done for transmission electron microscopy with selected area electron diffraction, and for two other microscopical analytical techniques, namely microprobe X-ray fluorescence with laboratory and synchrotron radiation sources and static secondary ion mass spectrometry.

Aerosol research was conducted in Arctic and sub-Arctic areas. This included studies within the framework of the Arctic Ocean Expedition 1996 (AOE-96), for Summit in Greenland, at the Zeppelin mountain station in Ny Ålesund, Spitsbergen, at Sevettijärvi in Finnish Lapland, and for two sites (i.e., Birkenes and Skreådalen) in southern Norway. For AOE-96, we performed chemical mass calculations and examined the detailed mass size distributions of various elements and species. Chemical mass closure calculations were also done for Sevettijärvi and the two Norwegian sites. The data sets from the three sites were also subjected to absolute principal component analysis in order to examine the interrelations between the various chemical species and elements, and to identify the major aerosol components and/or source types. For Sevettijärvi, we also applied trajectory statistics in order to identify the major source regions of sulphate and of selected elements and heavy metals.

Our contribution to the AEROSOL subproject includes the development, evaluation and application of analytical methods for OC and EC and for detailed organic compounds. During 1998, the methods were evaluated and applied to aerosol samples collected in Gent, during two different seasons (winter and summer). In both seasons, daily samples were taken with three types of filter collection devices. Particulate mass (PM) was determined for all filters by weighing, and all quartz filters were subjected to analyses for OC and EC; selected filters from one sampler were analysed for detailed organic compounds by capillary GC-FID and GC/MS. About two thirds of the PM10 (that is particles smaller than 10 μm) aerosol mass was contained in the fine (<2 μm) size fraction at Gent during the sampling campaigns. During both winter and summer, total carbon (TC = OC + EC) was responsible for around one quarter of the aerosol mass and EC represented about 25% of TC. Considering that the organic aerosol also contains other atoms (such as hydrogen, oxygen, nitrogen) besides carbon, the OC data have to be multiplied by a conversion factor in order to obtain organic aerosol mass (organic matter, OM). Multiplication factors of 1.4 are commonly used for urban aerosols. Using this factor, one arrives at

a percentage of carbonaceous aerosol (that is the sum of OM plus EC) of one third of the PM. By the detailed analyses for organic compounds, over 100 compounds belonging to different classes could be identified. Their total mass represented on average only 3% of the mass of the OM, though. *n*-Alkanes and fatty acids were the prevailing organic compounds in both seasons, but the distribution patterns of individual components within each class showed seasonal differences. The *n*-alkane pattern for summer aerosols was clearly affected by emissions from the vegetation, while that of fatty acids revealed a lower relative abundance of unsaturated fatty acids in summer than winter, that can be related to more extensive atmospheric oxidation of unsaturated fatty acids during summer. Concentrations of dicarboxylic acids and related products that are believed to be oxidation products of hydrocarbons and fatty acids were highest in summer aerosols. Some individual compounds in the latter class could only be detected in summer samples and showed the highest concentrations on hot summer days that were characterised by maximum temperatures above 25°C and increased ozone concentrations. The latter compounds included novel, recently identified glutaric acid derivatives. Several compounds were found that are markers of wood combustion, including diterpenoic acids, lignin pyrolysis products, and levoglucosan. The quantitative results obtained for diterpenoic acids and lignin pyrolysis products indicated that contributions from wood combustion are more important in winter than in summer. There was evidence that both soft and hard wood burning contribute to the organic aerosol, but that hard wood burning prevails during winter. Polyaromatic hydrocarbons were also more prevalent in winter than in summer.

Besides work on OC, EC, and detailed organic compounds, our contribution to the AEROSOL subproject includes intercomparison and evaluation of methods for measuring important aerosol parameters, such as the PM, carbon, determination of the detailed mass size distribution for the PM, OC, EC and other important aerosol species, chemical mass closure work, and source (type) apportionment. Various intercomparisons were made at Gent of filter collections and in-situ measurements for the aerosol particulate mass and elemental/black carbon (all for the PM2.5 aerosol, that is for the particles smaller than 2.5 μm). The in-situ instruments were a Rupprecht and Patashnick tapered element oscillating microbalance (TEOM) for the PM and a Magee Scientific aethalometer for black carbon (BC). The TEOM value was on average only two thirds of the gravimetric mass derived from quartz fibre filters. Discrepancies between TEOM and gravimetric aerosol data have been observed by others and are attributed to the heating to 50°C (and loss of semi-volatile aerosol) in the TEOM. Comparisons of gravimetric fine PM determinations were also done with filter holders that used different types of filters. It was found that the fine PM derived from Nuclepore polycarbonate filters and Teflo filters was only

around 75% of that derived from the quartz fibre filters. The difference may be due to the loss of semi-volatile aerosol for the Nuclepore and Teflo filters or to the collection of gaseous species by the quartz filters or to a combination of both. Further investigations should clarify this. In fall 1999, we examined the detailed mass size distribution of the PM, OC, EC, and various elements at Gent, and used the data for aerosol chemical mass closure calculations as a function of particle size. Six aerosol types were considered in the mass closure calculations: (1) organic aerosol, (2) EC, (3) ammonium sulphate, (4) sea salt, (5) crustal matter, and (6) biomass smoke. The major aerosol types in the submicrometer size fraction were organic aerosol (on average responsible for 32% of the PM), ammonium sulphate (27%) and EC (10%). In the supermicrometer size range, organic aerosol (28% of the PM) and crustal material (24%) prevailed; ammonium sulphate and sea salt were responsible for about 10% each. On average, 74% of the gravimetric PM was accounted for by the aerosol types considered. The unexplained mass is likely attributable to ammonium nitrate and water.

In addition to our aerosol research at Gent, we conducted aerosol research at various other urban sites, including for Cracow, Helsinki, and Budapest. These urban studies were to some extent linked to the EUROTRAC-2 AEROSOL subproject. Furthermore, the work in Helsinki fitted within the EUROTRAC-2 project SATURN.

We also participated in the INTERCOMP 2000 experiment of the EUROTRAC-2 AEROSOL subproject. The field work for INTERCOMP 2000 took place in April 2000 at the Institute for Tropospheric Research (IfT) research station Melpitz, about 50 km north-east of Leipzig, Germany.

A large part of our project dealt with comprehensive studies on chemical, physical, and optical (radiative) aerosol properties in the eastern Mediterranean and the assessment of the direct radiative forcing by aerosols in the area. These studies were performed in close co-operation with foreign research groups, especially with the Biogeochemistry Department of the Max Planck Institute for Chemistry, Germany. Both long-term and intensive aerosol measurements were conducted at Sde Boker in the Negev desert, Israel. The long-term measurements started in January 1995 and are still going on. The intensive measurements were conducted during two campaigns (of about 4 weeks each), the first one, called ARACHNE-96, in June-July 1996, the other, ARACHNE-97, in February-March 1997. In the long-term measurements, aerosol samples are collected with a Gent PM10 stacked filter unit sampler according to a 2-2-3-day schedule and analysed for the PM, BC, and over 40 elements. From December 1995 through September 1997, an integrating nephelometer was used for the continuous measurement of the aerosol scattering and backscattering coefficients at 3 wavelengths (450, 550, and 700 nm), and it was

then replaced by a unit which only measures the scattering at 550 nm. Furthermore, measurements of vertical column-integrated aerosol optical depth and aerosol properties are conducted at the site on a nearly continuous basis with an automatic tracking combined sunphotometer/sky radiometer. During the intensive campaigns, a wide array of instruments was used for measuring the aerosol chemical, physical, and optical (radiative) properties and for measuring selected atmospheric trace gases (CO, CO_2, SO_2, O_3). Comprehensive articles on the ARACHNE-96 and ARACHNE-97 campaigns were published. During ARACHNE-96, the average aerosol dry single scattering albedo (ω_0) characterising polluted conditions was 0.89, whereas during "clean" periods ω_0 was 0.94. The direct radiative effect of the pollution aerosols was estimated to be cooling. With regard to the long-term measurements, the data from the 3-wavelength nephelometer and the Gent PM10 stacked filter unit sampler were interrelated. This was done for the period December 1995 through September 1997. The total scattering coefficient at 550 nm showed a median of 66.7 Mm^{-1}, typical of moderately polluted continental air masses. Values of 1000 Mm^{-1} and higher were encountered during severe dust storm events. Mass scattering efficiencies were obtained by multivariate regression of the scattering coefficients on dust, sulphate, and residual components. An analysis of the contributions of the various aerosol components to the total scattering observed showed that anthropogenic aerosol accounted for about 70% of the scattering. The rest was dominated by the effect of the large dust events mentioned above, and of small dust episodes typically occurring during mid-afternoon. The radiative forcing by anthropogenic aerosols in the study region at the top of the atmosphere was estimated using two different approaches. The most detailed of these yielded an all-sky radiative forcing of -2.5 and -4.9 Watt m^{-2} over desert and ocean surfaces, respectively. These data are in good agreement with predictions from global models of aerosol radiative forcing. Overall, we concluded that our data provide strong support for a negative radiative forcing due to anthropogenic aerosols in the eastern Mediterranean region, and that the magnitude of this forcing is in good agreement with current model predictions. Further with regard to the long-term collections, we applied trajectory statistics in order to assess the source regions of some important aerosol constituents. The stacked filter unit data set for the 3-year period from 1995 through 1997 was used for this purpose. The air masses, which arrived at Sde Boker slightly above ground (i.e., at a level corresponding to 950/960 hPa), originated mainly from the north-west, and had remained in the atmospheric boundary layer (below 2000 meters) during the 5 days preceding their arrival. The same was true for the 900 hPa arrival level. The highest levels of fine sulphur were associated with air masses that originated in the North; the dominant source region appeared to be Ukraine, followed by the West coast of the Black Sea, and Greece. In contrast, fine V and fine Ni (two indicators of residual oil burning) were from local/regional origin,

including from the power plants along the Israeli coast. Russia seemed to be the major source area of fine Zn. Coarse Ca, an indicator for the carbonate mineral dust, was highest for air masses coming from the south-east and west, consistent with the location of the desert source regions.

Our aerosol research in tropical and subtropical regions included studies in Africa (the Republic of Congo, Zimbabwe, South Africa), the Brazilian Amazon region, northern Australia, and Indonesia. It involved both long-term and campaign-type measurements. The emphasis in the studies was placed on the impact of biomass burning and of natural biogenic emissions on the climatically active fine aerosol. Part of our work for Brazil was performed within the framework of the "Smoke, Clouds, Aerosols and Radiation - Brazil (SCAR-B) Experiment" and the "Large Scale Biosphere-Atmosphere Experiment in Amazonia" (LBA), and some of our research in South Africa was done as part of the Southern African Regional Science Initiative (SAFARI 2000).

With regard to the valorisation of our work, this is partly done through traditional channels, such as publications in international journals and presentations at international conferences. For our research that is done within intensive campaigns, we also relate our data with results of the other participants, which leads to joint publications and presentations. The results are further used in workshops, activities and reports that aim at transfer of knowledge to policy advisers and policy makers. Our long-term and other data sets with concentrations and compositions of fine atmospheric aerosols for various European sites are being used for advice to the European Commission, in particular within work for the 2003 revision of the EU Particulate Matter Directive.

Our research has shown that the determination of seemingly simple aerosol parameters, such as the PM, is much less straightforward than usually thought. The measurement of the PM is complicated by both positive and negative artifacts. Work on the control, elimination, and assessment of the artifacts is needed. This work will assist regulatory bodies which are setting and imposing guidelines for particulate matter. Carbonaceous particles make up a very large fraction (often over 30%) of the aerosol in many areas. Yet, our knowledge on the detailed molecular composition of the carbonaceous aerosol, its sources, and its effects on human health and climate is still quite poor. Further research on these topics is highly recommended. There are still large uncertainties associated with the radiative forcing of aerosols on climate. In the past few years, much progress has been made with regard to the *direct* radiative aerosol forcing. However, with regard to the *indirect* radiative forcing (that is through the effects of aerosols on clouds) much work remains to be done.

1. CONTEXT AND OBJECTIVES

Aerosols are tiny liquid or solid particles that are present in the atmosphere. They have diameters in the range from 1 nm to over 10 μm, but most of their mass is in the size range from about 0.1 to 10 μm. They originate from a wide variety of natural and anthropogenic (man-made) processes that exhibit a large spatial and temporal variability [Andreae, 1995; Jonas et al., 1995]. The production mechanisms are: (1) direct injection of particles in the atmosphere, mostly by dispersion processes, resulting in so-called primary (and coarse, that is >1 μm) aerosols, and (2) transformation of inorganic and organic gaseous precursors into secondary (and fine, <1 μm) aerosols. Aerosols play an important role in atmospheric chemistry, have effects on human and animal health and welfare, and they influence climate. In the 1990s renewed interest in the health risks of aerosols has been generated by the finding of a correlation between increased mortality and the concentration of (fine) airborne particles in metropolitan areas in the United States [Dockery et al., 1993].

The climatic effect of aerosols stems from the fact that they physically affect the heat balance of the Earth, both *directly* by reflecting and absorbing solar radiation and by absorbing and emitting some terrestrial infrared radiation, and *indirectly* by influencing the properties and processes of clouds, and, possibly, by changing the heterogeneous chemistry of reactive greenhouse gases (e.g., O_3) [Charlson and Heintzenberg, 1995]. Changes in the heat balance due to anthropogenic or externally imposed changes are referred to as forcings. The climatic effect of aerosols is in the direction of cooling (under most circumstances) and is of a magnitude comparable to that of the greenhouse gas warming [Charlson et al., 1992; IPCC, 1994]. Due to the spatial and temporal variability of anthropogenic aerosols, the forcing has strong regional character [Kiehl and Rodhe, 1995], so that also the climate response to the aerosol forcing is regionally heterogeneous [Taylor and Penner, 1994]. In 1995, the global mean radiative forcing by anthropogenic aerosols was estimated to be -(0.25-2.5) W m^{-2} [Houghton et al., 1996]. The large range of uncertainty associated with the aerosol forcing estimate reflects the poor state of knowledge regarding the sources, distributions, and properties of atmospheric aerosols. Kiehl and Briegleb [1993] stressed that studies on the regional characteristics of aerosols were urgently needed to reduce this uncertainty. Penner et al. [1994] suggested a research strategy which encompasses surface-based observations of aerosol chemical and physical properties.

Over Europe, fine sulphate, which is formed by the gas-to-particle conversion of SO_2 from fossil fuel burning and smelting activities, is thought to be mostly responsible for both the *direct* and *indirect* aerosol forcing on climate. Over tropical and equatorial continental regions, fine pyrogenic (biomass burning) particles and natural emissions

from the vegetation, which both consist mainly of carbonaceous particulates, are the prevailing climatically active aerosol species. In addition, organic aerosols from anthropogenic continental origin have been shown to account for the major part of the cloud condensation nuclei (and thus the *indirect* forcing) in marine air [Novakov and Penner, 1993]. However, it is difficult to discriminate between the natural and anthropogenic contributions to the carbonaceous aerosols, and this is especially so for tropical and subtropical areas [e.g., Radzi bin Abas and Simoneit, 1996; Maenhaut et al., 1996c]. This difficulty stems partly from the difficulties in collection and preservation of carbonaceous particles (which are often semi-volatile), but even more from the lack of suitable analytical methods to measure polar organic compounds in the aerosols. In the studies on natural and combustion aerosols from the vegetation, one has until now mainly concentrated on the determination of solvent extractable organic compounds, including *n*-alkanes, *n*-alkanoic acids, *n*-alkanols, and terpenoids [e.g., Rogge et al., 1993a; Radzi bin Abas and Simoneit, 1996]. A major component of the aerosol on a global scale is mineral dust (soil dust). While most of this dust is of natural origin (i.e., generated by dust storms in desert regions of North Africa and Central Asia), changes in land use must have increased the amounts of dust injected into the atmosphere [Andreae, 1995; Tegen and Fung, 1995]. Tegen et al. [1996] calculated the climate forcing of mineral aerosols from disturbed soils, and they indicated that additional field (and other) measurements are required to improve the estimates of the radiative forcing and to assess uncertainties.

In principle, the radiative (optical) properties of atmospheric aerosols can be predicted from their physical and chemical characteristics by using theoretical formalisms (Mie theory) or empirical relationships [e.g., Kiehl and Briegleb, 1993]. This requires the knowledge of the contribution from the various aerosol types (sulphates, combustion particles, dust, etc.), of the size distribution of these aerosol types, their surface composition and their chemical composition as a function of size, the particle shape, and the state of particle mixing (external or internal). Conversely, the optical characteristics of the aerosol (scattering and absorption coefficients) can be measured experimentally. These experimental optical data can then be compared with the calculated values in order to examine to which extent agreement ("closure") between them can be obtained. As indicated by Ogren [1995] and others, such closure experiments on various temporal and spatial scales are essential to minimise the uncertainties of current estimates of aerosol climate forcing.

In studies on the climatically active fine aerosol (and on fine aerosols in general), a major fraction of the fine particulate mass (PM) remains often unexplained by the particle types measured [e.g., Maenhaut et al., 1996a]. This observation formed the impetus for the EUROTRAC-2 AEROSOL subproject, which aims at obtaining chemical mass "closure" for fine aerosols in key urban and rural areas in Europe.

Assessing the various fine aerosol constituents and their sources is needed for determining the role of aerosols in regional and global climate forcing (and incidentally also for elucidating the causes of the health risks of aerosols). The relative contributions from natural and anthropogenic particle types (and source identification and apportionment in general) are usually obtained by applying receptor models [Gordon, 1988] to multivariate data sets that result from "bulk" analyses. For such data sets, there are, however, severe difficulties in apportioning the contributions from source types with similar bulk compositions of the emitted particles. To arrive at a better discrimination one can resort to individual particle techniques [e.g., Van Borm and Adams, 1988]. Most commonly used is electron probe X-ray microanalysis (EPXMA). While EPXMA is undoubtedly of great value, it suffers from the fact that its detection limits are of the order of 0.1% only. Therefore, continuous efforts are directed towards the development of more sensitive micro-analytical techniques and their application to environmental samples. Besides the identification and apportionment of sources and source types, similar tasks are increasingly performed with regard to source regions, particularly for areas that are down wind of major source regions. In the 1980s attempts were made to address this issue with receptor models, but nowadays there is a clear tendency to utilise air mass back trajectories in combination with the aerosol data sets [e.g., Stohl, 1996].

The overall aim of the project was to contribute to the reduction of the uncertainties in our knowledge of the sources, spatial distributions, and properties of the aerosols that are of relevance for climate forcing. Therefore, studies were performed at a number of sites that are representative for fairly large regions, and that are located in (or downwind of) areas where the radiative forcing from anthropogenic aerosols is expected to be substantial. The studies were done (1) at selected sites in Europe within the framework of the EUROTRAC-2 AEROSOL subproject, (2) at sites in the eastern Mediterranean and in the Arctic, which are receptor areas of the European pollution plume, and (3) in tropical and subtropical regions.

As indicated above, over Europe and downwind of it, fine sulphate is thought to be mostly responsible for the aerosol forcing on climate. However, the forcing by carbonaceous aerosols from fossil fuel use may also be substantial, and over the Mediterranean, mineral dust from arid and desert regions in North Africa and Arabia forms an important radiatively active aerosol component. One objective of the research was therefore to determine the relative contributions from the three aerosol types at various study sites and to determine their sources, source processes, source regions, and transport pathways (and to examine how all these parameters vary with season). While most of the climatically active fine sulphate is undoubtedly from anthropogenic origin, at certain times of the year (i.e., spring and summer) and in certain regions (e.g., the Arctic), there may be a significant contribution from

sulphate that is formed by gas-to-particle conversion of dimethylsulphide and other reduced sulphur gases emitted by marine and terrestrial plants. Similarly, the primary and secondary organic carbon (OC) component of the fine aerosol over Europe may also originate in part from natural emissions of the vegetation. In tropical and equatorial regions, the contribution from vegetative emissions to the OC particles may even be higher, especially during the wet season when biomass burning is much reduced. It was therefore a major objective to assess the relative contributions from natural and anthropogenic sources for both the fine sulphate and OC.

Because the submicrometer-sized aerosol particles are of major relevance for both the direct and indirect forcing of climate, the emphasis was placed on the comprehensive chemical and physical characterisation of the fine aerosol. This was done through collections with a variety of aerosol samplers, whereby the fine aerosol is collected in a separate fraction or is fractionated in several size classes (such as is the case with cascade impactors), and subsequent bulk chemical analysis of the fractionated aerosols. Depending upon the sampler used, the bulk analyses included determination of the particulate mass (PM), of organic carbon (OC) and elemental (or black or soot) carbon (EC or BC), of water-soluble inorganic species (sulphate, nitrate, ammonium) and some water-soluble organic compounds (e.g., methanesulphonate, lower molecular weight (MW) organic acids), of major, minor and trace elements, and of selected higher MW organic compounds. These bulk analyses were complemented by microscopical analyses on selected samples, which aimed at determining the shape (morphology) and composition of individual particles, the state of particle mixing (external versus internal), and the presence of water-soluble or hydrophilic coatings on mineral and carbonaceous particles (such coatings have the effect that the particles can act as cloud condensation nuclei (CCN)). At a number of sites, the physico-chemical aerosol measurements were complemented by purely physical aerosol measurements (of the number of condensation nuclei, of CCN, and of the detailed aerosol number size distribution), with the determination of in-situ optical (radiative) aerosol parameters (scattering, backscattering, absorption coefficients) and of vertical-column integrated aerosol properties (optical depth, aerosol size distribution, and scattering), and with measurements of aerosol precursor gases (SO_2) or of useful tracers for polluted air (CO, CO_2, O_3). The research involved both long-term measurements and intensive campaigns, and a much wider array of instrumentation was used in the latter. Most of the work consisted of surface-based aerosol measurements, but some measurements were performed with an airplane in order to examine the vertical structure of the physical, chemical, and optical aerosol parameters.

The various aerosol data sets were interrelated to each other and used for model calculations of the aerosol optical properties or radiative forcing. The objectives

hereby were: (a) to investigate how well the experimentally measured radiative properties of the aerosol could be predicted from the measured chemical and physical aerosol characteristics (and thus closure can be obtained between measurement and theory), (b) to assess the direct radiative forcing by aerosols, and (c) to assess to which extent the ground-level in-situ aerosol characteristics are related to or can be used for the prediction of the chemical, physical and optical aerosol properties in the entire vertical column. Another major objective was to examine to which extent the fine PM could be reconstituted on the basis of the various aerosol types measured, and if it appeared that a substantial fraction of the PM is unexplained, to take appropriate actions for identifying that "missing" mass.

The aerosol collections and chemical analyses were largely performed with instrumentation that was already available at the start of the project, but some new developments were also necessary and were made, especially for the bulk analysis of OC/EC and organic compounds and for the microscopical examination of submicrometer-sized individual particles. The developments were needed to obtain chemical mass closure for the PM, to extend the range of marker compounds or species for discrimination between natural and anthropogenic particle types, and to obtain the information required for the calculation of the optical aerosol characteristics.

To determine the relative contributions from the major aerosol types and/or source categories to the total aerosol concentration and to discriminate between the natural and anthropogenic contributions for the important particle types, we relied mostly on receptor modelling by chemical mass balance and multivariate techniques. In addition, efforts were made for assessing the dominant source regions and transport pathways. This work involved the use of air mass back trajectories.

The overall goal of the project was thus to contribute to the reduction of the uncertainties in our knowledge of the sources, spatial distribution, and characteristics of the tropospheric aerosols that are of importance for climate. In summary, the objectives of the project were:

- to provide a comprehensive physico-chemical characterisation of the fine (submicrometer-sized) aerosol in the areas of study;
- for some study areas, to complement this with purely physical aerosol measurements, with the determination of in-situ optical aerosol parameters and of vertical-column aerosol characteristics, and with measurements of atmospheric trace gases;
- to determine the relative contributions of the three aerosol types (fine sulphate, organic aerosols, and mineral dust), which are mainly responsible for the aerosol forcing on climate; to differentiate between the natural and

anthropogenic contributions to the fine sulphate and the organic aerosols; and to assess the sources, source processes, source areas, and transport mechanisms for the three important radiatively active aerosol types;

- to investigate to which extent the fine aerosol mass can be reconstituted on the basis of the measured aerosol types;
- to interrelate the various aerosol data sets and to utilise them for model calculations of optical aerosol characteristics or radiative forcing.

The project involved the development and implementation of novel methods and approaches for aerosol collection, for "bulk" and individual particle analysis, and for data interpretation and interrelation.

2. METHODS AND TECHNIQUES

2.1 Aerosol collections for subsequent "bulk" chemical analysis or investigation by individual particle techniques

A wide variety of aerosol collectors are employed, but those actually used at a given site depend on the logistical support, on the type of measurement (long-term, campaign, aircraft), on the subsequent analyses, and on the co-operating institutions. The collection devices used in the current project included "total" filter samplers, PM10 (particulate matter <10 µm equivalent aerodynamic diameter (EAD)) and PM2.5 (particulate matter <2.5 µm EAD) devices, and several types of cascade impactors. Most commonly used was the "Gent" PM10 stacked filter unit (SFU) sampler [Maenhaut et al., 1994b; Hopke et al., 1997]. This device separates the aerosol particles into a coarse and a fine size fraction, with the division between the two fractions at around 2 µm EAD. Filters of organic material (polycarbonate, Teflon, cellulose, cellulose esters) were used for measuring major, minor, and trace elements and water-soluble inorganic and organic species. For organic and elemental carbon and higher molecular weight organic compounds, the filter material consisted of quartz fibre, glass fibre or Teflon-coated glass fibre. As cascade impactors we mainly used the 8-stage, 1-L/min PIXE Int. cascade impactor (PCI) [Bauman et al., 1981] or reduced versions thereof, the 12-stage, 11-L/min small deposit area low pressure impactor (SDI) [Maenhaut et al., 1996b], and the 10-stage rotating microorifice uniform deposit impactor (MOUDI) [Marple et al., 1991].

2.2 Measurement of in-situ optical and physical aerosol characteristics and of vertical column integrated parameters

The optical (radiative) parameters of the in-situ aerosol are measured by means of an aethalometer (Magee Scientific) and a 3-wavelength integrating nephelometer with backscatter shutter (TSI 3563). The aethalometer [Hansen et al., 1984] is used for the measurement of the absorption coefficient (b_a). The TSI 3563 nephelometer [Anderson et al. 1996; Anderson and Ogren 1998] is used for the continuous measurement of the total scattering and backscattering coefficients at 3 wavelengths (450, 550, and 700 nm).

The physical characteristics of the in-situ aerosol are measured with a condensation nuclei (CN) counter (TSI Model 3022A) to determine the total number of particles (with diameter> 10 nm), a laser-optical particle probe to determine the aerosol number size distribution, and a cloud condensation nuclei (CCN) counter.

The column-integrated optical and physical aerosol parameters (optical depth, scattering, and volume size distribution) are determined by means of an automatic tracking combined sunphotometer/sky radiometer (CIMEL Electronique 318A) and by an automated multifilter rotating shadow-band radiometer [Harrison et al., 1994].

Most of the optical and physical aerosol measurements were performed through international co-operations, in particular with the Biogeochemistry Department (director: Prof. Dr. M.O. Andreae) of the Max Planck Institute for Chemistry (MPIC), Mainz, Germany.

2.3 Bulk chemical analyses

The bulk analyses included determination of the particulate mass (PM), of organic carbon (OC) and elemental (or black or soot) carbon (EC or BC), of water-soluble inorganic species (sulphate, nitrate, ammonium) and some water-soluble organic compounds (e.g., methanesulphonate (MSA), lower molecular weight (MW) organic acids), of major, minor, and trace elements, and of selected higher MW organic compounds. Many of these species and elements were measured with techniques and methods which were already used by us before the start of this project. The techniques include gravimetry (for PM), a simple light reflectance technique (for BC), ion chromatography (IC), particle-induced X-ray emission (PIXE) and instrumental neutron activation analysis (INAA). More details on them can be found in Maenhaut [1993, 1996]. For other species, in particular OC, EC, and organic compounds, methodology was developed as part of the current project.

2.4 Microscopical (individual particle) analyses

Selected aerosol filter samples and/or cascade impactor samples were examined by individual particle analysis techniques. The techniques include electron probe X-ray microanalysis (EPXMA), transmission electron microscopy (TEM), nuclear microprobe (NMP) analysis, synchrotron microprobe X-ray fluorescence (μ-XRF), and static secondary ion mass spectrometry (S-SIMS). EPXMA, TEM, the NMP and μ-XRF were used for the determination of the size, shape (morphology), and elemental composition of the individual particles. EPXMA was already a well-established technique at the start of the project, but for the other techniques methodological work was carried out as part of the current project.

2.5 Chemical mass closure calculations. Identification and apportionment of the major aerosol types and/or source categories and assessment of the dominant source regions and transport pathways. Determination of the relative contributions from natural and anthropogenic sources

The chemical analysis of the aerosol samples provides concentration data for several indicators and tracers of major aerosol types and source categories, and for discriminating between the natural and anthropogenic contributions. It is especially examined to which extent the measured fine PM can be reconstituted by the various aerosol types and/or components (and thus chemical mass closure can be obtained). The aerosol types and/or components include crustal material (which may consist of soil dust, road dust, and coal fly ash in variable proportions, depending upon the site), sea salt, carbonaceous aerosols, sulphate, nitrate, ammonium, and water. In the chemical mass closure calculations, we obtained the mass of crustal material from the mass of Al and other crustal elements, whereas the mass of sea salt was estimated on the basis of the sea-salt elements Na and Cl. By examining the relationships and correlations among the various variables in aerosol composition data sets, the major aerosol types and/or source categories (e.g., mineral dust dispersal, sea spray, fossil fuel combustion, industrial emissions, biomass burning, waste burning) are identified. Subsequently, we calculate the contribution from each aerosol type and/or source category to the concentrations of the fine PM and of the various species and elements. The calculations involve the use of chemical mass balance (CMB) models and of multivariate receptor models (such as absolute principal component analysis (APCA)) [Henry et al., 1984; Lowenthal et al., 1987; Maenhaut and Cafmeyer, 1987].

The concentrations of the aerosol types and/or source categories, as obtained by APCA or CMB, or of good indicators for the aerosol types are related to air mass back trajectories in order to assess the source regions and transport pathways. For

large data sets (of at least 100 samples collected over long time spans), we also implement statistical approaches to pinpoint the source areas [Seibert and Jost, 1994; Stohl, 1996].

For aerosol types, such as sulphate and carbonaceous particles, the natural and anthropogenic contributions are resolved by relating their concentrations to data of suitable indicator species. The apportionment involves the use of multiple linear regression (MLR) analysis [Maenhaut et al., 1994a], APCA or CMB.

2.6 Interrelation of the radiative and physicochemical characteristics for in-situ aerosols. Calculation of the direct radiative forcing of aerosols

From the nephelometer and aethalometer data, we obtain the extinction coefficient for up to 3 wavelengths and some other radiative characteristics for the in-situ aerosol. The radiative characteristics can also be calculated (modelled) from Mie theory [Bohren and Huffman, 1983] and the physicochemical aerosol properties, and it can be examined to which extent agreement (closure) is obtained between the experimentally determined and model-predicted radiative aerosol characteristics.

The optical/radiative aerosol characteristics can also be used to calculate the direct radiative forcing. For these calculations, one can employ the approaches of Penner et al. [1992, 1998], Kiehl and Briegleb [1993], Haywood and Shine [1995], Key and Schweiger [1998], Anderson et al. [1999] or modifications and/or extensions thereof.

This interrelation and modelling work was done in close collaboration with the MPIC.

3. DEVELOPMENT AND IMPLEMENTATION OF NOVEL TECHNIQUES AND METHODS FOR COLLECTION AND BULK AND MICROSCOPICAL (INDIVIDUAL PARTICLE) ANALYSIS OF ATMOSPHERIC AEROSOLS

3.1 Development of analytical methods for organic and elemental carbon

The carbonaceous fraction of atmospheric aerosols consists of elemental carbon (EC) and a variety of organic compounds (organic carbon (OC)). The distinction between OC and EC is mostly based on the difference in temperature at which they volatilise. For measuring OC and EC we acquired an OC/EC thermal-optical transmission (TOT) carbon aerosol analyser from Sunset Laboratory (Oregon, U.S.A.). This instrument is built for analysing aerosol samples collected on quartz filter samples. During the stepwise heat treatment in different atmospheres (first in pure He, then in an O_2/He mixture) the light transmission through the filter is continuously monitored, so that one can correct for the artifact EC that is formed by

charring during the pyrolysis of organic material [Birch and Cary, 1996]. Our analyses were generally performed using temperature, time and other instrumental parameters suggested by the manufacturer, and OC and EC were derived from the thermogram with the calculation software that was supplied with the instrument. This software sets an automatic EC/OC "split point" at that point (time) in the thermogram when the transmission through the filter is the same as the initial transmission, but one can override this and set the "split point" manually. The software also allows one to correct the OC concentration for the contribution from inorganic carbonate carbon (CC), provided the CC consists essentially of calcium carbonate and the peak arising from it is clearly identifiable in the thermogram. An alternative correction for CC is to perform the OC/EC analyses on sample sections that have been subjected to an HCl treatment to convert the inorganic carbonate into CO_2 and thus to volatilise it prior to analysis.

The capabilities and limitations of the instrument were examined by analysing filter samples from different locations and different seasons and by participating in international intercomparison exercises. We participated in the EUROTRAC-2 AEROSOL Carbon Shootout Stages I and II, which were organised by Prof. Dr. H. Puxbaum (Technical University, Vienna), and in an intercomparison, organised by Dr. X.D. Liu (National Research Centre for Environmental Analysis and Measurements (NRCEAM), Beijing, China). In the Carbon Shootout Stage I, urban aerosol samples were collected on quartz fibre filters at a site in Berlin and distributed to participants from about 20 universities and research institutions. For the Shootout Stage II the filters were collected at a rural site in Austria and there were again about 20 participating groups. The objectives of the Shootout were to compare the OC/EC analysis methods of the various participants and to arrive at improved methods for the determination of and differentiation between OC and EC. Good agreement was obtained for total carbon (TC = OC + EC), but there were large differences for the differentiation between OC and EC. The differences were clearly worse for the rural samples from Austria (with high biopolymer content) than for the urban samples from Berlin. Furthermore, for the rural samples, the EC/TC ratio depended strongly on the temperature program used. Higher EC/TC ratios were obtained when a lower maximum temperature was used in the first stage of the analysis (in pure He) or when the maximum temperature was sustained for a shorter time. This phenomenon also existed to some extent for the urban samples, but not as much as for the rural samples. Among the participants of the Shootout there is a consensus that methods which rely on an optical correction (as is the case with our method) provide more accurate results, at least for urban samples [Schmid et al., 2001]. For samples with high biopolymer content, further research is in progress. In the intercomparison of Dr. Liu, quartz fibre filter samples with aerosol collected in Beijing were distributed to participants from China, Japan, France, and ourselves.

The results of this exercise were similar as for the Carbon Shootout Stage I.

From the other evaluation work with our instrument it appeared that the automatic "split point" is set too late and provides too low EC/TC ratios for urban samples when their TC loading becomes larger than 100 μg cm^{-2}. This was concluded from the analysis of samples which had been taken in parallel with a high-volume sampler (with large areal aerosol mass density) and a low-volume sampler (with about 10 times lower areal aerosol mass density) at Gent during 1998 [Kubátová et al., 1999] and 1999. However, by manually adjusting the split point for the heavily loaded samples to the same time as automatically obtained for the lightly loaded samples collected in parallel, good agreement could be obtained between the EC/OC ratios for both types of filter samples. Another weak point of our instrument is that the HCl treatment led to a decrease in the response of the FID detector used for quantifying the carbonaceous compounds (after their conversion into methane). This problem is also seen in other instruments from the same company, it is unclear why it occurs, but because of it, the HCl treatment cannot be recommended for routine use [Cary, 1998]

We also developed procedures for measuring the water-soluble and the organic solvent extractable OC in aerosol filter samples. As the OC/EC instrument is built for analysing filter sections, it had to be adapted, so that also a quartz vessel (boat) with the residue of the solute or extract could be introduced into it. The reproducibility of this "boat" technique was evaluated with standard solutions of sucrose and EDTA and was typically better than 5%. The technique was applied to determine the water-soluble OC (WSOC) in total filter samples collected in summer and fall of 1998 in Gent. About 20% of the total OC appeared to be WSOC.

It should be indicated here that the OC, as obtained with the TOT technique, represents only the carbon in the organic aerosol and that other atoms (such as H, O, N) besides C are also present. Therefore, the OC data have to be multiplied by a conversion factor in order to obtain organic aerosol mass (organic matter, OM). For urban aerosols, one commonly uses a multiplication factor of 1.4 [Seinfeld and Pandis, 1998; Turpin et al., 2000].

3.2 Development of analytical methods for organic compounds in aerosols

The objectives of the analyses for organic compounds were to achieve a more complete molecular characterisation of the carbonaceous aerosol, to identify and quantify the compounds that provide the largest contribution to the OM, and to provide data for marker (indicator) species which allow one to differentiate between the natural and anthropogenic contributions to the carbon aerosol.

At the outset of the project it was decided to measure the organic compounds by capillary gas chromatography (GC) - flame ionisation detection (FID) and by GC/ mass spectrometry (MS), whereby GC/MS is used for qualitative analysis (identification) and GC-FID for the quantitative analysis, and to start by implementing and adapting a method which was originally described by Mazurek et al. [1987]. This method was selected because it was designed to monitor component losses during sample work-up, it can be applied to quantify low-microgram levels of extractable organic matter in aerosol samples, and allows one to determine over 100 compounds simultaneously. For the development work, we mostly used samples that were taken on Whatman QM-A quartz fibre filter with a total filter sampler (Qtot) at Gent. Special emphasis was placed on attempting to increase the fraction of extractable and elutable organic aerosol mass (EEOM). The EEOM is the sum of the resolved and unresolved mass in the GC-FID chromatograms. We compared the EEOM yields of (a) extraction with dichloromethane (CH_2Cl_2), (b) extraction with benzene, and (c) extraction with dichloromethane followed by extraction with the more polar solvent 2-propanol. Using (c), the EEOM yield was approximately 15-20% higher than with (a), but the increase was mainly in the unresolved complex mixture (UCM). Disadvantages of 2-propanol are that it gave rise to contamination, even when using a high-purity solvent, and that evaporation of the extracts is more difficult, and it was therefore not retained. Evaluation of benzene as extraction solvent showed that the EEOM and the composition of the extracts were very similar to those obtained with dichloromethane. Considering the high toxicity of benzene, preference was given to the use of dichloromethane as extraction solvent.

The yield of EEOM, relative to the OM, as derived from the TOT instrument, was of the order of 17% for the total filter samples from Gent, but only around 4% for the total filter samples from Amazonia. Taking into account that organic acids can also occur in the salt form, it was evaluated whether acidification of the filters results in an enhancement of the EEOM yield. In preliminary tests with total filter samples from Gent, the filters were first extracted with dichloromethane, then acidified with acetylchloride and extracted again. By this additional step, another 5% of the OM was recovered as EEOM. Following up on this good result, it was decided to evaluate the extraction yield itself for 5 different extraction procedures. For these experiments we used again total filter samples that were collected at Gent and were analysed for OM and EC with the TOT instrument. After the extraction, the filters were (when possible) again analysed for OM and EC, and also the organic extracts themselves were analysed for OM and EC. The five extraction procedures were:

i. 3 x 30 min ultrasonic extraction in CH_2Cl_2;
ii. 2 x 30 min + 1 x 16 hours ultrasonic extraction in CH_2Cl_2;
iii. in a Soxhlet apparatus: 4 hours in CH_2Cl_2;
iv. acidification with acetylchloride, followed by 3 x 30 min ultrasonic extraction in

CH_2Cl_2;

v. soft saponification with NaOH.

The extract of procedure (i) contained on average 40% of the original OM, that of procedure (ii) 45%, that of procedure (iii) 40%, that of procedure (iv) 40%, and after procedure (v) 8% of the OM was found in the saponified (acidic) fraction and 35% in the non-saponified fraction. It is striking that for each of the 5 procedures a similar percentage of 40% of the OM was found in the extract. Although acidification does not result in a higher yield of extracted OM (at least not for urban samples from Gent), it was nevertheless decided to retain it since more compounds could be identified and quantified by GC-FID and GC/MS in the extracts and it also gave higher EEOM yields, especially for tropical samples [Kubátová et al., 2000]. However, it was also found that acidification with acetylchloride resulted in partial methylation of the fatty acids of the OM, which is undesirable. It was therefore decided to replace extraction procedure (iv) by:

vi. acidification with acetic acid, followed by 3 x 30 min ultrasonic extraction in CH_2Cl_2.

This extraction procedure is currently used for our routine analyses by GC-FID and GC/MS.

The extraction efficiency was not only dependent on the actual extraction procedure used, but to a much larger extent on the sampling location and thus on the type of carbonaceous aerosol. This became evident by reanalysing filter samples from various locations (Balbina and Rondônia in Brazil and Sde Boker in Israel) for OM and EC, after they had been analysed for OM and EC and subsequently extracted for detailed organic analyses with procedures (i) and (iv). The OM extraction yield was much lower for total filter samples from Brazil than for similar samples from Israel (the results for Israel were similar to those for Gent). Also the particle size of the aerosol plays an important role. For filter collections from Balbina, whereby the aerosol was separated in two size fractions, a much larger extraction yield was noted for the fine size fraction than for the coarse. This was essentially due to the difference in composition between the two size fractions.

As to the GC-FID and GC/MS analyses themselves, they were done after concentrating the combined extracts to 1 mL, filtering and drying this, and redissolving the residue. Part of this solution was then analysed directly, and the remainder was methylated with diazomethane and also analysed. Our GC/FID and GC/MS procedures for routine analyses have changed somewhat over the years. Those originally used are described in detail in Kubátová et al. [2001b]. The more recent procedures are presented in Kubátová et al. [2000].

There is a substantial difference between the extracted OM yield and the EEOM yield (these are respectively 40% and 17% of the OM for total filter samples from Gent). On the other hand, it appeared from our routine GC-FID and GC/MS analyses that certain compounds, such as levoglucosan (which is a general marker for wood combustion), were present in high concentrations, but could not be quantified. Therefore, we started developing a method for the quantitative determination of levoglucosan and related monosaccharide anhydrides in aerosol samples. The method involves addition of a recovery standard (1,2,3-trihydroxyhexane), extraction with the new extraction procedure (vi), and trimethylsilylation.

In the course of our GC-FID and GC/MS analyses of urban and tropical aerosol samples it was found that several unknown compounds were present in notable concentration. Various types of derivatisations and solid-phase extraction in combination with GC/MS were employed for the characterisation and structure elucidation of these unknowns [Kubátová et al., 2000; Zdráhal et al., 2001a, 2001b].

3.3 Analytical-methodological development on individual particle analysis

Methodological development work was done for transmission electron microscopy (TEM) with selected area electron diffraction (SAED), and for two other microscopical analytical techniques, namely microprobe X-ray fluorescence (μ-XRF) with laboratory and synchrotron radiation sources and static secondary ion mass spectrometry (S-SIMS).

The TEM investigations were carried out on a JEOL JEM 1200EX at 80 kV, whereby EDX analyses were done with a Tracor Northern TN5500 X-ray microanalysis. The electron diffraction measurements were performed on a Philips CM 20 at 200 kV (EMAT-RUCA-University of Antwerp) [Sobanska et al., 2000].

With regard to μ-XRF and related techniques, methodological studies with aerosol particles were done at Hasylab in Hamburg and at the European Synchrotron Radiation Facility (ESRF) in Grenoble. As a preparation for the activities with beam line ID 22 of ESRF and to test the methodology, a number of measurements were performed on fly ash particles with dimensions of 10 to 50 μm. This was done, on one side, with a laboratory μ-XRF and μ-tomography instrument based on a rotating anode X-ray tube and capillary X-ray optics (built in the laboratory), and, on the other side, with the microfocus beam line, BL 1, of ESRF. The samples investigated were fly ash particles from a lignite fired power plant in Japan. This material was selected because it had been studied earlier with other microanalytical methods amongst others at other synchrotron facilities. Also, the particles were of a size (i.e., in excess of 10 μm EAD) which is compatible with the X-ray beam size of beam line BL 1. In accordance with the earlier measurements it was found that the particles are

inhomogeneous in composition and structure. Two-dimensional images with μ-XRF and microprobe X-ray diffraction (μ-XRD) were obtained with a lateral resolution of the order of 1 μm [Rindby et al., 1997]. The methodology, which also includes preliminary measurements with the tube excited system, is further described by Adams et al. [1998] and Vincze et al. [1998].

With the new beamline ID 22 we performed preliminary measurements on fallout particles from the Chernobyl explosion sampled in rural areas in Norway. The intention was to test the possibilities of imaging with X-ray absorption spectrometry, namely with X-ray absorption fine structure analysis (XANES). The 3 D repartition of uranium in 10 to 30 μm size particles and its different valence states could be established. Inside the particles, uranium seemed to be reduced to the elemental state, probably as a result of reactions with graphite or elemental carbon at the moment of the explosion.

S-SIMS allows the determination, with a lateral resolution of the order of 100 nm, of the elementary composition, the chemical composition of elemental constituents (speciation), and organic compounds at the surface of the microscopical object and in a subsurface shallow layer. In May 1997, a S-SIMS instrument (Cameca TOF SIMS) was acquired. The analytical methodology of SIMS for atmospheric particles had not been explored previously and was therefore studied within the current project. In a first phase, the characteristics of a number of collection substrates for aerosol sampling (aluminium foil, indium foil, and silver membranes) were studied with scanning electron microscopy with energy-dispersive X-ray analysis attachment (SEM-EDS) and the TOF-SIMS instrument. The results with SEM showed that the Ag-membranes are not appropriate as their pore size of 2-3 μm interferes with the observation of the particles. The purity of the three substrates was studied with TOF-SIMS and it was found that the impurity levels are comparable for the three substrates. It was concluded that indium foils are the best substrates for the collection of the air particulates. Aluminium substrates are less suitable as they prevent the determination of Al, which is one of the most important elements in aerosols. The general aspects of the methodology were described by Van Vaeck et al. [1998a]. Subsequently, we concentrated on the speciation of pure inorganic compounds as a preparation stage for obtaining molecular information on real atmospheric samples. A set of binary salts was analysed in which the mass spectra were systematically studied to characterise the different type of features, such as fragment ions, adduct ions, molecular ions, cluster ions and recombination clusters. Special attention was given to the development of a suitable sample preparation procedure and the influence of the instrumental parameters on the reproducibility of the measurements. Results showed that the SIMS spectra yield sufficient qualitative information to deduce the molecular formula of the salts. In addition, fine speciation

is possible (e.g., to distinguish between CuCl and $CuCl_2$) by ratio-ing adduct ions. The speciation of individual compounds in multi-component systems can, however, be inherently limited by the occurrence of "cross contamination" (e.g., a neutral from component A combines with an ion of component B). It was therefore necessary to expand the work to mixtures of two pure compounds before addressing speciation analysis in real atmospheric samples. Applications of the method on atmospheric particles sampled near a smelter in Genoa are given in Van Ham et al. [2001]. In this work, S-SIMS supplemented work obtained by micro-PIXE. Measurements were also made for the characterisation of these aerosols on pure Si wafers. Fourier transform laser microprobe mass spectrometry relying on the "selvedge" ionisation appeared to be a valuable technique for the validation of some of the results obtained [Van Vaeck et al., 1998a, 1998b]. An application of the latter technique was the analysis of polycyclic hydrocarbons (PAHs) adsorbed on soot particles. The variation of PAH patterns at different positions in the combustion chamber of an incineration plant was investigated [Zimmermann et al., 2000].

4. AEROSOL RESEARCH IN ARCTIC AND SUB-ARCTIC AREAS

Research was done within the framework of the Arctic Ocean Expedition 1996 (AOE-96), for Summit (72°34'N, 37°38'W, 3170 m asl) in Greenland, at the Zeppelin mountain station (78°54'N, 11°53'E, 474 m asl) in Ny Ålesund, Spitsbergen, at Sevettijärvi (69°35'N, 28°50'E, 130 m asl) in Finnish Lapland, and for two sites in southern Norway, i.e., Birkenes (58°23' N, 8°15' E, 190 m asl) and Skreådalen (58° 49' N, 6°43' E, 465 m asl).

AOE-96 took place in summer 1996. Aerosol filter and cascade impactor samples were collected for chemical analysis by us onboard the Swedish icebreaker *Oden* during Leg-1 of the expedition, i.e. from 20 July to 24 August and between 75°N and 87°N. About 5 days were spent in the open waters between Norway and the ice edge (at about 60°E and 80°N), and the rest of the time was spent in the permanent pack ice of the Nansen and Amundsen basins. Our samplers were a PM10 Teflon filter unit (TF), a Gent PM10 SFU sampler, which provided two size fractions (coarse: 2-10 µm EAD; fine <2 µm EAD) on Nuclepore polycarbonate filters, and a 12-stage small deposit area low pressure impactor (SDI). Particulate matter (PM) was determined for the filters from the TF and SFU devices by weighing at 20°C and 50% RH. All samples were subjected to multi-elemental analysis by PIXE and INAA (for the SDI samples only by PIXE) and the TF samples were also analysed for major anions (methanesulphonate (MSA^-), SO_4^{2-}, Cl^-, Br^-, NO_3^-, NO_2^-) and cations (NH_4^+, Na^+, K^+, Mg^{2+}, Ca^{2+}) by IC. The results indicated that the atmospheric concentrations of the

continental aerosol species (or elements) were substantially lower during AOE-96 than during the 1991 International Arctic Ocean Expedition (IAOE-91). The data from the TF and SFU samplers were used to assess which fraction of the experimentally determined aerosol mass could be reconstituted on the basis of the measured species and elements, and thus aerosol chemical mass closure could be obtained. The dry reconstituted mass was estimated as follows:

(dry PM) = Sea salt + Crustal matter + Sum [nss/ncr-elements(INAA/PIXE)]

$$+ MSA^- + nss\text{-}SO_4^{2-} + NO_3^- + NH_4^+ \quad (1)$$

with nss standing for non-sea-salt and ncr for noncrustal. Sea salt was estimated from Na and Cl using the approach of Virkkula et al. [1999] and crustal matter was estimated from a number of crustal elements, as done by Cahill et al. [1989] and Chan et al. [1997], so that equation (1) became:

(dry PM) = [Cl + 1.4486 Na] + [1.16 (1.90 Al + 2.15 Si + 1.41 nss-Ca + 1.67 Ti

+ 2.09 Fe)] + Sum [nss/ncr-elements(INAA/PIXE)]

$$+ MSA^- + nss\text{-}SO_4^{2-} + NO_3^- + NH_4^+ \quad (2)$$

One aerosol constituent not considered so far is water, so that the reconstituted PM is actually the dry PM, as indicated. Since the gravimetric PM was determined at 50% RH and the aerosol samples contained large proportions of hygroscopic components, such as sea salt and sulphate, water cannot be neglected. It was estimated from the composition of the samples using a thermodynamic model described by Clegg et al. [1998]. Water estimated in this way should be considered as an upper limit (maximum value) for the actual water mass in the samples. The difference between the gravimetric PM and the sum of (dry PM) + water (at 50% RH) varied from +23 to -6% for the TF samples, but it was only significant (and positive) for two of the eight samples, so that it was concluded that other aerosol types or species than those considered provided a significant contribution to the gravimetric PM in those two samples. A plausible candidate for the missing aerosol type is the carbonaceous aerosol (including so-called biological aerosols). Bigg and Leck [2001] examined individual particles collected during AOE-96 by transmission electron microscopy and found that particles larger than 100 nm contained significant organic material. This was even the case for most sea-salt particles. In addition to organic compounds, bacteria and diatoms were observed. The volume or mass contribution of the organics to the aerosol was not quantified by Bigg and Leck [2001], however, and it is also unclear which variability one may expect in the levels of the organic/biological PM when considering long collection periods, such as those used

for the TF samples. It is noteworthy that the two TF samples with significant unexplained PM are among the three TF samples with lowest gravimetric PM levels. This suggests that closure was obtained for the other samples because the relative contribution from the organic and biological aerosols became less important. The missing PM (± 1s) was 46 ± 20 ng m^{-3} and 85 ± 20 ng m^{-3} in the two TF samples. These data represent rough first estimates of the organic/biological aerosol PM10 level in the high Arctic during summer. Clearly, they should be confirmed by actual OC/EC measurements in future expeditions. The data indicated that sea salt was normally the dominant aerosol type, followed by water, and then nss-sulphate. When averaging the percentage contributions over all 8 samples, the following results were obtained: 45% for sea-salt, 27% for water, 10% for nss-sulphate, 6% for crustal matter, 2.8% for MSA, 2.3% for NH_4^+, 1.5% for NO_3^-, and 0.4% for the nss/ncr-elements. For the SFU samples, separate mass closure calculations were performed for the fine (<2 µm EAD) size fraction, the coarse fraction (2-10 µm EAD), and the sum of both (SFU-sum). The results of the chemical mass closure calculations for the sum of the fine and coarse filters agreed overall quite well with the results for the TF filters. The separate data for the coarse and fine SFU filters indicated that there was only missing mass for two fine filters. Considering that we attributed the missing mass essentially to organic/biological aerosols, it is tentatively concluded that these aerosols are mainly present in the fine (<2 µm EAD) size fraction. When averaging the percentage contribution of the various aerosol types and species to the gravimetric SFU fine PM over all 8 samples, the results were as follows: 38% for sea-salt, 27% for water, 18% for nss-sulphate, 3.5% for crustal matter, 3.1% for MSA, 3.3% for NH_4^+, 1.5% for NO_3^-, and 0.4% for the nss/ncr-elements. Compared to the PM10 aerosol, sea-salt is less important in the fine aerosol, but is on average still the main contributor to the fine PM. The contribution of nss-sulphate to the fine PM is substantially larger than that to the total PM (on average 18% versus 10%), and for three of the eight sampling periods, fine nss-sulphate was more important than fine sea-salt.

During AOE-96 SDI samples had also been taken by the Finnish Meteorological Institute (FMI) and analysed for anionic and cationic species by IC. The data set obtained was combined with the PIXE data of our SDI samples. Continuous particle size spectra were extracted from the raw data using a data inversion method. Log-normal size distribution modes were fitted to the continuous spectra. Clear and varying modal structures for aerosols consisting of primary sea salt particles or of secondary particles related to dimethylsulphide emissions were found. The concentration levels of all modes decreased rapidly when the distance from open sea increased. The major ions in the submicrometer size range were MSA, sulphate, and ammonium. They had most of the time a clear Aitken mode and one or two accumulation modes, with aerodynamic mass median diameters around 0.1 µm, 0.3

μm, and between 0.5-1.0 μm, respectively. Primary sea-salt particles formed a mode with an aerodynamic mass median diameter around 2 μm. The observed modal structure of the submicron SO_4^{2-}, MSA, and NH_4^+ mass size distributions was consistent with the mass size distribution derived from the number size distribution measured with a differential mobility particle sizer. More details on this SDI work are given by Hillamo et al. [2001].

With regard to the aerosol research at Summit, we refer to three published papers [Maenhaut et al., 1997c; Jaffrezo et al., 1998; Kerminen et al., 1998]. Notable was that biomass burning plumes from forest fires in Canada could be detected on top of the Greenland Ice Sheet [Jaffrezo et al., 1998].

For the Zeppelin station at Ny Ålesund, we combined our long-term aerosol composition data sets with aerosol light scattering data sets from the Department of Meteorology of the University of Stockholm (MISU), and studied the interrelations between the chemical composition and light scattering. It was found that fine non-sea-salt sulphate provided the largest contribution to the total light scattering coefficient. More details on this study can be found elsewhere [Maenhaut et al., 1999e].

From July 1992 until January 1996 atmospheric aerosol samples had been collected nearly continuously in two size fractions at Sevettijärvi in northern Finland. The samples were analysed for the PM, BC, major anions and cations (by IC), and up to 46 elements (by a combination of INAA and PIXE). The fine fraction data set was subjected to absolute principal component analysis (APCA) [Maenhaut and Cafmeyer, 1987] in order to examine the interrelations between the various chemical species and elements, and to identify the major aerosol components and/or source types. Furthermore, trajectory statistics [Stohl, 1996] was employed to identify the major source regions of sulphate and of selected elements and heavy metals. The trajectories used were 3-dimensional 96-hour back-trajectories arriving at 950 hPa. Six components were identified by APCA. The first component had high loadings (of 0.7 to 0.9) for S, K, V, Mn, Zn, ammonium, BC, and the PM; it represents a general pollution component. The second component was highly loaded with Cu and Ni (loadings of 0.9) and is most likely mainly due to the Cu-Ni smelters of Nikel and Zapolyarni on the Kola peninsula, at about 60 km to the east of Sevettijärvi. The third component was a crustal component (with Al, Si, and Fe); the fourth component sea salt (Na, Cl). The fifth component was mostly loaded with As, and to a lesser extent also with Se and Sb. And the sixth component was a nearly pure nitrate component. The air trajectories indicated that there was no predominant pathway for air mass transport to the Sevettijärvi site. The air masses came from all directions, but there was some preference for transport from over the sea. The trajectory statistics

analysis showed that the highest levels of fine S at the site were observed for air masses that had passed over Ukraine and European Russia. The maps for K, ammonium, and the PM were rather similar to that for S. Also those for BC, V, Mn, Zn, Sb, and Pb showed some resemblance to that of S, but European Russia was much more important than Ukraine as potential source region for these species and metals. It is noteworthy that most of these species (and metals) which have Ukraine and European Russia as potential source region were also highly correlated with the APCA component 1. This strongly suggests that this component also had the same source regions. The maps for Cu and Ni suggested that these elements had source regions in the Kola peninsula, but also (and even more important ones) in northern Siberia. However, only few trajectories had passed over the latter region, so that the attribution to this region should be considered with caution. The map for As clearly indicated that the Kola peninsula was the most important source area for this element. An article about this study has been published [Maenhaut et al., 1999f]. Other features about our long-term research at Sevettijärvi, including results from chemical mass closure work, were described by Virkkula et al. [1999].

Further with regard to Sevettijärvi, we contributed to the work of the three intensive field campaigns of the European Arctic Aerosol Study (EAAS). These campaigns took place in summer 1997, winter 1998, and summer 1998. Results from this research are described elsewhere [Hillamo et al., 1999; Maenhaut et al., 1999b; Ricard et al., 2001].

As to Birkenes and Skreådalen in southern Norway, we examined the data sets from our 5-year aerosol study. From 29 January 1991 to 6 March 1996, Gent PM10 SFU samplers had been deployed at the two sites for continuous collections in parallel according to a 2-2-3 day schedule. The coarse and fine filters of the nearly 800 SFU samples from each site were analysed for the PM, BC, and over 40 elements. APCA was used to identify the major source types, and chemical mass closure calculations were performed using an approach described by Chan et al. [1997]. The concentrations of PM, BC and the sea-salt elements were very similar at the two sites; the S levels at Skreådalen were 80% of those at Birkenes, and for the crustal elements and anthropogenic metals, the Skreådalen/Birkenes concentration ratio was around 0.6. Scatter plots and time trends indicated that the fine PM and the anthropogenic species (e.g., BC, non-sea-salt (nss) S, noncrustal V) were generally well correlated between the two sites, thus strongly suggesting that their atmospheric levels in southern Norway are mainly due to long-range transport. There was quite some variability in the concentrations from sample to sample, which presumably resulted mainly from variations in meteorological conditions and in air mass origin [Maenhaut et al., 1997b]. Nevertheless, clear seasonal variations were observed for several elements (species). The crustal elements exhibited highest levels during

spring and summer (especially during May). This was also observed by Amundsen et al. [1992] in their study on the total aerosol at Birkenes. Fine iodine showed a maximum in spring and BC was most elevated during the winter months. APCA on the fine data set from Birkenes (with 27 variables included) resulted in five components, i.e., a general pollution component (with loadings in the range 0.7-0.9 for PM, BC, S, K, V, Ni, Cu, Zn, As, Se, Br, In, Sb, I, and Pb), a crustal component (with loadings around 0.9 for Al, Si, Ca, Sc, Ti, Fe, La, and Sm), sea salt (with Na, Mg, and Cl), a weak residual oil burning component (loadings of 0.5 for V and of 0.4 for Ni and S), and a nearly pure Mn component. This last component originates from local Mn sources in southern Norway [Pakkanen et al., 1996; Maenhaut et al., 1997b]. For the chemical mass closure calculations 5 aerosol types were considered, i.e., crustal matter, sea salt, BC, smoke (actually noncrustal K = K - 0.6 Fe), and ammonium sulphate. The 5 aerosol types explained, on average, 70% of the experimental fine PM, and there was no seasonal variation in this percentage. For the coarse size fraction at Birkenes, 63% of the experimental PM was, on average, attributed to the 5 aerosol types, but this percentage exhibited a clear seasonality, and was around 50% in summer versus 70% in winter. The results for Skreådalen were similar to these for Birkenes, but the mass closure was somewhat poorer at that site. The unexplained mass is thought to be mostly attributable to organic aerosol (i.e., to mainly secondary organic particles in the fine size fraction and to primary organic aerosol (including biological aerosol particles) in the coarse fraction) and to a lesser extent to nitrate. Two articles about this work have been published [Hanssen et al., 2000; Maenhaut et al., 2000c]

5. RESEARCH WITHIN THE FRAMEWORK OF THE EUROTRAC-2 AEROSOL SUBPROJECT

Our contribution to the AEROSOL subproject includes the development of analytical methods for OC and EC and for detailed organic compounds, described above in subsections 3.1 and 3.2. During 1998 the methods were evaluated and applied to aerosol samples collected in Gent, during two different seasons (winter and summer). In both seasons, daily samples were taken with three types of collection devices, each with 47-mm diameter filters. Sampler #1 was a Gent PM10 SFU sampler [Maenhaut et al., 1994b], in which the coarse size fraction (2-10 µm EAD) was collected on a Nuclepore polycarbonate filter and the fine size fraction (further denoted as PM2) on a Whatman quartz fibre filter (type QM-A). Sampler #2 was similar to #1, but contained only a single Whatman QM-A filter which collected the PM10 aerosol. Sampler #3 was a “total” filter sampler (Qtot); it also used a Whatman QM-A filter; the particles collected by it are further denoted as PMtot aerosol.

Samplers #1 and #2 operated at 17 L/min, sampler #3 at 150 L/min. Particle mass (PM) was determined for all filters; and all quartz filters were subjected to OC/EC analysis with the TOT technique. Selected filters from sampler #3 were also analysed for detailed organic compounds by GC-FID and GC/MS.

The average aerosol mass concentrations, and the TC/(particle mass) and EC/TC ratios (with TC = OC + EC) for the 1998 winter and summer seasons, as derived from each of the three collection devices, are presented in Table I. For sampler #3 (Qtot), the EC/TC data were recalculated with manual "split point" setting, as described in subsection 3.1. The average PM2/PM10 mass ratio and associated standard deviation (sampler #1) were 0.69 ± 0.10 (N: 34) during winter and 0.67± 0.07 (N: 51) during summer. Clearly, most of the aerosol mass was contained in the fine (<2 μm EAD) size fraction at Gent during the sampling campaigns. PMtot is, on average, very similar to PM10, indicating that there was either relatively little aerosol mass in the size fraction above 10 μm EAD or that this size fraction was not efficiently collected by our "total" aerosol sampler. The mean levels of PM2, PM10 and PMtot for the summer campaign are only 50% of the respective levels during the winter campaign. This difference is mainly attributed to the frequent occurrence of surface inversions during the winter campaign. During both winter and summer, TC was responsible for around one quarter of the aerosol mass, with somewhat higher percentages for the PM2 aerosol than for the PM10 aerosol. EC represented about 25% of TC and was slightly more pronounced in the PM2 aerosol. As already indicated in subsection 3.1, the organic aerosol also contains other atoms (such as H, O, N) besides C, so that the OC data have to be multiplied by a conversion factor in order to obtain organic aerosol mass (organic matter, OM). Using a multiplication factor of 1.4, as is commonly used for urban aerosols [Seinfeld and Pandis, 1998; Turpin et al., 2000], one arrives at a percentage of carbonaceous aerosol (that is the sum of OM plus EC) of one third of the particle mass.

The detailed analyses for organic compounds enabled us to construct organic aerosol apportionments. The average apportionments for the winter and summer samples are shown in Figure 1. The extractable and elutable organic matter (EEOM) fraction, which is determined as the sum of resolved and unresolved mass, corresponded on average to 19(± 7)% and 15(± 3)% of the OM for the winter and summer samples, respectively. The unresolved complex mixture (UCM) was the major part of the EEOM and corresponded to 75% and 65% of it for winter and summer samples, respectively.

Table I: *Average aerosol mass concentrations, (TC/particle mass) ratios, and EC/TC ratios at the Gent sampling site during the 1998 winter and summer sampling campaigns.*

Size fraction (sampler)	part. mass (µg m^{-3})	TC/(part. mass)	EC/TC
Winter [a]			
PM2 (sampler #1)	41 ± 20	0.28 ± 0.07	0.25 ± 0.04
PM10 (sampler #1)	58 ± 28		
PM10 (sampler #2)	60 ± 30	0.24 ± 0.05	0.23 ± 0.03
PMtot (sampler #3)	58 ± 32	0.24 ± 0.05	0.24 ± 0.03
Summer [b]			
PM2 (sampler #1)	20 ± 9	0.26 ± 0.06	0.28 ± 0.05
PM10 (sampler #1)	29 ± 12		
PM10 (sampler #2)	30 ± 13	0.23 ± 0.04	0.25 ± 0.04
PMtot (sampler #3)	29 ± 13	0.23 ± 0.03	0.23 ± 0.03

[a] Winter: period 12 January - 11 March 1998 (number of samples N: 34)
[b] Summer: period 12 June - 21 August 1998 (number of samples N: 51)

The UCM consists mainly of branched and cyclic hydrocarbons and originates from car exhaust [Simoneit, 1984; Rogge et al., 1993b]. For urban aerosols, large percentages of UCM are quite typical. In the resolved OM, over 100 compounds belonging to different classes could be identified. *n*-Alkanes and fatty acids were the prevailing resolved organic compounds in both seasons, but the distribution patterns of individual components within each class showed seasonal differences. The *n*-alkane pattern for summer aerosols was clearly affected by emissions from the vegetation, while that of fatty acids revealed a lower relative abundance of unsaturated fatty acids in summer than winter, that can be related to more extensive atmospheric oxidation of unsaturated fatty acids during summer.

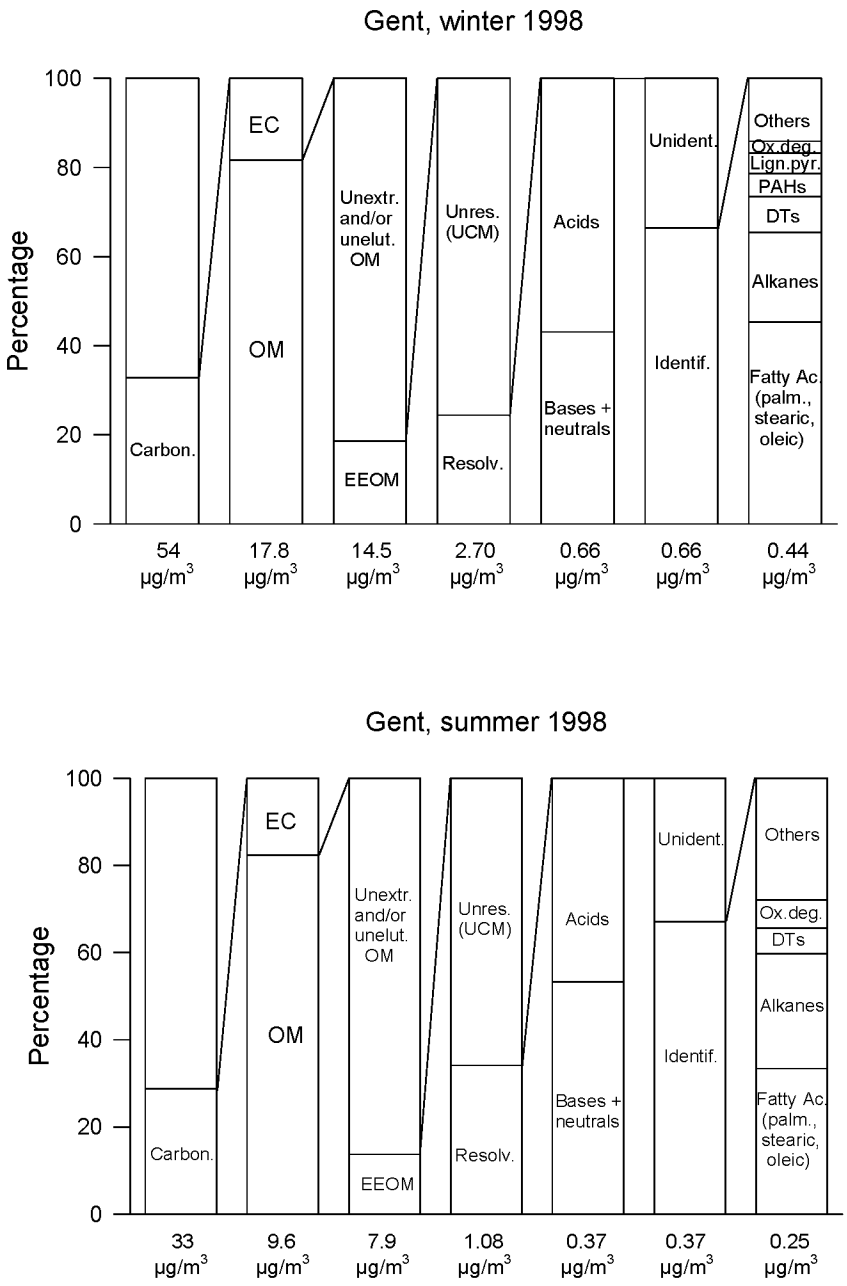

Figure1: *Percentage contributions of different carbonaceous and organic compound classes in winter and summer 1998 "total" filter samples from Gent, Belgium (based on 22 samples from each season). The first column represents the contributions of the carbonaceous (OM + EC) and the inorganic aerosol to the particulate mass (PM). The atmospheric concentrations under the columns indicate the average concentration for the sum of the species in the column. Thus, the concentration under the first column indicates the average PM, that under the last column the average concentration of the sum of identified organic compounds.*

Concentrations of dicarboxylic acids and related products (Ox. deg.) that are believed to be oxidation products of hydrocarbons and fatty acids were highest in summer aerosols. Some individual compounds in the latter class could only be detected in summer samples and showed the highest concentrations on hot summer days that were characterised by maximum temperatures above 25°C and increased ozone concentrations. The latter compounds included novel, recently identified glutaric acid derivatives, namely, 3-isopropyl and 3-acetyl pentanedioic acid, likely originating from atmospheric oxidation of reactive mono- or sesquiterpene precursors that still need to be identified. Two other novel compounds were 3-acetyl hexanedioic acid, and, interestingly, a tricarboxylic acid, 3-carboxy heptanedioic acid. Several compounds were found that are markers of wood combustion, including diterpenoic acids (DTs), lignin pyrolysis products, and levoglucosan. The quantitative results obtained for diterpenoic acids and lignin pyrolysis products indicated that contributions from wood combustion are more important in winter than in summer. There was evidence that both soft and hard wood burning contribute to the organic aerosol, but that hard wood burning prevails during winter. Polyaromatic hydrocarbons (PAHs) were also more prevalent in winter than in summer. More details about this study are given by Claeys et al. [1999] and Kubátová et al. [1999, 2001a, 2001b].

Besides work on OC, EC, and detailed organic compounds, our contribution to the AEROSOL subproject includes intercomparison and evaluation of methods for measuring important aerosol parameters such as the PM and carbon, determination of the detailed mass size distribution for PM, OC, EC and other important aerosol species, chemical mass closure work, and source (type) apportionment.

During 1999 and 2000, intercomparisons were made at Gent of filter collections and in-situ measurements for the aerosol particle mass and elemental/black carbon. The filter collections (of typically 24 hours) were performed with a PM2.5 sampler, using a Whatman QM-A quartz fibre filter, and the samples were analysed for the PM by weighing (at 20°C and 50% relative humidity) and for OC and EC by the TOT technique (see subsection 3.1). In parallel with the filter collections, the PM and BC in the PM2.5 size fraction were measured in-situ and in real time with a Rupprecht and Patashnick tapered element oscillating microbalance (TEOM, model 1400A) and a Magee Scientific aethalometer (tape-feeder model AE-14U), respectively. Both instruments were operated with 5 min time resolution, but the results were averaged for each filter collection period. During 1999 and 2000, the TEOM values were on average 77 (± 13) % [N = 64] and 59 (± 11) % [N = 85], respectively, of the gravimetric mass derived from the quartz fibre filters. Discrepancies between TEOM and gravimetric aerosol data have been observed by others [e.g., Ayers et al., 1999]

and are attributed to the heating to 50°C (and loss of semi-volatile aerosol) in the TEOM. The comparison of the aethalometer BC data with the EC results from the PM2.5 filter sampler showed that good agreement between both could be obtained when the original BC data were subjected to an empirical correction, as used by Reid et al. [1998]. The average ratios (corrected BC)/EC and associated standard deviations were 0.96 ± 0.08 [N = 65] and 0.88 ± 0.13 [N = 83] for 1999 and 2000, respectively. The average ratios (uncorrected BC)/EC for 1999 and 2000 were 1.38 ± 0.12 [N = 65] and 1.28 ± 0.19 [N = 83]. The results from the study during 1999 are discussed in more detail by Maenhaut et al. [2001a].

Weighing of aerosol filter samples at a specified temperature and relative humidity (normally 20°C and 50% relative humidity) is the reference method for PM determination. However, during the actual filter collection, various artifacts can occur, which may depend upon the type of filter material used. We examined the importance of such artifacts for the fine aerosol at Gent. In January-February 2000, aerosol collections (of typically 24 hours) were done with 3 different Gent PM10 SFU samplers, operating in parallel. The coarse filter was always an Apiezon-coated 8-µm pore size Nuclepore polycarbonate filter, but as fine filter (which collects the <2-µm EAD size fraction), we used a 0.4-µm pore size Nuclepore polycarbonate filter in the first SFU sampler, a Gelman Teflo filter (pore size 2 µm) in the second, and a Whatman QM-A quartz fibre filter in the third. The PM was determined for all filters by weighing at 20°C and 50% relative humidity. It was found that the Nuclepore polycarbonate filters and the Teflo filters collected on average only 74 (± 12) % [N = 37] and 73 (± 10) % [N = 26] of the PM2 PM derived from the quartz fibre filters. The difference may be due to the loss of semi-volatile aerosol for the Nuclepore and Teflo filters or to the collection of gaseous species by the quartz filters or to a combination of both. Further investigations should clarify this.

In September-October 1999, we examined the detailed mass size distribution of the PM, OC, EC, and various elements at Gent, and used the data for aerosol chemical mass closure calculations as a function of particle size. The aerosol collections were done with a 10-stage rotating microorifice uniform deposit impactor (MOUDI) and a 12-stage small deposit area low pressure impactor (SDI). The collection surfaces in the MOUDI consisted of pre-baked aluminium foils, whereas thin polycarbonate films were used in the SDI. Thirty-four parallel samples (of typically 24 hours) were collected. The MOUDI samples were analysed for the PM and for OC and EC. The SDI samples were analysed for up to 27 elements by PIXE. Examples of mass size distributions are shown in Figure 2, which presents the results for PM, OC, EC, and several elements for the samplings of 5-6 October 1999. From looking at the entire data set, it could be concluded that PM and OC exhibited typically a rather similar bimodal size distribution, with most of their mass in the submicrometer size range.

EC was predominantly associated with fine particles, with maximum typically at around 0.2 µm EAD. EC is expected to have a large contribution from traffic (mainly heavy duty vehicles) at the sampling site. Sulphur was also mainly in the fine size range, but with maximum at 0.5 µm EAD. Other elements with mainly a fine mode were V and Ni (both are excellent indicators of residual oil combustion), As, Se, and Pb. The crustal elements (Al, Si, Ti, Fe, Zr) exhibited mostly a unimodal coarse mode size distribution, with maximum at about 4 µm EAD. Soil dust, road dust, and coal fly ash all contribute to the concentrations of these elements. Other elements with mainly a coarse mode were Na, Mg, P, Ca, Cr, Mn, Cu, Ga, and Sr. The element K was generally bimodal. Its fine mode is most likely predominantly due to emissions from biomass burning and waste burning (incinerators). Also Zn and Rb were mostly bimodal.

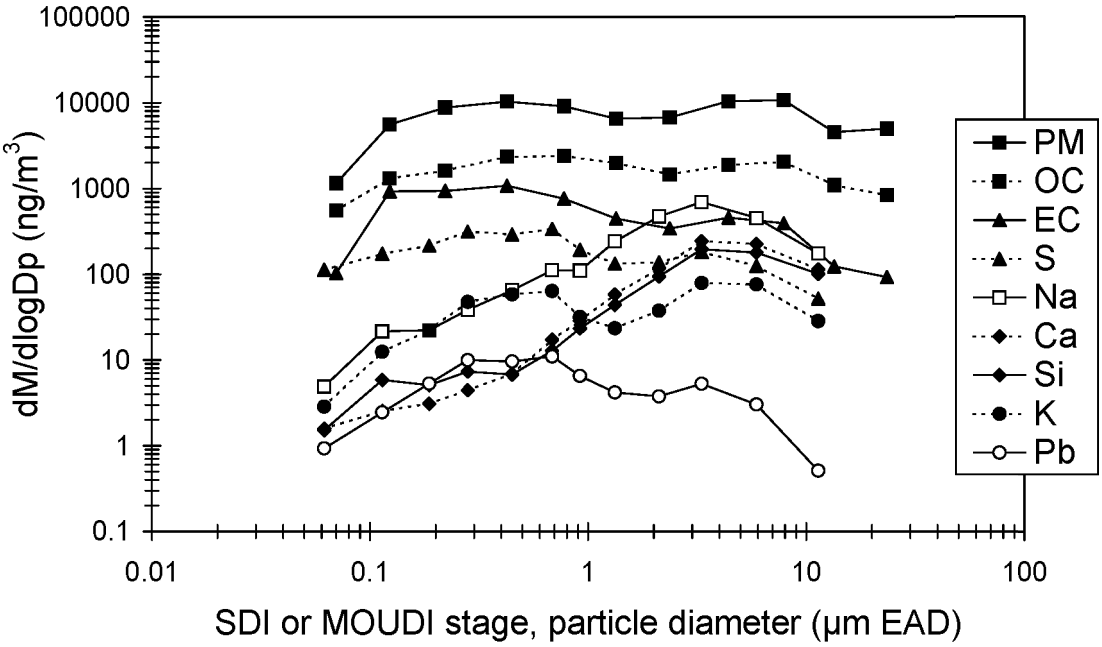

Figure 2: *Mass size distributions for PM, OC, EC, and several elements for the sampling period of 5-6 October 1999. The data for PM, OC, and EC were derived from the MOUDI sample, those for the elements from the SDI sample collected in parallel.*

Mass closure calculations were performed in a similar way as done by Chan et al. [1997]. Six aerosol types were considered: (1) organic aerosol, which was estimated as 1.4 OC, (2) EC, (3) ammonium sulphate, (4) sea salt, (5) crustal matter, and (6) smoke (actually, noncrustal K = K - 0.6 Fe). The average percentage (averaged over all samples) of the gravimetric PM attributed to each of the six aerosol types as a function of particle size in shown in Figure 3. As expected, crustal matter and sea salt provide a larger contribution in the supermicrometer size range than they do in the submicrometer size range. The opposite is noticed for ammonium sulphate and

EC. The percentage contribution from organic aerosol to the gravimetric PM is rather constant in the size range from 8 µm EAD down to 0.2 µm EAD, but increases clearly with decreasing particle size below 0.2 µm EAD. The very fine organic aerosol consists undoubtedly predominantly of secondary organic aerosol (SOA) and emissions from traffic are expected to provide the largest contribution to it. Average percentage attributions of the gravimetric PM to each of the 6 aerosol types were calculated for the submicrometer (<1 µm EAD) and supermicrometer (1-10 µm EAD) size ranges. The major aerosol types in the submicrometer fraction are organic aerosol (on average responsible for 32% of the PM), ammonium sulphate (27%) and EC (10%). In the supermicrometer size range, organic aerosol (28% of the PM) and crustal material (24%) prevail; ammonium sulphate and sea salt are responsible for about 10% each. On average, 74% of the gravimetric PM is accounted for by the aerosol types considered. The unexplained mass is likely attributable to ammonium nitrate and water. The percentage of organic aerosol, obtained in this study in fall 1999, is quite similar to that derived from the filter collections in winter and summer 1998. The fall 1999 study is described in more detail by Maenhaut et al. [2001b, 2001c].

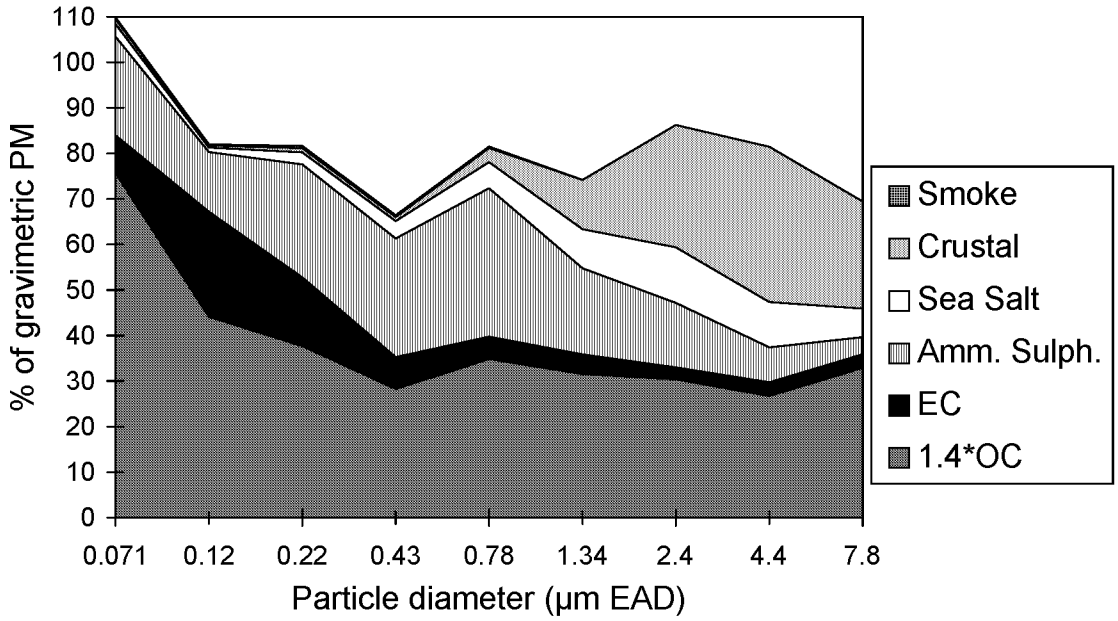

Figure 3: *Average percentage attribution of the gravimetric aerosol mass (PM) to 6 aerosol types as a function of particle size during fall 1999 at Gent (based on 34 samples).*

During 2000 we participated in the INTERCOMP 2000 experiment of the EURO-TRAC-2 AEROSOL subproject. The field work for INTERCOMP 2000 took place from 4 to 14 April 2000 at the Institute for Tropospheric Research (IfT) research station Melpitz, about 50 km north-east of Leipzig, Germany. Eight European research groups participated in the field work, and 6 other groups received samples for analysis. The objectives of the experiment were (1) to intercompare instruments and

methods for measuring the particulate mass (PM) and various aerosol types (e.g., crustal matter, nitrate, carbonaceous aerosols), (2) to assess to which extent the gravimetric particulate mass could be reconstituted on the basis of the various aerosol types (or components) measured, and thus aerosol chemical mass closure could be obtained for the site, and (3) to identify the source categories of the aerosol particles and to apportion the PM and the major aerosol types to these categories. We participated in the field work of the experiment and deployed various filter collectors, two cascade impactors, and two in-situ instruments at the site. Most of our analyses were completed before the end of the OSTC project, but the intercomparisons of our data with the data from the other groups and the chemical mass closure work were started in 2001.

In preparation for the EC-EUROTRAC aerosol phenomenology workshop at Ispra in January 2001, we started doing chemical mass closure calculations for our various long-term aerosol data sets for European sites. These sites are (1) Sevettijärvi (69° 35'N, 28°50'E, 130 m asl) in northern Finland (data set for the period from 27 October 1993 to 14 December 1994 and from 4 March 1995 to 15 January 1996); (2) Birkenes (58°23' N, 8°15' E, 190 m asl) and (3) Skreådalen (58°49' N, 6°43' E, 465 m asl) in southern Norway (data sets from 29 January 1991 to 6 March 1996); (4) Gent (51°01' N, 3°44' E, 10 m asl) in Belgium (data set from 26 May 1993 to 14 July 1994); and (5) Waasmunster (51°07' N, 4°05' E, 20 m asl) in Belgium (data set from 16 July 1994 to 23 November 1995). The results from the chemical mass closure calculations for the two sites in southern Norway (Birkenes and Skreådalen) were partially discussed in Section 4.

6. COMPREHENSIVE STUDIES ON CHEMICAL, PHYSICAL, AND OPTICAL AEROSOL PROPERTIES IN THE MEDITERRANEAN AND ASSESSMENT OF THE DIRECT RADIATIVE FORCING BY AEROSOLS

These studies are performed in close co-operation with foreign research groups, especially with the Biogeochemistry Department (director: Prof. Dr. M.O. Andreae) of the Max Planck Institute for Chemistry (MPIC), Mainz, Germany, and the Ben Gurion University (BGU) of the Negev, Israel (Dr. A. Karnieli), and in part also with the Laboratory of Atmospheric Physics, Aristotle University of Thessaloniki (AUTH), Greece (Prof. Dr. C. Zerefos).

Both long-term and intensive chemical, physical, and optical (radiative) aerosol measurements were conducted at Sde Boker (30°51'N, 34°47'E, 470 m asl), Israel. The long-term measurements started in January 1995 and are still going on. The intensive measurements were conducted during two campaigns (of about 4 weeks

each), the first one, called ARACHNE-96, in June-July 1996, the other, ARACHNE-97, in February-March 1997.

In the long-term measurements, aerosol samples are collected with a Gent PM10 SFU sampler according to a 2-2-3-day schedule and analysed for the PM, BC, and over 40 elements. From December 1995 through September 1997, an integrating nephelometer (TSI 3563) was used for the continuous measurement of the aerosol scattering and backscattering coefficients at 3 wavelengths (450, 550, and 700 nm), and it was then replaced by a Radiance Research unit which only measures the scattering at 550 nm. Furthermore, measurements of vertical column-integrated aerosol optical depth and aerosol properties are conducted at the site on a nearly continuous basis with an automatic tracking combined sunphotometer/sky radiometer (CIMEL Electronique 318A).

During the intensive campaigns, a wide array of instruments was used for measuring the aerosol chemical, physical, and optical (radiative) properties and for measuring selected atmospheric trace gases (CO, CO_2, SO_2, O_3). Details on most of the instruments used can be found in publications by Maenhaut et al. [1999d], Ichoku et al. [1999], and Formenti et al. [2001b].

A comprehensive article on the physical and chemical aerosol characteristics and their interrelation for ARACHNE-96 was written by Formenti et al. [2001b]. In brief, fine non-sea-salt (nss)-SO_4^{2-} averaged 9 ± 3 μg m^{-3} and fine black carbon averaged 1.4 ± 0.5 μg m^{-3}, comparable to values observed off the east coast of the United States. Optical parameters relevant for radiative forcing calculations were determined. The backscatter ratio was β = 0.13 ± 0.01. The mass absorption efficiency for fine black carbon ($\alpha_{a,BCEf}$) was estimated as 8.9 ± 1.3 m^2 g^{-1} at 550 nm, while the mass scattering efficiency for fine nss-SO_4^{2-} ($\alpha_{s,nss\text{-}SO4^{2-}f}$) was 7.4 ± 2.0 m^2 g^{-1}. The average dry single scattering albedo (ω_0) characterising polluted conditions was 0.89, whereas during "clean" periods ω_0 was 0.94. The direct radiative effect of the pollution aerosols was estimated to be cooling. At low altitudes (below 800 hPa), the area was generally impacted by air masses travelling over the Balkan region, Greece, and Turkey. Additional pollution was often added to these air masses along the Israeli Mediterranean coast, where population and industrial centres are concentrated. At higher levels (700 and 500 hPa), air masses came either from eastern Europe or from North Africa (Algerian or Egyptian deserts). The combination of measurements of SO_2, CO, condensation nuclei (CN), and accumulation mode particles allowed us to characterise the air masses impacting the site in terms of a mixture of local and long-range transported pollution. In particular, the lack of correlation between SO_2 and nss-SO_4^{2-} indicated that the conversion of regional SO_2 into the particulate phase is not an efficient process in summer and that aged

pollution dominates the accumulation mode particle concentrations. The elemental mass size distributions, as derived from cascade impactor samplings during ARACHNE-96, were also examined. Details on this work are given by Maenhaut et al. [1999d].

Also for ARACHNE-97 we examined interrelationships between aerosol characteristics and light scattering [Ichoku et al., 1999]. During this campaign, average background scattering coefficients were about 25 Mm^{-1} at 550 nm wavelength, but strong dust events caused this parameter to rise up to about 800 Mm^{-1}. Backscattering fractions did not depend on aerosol loading, and generally fell in the range of 0.1 to 0.25, comparable to values reported for marine and Arctic environments. Chemical analysis of the aerosol revealed that, in the coarse size range (2-10 μm EAD), Ca was by far the most abundant element followed by Si, both of which are indicators for mineral dust. In the fine size fraction (<2 μm EAD), S generally was the dominant element, except during high dust episodes when Ca and Si were again the most abundant. A preview of the short-term effect of aerosol loading on radiative forcing was provided by measurements of global and diffuse solar radiation, which showed that during high turbidity periods (strong dust events), almost all of the solar radiation reaching the area was scattered or absorbed.

During ARACHNE-97, samples had also been collected for OC/EC analysis and for the determination of detailed organic compounds. The mean ratio of OC to the particulate mass (PM) in the fine size fraction was 0.120 ± 0.046 [N = 25], and the mean ratio EC/PM in the same size fraction: 0.022 ± 0.012 [N=25]. As to the detailed organic compounds, a series of higher alkanes with uneven C-number (range: C_{25}-C_{35}) originating from waxes of higher plants were found in samples taken during intense dust storm episodes.

With regard to the long-term measurements, the data from the TSI 3563 nephelometer and the Gent PM10 SFU sampler were interrelated. This was done for the period December 1995 through September 1997 [Andreae et al., 2001]. The total scattering coefficient at 550 nm showed a median of 66.7 Mm^{-1} (mean value 75.2 Mm^{-1}, std. dev. 41.7 Mm^{-1}) typical of moderately polluted continental air masses. Values of 1000 Mm^{-1} and higher were encountered during severe dust storm events. During the study period, 31 such dust events were detected, which were characterised by a sharp drop in the Ångström coefficient (i.e., the spectral dispersion of the light scattering) to values near zero. When considering the full data set, there was a clear linear relationship between the Ångström coefficient and the log of the (coarse PM/fine PM) ratio, with values around 2 when the (coarse PM/fine PM) ratio was below 1 to values around zero during dust storms, in good agreement with the behaviour expected from Mie theory [Seinfeld and Pandis, 1998]. Mass

scattering efficiencies were obtained by multivariate regression of the scattering coefficients on dust, sulphate, and residual components. Various multiple linear regressions (MLRs) were performed [Maenhaut et al., 1997a; Andreae et al., 2001], including MLRs according to the following equation:

$$\sigma_{sp,\lambda} = k + \alpha_{\lambda,CPM}\,[CPM] + \alpha_{\lambda,Fsulphate}\,[Fsulphate] + \alpha_{\lambda,Fres}\,[Fres] \qquad (3)$$

with $\sigma_{sp,\lambda}$: scattering coefficient, in Mm^{-1}, at wavelength λ (450, 550 or 700 nm)
α: mass scattering efficiency (MSE), in $m^2\ g^{-1}$
in brackets: aerosol type concentration, in $\mu g\ m^{-3}$
CPM: Coarse (2-10 µm EAD) PM
Fsulphate: Fine (<2 µm EAD) sulphate
Fres: Fine residual PM = Fine PM - Fsulphate

For comparison with the literature, we have also computed this regression without the Fres term, which provides information on the scattering efficiency of the combination of fine sulphate itself and the other components associated with it (termed $\alpha_{\lambda,Fsulphate+}$ in Table II).

In Table II we compare our mass scattering efficiencies for 550 nm, as obtained from the above and other MLRs, to values found in the literature. It is important to note, that due to differences in the sampling and analysis regimes, such as the size cut-off for the fine and coarse mode, humidity of the sampled air, and chemical apportionment of the aerosols, the calculated α values are not always directly comparable. Our sulphate scattering efficiency, $\alpha_{550,Fsulphate}$ falls within the range reported for low-humidity conditions by other authors, and coincides with the theoretically predicted value for sulphate particles with a diameter of 0.4-0.5 µm [Charlson et al., 1999]. In contrast, our mass scattering efficiency of 5.2 $m^2\ g^{-1}$ for total FPM, $\alpha_{550,FPM}$, is above the range of literature values (2.4 to 4.7 $m^2\ g^{-1}$). This discrepancy may be partially due to differences in cut-off size, since the frequently used cut-off at 2.5 µm would result in more dust aerosol being included, and therefore a lower α. Another factor is the fact that the fine aerosol at Sde Boker, because of its aged character, is relatively large, with a sulphate mass median diameter around 0.4-0.5 µm [Maenhaut et al., 1999d], and therefore near the maximum in the scattering efficiency/size relationship [Charlson et al., 1999]. In studies conducted in or near urban regions, such as those by Dzubay et al. [1982], White et al. [1994], or Hegg et al. [1995], the effective fine aerosol diameter is often only about half that typical of our region. Finally, since sulphate dominates the composition of the fine aerosol at Sde Boker, it is to be expected that sulphate and fine-mass α have similar values.

Table II: *Estimates of mass scattering efficiencies for four categories of aerosol. Fsulphate+ refers to the scattering from fine SO_4^{2-} and other, correlated aerosol ingredients present in the sampled air.*

General Location	Date	Altitude	α_{550} (m^2 g^{-1})				Reference
			Fine	Coarse	fine SO_4^{2-}	Fsulphate+	
Southern Sweden	1973-74	Aircraft	--	--	--	5±2 (450 nm)	[Waggoner et al., 1976]
New York City, U.S.A.	1976-77	Surface	--	--	8.8±0.5	--	[Leaderer et al., 1981]
--	--	--	3.1±0.2	--	--	--	[Waggoner et al., 1981]
Houston, U.S.A.	--	Surface	3.5	--	--	--	[Dzubay et al., 1982]
Canadian Arctic	1979-84	Surface	--	--	10.9±1.1	--	[Barrie and Hoff, 1985]
Maryland, Long Island, U.S.A.	1980-83	Aircraft	--	--	--	12.0±1.4	[ten Brink et al., 1987]
Eastern U.S.A.	--	Surface	--	--	5	--	[White, 1990]
--	--	--	--	--	5	8.5	[Charlson et al., 1991, 1992]
NE Atlantic, Azores Islands	1992	0-2.7 km	--	--	2.8±0.14	2-26.3	[Hegg et al., 1993]
Southwest U.S.A.	1989	Surface	2.4-2.5	0.34-0.45	--	--	[White et al., 1994]
Northeastern Atlantic Seaboard	1993	0.3-2 km	3.2	--	2.2±0.4	2.1±0.8	[Hegg et al., 1995]
Pacific Ocean	1991-92	Surface	--	--	3.6±1.1	--	[Quinn et al., 1995]
NE Atlantic (ASTEX)	--	0-3 km	4±0.7	1.1±0.2	~5	5-16	[Clarke et al., 1996]
Barbados	1994	Surface	--	0.83±0.4	--	--	[Li et al., 1996]
Pacific Ocean	1993-94	Surface	--	--	4.3-7.5	--	[Quinn et al., 1996]
North Sea, Netherlands	1993	Surface	--	--	--	20	[ten Brink et al., 1996]
mid Atlantic coast, U.S.A.	1996	0-4 km	2.8	--	2.7±1.3	--	[Hegg et al., 1997]
Hungary, rural winter	1994-95	Surface	--	--	8.3	--	[Meszaros et al., 1998]
Hungary, rural summer	1995	Surface	--	--	5.9±2	--	[Meszaros et al., 1998]
Negev Desert, Israel, winter	1997	Surface	3.7±0.6	0.12±0.05	--	--	[Ichoku et al., 1999]
Negev Desert, Israel, summer	1996	Surface	--	--	7.4±2.0	--	[Formenti et al., 2001b]
Negev Desert, Israel	1995-97	Surface	5.2±0.2	0.31±0.03	5.5±0.4	7.9±0.5	This work

An analysis of the contributions of the various aerosol components to the total scattering observed showed that anthropogenic aerosol accounted for about 70% of scattering. The rest was dominated by the effect of the large dust events mentioned above, and of small dust episodes typically occurring during mid-afternoon.

To obtain an initial, rough estimate of the radiative forcing by anthropogenic aerosols in the study region, we estimated the radiative forcing efficiency (RFE) at the top of the atmosphere (TOA), i.e., the amount of radiative forcing corresponding to a unity increase in aerosol optical thickness using an equation given by Anderson et al. [1999], based on the analysis of Haywood and Shine [1995]. In this estimation we used the average dry single scattering albedo (ω_0) of 0.92 ± 0.03 obtained during ARACHNE-96 [Formenti et al., 2001b]. We obtained a RFE of -12.8 W m^{-2} over land and -55.2 W m^{-2} over the sea. Using the long-term average aerosol optical thickness (AOT) at 670 nm measured at Sde Boker of 0.16 [Holben et al., 2001] and a 70% anthropogenic contribution to AOT based on the 70% anthropogenic contribution to total scattering, we obtained TOA forcing estimates of -1.4 and -6.2 W m^{-2} over land and sea, respectively. As an alternative to this rough estimate of radiative forcing, we computed the TOA forcing due to the anthropogenic aerosol using the Streamer radiative code [Key and Schweiger, 1998] for the same aerosol optical depth and the aerosol optical properties derived from our measurements. This yielded an annually averaged clear-sky radiative forcing of -3.5 and -6.9 W m^{-2} over desert and ocean surfaces, respectively. Assuming a negligible aerosol direct effect in cloudy sky and using the climatological mean cloud cover of 29%, this translates into an all-sky radiative forcing of -2.5 and -4.9 W m^{-2} over desert and ocean surfaces, respectively. Both our crude estimate, based on the formula by Anderson et al. [1999], and the detailed radiative transfer calculation are in good agreement with predictions from global models of aerosol radiative forcing. For example, Haywood and Shine [1995] predicted a TOA forcing of -2 to -3 W m^{-2} for our study region (without explicitly distinguishing between land and sea areas).

For further comparison with model predictions of forcing, we estimated the sulphate forcing alone and obtained values of -2.3 and -4.7 W m^{-2} over land and sea, respectively. These values are in good agreement with the model predictions for climate forcing due to sulphate in our region, which fall in the range of -2 to -5 W m^{-2} [Charlson et al., 1991; Boucher and Anderson, 1995; Feichter et al., 1997; Langmann et al., 1998; Penner et al., 1998]. Overall, we conclude that our data provide strong support for a negative radiative forcing due to anthropogenic aerosols in the eastern Mediterranean region, and that the magnitude of this forcing is in good agreement with current model predictions.

For the long-term fine and coarse aerosol chemical data sets, covering the 4-year period from January 1995 through November 1998, it was examined to which extent the experimental PM could be explained by the sea salt, mineral dust, and nss-sulphate aerosol types (which were derived on the basis of the PIXE/INAA elemental data) and by some additional components, such as nitrate, ammonium, OC and EC (these additional components were only measured in a limited number of samples). This work involved a combination of chemical mass balance (CMB) and pure chemical mass closure calculations.

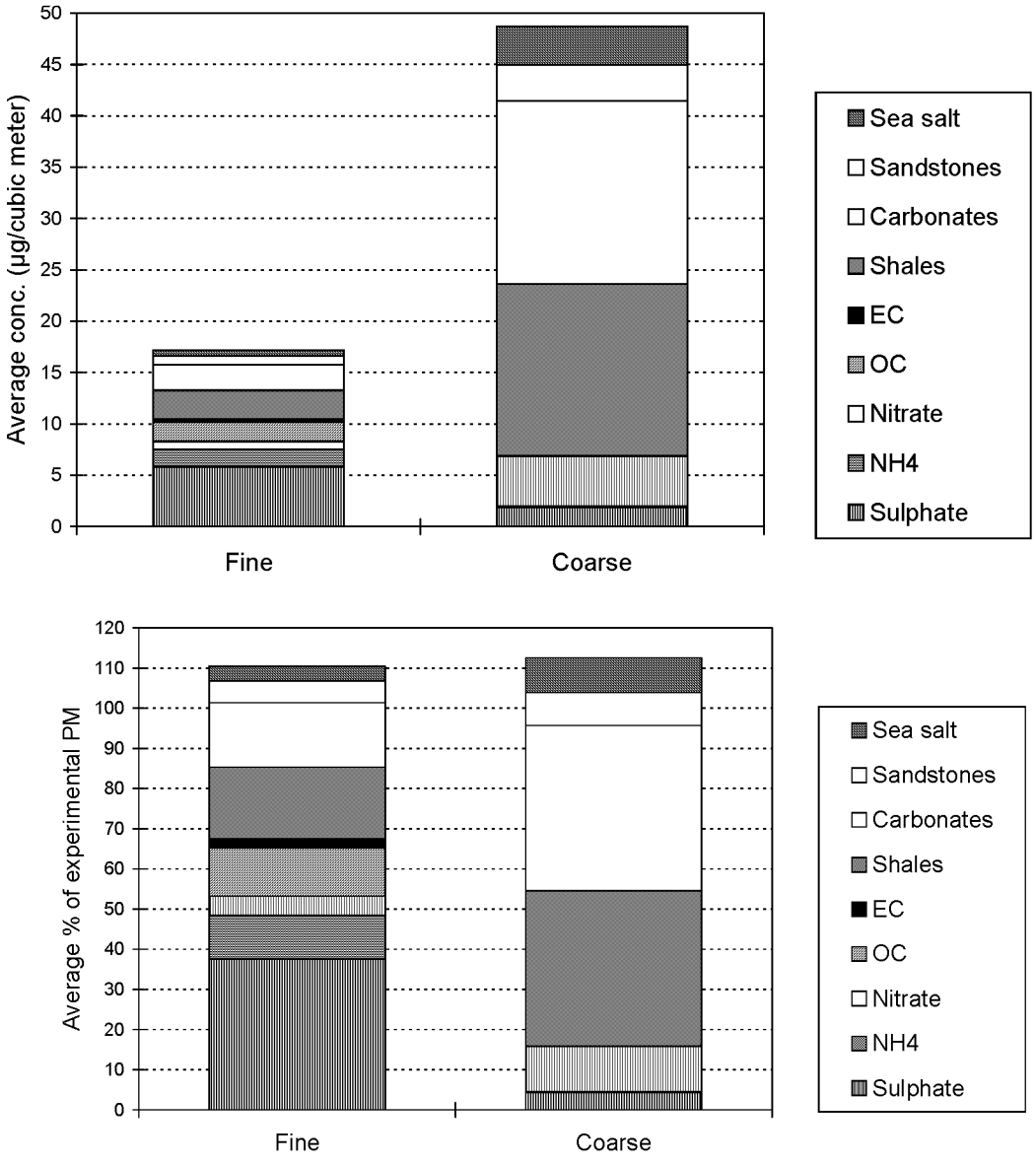

Figure 4: *Average absolute (top) and percentage (bottom) apportionment of the gravimetric aerosol mass (PM) to various aerosol types and components in the fine and coarse size fractions at Sde Boker (4-year period, Jan. 1995 through Nov. 1998, 622 SFU samples).*

In the CMB calculation, three different mineral dust profiles were included, i.e., shales, carbonates, and sandstones. The average apportionments (averaged over all samples) of the gravimetric PM to the various aerosol types and components in the fine and coarse size fractions are shown in Figure 4. Both absolute apportionments (average atmospheric concentrations of the various components) and percentage apportionments (average percentages of the aerosol types/components relative to the gravimetric aerosol mass (PM)) are shown. In both size fractions very good mass closure was obtained. On average, nss-sulphate contributed for 38% to the fine PM, ammonium for 11%, and mineral dust for 39%.

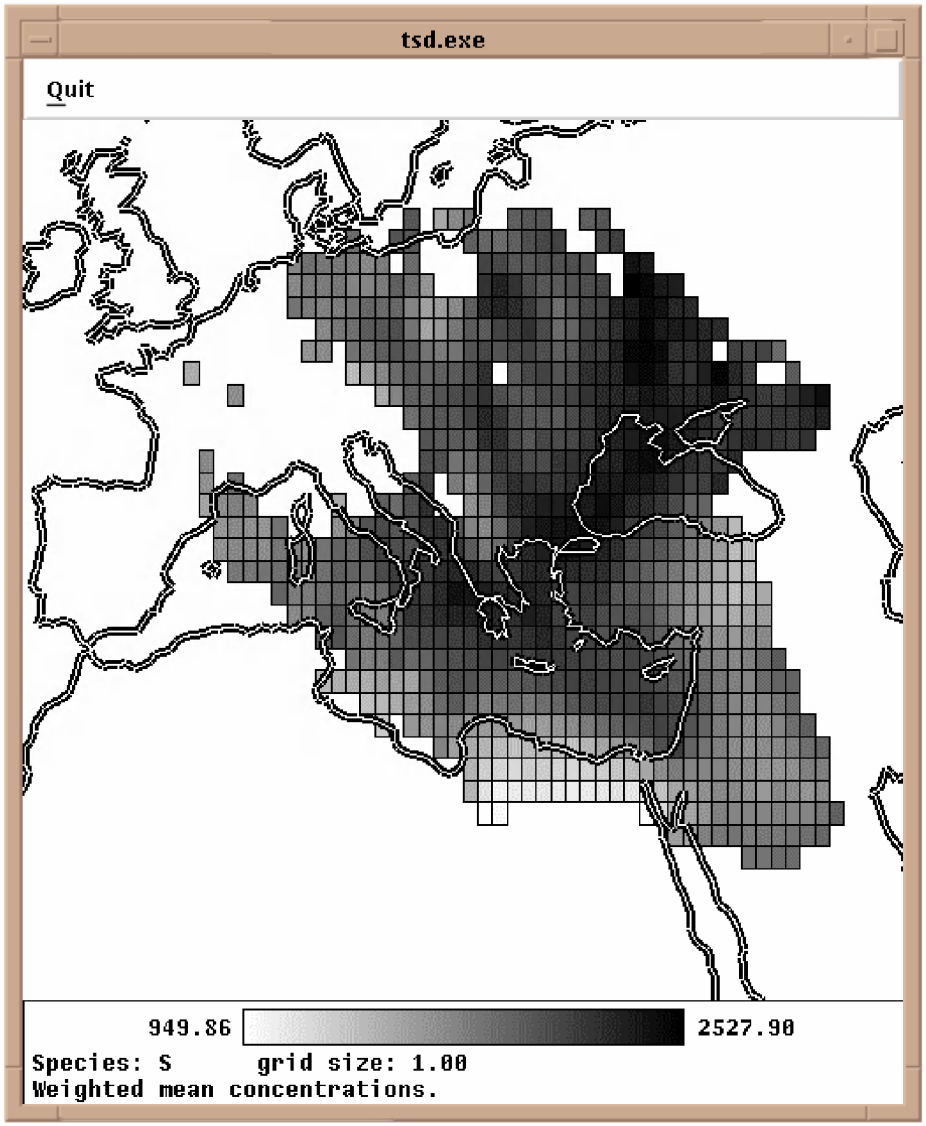

Figure 5: *Concentration field for fine S for the Sde Boker receptor site, as computed using trajectory statistics (see text for details). The grey scale indicates the S concentration in ng* m^{-3}.

Further with regard to the long-term collections, we applied trajectory statistics in order to assess the source regions of some important aerosol constituents [Ptasinski et al, 1998]. The SFU data set for the 3-year period from 1995 through 1997 (493 samples in total) was used for this purpose. The air masses, which arrived at Sde Boker slightly above ground (i.e., at a level corresponding to 950/960 hPa), originated mainly from the north-west, and had remained in the atmospheric boundary layer (below 2000 meters) during the 5 days preceding their arrival. The same was true for the 900 hPa arrival level. Using trajectory statistics, concentration fields were calculated for several fine and coarse species and elements. The concentration field for fine S (obtained by subdividing the domain of interest in grid cells of 1° x 1°) is shown in Figure 5. The concentration in each grid cell indicates the average concentration obtained at the receptor site (i.e., Sde Boker) when the air masses passed over that cell. Figure 5 shows that the highest levels of fine S were associated with air masses that originated in the North; the dominant source region appeared to be Ukraine, followed by the West coast of the Black Sea, and Greece. In contrast, fine V and fine Ni (two indicators of residual fuel burning) were from local/regional origin, including from the power plants along the Israeli coast. Russia seemed to be the major source area of fine Zn. Coarse Ca, an indicator for the carbonate mineral dust, was highest for air masses coming from the south-east and west, consistent with the location of the desert source regions.

Selected SFU filter samples from both ARACHNE-96 (summer) and ARACHNE-97 (winter) were subjected to automated scanning electron microscopy (SEM) with X-ray microanalysis (EPXMA). All together, about 20,000 individual particles were examined. Hierarchical cluster analysis was performed to interpret the data on the basis of particle diameter and composition. Eleven particle classes (groups) were identified and these provided clues on the sources and/or formation processes of the particles. These 11 particle classes were (1) alumino-silicates, (2) $CaCO_3$ particles, (3) $CaSO_4$ particles, (4) other mineral dust particles, (5) sea-salt particles, (6) aged sea salt, (7) transformed mineral dust, (8) pure S particles (which actually consist of ammonium sulphate, ammonium bisulphate or sulphuric acid), (9) industrial particles, (10) P-rich particles, and (11) a particle group with composition that differed from that of the other 10 particle groups. The average contribution, as a function of particle size, of the 11 particle types to the summer and winter samples is shown in Figure 6. This figure shows that there were substantial differences between the two campaigns. The summer samples were enriched in sulphates and mineral dusts, while the winter samples contain more sea salts, aged sea salts, and industrial particles. As expected, mineral dust and sea salt particles become relatively more abundant with increasing particle size, while sulphates and other sulphur containing particles are more pronounced with decreasing particle size. The fine size fraction is enriched in secondary particles, largely below 1 μm diameter, and it showed

evidence of chemical processing in the atmosphere. The secondary sulphate particles were mainly attributed to long-range transport. Regional conversion from calcite to sulphate occurred during summer. Industrial particles originating from local pollution sources were present during winter. More details about this study can be found in a submitted manuscript (S. Sobanska, C. Coeur, W. Maenhaut and F. Adams, SEM-EDX characterization of tropospheric aerosols in the Negev desert (Israel), 2001).

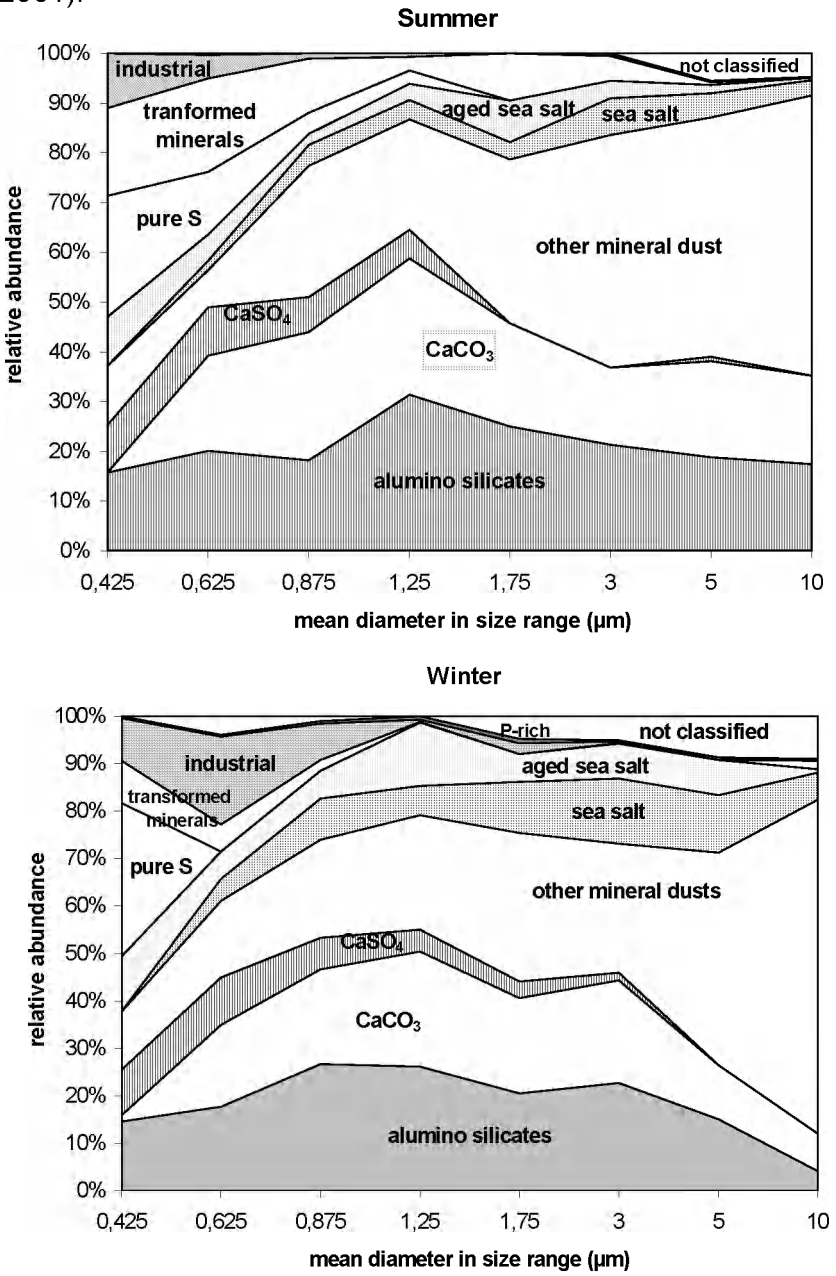

Figure 6: *Average contribution, as a function of particle size, of 11 particle types to the aerosol samples from the 1996 summer and 1997 winter campaigns at Sde Boker.*

During the two campaigns, samples had also been collected on Cu-grids for analysis by transmission electron microscopy (TEM), energy-dispersive X-ray spectrometry (EDX), and selected area electron diffraction (SAED). In the summer samples several types of S-containing particle types could be distinguished, including acidic sulphates and ammonium sulphates, and particles that contained soot, K, Na, and/or Ca in addition to S. Among the soot-containing particles, both internal and external mixtures of soot and sulphate were discerned. Examples of the two different soot-containing particle types and of pure ammonium sulphate particles are shown in Figure 7.

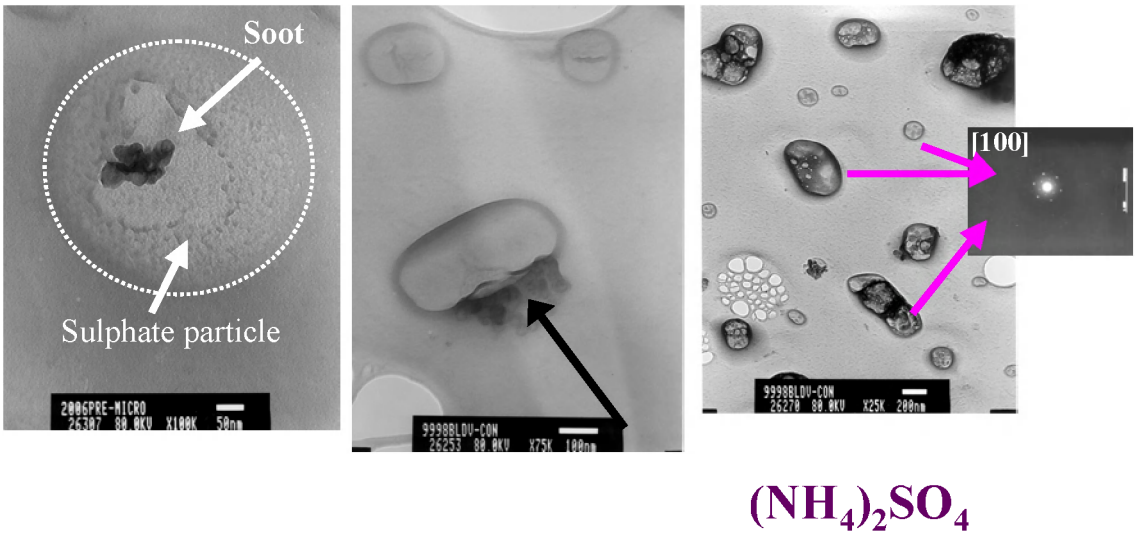

Figure 7: *Examples of internally-mixed (left) and externally mixed (center) soot-containing sulphate particles and of pure ammonium sulphate particles (right), as identified by TEM/EDX/SAED of samples collected during the 1996 summer campaign at Sde Boker.*

Besides the work at the Sde Boker site, work was done at Ouranoupolis (40°23'N, 23 °57'E), a site near Mount Athos in Greece. The research at this site is essentially an effort of the MPIC and AUTH teams, with whom we co-operate. At the Mount Athos site, an integrating nephelometer (TSI 3563) and an automatic tracking combined sunphotometer/sky radiometer (CIMEL Electronique 318A) are continuously operated since fall 1997. From these instruments spectral measurements of the aerosol particle scattering coefficient σ_s and the aerosol optical depth τ_a are obtained. For the period between June and September 1998, such spectral measurements were conducted simultaneously at the Mount Athos and Sde Boker sites. The data were related to 5-day three-dimensional back trajectories at 950, 850, and 550 hPa calculated daily, to assess the influence of long-range transport from particular source regions to the aerosol load at the two sites. It appeared that the eastern Mediterranean basin is severely polluted during summer. Daily average σ_s values at 550 nm were typically in the range of 30-200 Mm^{-1} at both sites. The range obtained

for the summer regional aerosol optical depth τ_a was 0.03-0.52 at 500 nm. Enhanced aerosol extinction was related to transport of polluted air masses from western and eastern Europe. High-altitude transport of mineral dust from northern Africa was observed at both sites, particularly in Israel. For further details on this study, see Formenti et al. [2001a].

7. AEROSOL RESEARCH IN TROPICAL AND SUBTROPICAL REGIONS

This research was conducted in Africa (the Republic of Congo, Zimbabwe, South Africa), the Brazilian Amazon region, northern Australia, and Indonesia. It was done in close co-operation with several foreign research groups, in particular with the Biogeochemistry Department (director: Prof. Dr. M.O. Andreae) of the Max Planck Institute for Chemistry (MPIC), Mainz, Germany, the School of Geosciences of the University of the Witwatersrand, Johannesburg, South Africa (Prof. Dr. H.J. Annegarn), the Institute of Physics of the University of Sao Paulo (USPIF), Brazil (Prof. Dr. P. Artaxo), and the School of Applied Science, Monash University, Churchill, Australia (Prof. Dr. M.A. Hooper). The studies involved both long-term and campaign-type measurements. The emphasis in the studies was placed on the impact of biomass burning and of natural biogenic emissions on the climatically active fine aerosol.

During the Experiment for Regional Sources and Sinks of Oxidants (EXPRESSO-96), SFU samples had been collected during the dry season (in November and December 1996) at a ground site in the tropical rain forest at the N'doki National Park (NNP) in the Republic of Congo. The samples were analysed for up to 26 elements by PIXE. Elements related to mineral dust and pyrogenic aerosol exhibited greater concentrations during the daytime, while aerosol produced by the rain forest exhibited higher concentrations at night. Samples were also collected at two levels on a tower, above and below the canopy, to characterise vegetation sources. APCA identified three major aerosol source types in both the fine and coarse fractions. The fine size fraction contained mineral dust (Al, Si, Ca, Ti, and Fe), pyrogenic (black carbon, K, and Zn), and marine/anthropogenic sulphur components. The coarse size fraction included a mineral dust (Al, Si, Ca, Ti, Mn, and Fe) and two primary biogenic components consisting of K, P, Zn, and S. Absolute principal component scores were calculated for the components of APCA, and temporal trends were compared to 7-day isopycnic backward trajectories. Consistent relationships between the temporal trends of the fine fraction aerosol components and meteorological patterns were observed. Trade wind air masses transported biomass burning and mineral dust aerosol to NNP during the first half of the

experiment. The fine fraction sulphur component correlated well with the pyrogenic activity before the change in meteorological patterns halfway through the experiment. The fine and coarse sulphur concentrations nearly doubled in the latter part of the experiment as a monsoon circulation brought sulphur-enriched aerosol from the Atlantic Ocean. Various industrial activities on the coast of Cameroon and Gabon probably contributed to the high sulphur concentrations as well. This study is described in detail by Roberts et al. [1998, 2001].

Since September 1994, a long-term aerosol study is being performed at Rukomechi (16°S, 29°30' E, 500 m asl), a site at 70 km to the ENE of lake Kariba in Zimbabwe [Maenhaut et al., 2000a]. The aerosols are collected with a Gent PM10 SFU sampler. The coarse and fine filters are analysed for PM, BC, and over 40 elements (from Na upward). The results for the period September 1994 through March 1998 (334 SFU samples) covering several transitions from dry to wet season, were examined by APCA and chemical mass balance (CMB) receptor modelling techniques in order to identify the major aerosol components and/or source types in each of the two size fractions and to apportion the PM and the various aerosol constituents to the aerosol components or source types. By APCA on the fine size fraction data set, 5 components were identified, viz., mineral dust, sea salt, and biomass burning (pyrogenic), pollution, and sulphate components. For the CMB calculations on this fine data set we used 4 source profiles, one for mineral dust, one for sea salt, one for pyrogenic aerosol [Maenhaut et al., 1996d], and a pure $(NH_4)_2SO_4$ profile. The pyrogenic component was the dominant contributor to the total CMB-modelled fine PM during the dry season (period July-November), see Figure 8. During the wet season, sulphate was the dominant aerosol type. The sulphate is thought to originate mainly from fossil fuel burning and industrial activities in sub-equatorial Africa. The 4 profiles reproduced the experimental fine PM rather well during the dry season, but during the wet season about 50% of the experimental fine PM remained unaccounted. Presumably, the unexplained fine PM consists mainly of organic matter from natural origin. For the CMB on the coarse data set 3 source profiles were used (i.e., the same ones as for the fine data with the exception of the pyrogenic profile). The 3-source solution reproduced the experimental coarse PM well during the period April-October. In the other months, and especially during December-January, a large fraction (up to 70% or more) of the coarse PM remained unexplained. This fraction consisted most likely mainly of organic matter from the vegetation.

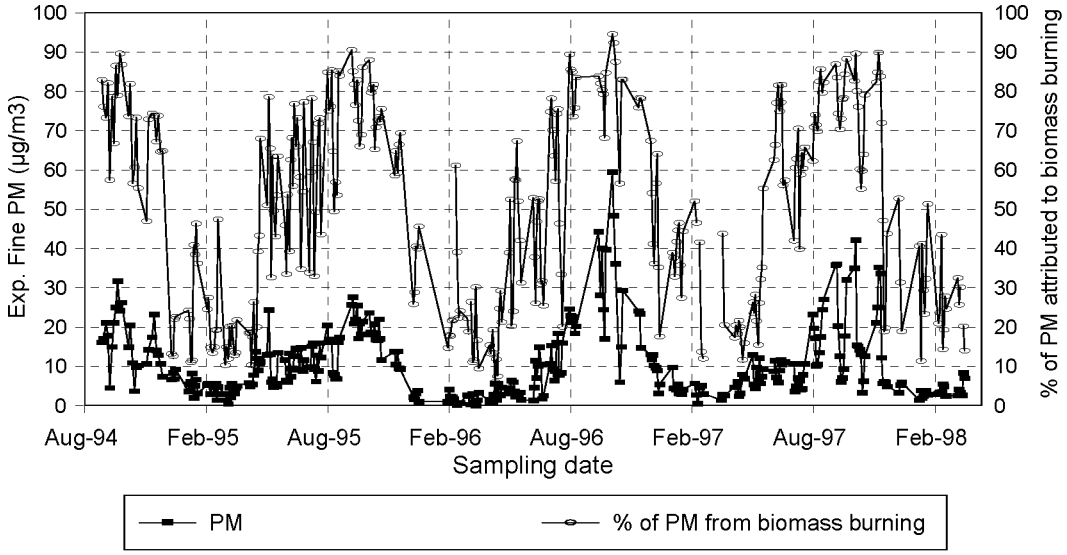

Figure 8: *Time trend of the fine (<2 µm EAD) PM at Rukomechi and percentage contribution of the pyrogenic aerosol to the total CMB-modelled fine PM.*

With regard to the aerosol research in South Africa, we completed an EPXMA study on aerosol samples that had been taken during SAFARI-92 [Liu et al., 1998, 2000a, 2000b], and we finished some other studies that resulted in publications [Andreae et al., 1998; Piketh et al., 1998].

In August-September 2000, we participated in the field work of the final dry season campaign of the Southern African Regional Science Initiative (SAFARI 2000). SAFARI 2000 is an international science initiative aimed at developing a better understanding of the southern African earth-atmosphere-human system (see at: http://safari.gecp.virginia.edu/ for details). Particular emphasis is placed upon biogenic, pyrogenic and anthropogenic emissions, their characterisation and quantification, their transport and transformations in the atmosphere, their influence on regional climate and meteorology, their eventual deposition, and the effects of this deposition on ecosystems. We contributed to SAFARI 2000 by performing various types of aerosol collections and measurements at Skukuza airport (25°01'S, 31°35'E, 260 m asl), in the Kruger National Park, South Africa. An aerosol collector was also deployed for us at Mongu, a site in Zambia. Some of our analyses were completed before the end of the OSTC project, but other analyses and the data interpretation were only started in 2001.

With regard to our research in Brazil, we contributed to the Smoke, Clouds, Aerosols and Radiation - Brazil (SCAR-B) Experiment, for which the field work took place in 1995, and to various activities of the "Large Scale Biosphere-Atmosphere Experiment in Amazonia" (LBA), and more specifically in its "Atmospheric Chemistry

Component" (ACC). Furthermore, we were involved in several long-term studies. For the work within SCAR-B and in the long-term studies we refer to a number of publications [Artaxo et al., 1996, 1998, 2000; Echalar et al., 1998; Maenhaut et al. 1999a, 2001d, 2001e].

As to our work within LBA, in March-April 1998, we participated in a large international measuring campaign, which was named LBA-CLAIRE-98 (CLAIRE = Cooperative LBA Airborne Regional Experiment). The field work for it took place in Brazil and Surinam, during the wet season. We participated in the ground component of the campaign, and especially in the component at Balbina (1°55'S, 59°24'W, 130 km North of Manaus), Brazil. At this site aerosol samples were taken from 23 March until 15 April 1998 (23 days) with various types of filter samplers and cascade impactors. The bulk analyses on the filter samples included measurements of PM, BC, OC/EC, up to 50 elements, and detailed organic compounds. The cascade impactor samples, in contrast, were only analysed for elements (by PIXE). PM, OC and most elements were predominantly associated with the coarse (supermicrometer-sized) particles. During the first 6 days (23-29 March), mineral dust was elevated and responsible for the bulk of the PM. The dust appeared to have been advected by long-range transport from northern Africa, as explained in some detail below. During the second part of the campaign (from 30 March to 15 April), PM was much reduced (coarse PM: 5 μg m^{-3}, fine PM: 1.6 μg m^{-3}) and the organic aerosol became the dominant aerosol type; it was responsible for about two thirds of the PM10 aerosol mass. From separate day and night SFU collections, it appeared that, during the second part of the campaign, there was a substantial difference between day and night in the concentrations of coarse PM and of the elements that were associated with the coarse organic aerosol (P, S, K, Zn, (Ca, Mn)). The average coarse PM level was 8.7 μg m^{-3} during the night versus 2.4 μg m^{-3} during the day. This difference is probably due to increased atmospheric stability and reduced vertical mixing during the night, so that the organic aerosol which is produced from the regional forest cannot be transported aloft. From the detailed analyses for organic compounds, it appeared that 4% of the OM was extractable and elutable (EEOM), and that the fatty acids (palmitic (C_{16}), stearic (C_{18}), and oleic ($C_{18:1}$) acid) were the major identified compounds in the EEOM. A number of dicarboxylic acids, indicative of atmospheric oxidation processes, could also be detected. The EEOM appeared mostly associated with the fine size fraction. The bulk of the organic aerosol is undoubtedly attributable to natural emissions from the vegetation, but its composition remains largely unknown. The following elements were associated with the coarse organic aerosol: P, K, and Zn, and to a lesser extent also S, Ca, Mn, Cl, Br, and I. On the basis of the cascade impactor measurements it was found that the mineral dust and sea-salt elements exhibited essentially a broad unimodal size distribution with geometric mean aerodynamic diameter of 2-3 μm.

Also the biogenic elements were only (P) or mainly (K, Zn) present in a coarse mode. Of the elements from Na upward, S was the only one with elevated concentrations in a submicrometer-sized fine mode. The fine S is presumably present as sulphate and it is expected to be a major contributor to the climatic effects of the Amazonian aerosol during the wet season. Using the size distribution data in combination with enrichment factors and time trends, it is suggested that the fine S was mainly from marine origin.

As indicated above, the detailed organic analyses of the aerosol samples from Balbina indicated that a number dicarboxylic acids were present. Special emphasis was placed on the characterisation and identification of several novel unknown dicarboxylic acids and related oxidative degradation products. This class of acidic products was enriched in the fine size fraction, suggesting that they were secondary organic aerosol products formed by gas-to-particle conversion. Some of the unknowns contributed more to the class of dicarboxylic acids than the major known compound, nonadioic acid (azelaic acid). The same unknowns were also observed in urban aerosol samples collected on hot summer days in Gent (see Section 5). Four unknowns were identified. The most abundant were two derivatives of glutaric acid, 3-isopropyl pentanedioic acid and 3-acetyl pentanedioic acid. The other two identified unknowns were another oxo homologue, 3-acetyl hexanedioic acid, and 3-carboxy heptanedioic acid. The biogenic precursors of the novel identified compounds could not be pinpointed, but most likely include monoterpenes and fatty acids. For further details on this study we refer to Kubátová et al. [2000].

Several SFU samples that we had collected at Balbina were provided to the research group of Prof. Dr. R. Van Grieken at the University of Antwerp for individual particle analysis by EPXMA. The EPXMA data sets were analysed by cluster analysis and around 10 clusters (particle types) were observed in each individual sample. During the first 6 days of the campaign (23-29 March), mineral dust particles dominated, but later on (from 30 March to 15 April) biogenic and organic particles became the most prominent ones. These results are consistent with those from the bulk analyses discussed above.

Further with regard to LBA-CLAIRE-98, the chemical and optical measurements during March 1998 in Brazil and Surinam were related to a large-scale outbreak of Saharan dust [Formenti et al., 2001c]. The observations in South America were supported by measurements in Israel and Tenerife (Canary Islands), where the dust outbreaks were also detected. In Brazil, the dust outbreak produced an increase of a factor of 3 in the daily mean mass concentration (up to 26 ± 7 μg m^{-3}) of particles smaller than 10 μm EAD, and in the daily mean aerosol particle scattering coefficient σ_s (up to 26 ± 8 Mm^{-1} STP, ambient humidity). Background levels of aerosol

scattering (ambient) were σ_s ~ 10 Mm^{-1}.

During 1999 two new large international campaigns took place in Brazil within the framework of LBA, this time in the state of Rondônia. Two sites were used, i.e., a "primary rain forest site" (Biological Reserve Jaru) and a "pasture site" ("Fazenda Nossa Senhora"). In the latter area, tropical forest had been converted to pasture for cattle. The first of the two campaigns took place during the wet season and the subsequent transition to dry season (February through May 1999), the second campaign occurred during the transition from dry to wet season (September-October 1999). Through co-operations with USPIF and MPIC, we obtained samples from both campaigns for analysis for OC and EC and detailed organic compounds. Two articles about this work have been published [Zdráhal et al., 2001a, 2001b], but the work on these samples is continued in 2001.

With regard to our aerosol research in northern Australia, the samplings for it took place at Jabiru (12°40' S, 132°53' E, at sea level) and some articles about this work were published [Vanderzalm et al. 1998a, 1998b; Maenhaut et al., 2000b]. As to Indonesia, we started long-term studies at two sites [i.e., at Bukit Tinggi (0°18'S, 100° 20'E, 864 m asl) in Sumatra and at Pontianak (0°5'S, 109°16'E) in Kalimantan]. The work at these Indonesian sites is still ongoing.

8. OTHER AEROSOL-RELATED STUDIES

Besides the research described so far, we performed a number of other aerosol-related studies, which resulted in papers that were published or are in press. The Gent PM10 sampler was further characterised [Hopke et al., 1997]; work was done on the applicability of XRF with capillary optics for analysing aerosol samples [Holynska et al., 1997], and on the use of the NMP for individual particle analysis [Maenhaut et al., 1997d]. The elemental mass size distributions, as derived from cascade impactor measurements, were examined for a site near Rome [Maenhaut et al., 1999c] and the long-term data set from SFU samplings on the Antarctic Peninsula was analysed [Correia et al., 1998]. The aerosol composition and deposition were examined in eastern Germany [Matschullat et al., 2000]. Urban aerosols were studied in Cracow, Poland [Wróbel et al., 1999, 2000], in Helsinki, Finland [Pakkanen et al., 1999, 2000, 2001a, 2001b, 2001c], and in Budapest, Hungary [Salma et al., 2000a, 2000b, 2000c, 2001a, 2001b, 2001c]. These urban studies were to some extent linked to the EUROTRAC-2 AEROSOL subproject. Furthermore, the work in Helsinki fitted within the EUROTRAC-2 project SATURN.

9. VALORISATION POTENTIAL OF THE RESULTS

With regard to the valorisation of our results, this is in part done through traditional channels, such as publications in international journals and presentations at international conferences. For our research that is done within intensive campaigns and/or in co-operation with other groups, we also relate our data with results of the other participants, which leads to joint publications and presentations. Several articles about our project have already been published and more are planned. The articles are published in peer-reviewed journals with high impact factor and/or broad distribution within the fields of atmospheric and environmental sciences, such as Atmospheric Environment, Journal of Geophysical Research, Journal of Atmospheric Chemistry, Environmental Science and Technology, and Journal of Aerosol Science, and also in journals that deal with analytical chemistry and/or with instrumental techniques and methods.

The presentations at the international level are done at scientific conferences, symposia, workshops, and meetings, such as the EUROTRAC-2 Symposia, International Global Atmospheric Chemistry (IGAC) Conferences, the European Aerosol Conference, the General Assembly of the European Geophysical Society, and workshops of the EUROTRAC-2 AEROSOL subproject.

The results can be used and are being used in workshops, activities and reports that aim at transfer of knowledge to policy advisers, policy makers, and the general public, and this at both the national and international levels. At the national level, the valorisation can be done through activities that are being organised by, for example, the Federal Office for Scientific, Technical and Cultural Affairs (OSTC). Furthermore, the results were and will be used for contributions to Impact and Assessment, Application and other reports and publications that are prepared for policy advisers and makers by, e.g., EUROTRAC-2, IGBP-IGAC, and the Intergovernmental Panel on Climate Change (IPCC). Within EUROTRAC-2, some of our results are used for progress reports, and we will contribute to the Synthesis and Integration document, i.e., to the chapter on “Tropospheric Aerosols and Clouds”. Our long-term and other data sets with concentrations and compositions of fine atmospheric aerosols and chemical mass closure results for various European sites are being used for advice to the European Commission, in particular within work for the 2003 revision of the EU Particulate Matter Directive. Also our findings on the differences on particulate matter values obtained with filter and in-situ measurements and between different filter types are of value for this revision.

Further at the national level, the project and its results can be and are being used in university teaching and education. Undergraduate and graduate students and

postdoctoral researchers are performing research that is closely related to this project, and this research enables them to write theses that lead to licentiate and doctoral degrees and to gain knowledge and experience on environmental issues, atmospheric aerosols and their impact on climate and health. The results are integrated in our course on Chemistry of the Global Atmosphere and in other courses.

The project is and will also be used to strengthen our existing co-operations with foreign research groups (of which several are of top quality, such as the Max Planck Institute for Chemistry (MPIC) in Mainz) and to initiate new co-operations with excellent European groups, and we will use the results of the project as a basis for joint applications in calls for proposals within the 6th Framework Programme of the European Union (EU). We hope to be able to contribute to the improvement of the Belgian competitiveness and participation in EU-funded projects.

10. CONCLUSIONS

As indicated in Section 1, the overall goal of the project was to contribute to the reduction of the uncertainties in our knowledge of the sources, spatial distribution, and characteristics of the tropospheric aerosols that are of importance for climate. The project definitely provided new, invaluable and important knowledge on these topics. Concentrations of climatically active aerosol types, including sulphate, carbonaceous aerosols and mineral dust, and of the aerosol mass itself were obtained at several sites in (and downwind of) Europe and at locations in tropical and subtropical regions in various continents. The relative contributions of the major aerosol types to the particulate mass were generally determined for the separate fine and coarse size fractions, and in a number of occasions also as a function of particle size down to around 50 nanometer (by using cascade impactors with 10 or more stages or size fractions). It was found and/or inferred from chemical mass closure calculations that the carbonaceous aerosol (organic aerosol and elemental carbon) is responsible for a very significant fraction (often over 30%) of the particulate mass, and this in both the coarse and fine size fractions. Valuable information was obtained on the sources, source types, and source regions of several aerosol types, acidic species and heavy metals. With regard to the organic aerosol, it is evident that this originates from natural emissions by the vegetation or biomass burning in tropical regions. However, its sources in urban areas are far less clear. Work for Gent has indicated that the contribution from car exhaust is very important, but there are also significant contributions from wood combustion and the vegetation. However, the relative contributions from these various source types and from other sources, such

as meat cooking and road dust, remain rather uncertain. The detailed analyses of the organic aerosol also indicated the importance of atmospheric processing. At Gent, we observed high concentrations of dicarboxylic acids and related oxidative degradation products on hot summer days with elevated ozone levels. This has implications for the climatic effects of aerosols. By such atmospheric processing, the organic aerosol particles may become more water-soluble and/or hydrophilic, and thus become possible cloud condensation nuclei (CCN) and contribute to the *indirect* radiative aerosol forcing. While the detailed analyses of the molecular composition of the organic aerosol provided invaluable information, only a minor fraction of the organic aerosol mass (e.g., in Gent only 3%) was accounted for the various organic compounds measured. Clearly, further work on the characterisation of the organic aerosol is urgently needed. This work will lead to a better source apportionment of the carbonaceous aerosol and will provide invaluable information for assessing the effects of the carbonaceous aerosols on human health and climate.

At a number of sites, and in close co-operation with foreign research groups, our physico-chemical aerosol measurements were complemented with measurements of pure physical and optical/radiative aerosol properties. This was especially the case for our extensive research in the eastern Mediterranean. The various data were interrelated and used to asses the *direct* radiative forcing by aerosols in the region. Our estimates for the all-sky radiative forcing were -2.5 and -4.9 W m^{-2} for land and sea surfaces, respectively; more than 90% of these forcings was due to fine non-sea-salt sulphate, and most of the sulphate came from source regions in Europe. Our forcing estimates were in good agreement with current model predictions.

The intensive work by several research groups in the past few years has led to significant progress in our knowledge on the *direct* radiative aerosol forcing. However, with regard to the *indirect* radiative forcing (that is through the effects of aerosols on clouds) much work remains to be done. The *indirect* effect is receiving increasing attention nowadays. It is normally split into two components corresponding to (1) the radiative forcing due to modification of the radiative properties of clouds (cloud albedo (or Twomey) effect) and (2) the effects of anthropogenic aerosols upon the lifetime of clouds (cloud lifetime (or Albrecht) effect) [Haywood and Boucher, 2000; Penner et al., 2001; Rotstayn and Penner, 2001]. With regard to the second *indirect* effect, it has been found that warm rain processes in convective tropical clouds infected by heavy smoke from forest fires are practically shut off [Rosenfeld, 1999]. The tops of the smoke-infected clouds must exceed the freezing level, i.e., grow to altitudes colder than about -10°C, for the clouds to start precipitating. Also urban and industrial air pollution can completely shut off precipitation from clouds that have temperatures at their tops of about -10°C over large areas [Rosenfeld, 2000]. A side-effect of the production of numerous small

droplets and of the suppression of the mean droplet size above polluted areas is that more cloud water can reach the mixed phase region where it is involved in the formation of precipitation and the separation of electric charge, leading to an enhancement of cloud-to-ground lightning [Orville et al., 2001]. The magnitude of the *indirect* forcing by aerosols is highly uncertain. More research on it is clearly needed. This work should include a better characterisation of the atmospheric aerosol in general and of the carbonaceous aerosol in particular.

Our project involved the development and implementation of novel methods and approaches for aerosol collection, for "bulk" and individual particle analysis, and for data interpretation and interrelation. Our work has shown that the determination of seemingly simple aerosol parameters, such as the particulate mass (PM), is much less straightforward than usually thought. Substantial differences are found between the PM data from filter and in-situ measurements and between the data from different filter types. The measurement of the PM is complicated by both positive and negative artifacts. Work on the control, elimination, and assessment of the artifacts is needed. This work will assist regulatory bodies which are setting and imposing guidelines for particulate matter. Also the important issue of the accurate differentiation between black (or elemental) carbon and organic carbon is not settled at all. And as already indicated, improved characterisation of the organic aerosol is strongly recommended. The latter work should include research on the water-soluble fraction and/or on organic aerosol components that cannot be extracted by organic solvents.

ACKNOWLEDGEMENTS

This project was funded by the Belgian State - Prime Minister's Service - Federal Office for Scientific, Technical and Cultural Affairs. Financial support was also received from other sources, in particular from the "Fonds voor Wetenschappelijk Onderzoek - Vlaanderen" and the "Instituut voor Wetenschappelijk and Technologisch Onderzoek". For the research team of W. Maenhaut, contributions were provided by K. Beyaert, J. Cafmeyer, X. Chi, D. De Ridder, S. Dubtsov, M.-T. Fernández-Jiménez, S. Mertens, I. Neefs, J. Ptasinski, I. Rajta and P. Van den Broeck. In the team of F. Adams, contributions were provided by A. Adriaens, C. Coeur, B. de la Calle, W. Dorriné, K. Janssens, F. Laturnus, S. Sobanska, R. Van Ham and H. Wille. Dr. Xiande Liu, Dr. Shuping Dong and Dr. Yuwu Li, guest scientists from the National Research Centre for Environmental Analysis and Measurements, Beijing, China, also participated in the activities. A. Kubátová, J. Jeko, J. Oliveira, H. Van den Heuvel, R. Vermeylen, V.G. Voinov and Z. Zdráhal contributed in the team of M. Claeys.

Furthermore, we benefited from co-operation with the following universities and institutes:

Biogeochemistry Department, Max Planck Inst. for Chemistry (MPIC), Mainz, Germany: M.O. Andreae, F.X. Meixner and others;

Institute of Physics, University of Sao Paulo, Brazil: P. Artaxo and others;

Laboratoire de Glaciologie et Géophysique de l'Environnement (LGGE), Saint-Martin-d'Hères, France: C. Boutron and J.-L. Jaffrezo;

Finnish Meteorological Institute (FMI), Helsinki, Finland: R. Hillamo, V.-M. Kerminen, T.A. Pakkanen and others;

Department of Meteorology, University of Stockholm, Sweden: C. Leck and others;
Norwegian Institute for Air Research (NILU), Kjeller, Norway: J.E. Hanssen and others;

J. Blaustein Institute for Desert Res., Ben Gurion University of the Negev, Sde Boker, Israel: A. Karnieli and others;

Laboratory of Atmospheric Physics, Aristotle University of Thessaloniki, Greece: C.

Zerefos;

University of the Witwatersrand, Johannesburg, South Africa: H.J. Annegarn and others;

Tsetse Control Branch, Department of Veterinary Services, Harare, Zimbabwe: J.W. Hargrove and others;

School of Applied Science, Monash University, Churchill, Australia: M.A. Hooper and others, and Department of Geography and Environmental Science, Monash University, Melbourne, Australia: N.J. Tapper;

National Research Centre for Environmental Analysis and Measurements (NRCEAM), Beijing, China: X.D. Liu and others;

Faculty of Physics and Nuclear Techniques, University of Mining and Metallurgy, Cracow, Poland: B. Holynska;

Institute of Physics, Jagiellonian University, Cracow, Poland: A. Wróbel and E. Rokita;

Department of Chemical Technology and Environmental Chemistry, L. Eötvös University, Budapest, Hungary: I. Salma;

Interdisciplinary Environmental Research Center, Freiberg Technical University and Bergakademie, Freiberg, Germany: J. Matschullat;

Forestry and Renewable Natural Resources, University of Agriculture, Vienna: P. Seibert;

Bioclimatology and Immission Research, Ludwig-Maximilians-University, Munich: A. Stohl;

Department of Chemistry and Department of Civil & Environmental Engineering, Clarkson University, Potsdam, N.Y., U.S.A.: P.K. Hopke;

Department of Materials, University of Oxford: G.W. Grime;

Department of Chemistry and Biochemistry, Arizona State University, Tempe, AZ, U.S.A.: J.R. Anderson;

Department of Chemistry, University of Antwerp (UIA), Belgium: A. Worobiec, R. Van Grieken and others;

Department of Physics, Chalmers University of Technology, Gothenburg, Sweden: A. Rindby;

European Synchrotron Radiation Facility (ESRF), Grenoble: C. Riekel, P. Engström, A. Snigirev and I. Snigireva; and synchrotron sources in Brookhaven: K.W. Jones; and Hamburg: A. Knöchel;

Laboratory for Analytical Chemistry, Agricultural University of Norway: B. Salbu;

GSF-Forschungszentrum GmbH, Oberschleisheim, Germany: R. Zimmermann;

Departimento di Fisica and Istituto Nazionale di Fisica Nucleare, Sezione di Genova, Italy: P. Prati and A. Zucchiatti.

The financial support by the funding agencies and the work and/or assistance of the internal and external contributors is very much appreciated.

REFERENCES

Adams, F., Janssens, K. and Snigirev, A. 1998. Microscopical X-ray fluorescence analysis and related methods with laboratory and synchrotron radiation sources. J. At. Anal. Spectrom. 13 : 319-331.

Amundsen, C.E., Hanssen, J.E., Semb, A. and Steinnes E. 1992. Long-range atmospheric transport of trace elements to southern Norway. Atmos. Environ. 26A : 1309-1324.

Anderson, T.L. and Ogren, J.A., Determining aerosol radiative properties using the TSI 3563 integrating nephelometer. 1998. Aerosol Sci. Technol. 29 : 57-69.

Anderson, T.L., Covert, D.S., Marshall, S.F., Laucks, M.L., Charlson, R.J., Waggoner, A.P., Ogren, J.A., Caldow, R., Holm, R.L., Quant, F.R., Sem, G.J., Wiedensohler, A., Ahlquist, N.A. and Bates, T.S. 1996. Performance characteristics of a high-sensitivity, three-wavelength, total scatter/backscatter nephelometer. J. Atmos. Ocean. Technol. 13 : 967-986.

Anderson, T.L., Covert, D.S., Wheeler, J.D., Harris, J.M., Perry, K.D., Trost, B.E., Jaffe, D.J. and Ogren, J.A. 1999. Aerosol backscatter fraction and single scattering albedo: Measured values and uncertainties at a coastal station in the Pacific Northwest. J. Geophys. Res. 104 : 26,793-26,807.

Andreae, M.O. 1995. Climatic effects of changing atmospheric aerosol levels. In: World Survey of Climatology, Volume XVI: Future Climates of the World. Henderson-Sellers, A. (Ed). Elsevier, New York: 341-392.

Andreae, M.O., Andreae, T.W., Annegarn, H., Beer, J., Cachier, H., le Canut, P., Elbert, W., Maenhaut, W., Salma, I., Wienhold, F. and Zenker, T. 1998. Airborne studies of aerosol emissions from savanna fires in southern Africa: 2. Aerosol chemical composition. J. Geophys. Res. 103 : 32119-32128.

Andreae, T.W., Andreae, M.O., Ichoku, C., Maenhaut, W., Cafmeyer, J., Karnieli, A. and Orlovsky, L. 2001. Light scattering by dust and anthropogenic aerosol at a remote site in the Negev desert, Israel. J. Geophys. Res., in press.

Artaxo, P., Fernandes, E.T., Martins, J.V., Yamasoe, M.A., Longo, K.M., Hobbs, P. and Maenhaut, W. 1996. Large scale elemental composition of atmospheric aerosols measured during SCAR-B. In: SCAR-B Proceedings. Kirchhoff, V.W.J.H. (Ed). Transtec, Sao José dos Campos, SP, Brazil: 9-14.

Artaxo, P., Fernandes, E.T., Martins, J.V., Yamasoe, M.A., Hobbs, P.V., Maenhaut, W., Longo, K.M. and Castanho, A. 1998. Large scale aerosol source apportionment in Amazonia. J. Geophys. Res. 103 : 31837-31847.

Artaxo, P., de Campos, R.C., Fernandes, E.T., Martins, J.V., Zifan Xiao, Lindqvist, O., Fernández-Jiménez, M.T. and Maenhaut, W. 2000. Large scale mercury and trace elements measurements in the Amazon basin. Atmos. Environ. 34 : 4085-4096.

Ayers, G.P., Keywood, M.D. and Gras, J.L. 1999. TEOM vs. manual gravimetric methods for determination of PM2.5 aerosol mass concentrations. Atmos. Environ. 33 : 3717-3721.

Barrie, L.A. and Hoff, R.M. 1985. Five years of air chemistry observations in the Canadian Arctic. Atmos. Environ. 19 :1995-2010.

Bauman, S., Houmere, P.D. and Nelson, J.W. 1981. Cascade impactor aerosol samples for PIXE and PESA analysis. Nucl. Instr. and Meth. 181 : 499-502.

Bigg, E.K. and Leck, C. 2001. Properties of the aerosol over the central Arctic Ocean. J. Geophys. Res., in press.

Birch, M.E. and Cary, R.A. 1996. Elemental carbon-based method for monitoring occupational exposures to particulate diesel exhaust. Aerosol Sci. Technol. 25 : 221-241.

Bohren, C.F. and Huffman, D.R. 1983. Absorption and Scattering of Light by Small Particles, Wiley, New York, 1983.

Boucher, O. and Anderson, T.L. 1995. General circulation model assessment of the sensitivity of direct climate forcing by anthropogenic sulfate aerosols to aerosol size and chemistry. J. Geophys. Res. 100 : 26,117-26,134.

Cahill, T.A., Eldred, R.A., Motallebi, N. and Malm, W.C. 1989. Indirect measurement of hydrocarbon aerosols across the US by nonsulphate hydrogen and remaining gravimetric mass correlations. Aerosol Sci. Technol. 10 : 421-429.

Cary, R.A. 1998. Personal communication.

Chan, Y.C., Simpson, R.W., McTainsh, G.H., Vowles, P.D., Cohen, D.D. and Bailey, G.M. 1997. Characterisation of chemical species in $PM_{2.5}$ and PM_{10} aerosols in Brisbane, Australia. Atmos. Environ. 31 : 3773-3785.

Charlson, R.J. and Heintzenberg, J. (Eds). 1995. Aerosol Forcing of Climate. Wiley, Chichester, 416 pages.

Charlson, R.J., Langner, J., Rodhe, H., Leovy, C.B. and Warren S.G. 1991. Perturbation of the northern hemisphere radiative balance by backscattering from anthropogenic sulfate aerosols. Tellus 43AB : 152-163.

Charlson, R.J., Schwartz, S.E., Hales, J.M., Cess, R.D., Coakley, J.A., Hansen, J.E. and Hofmann, D.J. 1992. Climate forcing by anthropogenic aerosols. Science 255 : 423-430.

Charlson, R.J., Anderson, T.L. and Rodhe, H. 1999. Direct climate forcing by anthropogenic aerosols: Quantifying the link between atmospheric sulfate and radiation. Contr. Atmos. Phys. 72 : 79-94.

Claeys, M., Vermeylen, R., Kubátová, A., Cafmeyer, J. and Maenhaut, W. 1999. Characterisation of organic compounds in atmospheric aerosols. In: Proceedings of EUROTRAC Symposium '98, Transport and Chemical Transformation in the Troposphere. Volume 1, Chemical Mechanisms; Photo-Oxidants; Aerosols and Clouds; Policy Applications. Borrell, P.M. and Borrell P. (Eds). WITpress, Southampton, United Kingdom: 501-505.

Clarke, A.D., Porter, J.N., Valero, F.P.J. and Pilewskie, P. 1996. Vertical profiles, aerosol microphysics, and optical closure during the Atlantic Stratocumulus Transition Experiment: Measured and modeled column optical properties. J. Geophys. Res. 101 : 4443-4453.

Clegg, S.L., Brimblecombe, P. and Wexler, A.S. 1998. A thermodynamic model of the system H^+-NH_4^+-Na^+-SO_4^{2-}-NO_3^--Cl^--H_2O at 298.15 K. J. Phys. Chem. 102A : 2155-2171.

Correia, A., Artaxo, P. and Maenhaut, W. 1998. Monitoring of atmospheric aerosol particles at the Antarctic Peninsula. Annals of Glaciology 27 : 560-564.

Dockery, D.W., Pope, C.A. III, Xu, X., Spengler, J.D., Ware, J.H., Fay, M.E., Ferris, B.G. Jr. and Speizer, F.E. 1993. An association between air pollution and mortality in six U.S. cities. N. Engl. J. Med. 329 : 1753-1759.

Dzubay, T.G., Stevens, R.K., Lewis, C.W., Hern, D.H., Courtney, W.J., Tesch, J.W. and Mason, M.A. 1982. Visibility and aerosol composition in Houston, Texas. Environ. Sci. Tech. 16 : 514-525.

Echalar, F., Artaxo, P., Martins, J.V., Yamasoe, M., Gerab, F., Maenhaut, W. and Holben, B. 1998. Long-term monitoring of atmospheric aerosols in the Amazon Basin: source identification and apportionment. J. Geophys. Res. 103 : 31849-31864.

Feichter, J., Lohmann, U. and Schult, I. 1997. The atmospheric sulfur cycle in ECHAM-4 and its impact on the shortwave radiation. Climate Dynamics 13 : 235-246.

Formenti, P., Andreae, M.O., Andreae, T.W., Galani, E., Vasaras, A., Zerefos, C., Amiridis, V., Orlovsky, L., Karnieli, A., Wendish, M., Wex, H., Holben, B.N., Maenhaut, W. and Lelieveld, J. 2001a. Aerosol optical properties and large-scale transport of air masses: observations at a coastal and a semiarid site in the eastern Mediterranean during summer 1998. J. Geophys. Res. 106 : 9807-9826.

Formenti, P., Andreae, M.O., Andreae, T.W., Ichoku, C., Schebeske, G., Kettle, A.J., Maenhaut, W., Cafmeyer, J., Ptasinsky, J., Karnieli, A. and Lelieveld, J. 2001b. Physical and chemical characteristics of aerosols over the Negev desert (Israel) during summer 1996. J. Geophys. Res. 106 : 4871-4890.

Formenti, P., Andreae, M.O., Lange, L., Roberts, G., Cafmeyer, J., Rajta, I., Maenhaut, W., Holben, B.N., Artaxo, P. and Lelieveld, J. 2001c. Saharan dust in Brazil and Suriname during the Large-Scale Biosphere-Atmosphere Experiment in Amazonia (LBA)- Cooperative LBA Regional Experiment (CLAIRE) in March 1998. J. Geophys. Res. 106 : 14,919-14,934.

Gordon, G.E. 1988. Receptor models. Environ. Sci. Technol. 22 : 1132-1142.

Hansen, A.D.A., Rosen, H. and Novakov, T. 1984. The aethalometer, an instrument for the real time measurement of optical absorption by aerosol particles. Sci. Total Environ. 36 : 191-196.

Hanssen, J.E., Maenhaut, W. and Semb, A. 2000. Chemical composition of PM2.5

and PM10 at Birkenes. In: EMEP/WMO Workshop on fine particles - emissions, modelling and measurements, Interlaken, Switzerland, 22-25 November 1999. Hanssen, J.E., Ballaman, R, and Gehrig R. (Eds). EMEP/CCC-Report 9/2000, O-98134: 111-116.

Harrison, L., Michalsky, J. and Berndt, J. 1994. Automated multifilter rotating shadow-band radiometer: an instrument for optical depth and radiation measurements. Appl. Opt. 22 : 5118-5125.

Haywood, J.M. and Shine, K.P. 1995. The effect of anthropogenic sulfate and soot aerosol on the clear-sky planetary radiation budget. Geophys. Res. Lett. 22 : 603-606.

Haywood, J. and Boucher O. 2000. Estimates of the direct and indirect radiative forcing due to tropospheric aerosols: A review. Rev. Geophys. 38 : 513-543.

Hegg, D.A., Ferek, R.J. and Hobbs, P.V. 1993. Light scattering and cloud condensation nucleus activity of sulfate aerosol measured over the Northeast Atlantic Ocean. J. Geophys. Res. 98 : 14,887-14,894.

Hegg, D.A., Hobbs, P.V., Ferek, R.J. and Waggoner, A.P. 1995. Measurements of some aerosol properties relevent to radiative forcing on the east coast of the United States. J. Appl. Meteor. 34 : 2306-2315.

Hegg, D.A., Livingston, J., Hobbs, P.V., Novakov, T. and Russell, P. 1997. Chemical apportionment of aerosol column optical depth off the mid-Atlantic coast of the United States. J. Geophys. Res. 102 : 25,293-25,303.

Henry, R.C., Lewis, C.W., Hopke, P.K. and Williamson, H.J. 1984. Review of receptor model fundamentals. Atmos. Environ. 18 : 1507-1515.

Hillamo, R., Kerminen, V.-M., Teinilä, K., Meriläinen, J., Jaffrezo, J.-L., Cachier, H., Liousse, C., Masclet, P. and Maenhaut, W. 1999. European Arctic Aerosol Study (EAAS): Presentation and preliminary results. In: Proceedings of EUROTRAC Symposium '98, Transport and Chemical Transformation in the Troposphere. Volume 1, Chemical Mechanisms; Photo-Oxidants; Aerosols and Clouds; Policy Applications. Borrell, P.M. and Borrell, P. (Eds). WITpress, Southampton, United Kingdom: 546-549.

Hillamo, R., Kerminen, V.-M., Aurela, M., Mäkelä, T., Maenhaut, W. and Leck, C.

2001. Modal structure of chemical mass size distribution in the high Arctic aerosol. J. Geophys. Res., in press.

Holben, B.N., Tanre, D., Smirnov, A., Eck, T.F., Slutsker, I., Abuhassan, N., Newcomb, W.W., Schafer, J.S., Chatenet, B., Lavenu, F., Kaufman, Y.J., Castle, J.V., Setzer, A., Markham, B., Clark, D., Frouin, R., Halthore, R., Karneli, A., O'Neill, N.T., Pietras, C., Pinker, R.T., Voss, K. and Zibordi, G. 2001. An emerging ground-based aerosol climatology: Aerosol optical depth from AERONET. J. Geophys. Res. 106 : 12067-12097.

Holynska, B., Ptasinski, J., Maenhaut, W. and Annegarn, H.J. 1997. Energy-dispersive X-ray fluorescence spectrometer with capillary optics for the chemical analysis of atmospheric aerosols with high time resolution. J. Aerosol Sci. 228 : 1455-1463.

Hopke, P.K., Xie, Y., Raunemaa, T., Biegalski, S., Landsberger, S., Maenhaut, W., Artaxo, P. and Cohen, D. 1997. Characterization of the Gent stacked filter unit PM10 sampler. Aerosol Sci. Technol. 27 : 726-735.

Houghton, J.T., Meira Filho, L.G., Callander, B.A., Harris, N., Kattenberg, A. and Maskell, K. (Eds). 1996. Climate Change 1995. The Science of Climate Change. Contribution of WGI to the Second Assessment Report of the Intergovernmental Panel on Climate Change. Cambridge University Press, Cambridge, UK.

Ichoku, C., Andreae, M.O., Andreae, T.W., Meixner, F.X., Schebeske, G., Formenti, P., Maenhaut, W., Cafmeyer, J., Ptasinski, J., Karnieli, A. and Orlovsky, L. 1999. Interrelationships between aerosol characteristics and light scattering during late-winter in an Eastern Mediterranean arid environment. J. Geophys. Res. 104 : 24371-24393.

IPCC (Intergovernmental Panel on Climate Change). 1994. Climate Change 1994: Radiative Forcing of Climate and an Evaluation of the IS92 Emission Scenarios. Houghton, J.T., Meira Filho, L.G., Bruce, J., Lee Hoesong, Callander, B.A., Haites, E.F., Harris, N. and Maskell, K. (Eds). Cambridge University Press, Cambridge, UK.

Jaffrezo, J.-L., Davidson, C.I., Kuhns, H.D., Bergin, M.H., Hillamo, R., Maenhaut, W., Kahl, J.W. and Harris, J.M. 1998. Biomass burning plumes over central Greenland: Sources, characteristics of the aerosol and record in the snow. J. Geophys. Res. 103 : 31067-31078.

Jonas, P.R., Charlson, R.J. and Rodhe, H. 1995. Aerosols. In: Climate Change 1994:

Radiative Forcing of Climate and an Evaluation of the IS92 Emission Scenarios. Houghton, J.T., Meira Filho, L.G., Bruce, J., Lee Hoesong, Callander, B.A., Haites, E.F., Harris, N. and Maskell, K. (Eds). Cambridge University Press, Cambridge, UK: 127-162.

Kerminen, V.-M., Hillamo, R.E., Mäkelä, T., Jaffrezo, J.-L. and Maenhaut, W. 1998. The physico-chemical structure of the Greenland summer aerosol and its relation to atmospheric processes. J. Geophys. Res. 103 : 5661-5670.

Key, J. and Schweiger, A.J. 1998. Tools for atmospheric radiative transfer: Streamer and Fluxnet. Computers and Geosciences 24 : 443-451.

Kiehl, J.T. and Briegleb, B.P. 1993. The relative role of sulfate aerosols and greenhouse gases in climate forcing. Science 260 : 311-314.

Kiehl, J.T. and Rodhe, H. 1995. Modeling geographical and seasonal forcing due to aerosols. In: Aerosol Forcing of Climate. Charlson, R.J. and Heintzenberg, J. (Eds). Wiley, Chichester: 281-296.

Kubátová, A., Vermeylen, R., Claeys, M., Cafmeyer, J. and Maenhaut, W. 1999. Carbonaceous aerosols and particulate organic compounds in Gent, Belgium, during winter and summer of 1998. J. Aerosol Sci. 30, Suppl. 1 : S905-S906.

Kubátová, A., Vermeylen, R., Claeys, M., Cafmeyer, J., Maenhaut, W., Roberts, G. and Artaxo, P. 2000. Carbonaceous aerosol characterisation in the Amazon basin, Brazil: Novel dicarboxylic acids and related compounds. Atmos. Environ. 34 : 5037-5051.

Kubátová, A., Vermeylen, R., Claeys, M., Cafmeyer, J. and Maenhaut, W. 2001a. Characterisation of novel dicarboxylic acids and related compounds in urban atmospheric aerosols. In: Transport and Chemical Transformation in the Troposphere. Proceedings of EUROTRAC Symposium 2000, Garmisch-Partenkirtchen, Germany, 27-31 March 2000. Midgley, P.M., Reuther, M. and Williams, M. (Eds). Springer Verlag Berlin, Heidelberg, 4 pages (published on CD-rom).

Kubátová, A., Vermeylen, R., Claeys, M., Cafmeyer, J. and Maenhaut, W. 2001b. Organic compounds in urban aerosols from Gent, Belgium: Characterization, sources, and seasonal differences. J. Geophys. Res., in press.

Langmann, B., Herzog, M. and Graf, H.F. 1998. Radiative forcing of climate by

sulfate aerosols as determined by a regional circulation chemistry transport model. Atmos. Environ. 32 : 2757-2768.

Leaderer, B.P., Tanner, R.L., Lioy, P.J. and Stolwijk, J.A.J. 1981. Seasonal variations in light scattering in the New York region and their relation to sources. Atmos. Environ. 15 : 2407-2420.

Li, X., Maring, H., Savoie, D., Voss, K. and Prospero, J.M. 1996. Dominance of mineral dust in aerosol light-scattering in the North Atlantic trade winds. Nature 380 : 416-419.

Liu, X., Li, Y., Adams, F. and Maenhaut, W. 1998. Identification of particle classes in African savanna fire samples based on EPMA data. J. Aerosol Sci. 29, Suppl. 1 : S227-S228.

Liu, X.D., Dong, S.P., Van Espen, P., Adams, F., Cafmeyer, J. and Maenhaut, W. 2000a. Size and chemical characterization of atmospheric aerosol and savanna fire samples in southern Africa. J. Aerosol Sci. 31, Suppl. 1 : S186-S187.

Liu, X.D., Van Espen, P., Adams, F., Cafmeyer, J. and Maenhaut, W. 2000b. Biomass burning in Southern Africa: Individual particle characterization of atmospheric aerosols and savanna fire samples. J. Atmos. Chem. 36 : 135-155.

Lowenthal, D.H., Hanumara, R.C., Rahn, K.A. and Currie, L.A. 1987. Effects of systematic error, estimates and uncertainties in chemical mass balance apportionments: Quail Roost II revisited. Atmos. Environ. 21 : 501-510.

Maenhaut, W. 1993. Composition and origin of the regional atmospheric aerosol at great distance from anthropogenic source areas. Assessment of the extent of the anthropogenic perturbation. In: Belgian Impulse Programme “Global Change”, Symposium 17 & 18 May 1993, Proceedings, Vol. 1. Belgian Science Policy Office: 5-30.

Maenhaut, W. 1996. Composition and origin of the regional atmospheric aerosol at great distance from anthropogenic source areas. Assessment of the extent of the anthropogenic perturbation. Belgian Impulse Programme “Global Change” 1990-1996, Final Report, Federal Office for Scientific, Technical and Cultural Affairs, 105 pages [published in 1997].

Maenhaut, W. and Cafmeyer, J. 1987. Particle induced X-ray emission analysis and

multivariate techniques: an application to the study of the sources of respirable atmospheric particles in Gent, Belgium. J. Trace Microprobe Techn. 5 : 135-158.

Maenhaut, W., Ducastel, G., Beyaert, K. and Hanssen, J.E. 1994a. Chemical composition of the summer aerosol at Ny Ålesund, Spitsbergen, and relative contribution of natural and anthropogenic sources to the non-sea-salt sulfate. In: The Proceedings of EUROTRAC Symposium '94. Borrell, P.M. et al. (Eds). SPB Academic Publishing bv, The Hague: 467-471.

Maenhaut, W., François, F. and Cafmeyer, J. 1994b. The "Gent" stacked filter unit (SFU) sampler for the collection of aerosols in two size fractions: Description and instructions for installation and use, In: Applied Research on Air Pollution using Nuclear-Related Analytical Techniques. NAHRES-19, IAEA, Vienna: 249-263.

Maenhaut, W., Fernández-Jiménez, M.-T., Polasek, M., Meixner, F.X., Torr, S., Hargrove, J.W., Chimanga, P. and Mlambo, J. 1996a. Long-term aerosol composition measurements at Rukomechi, Zimbabwe. Annales Geophysicae, Suppl. II to Vol. 14 : C598.

Maenhaut, W., Hillamo, R., Mäkelä, T., Jaffrezo, J.L., Bergin, M.H. and Davidson, C.I. 1996b. A new cascade impactor for aerosol sampling with subsequent PIXE analysis. Nucl. Instr. and Meth. B109/110 : 482-487.

Maenhaut, W., Koppen, G. and Artaxo, P. 1996c. Long-term atmospheric aerosol study in Cuiabá, Brazil: Multielemental composition, sources, and impact of biomass burning. In: Biomass Burning and Global Change. Volume 2: Biomass Burning in South America, Southeast Asia, and Temperate and Boreal Ecosystems, and the Oil Fires of Kuwait. Levine, J.S. (Ed). MIT Press, Cambridge, Mass., Chapter 61: 637-652.

Maenhaut, W., Salma, I., Cafmeyer, J., Annegarn, H.J. and Andreae, M.O. 1996d. Regional atmospheric aerosol composition and sources in the eastern Transvaal, South Africa, and impact of biomass burning. J. Geophys. Res. 101 : 23631-23650.

Maenhaut, W., Cafmeyer, J., Ptasinski, J., Andreae, M.O., Andreae, T.W., Elbert, W., Meixner, F.X., Karnieli, A. and Ichoku, C. 1997a. Chemical composition and light scattering of the atmospheric aerosol at a remote site in the Negev desert, Israel. J. Aerosol Sci. 28, Suppl. 1 : S73-S74.

Maenhaut, W., François, F., Cafmeyer, J., Gilot, C. and Hanssen, J.E. 1997b. Long-term aerosol study in southern Norway, and the relationship of aerosol components to source regions. In: Proceedings of EUROTRAC Symposium '96, Volume 1: Clouds, Aerosols, Modelling and Photo-oxidants. Borrell, P.M., Borrell, P., Kelly, K., Cvitas, T. and Seiler, W. Computational Mechanics Publications, Southampton, United Kingdom: 277-280.

Maenhaut, W., Hillamo, R., Mäkelä, T., Jaffrezo, J.-L., Bergin, M.H. and Davidson, C.I. 1997c. Concentrations and mass size distributions of particulate trace elements at Summit, Greenland: Impact of boreal forest fires. J. Aerosol Sci. 28, Suppl. 1 : S565-S566.

Maenhaut, W., Salomonovic, R., Ptasinski, J. and Grime, G.W. 1997d. Nuclear microprobe analysis of atmospheric aerosol samples: Comparison with bulk measurements and analyses of individual particles. Nucl. Instr. and Meth. B130 : 576-581.

Maenhaut, W., Fernández-Jiménez, M.-T. and Artaxo, P. 1999a. Long-term study of atmospheric aerosols in Cuiabá, Brazil: Multielemental composition, sources and source apportionment. J. Aerosol Sci. 30, Suppl. 1 : S259-S260.

Maenhaut, W., Jaffrezo, J.-L., Hillamo, R.E., Mäkelä, T. and Kerminen, V.-M. 1999b. Size-fractionated aerosol composition during an intensive 1997 summer field campaign in northern Finland. Nucl. Instr. and Meth. B150 : 345-349.

Maenhaut, W., Kohl, F., Hillamo, R.E. and Allegrini, I. 1999c. Detailed size distributions of aerosol species and elements during a 1995 summer field campaign near Rome, Italy. In: Proceedings of EUROTRAC Symposium '98, Transport and Chemical Transformation in the Troposphere. Volume 1, Chemical Mechanisms; Photo-Oxidants; Aerosols and Clouds; Policy Applications. Borrell, P.M. and Borrell, P. (Eds), WITpress, Southampton, United Kingdom: 490-494.

Maenhaut, W., Ptasinski, J. and Cafmeyer, J. 1999d. Detailed mass size distributions of atmospheric aerosol species in the Negev Desert, Israel, during ARACHNE-96. Nucl. Instr. and Meth. B150 : 422-427.

Maenhaut, W., Rajta, I., Beyaert, K., Leck, C., Holmen, K. and Hanssen, J.E. 1999e. Interrelations between chemical composition and light scattering of the atmospheric aerosol at Ny Ålesund, Spitsbergen. J. Aerosol Sci. 30, Suppl. 1 : S119-S120.

Maenhaut, W., Rajta, I., François, F., Aurela, M., Hillamo, R. and Virkkula, A. 1999f. Long-term atmospheric aerosol study in the Finnish Arctic: Chemical composition, source types and source regions. J. Aerosol Sci. 30, Suppl. 1 : S87-S88.

Maenhaut, W., Fernández-Jiménez, M.-T., Rajta, I., Dubtsov, S., Meixner, F.X., Andreae, M.O., Torr, S., Hargrove, J.W., Chimanga, P. and Mlambo, J. 2000a. Long-term aerosol composition measurements and source apportionment at Rukomechi, Zimbabwe. J. Aerosol Sci. 31, Suppl. 1 : S228-S229.

Maenhaut, W., Fernández-Jiménez, M.-T., Vanderzalm, J.L., Hooper, B., Hooper, M.A. and Tapper, N.J. 2000b. Aerosol composition at Jabiru, Australia, and impact of biomass burning. J. Aerosol Sci. 31, Suppl. 1 : S745-S746.

Maenhaut, W., François, F., Ptasinski, J., Mertens, S.F. and Hanssen, J.E. 2000c. Five-year study of the atmospheric aerosol composition, sources and chemical mass closure at two sites in southern Norway. J. Aerosol Sci. 31, Suppl. 1 : S180-S181.

Maenhaut, W., Cafmeyer, J., Chi, X. and Dubtsov, S. 2001a. Intercomparison of filter collections and in-situ measurements for the aerosol particle mass and elemental/black carbon at Gent, Belgium. In: Transport and Chemical Transformation in the Troposphere. Proceedings of EUROTRAC Symposium 2000, Garmisch-Partenkirtchen, Germany, 27-31 March 2000. Midgley, P.M., Reuther, M. and Williams, M. (Eds). Springer Verlag Berlin, Heidelberg, 4 pages (published on CD-rom).

Maenhaut, W., Cafmeyer, J., Dubtsov, S. and Chi, X. 2001b. Detailed mass size distributions of aerosol species and elements, and aerosol chemical mass closure during fall 1999 at Gent, Belgium. In: Transport and Chemical Transformation in the Troposphere. Proceedings of EUROTRAC Symposium 2000, Garmisch-Partenkirtchen, Germany, 27-31 March 2000. Midgley, P.M., Reuther, M. and Williams, M. (Eds). Springer Verlag Berlin, Heidelberg, 4 pages (published on CD-rom).

Maenhaut, W., Cafmeyer, J., Dubtsov S. and Chi X. 2001c. Detailed mass size distributions of elements and species, and aerosol chemical mass closure during fall 1999 at Gent, Belgium. Nucl. Instr. and Meth. B, in press.

Maenhaut, W., Fernández-Jiménez, M.-T., Rajta, I. and Artaxo, P. 2001d. Two-year study of atmospheric aerosols in Alta Floresta, Brazil: Multielemental composition, sources and source apportionment. J. Aerosol Sci. 32, Suppl. 1 : S469-S470.

Maenhaut, W., Fernández-Jiménez, M.-T., Rajta, I. and Artaxo, P. 2001e. Two-year study of atmospheric aerosols in Alta Floresta, Brazil: Multielemental composition and source apportionment. Nucl. Instr. and Meth. B, in press.

Marple, V.A., Rubow, K.L. and Behm, S.M. 1991. A microorifice uniform deposit impactor (MOUDI): description, calibration and use. Aerosol Sci. Technol. 14 : 434-446.

Matschullat, J., Maenhaut, W., Zimmermann, F. and Fiebig, J. 2000. Aerosol and bulk deposition trends in the 1990's, Eastern Erzgebirge, Central Europe. Atmos. Environ. 34 : 3213-3221.

Mazurek, M.A., Simoneit, B.R.T., Cass, G.R. and Gray, H.A. 1987. Quantitative high-resolution gas chromatography and high-resolution gas chromatography/mass spectrometry analysis of carbonaceous fine aerosol particles. Int. J. Environ. Anal. Chem. 29 : 119-139.

Meszaros, E., Molnar, A. and Ogren, J. 1998. Scattering and absorption coefficients vs. Chemical composition of fine atmospheric aerosol particles under regional conditions in Hungary. J. Aerosol Sci. 29 : 1171-1178.

Novakov, T. and Penner, J.E. 1993. Large contribution of organic aerosols to cloud-condensation-nuclei concentrations. Nature 365 : 823-826.

Ogren, J.A. 1995. A systematic approach to in situ observations of aerosol properties. In: Aerosol Forcing of Climate. Charlson, R.J. and Heintzenberg, J. (Eds). Wiley, Chichester: 215-226.

Orville R.E., Huffines G., Nielsen-Gammon J., Zhang R.Y., Ely B., Steiger S., Phillips S., Allen S. and Read W. 2001. Enhancement of cloud-to-ground lightning over Houston, Texas. Geophys. Res. Lett. 28 : 2597-2600.

Pakkanen, T.A., Hillamo, R.E., Keronen, P., Maenhaut, W., Ducastel, G. and Pacyna, J.M. 1996. Sources and physico-chemical characteristics of the atmospheric aerosol in southern Norway. Atmos. Environ. 30 : 1391-1405.

Pakkanen, T., Ojanen, C., Hillamo, R., Aurela, M., Aarnio, P., Koskentalo, T. and Maenhaut, W. 1999. Mass balance of atmospheric fine particles in the Helsinki area. J. Aerosol Sci. 30, Suppl. 1 : S275-S276.

Pakkanen, T.A., Korhonen, C.H., Hillamo, R.E., Aurela, M., Aarnio, P., Koskentalo, T. and Maenhaut, W. 2000. Ultrafine particles ($PM_{0.1}$) in the Helsinki area. J. Aerosol Sci. 31, Suppl. 1 : S522-S523.

Pakkanen, T.A., Kerminen, V.-M., Korhonen, C.H., Hillamo, R.E., Aarnio, P., Koskentalo, T. and Maenhaut, W. 2001a. Urban and rural ultrafine particles ($PM_{0.1}$) in the Helsinki area. Atmos. Environ. 35 : 4593-4607.

Pakkanen, T.A., Kerminen, V.-M., Korhonen, C.H., Hillamo, R.E., Aarnio, P., Koskentalo, T. and Maenhaut, W. 2001b. Use of atmospheric elemental size distributions in estimating aerosol sources in the Helsinki area. Atmos. Environ., in press.

Pakkanen, T.A., Loukkola, K., Korhonen, C.H., Aurela, M., Mäkelä, T., Hillamo, R.E., Aarnio, P., Koskentalo, T., Kousa, A. and Maenhaut, W. 2001c. Sources and chemical composition of atmospheric fine and coarse particles in the Helsinki area. Atmos. Environ., in press.

Penner, J.E., Dickinson, R.E. and O'Neill, C.A. 1992. Effects of aerosol from biomass burning on the global radiation budget. Science 256 : 1432-1434.

Penner, J.E., Charlson, R.J., Hales, J.M., Laulainen, N.S., Leifer, R., Novakov, T., Ogren, J., Radke, L.F., Schwartz, S.E. and Travis, L. 1994. Quantifying and minimizing uncertainty of climate forcing by anthropogenic aerosols. Bull. Am. Meteorol. Soc. 75 : 375-400.

Penner, J.E., Chuang, C.C. and Grant, K. 1998. Climate forcing by carbonaceous and sulfate aerosols, Climate Dynamics 14 : 839-851.

Penner J.E., Hegg D. and Leaitch R. 2001. Unraveling the role of aerosols in climate change. Environ. Sci. Technol. 35 : 332A-340A.

Piketh, S.J., Formenti, P., Freiman, M.T., Maenhaut, W., Annegarn, H.J. and Tyson, P.D. 1998. Industrial pollutants at a remote site in South Africa. In: Papers of the 11th World Clean Air and Environment Congress, Durban, South Africa, 13-18 September 1998, Volume Six. National Association for Clean Air, Parklands, South Africa: paper # 17E-5, 6 pages.

Ptasinski, J., Maenhaut, W., Meixner, F.X. and Stohl, A. 1998. Source areas of radiatively active and anthropogenic aerosol constituents at a remote site in the

Negev desert, Israel. EOS Transactions of the American Geophysical Union 79, No. 45/supplement (1998) F84.

Quinn, P.K., Marshall, S.F., Bates, T.S., Covert, D.S. and Kapustin, V.N. 1995. Comparison of measured and calculated aerosol properties relevant to the direct radiative forcing of tropospheric sulfate aerosol on climate. J. Geophys. Res. 100 : 8977-8991.

Quinn, P.K., Kapustin, V.N., Bates, T.S. and Covert, D.S. 1996. Chemical and optical properties of marine boundary layer aerosol particles of the mid-Pacific in relation to sources and meteorological transport. J. Geophys. Res. 101 : 6931-6951.

Radzi bin Abas, M. and Simoneit, B.R.T. 1996. Composition of extractable organic matter of air particulates from Malaysia: an initial study. Atmos. Environ. 30 : 2779-2793.

Reid, J.S., Hobbs, P.V., Liousse, C., Martins, J.V., Weiss, R.E. and Eck, T.F. 1998. Comparisons of techniques for measuring shortwave absorption and black carbon content of aerosols from biomass burning in Brazil. J. Geophys. Res. 103 : 32031-32040.

Ricard, V., Jaffrezo, J.-L., Kerminen, V.-M., Hillamo, R.E., Teinila, K. and Maenhaut W. 2001. Size distributions and modal parameters of aerosol constituents in Northern Finland during the European Arctic Aerosol Study. J. Geophys. Res., submitted.

Rindby, A., Engström, P. and Janssens, K. 1997. The use of a scanning X-ray microprobe for simultaneous XRF/XRD studies of fly-ash particles. J. Synchrotron Rad. 4 : 228-235.

Roberts, G., Andreae, M.O., Maenhaut, W. and Fernández-Jiménez, M.-T. 1998. Inorganic composition and sources of aerosols in a central African rainforest during the dry season. J. Aerosol Sci. 29, Suppl. 1 : S727-S728.

Roberts, G.C., Andreae, M.O., Maenhaut, W. and Fernández-Jiménez, M.-T. 2001. Composition and sources of aerosol in a Central African rainforest during the dry season. J. Geophys. Res. 106 : 14423-14434.

Rogge, W.F., Mazurek, M.A., Hildemann, L.M., Cass, G.R. and Simoneit, B.R.T. 1993a. Quantification of urban organic aerosols at a molecular level: Identification, abundance and seasonal variation. Atmos. Environ. 27A : 1309-1330

Rogge, W.F., Hildemann, L.M., Mazurek, M.A., Cass, G.R. and Simoneit, B.R.T. 1993b. Sources of fine organic aerosol. 2. Noncatalyst and catalyst-equipped automobiles and heavy-duty diesel trucks. Environ. Sci. Technol. 27 : 636-651.

Rosenfeld D. 1999. TRMM observed first direct evidence of smoke from forest fires inhibiting rainfall. Geophys. Res. Lett. 26 : 3105-3108.

Rosenfeld D. 2000. Suppression of rain and snow by urban and industrial air pollution. Science 287 : 1793-1796.

Rotstayn L.D. and Penner J.E. 2001. Indirect aerosol forcing, quasi forcing, and climate response. J. Clim. 14 : 2960-2975.

Salma, I., Maenhaut, W., Dubtsov, S., Zemplén-Papp, É. and Záray, G. 2000a. Impact of phase out of leaded gasoline on the air quality in Budapest. Microchem. J. 67 : 127-133.

Salma, I., Maenhaut, W., Weidinger, T., Záray, G. and Zemplén-Papp, É. 2000b. Elemental size distributions in the urban atmospheric aerosol. J. Aerosol Sci. 31, Suppl. 1 : S747-S748.

Salma, I., Maenhaut, W., Zemplén-Papp, É. and Bobvos, J. 2000c. Chemical characteristics and temporal variation of size-fractionated urban aerosols and trace gases in Budapest. In: Aerosol Chemical Processes in the Environment. Spurny, K.R. (Ed). CRC Press Lewis, Boca Raton: 415-430.

Salma, I., Maenhaut, W., Zemplén-Papp, É. and Záray, G. 2001a. Comprehensive characterization of atmospheric aerosols in Budapest: Physicochemical properties of inorganic species. Atmos. Environ. 35 : 4367-4378.

Salma, I., Maenhaut, W., Zemplén-Papp, É. and Záray, G. 2001b. Comparative study of elemental mass size distributions in urban atmospheric aerosols. J. Aerosol Sci., in press.

Salma, I., Weidinger, T., Maenhaut, W. and Záray, G. 2001c. Sources of atmospheric coarse and fine particles in Budapest. J. Aerosol Sci. 32, Suppl. 1 : S769-S770.

Schmid, H., Laskus, L., Abraham, H.J., Baltensperger, U., Lavanchy, V., Bizjak, M., Burba, P., Cachier, H., Crow, D., Chow, J., Gnauk, T., Even, A., ten Brink, H.M.,

Giesen, K.-P., Hitzenberger, R., Hueglin, C., Maenhaut, W., Pio, C., Carvalho, A., Putaud, J.-P., Toom-Sauntry, D. and Puxbaum, H. 2001. Results of the "carbon conference" international aerosol carbon round robin test stage I. Atmos. Environ. 35 : 2111-2121.

Seibert, P. and Jost, D.T. 1994. Investigation of potential source areas by statistical analysis of ALPTRAC aerosol measurements. EUROTRAC Newsletter no. 14 : 14-17.

Seinfeld, J.H. and Pandis, S.N. 1998. Atmospheric Chemistry and Physics: From Air pollution to Climate Change. John Wiley, New York, 1326 p.

Simoneit, B.R.T. 1984. Organic matter of the troposphere: III - characterization and sources of petroleum and pyrogenic residues in aerosols over the Western United States. Atmos. Environ. 18 : 51-67.

Sobanska, S., Coeur, C., Pauwels, B., Maenhaut, W. and Adams, F. 2000. Micro-characterisation of tropospheric aerosols from the Negev desert, Israel. J. Aerosol Sci. 31, Suppl. 1 : S344-S345.

Stohl, A. 1996. Trajectory statistics - a new method to establish source-receptor relationships of air pollutants and its application to the transport of particulate sulfate in Europe. Atmos. Environ. 30 : 579-587.

Taylor, K.E. and Penner, J.E. 1994. Response of the climate system to atmospheric aerosols and greenhouse gases. Nature 369 : 734-737.

Tegen, I. and Fung, I. 1995. Contribution to the mineral aerosol load from land surface modification. J. Geophys. Res. 100 : 18707-18726.

Tegen, I., Lacis, A.A. and Fung, I. 1996. The influence on climate forcing of mineral aerosols from disturbed soils. Nature 380 : 419-422.

ten Brink, H.M., Schwartz, S.E. and Daum, P.H. 1987. Efficient scavenging of the aerosol sulfate by liquid-water clouds. Atmos. Environ. 21 : 2035-2052.

ten Brink, H.M., Veefkind, J.P., Waijers-Ijpelaan, A. and van der Hage, J.C. 1996. Aerosol light-scattering in the Netherlands. Atmos. Environ. 30 : 4251-4261.

Turpin, B.J., Saxena, P. and Andrews, E. 2000. Measuring and simulating particulate organics in the atmosphere: problems and prospects. Atmos. Environ. 34 : 2983-

3013.

Van Borm, W. and Adams, F. 1988. Cluster analysis of electron microprobe data for source apportionment of air particulate matter. Atmos. Environ. 22 : 2287-2307.

Vanderzalm, J.L., Hooper, M.A., Maenhaut, W. and Tapper, N.J. 1998a. Particulate air quality and polycyclic aromatic hydrocarbons in regional northwest Australia and southeast Asia. In: Proceedings 14th International Clean Air and Environment Conference, Melbourne, Australia, 18-22 October, 1998. Clean Air Society of Australia and New Zealand Inc.: 433-438.

VanderZalm, J.L., Hooper, M.A., Tapper, N.J., Maenhaut, W., Ryan, B. and Martin, P. 1998b. An aerosol study of regional haze in northwest Australia and southeast Asia: A preliminary report on methods and first results. In: Proceedings 13th Conference on Fire and Forest Meteorology, Lorne, Australia, 1996, International Association of Wildland Fire, PO Box 327, Moran, WY USA 83013: 127-131.

Van Ham, R., Adriaens, A., Prati, P., Zucchiatti, A., Van Vaeck, L. and Adams F. 2001. Static secondary ion mass spectrometry as a new analytical tool for measuring atmospheric particles on insulating substrates. Atmos. Environ., revised version submitted.

Van Vaeck, L., Adriaens, A. and Adams, F. 1998a. Microscopical speciation analysis with laser microprobe mass analysis and static secondary ion mass spectrometry. Spectrochim. Acta 53B : 367-378.

Van Vaeck, L., Cuynen, E., Van Espen, P. and Adams, F. 1998b. Microscopical speciation analysis with laser microprobe mass spectrometry and static secondary ion mass spectrometry. In: Proceedings of the Second Biennial International Conference on Chemical Measurements and Monitoring of the Environment, Ottawa, Canada, 11-14 May 1998. Clement, R. and Burk, B. (Eds). Carleton University, Ottawa, Canada: 535-540.

Vincze, L., Janssens, K., Adams, F., Rindby, A., Engström, P. and Riekel, C. 1998. Optimization of tapered capillary optics for use at the microfocus beamline (ID 13) at the European Synchrotron Radiation Facility (ESRF). Adv. X-ray Anal. 41: 252-261.

Virkkula, A., Aurela, M., Hillamo, R., Mäkelä, T., Pakkanen, T., Kerminen, V.-M., Maenhaut, W., François, F. and Cafmeyer, J. 1999. Chemical composition of

atmospheric aerosol in the European subarctic: Contribution of the Kola Peninsula smelter areas, Central Europe and the Arctic Ocean. J. Geophys. Res. 104 : 23681-23696.

Waggoner, A.P., Vanderpol, A.J., Charlson, R.J., Larsen, S., Granat, L. and Tradgard, C. 1976. Sulfate light scattering ratio as an index of the role of sulfur in the tropospheric optics. Nature 261 : 120-122.

Waggoner, A.P., Weiss, R.E., Ahlquist, N.C., Covert, D.S. and Charlson, R.J. 1981. Optical characteristics of atmospheric aerosols. Atmos. Environ. 15 : 1891-1909.

White, W.H. 1990. Contributions to light extinction. In: Visibility: Existing and Historical Conditions - Causes and Effects. NAPAP Rep. 24, by Trijonis, J.C., Malm, W.C., Pitchford, M., White, W.H., Charlson, R. and Husar, R. Natl. Acid Precip. Assess. Program, Washington D.C.: 85-102.

White, W.H., Macias, E.S., Nininger, R.C. and Schorran, D. 1994. Size-resolved measurements of light scattering by ambient particles in the Southwestern USA. Atmos. Environ. 28 : 909-921.

Wróbel, A., Rokita, E. and Maenhaut, W. 1999. The influence of meteorological parameters on short range transport of aerosols. Nucl. Instr. and Meth. B150 : 403-408.

Wróbel, A., Rokita, E. and Maenhaut, W. 2000. Transport of traffic-related aerosols in urban area. Sci. Total Environ. 257 : 199-211.

Zdráhal, Z., Vermeylen, R., Claeys, M., Maenhaut, W., Guyon, P. and Artaxo, P. 2001a. Characterization of novel di- and tricarboxylic acids in fine tropical aerosols. J. Mass Spectrom. 36 : 403-416.

Zdráhal, Z., Vermeylen, R., Claeys, M. and Maenhaut, W. 2001b. Characterization of tricarboxylic acids in tropical biomass burning aerosols. In: Proceedings of the 49th ASMS Conference on Mass Spectrometry and Allied Topics, Chicago, Illinois, May 27-31, 2001, 2 pages (published on CD-rom).

Zimmermann, R., Van Vaeck, L., Davidovic, M., Beckmann, M. and Adams, F. 2000. Analysis of polycyclic hydrocarbons (PAHs) adsorbed on soot particles by Fourier

transform laser microprobe mass spectrometry (FT LMMS) : Variation of the PAH patterns at different positions in the combustion chamber of an incineration plant. Environ. Sci. Technol. 34 : 4780-4788.

AS/00/10

BELEUROS: IMPLEMENTATION AND EXTENSION OF THE EUROS (EUROPEAN OPERATIONAL SMOG) MODEL FOR POLICY SUPPORT IN BELGIUM

VITO
Boeretang 200
B-2400 MOL
L. DELOBBE (coordinator AS/00/10)
C. MENSINK

UNIVERSITÉ CATHOLIQUE DE LOUVAIN (UCL)
INSTITUT D'ASTRONOMIE ET DE GÉOPHYSIQUE GEORGES LEMAITRE
Chemin du Cyclotron, 2
B-1348 LOUVAIN-LA-NEUVE
G. SCHAYES (partner)
O. BRASSEUR

FACULTÉ POLYTECHNIQUE DE MONS (FPMs)
Service Fluides - Machines
Rue du Joncquois
B-7000 MONS
C. and D. PASSELECQ (partners)

INSTITUT ROYAL MÉTÉOROLOGIQUE DE LA BELGIQUE
Avenue Circulaire 3
B-1180 BRUXELLES
A. QUINET (partner)

INTERREGIONALE CEL VOOR HET LEEFMILIEU (IRCEL/CELINE)
Kunstlaan 10-11
B-1210 BRUSSEL
G. DUMONT and C. DEMUTH (associate partners)

RIJKSINSTITUUT VOOR VOLKSGEZONDHEID EN MILIEU (RIVM)
P.O. Box 1
NE-3720 BA Bilthoven
D. VAN LITH and J. MATTHIJSEN (external partner)

TABLE OF CONTENTS

ABSTRACT 1

1. INTRODUCTION 2

2. A DYNAMIC EMISSION INVENTORY FOR THE EUROS MODEL 4

2.1 Introduction 4
2.2 Inventory of the available emission data 6
2.2.1 Emission data for the regions inside Belgium 7
2.2.2 Emission data for the regions outside Belgium 8
2.2.3 Emission data for scenario building 9
2.2.4 Summary of the available emission data 12
2.3 Spatial distribution of emissions in Euros 12
2.3.1 GIS Implementation and shifted pole transformation 13
2.3.2 Emission distribution on refined grids 14
2.4 Temporal distribution of emissions in EUROS 15
2.4.1 Emission time factors 16
2.4.2 Temperature dependencies 17
2.5 Partition of emissions into specific substances 18
2.5.1 NMVOC, NO_2/NO and SO_2/SO_4 Split 18
2.5.2 Biogenic NMVOC emissions 19
2.6 Conclusions and suggestions for improvements 19
2.7 References 21
2.8 Figures 23

3. IMPLEMENTATION OF METEOROLOGICAL DATA IN EUROS 26

3.1 Introduction 26
3.2 The Euros Model 26
3.3 Description of the meteorological data 28
3.3.1 ECMWF meteorological data 28
3.3.2 ALADIN meteorological data 29
3.3.3 Processing of the meteorological data 29
3.4 Mixing height from meteorological data sets 30
3.4.1 Description of methods to estimate mixing heights 30
3.4.1.1 Virtual potential temperature (VPT) method 31
3.4.1.2 Bulk Richardson number (BRN) method 32
3.4.1.3 Modified Bulk Richardson number (MBRN) method 34

3.4.2 Results from ECMWF data set 35
3.4.3 Results from ALADIN data set 37
3.4.4 Comparison with observed vertical soundings and discussion 39
3.5 Mixing height from model simulations 41
3.5.1 Overview of the MAR model 42
3.5.2 Description of experiments 42
3.5.3 Validation of MAR simulations 43
3.5.4 Mixing-layer heights 45
3.5.5 Boundary-layer height 50
3.5.6 Temporal evolution of mixing and boundary-layer heights 53
3.5.7 Conclusions of simulation results 57
3.6 Conclusions 58
3.7 References 60

4. OPTIMIZATION OF CHEMICAL AND ADVECTION MODULES IN EUROS 63

4.1 Introduction 63
4.2 Parameterization of the mixing layer height in Euros 64
4.2.1 General description 64
4.2.2 Improvements 66
4.2.2.1 Distinction land/sea 66
4.2.2.2 Comparison with LIDAR observations 67
4.2.2.3 Choice of parameters 69
4.2.2.4 Update of the ML height formulations 70
4.3 Horizontal transport 70
4.4 Simulations with a variable mixing height 73
4.4.1 Land procedure used everywhere 73
4.4.2 Distinction land/sea 75
4.4.3 Impact of the vertical discretisation used for the advection 76
4.4.4 Comparison with measurements 78
4.5 Chemistry: selection of relevant components and reactions 80
4.5.1 Definition of the problem 80
4.5.2 Database 81
4.5.3 Selection of compounds 82
4.5.3.1 Organic compounds 82
4.5.3.2 Methods to select organic compounds relevant to atmospheric chemistry 83
4.5.4 Conclusion 84
4.6 Conclusions 84
4.7 Acknowledgements 85
4.8 References 87
4.9 Figures 90

5. USER INTERFACE **104**

5.1 Introduction **105**
5.2 Procédure d'acquisition du logiciel **106**
5.3 Présentation générale des fonctionnalités **109**
5.3.1 Option «Start» *110*
5.3.2 La ligne de menu «Emissions factors» *115*
5.3.3 La ligne de menu «Point Sources» *121*
5.3.4 La ligne de menu «Meteo» *128*
5.3.5 La ligne de menu «EurosFile» *130*
5.3.6 La ligne de menu «Internet» *136*
5.3.7 La ligne de menu «Results» *141*
5.4 Actions pour créer un scénario **147**
5.5 Conclusions **154**

6. IMPACT MODELLERING **154**

6.1 Inleiding **154**
6.2 Effect van ozon op gezondheid en vegetatie **155**
6.2.1 Effect op gezondheid *155*
6.3 Blootstellings-effect relaties voor gezondheid **155**
6.3.1 Effect op vegetatie *158*
6.3.2 Blootstelling-effect relaties voor vegetatie *159*
6.4 Wetgeving betreffende luchtverontreiniging door ozon **161**
6.5 Samenvatting van alle indicatoren **163**
6.6 Impact evaluatie met behulp van Euros **164**
6.7 Conclusies **166**
6.8 References **167**

7. GENERAL CONCLUSIONS **170**

ANNEX **173**
A1: Scientific publications related to the project **173**
A2: List of the contributors to the project **175**
A3: Annexe au chapitre 5: "User interface" **176**

ABSTRACT

In the framework of the BelEUROS project, a new version of the EUROS model coupled with a state of the art user interface has been installed at IRCEL/CELINE as a tool for policy support with respect to tropospheric ozone. This tool allows evaluating the impact of potential emission reduction strategies on ozone concentrations.

The EUROS model is an Eulerian atmospheric model that simulates tropospheric ozone over Europe on a long term basis (up to several years). The model was developed at the Rijksinstituut voor Volksgezondheid en Milieu (RIVM, The Netherlands). For its implementation in Belgium, the model has been further developed in collaboration with the RIVM and some input data have been adapted. The new developments concerned the representation of the atmospheric boundary layer processes. The calculation of the horizontal transport has been improved and a spatially variable mixing height has been implemented. The model is now provided with a three dimensional grid structure.

As far as the input data are concerned, a new meteorological data set has been generated from the meteo data of the European Centre for Medium-Range Weather Forecast (ECMWF, Reading, UK). A dynamic emission inventory has been compiled for the European countries that are covered by the EUROS domain. The inventory provides the spatial and temporal variations in anthropogenic emissions for six emission sectors (traffic, space heating, refinery, solvents use, combustion, industry) and the distribution of biogenic emissions varying with temperature. This inventory was implemented in a GIS (Arcview).

The new version of the model has been coupled with a user friendly interface on a Windows platform written in VISUAL-C++. It allows the user to define the emission reduction scenarios, to start the simulation from his own computer through internet exchanges with IRCEL/CELINE and to visualise and analyse the simulation results.

The user has the possibility to modify the emission rates of a given pollutant (NOx or VOC) for a given emission sector and for a given geographical area. Monthly, daily and hourly emission factors can also be modified for each sector. These factors account for the influence of the month, the day in the week, and the hour of the day.

The simulation results allow estimating the indicators currently used to evaluate the effect of ozone on vegetation and human health, such as AOTs (Accumulated exposure over a Threshold) and NETs (Number of Exceedances of Threshold). These indicators are also used in the European legislation relating to ozone in

ambient air. EUROS is therefore an appropriate tool for the evaluation of possible emission reduction measures.

1. INTRODUCTION

During summertime, high ozone concentrations in the ambient air are a threat for public health and vegetation. This concern is shared at various policy levels. At the European level, long-term objectives for the reduction of ozone concentrations have been defined in the framework of the Directive 96/62/EC. According to the daughter directive in preparation, the target values should be attained by the member states by the year 2010.

In order to reach these objectives, most of the member states will have to reduce drastically the emission of pollutants responsible for ozone formation, i.e. nitrogen oxides (NOx = NO + NO_2) and non-methane volatile organic compounds (VOC). In this perspective, it is essential to provide the policy makers with adequate tools for evaluating the impact of possible emission reduction strategies on the ozone concentrations. Numerical atmospheric models are well suited for this task. These models represent the various atmospheric processes responsible for ozone formation and destruction: pollutant emission, atmospheric dispersion and transport, chemical transformations and deposition. Model simulations allow estimating the effect of specific emission reduction measures on ozone concentrations.

The aim of the BelEUROS project is to provide the Belgian authorities with such a modelling tool for policy support with respect to tropospheric ozone. The EUROS model (EURopean Operational Smog model) was earlier selected for this purpose (van Loon, 1996). EUROS is a regional chemistry-model which has been developed at the RIVM (Rijksinstituut voor Volksgezondheid en Milieu, Bilthoven, The Netherlands). It simulates ozone formation over Europe with a standard resolution of 60 km. A grid refinement procedure allows to refine the spatial resolution in certain areas of the model domain, for example Belgium. A detailed emission module describes the emission of three pollutant categories (NOx, VOC, SO_2) for 6 different economical sectors.

The implementation of the EUROS model in Belgium required the adaptation of some input data (emission and meteorological data) and the modification of some intrinsic features of the model. These model developments were related to the representation of the atmospheric boundary layer and were motivated by the differences in topography between Belgium and The Netherlands. It mainly concerned the implementation of a spatially variable mixing height and of a multi-layer

representation of the horizontal transport. This work has been carried out in close collaboration with the RIVM.

The final goal of this project was to install the new version of the EUROS model at the Interregional Cell for the Environment (IRCEL/CELINE) in Brussels and to make it available to user groups in the three Belgian Regions. A complex model as EUROS can not be used efficiently by policy makers if it is not provided with a user friendly interface allowing the user to define the general characteristics of his simulation, to specify the emission scenarios and to visualise and analyse the output results. Therefore, an important task of this project was the development of an effective windows user interface. This interface must also control the Internet exchanges between the local computer of the user and the central computer at IRCEL where the model runs. This allows the user to start a simulation from a remote location through internet connection.

The distribution of the tasks between the various partners was organised as follows. VITO (Mol) was in charge for the development of a new emission inventory. The new developments on the EUROS model itself were realised by VITO in collaboration with UCL (Louvain-la-Neuve) for the meteorological aspects. FPMs (Mons) was in charge for the development of the user interface and for the installation at IRCEL in collaboration with the VITO and IRCEL. The task of RMI (Brussels) was to provide the meteorological data. VITO was also in charge of a study concerning the impact modelling of ozone on human health and vegetation. As user and associate partner, IRCEL has played an important role as adviser throughout the whole project. The co-ordination of these tasks was ensured by the VITO.

This final report gives a complete overview of the work, which has been carried out in the framework of the BelEUROS project. In chapter 2, we describe the development of dynamic emission inventory for the European countries that are covered by the EUROS domain. This inventory provides the spatial and temporal variations in anthropogenic emissions for six economical sectors and the spatial distribution of biogenic emissions varying with temperature.

The implementation of the meteorological data in EUROS is described in chapter 3. After a short description of the EUROS model, the meteorological data sets are presented. These data are used to determine the meteorological forcing applied to the EUROS model. An important atmospheric feature is the mixing height. Several methods are described to estimate the mixing height from the meteorological data. The results of these methods are evaluated through comparison with observational data and with results of more sophisticate models.

The development of a new version of the EUROS model is described in chapter 4. The new version includes a spatially variable mixing layer and a multi-layer representation of the horizontal transport. The model is now provided with a three-dimensional grid structure. In this section various methods are also briefly described allowing to select the relevant chemical components and reactions in order to reduce the complexity of the chemical module.

The input/output user interface and the installation at IRCEL are presented in chapter 5. It consists of a user friendly Windows interface developed in VISUAL-C++. It allows the user to define emission reduction scenarios, to start the simulation from his own computer through internet exchanges with IRCEL/CELINE and to visualise and analyse the simulation results. The general characteristics of the software are presented as well as an extended user guide. The control of the Internet exchanges and the model administration are also described.

Chapter 6 is devoted to the impact modelling. The impact of ozone on human health and vegetation are briefly described and a short overview of currently used dose-response relationships is given. The current European legislation with respect to ozone is also described and the main indicators currently used to evaluate the impact of ozone are summarised. Finally, the main results of this project are summarised and general conclusions are drawn.

2. A DYNAMIC EMISSION INVENTORY FOR THE EUROS MODEL [1]

2.1 Introduction

The EUROS (EURopean Operational Smog) model is a regional atmospheric model developed and implemented to simulate photochemical smog situations on a long-term base. EUROS can provide policy support by modelling the impact of emission reduction strategies and emission reduction measures on ozone formation. The model has originally been developed at the National Institute of Public Health and Environmental Protection (RIVM, Bilthoven, The Netherlands) (van Loon, 1996). Its implementation for Belgium requires an adaptation of the input data (emissions, meteorology, geography) and a modification of some intrinsic features of the model.

The first work package of the OSTC project “Implementation and extension of the EUROS model for policy support in Belgium” (Contract AS/00/10) deals with the

[1] The content of this chapter is taken from the intermediary report: Mensink C and L. Janssen, 2000. A dynamic emission inventory for the EUROS model. Scientific report. 2000/TAP/R/6, VITO, Mol.

construction of a dynamic emission inventory for the European countries that are covered by the EUROS domain.

The objective of work package 1 was to determine the emissions of the relevant ozone precursors inside and outside of Belgium and to describe in detail (especially for Belgium) their spatial and temporal variations, as well as their temperature dependency. Besides an inventory and acquisition of the most recent available emission data, the construction of emission scenarios was a second objective of this work package.

Starting point of the construction of a dynamic emission inventory for the EUROS model are the existing and available national (and regional) emission inventories. Section 2.2 of this report describes the emission data and data sources that were used to describe the emissions inside and outside of Belgium. Emission data for the construction of scenarios up to 2010 are presented as well.

In section 2.3 a methodology is describes which can provide a spatial distribution of the emission data over Europe at the desired grid levels, ranging from 60 km x 60 km (base grid level) to 7.5 km x 7.5 km (3^{rd} refinement level). As EUROS has the possibility to apply grid refinement in a static way at locations of interest or in a dynamic way, i.e. following strong gradients in the concentration field, the emissions have to be provided at the corresponding grid levels. The methodology was implemented in a GIS (Arcview) which was very useful in this context.

In section 2.4 the temporal variations and temperature dependencies of the emissions are described. The methodology to specify emissions in function of time is based on so called emission time factors. These factors yield *typical* emission patterns, rather than *actual* emissions at a certain moment. A better representation of actual emission data can be obtained by using the temperature as an input variable to describe temporal emission variations. Especially NMVOC emissions are very sensitive to temperature changes.

Section 2.5 deals with the further distribution or "split" of the emissions into classes of specific substances. This is very important for the NO_x and NMVOC emissions, since they are the driving force for the (photo)chemical activities modelled by the chemistry module in EUROS. The resulting ozone concentrations depend strongly on how the total NMVOC emissions are split into the individual components. Section 5 described also how biogenic emissions (isoprenes and monoterpenes) are modelled spatially and in function of the temperature.

In section 2.6 conclusions and suggestions for further improvements are given.

It must be noted that the number of Figures has been limited in the present document. More illustrations can be found in Mensink and Janssen (2000).

2.2 Inventory of the available emission data

National and regional emission inventories form the starting point for the construction of a dynamic emission inventory. At a European level data sources are EMEP (Mylona, 1999), CORINAIR 1985 (EC, 1995), CORINAIR 1990 (EEA, 1995), CORINAIR 1994 (EEA, 1997) and various national and regional inventories. However, on a very detailed level, various data (e.g. industrial point sources and their locations) are not always available because of various reasons (lack of registration, confidentiality, organisational or political reasons (Jol, 1999), etc.). To overcome these problems, available data on NUTS3 level (NUTS = Nomenclature des Unités Territoriales Statistiques) were exploited as much as possible and combined with detailed geographical information on point source locations, traffic routes, population densities, distribution of industrial activities, etc.

On the other hand national statistics were used, not only to disaggregate emissions over individual source categories, but also to describe e.g. sector dependent source heights and time dependent emission patterns (see section 2.4). In this way a mixture of a top down and bottom up approach is obtained. The result is an inventory which complies with the official reported national emission data, but which represents *typical* emission distributions and emission patterns, rather than *actual* emission patterns described with all possible geographical details. This somehow represents a balance between available information and the difficulties to obtain more detailed information on one hand and the required detail by the EUROS model on the other hand. Improvements are always possible, but are not always effective.

The substances for which emission data are needed in EUROS are sulphur dioxide (SO_2), nitrogen oxides (NO_x) and non-methane volatile organic compounds (NMVOC). The anthropogenic emission source categories (emission sectors) included in the EUROS model are:

- Combustion (power plants & industry)
- Space heating
- Refineries
- Chemical processes
- Solvent use
- Road traffic

In section 2.2.1 the emission data sources for the regions inside Belgium are discussed. Section 2.2.2 gives an overview of the data sources that were used to specify emissions outside Belgium. Section 2.2.3 deals with the data sources that were used to specify emission scenario's up to 2010.

2.2.1 Emission data for the regions inside Belgium

The Emission Inventory for the Flemish Region (EIVR) (VMM, 1999) provides a very detailed spatial distribution of registered industrial point source emissions, emissions from space heating (1 km x 1 km) and traffic emissions (1 km x 1 km). The actual emission inventory includes the period 1980-1998 and was used earlier to supply the OPS (Operational Priority Substances) model with emission data (Mensink et al. 1998). From all registered industrial point sources only sources with emission rates higher than 10 tons/year for SO_2 and 1 ton/year for NO_x and NMVOC were selected. This covers 94% of the industrial SO_2 emissions, 96% of the industrial NO_x emissions and 100% of the NMVOC emissions from industrial point sources in Flanders. Correction factors were used to recover 100 % of the emissions. In this way 304 point sources for SO_2 , 392 point sources for NO_x and 239 point sources for NMVOC were obtained.

From the large number of selected point sources, the average source height and average flue gas temperature could be calculated. This information is needed in the EUROS model to compute the effective plume height. Unfortunately this information is very seldom available. Therefore it was assumed that the large amount of point source data for Flanders provide a sound statistical base to calculate average stack heights and flue gas temperatures representative for each emission source category. These Figures were then used for the source categories outside Flanders, where no detailed information is available. The results are given in Table 1. In the calculation of the average flue gas temperature, the individual values are weighted by the flue gas volumes.

Table 1: *Average stack height and flue gas temperature per source category.*

Source category	Average stack height (m)	Average flue gas temperature (K)
Combustion:		
power plants	107	398
industry	36	465
Refineries	65	611
Chemical processes	51	433

Very recently, additional estimations of non-registered and diffusive emissions were made (Van Rompaey, 2000). They were not yet included in the dynamic emission inventory for the EUROS model in order to stay with the officially reported emission data for Flanders. This also enhances the implementation of scenarios as described in section 2.2. However, the diffusive emissions can be added as soon as the EIVR will publish these data officially.

For space heating and road traffic, area sources of 1 km x 1 km are available for SO_2, NO_x and NMVOC. They are aggregated to obtain the desired grid level, ranging from 60 km x 60 km (base grid level) to 7.5 km x 7.5 km (3rd refinement level). The aggregation procedure is carried out by a Fortran program in combination with GIS scripts. This will be discussed in section 2.3.

The distribution of emissions in the Walloon region were derived visually from the *Altas de l'air de la Wallonie* (Ministère de la région Wallonne, 1998). This atlas provides the spatial distribution (5 km x 5 km) of SO_2, NO_x and NMVOC emissions for 1996. The emissions for the period 1990-1998 were derived from additional information given by EMEP, CORINAIR and information published by the Walloon government (EMIS, 2000). Detailed information on industrial point sources was not available, therefore the data at NUTS3 level were used in combination with the information from Table 1 and with the geographical information (point source locations) provided by the atlas and other maps.

For the Brussels region the inventory obtained by Institut Wallon (1995) was used. Except for a few point sources, the emissions were evenly distributed over the Brussels area (161 km²), because no further information on the spatial distribution of the emissions could be obtained so far.

2.2.2 Emission data for the regions outside Belgium

The CORINAIR emission inventory 1985 (EC, 1995) gives the spatial distribution for SO_2, NO_x and NMVOC emissions in the (at that time) 12 EU countries. The Figures are given at NUTS3 level which is equivalent to "counties" in the UK, "arrondissements" in France and "Kreise" in Germany.

CORINAIR 1990 (EEA, 1995) does not provide a spatial distribution at NUTS3 level. Yearly averaged emissions are reported for 29 European countries. The emissions are split into 11 subcategories, following the SNAP (Selected Nomenclature for Air Pollution) code (McInnes, 1996). In order to construct an emission inventory for the base year 1990 which contains sufficient spatial detail, the data from CORINAIR 1985 and 1990 were combined into one data base. Additional statistical data (like population densities, etc.) and geographical maps were used to distribute emissions

in the countries where no NUTS3 level data were available. This implementation was done using a GIS (Arcview), as will be discussed in section 2.3. For the countries and important industrial regions neighbouring Belgium, geographical maps were used to refine the spatial detail (e.g. by locating industrial areas).

At the moment the combination of CORINAIR 1985 and CORINAIR 1990 provide sufficient information to split the emissions into the 6 emission source categories included in EUROS. A more detailed category split inside each of the 11 SNAP categories can be obtained by using the CORINAIR 1994 data set (EEA, 1998). However, for the moment the extension of the source category split is not a priority.

For the actualisation of the CORINAIR 1990 data EMEP (Mylona et al., 1999) is used. Under the Convention on Long Range Transboundary Air Pollution (LRTAP) the Task Force of Emission Inventories under EMEP presents yearly the state of the emission data. This is a combination of the official national submissions and emission data used for modelling at MSC-W. The latter contains also emissions for parts of the modelling domain that are not fully covered by official submissions. Furthermore possible gaps in the inventory are filled with estimates from available open sources. Annual emission data per country are given for the period 1980-1997. These data are used to transform the spatially distributed emission inventory for the base year 1990 to any desired year between 1980 and 1997. At the moment this is done by calculating a emission coefficient per year and per country. In the near future EMEP will provide data per sector for the 11 SNAP categories, which will allow a calculation of the emission coefficient per source category as well.

2.2.3 Emission data for scenario building

For the period 1998-2010 no emission data are registered or available for the countries in the EUROS domain. Therefore one has to use scenarios in order to explore future emissions. Three scenarios for the period 1998-2010 have been set up, allowing an assessment of the impact of current and future abatement strategies.

A first scenario is called the reference (REF) scenario. It incorporates the current reduction plans, in which former officially adopted national emission ceilings are included, as well as the current legislative actions that are needed to comply with the adopted national and international regulations on emission control. These legislative actions include not only national emission control regulations in the individual European countries (e.g. Vlarem II in Flanders), but also the relevant European Directives and the obligations for the protocols under the Convention on Long Range Transboundary Air Pollution, e.g. the Second Sulphur Protocol. Implementation of the Auto/Oil-1 programme is included in the legislative actions as well. The REF scenario selects the more stringent emission reduction from the current reduction plans and

the current legislative actions. It was used as a reference scenario in the exploration of possible cost-effective abatement strategies on acidification and ozone for the European Commission (Amman et al., 1999). The main reduction measures included in the REF scenario are given in Table 2. The resulting emissions for the 15 EU countries are given in Table 3.

The second scenario is known as the National Emission Ceilings (NEC) scenario. The emission ceilings were laid down in the 8th Protocol to the Convention on Long-Range Transboundary Air Pollution abating acidification, eutrophication and ground-level ozone (Europe environment, 1999). The European Commission's emission reduction strategies aim at a reduction of the area of unprotected ecosystems in Europe by at least 50% in 2010 compared to 1990. For ozone formation the AOT60 (Accumulated exposure Over a Threshold value of 60 ppb) is used as an indicator for the protection of human health. An eight-hour maximum value of 60 ppb is considered as a level at which acute adverse effects occur in the population (WHO, 1997). In the NEC scenario a 67% reduction of the AOT60 as estimated for 1990 is aimed at. For damage on vegetation the AOT40 (Accumulative exposure Over a Threshold value of 40 ppb) is used as indicator. The NEC scenario aims at a reduction of 33% of the AOT40 as compared to the situation in 1990. The main reduction measures included in the NEC scenario are given in Table 2. The emission ceilings per country are given in Table 3.

Table 2: *Main reduction measures included in the REF & NEC scenarios.*

	REF	NEC
SO_2	• Large combustion plant directive	• Stage 1,2,3 Abatement technologies for process emissions
	•Directive on sulphur content of gas oil	• Low sulphur heavy oil fuel
	• Second Sulphur Protocol	• Low sulphur coal
	• Best Available Technologies (BAT) for new plants	• Flue gas desulphurisation
NOx	• Large combustion plant directive	• Stage 1,2,3 Abatement technologies for process emissions
	• Best Available Technologies (BAT) for new plants	• Selective catalytic and non-catalytic reduction
	• Auto Oil I	• EUR3 Post 2000 standards for heavy duty diesel vehicles
	• Inspection and maintenance programs	• Improved inspection and maintenance programs
NMVO	• Stage 1	• Stage 1,2,3 Abatement technologies for process emissions
	• EU Solvent Directive	• New technologies for solvent use
	• Regulations on carbon canisters	• EUR3 Post 2000 standards for heavy duty diesel vehicles
	• Auto Oil I & inspection and maintenance programs	• Improved inspection and maintenance programs

Table 3: *Emissions per country for the REF & NEC scenarios in 2010.*

	SO2 REF	SO2 NEC	NOx REF	NOx NEC	NMVOC REF	NMVOC NEC
Albania	55		36		41	
Armenia		73		46		81
Austria	40	39	103	107	205	159
Belarus	494	480	316	255	309	309
Belgium	193	106	191	181	193	144
Bosnia-H.	415		60		48	
Bulgaria	846	856	297	266	190	185
Croatia	70	70	91	87	111	90
Czech Republic	366	283	296	286	305	220
Denmark	90	55	128	127	85	85
Estonia	175		73		49	
Finland	116	116	152	170	110	130
France	448	400	858	860	1223	1100
Germany	581	550	1184	1081	1137	995
Greece	546	546	344	344	267	261
Hungary	546	550	198	198	160	137
Ireland	66	42	70	65	55	55
Italy	567	500	1130	1000	1159	1159
Latvia	104	107	118	84	56	136
Liechtenstein		0,11		0,37		0,86
Lithuania	107	145	138	110	105	92
Luxembourg	4	4	10	11	7	9
Netherlands	73	50	280	266	233	191
norway	32	22	178	156	195	195
Poland	1397	1397	879	879	807	800
Portugal	141	170	177	260	144	202
Republic of Moldova	117	135	66	90	42	100
Romania	594	918	458	437	504	523
Russian Federation	2344		2653		2787	
PEMA		635		265		165
Slovakia	137	110	132	130	140	140
Slovenia	71	27	36	45	40	40
Spain	774	774	847	847	669	669
Sweden	67	67	190	148	290	241
Switzerland	26	26	79	79	144	144
FYR Macedonia	81		29		19	
Ukraine	1488	1457	1433	1222	851	797
United Kingdom	980	625	1186	1181	1351	1200
Yugoslavia			152		139	
European Community	4687	4059	6849	6671	7128	6600
Non-EU	9732		7718		7041	
Total	14419		14567		14169	

A third scenario is called a User Defined Scenario (UDS) where the user can provide emission reductions per sector and per country or region. The options to specify this scenario have to be provided through the user interface (section 5).

2.2.4 Summary of the available emission data

Summarising the three previous sections, the following options are available for the calculation of emissions for the EUROS model:

- Emission substances: SO_2, NO_x and NMVOC
- Time period (annual averages) 1980-1997: officially reported data (EMEP)
- Time period 1998-2010: emission scenario's:
- REF scenario
- NEC scenario
- UDS scenario
- Geographical units: NUTS3 level + more spatial details for Belgium and its surrounding areas and regions.
- Source categories:
- Combustion (power plants & industry)
- Space heating
- Refineries
- Chemical processes
- Solvent use
- Road traffic
- Nature (treated separately)

2.3 Spatial distribution of emissions in EUROS

As described in section 2.2, the dynamic emission inventory is based on a spatial distribution on NUTS3 level. The polygons describing the districts, counties and provinces that make up the NUTS3 level areas are available in a GIS environment.

However, the EUROS grid is defined in shifted pole coordinates where the longitude and latitude coordinates are shifted and transformed in order to obtain approximately equally sized grid cells. Equally spaced grid cells reduce numerical errors due to the

discretisation of the equations and the spatial domain. Furthermore they enhance the maximum allowable time step that is used in the advection scheme in order to obtain a stable solution.

As a result the emissions, as spatially provided on NUTS3 level, had to be redistributed on the EUROS grid. The transformation, interpolation and quality control techniques that were used to do this are described in section 2.3.1. Except for the base grid (60 km x 60 km) the emissions have to be provided at the desired grid refinement level as well. This is described in section 2.3.2.

2.3.1 GIS Implementation and shifted pole transformation

The source data sets used for the implementation of the dynamic emission inventory in GIS (Arcview) are the GeoDataset NUTS0 – European NUTS first level - and the GeoDataset NUTS3 – European NUTS fourth level. These data sets are a subset of ESRI Data & Maps 1998. The NUTS0 data set consists of a statistical data and country borders for the European countries. In total the database includes 45 polygons and 173 descriptive fields per polygon. The NUTS3 level database includes 1335 polygons and 5 descriptive fields per polygon containing statistical information.

One of the 5 fields contains an ID number, i.e. a unique Region-Group ID Code. This ID number could be connected to the ID number used in the CORINAIR 1985 database where the emissions are provided on NUTS3 level. In a next step the SO_2, NO_x and NMVOC emissions are added to each of the 1335 polygons. By using the CORINAIR 1990 data the emissions in each polygon were updated for 1990 and redistributed over 6 emission source categories.

The shifted pole transformation is applied as follows. First of all, the vector coordinates of the polygons (country borders) are written in an ASCII table using an Arcview script. In a next step the shifted pole transformation is applied using a Fortran program. The transformed coordinates (X,Y) are then read in again by a second Arcview script, so that they can be used for further processing. The tables with the SO_2, NO_x and NMVOC emissions are linked again to the new (transformed) polygons by means of the unique ID number. As a quality check, the sum of the areas before and after the transformation was compared. The total surface area of the polygons before the transformation was 6.731.370 km². After the transformation the total surface area of the polygons was 6.736.575 km². This means that due to the transformation procedure an error of less than 0.08% was introduced.

As a final step in the GIS implementation the emission values per unit area (km²) were calculated. As a result Figure 1 shows the distribution of the total SO_2 emissions for 1990 over the NUTS3 areas in Europe. Note that the surface areas are

not equally distributed when different countries are compared. However, the emissions are expressed in tons/km² so the colors give a good indication of the differences in emission densities. Similar Figures can be obtained for the 6 emission sectors. For space heating and combustion, the larger contributions can be found in East Europe. For NO_x emissions the opposite is true, as can be seen in Figure 4 for the total NO_x emissions.Also for the NMVOC emissions the emission densities are highest in West Europe..

Biogenic NMVOC emissions are described separately in section 2.5.2.

2.3.2 Emission distribution on refined grids

The EUROS domain in shifted pole coordinates stretches out between -8.25° and 20.35° in longitudinal direction and between –23.10° and 7.15° in lateral direction. The base grid consists of 52 x 55 grid cells with a grid spacing of 0.55° x 0.55° (+/- 60 km x 60 km).

In Arcview the polygons are converted into grid cells by means of an interpolation routine. In this routine the coordinates of the centers of the grid cells are allocated to the polygon in which they are located. The aim is to obtain mass conservation during this conversion. This was tested for 5 different grid cell sizes:

base grid: 0.55° (+/- 60 km)

1st refinement level: 0.275° (+/- 30 km)

2nd refinement level: 0.1375° (+/- 15 km)

3rd refinement level: 0.06875° (+/- 7.5 km)

4th refinement level: 0.034375° (+/- 3.75 km)

In a first method a direct interpolation in GIS was applied. When comparing the total surface area and the total emissions obtained from the polygons with the ones obtained from the grid cells, it was found that the differences were too large and not acceptable (> 5%). In an improved method, the exact surface area of the grid cells was calculated outside GIS by a Fortran routine and multiplied by the emission density found in the allocated polygon. The results for each of the six grid cell sizes are found in Table 4.

Table 4: *Errors in surface area and emission mass conservation.*

Grid cell size	Error in calculated surface area	Error in calculated emissions
0.55°	0.44%	1.21%
0.275°	0.38%	1.12%
0.1375°	0.35%	1.08%
0.06875°	0.15%	0.73%
0.034375°	0.11%	0.83%

The second column in Table 4 gives the error in the total surface area obtained from the grid cells compared to the total surface area obtained from the polygons. The last column in Table 4 shows the error in the total NO_x emissions obtained by multiplying the emission densities per grid cell by the surface area per grid cell, compared to the total NO_x emissions distributed over the NUTS3 polygons. The errors made in the procedure are probably due to the discretisation of the emission values, the representation of the surface areas in GIS and the 3D projection of areas on the 2D surfaces in shifted pole co-ordinates.

For emissions due to space heating and road traffic, area sources of 1 km x 1 km are available for the Flanders region. They are aggregated into the desired grid level by means of a Fortran program which scans the individual area sources in order to find out in which grid cell they belong.

Examples of the emission distribution on refined grids are shown in Figures 10 and 13. Figure 10 shows the total NO_x emissions distributed on the base grid (0.55°). Figure 13 shows the total NO_x emissions on the 3rd refinement level (0.06875°).

2.4 Temporal distribution of emissions in EUROS

The temporal emission variations are modelled using temporal emission factors based on various sources of emission measurements and national statistics (e.g. traffic counts and several years of degree days measured at different locations). The procedure to obtain these temporal emission factors is also described in the EMEP/CORINAIR Atmospheric Emission Inventory Guidebook (McInnes, 1996). Section 2.4.1 summarises the results of this procedure.

For some cases it is more interesting to describe the temporal behaviour of emissions as a function of temperature, rather than prescribing it with time factors. In

this way a more actual emission pattern can be obtained. This is especially the case for emissions due to space heating, as will be discussed in section 2.4.2.

2.4.1 Emission time factors

Hourly variations in emissions can be obtained by multiplying the annual emissions with three emission time factors Γ_m, Γ_d and Γ_h where

Γ_m for monthly variations;

Γ_d for daily variations (weekdays) and

Γ_h for hourly variations

are determined per emission category, such that:

$$(12 \cdot 7 \cdot 24)^{-1} \sum_{m,d,h} (\Gamma_m \cdot \Gamma_d \cdot \Gamma_h) = 1$$

At the moment the emission time factors have been determined for the categories industrial combustion (including power stations, refineries and large industrial plants), space heating and road traffic. Figures 16, 17 and 18 show, per source category, the time factors for the monthly, daily and hourly variations respectively (Mensink et al., 1999).

The monthly time factors for industrial combustion are based on the monthly fuel consumption. The daily and hourly time factors were adopted from the emission guide book (McInnes, 1996).

The monthly time factors for space heating are based on the calculated monthly averaged degree days (15/15) for Antwerp, Gent and Mol over the period 1987-1991 and for Mol over the preiod 1964-1993. The differences in time factors during winter months between these cities was only 3-4%. Daily variations for space heating were not considered, because of insufficient data. Thus the time factor concerned was set to Γ_d = 1.0. The hourly variations were adopted from the OPS model (van Jaarsveld, 1990). Note again that by using time factors for the space heating emissions a typical emission pattern is obtained. An actual picture of the space heating emissions can be obtained by expressing the emissions as a function of temperature (see section 2.4.2).

The monthly, daily and hourly variations in road traffic emissions are based on traffic counts carried out in 1993 in Flanders (Ministerie van de Vlaamse Gemeenschap, 1996). The time factors were based on the results of 8 counting stations along

highways and 10 counting stations along national roads. The factors obtained for both road categories were weighted with a factor of 0.33 for the highways and a factor of 0.67 for the national roads.

The time factors specified in this section are basically derived from available data for the Flanders region. At the moment it is assumed that the time factors can be used for the whole of Europe. This will of course not be correct (e.g. for space heating in South Europe). An improvement would be to specify the emission time factors per country or region. However, at the moment sufficient data are lacking in order to do this exercise.

Local time is used as input to determine the actual value of Γ_h. In the EUROS model the local time is used depending on the time zone to which the country belongs.

2.4.2 Temperature dependencies

For the determination of actual hourly space heating emissions it is suggested to use an expression in which the emission is a function of the actual temperature. Such a function could look like this:

$$E_{space}(t) = E_{annual} * (15°C - T(t)) / (\sum_{i=1,8760} (15°C - T_i)) \qquad \forall \; T(t) < 15°C$$

$$= 0 \qquad \forall \; T(t) \geq 15°C$$

where:

E_{space} : actual calculated hourly averaged emission for space heating (kg/h)

E_{annual} : annual emission for space heating (kg/yr)

$T(t)$: actual temperature (°C)

T_i : temperature for hour i (summed over the 8760 hours per year)

One problem is of course to find the annual sum of hourly temperatures in case of actual situations. However this value could be estimated from long term averages. In some cases the space heating emissions are not zero for temperatures above 15°C. Water heating for sanitary purposes could for example contribute to the space heating emissions. For countries in North West Europe this is estimated to make up 10% of the total emissions for space heating (McInnes, 1996).

Biogenic emissions are very dependent on temperature variations. This temperature dependency is included in the model equation used to estimate the biogenic emissions. This is discussed in section 2.5.2.

2.5 Partition of emissions into specific substances

For the chemistry models that are used to describe the formation of ozone, the emissions of SO_2, NO_x and NMVOC do not contain sufficient detail with respect to the reaction substances and products that play a role in the (photo)chemical processes. Therefore these principal emissions are split into specific substances. This subdivision depends on the type of chemistry model that is used. Section 2.5.1 shows how SO_2, NO_x and NMVOC are split into the various substances for the EUROS model.

Biogenic emissions are treated in EUROS as a separate emission source category. Basically isoprenes and monoterpenes are the emitted NMVOC species for this category. In section 2.5.2 it is described how these emissions are modelled in function of the forest or vegetation type, the spatial distribution of these types and in function of temperature.

2.5.1 NMVOC, NO_2/NO and SO_2/SO_4 Split

Preliminary tests with different chemical models used in EUROS have shown the importance of applying an emission category specific NMVOC split instead of one NMVOC split for all emission categories (Hammingh, 1999). The results of the study by Hammingh (1999) are adopted in this section. For the 6 emission categories specified in the EUROS model the NMVOC split has been derived for the EMEP chemistry model and for two versions of the Carbon Bound IV chemistry models (CB-IV_V and CB-IV_99) actual in use. Starting point is the NMVOC split by Barrett and Berge (1996) as used in EMEP for 10 individual emission source categories. This is shown in Table 5. By aggregating the 10 sectors into the 6 EUROS source categories the results in Table 6 are obtained. The translation from the NMVOC components in EMEP to the lumped NMVOC species in the CB-IV models is given in Table 7. The resulting emission category specific NMVOC split is given in Table 8 and Table 9 for the CB-IV_V version and the CB-IV_99 version, respectively.

For the split of NO_x emissions into NO and NO_2 a fixed partition is used:

$$NO_x = 95\%\ NO + 5\%\ NO_2$$

In case of temperatures lower than 5°C the contribution of NO_2 increases to 15% due to the contribution of so called "cold start" emissions. For the SO_2 emissions it is assumed that 3% of the emissions is initially converted into SO_4.

2.5.2 Biogenic NMVOC emissions

Biogenic NMVOC emissions have to be expressed in terms of isoprene and monoterpenes, being the most important species for regional ozone formation. Sources are forests (foliar emissions), natural grasslands and other low vegetation and wet lands (Simpson et al., 1999). Forests are the main source of biogenic NMVOC. These emissions are strongly dependent on season, temperature and light intensity. On warm summer days biogenic emissions might in some cases become dominant in the ozone formation process. Large uncertainties exist in the estimates of biogenic emissions. This is due to ill-defined land use classifications, uncertainties in emission factors and emission algorithms. A detailed calculation method is given by Simpson et al. (1999). This method is used to estimate the biogenic emissions as input for the EUROS model. In the method, the biogenic flux F (µg $m^{-2}h^{-1}$) is calculated by

$$F = \varepsilon \cdot D \cdot \gamma$$

Where ε ($m^{-2}s^{-1}$) is the emission rate expected for a particular plant species at a reference temperature of 30°C and PAR of 1000 µmol photons (400-700 nm), D (g m^{-2}) is the foliar biomass density and γ is a dimensionless environmental correction factor accounting for the effect of temperature and in some cases solar radiation:

$$\gamma = \exp[\beta (T-T_s)]$$

where β is an empirical constant (β = 0.09 K^{-1}) and T_s the standard temperature (T_s = 303 K). Values of D and ε for common European forest species are given by Simpson et al. (1999). The biogenic emissions were calculated for the species provided by the CORINE land use map.

2.6 Conclusions and suggestions for improvements

A dynamic emission inventory has been compiled for the European countries that are covered by the EUROS domain. The inventory provides the spatial and temporal variations in anthropogenic emissions for six source categories and the spatial distribution of biogenic emissions varying with temperature. The emission inventory is supported by various sets of input data from different sources. Emission modelling techniques were used to complete the inventory and to make it homogeneous. The

dynamic emission inventory was implemented in a GIS (Arcview) which was found to be very helpful in this context.

Although improvements in the emission inventory for the EUROS model can always be made, this will not always be effective, because of the limited resolving capacity of the EUROS model.

The following suggestions for improvements are made in function of their priority:

- More specific information is needed to describe in more detail the spatial distribution of emissions in the Walloon region and Brussels. Access to data sources for these regions could not yet be provided.

- Specification of the emission time factors per country. This will, however, require a lot of additional information.

- A further disaggregation of emissions into various source (sub)categories, e.g. in 11 categories following the SNAP code, is proposed in order to enhance the implementation of emission reduction strategies and to provide the possibility of linking specific emission reduction measures with specific economic sectors.

- Improvements in biogenic emissions by including more accurate, seasonal dependent land cover data.

- Including missing emission source categories in the dynamic emission inventory, like air and ship transport, in order to complete it. Including diffusive emission sources.

- NO_x split per emission source category.

2.7 References

Amman, M., Bertok, I., Cofala, J., Gyarfas, F., Heyes, C., Klimont, Z., Makowski, M., Schopp, W. and Syri, S. (1999), *Cost-effective Control of Acidification and Ground-Level Ozone,* Seventh Interim Report to the European Commission, DG-XI, IIASA, Laxenburg.

Barrett, K. and Berge, E. (1996) *Transboundary air pollution in Europe*. Part 1: Estimated dispersion of acidifying agents and of near surface ozone. Emep MSC-W Status Report 1996, Oslo

EC (1995) CORINAIR, *Inventaire des émissions de dioxyde de soufre, d'oxydes d'azote et de composés organiques volatils dans la Communauté européenne en 1985*, Corine, EC publication EUR 13232 FR, Luxembourg.

EEA (1995) *CORINAIR 1990 summary tables*: Fifth Set, European Environmental Agency, August 1995, Copenhagen.

EEA (1997) *CORINAIR 1994,* Copenhagen.

EMIS (2000) http://www.emis.vito.be/index.htm

Europe environment (1999) *Transboundary pollution: protocol to abate acidification and ground-level ozone,* Europe environment n° 557, November 30, 1999

Hammingh P. (1999) Emission sector specific split on the non methane volatile organic compounds emissions in Euros. Technical Note, RIVM, Bilthoven

Institut Wallon: 1995, *Bilan energetique de la région de Bruxelles-capitale 1994*, Namur.

Jaarsveld, J.A. van (1990) *An Operational atmosferic transport model for Priority Substances; specification and instructions for use*, RIVM rapport nr. 222501002, Bilthoven.

Jol, A. (1999) *Private communication*, European Environmental Agency, Copenhagen.

Loon M. van (1996) *Numerical methods in smog prediction*, PhD thesis, University of Amsterdam.

Mc Innes G. (ed. (1996) *Atmospheric emission inventory guide book*, A joint EMEP/CORINAIR Production, EEA, B710/9-11, Copenhagen.

Mensink, C. and De Vlieger, I. (1998) Regional scale modelling of acidification associated with road transport and road transport scenarios, *Int. J. Vehicle Design*, Vol 20, Nos. 1-4, pp. 335-343, 1998

Mensink, C., Van Rensbergen, J., Viaene, P., De Vlieger, I. and Beirens, F. (1999) Temporal and spatial emission modelling for urban environments using emission measurement data, in: Borell, P.M. and Borell P. (eds.) *Proceedings of EUROTRAC Symposium '98*, Vol 2, p. 711-714, WIT Press, Southampton.

Ministère de la Région Wallone (1998) *Atlas de l'air de la Wallonie*, Institut Wallone, Namur.

Ministerie van de Vlaamse Gemeenschap (1996) *Verkeerstellingen in Vlaanderen 1993*, Departement Leefmilieu en Infrastructuur, Administratie Wegeninfrastructuur en Verkeer Rapport nr 186, Brussel.

Mylona, S. (1999) *EMEP EMISSION DATA*, Status Report 1999 Emep MSC-W Report 1/99, Oslo.

Simpson D. et al. (1999) Inventorying emisions from nature in Europe, *Journal of Geophysical Research*, Vol 104, D7, pp 8113-8152

Van Rompaey (2000) *Private communication,* Vito, Mol

Vlaamse Milieumaatschappij (VMM) (1999) *Lozingen in de lucht 1997-1998*, Vlaamse Milieumaatschappij, Erembodegem.

WHO (1997), *Air quality guidelines for Europe*, Second edition, Copenhagen.

2.8 Figures

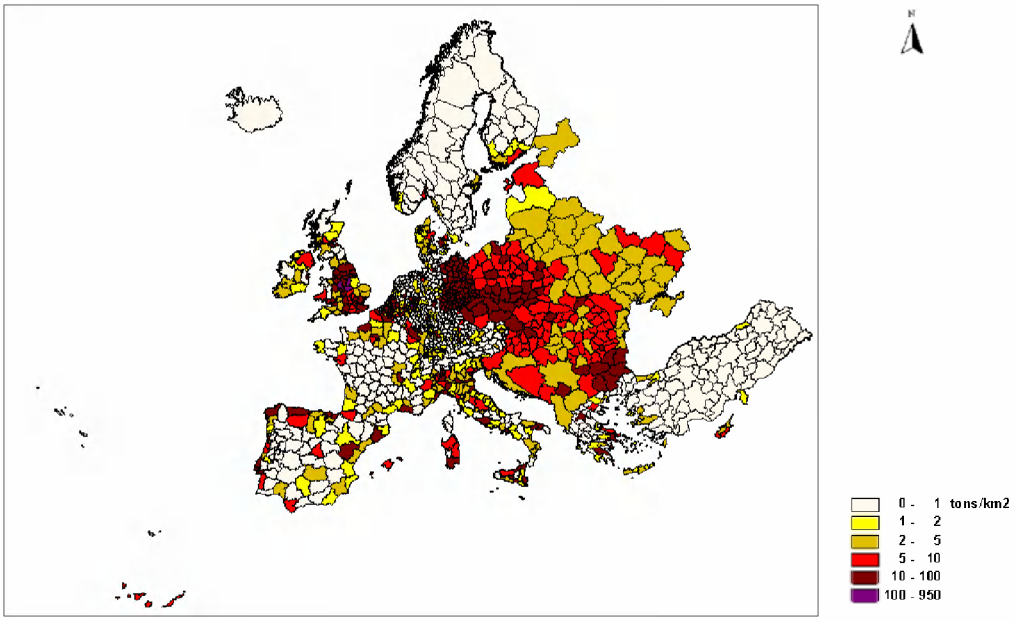

Figure 1: Total SO2 - emissions for 1990

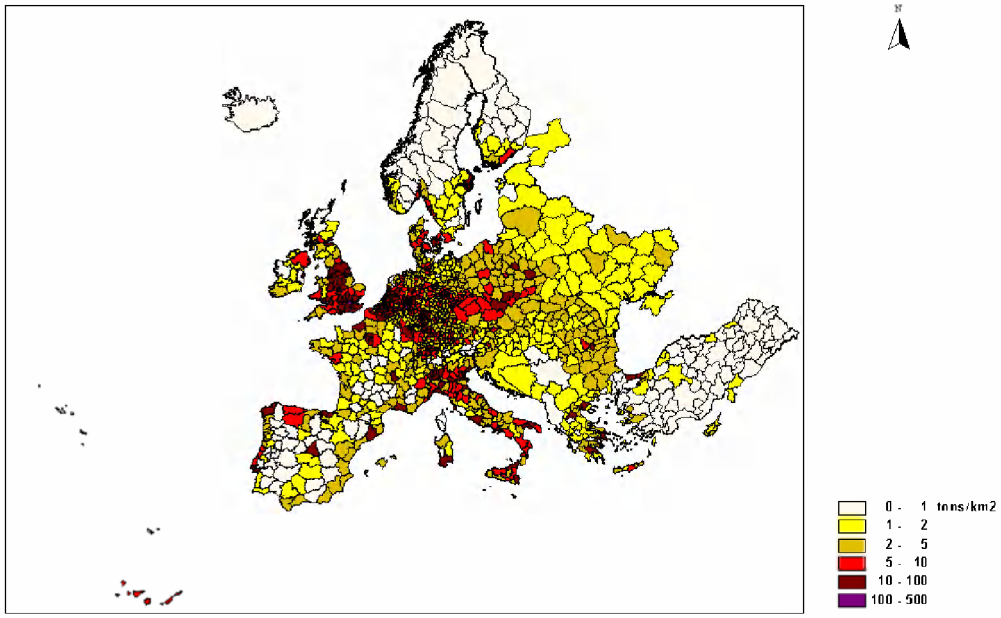

Figure 4: Total NOx - emissions for 1990

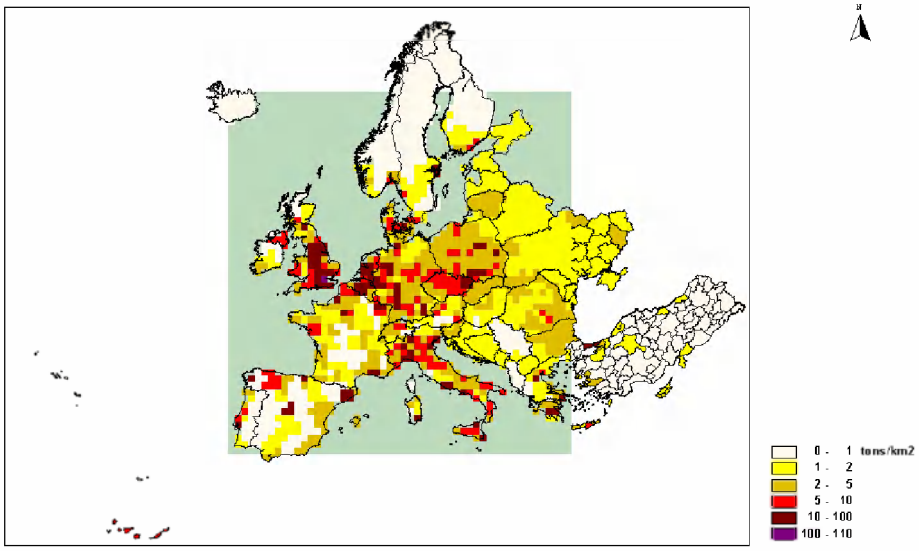

Figure 10: Total NOx - emissions for 1990.
Model domain (-8.25°, 20.35° en 7.15°, -23.1°) , grid cell size = 0.55° (base grid)

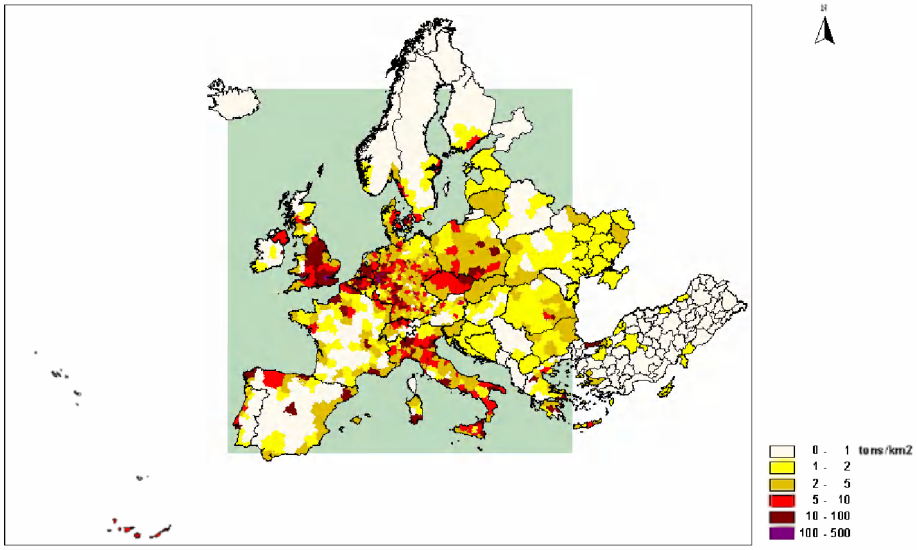

Figure 13: Total NOx - emissions for 1990.
Model domain (-8.25°, 20.35° en 7.15°, -23.1°) , grid cell size = 0.06875° (3rd refinement level)

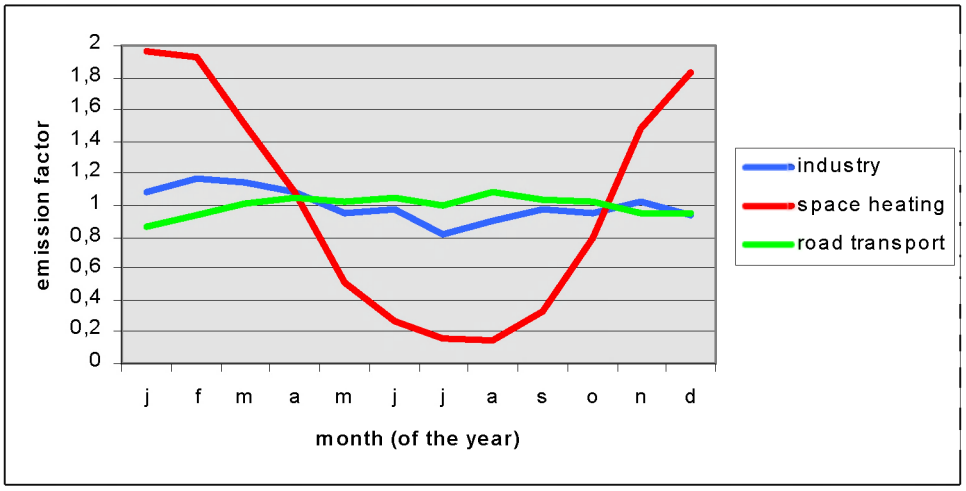

Figure 16: *Emission time factors representing monthly variations.*

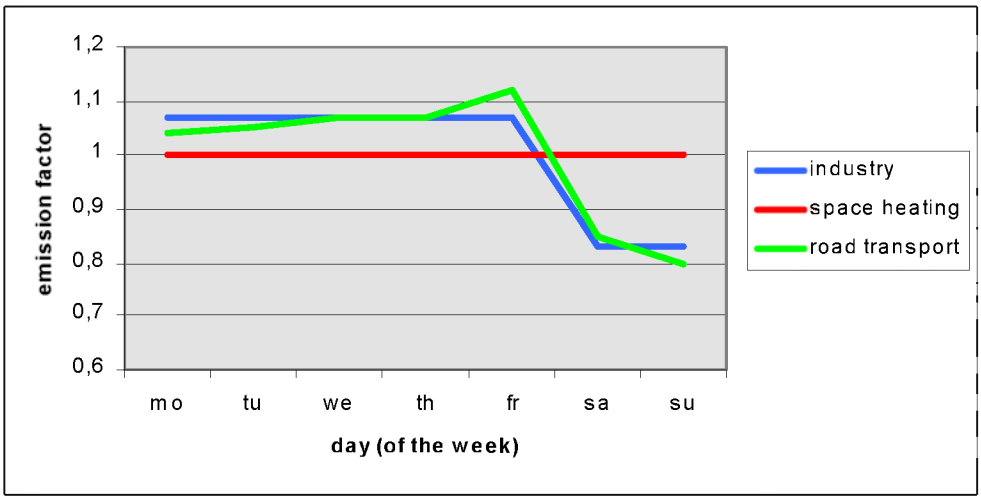

Figure 17: *Emission time factors representing daily variations.*

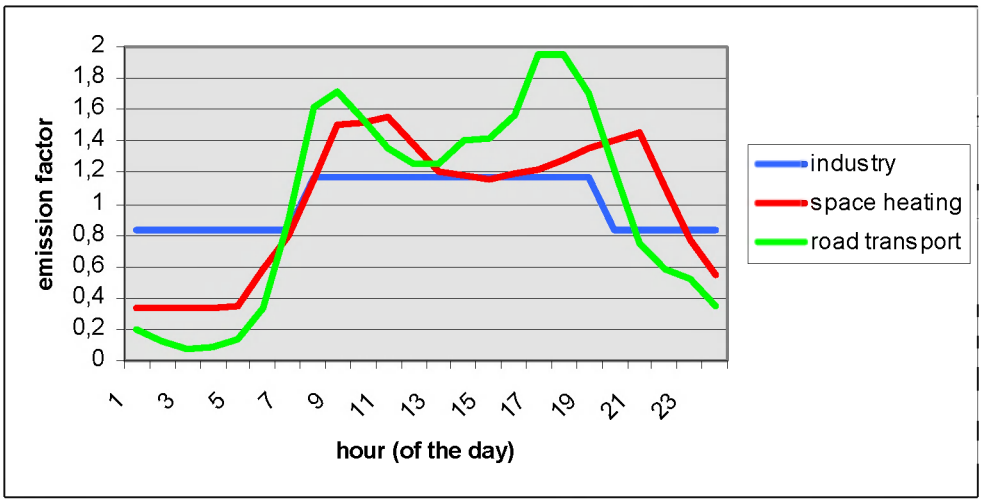

Figure 18: *Emission time factors representing hourly variations.*

3. IMPLEMENTATION OF METEOROLOGICAL DATA IN EUROS [2]

3.1 Introduction

The implementation of the EUROS model in Belgium requires to adapt the input data (emissions, meteorology, geography) and to modify some intrinsic features of the model. This chapter describes the meteorological aspect of this implementation.

In contrast to the Netherlands, variations of topography over Belgium may cause significant variations in the local meteorological situations especially in situations where the large scale forcing is not dominant. Therefore, an adequate representation of the meteorological forcing of the model is required. This includes high resolution wind, temperature and humidity fields but also an efficient representation of the time and spatial variations of the mixing height.

This chapter is organised as follows. In the next section, the EUROS model is shortly described focusing more particularly on the physical processes related to meteorology. The meteorological data sets and the processing of these data are described in the section 3.3. The rest of the chapter is devoted to the representation of the mixing layer height. On the one hand, the mixing layer height has been estimated from two different meteorological data sets and using various methods. These methods and the results are presented in section 3.4. On the other hand, regional atmospheric models have been run to get additional estimates of the mixing layer height. These simulations are analysed and discussed in section 3.5. Conclusions and recommendations for future work are presented in section 3.6.

3.2 The EUROS Model

A detailed description of the EUROS model can be found in (van Loon, 1996). It is an Eulerian grid model which covers the whole Europe. The spatial resolution is about 60 km but a grid refinement procedure allows to refine the spatial resolution in certain areas of the model domain, for example in areas where strong concentration gradients occur. This procedure can also be applied automatically for specific areas of interest, for example Belgium. The highest possible resolution is 7.5 km.

The model includes the representation of (photo)-chemical and physical processes. The (photo)-chemical module is the CB4 mechanism (reference LD ???). The essential characteristics of photochemical ozone formation are retained. It includes

[2] The content of this chapter is taken from the intermediary report: Delobbe L., C. Mensink, O. Brasseur, G. Schayes, and A. Melikechi, 2000. Implementation of meteorlogical data in EUROS. Scientific report, 2000/TAP/R/001, Vito, Mol.

32 chemical species and 87 reactions. The physical processes which affect the concentrations of the various chemical species are the following: advection, horizontal diffusion, vertical diffusion, fumigation, dry deposition and wet deposition. The four latter processes cause vertical exchanges between the atmospheric layers. To depict how they are represented in EUROS it is useful to describe the vertical structure of the model.

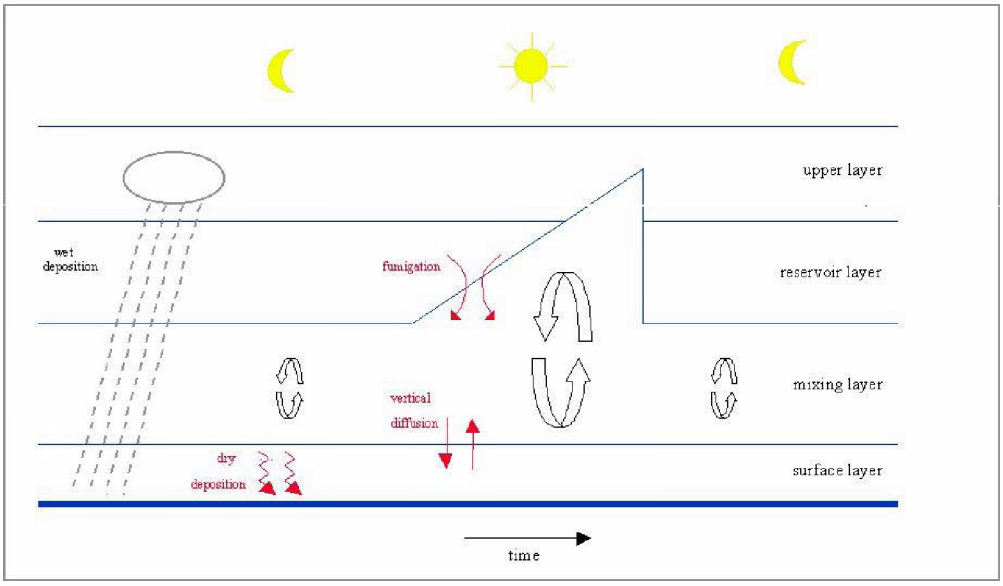

Figure 19: *Vertical structure of EUROS and time evolution of the mixing layer height.*

Vertical structure

The vertical structure is modeled by 4 layers (Figure 19). In each layer, the concentrations are taken vertically homogeneous. The surface layer extents to a 50m height. Dry deposition and emissions by traffic and space heating take place in this layer. The surface layer interacts with the overlying layer (the mixing layer) through vertical diffusion. The mixing layer is characterized by a strong turbulent mixing of the atmosphere. It has a constant depth during the night, grows during daytime and rapidly decreases after sun set. The depth variations of the mixing layer lead to exchanges of pollutants between the mixed layer and the overlying reservoir layer. This process is called the fumigation process. The top of the reservoir layer is determined by the effective height of the highest emission sources. It means that pollutants emitted during the night in the reservoir layer can be entrained into the

mixed layer during the next day. Note that the reservoir layer may vanish in the afternoon. In this case, the fumigation process operates between the mixing layer and the upper layer of the model, which serves as a "semi-permanent" reservoir layer.

In the current version of the model, the mixing layer depth grows during daytime but remains uniform over the whole domain. The growth rate of the mixing layer is everywhere the same and is fixed to 75 meters per hour for summer time. This representation fails in accounting for local variations in the meteorological situations. Therefore, an important improvement consists in implementing a space-varying mixing height which would be determined using the meteorological data. These data are presented in the following section.

3.3 Description of the meteorological data

The Royal Meteorological Institute of Belgium (RMI) provided us with 2 meteorological datasets for the time period May-September 1997: the ECMWF and the ALADIN datasets. The ECMWF (European Center for Medium-Range Weather Forecasts, Reading UK) is an international organization which produces operational medium-range forecasts (up to 10 days) for distribution to the meteorological services of the Member States. The ECMWF atmospheric model is global, i.e. it simulates the whole Earth atmosphere. The ALADIN model is a limited-area model which was developed by METEO-FRANCE and which is now used in several countries (among them Belgium) to produce regional operational weather forecasts.

3.3.11 ECMWF meteorological data

The geographical area for which we received the data and the horizontal grid of the ECMWF model are shown in Figure 3.1. The spatial horizontal resolution is 0.5 degrees in latitude and longitude. Over Europe, it means that the grid points are separated by about 60 km. The variables are calculated on 31 vertical levels. The meteorological fields are given every 6 hours. For each grid point of the three-dimensional grid, the available variables are the 3 components of the wind (u,v,w), the temperature and the specific humidity. At the surface, temperature, humidity, and pressure are also given.

On the European scale, a spatial resolution of 60 km is a reasonably high resolution. It is not the case on the Belgian scale. Less than 10 grid points are located in Belgium which means that some meteorological features over Belgium will be poorly represented. Since the EUROS model can be run with a spatial resolution up to 7.5 km it is useful to provide it with meteorological fields having a similar spatial resolution, at least in the areas of interest (mainly Belgium).

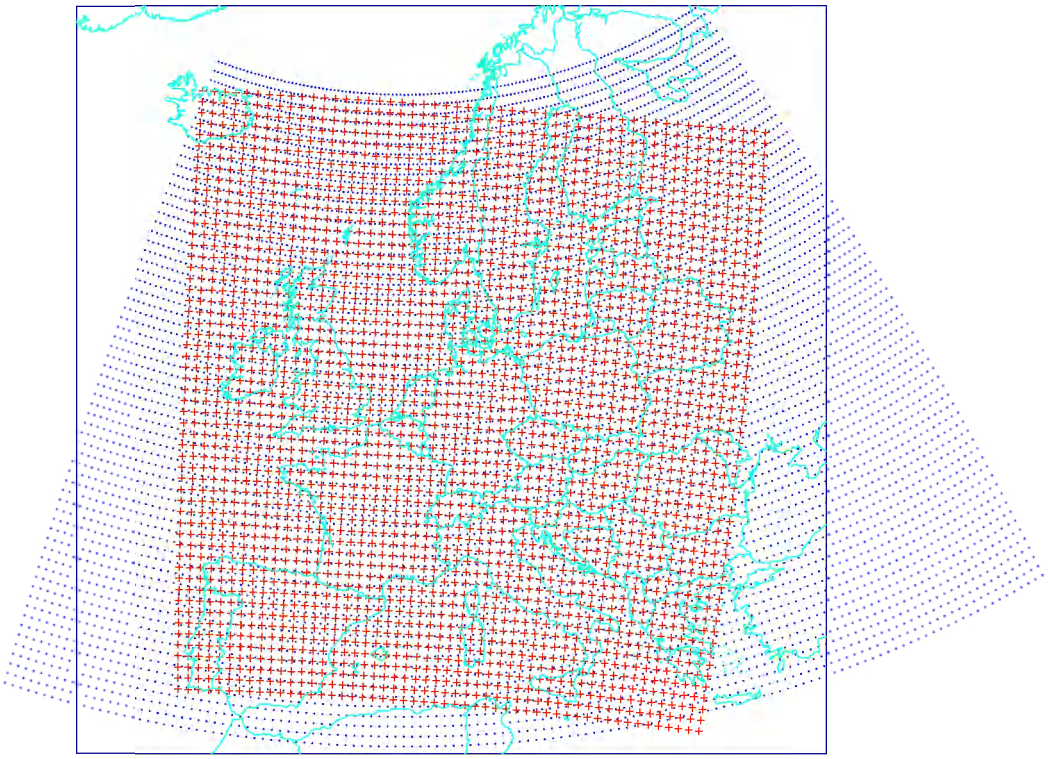

Figure 20: *Grid structure of the ECMWF data set (blue points) and standard grid structure of the EUROS model (red crosses).*

3.3.12 ALADIN meteorological data

The ALADIN model computes the meteorological fields on a limited area. For the ALADIN simulations carried out at the RMI, the model domain covers Belgium, the Netherlands and the North of France (Figure 21). The spatial resolution is 7 km and there are 27 vertical levels. The data are available every 3 hours. The variables are the same as in the ECMWF data set.

3.3.13 Processing of the meteorological data

As is apparent in Figure 20 and 21, the horizontal grid in the ALADIN and ECMWF models do not match the base grid of the EUROS model (60 km resolution) neither the various refined grid levels. An interpolation procedure is therefore necessary to obtain the meteorological fields on the various grid levels of the EUROS model. A linear interpolation has been used. The ECMWF data have been interpolated on the base grid of the EUROS model (60 km resolution). The ALADIN data have been interpolated on the finest EUROS grid (7.5 km).

High resolution data are available on the ALADIN domain. Out of this domain the coarser resolution ECMWF data must be used. These data will be used for the estimation of the mixing height but also as input for the calculation of some physical processes such as advection. In both cases it is crucial to avoid large discontinuities in the meteorological fields at the boundaries of the ALADIN domain. Therefore, a specific treatment will be necessary to ensure a smooth transition between the meteorological fields of ALADIN and ECMWF.

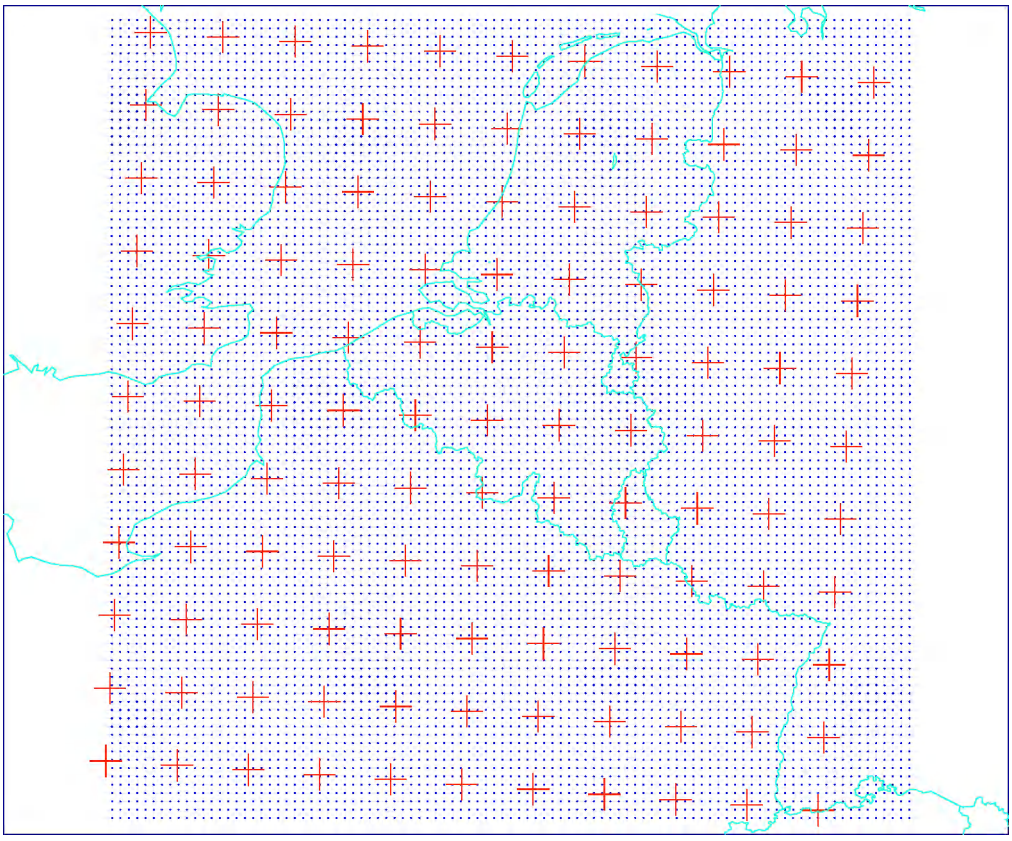

Figure 21: *Domain and Grid structure of the ALADIN data set (blue points) and standard grid structure of the EUROS model (red crosses).*

3.4 Mixing height from meteorological data sets

3.4.1 Description of methods to estimate mixing heights

The boundary layer is the part of the troposphere that is directly influenced by the presence of the earth's surface, and responds to surface forcings with a time scale of about an hour or less (Stull, 1988). These forcings include frictional drag, evaporation and transpiration, heat transfer, pollutant emission, and terrain induced flow modification. The boundary layer depth is quite variable in time and space, ranging

from hundred meters to a few kilometers. The turbulence is the primary agent that determines the height to which a quantity from a lower level can be transported up to a higher level.

Several methods to determine the mixing height will be discussed in this section. However the mixing height is not exactly the same concept as the boundary-layer height, even if their physical meanings present some evident similarities.

The *mixing-layer height* corresponds to the thickness of the layer of air, adjacent to the earth's surface and characterized by vertical transport by convective motions (convective bounday layer) and dispersion by atmospheric turbulence. Mixing is a term normally used in relation to a process of vertical, adiabatic lifting up to the level where the temperature of the lifted air parcel equals the ambient temperature. As a consequence, the local vertical temperature gradient can importantly influence the turbulent state of the atmospheric layer. The concept of mixing-layer height is used in the field of air pollution, for which atmospheric stability is a very important meteorological aspect.

The *boundary-layer height* is the height up to which the fluid motion is affected by the presence of the earth's surface. This height is directly related to the turbulence intensity (or the turbulent kinetic energy) that determines the vertical transport of a quantity. The turbulent kinetic energy (denoted TKE) is itself influenced by buoyancy, wind shear, and dissipation for the source and sinks terms, and by advection and turbulent diffusion for the transport terms.

3.4.1.1 Virtual potential temperature (VPT) method

This method is based on parcel theory. Buoyancy is one of the driving forces for turbulence in the boundary layer. Thermals of warm air rise because they are less dense than the surrounding air, and hence positively buoyant. Virtual potential temperature is currently used in turbulence parameterizations because it is the temperature that the dry air must have to equal the density of moist air at the same pressure. Consequently, variations of virtual temperature can be studied in place of variations in density.

Using this conservative variable, it can be stated that upward motions take place over a depth where the virtual potential temperature of the parcel (denoted θ_{vp}) is higher than environmental virtual potential temperature (denoted θ_{ve}). The boundary-layer depth is therefore simply defined as the height of the layer starting from the surface and where θ_{vp} is always greater than θ_{ve}. An example is presented in Figure 4.1 for a convective boundary layer.

The main advantage of this technique is that it is very fast and easy to implement. But it is effective only for well-mixed layers. It fails when layers are stable or weakly stable. For instance, let us consider a boundary layer globally characterized by a temperature gradient close to neutral, but nearly neutral (slightly stable) in a thin layer of the boundary layer. The boundary-layer depth predicted with the VPT method will be limited by the height of this thin stable layer, which is clearly too restrictive. Indeed vertical motions can be sufficient to pass through this thin layer. Consequently, the present technique will tend to underestimate the mixing height.

Another disadvantage is the sensitivity to the surface temperature. If the temperature gradient is weak above the mixing height, a high sensitivity of the mixing-layer height is expected. In this case, the results are completely dependent on the accuracy of the surface fields simulated by atmospheric models.

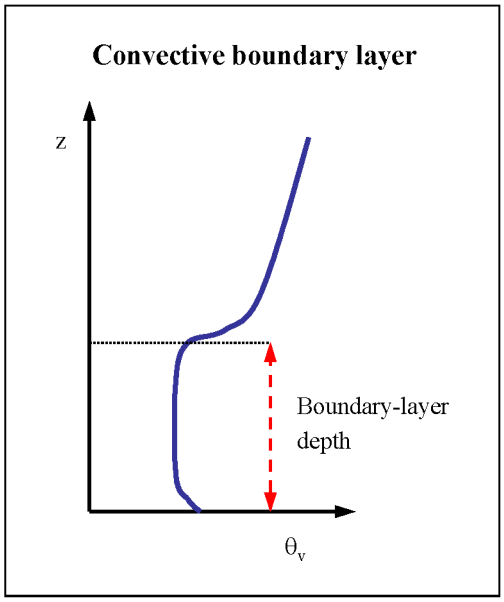

Figure 22: *Determination of the depth of a convective boundary layer using the method of virtual potential temperature profile.*

3.4.1.2 Bulk Richardson number (BRN) method

Another technique currently used to determine the mixing-layer height is the bulk Richardson number method (e.g. Sorensen et al., 1997; Sorensen and Rasmussen, 1997; Van der Auwera, 1992; Vogelezang and Holtslag, 1996). The Richardson number provides quantitative information on the relation between the stabilizing effect of buoyancy and the destabilizing effect of wind shear. The method is robust and fairly accurate. It is suited for use in situations where the vertical resolution of

temperature and wind is limited as e.g. output from models for numerical weather prediction.

The bulk Richardson number at height z above the ground is given by the following expression:

$$\mathrm{Ri}_B = \frac{g\, z\left(\theta_v - \theta_{vs}\right)}{\theta_{vs}\left(U^2 + V^2\right)} \qquad (4.1)$$

The quantities θ_v and θ_{vs} are the virtual potential temperature at the surface and height z, respectively, and U and V are the horizontal wind components at height z, g is the gravitational acceleration.

The method simply defines the boundary-layer height at a height where a transition from turbulent to laminar conditions is diagnosed. Starting from the surface upwards, the boundary layer is diagnosed as the first level at which the Richardson number exceeds a critical value of the Richardson number (denoted $\mathrm{Ri}_{\mathrm{Crit}}$). Therefore, the depth of the boundary layer is given by the height at which the bulk Richardson number reaches $\mathrm{Ri}_{\mathrm{Crit}}$. Everywhere below this height Ri_B is lower than $\mathrm{Ri}_{\mathrm{Crit}}$. The choice of the bulk Richardson number is justified by the fact that it incorporates the dynamic and thermal characteristics of the fluid. The threshold $\mathrm{Ri}_{\mathrm{Crit}}$ thus delimits laminar from turbulent regions.

An important parameter of the method is therefore $\mathrm{Ri}_{\mathrm{Crit}}$. The value attributed to this parameter is generally experimental. According to Troen and Mahrt (1986), the normally applied value for the critical bulk Richardson number varies between 0.3 and 1. The choice of $\mathrm{Ri}_{\mathrm{Crit}}$ depends on the atmospheric model. For instance, critical values of $\mathrm{Ri}_{\mathrm{Crit}}$ in the range 0.15-0.35 appears adequate for the DIM-HIRLAM, while it is 0.3-0.6 for ECMWF data (Sorensen and Rasmussen, 1997). A value of 0.38 is chosen with the Deutschland-Modell. The difference between the various ranges of critical values owes to differences in vertical resolution and physical parameterizations of the models. Consequently, this method needs calibration of $\mathrm{Ri}_{\mathrm{Crit}}$ before any operational application.

The BRN method limits the deficiency of the VPT method for weakly stable layers. The critical threshold is indeed positive in order to allow the presence of layers characterized by a slightly positive vertical gradient of virtual potential temperature. Nevertheless, the method is (as the VPT method) sensitive to the surface temperature and the specification of θ_{vs} is particularly important.

In the case of stable layer, Troen and Mahrt (1986) suggest to use the measured virtual potential temperature at the lowest level. For unstable atmosphere, it is well known that mixing is not only due to local down-gradient fluxes but also to thermals or energetic eddies of the size of the whole boundary-layer depth. This non-local effect is translated into a temperature excess over the temperature at the first level. As shown by Troen and Mahrt (1986), this temperature correction is consistent with the formulation of the counter-gradient heat flux. They calculate the surface temperature θ_{vs} from the following relation:

$$\theta_{vs} = \theta_v(\text{level 1}) + \theta_E \qquad (4.2)$$

with θ_E the surface temperature excess given by:

$$\theta_E = C\frac{\overline{w'\theta'_v}}{w_s} \qquad (4.3)$$

where $\overline{w'\theta'_v}$ is the surface upward turbulent heat flux, and C is a constant set to 6.5 (Troen and Mahrt, 1986). The velocity scale w_s is computed from:

$$w_s = \left[u_*^3 + cw_*^3\right]^{1/3} \qquad (4.4)$$

In relation (4.4), c is equal to 0.28, u_* is the friction velocity, and w_* is the convective velocity scale. Note that the correction θ_E is applied only when it is positive, i.e. with upward heat fluxes. As can be seen from equation (4.2), the procedure for estimating θ_{vs} is continuous for the transition between stable and unstable situations.

Let us remark from relation (4.1) that, in the case of vanishing wind speed, the BRN method reduces to the VPT method, with the well known disadvantages of this technique (see the previous section).

The correction of the surface temperature given by the relation (4.3) requires the determination of the surface heat flux. However this quantity is not always available from data sets such as ECMWF analysis. In this case, the correction is not taken into account and θ_E is equal to zero. In order to clarify this distinction, the BRN method with $\theta_E = 0$ is named “BRN1”, while the BRN method with $\theta_E \neq 0$ is named “BRN2”.

3.4.1.3 Modified bulk Richardson number (MBRN) method

Both VPT and BRN methods fail when the boundary layer includes a thin stable layer and when the wind speed is weak. In order to avoid such deficiencies, it is suggested to modify the BRN method as follows.

Before presenting the modification to the BRN method, let us define the integrated buoyant energy (denoted IBE):

$$IBE = \int_0^h g \frac{\Delta\theta_v}{\theta_v} dz \qquad (4.5)$$

The IBE is closely related to vertical motions. If equilibrium is assumed between buoyant (potential) energy and kinetic energy, the vertical velocity at the height h can be written as:

$$w(h) = \sqrt{2.IBE} \qquad (4.6)$$

From this relation, vertical motions take place only if IBE is positive. For clarity, the layer where IBE > 0 will be named "buoyant layer". In this case, any parcel at the surface is able to reach the top of the considered sub-layer, and any parcel at the top is able to reach the surface. Therefore, if vertical exchanges are possible, the sub-layer should be necessarily contained in the boundary layer.

Consequently, whatever the value of Ri_B, the boundary layer is assumed to include the buoyant layer. Above this layer, the BRN method is applied without any modification. The consideration of the buoyant layer allows avoiding unrealistic mixing heights due to the presence of thin stable layer.

3.4.2 Results from ECMWF data set

The various methods described in the previous section have been applied to the ECMWF data set. The ECMWF vertical profiles of temperature, geopotential, specific humidity, and wind allow to evaluate for each vertical level the virtual potential temperature and the bulk Richardson number. The surface heat and momentum fluxes are however not available which does not allow to estimate the surface temperature excess θ_E in the expression (4.2) of the surface virtual potential temperature. It is therefore not possible to apply the BRN2 method. No surface temperature correction may cause an underestimation of the mixing height when using the BRN1 (Bulk Richardson Method) and MBRN (Modified BRN) methods in the case of convective meteorological situations. For BRN1 and MBRN, the value of the critical Richardson Number has been fixed to 0.3. All our results have shown a very low sensitivity to this parameter in the range 0.15-1.

First, we have tested the VPT (Virtual Potential Temperature) method. This method is only based on the virtual potential temperature profile and does not account for the wind shear production of turbulence. This method tends to strongly underestimate the mixing height. In many cases, mixing heights as low as 200 m are obtained for daytime situations over land. These unrealistic results led us to reject this first method.

The BRN1 method takes the effect of wind shear into account and therefore produces more realistic results than the VPT method. Figure 23 (left panel) illustrates the results obtained with this method over Belgium for July 11, 12 and 13 1997 at 1200 UT. An important feature is the low values of the mixing height over sea. This is not surprising since, during summer, the sea surface is relatively cold compared with daytime atmospheric temperatures. This causes a strong stabilizing effect near the surface. In these conditions, the turbulence is only created through wind shear, which gives rise to a relatively thin mixed layer. For July 11, the estimated mixing heights over land turn around 1500 m. It must be noted that the spatial resolution of the ECMWF meteorological data does not allow to accurately locate the coastline. Over the domain represented in Figure 23, one ECMWF grid point located in the North of France is characterized by an extremely low value of the mixing height which is not realistic for a day time summer situation. The ECMWF atmospheric profile exhibits on this grid point a thin and slightly stable layer near the ground and above this layer a relatively deep unstable layer. As described in section 3.4.1, this causes the BRN1 algorithm to strongly underestimate the mixing height. The MBRN algorithm aims to remedy to this deficiency. The right panel on Figure 23 shows the results obtained with the MBRN method. As expected, this method allows to significantly improve the estimate of the mixing height.

The results obtained for July 12 are quite different. The estimated mixing layer is thinner. The mean value over Belgium is around 800 m. As we will see later, this thinning of the mixing layer for July 12 was also observed in the RMI atmospheric soundings of Uccle (Brussels). Near the eastern border of Belgium, the estimated mixing height is extremely low, which is probably the result of an underestimation by the tested algorithms. Results obtained with the BRN1 and MBRN methods are almost identical. Therefore, low mixing height values can not be attributed to the presence of a stable layer near the ground. The absence of the surface temperature correction is a possible explanation.

In contrast with July 12, the estimated mixing height for July 13 using the MBRN method strongly differs from the estimation with the BRN1 method. The BRN1 method completely fails while the MBRN method generates a realistic mixing height pattern. Based upon these results, it appears that the MBRN method is much more adequate for estimating the mixing height than the other methods presented in 3.4.1. The comparison with the mixing height estimation from atmospheric soundings (see section 3.4.4) will allow to better point out the good points and the deficiencies of this method.

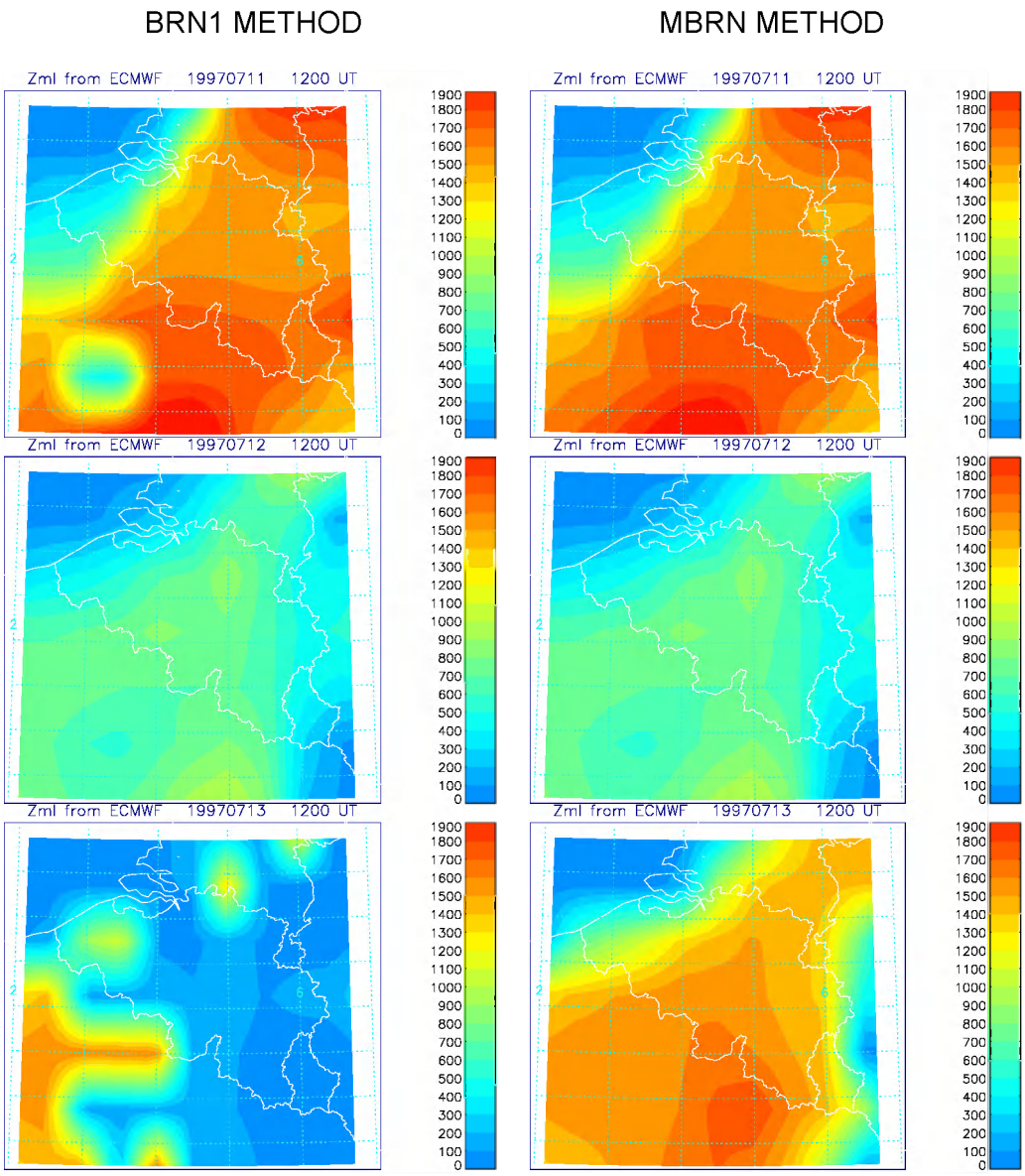

Figure 23: *Mixing layer heights (m) derived from the ECMWF data set using the standard Bulk Richarson Method (left panel) and the Modified Bulk Richardson Method (right panel). The upper, middel and bottom panels correspond respectively to July 11, 12 and 13 1997 at 12OO UT.*

3.4.3 Results from ALADIN data set

The ALADIN meteo fields have been also used to estimate the mixing height from the various algorithms presented in section 3.4.1. In contrast with the results obtained using the ECMWF data, the differences in the mixing height estimates using BRN1 and MBRN are very limited. The MBRN estimate is larger or equal to the BRN1 estimate but the mixing height values are always significantly smaller than the estimates from the ECMWF data. Figure 26 shows the mixing height estimated from

the ALADIN data for the period July 11-July 14 using the MBRN algorithm. The four patterns exhibit a relatively thin mixing layer. The estimated mixing height rarely exceeds 1000 m, which is not realistic for daytime situations during summer. The various algorithms have been used for other time periods in the summer 1997 and it appears that the ALADIN data never generate relatively deep mixing layers. This surprising result led us to carefully analyze the vertical profiles of the ALADIN data set. It seems that the ALADIN model tends to produce excessively stable vertical profiles, which causes the various algorithms to generate very low values of the mixing height.

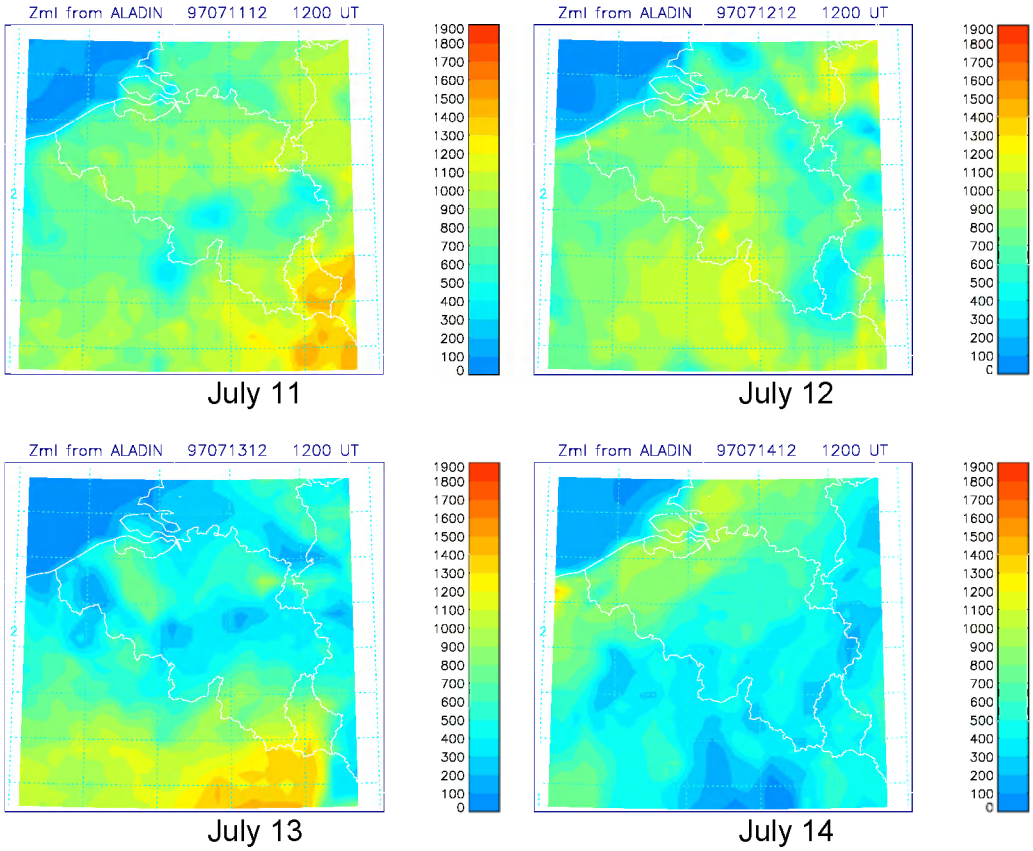

Figure 26: *Mixing layer heights (m) derived from the ALADIN data set using the MBRN method for the time period July 11-14 1997 at 12OO UT.*

It must be noted that the ALADIN meteo data set corresponds to short term weather prediction. The meteorological situation produced by ALADIN at 1200UT is a model prediction from the initial state at 00 UT. In contrast, the ECMWF data at each time step result from an assimilation procedure that combines simulation results and meteorological observations. The fact that the ALADIN data only result from model integration, even short, may cause significant errors in the vertical meteorological profiles as well as in the surface temperature. The accuracy of the surface temperature is not expected to be better than 2 degrees, which may result in significant errors on the estimated mixing height. Further investigation should be

necessary to clearly identify the causes of the deficiencies in our results. However, it appears difficult to use these data to estimate the height of the mixing layer.

3.4.4 Comparison with observed vertical soundings and discussion

For July and August 1997, meteorological data from high resolution vertical soundings are available in Uccle (RMI, Brussels) twice a day: at 10 UT and 22 UT. For May, June and September, these soundings are only available two days per week. The accuracy of the measurements and the high vertical resolution (around 60m) allow a very good view of the vertical structure of the atmosphere and, therefore, a good estimate of the mixing layer height. A simple visualization of the observed vertical profiles allows in most cases to determine the mixing height since the top of the mixing layer is generally marked by a strong discontinuity in the vertical structure. The use of the MBRN method confirms this first guess except in cases of complex vertical structures which are encountered in frontal situations or in cases with deep cloudiness, for example.

Figure 27 shows the time evolution for July and August 1997 of the mixing height estimated from the daytime RMI sounding. For the same time period, the mixing height over Brussels has been estimated from the ECMWF data as the averaged value for the four ECMWF grid points surrounding Brussels. The ECMWF time series are also represented in Figure 27. The comparison of the two time series allows getting an idea of the reliability of the estimation of the mixing height using the MBRN algorithm applied on the ECMWF data set. The two time series let appear significant discrepancies even if some important features are well represented. For example, the thinning of the mixing layer on the 12th of July is present in the ECMWF time evolution in agreement with the observed sounding in Brussels. This day correspond to an important ozone peak in Brussels and Belgium due to the confinement of the emitted pollutants in the thin atmospheric mixing layer.

Many factors may cause discrepancies between the sounding estimate and the ECMWF estimate. First of all, it must be stressed that the vertical resolution of the ECMWF data is coarse. The vertical levels between 500m and 2500m are approximately 640m, 980m, 1370m, 1800m, 2270m, and 2770 m. As a consequence, the accuracy of the estimated mixing height can not be expected to be better than 300 or 400m. The scatter plot of the ECMWF estimate versus the sounding estimate shows that most points are located in this error margin (Figure 28). It is apparent on this Figure that the range of mixing height values is narrower when estimated from ECMWF than from the RMI soundings. This larger variability in the estimates from the RMI sounding can be due to the fact that the sounding is located on a particular geographical point which makes it more sensitive to local meteorological conditions such as local updraft or downdraft in convective situations.

The estimate from the ECMWF is an average over 4 grid points, which introduces a smoothing effect. Besides, the MBRN algorithm does not include the temperature correction (4.3) which may induce significant underestimation of the mixing height in cases of convective meteorological conditions. This may contribute to large errors obtained for example the 2nd of July for which the Sounding estimate is around 1500m while the ECMWF estimate barely exceeds 500m. Another source of discrepancies is the difference in time between the ECMWF data (1200 UT) and the RMI sounding (1000 UT). If the morning mixing layer growth is relatively slow, this layer may be not completely developed at the time of the RMI sounding.

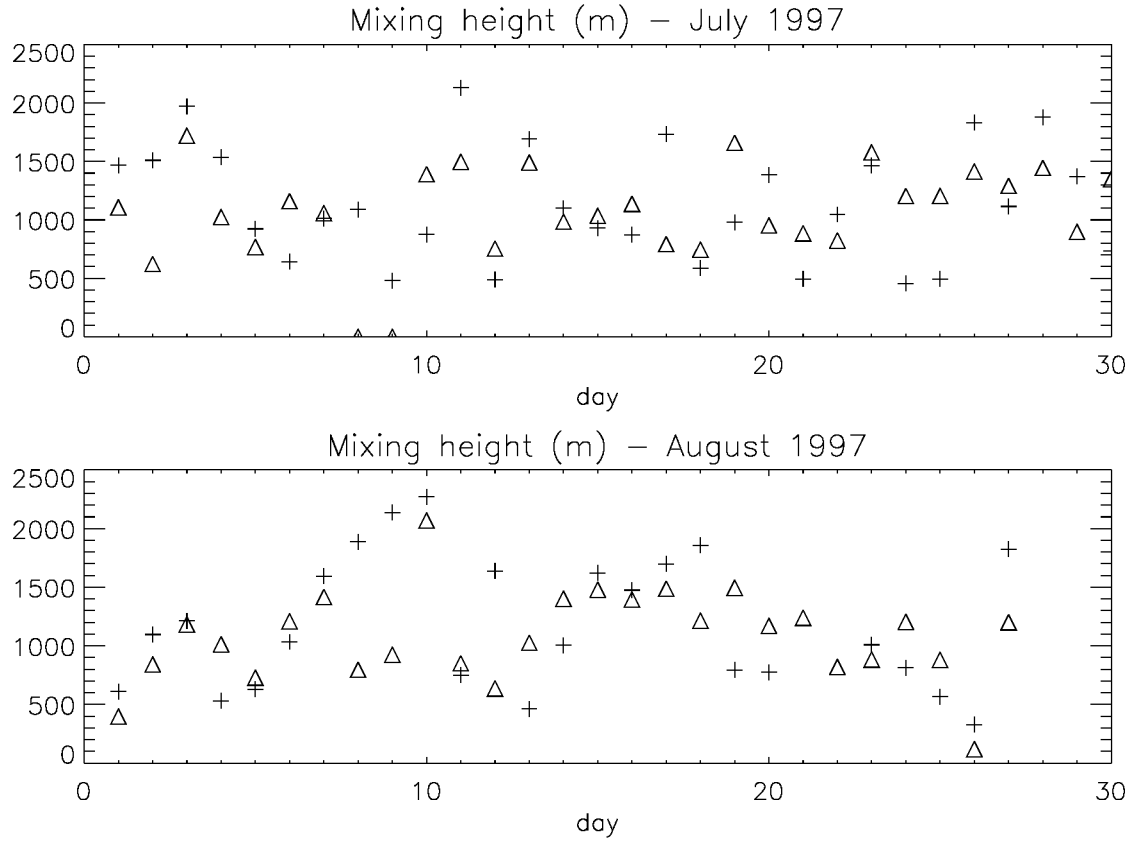

Figure 27: *Time series of the mixing layer height at noon over Brussels for July and August 1997. Crosses correspond to the estimation from the RMI soundings. Triangles correspond to the estimation from the ECMWF data set.*

The results obtained using the MBRN method applied to the ECMWF data are not fully satisfying. However, this method appears much more adequate than the other tested methods and, keeping in mind the vertical resolution of the ECMWF data, the errors are generally acceptable. An important improvement to this method should be to include the surface temperature correction as described in section 3.4.1. However, this improvement requires the knowledge of the surface heat fluxes, which are not available in our meteorological data sets. The magnitude of this correction and its

effect on the estimation of the mixing height will be investigated using mesoscale atmospheric simulations. These simulations are presented in the next section.

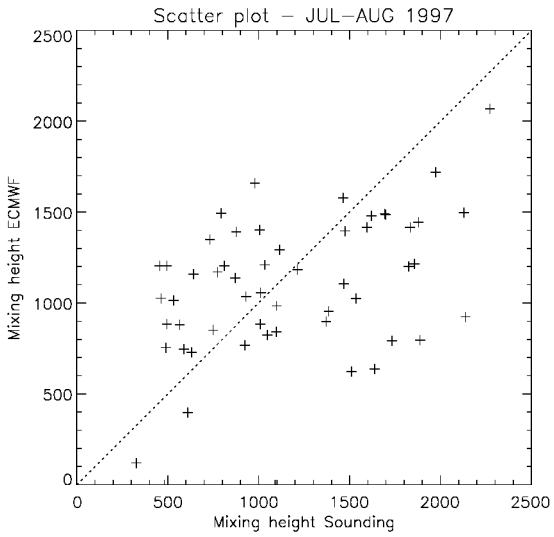

Figure 28: *Scatter plot for the period July-August 1997: mixing heights estimated from ECMWF versus mixing heights estimated from RMI soundings.*

3.5 Mixing height from model simulations

In section 3.4, three methods to estimate mixing heights have been presented. In the present section, it is proposed to compare the computed mixing heights with the boundary-layer heights. The difference in the definitions of mixing and boundary layer heights have been already reminded in section 3.4.

The main difficulty for the determination of the boundary-layer height is the turbulent kinetic energy. This quantity is not available in ECMWF and ALADIN data sets. Moreover, it is not possible to diagnose it from these data sets, since TKE is intrinsically a prognostic variable that interacts with the mean quantities such as wind and temperature. Therefore it is suggested to compare the mixing heights obtained by the methods described in section 3.4 with the boundary-layer heights using a mesoscale model nested in the ECMWF fields. The objective of this comparison is not to assess the accuracy of the simulated meteorological fields, but rather to assess the validity of the methods to determine the mixing heights.

3.5.1 Overview of the MAR model

The formulation of the present version of MAR is described in Gallée and Schayes (1994) and Gallée (1995, 1996). MAR is a hydrostatic primitive equation model in which the vertical coordinate is the normalized pressure $\sigma = (p - p_t)/(p_s - p_t)$, where p, p_s and p_t are the actual pressure, the surface pressure and the model top pressure respectively. All one-dimensional experiments are treated with a vertical grid containing 60 levels, all two and three-dimensional simulations use generally 30 levels. The vertical grid size is determined with arithmetic and geometric progressions, producing a higher resolution close to the surface layer and in the boundary layer. The solar radiation scheme is that of Tricot and Berger (1988) modified by Gallée et al. (1991). The longwave radiation scheme follows a wide-band formulation of the radiative transfer equation (Morcrette 1984). The heat and moisture exchanges over land are represented with the surface model of Deardorff (1978). The hydrological cycle is fully described in Gallée (1995). The MAR includes also a convective adjustment scheme derived from Fritsch and Chappell (1980) for the representation of deep convection. The boundaries are treated according a dynamic relaxation that includes a Newtonian term (Davies 1976) and a diffusion term (Davies 1983; Anthes et al. 1989).

The parameterization scheme for the surface layer is based on Businger (1973) and Duynkerke (1991) formulations. Brasseur et al. (1998) have shown that one-and-a-half order closures allow generally a good compromise between accuracy and computing cost, and the differences with second order closures have no significant impact on the mean variables. Therefore the vertical sub-grid scale fluxes are treated according the one-and-a-half order turbulent closure of Dunykerke (1988).

3.5.2 Description of experiments

For all experiments presented with the MAR model, two three-dimensional simulation domains are considered. The horizontal resolution is fixed at either 8 km (which can be considered as the limit for a hydrostatic model) or 50 km. The horizontal mesh at 8-km resolution covers Belgium (and partly the neighbouring countries) with a horizontal extent of 592 by 592 km^2 (i.e. 74 by 74 grid points) and is centred on 51.2N, 4.5E. The second simulation domain covers Western Europe. The vertical discretization includes 30 levels. The vertical grid size is determined with arithmetic and geometric progressions, producing a higher resolution close to the surface layer and in the boundary layer. The vertical discretization contains 30 levels, with an increased resolution close to the surface. The first model level is at 10-m height. The atmospheric and surface variables are initialized and forced at the boundaries with the ECMWF (European Center for Medium-range Weather Forecast) analysis.

The considered periods for the MAR simulations are the same as mentioned in previous sections, i.e. from 10 to 15 July 1997, and from 6 to 15 August 1997. Both these periods were characterized by ozone peaks exceeding the threshold of 180 $\mu g / m^3$. In this report, we propose to present only the results related to the first period, because the properties of the boundary layer appear particularly difficult to represent during the 12, 13, and 14 July.

3.5.3 Validation of MAR simulations

Before any discussion about the mixing and boundary layer heights obtained with MAR, it is important to assess the accuracy of the simulated meteorological fields. Since the simulation domain mostly includes Belgium, it is proposed to compare with the synoptic data (surface temperature and wind) available with a time frequency of 3 hours for about 18 stations.

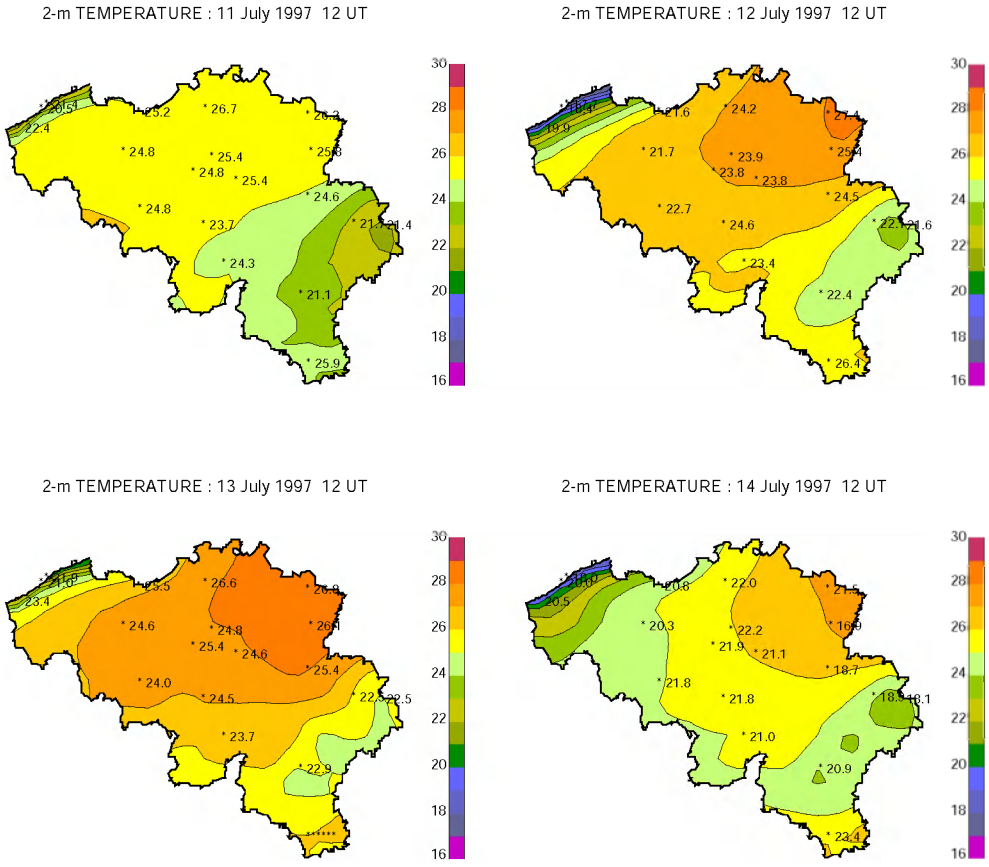

Figure 29: *Comparison between simulated and observed 2-m temperatures (units, °C) over Belgium for the 11, 12, 13, and 14 July at 12 UT. Simulations results obtained with the MAR at 8-km resolution are represented by filled contours. Observations come from the synoptic stations scattered in Belgium and are overplotted.*

Figures 29 and 30 present the comparison between observed and simulated surface temperatures at 2-m height, respectively with the 8- and 50-km resolutions. The assessment of the simulated 2-m temperature is important because it is a key parameter in the VPT, BRN and MBRN methods.

The analysis of the results presented in Figure 29 shows that the simulated temperature is in very good agreement with the observations on the 11th July at 12UT, but are overestimated (generally by 2 to 3 K) on the 12th and 13th July. A possible explanation to this fact is an incorrect representation of the cloudiness: during the whole period, the simulated cloudiness was nearly zero. Only a few cumulus clouds have simulated during daytime. As a consequence too large thermal amplitudes can result from underestimated cloud cover. Nevertheless, spatial tendencies are satisfyingly reproduced: the highest temperatures are found in Campine (due to the properties of sandy soil), the temperature decreases with surface elevation over Ardennes, and the Belgian coast is refreshed by the sea breeze.

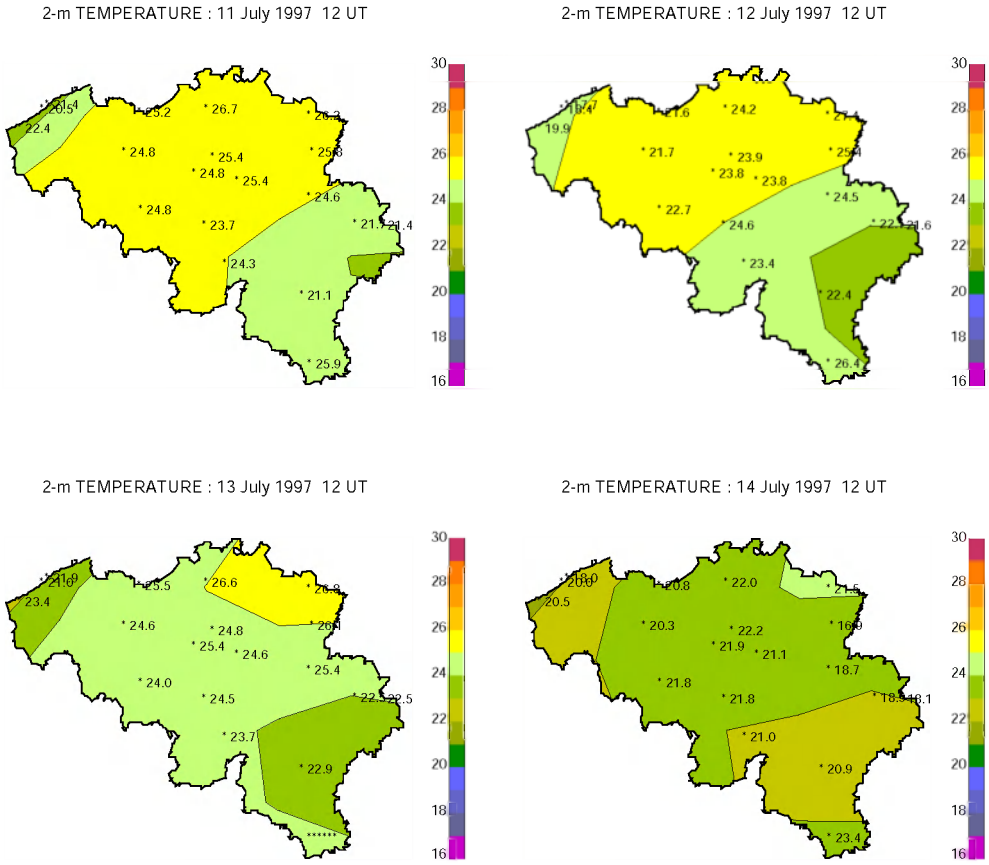

Figure 30: *As in Figure 29, except that the simulation domain at 50-km resolution is considered.*

The situation of 14th July is poorly simulated because of an incorrect representation of a cold front and its associated cloudiness. Such a deficiency could be expected for two reasons. (i) The simulation domain is not sufficiently large to include the characteristics of the circulation at the synoptic scale, and in addition, the transition from the ECMWF fields at 50 km resolution to the MAR grid at 8 km resolution can be somewhat abrupt. As a consequence, the depression and the associated frontal zones cannot be correctly represented. (ii) The lateral boundary forcing does not include the relaxation of microphysical variables. This means that no cloud can enter from the inflow boundary and as a consequence of the very limited horizontal extent of the 8-km domain, no cloud can be generated over Belgium.

Figure 30 presents the simulated temperature obtained with the 50-km resolution. It confirms the hypothesis of the incorrect representation of the cloudiness with the 8-km resolution. Indeed the simulation at 50-km resolution considers a much larger domain, and includes the characteristics of the large-scale circulation. On the contrary to the 8-km simulation that was characterized by a nearly permanent clear sky, the 50-km simulation has been able to represent the cloud cover on the 12th, 13th, and 14th July. The cloudiness seems in satisfying agreement with the total cloud cover given in the ECMWF analysis. These considerations explain why simulated 2-m temperatures with the 50-km resolution are in better agreement with the observations.

As shown in the next sub-sections, the consequences of an incorrect representation of the surface temperature can be important for the determination of the mixing layer. This is particularly the case when the vertical thermal gradient is weak in the low troposphere.

3.5.4 Mixing-layer heights

Figures 31 and 32 present the mixing-layer heights obtained with the BRN1, and BNR2 methods applied to the meteorological fields simulated by MAR at 8-km resolution.

The results obtained with the MBRN method are not presented, since they are exactly the same as those obtained with the BRN1 method. The similarities between the BRN1 and the MBRN mixing heights are explained by the absence of thin stable layer in the boundary layer simulated by MAR. The criterion on the integrated buoyancy is not useful in this case.

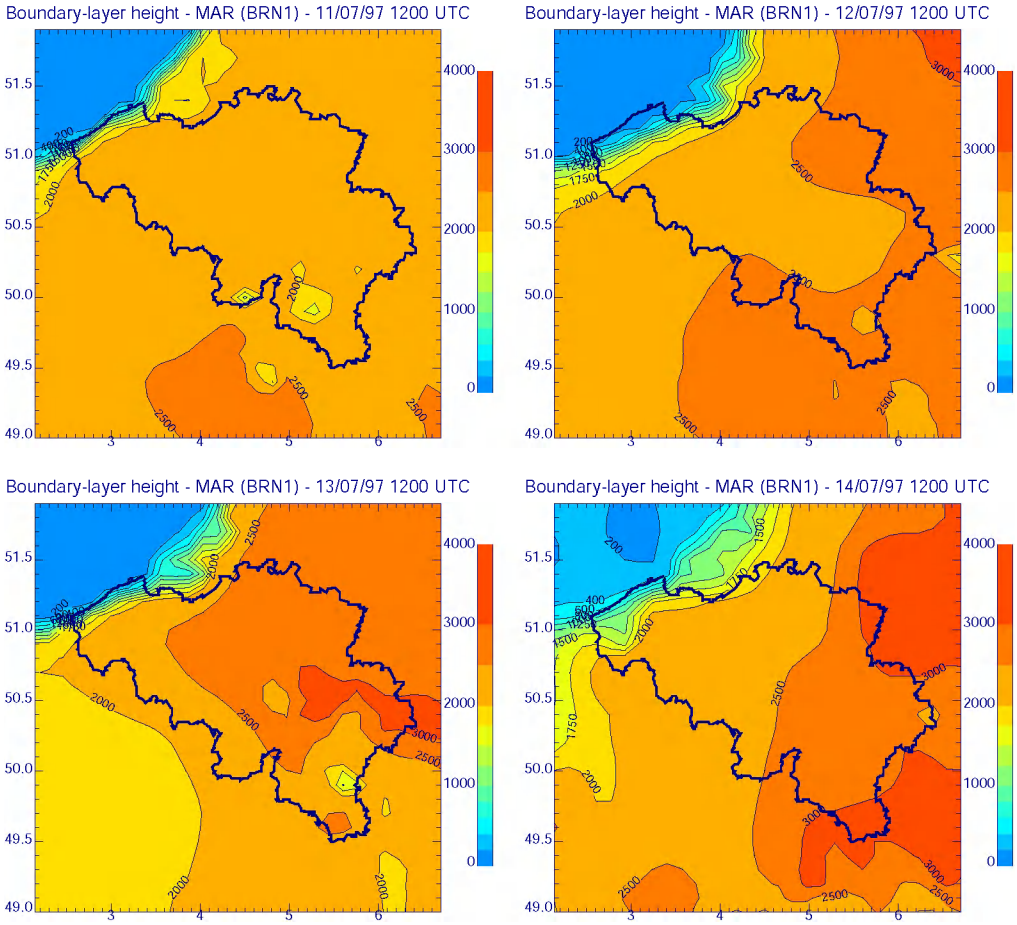

Figure 31: *Mixing-layer heights (units, m) obtained with the BRN1 method applied to the meteorological fields from the MAR simulation at 8-km resolution. The considered dates are 11, 12, 13 and 14 July 1997 at 12 UT.*

The differences between BRN1 and BRN2 methods are the most important during daytime, when the upward surface heat flux is positive. The magnitude of the correction θ_E on the surface temperature (i.e. the only difference between BRN1 and BRN2) is shown in Figure 33, and is generally about 0.8 K at 12 UT for a Julian day. As a consequence of the increased surface temperature θ_{vs}, one notes higher mixing heights with the BNR2 method, and the mean difference of heights between the two methods is about 250 m.

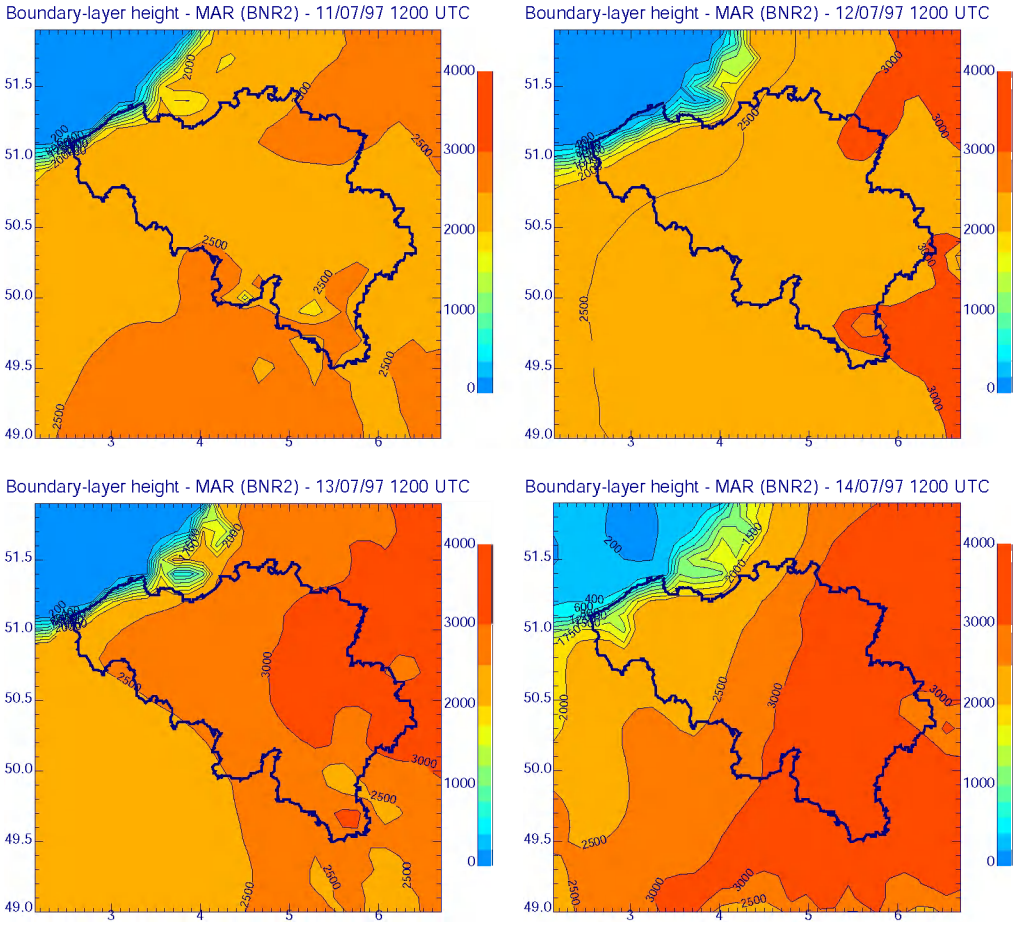

Figure 32: *As in Figure 31, except that the BRN2 method is used instead of BRN1.*

The differences between BRN1 and BRN2 methods are the most important during daytime, when the upward surface heat flux is positive. The magnitude of the correction θ_E on the surface temperature (i.e. the only difference between BRN1 and BRN2) is shown in Figure 33, and is generally about 0.8 K at 12 UT for a Julian day. As a consequence of the increased surface temperature θ_{vs}, one notes higher mixing heights with the BNR2 method, and the mean difference of heights between the two methods is about 250 m.

Figures 34 and 35 present the mixing-layer heights obtained with the BRN1 and BRN2 methods applied to the meteorological fields simulated by MAR at 50-km resolution. The magnitude of θ_E corresponding to the 50-km run is shown in Figure 36.

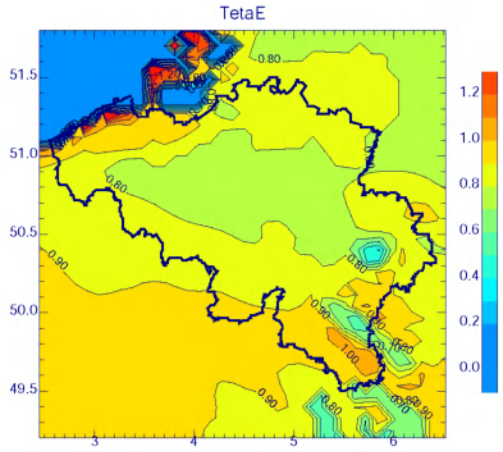

Figure 33: *θ_E field for the situation of 12 UT 13th July 1997, deduced from the surface heat flux obtained with the simulation at 8-km resolution.*

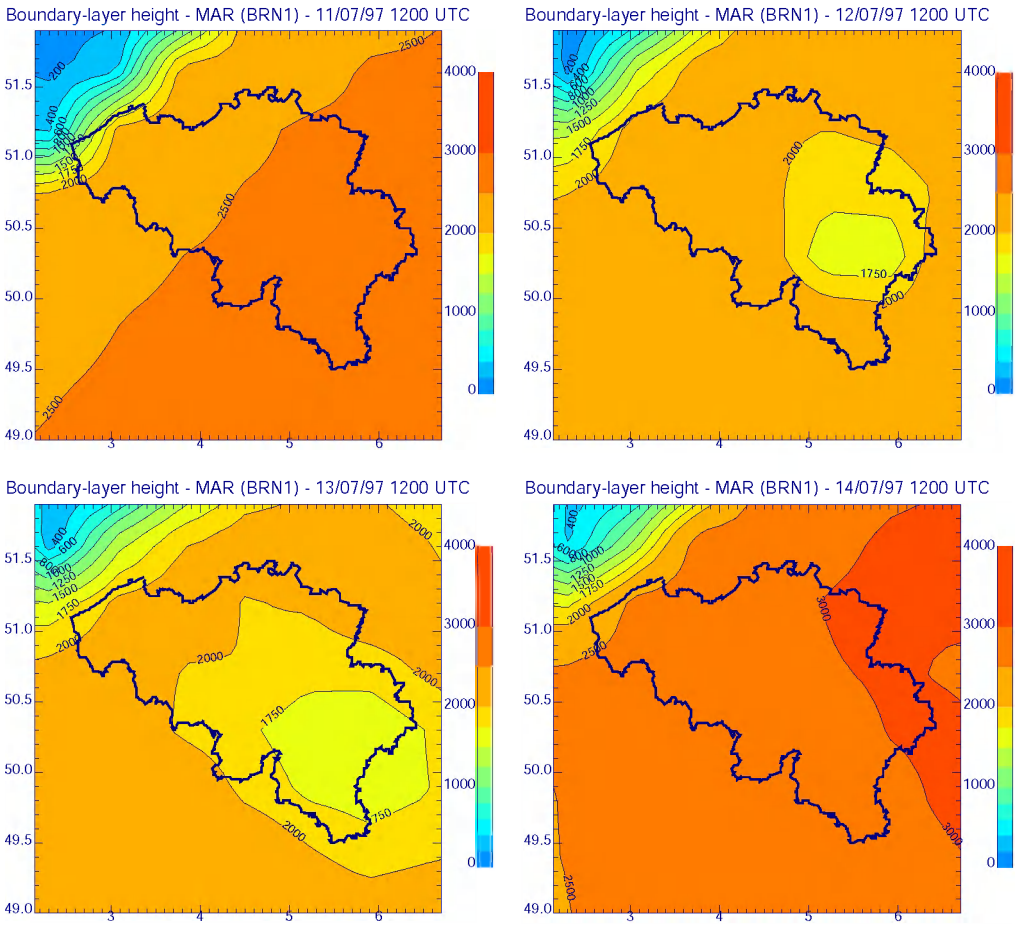

Figure 34: *Mixing-layer heights (units, m) obtained with the BRN1 method applied to the meteorological fields from the MAR simulation at 50-km resolution. The considered dates are 11, 12, 13 and 14 July 1997 at 12 UT.*

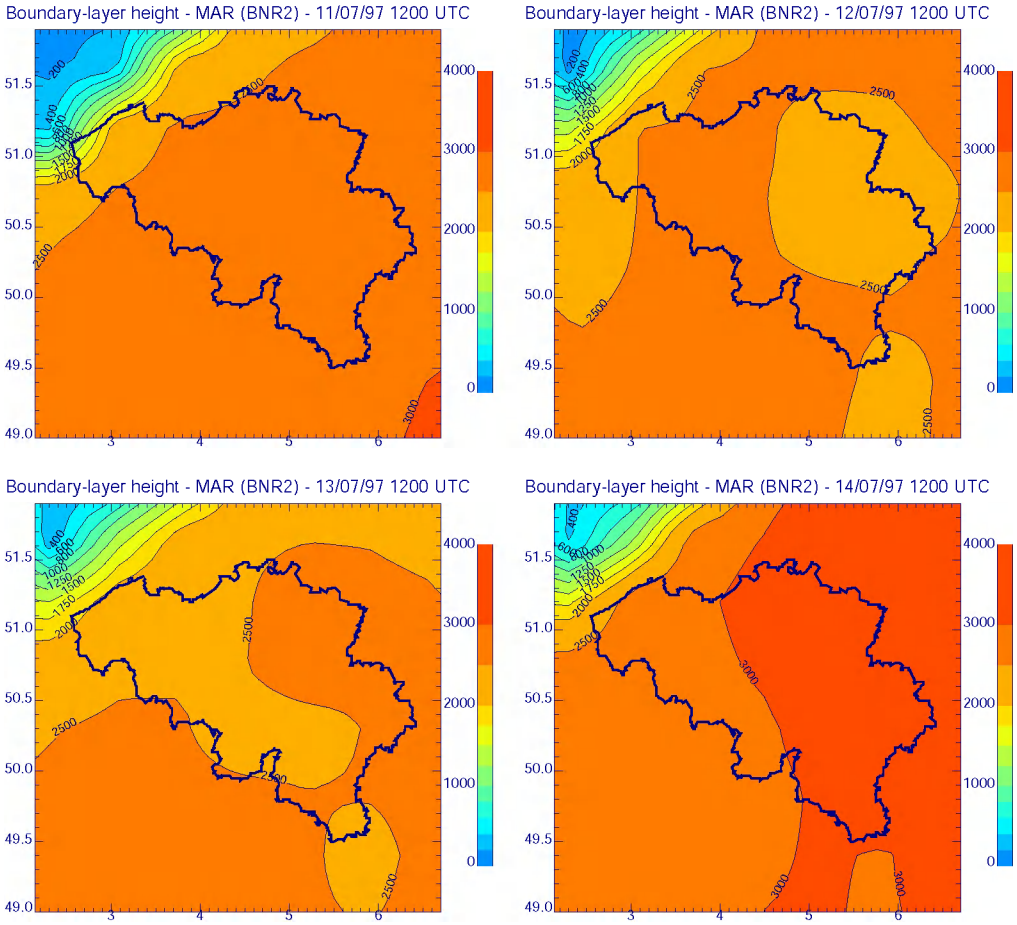

Figure 35: *As in Figure 34, except that the BRN2 method is used instead of BRN1.*

The comparison of the BRN1, BRN2, and MBRN methods based on the output of the 50-km simulation leads to the same conclusions as with the 8-km resolution. However the mixing-layer heights from the simulations at 8- and 50-km resolution are not the same. The mixing heights with the 50-km simulation are in satisfying agreement with the estimates from soundings on the 13th July, with a simulated height around 2000 m. These values appear more realistic than with the 8-km simulation. This is a direct consequence of the better representation of the cloudiness and, consequently, of the surface temperature. The mixing height of the 12 July is better represented with the 50-km resolution, but it remains widely overestimated (see Figure 27). For the 11 and 14 July, the 50-km resolution leads to higher mixing heights than with the 8-km resolution. Such results were not expected for the 14 July, since the 2-m temperature is better simulated with the 50-km resolution than with the 8-km resolution. The only possible explanation is the representation of the vertical structure of the atmosphere and the related turbulent motions, which are implicitly dependent on the horizontal resolution. This fact will be discussed in the next sub-section.

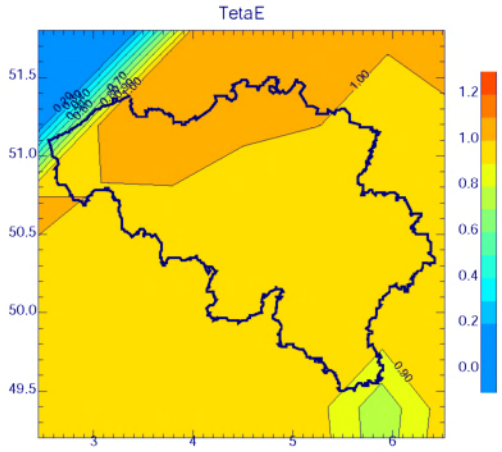

Figure 36: *θ_E field for the situation of 12 UT 13th July 1997, deduced from the surface heat flux obtained with the simulation at 50-km resolution.*

3.5.5 Boundary-layer height

The boundary-layer height z_{BL} is defined in the model as the height where the turbulent kinetic energy is a fraction of its surface value:

$$E(z_{BL}) = 0.05 * E_{surface} \qquad (5.1)$$

where $E_{surface}$ and $E(z_{BL})$ are the turbulent kinetic energy respectively at the surface and at the top of the boundary layer.

Even if mixing-layer and boundary-layer heights are computed with methods that differ on a theoretical point of view, these two quantities present some similarities on a physical point of view. Both represent the depth of the layer affected by the surface through the presence of vertical exchanges. Consequently, it can be useful to compare the two approaches. In Figures 37 and 38, the boundary-layer heights are presented for the same situations as in Figures 31, 32, 34, and 35.

Let us first comment the 8-km simulation. The boundary-layer height is generally in better agreement with the observations (from sounding) than the mixing height. For the four considered situations and if one excepts some local peaks, the mean boundary-layer height over Belgium is about 1750 to 2000 m. The local peaks are explained by the presence of updrafts that are usual during a summer day.

The analysis the boundary-layer heights from the 50-km simulation give a completely different conclusion than with the 8-km resolution. The simulated boundary-layer heights are much less convincing than the 8-km simulation, and than the mixing heights. The TKE method is fully based on the field of turbulent kinetic energy. On

one hand, it can be shown that the horizontal resolution has a significant impact on the representation of turbulent processes (e.g. Brasseur, 1999) and, on this point of view, the 8-km resolution has a significant advantage on the 50-km resolution.

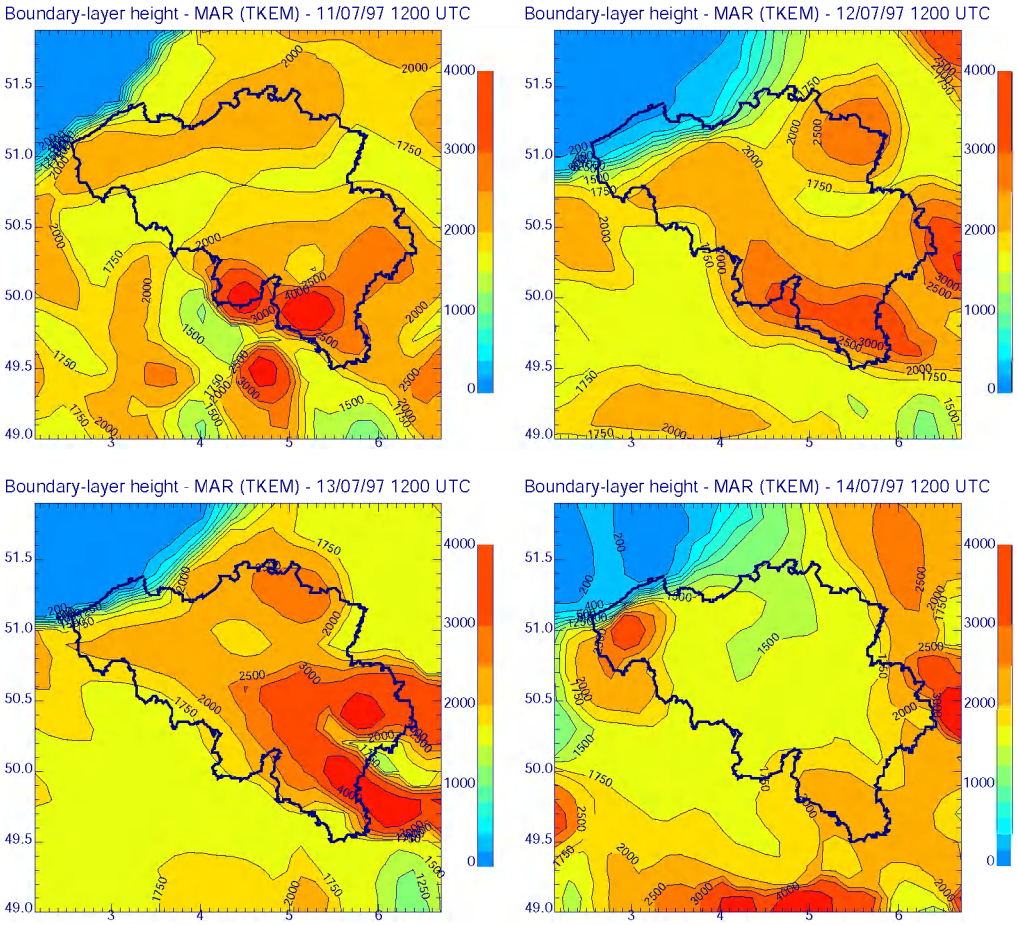

Figure 37: *Boundary-layer heights (units, m) obtained from the meteorological fields of the MAR simulation at 8-km resolution. The considered dates are 11, 12, 13 and 14 July 1997 at 12 UT.*

On the other hand, the simulation at the highest resolution has not correctly reproduced the cloud cover, with the above-mentioned implications on the surface temperature. But the TKE method seems less sensitive to the surface temperature than the methods for the determination of the mixing height. This is explained by the intrinsic nature of the two methods. The BRN1, BRN2, and MBRN methods are directly influenced by the surface temperature (since this variable is explicitely used in the diagnostic of mixing height), while the TKE method is only based on the turbulent kinetic energy that is prognostically affected by the surface temperature. In addition, the turbulent kinetic energy also depends on other factors. This means that a change or a perturbation of the surface temperature will imply a direct and

immediate response with the BRN methods, while the TKE method will progressively adjust the vertical profiles to the new conditions and will require a non negligible adjustment time. The adjustment time depends on the global vertical structure of the atmosphere (i.e. vertical profiles of temperature, …).

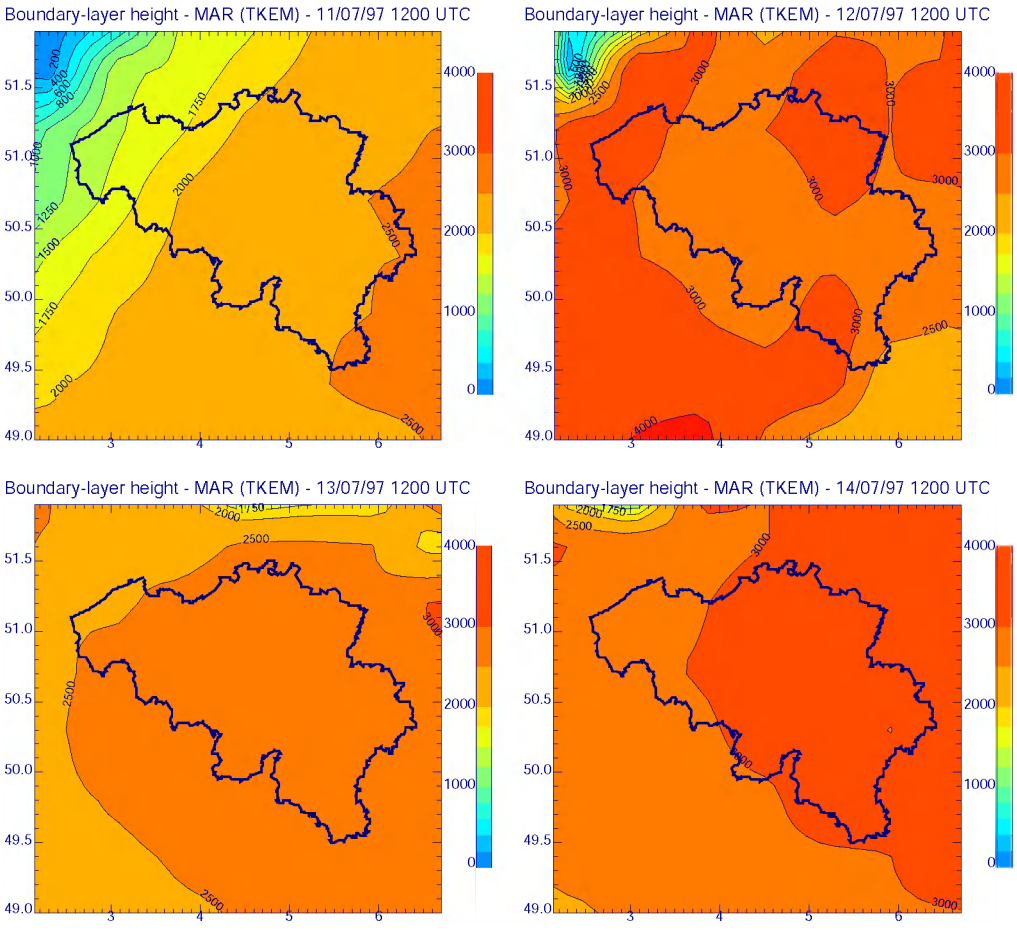

Figure 38: *As in Figure 37, except that boundary-layer heights are computed from the MAR simulation at 50-km resolution.*

3.5.6 Temporal evolution of mixing and boundary-layer heights

In the previous sub-sections, we have presented only results for the situations of 11, 12, 13, and 14 July at 1200 UT, which corresponds to a period of the day characterized by convective boundary layer. However it is also important to assess and compare the different methods on various situations of atmospheric stability. Since a diurnal cycle includes changing conditions of stability (stability during the night, convective layer during the day, …), it is suggested to analyze the diurnal cycle of mixing-layer heights during the whole considered period.

Figures 39 and 41 present the mixing-layer heights deduced from the BRN1, BRN2, and MBRN methods respectively based on the results of the 8- and 50-km experiments. Each Figure includes a sensitivity test to the surface temperature (perturbations from –2 to +3 K), since this variable is one of the most important in the BRN and MBRN methods. All methods show a high sensitivity to the surface temperature: a temperature change of 1 K can induce a modification of the mixing-layer height of a few hundred meters. This sensitivity is more marked with the 50-km resolution than with the 8-km resolution.

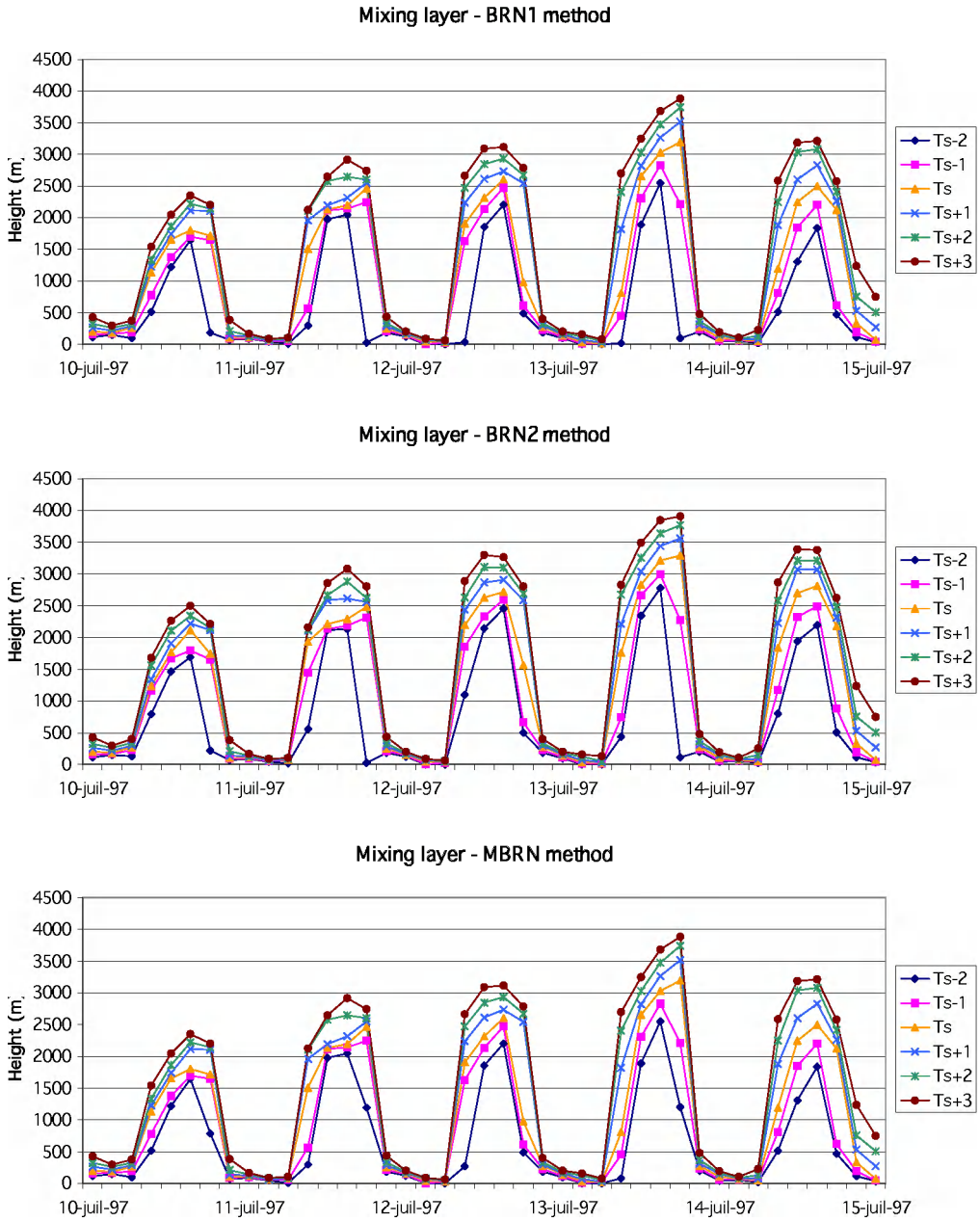

Figure 39: *Sensitivity of mixing-layer heights to perturbations (respectively –2, -1, 0, +1, +2, +3) of the surface temperature. Results are presented for the BRN1, BRN2, and MBRN methods applied to the period from 10 to 15 July 1997, and are based on the MAR simulation at 8-km resolution. The temporal resolution is 3 hours. The analyzed grid point corresponds to Uccle station.*

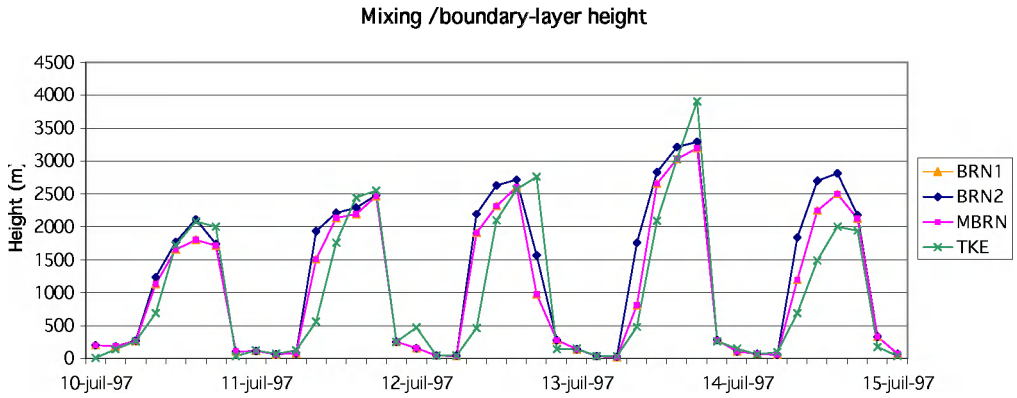

Figure 40: *Comparison of the mixing-layer heights obtained from BRN1, BRN2, and MBRN methods with the boundary-layer height deduced from the TKE method. Results are presented for the period from 10 to 15 July 1997, and are based on the MAR simulation at 8-km resolution. The temporal resolution is 3 hours. The analyzed grid point corresponds to Uccle station.*

The comparison between the different methods and the TKE method are presented in Figures 40 and 42 respectively for the 8- and 50-km resolutions. First of all, let us remark that the BRN1 and MBRN methods give exactly the same results. The additional criterion on the integrated buoyancy in the MBRN method is not necessary for the meteorological fields simulated by MAR. As expected, the BRN2 method leads to higher mixing heights. During daytime, the differences of the mixing heights computed with BRN1 and BRN2 can reach 500 m. Since the typical magnitude of θ_E is about 1K (see Figures 33 and 36), the differences between BRN1 and BRN2 methods can be also investigated with the sensitivity study to the surface temperature, in particular considering the perturbation of +1 K during daytime.

The boundary-layer height obtained with the TKE method generally shows a lot of similarities with those computed with the BRN and MBRN methods. This is particularly the case with the 8-km experiment in Figure 40. With the 50-km resolution, the TKE method produces widely overestimated boundary-layer heights – up to more than 1000 m – compared to the estimates from soundings and compared to the results from the methods based on the Richardson number. This confirms the explanation – mentioned in the previous section – about the loss of accuracy in the representation of the turbulent kinetic energy (related to the representation of the meteorological fields) as the horizontal resolution decreases.

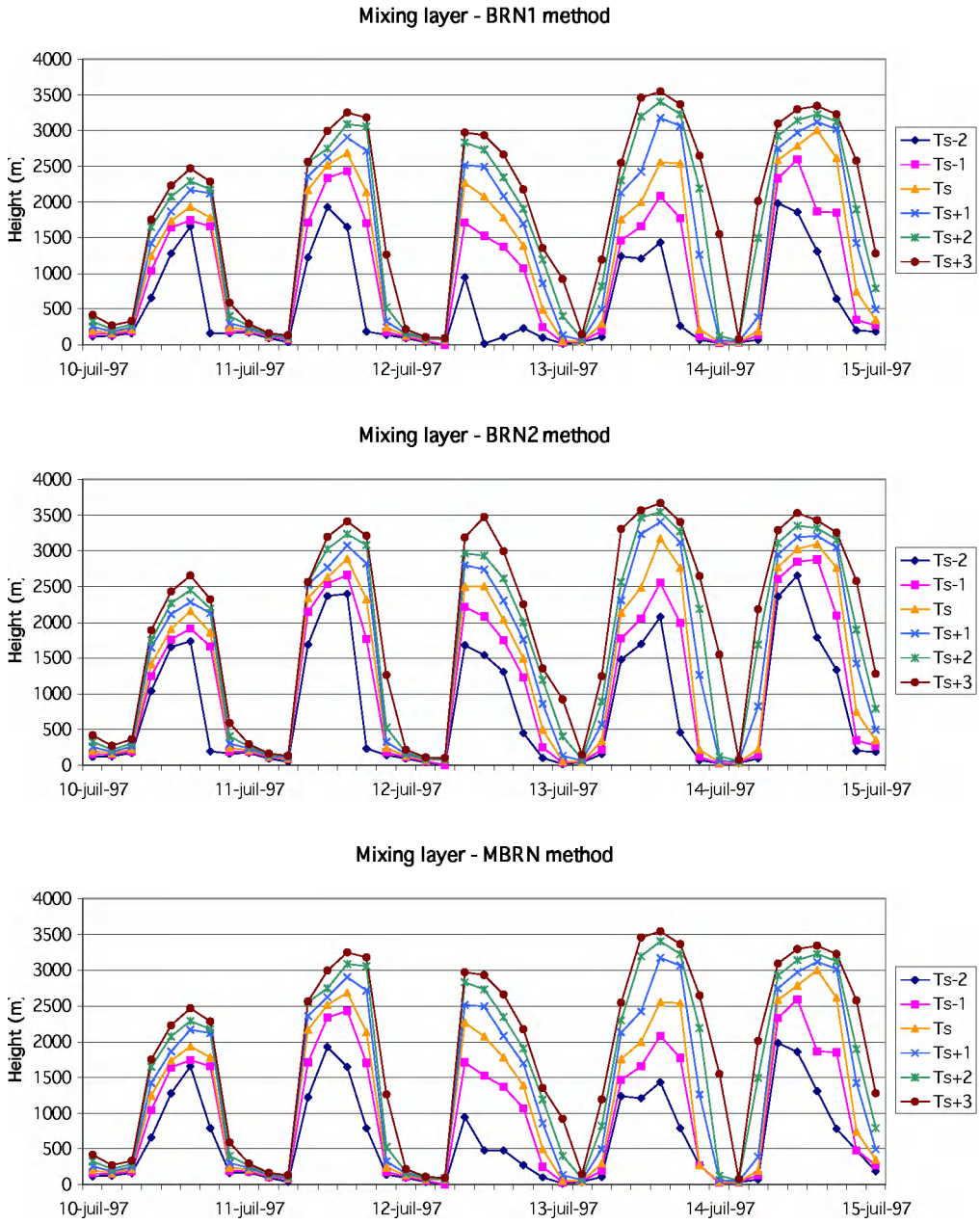

Figure 41: *As in Figure 39, except that mixing heights are computed with the simulation results at 50-km resolution.*

Considering the observations from soundings and the ECMWF data sets, it can be noted a decrease of the mixing height on the 12th July (see section 3.4) compared to the other days. The sounding at 1200 UT 12 July indicates a mixing height of about 500 m. This sudden decrease is not at all simulated in the experiment at 8-km resolution (e.g. Figure 40), while a tendency of decreasing (but without the correct intensity) the mixing height is reproduced in the 50-km simulation. This is not the case for the boundary-layer height – computed ith the TKE method – that is not in

agreement with the observations for both the experiments at 8 - and 50-km resolution.

From all these considerations, it is observed that the 8-km resolution gives a better representation of the turbulent kinetic energy field (required with the TKE method), while the best meteorological fields (temperature, required with the BRN methods) have been obtained with the 50-km resolution that considers a much larger simulation domain able to take into account the large-scale circulation.

Consequently the representation of the meteorological fields has a fundamental importance with the methods based on the Richardson number, while a particular care to the simulation of the turbulent kinetic energy has to be considered with the TKE method.

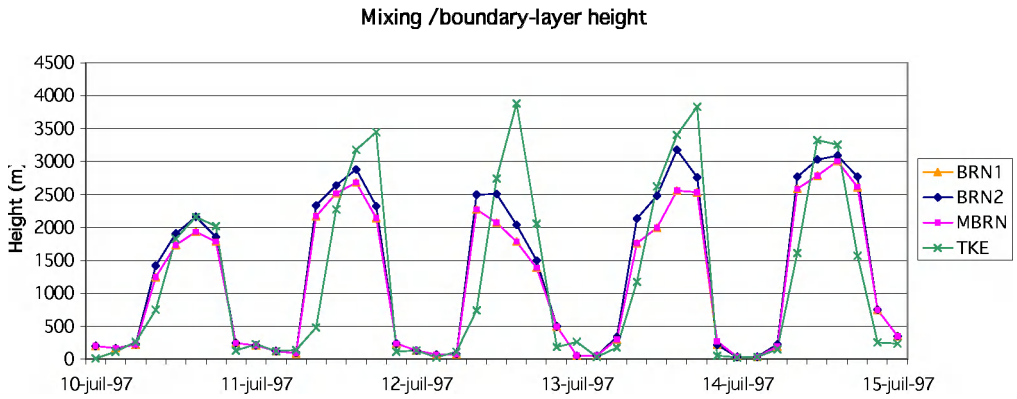

Figure 42: *As in Figure 40 except that mixing and boundary-layer heights are computed with the simulation results at 50-km resolution.*

3.5.7 Conclusions of simulation results

In this section, two simulations performed with the MAR mesocale model at 8- and 50-km resolution are presented for the period from 11 to 14 July 1997. The objective of this study consists of establishing a detailed comparison between all methods presented in section 3.4.1, and the TKE method. Such a comparison was not possible with the other data sets, because the surface turbulent fluxes (required by BRN2 method) and the turbulent kinetic energy (required by TKE method) are not available.

The analysis of the results has led to the following conclusions:

The methods based on the Richardson number are particularly dependant on the surface temperature. Compared to the observations from soundings, the best

estimates of the mixing height computed with the BRN1, BRN2, and MBRN methods are obtained with the 50-km simulation that gives the best representation of the 2-m temperature field.

BRN1 and MBRN methods have given the same mixing heights with the MAR fields.

The correction of the surface temperature prescribed in BRN2 method is not negligible during daytime. Compared to BRN1 method, the subsequent increase of the mixing height can reach 500 m.

The TKE method seems sensitive to the horizontal resolution. The best estimates of the boundary-layer height are obtained with the highest resolution.

The comparison of the results computed with methods based on the Richardson number and the TKE method appears particularly difficult due to the fundamental differences in the concepts of the two approaches.

3.6 Conclusions

In this study, we have mainly focused on the estimation of the mixing height from meteorological three-dimensional data sets. The aim is to introduce in the EUROS model a spatial and time varying mixing height as a function of the meteorological situation.

The data sets we have used are the ECMWF data (coarse resolution, domain covering the whole Europe) and the ALADIN data (high resolution, domain limited to the BENELUX and the North of France). Various methods have been presented to determine the mixing height from the meteorological fields and have been applied to the two meteo data sets. Based upon our results with the ECMWF meteo data, it appears that the Modified Bulk Richardson Number (MBRN) method is the most adequate. This method combines the usual criterion based on the Richarson Number and a criterion based on the integrated buoyant energy. This algorithm allows to strongly improve the results when a thin stable layer is present near the ground. The ALADIN data have also been used to estimate the mixing height with the various algorithms but the results exhibit a systematic underestimation of the mixing height.

Even if the MBRN algorithm appears to be the most appropriate, the estimated mixing heights from the ECMWF data show significant discrepancies compared with more accurate estimations obtained from observed vertical soundings. Inaccuracies in the meteo fields can cause important errors in the estimated mixing height. The limitations of the estimation algorithms constitute another source of errors. To better understand the behavior of these algorithms, numerous model simulations have been

carried out with a regional atmospheric model. The various algorithms have been applied to the simulated atmospheric fields. An important result is the large sensitivity of these algorithms to the surface temperature. A surface temperature change of 1 K can induce a modification of the estimated mixing height of a few hundred meters.

In the methods based on the Bulk Richardson Number, a correction must in theory be applied to the surface temperature in the cases of convective meteorological conditions. This correction is based on the surface turbulent heat flux. Since this variable is not available in our data sets, it was not possible to introduce this correction in the algorithms. Nevertheless, the model simulations allowed to get an idea of the magnitude of the correction for summer conditions in Belgium. This magnitude is around 1K, which shows that the surface temperature correction could have a significant impact on the estimated mixing heights.

An interesting study for the future will be to evaluate the sensitivity of the results simulated by EUROS to the mixing height values. If it appears that an accurate estimation of the mixing height is of crucial importance for a realistic simulation of the photochemical smog formation, the introduction of the surface temperature correction could be considered.

3.7 References

Anthes, R.A., Kuo, Y.-H., Hsie, E.-Y., Low-Nam, S., and Bettge, T.W., 1989 : Estimation of skill and uncertainty in regional numerical models. Quart. J. Roy. Meteor. Soc., 115, 763-806.

Barrett, K., and Berge, E (editors), 1996: Transboundary Air Pollution in Europe, Part 1: Estimated dispersion of acidifying agents and of near surface ozone, EMEP MSC-W Status Report, 1996.

Brasseur, O., 1999: Mesoscale modeling of extreme meteorological events over Belgium. Université catholique de Louvain, unpublished thesis.

Brasseur, O., Gallée, H., Schayes, G., Tricot, C., and De Ridder, K., 1998 : Impact of Turbulent Closures on Diurnal Temperature Evolution for Clear Sky Situations over Belgium. Bound.-Layer Meteor., 87, 163-193.

Businger, J.A., 1973: Turbulent transfer in the atmospheric surface layer. Workshop on Micrometeorology, Amer. Meteorol. Soc., 67-100.

Davies, H.C., 1976: A lateral boundary formulation for multi-level prediction models. Quart. J. Roy. Meteorol. Soc., 102, 405-418.

Davies, H.C., 1983: Limitations of some common lateral boundary schemes used in regional NWP models. Mon. Wea. Rev., 111, 1002-1012.

Deardorff, J.W., 1978: Efficient prediction of ground surface temperature and moisture, with inclusion of a layer of vegetation. J. Geophys. Research, 83, 1889-1903.

Duynkerke, P.G., 1988: Application of the E-e turbulence closure model to the neutral and stable atmospheric boundary layer. J. Atmos. Sci. 45, 865-880.

Duynkerke, P.G., 1991: Radiation fog: a comparison of model simulation with detailed observations. Mon. Wea. Rev. 119, 324-341.

Fritsch, J. M., and Chappell, C. F., 1980: Numerical prediction of convectively driven mesoscale pressure systems. Part I: Convective parameterization. J. Atmos. Sci., 37, 1722-1733.

Gallée, H., 1995: Simulation of the mesocyclonic activity in the Ross Sea, Antarctica. Mon. Wea. Rev. 123, 2051-2069.

Gallée, H., 1996: Mesoscale atmospheric circulations over the Southwestern Ross Sea sector, Antarctica. J. Appl. Meteor. 35, 1142-1152.

Gallée, H., van Ypersele, J.P., Fichefet, T., Tricot, C., and Berger, A., 1991: Simulation of the last glacial cycle by a coupled 2-D climate-ice sheet model, 1, The Climate Model. J. Geophys. Res. 96, 13139-13161.

Gallée, H., and Schayes, G., 1994: Development of a three-dimensional meso-g primitive equations model, katabatic winds simulation in the area of Terra Nova Bay, Antarctica. Mon. Wea. Rev. 122, 671-685.

Loon, M. van, 1996: Numerical methods in smog prediction, PhD thesis, Univesrity of Amsterdam.

Morcrette, J.-J., 1984: Sur la paramétrisation du rayonnement dans les modèles de la circulation générale atmosphérique. Unpublished thesis, Université de Lille, France.

Simpson, D., Anderson-Sköld, Y., and Jenkin, M.E., 1993: Updating the chemical scheme for the EMEP MSC-W oxidant model: current status. Technical Report note 2/93, EMEP MSC-West, Oslo, Norway.

Sorensen, J.H., and Rasmussen, A., 1997: Method for calculation of atmospheric boundary-layer height used in ETEX dispersion modeling. Proceedings of the Sixth Topical Meeting on Emergency Preparedness and Response, San Francisco, California, April 22-25, 1997, pp. 503-506.

Sorensen, J.H., Rasmussen, A., and Svensmark, H., 1997: Forecast of the atmospheric boundary-layer height utilized for ETEX real-time dispersion modeling. Physics and Chemistry of the Earth.

Stull, R.B., 1988: An introduction to boundary layer meteorology. Kluwer Academic Publishers, 666 pp.

Tricot, C., and Berger, A., 1988: Sensitivity of Present-Day Climate to Astronomical Forcing. Long and Short Term Variability of Climate. Lect. Notes Earth Sci. 16, edited by H. Wanner and U. Siegenthaler, 132-152.

Troen, and Mahrt, 1986: A simple model of the atmospheric boundary layer. Boundary-Layer Meteorology, 37, 129-148.

Van der Auwera, L., 1992: Inversion and mixing heights calculated from radiosonde profiles taken between 1968 and 1991. IRM internal publication, Misellanea serie B, n° 66.

Vogelezang, D.H.P., and Holtslag, A.A.M., 1996: Evaluation and model impacts of alternative boundary-layer heights. Boundary-Layer Meteorology, 81, 245-269.

4. OPTIMIZATION OF CHEMICAL AND ADVECTION MODULES IN EUROS [3]

4.1 Introduction

The EUROS (EURopean Operational Smog) model is an atmospheric model that has been developed at the National Institute of Public Health and Environmental Research (RIVM, Bilthoven, The Netherlands). For its implementation in Belgium, the EUROS model has been further developed in order to improve the representation of some important atmospheric processes. This chapter describes these new developments, which have been carried out in close collaboration with RIVM. In order to run the EUROS model for Belgium it was also necessary to adapt the emission and meteorological data. These tasks have already been carried out in the framework of work package 1 and 3 of BeleEUROS and are described in chapters 2 and 3.

The main developments on the EUROS model concern the representation of the mixing layer processes and the calculation of the horizontal transport. In the original version of the EUROS model, the mixing layer is uniform over Europe and its diurnal growth is determined from a climatological mean. A new version has been developed in which the mixing layer height is calculated for each grid point from surface meteorological parameters. The implementation of this spatially variable mixing layer required the adaptation of the horizontal advection scheme. A multi-layer structure has been introduced for the calculation of the advection. The model is now provided with a three-dimensional grid structure. In the framework of this work package 4, the optimization of the chemical module has also been addressed. Various methods have been proposed in the literature to select relevant chemical components and reactions in order to reduce the complexity of chemical modules. These methods are shortly described in this report.

In the next section, the implementation of a spatially variable mixing height is described. The comparison of simulated mixing heights with LIDAR observations is also presented. The adaptation of the horizontal advection scheme is described in section 4.3. The new version of EUROS has been extensively tested. The results are analyzed and compared with the observations in section 4.4. Optimization methods for the chemical scheme are shortly depicted in section 4.5. Finally, general conclusions are drawn in section 4.6.

[3] The content of this chapter is taken from the intermediary report: Delobbe L., L. Kinnaer and C.Mensink, 2000. Optimization of chemical and advection modules in EUROS. Sceintific report, 2000/TAP/R/063, Vito, Mol.

4.2 Parameterization of the mixing layer height in EUROS

4.2.1 General description

In the original version of the EUROS model (van Loon, 1996, hereafter referred to as VL), a very simple representation of the mixing layer (ML) is used. The ML height is constant during the night (300m in VL) and grows during the day hours. After the sunset, the nocturnal mixing layer is quickly established again. The growth rate of the ML during the day is prescribed according to climatological values. In VL, the growth rates are 50 and 75 meters per hour, for winter and summer, respectively. The ML height varies in time but is the same for the whole Europe.

This representation of the ML has been recently updated and a new calculation of the ML height has been implemented in EUROS. This calculation is based on diagnostic formulae which relate the ML height (also referred to as the mixing height MH) to surface meteorological parameters (see technical note from Addo van Pul: "EUROS testruns: new calculations of the mixing layer height). These parameters are the friction velocity (u_*), the Obukhov length (L), and the sensible heat flux (h_s). Three different cases are considered for the calculation of the ML height:

Stable atmospheric conditions (L > 0):

The atmospheric boundary layer is considered as stable if the Obukho length is positive. In this case, the ML height is calculated following Nieuwstadt (1981):

$$\frac{H}{L} = \frac{c_1 u_* / fL}{1 + c_2 H/L} \qquad (2.1)$$

where c_1 = 0.15, c_2 = 0.31 and Coriolis parameter, f, is 0.0001.

This formulation is also discussed in Holtslag and Westrhenen (1989). It must be solved iteratively. The initial value is given by the ML height value under neutral conditions.

Neutral conditions (L < -1000):

For strongly negative Obukhov lengths, the boundary layer is considered as neutral. The following expression is then used:

$$H = c_1 u^* / f \qquad (2.2)$$

Let us remark that (2.2) is the limit of (2.1) for increasing values (negative or positive) of the Obukhov length (L).

Unstable conditions (- 1000 < L < 0):

In unstable cases, the growth of the convective boundary layer is described through a prognostic equation. The formulation of Tennekes (1973) is used:

$$\frac{\partial H}{\partial t} = \frac{h_s}{\gamma H} \tag{2.3}$$

where H is the convective layer height, and γ is the vertical gradient of potential temperature above the convective boundary layer. This model considers the surface heating flux as the only relevant driving force, neglecting the mechanical turbulence production due to surface friction. The parameter γ expresses the stability of the layer above the convective layer. Its value is fixed to the climatological value of 0.005 K/m. The integration of (2.3) over one time step results in:

$$H_{t+1} = \sqrt{abs(H_t^2 + \frac{2\,\Delta t\, h_{s,t}}{\gamma})} \tag{2.4}$$

The surface meteorological parameters u_*, L, and h_s are calculated using a software library developed at the KNMI by Beljaars and Holtslag (1989). The input parameters are the wind (at 10m for example), the surface air temperature (at 2 m), aerodynamic roughness length and the cloud cover from SYNOP observations. The input data are taken from the ODS data set.

In order to keep a uniform mixing layer over Europe, the calculation of the mixing layer height is carried out for a single grid point located in The Netherlands and this value is applied to the whole Europe. The following step consists in calculating the ML for each grid point of the EUROS domain. This improvement is only possible if the advection scheme can support a spatially variable mixing layer. The adaptation of the advection scheme is described in section 4.3.

It is worth noting that the KNMI software for the calculation of the surface parameters was developed for use over horizontally homogeneous flat terrain and validated with observations at Cabauw in The Netherlands. Over complex terrains, these routines are not expected to yield accurate results. This must be kept in mind when using these routines over all European regions. Besides, some internal parameters used in these routines (the albedo for example) are not adapted to regions other than The

Netherlands. This point will be discussed in section 4.2.2.3. Finally, the KNMI routines which have been implemented in EUROS are designed for the calculation of the ML over land. The calculation of the surface meteorological parameters over sea needs the implementation of new routines suited to sea conditions.

4.2.2 Improvements

4.2.2.1 Distinction land/sea

An important improvement of the ML representation in EUROS consists in calculating the ML height for each EUROS grid point and not only for a single grid point located in The Netherlands. Large areas of the EUROS domain are sea areas and it is therefore necessary to adapt the determination of the ML height to sea conditions. The expressions used in EUROS for the calculation of the ML height, as well as those reviewed in Seibert et al. (2000) are based on three meteorological parameters i.e., the Obukhov length, the friction velocity and the sensible heat flux. To evaluate these parameters over sea, the adequate routine from the KNMI software library must be implemented in EUROS, i.e. the routine FLXSE1 from Beljaars and Holtslag (1989).

The input meteorological data for the routine FLXSE1 are the sea surface temperature (SST), the air temperature and a single wind speed. The two latter parameters can be extracted from the ODS dataset but it is not the case for the SST. Since the SST evolution along the year is relatively slow and remains similar from a year to another, the SST data can be extracted, as a first approximation, from climatological values. The monthly SST climatology from Trenberth and Reynolds from NCAR (Boulder, USA) can be used (Shea et al., 1990; Shea et al., 1992). It provides monthly averaged SSTs with a regular 2 degrees spatial resolution.

The calculation of the three parameters u*,L, h_0 through FLXSE1 does not converge if the wind velocity is too small. In unstable conditions (sst larger than the surface air temperature), the wind velocity must be at least 1.5 m/s to ensure convergence. In stable conditions (sst smaller than surface air temperature), the wind must be at least 3.8 m/s. To avoid divergence in the calculation of the meteo parameters, minimal values of the wind velocity have been set to 2 and 4 m/s for unstable and stable conditions respectively.

Figures 2.1 and 2.2 illustrate the impact of the land-sea distinction on the geographical pattern of the mixing layer height (runs 615 and 641). The mixing layer depth calculated by EUROS is shown for the 30th of July 1990 at 04 UT (Figures 2.1 and 2.2) and at 16 UT (Figures 2.3 and 2.4). Note that the top of the mixing layer is given by the ML depth plus 50m, which is the depth of the surface layer. When the

land-sea distinction is not included, the calculated mixing layer heights are similar over land and over sea, as well during the night as during the day. This is not realistic. In contrast with land, the sea surface temperature is almost constant at the day scale. No diurnal cycle is observed. This results in a stabilizing effect during the day (SST is cooler than the atmospheric temperature) and a destabilizing effect during the night. Over land, the opposite effect is observed with strong destabilizing effect during the day, due to surface heating and a strong stabilization during the night due to the longwave cooling of the land surface. When the "land routines" are used everywhere, this effect can not be accounted for, which results in an unrealistic ML height geographical pattern. As shown in Figures 2.2 and 2.4, the calculated ML height geographical pattern is significantly improved. During the night, higher ML heights are obtained over sea while during the day, stabilization over sea results in relatively low ML values in comparison with those obtained over land.

A common feature of Figures 2.2 and 2.4 is that the western border of some land areas exhibit a systematic higher ML height than the sea and land grid points around. This is particularly true for the north of UK and Ireland, and the south of Portugal. This shortcoming is probably related to the interpolation of surface meteo data for grid cells that are partly over land and partly over sea. Note that for sea grid cells, this deficiency disappears when the land-sea distinction is introduced (see north of UK).

Finally, let us remark that the ML height geographical patter lets clearly appear that significant areas of The Netherlands located near the coast are considered as sea areas. This must be kept in mind when the simulated results are compared with measurements collected in stations near the coast.

4.2.2.2 Comparison with LIDAR observations

The validation of the parameterizations used for the calculation of the mixing layer height is of crucial importance but remains a problematic issue. Observations of the atmospheric boundary layer are only available for some specific locations, most of them over land, which makes diffcult a validation at the European scale.

In this study, we have compared the ML height calculated by EUROS for the grid cell where Bilthoven is located with the LIDAR observations at RIVM. The LIDAR determination of the ML height is based on the backscatter of a laser beam by aerosol particles present in boundary layer (van Pul et al., 1994). The top of the ML height is marked by a discontinuity in the backscatter profile. The comparison has been performed for August 1994. Figure 2.5 shows the two time evolutions of the ML height. Significant discrepancies between the two time series are found. The LIDAR observations exhibit a much larger variability then the EUROS values. For most days,

the EUROS ML height is 100 m during the night and grows in a motonic way up to a value around 1000m in the late afternoon. According to the LIDAR observations the night values of the ML height are mostly between 200m and 700m. In the day, the ML height is usually comprised between 1000 and 1500m but sometimes exceeds 2000m. LIDAR observations exhibit significant variations during the day hours in contrast with the day values obtained with the EUROS parameterization.

Figure 2.6 shows the averaged diurnal cycle for August 1994 as observed with the LIDAR and simulated by EUROS. It is clearly apparent that EUROS tends to underestimate the ML height. During the day the mean difference between the LIDAR and EUROS values for August 1994 is limited to about 200m. In the night the differences in the mean ML height are considerably larger. It must be noted that the lowest ML top that can be detected by the LIDAR is about 200m. If the actual ML top is lower than 200 m, the LIDAR may consider the top of the residual layer as the ML top leading to an unrealistically high ML height. The night mean values are strongly affected by these erroneous LIDAR estimates. In the evening, it may also take some time until the LIDAR may detect the top of the new boundary layer, within the previously well-mixed layer. Figure 2.7 shows the boundary layer climatology for August at Bilthoven, based on the lidar observations for 1992 to 1999. During the night, the mean value strongly differs from the most frequent value, which is around 300m. For the EUROS results, the differences between the mean values, the most frequent values and the 50-percentile are much more limited. The comparison between the average diurnal cycle for August 1994 and the averaged LIDAR diurnal cycle of Figure 2.6 shows a relatively good agreement.

As far as the time series for the month August are concerned (Figure 2.5), several causes of discrepancies can be mentioned. First of all, the method used in EUROS for the calculation of the ML height has its own limitations. Errors may arise from the calculation of the surface meteorological parameters (Obukhov length, friction velocity and heat flux) through the KNMI routines but also from the determination of the MH from these parameters using expressions (2.1), (2.2) and (2.4) in stable, neutral and unstable conditions respectively. The meteo input used for the calculation of the surface meteo parameters, i.e. the 2m-temperature, 10-m wind, cloudiness, may also induce some errors. The meteo input used in EUROS results from a spatial interpolation from synoptic observations and a time interpolation from the 4 input times of these synoptic observations (00, 06, 12, 18 UT). This interpolation partly explains the fact that the ML diurnal cycles simulated by EUROS are much smoother than the observed diurnal cycles from the LIDAR. Another possible cause of discrepancies arises from the fact that the LIDAR observations are local while the EUROS estimate is an average over a 60 x 60 km^2 grid cell. Finally, the determination of the ML height from LIDAR measurements has also its own

limitations. We have already mentioned the minimal detectable value of 200m which may result in large errors for the night estimates. Another shortcoming is the large inaccuracies in case of rain or if the amount of aerosol or trace gas in the boundary layer is too low.

A deeper validation of the ML parameterization would need to compare with various observational data, including both LIDAR and soundings, but also with results of atmospheric models including a detailed representation of the boundary layer processes.

4.2.2.3 Choice of parameters

The parameterizations used to calculate the surface parameters (u_*, L, and $h_{s)}$ contain a number of empirical coefficients which have been optimized for data gathered at Cabauw in The Netherlands (Beljaars and Holtslag, 1990). The values of these coefficients are typical for grass land with sufficient water supply on a clay soil. Beljaars and Holtslag mention that the most important parameters are the albedo, the modified Priestley-Taylor parameter (which controls the partitioning of available surface energy between latent and sensible heat flux), and the bulk soil heat transfer coefficient (which relates the heat flux into the soil to the temperature difference between the top of the vegetation layer and the deep soil). When the KNMI software library is used for different terrain types, it is recommended to adapt these parameters. The authors suggest some guidelines to determine the parameters from local land-use conditions. The relationships they propose are mainly based on Stull (1988).

In the new version of EUROS including a variable mixing layer height over Europe, it could be useful to adjust the above-mentioned parameters for each grid point as a function of the land-use conditions. Since the mesh of the base grid of Euros may contain various land-use types, an adequate interpolation procedure should be applied.

Another parameter which influences the calculation of the ML height is γ is the vertical gradient of potential temperature above the convective boundary layer (γ in equation). This parameter controls the growth of the convective boundary layer in unstable conditions. Its value is fixed to 0.005 K/m in EUROS. Observations show a large variability of γ (e.g., van Pul et al., 1994). A better determination of this parameter could be investigated.

4.2.2.4 *Update of the ML height formulations*

The expressions (2.1), (2.2) and (2.4) for the calculation of the mixing height (MH) are not the only one proposed in the literature. A review of operational methods for the determination of the mixing height (MH) is made in Seibert et al. (2000).

The calculation of the MH in stable or neutral conditions remains a very controversial issue and a large variety of formulations have been proposed. These formulations differ through the choice of the meterological input parameters (Obukhov length, Ekman length, friction velocity, Brunt-Vaisala frequency, …). A wide range of different constants is also used for the same formulations. So far, none of these formulations appears to be fully satisfying and further development and validation work is needed.

In case of convective situations, the MH is usually determined through a prognostic equation similar to (2.3) describing the growth of the mixing layer through surface heating. The basic input paramters of these formulations are the surface heat flux and an initial temperature gradient as in the expression (2.3) used in EUROS. These formulations can be improved by taking into account the additional turbulence production due to surface friction as well as the entrainment heat flux at the top of the boundary layer. The entrainment flux is generally parameterised in term of the surface heat flux. For example, the following expression proposed by Gryning (1991) can be used:

$$\frac{dh}{dt} = (1+2A)\frac{Q_0}{\gamma_\theta h} + 2B\frac{u_*^3}{\gamma_\theta \beta h^2}$$

where Q_0 is the surface heat flux, u_* the friction velocity, γ_θ the potential temperature gradient above the MH, and β is the buoyancy parameter ($\beta = g/T$). The parameters A and B given in the literature differ considerably ranging between 0 and 1 for A (A = 0 correspond to no entrainment flux) and between 0 and >10 for B (B = 0 corresponds to no mechanical production of turbulence). A discussion about these parameters can be found in Seibert et al. (2000).

4.3 Horizontal transport

The vertical structure of the EUROS model consists in four layers: the surface layer (up to 50 m), the mixing layer, the reservoir layer, and the top layer (up to the model top at 3000 m). The advection process is taken into account in the mixing layer and the reservoir layer. Since the depths and the heights of these two layers are uniform over the whole domain, the computation of the horizontal advection can be easily performed. The implementation of a variable mixing layer height in EUROS requires to adapt the representation of the advection process. Several options have been

considered. An important criterion in evaluating the various options is the possibility to extend it to the vertical advection process, allowing EUROS to evolve towards a fully three-dimensional structure. Hereafter we only describe the option which has been selected.

A new vertical structure is used for the calculation of the horizontal advection. It includes a larger number of layers than the initial 4 layers structure. The multi-layer structure is uniform over the whole domain allowing to calculate the advection in each advection layer using the same advection scheme as in the four-layer structure. In order to keep the computational cost acceptable, the four-layer structure is conserved for the calculation of the other processes, i.e. chemistry, fumigation, dry and wet deposition, and diffusion.

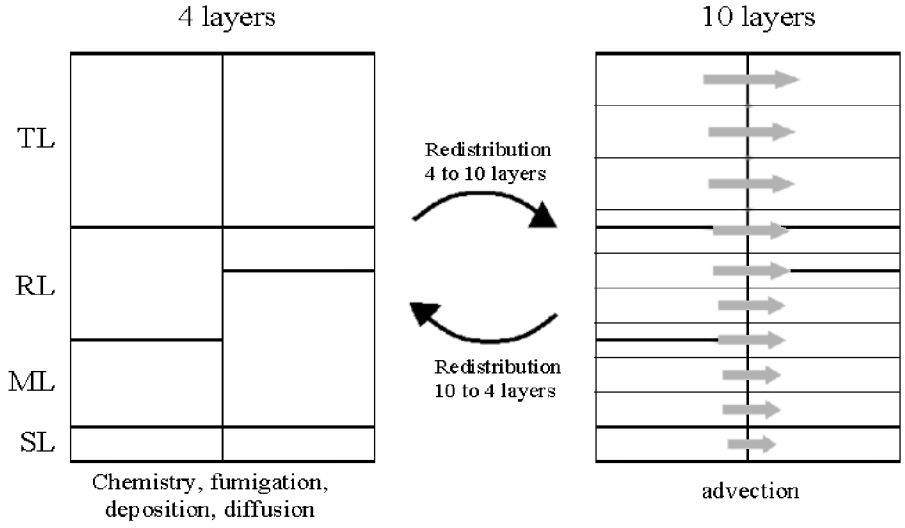

Even if the advection and the fumigation (exchange between the ML and the RL due to change in the mixing layer depth) are coupled in the reality, these two processes are treated separately in the model leading to mass exchange between the ML and the RL through horizontal advection. This approach is similar to the approach followed in 3D atmospheric models: the advection scheme computes the transport by the mean wind while the turbulence computes the fluxes (mainly vertical) due to turbulence. The mixing layer concept used in EUROS can be considered as a very simple turbulence scheme: a mixing height is determined from meteo data and it is

assumed that the atmosphere is perfectly mixed from the ground up to the mixing height.

A strong advantage of this method is that it provides the model with a 3D grid structure which allows an easy implementation of a 3D advection scheme. Besides, it gives also the possibility to implement a more sophisticated turbulence scheme.

Another improvement in respect to other approaches, in which a four-layer structure is conserved for the advection, is that the vertical profile of the horizontal wind can be better represented. The approximation of considering one horizontal wind for the ML and one horizontal wind for the RL can be relaxed. It allows also a better calculation of the vertical wind when 3D advection is considered.

The main disadvantage is of course the relatively high computing cost. The number of layers must be chosen so as to keep this cost acceptable. In a first step we will consider 10 layers for the calculation of the advection. The impact of the number of layers and the heights of these layers will be investigated in section 4.4.3.

Another difficulty arises from the fact that the mixing height does not necessarily correspond with one of the vertical levels of the multi-layer structure. Just before and after the advection step, mass must be redistributed from the four meteorological layers to the advection layers, using linear interpolation. This means that numerically induced mass exchange between the vertical layers will occur. Even if the ML height remains constant in time, artificial exchange between the ML and the RL will occur through the redistribution procedure between the two vertical structures. Another approach could be to enforce the top of the mixing layer at one of the advection layers. This approach consists in using an approximate value of the mixing height which is equal to one of the advection levels. It must be kept in mind that the mixing height can not be estimated with great accuracy. If the error on this estimate is of the same magnitude as the depth the advection layers, it is justified to approximate the mixing height to the closest vertical level of the multi-layer structure. In a first step, the redistribution procedure will be used. The impact of this procedure will be investigated in section 4.3 devoted to the sensitivity to the vertical resolution.

The standard vertical grid structure includes ten advection levels: 50, 100, 200, 400, 600, 900, 1200, 1500, and 2000 m. The advection layers are between the advection levels. The horizontal wind used in each advection layer is computed through a linear inerpolation from the 5 vertical levels of the meteo input data. Note that the number of layers and the heights of these layers can be easily modified.

4.4 Simulations with a variable mixing height

A large number of simulations have been carried out to test the new version of EUROS including a spatially variable mixing height and a multi-layer vertical structure for the representation of the horizontal advection. In a first step, the mixing layer height has been calculated using the "land procedure" everywhere. It means that the MH is spatially variable over Europe but the same calculation method is used without distinction over land and over sea. The results are presented in the next section. The simulations including the land sea distinction are described in section 4.4.2. The sensitivity to vertical discretisation is addressed in section 4.4.3. The last section is devoted to the comparison of the EUROS results with observational data.

The time period of these simulations is the summer 1990. Hereafter, we summarize the most relevant results and only a limited number of runs will be mentioned.

4.4.1 Land procedure used everywhere

The impact of a spatially variable mixing height is illustrated in Figure 4.1. This Figure shows the ozone evolution at observational height for runs 618 and 619. In run 618, the MH is uniform over Europe and calculated according to a climatological growth rate during the day. In run 619, the MH height varies from one grid point to another and is calculated from surface meteo parameters following the procedure described in section 4.2.1. In both simulations, the advection is calculated using a 10-layer vertical structure. The simulation period extends over 6 days from July 30 to August 4 1990. The ozone evolutions have been checked for 14 locations in Europe (most in The Netherlands). It appears that the differences between the two simulations are extremely limited and do not tend to grow with time. This is illustrated in Figure 4.1. for two specific locations: Cabauw in The Netherlands (between Rotterdam and Utrecht) and Waldhof in Germany (South of Hamburg).

The comparison between the two simulations shows that the impact of the ML representation is much more limited than expected. The MH seems not to be a dominant factor in the evolution of ozone concentrations as simulated by EUROS. A possible explanation is related to the representation of the vertical exchange between the mixing layer, the reservoir layer and the top layer in EUROS. In particular, the altitude of the top of the reservoir layer, which is prescribed, seems to play an important role. In the standard version of EUROS, the RL top is fixed to 600 m. In the morning hours, the growth of the mixing layer gives rise to mass exchange between the mixing layer and the reservoir layer, provided that the ML top does not exceed 600 m. If the ML height exceeds 600 m, the reservoir layer vanishes and the fumigation process acts between the mixing layer and the top layer. Since the concentrations in the top layer are fixed, the entrainment of mass from the top layer

into the ML constitutes a restoring toward the top layer background concentrations. The exchange mechanism also implies an intense outflow of concentrations from the ML to the top layer at the end of the day when the ML collapses. This outflow flux is implicitly controlled by the prescribed height of the reservoir layer.

These considerations let appear that the ozone concentrations may be much more affected by the height of the reservoir layer and the top layer concentrations than by the mixing layer height. In order to point out the impact of the reservoir layer height, a run with a prescribed height of 1500 m has been carried out (run 620). The comparison between run 618 and run 620 is illustrated in Figure 4.2. The only difference between the two runs is the prescribed height of the reservoir layer. Significant differences between the two simulated ozone evolutions are clearly apparent. A factor 2 difference in ozone concentrations can be reached in the afternoon hours. The ground level simulated ozone concentrations are higher when the reservoir layer top is set to 1500 m. This probably results from the reduced mass outflow from the mixed layer to the top layer at sunset. The MH estimated by EUROS rarely exceeds 1500 m. At the end of the day, when the mixing layer collapses, the mixing layer concentrations are injected in the reservoir layer and not in the top layer. The day after, these reservoir concentrations can be entrained again into the mixing layer during the mixing layer growth that occurs in the morning hours.

In order to better catch the impact of the reservoir layer top, 1-month simulations with various RL tops ranging from 600 to 1500 m have been carried out. The results are illustrated in Figure 4.3. For a better visualization, only the first 8 days of the simulation are plotted. A similar behavior is found for the following days. The simulated ozone evolution at Cabauw lets again appear a large sensitivity to the reservoir layer top. The differences between the various runs are significant. When the RL top is set to 600 m, the exchange with the top layer is very intense which amplifies the restoring towards the background concentrations of the top layer. When the RL top is set to 1500 m, the exchange with the top layer is extremely low. All pollutants present in the surface layer, in the mixing layer and the reservoir layer remain in these layers. Mass exchanges occur between these three layers but the global mass remains constant.

As a consequence, the peak concentrations will be higher. Figure 4.3 shows that peak concentrations are even larger when the RL top is fixed to 900 or 1200m. The reason of this feature is that the mixing layer top rarely exceeds 1000m, which means that, even with a RL top around 1000m, the exchanges with the top layer will be very limited. With a RL around 1000m instead of 1500m, the pollutants are dispersed over a thinner atmospheric layer, which causes the concentrations to

increase. In short, the peak concentrations tend to be higher if the RL top is fixed to the maximum value of the ML height.

In order to limit the computing cost, the above-described simulations have been carried out with the 4-layer vertical structure for the representation of the advection and a uniform mixing layer height. The simulation results with a RL top at 600 m appear to be slightly different from the results obtained with a uniform MH but using a 10-layer structure for the advection. This suggests that the the number layers used for the advection could have a significant impact. This will be further investigated in section 4.4.3.

4.4.2 Distinction land/sea

As described in section 4.2.2.1, new routines have been implemented in order to make a distinction between land and sea for the calculation of the mixing height. The impact on the estimated MH pattern has already been shown in Figures 2.1 to 2.4. In this section, we point out the impact on the simulated ozone concentrations.

Figure 4.4 illustrates the comparison between run 626 and run 644. These are two 1-month simulations with a spatially variable MH and a 10-layer vertical structure for the horizontal advection. In both simulations, the top of the reservoir layer is set to 600 m. In run 626, the MH is calculated using everywhere the “land routines” while a distinction is made between land and sea grid cells in run 644. This allows a better representation of the land sea contrast in the development of the mixing layer, especially during the day where convective conditions mostly prevail over land while stable conditions and thin mixing layers are found over sea. Over land, the calculated MH is the same in the two simulations. The ozone evolutions are shown for 3 locations: Cabauw, Waldhof, Kollumerwaard. For Cabauw and Waldhof, the ozone evolutions are almost identical. This shows that a change in the MH over sea does not influence the ozone evolution in these two locations. The same conclusion is found for all stations located over land. For stations located at the coast, things can be quite different. Kollumerwaard is located at the northern coast of The Netherlands. As apparent in Figure 4.4, significant discrepancies are found between the two simulations. In fact, the grid cell where Kollumerwaard is located is considered by the EUROS model as a sea grid cell. During the day hours, the pollutant concentrations remain confined in a relatively shallow mixing layer, which probably explains the higher ozone peaks which are obtained when the land/sea distinction is taken into account. This example shows that results obtained for coast grid cells must be carefully interpreted.

4.4.3 Impact of the vertical discretisation used for the advection

Until now, all the simulations have been carried out with a ten-layer structure for the representation of the horizontal advection process. The heights of the ten levels were 50, 100, 200, 400, 600, 900, 1200, 1500, 2000 and 3000 m. The number of levels and the heights of these levels influence the re-distribution of the concentrations from the four-layer structure (SL, ML, RL and TP) to the multi-layer structure used for the advection. Therefore, it is useful to investigate how the results are sensitive to the vertical discretisation used for the advection. The vertical grid structures which have been tested are represented in table 1.

The period of simulation is august 1990. In all the simulations, the mixing layer is calculated from the surface meteo parameters with distinct procedure for land and sea. The top of the reservoir layer is fixed to 600m

The simulated ozone evolutions for Cabauw and Waldhof are presented in Figure 4.5. It is not apparent on the plot but the simulations 660 and 665 give exactly the same results (the black line is hidden behind the light blue line). The simulation 663 gives also almost identical results.

In the first four runs, the advection is calculated using 10 layers. It appears that the simulation 662 strongly differs from the three other simulations with ten layers. The only difference between the vertical discretisation in runs 662 and 663 is the height of the fifth level, which is respectively at 700 and 600m. In run 662, no level is located at the top of the reservoir layer, which is set at 600 m. It means that at each advection step, an artificial exchange between the reservoir layer and the top layer occurs through the redistribution procedure. This shortcoming does not occur when the reservoir layer has vanished due to the growth of the mixing layer. Nevertheless, during the night and the morning hours, the artificial exchange with the top layer causes a strong restoring toward the top layer background concentrations. During the night, the reservoir ozone concentrations are usually lower than the background concentrations. As a consequence, this spurious process results in the entrainment of ozone from the top layer into the reservoir layer. When the mixing layer starts growing in the morning, these concentrations are then entrained into the mixing layer. This explains why higher ozone concentrations are obtained when the top of the reservoir layer does not match one of the advection levels

Run :	660	661	662	663	664	665
# layers	10	10	10	10	15	15
3000						
2900						
2800						
2700						
2600						
2500						
2400						
2300						
2200						
2100						
2000						
1900						
1800						
1700						
1600						
1500						
1400						
1300						
1200						
1100						
1000						
900						
800						
700						
600						
500						
400						
300						
200						
100						
50						

Table 1: *Various vertical grid structures.*

In runs 664 and 665, the advection is calculated using 15 layers. In run 664, a fine resolution is used in the lower layers while in run 665, a more uniform distribution is used from the surface up to 3000 m. Note that in both cases, one of the advection levels is located at 600m. In run 665, the vertical levels up to 1200 m are exactly the same as in run 660. The results of run 660 and 665 are identical which means that it has no use to refine the resolution in the higher layers.

Another interesting feature is that the highest ozone peaks are obtained in runs 661 and 664. These two simulations are characterized by a very fine resolution in the lower layers. In run 664, a resolution of 100m is used up to 1200 m. Figure 4.3 clearly shows that using thinner advection layers lead to higher ozone peaks. This feature must be related to the re-distribution procedure between the multi-layer structure used for the advection and the four-layer structure used for the other processes. With thinner advection layers, the artificial exchange between the model layers due to this redistribution procedure is reduced. This is particularly important in the afternoon when the reservoir layer has vanished. Reducing the artificial exchange between the mixing layer and the top layer causes to attenuate the restoring toward the background concentrations. This results in an amplification of the ozone peaks.

The sensitivity experiments to the vertical resolution have shown that the effect of the redistribution procedure is not negligible. The comparison of simulations 628 and 629 allows to clearly identify the impact of this redistribution. In the two simulations, the MH is uniform over Europe and calculated using a climatological growth rate. In run 628, the advection is calculated using the four-layer vertical structure which is possible since the MH is uniform. In run 629, the 10-layer structure is used as in run 660. The only difference between the two simulations arises from the re-distribution procedure needed in run 629. The ozone time evolutions for Cabauw and Waldhof are shown in Figure 4.6.As expected, the ozone peaks are higher when the advection is computed with 10 layers. For the highest peaks, the difference between the two simulations can reach 40 μm^{-3} which clearly shows that the redistribution procedure significantly affects the simulated ozone evolution. It must be noted that the effect of the redistribution procedure is probably higher in the case of uniform MH since the same redistribution is applied to the whole domain.

As mentioned in section 4.3, an alternative solution to the redistribution procedure consists in approximating the mixing layer height by the nearest advection level. In this case, the redistribution procedure becomes unnecessary. Since the MH can not be estimated with great accuracy, this approach seems perfectly justified. Only preliminary tests have been carried out to evaluate this new approach and the results seem to be strongly dependent to the heights of the advection levels. Further investigation is needed to implement this method in the operational version of EUROS.

From all the simulations which have been presented in this section, two important conclusions can be drawn. First, it is crucial to use a vertical grid structure in which one of the advection levels is equal to the prescribed height of the reservoir layer. Secondly, a relatively fine resolution must be chosen in the lower part of the atmosphere (up to 1000 m) in order to limit the artificial exchanges between the mixed layer, the reservoir layer and the top layer due to the redistribution procedure. To limit the computing cost, the number of advection layers can not be too large. Using 15 layers instead of 10 layers causes the CPU to increase by a factor 1.16 (1 month simulation = 12h30 CPU with 10 layers and 14h30 CPU with 15 layers). A compromise must be find between accuracy and computing cost. Nevertheless, if the CPU time necessary to run the model with 15 layers is acceptable, it is recommended to use the vertical resolution of run 664.

4.4.4 Comparison with measurements

Up to now, we have carried out a wide variety of simulations in order to better understand the model behavior and its sensitivity to some parameters. We have

found that the prescribed value of the reservoir layer top has a strong impact on the simulation results since it implicitly controls the exchange between the top layer and the lower layers (reservoir layer and mixing layer). In other words, it controls the concentration exchanges between the boundary layer and the free troposphere.

On the other hand, we have seen that the redistribution procedure was responsible for artificial exchanges between the model layers. This spurious mechanism can be reduced by increasing the number of advection layers.

In this section, we compare the results obtained with various versions of the model with ozone measurements collected at some measuring stations over Europe. In particular, we will test the effect of the reservoir layer top and of the number of advection layers. The comparison concern the month august 1990. It must be stressed that this comparison with the measurements can not be considered as a model validation. This would need to run the model over a longer time period and to compare the results with a large number of station measurements. Nevertheless, this comparison study allows to get a first idea of the model performances and to propose some guidelines for the choice of the above-mentioned model parameters.

First we have compared the results of simulations 660 to 665 to measured ozone values. The results of these runs have been compared with the measurements in 13 stations. In Figure 4.7, we show the results of simulations 660 and 664 and the measurements as well, for Cabauw, Waldhof and Vredepeel (South of The Netherlands, near the Belgian border). The run 660 is the standard simulation including 10 layers for the representation of the advection. In run 664, 15 layers are used for the advection and the vertical grid is chosen so as to minimize the artificial exchange due to the redistribution procedure. The ozone peaks are higher in run 664 and for most stations, in better agreement with the measurements. It seems that a reduction of the artificial exchange between the model layers allows to improve the performances of the model. However, for many station, the ozone peaks in Augustus 1990 are still underestimated in run 664. This can be due to an overestimation of the exchanges with the top layer. To modify this exchange, we have carried out simulations with different reservoir layer heights, using the vertical discretisation of run 664. The results are illustrated in Figure 4.8. for three reservoir layer tops : 600m (run 664), 800m (run 667), and 900m (run 666). When the reservoir layer top is set to 900m, the exchanges with the top layer are extremely limited and the restoring to the background concentrations very low. In most stations, it leads to a significant overestimation of the ozone peaks. Better results are obtained with a reservoir layer top set to 800m. For many stations, the observed ozone peaks are relatively well reproduced by simulation 667. Nevertheless, in some stations like Waldhof (see Figure 4.8), the simulated peaks are higher than those observed.

The results presented here show that the vertical discretisation and the control of the restoring toward the background concentrations may significantly affect the ability of the model to reproduce the observed ozone episodes. A deeper analysis of these results must be performed but, based upon the present study, some conclusions can be already drawn. First, it is recommended to use more advection layers than the 10 layers used in our standard simulations. The 15-layer structure of run 664 seems quite appropriate to limit the artificial exchanges between the model layers. On the other hand, our results suggest that using a reservoir layer top at 600m causes to overestimate the concentration exchanges with the top layer. The use of another prescribed value of the reservoir layer top must be considered. An intermediate value between 600m and 800m seems more appropriate. Let us remind here that one of the advection levels must be equal to the prescribed top of the reservoir layer.

4.5 Chemistry: selection of relevant components and reactions

4.5.1 Definition of the problem

The atmosphere is a very complex chemical reactor, consisting of thousands of components with numerous chemical interactions. The chemical reactions between these components have some common features, namely:

- all reagents are at low pressure except for the normal atmospheric components like O_2, the order of magnitude for the others is within the ppb range
- most of the reactions are coupled, running from one parent to a series of daughters
- there is a large difference between the different components as far as the rate of the reaction is concerned, from very slow tot extreme fast leading to a very stiff system of differential equations (ODEs)
- there are different types for the initiation of the reactions:
    - thermal initiation
    - photolytic initiation leading to fast reacting components like radicals and charged fragments

The rate of the reaction between the different compounds in the atmosphere differs by several orders of magnitude. This leads to a very stiff system of ODEs. This means that special solvers are needed to solve the system. A detailed description can be found in the documentation of the Kinetic PreProcessor (KPP) (Damian-Iordache, 1996).

The system of ODEs takes a long time to be solved (about 80 % of the CPU time of an atmospheric model run). Therefore there is a strong need to limit the number of species and reactions describing the chemistry as much as possible in order to get a chemical meaningful solution.

4.5.2 Database

Definition

To calculate the solution of the chemical reactions running in the atmosphere, one needs kinetic data. There are several kinetic data bases, the most extensive is MCM2 (Master Chemical Mechanism v.2) from the University of Leeds, U.K. This one gives all the possible atmospheric reactions of several hundred compounds, leading to a few thousand reactions. Another one is CB4_99 (Carbon Bond mechanism v4_99) from the University of Carolina and developed by Zac Adelman. (http://airsite.unc.edu/soft/cb4/CB4main.html).

The rates of the reaction are given for the two types of initions, thermal and photolytic.

thermal reaction initiation:
the rate constant is defined by the Arrhenius law, which is of the following form

$$k = A.\exp\left(-\frac{Ea}{RT}\right)$$

where A is the frequency factor ([s^{-1}] for a first order reaction, [$l.mol^{-1}s^{-1}$] for a second order reaction, Ea is the activation energy [$kJ.mol^{-1}$] and T is the temperature [K]

photolytic reaction

the rate constant is given by:

$$Ja = \int_{\lambda_1}^{\lambda_2} \sigma_A(\lambda.T)\phi_A(\lambda.T)I(\lambda)d\lambda$$

in [$molecule.cm^{-3}.s^{-1}$]. The quantities σ_A, ϕ_A, and I are respectively the absorption cross-section [cm^2 $molecule^{-1}$], the quantum yield for photolysis, and the spectral actinic flux [$photons.cm^{-2}.s^{-1}.nm^{-1}$]

Use of the data bases

The use of the data bases consists in selecting the reaction mechanisms together with the rate constants for these components which are responsible for the O_3 production in the atmosphere. The huge number of compounds that enter the

atmosphere (biogenic as well as anthropogenic) leads to a large stiff system of ODEs. To keep the CPU time acceptable one has to select these compounds which are crucial for the O_3 formation. The methods to perform this selection are described hereafter.

4.5.3 Selection of compounds

4.5.3.1 Organic compounds

Organic compounds, as well as from biogenic as anthropogenic sources, can be divided in groups based on molecular structure and reactivity.

The following division is a general one:

- homologues series:
  These are compounds, which can be defined by a general bruto formula. The simplest homologues series are the n-alkanes which have the general formula:
  C_nH_{2n+2}
  Examples: methane (CH_4), ethane (C_2H_6)….
  Another series is formed by the alkenes: C_nH_{2n}
  Examples: ethene (C_2H_4), propene (C_3H_6)….

- functional groups:
  The reactivity of organic compounds is generaly defined by the functional groups residing on the molecules. These groups are responsible for the delocalisation of the electrons in the molecule. The effect is that some of the bonds in the molecule are weakened, while others become stronger.

  Examples of functional groups are:

°	alcohol:	OH	CH_3OH	methanol
°	carboxyl:	COOH	CH_3COOH	acetic acid
°	ether:	C-O-C	CH_3-O-CH_3	dimethylether
°	aldehyde:	CO	CH_2O	formaldehyde
°	amines:	NH_2	CH_3-NH_2	methyl amine

This summation is very limited, but gives a good idea of the possibilities of the functional groups to select compounds based on their reactivity.

4.5.3.2 *Methods to select organic compounds relevant to atmospheric chemistry*

Chemical bonds

The reaction database CB4_99 takes into account the similarity in reactivity of the carbon-carbon bonds within different groups of compounds. In general, a triple carbon-carbon bond is more reactive then a double bond and these more then a single bond. The kind of the functional groups and its position on the molecule are also taken into account. The parameters to perform a selection on this base are those from the Arrhenius equation (frequency factor and activation energy). This method is a very useful one.

QSAR methods

QSAR stands for Quantitative Structure Activity Relationship (Karcher and Devillers, 1990). The QSAR methods were originally developed to predict the pharmacological and/or the toxicological effects of existing drugs which were chemically changed. For the last decades the QSAR methods have been more and more used in environmental studies. (Environmental chemistry and toxicology) In this domain QSAR stands for Quantitative Similarity Activity Relationship. This means that compounds belonging to different chemical groups have the same environmental impact. Two QSAR methods which can be used in atmospheric chemistry are described hereafter.

b.1. Electron polarisation

The electron polarisation Pe is the possibility for the electrons in an atom, a group of atoms or a molecule to be delocalized by an electro-magnetic field. As mentioned before the effect is that some bonds become stronger while others become weaker. The Pe is defined by the molar refractivity and is given by following relationship:

$$Pe = \left(\frac{n^2 - 1}{n^2 + 1} . \frac{M}{\rho} \right) . \frac{3}{4} . \frac{1}{\pi . N}$$

where n is the refractive index, M the molecular mass, ρ the density and N the Avogadro number. Compounds with a similar Pe can be lumped in the atmospheric chemistry system or one of them can be selected as relevant for the whole group.

b.2. Connectivity index Chi

The connectivity indexes are derived from topological indices. These are the numerical expressions of the topology of a chemical compound. The most important feature is that the index is calculated on a sound chemical and mathematical basis.

There are extensively used in the quantitative description of the physical, chemical, biological and environmental properties of chemicals.

The information used to derive the indices is:

- the number and type of atoms in the molecule
- the type of the bonds between the atoms
- the number of valence and non-valence electrons.

A detailed treatment is beyond the scope of this study, but the method can easily be adapted to the atmospheric chemistry.

4.5.4 Conclusion

The most important reason to select a small number of compounds and reactions to simulate the chemistry of the atmosphere is to reduce the CPU to a reasonable value.

As a matter of fact one has to reduce the number of compounds and reactions, but one must select those which describe the chemistry in a sufficiently realistic way.

Different methods are available to do this:

- chemical structure

  homologous series

  functional groups

- electronic structure and QSAR

  electron polarisation

  connectivity indices

Once the compounds are selected the proces, the construction of the chemistry module can be performed.

4.6 Conclusions

A new version of the EUROS model has been developed in close collaboration with the RIVM. This new version includes a spatially variable mixing height. In the previous version, a uniform mixing layer was used over the whole Europe. This

improvement allows a better representation of the mixing height pattern over Europe. In particular, the representation of the land-sea contrast is now much more realistic.

The implementation of the variable mixing layer required the adaptation of the horizontal advection scheme. A multi-layer vertical grid structure has been implemented and tested. The number of the advection layers and the height of these layers can be easily modified. We recommend using a vertical structure with 15 layers and with a vertical resolution of 100m up to 1000m.

The new version of EUROS has been extensively tested and the simulated ozone concentrations have been compared with the observations. It has been found that the impact of the mixing layer height is much more limited than expected. In contrast, the simulation results are strongly sensitive to the prescribed height of the reservoir layer, which overlies the mixing layer. The height of the reservoir layer top controls the mass exchanges with the top layer and, as a consequence, the restoring toward the background concentrations. Our results suggest that the model tends to overestimate the mass exchanges with the top layer. A possible technique to reduce this mass exchange consists in slightly elevating the reservoir layer top. In the standard version of EUROS, the reservoir layer top is set to 600m. It could be considered to increase this value to 700m or 800m. A more fundamental solution to this problem consists in including a more explicit representation of the vertical exchanges between the atmospheric layers through advection and diffusion. In the current version of EUROS, only an explicit representation of the horizontal component of these processes is included. The three-dimensional grid structure that has been implemented in EUROS is a first step towards a fully three-dimensional representation of the advection and diffusion processes.

An important limitation factor in the extensive use of EUROS for policy support is the computing cost. The new version with a multi-layer advection scheme is slightly more expensive than the previous version (16 %). The chemical module strongly contributes to the computing time. Therefore, it is of crucial importance to reduce its complexity by limiting the number of components and reactions which are taken into account. A short review of the various methods allowing to select the relevant components and reactions have been made. The use of these methods to simplify the chemical module of EUROS could be the subject of further investigations.

4.7 Acknowledgements

The development work on the EUROS model has been carried out during a temporary staying of Laurent Delobbe at the Laboratorium voor Lucht Onderzoek of RIVM. Laurent Delobbe wish to thank Jan Matthijsen, Ferd Sauter, Liesbeth de Waal,

Wilco de Vries and all the members of the Laboratory for their hospitality, and the friendly and fruitful collaboration. We also thank Hans Bergwerff and Daan Swart for supplying us with the LIDAR data from RIVM.

4.8 References

Barrett, K., and Berge, E (editors), 1996: Transboundary Air Pollution in Europe, Part 1: Estimated dispersion of acidifying agents and of near surface ozone, EMEP MSC-W Status Report, 1996.

Beljaars, A.C.M., and Holtslag, A.A.M., 1990. A software library for the calculation of surface fluxes over land sea. Environmental software, 5, 60-68.

Businger, J.A., 1973 : Turbulent transfer in the atmospheric surface layer. Workshop on Micrometeorology, Amer. Meteorol. Soc., 67-100.

Damian – Iordache, V: 1996. KPP – Chemistry Simulation Development Environment. The University of Iowa.

Deardorff, J.W., 1978 : Efficient prediction of ground surface temperature and moisture, with inclusion of a layer of vegetation. J. Geophys. Research, 83, 1889-1903.

Delobbe, L., C. Mensink, O. Brasseur. G. Schayes, and A. Melikechi, 2000. Implementation of meteorological data in EUROS. Scientific report 2000/TAP/R/001, VITO, Mol.

Duynkerke, P.G., 1988 : Application of the E-e turbulence closure model to the neutral and stable atmospheric boundary layer. J. Atmos. Sci. 45, 865-880.

Holtslag, A.A.M., and van Westrhenen, R.M., 1989. Diagnostic derivation of boundary layer parameters from the outputs of atmospheric models. Sci. Rep. KNMI WR 89-04.

Karcher W. and J. Devillers, 1990. Practical Applications of Quantitative Structure-Activity Relationships (QSAR) in Environmental Chemistry and Toxicology. Kluwer Academic Publishers, 1990.

Loon, M. van, 1996 : Numerical methods in smog prediction, PhD thesis, University of Amsterdam.

Mensink, C and L. Janssen, 2000. A dynamic emission inventory for the EUROS model. Scientific report , VITO, Mol.

Nieuwstadt, F.T.M., 1981. The nocturnal boundary layer : theory and experiments. Sc. Rep. KNMI, WR 81-1.

Nieuwstadt, F.T.M., 1981. The steady-state height and resistance laws of the nocturnal boundary-layer : Theory compared with Cabauw observations. Boundary-Layer Meteorology, 20, 3-17.

Seibert, P., Beyrich, F., Gryning, S.-E., Joffre, S., Rasmussen, A., and Tercier, P., 2000. Review and intercomparison of operational methods for the determination of the mixing height. Atmospheric Environment, 34, 1001-1027.

Shea, D.J., K.E. Trenberth, and R. W. Reynolds, 1990: A global monthly sea surface temperature climatology. Technical note NCAR/TN 345+STR, NCAR, Boulder, 167_pp.

Shea, D.J., K.E. Trenberth, and R. W. Reynolds, 1992: A global monthly sea surface temperature climatology. J. Climate, 5, 987-1001.

Simpson, D., Anderson-Sköld, Y., and Jenkin, M.E., 1993 : Updating the chemical scheme for the EMEP MSC-W oxidant model: current status. Technical Report note 2/93, EMEP MSC-West, Oslo, Norway.

Sorensen, J.H., and Rasmussen, A., 1997: Method for calculation of atmospheric boundary-layer height used in ETEX dispersion modeling. Proceedings of the Sixth Topical Meeting on Emergency Preparedness and Response, San Francisco, California, April 22-25, 1997, pp. 503-506.

Sorensen, J.H., Rasmussen, A., and Svensmark, H., 1997: Forecast of the atmospheric boundary-layer height utilized for ETEX real-time dispersion modeling. Physics and Chemistry of the Earth.

Stull, R.B., 1988: An introduction to boundary layer meteorology. Kluwer Academic Publishers, Dordrecht, 666 pp.

Troen, and Mahrt, 1986: A simple model of the atmospheric boundary layer. Boundary-Layer Meteorology, 37, 129-148.

Van der Auwera, L., 1992: Inversion and mixing heights calculated from radiosonde profiles taken between 1968 and 1991. IRM internal publication, Misellanea serie B, n° 66.

van Pul, W.A.J., Holtslag, A.A.M., Swart, D.P.J., 1994. A comparison of ABL-heights inferred routinely from lidar and radiosonde at noon time. Boundary-Layer Meteorology, 68, 173-191.

Vogelezang, D.H.P., and Holtslag, A.A.M., 1996: Evaluation and model impacts of alternative boundary-layer heights. Boundary-Layer Meteorology, 81, 245-269.

4.9 Figures

Figure 2.1: Mixing layer depth at 04 UT for July 30, 1990. Spatially variable mixing height. No land-sea distinction in the calculation procedure.

Figure 2.2: Mixing layer depth at 04 UT for July 30, 1990. Spatially variable mixing height with land-sea distinction.

Figure 2.3: Mixing layer depth at 04 UT for July 30, 1990. Spatially variable mixing height. but no land-sea distinction in the calculation procedure.

Figure 2.4: Mixing layer depth at 04 UT for July 30, 1990. Spatially variable mixing height with land-sea distinction.

Figure 2.5: Comparison of the mixing layer height estimated by the EUROS model and derived from LIDAR observations at RIVM.

Figure 2.6: Mean values and most frequent values of the mixing layer height at Bilthoven averaged over August 1994, as estimated by the EUROS model and derived from the LIDAR measurements at RIVM.

Figure 2.7: Mixing height diurnal cycle. Climatology for August as derived from LIDAR measurements at Bilthoven. From Hans Bergwerff and Daan Swart (RIVM).

Figure 4.1: Ground level ozone evolution as simulated by EUROS with a uniform mixing height over Europe, and with a spatially variable mixing height. No land/sea distinction is included. The reservoir layer top is set to 600m.

Figure 4.2: Impact of the reservoir layer top on the ozone evolution as simulated by EUROS. The mixing height is spatially variable No land/sea distinction for the calculation of the mixing height.

Figure 4.3: Impact of the reservoir layer top on the simulated ozone concentrations. A uniform mixing height is used in all simulations.

Figure 4.4: Ozone evolution as simulated by EUROS. Impact of the land/sea distinction in the calculation of the mixing height.

Figure 4.5: Euros simulations with various vertical discretisations for the calculation of the advection. The various discretisations are described in table 1 of section 4.3.

Figure 4.6: Ozone evolution simulated by EUROS using 4 layers for the advection and using 10 layers for the advection. The MH is uniform over the whole domain.

Figure 4.7: comparison between EUROS simulation results (run 660 and 664) and measurements.

Figure 4.8: comparison between EUROS simulations (runs 664, 666, and 667) and measurements.

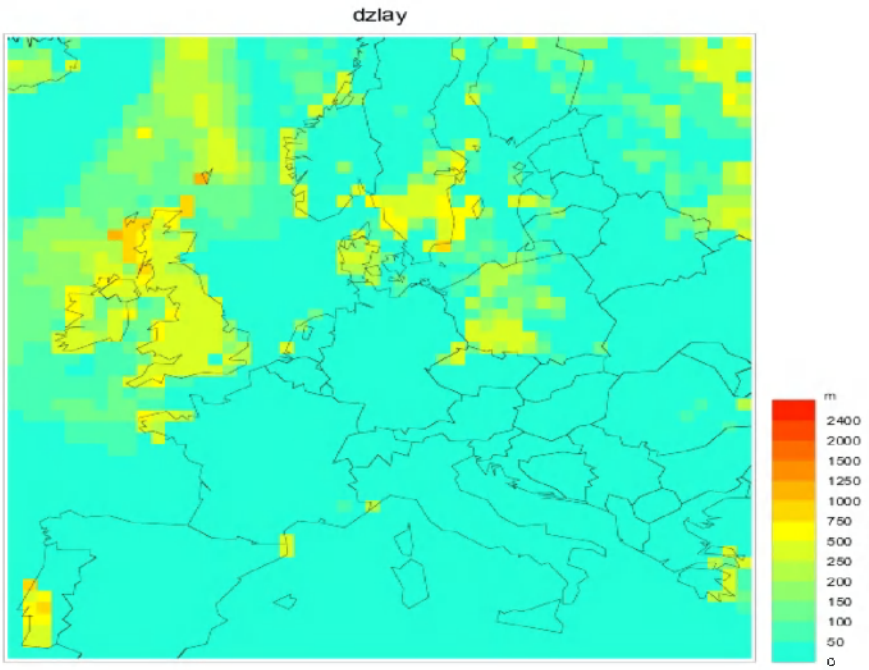

Figure 2.1: *Mixing layer depth at 04 UT for July 30, 1990. Spatially variable mixing height. No land-sea distinction in the calculation procedure.*

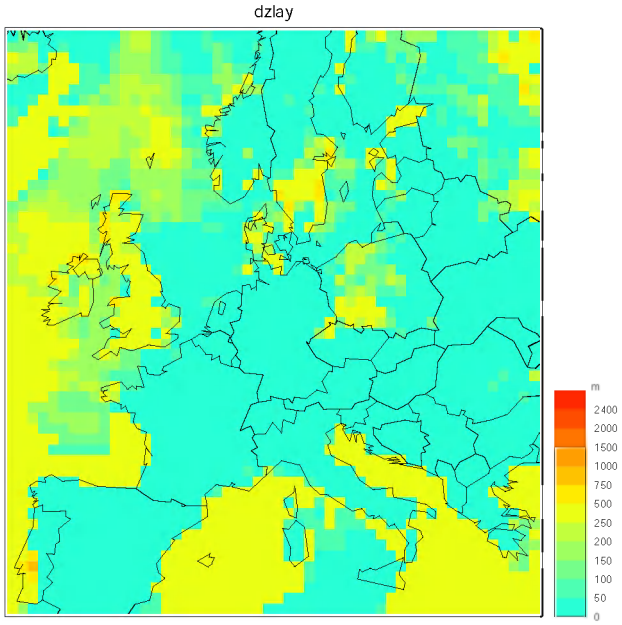

Figure 2.2: *Mixing layer depth at 04 UT for July 30, 1990. Spatially variable mixing height with land-sea distinction.*

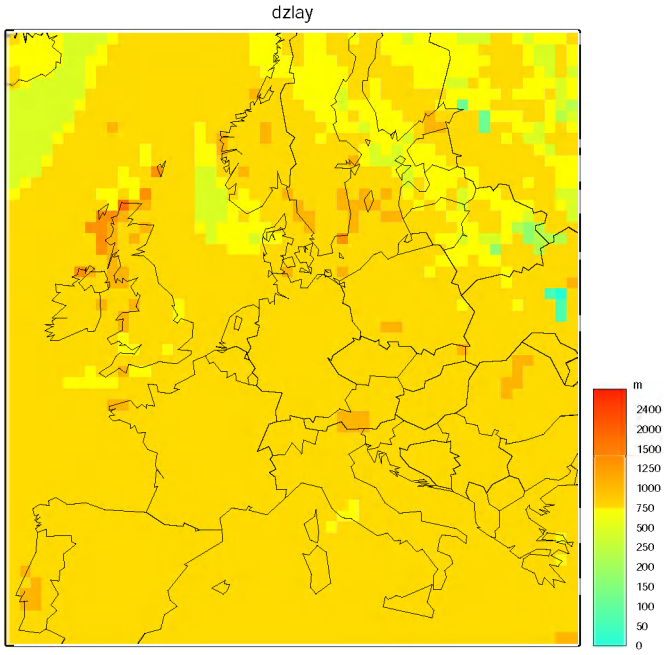

Figure 2.3: *Mixing layer depth at 16 UT for July 30, 1990. Spatially variable mixing height. but no land-sea distinction in the calculation procedure.*

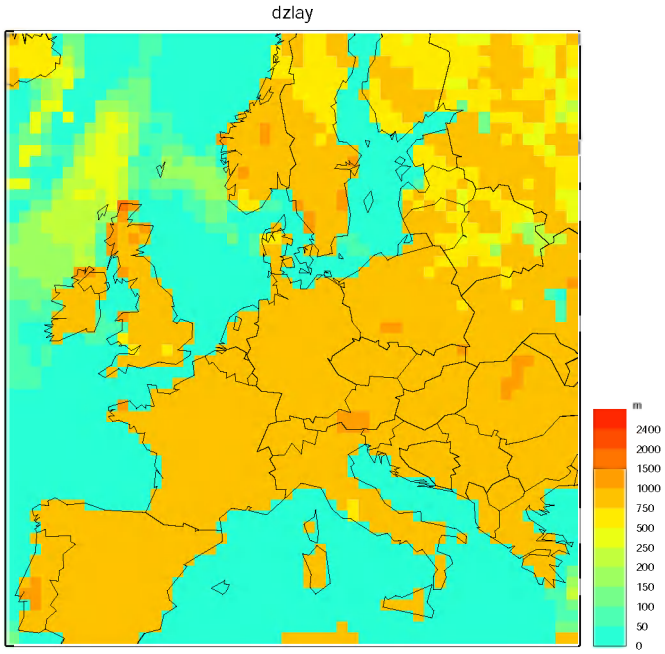

Figure 2.4: *Mixing layer depth at 16 UT for July 30, 1990. Spatially variable mixing height with land-sea distinction.*

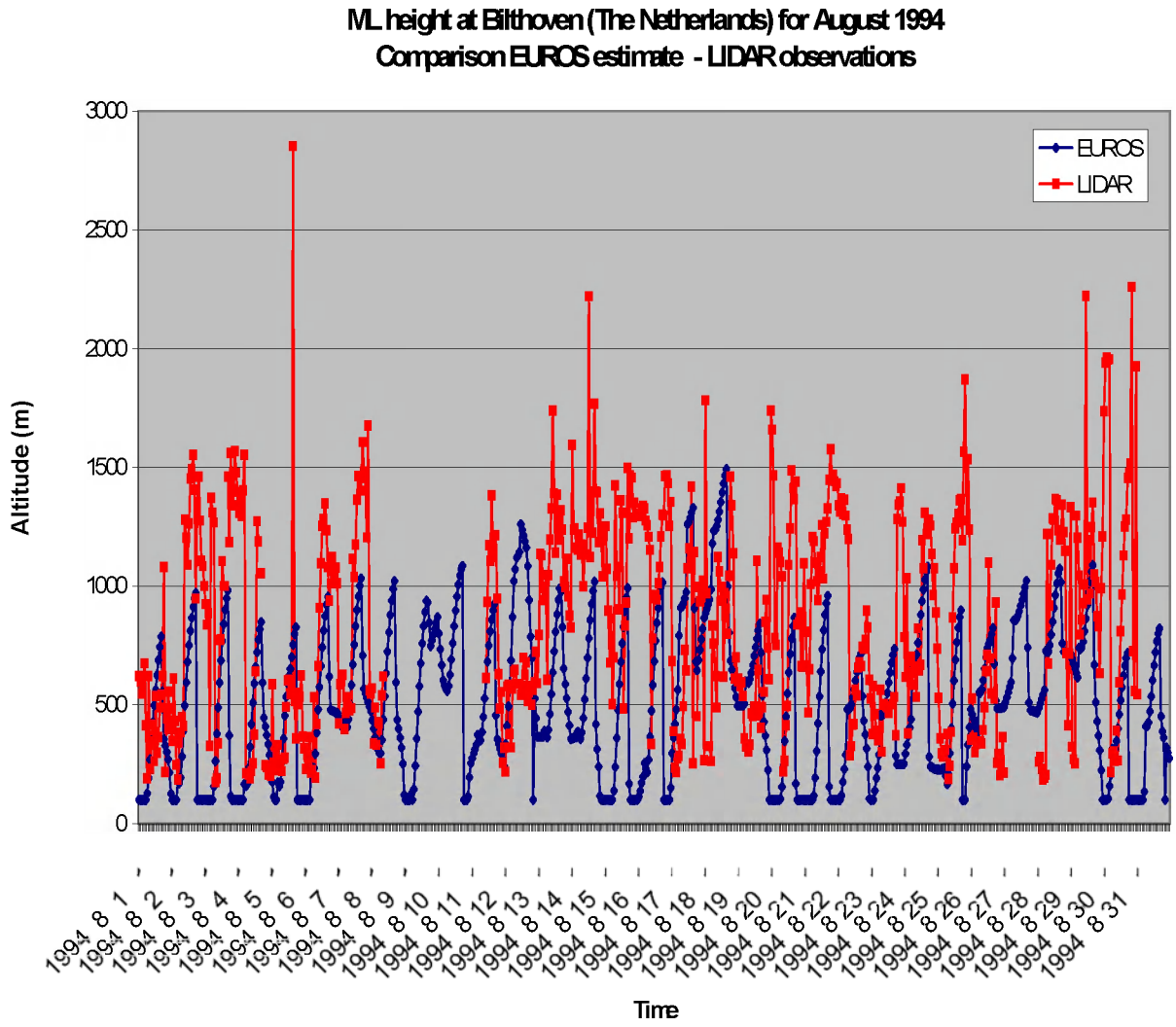

Figure 2.5: *Comparison of the mixing layer height estimated by the EUROS model and derived from LIDAR observations at RIVM.*

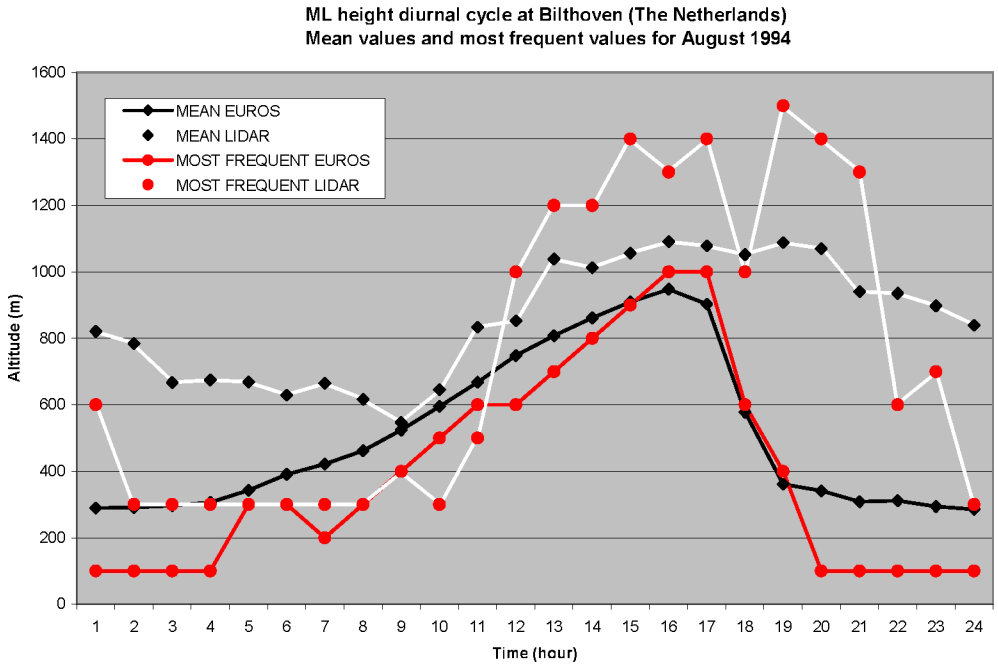

Figure 2.6: *Mean values and most frequent values of the mixing layer height at Bilthoven averaged over August 1994, as estimated by the EUROS model and derived from the LIDAR measurements at RIVM.*

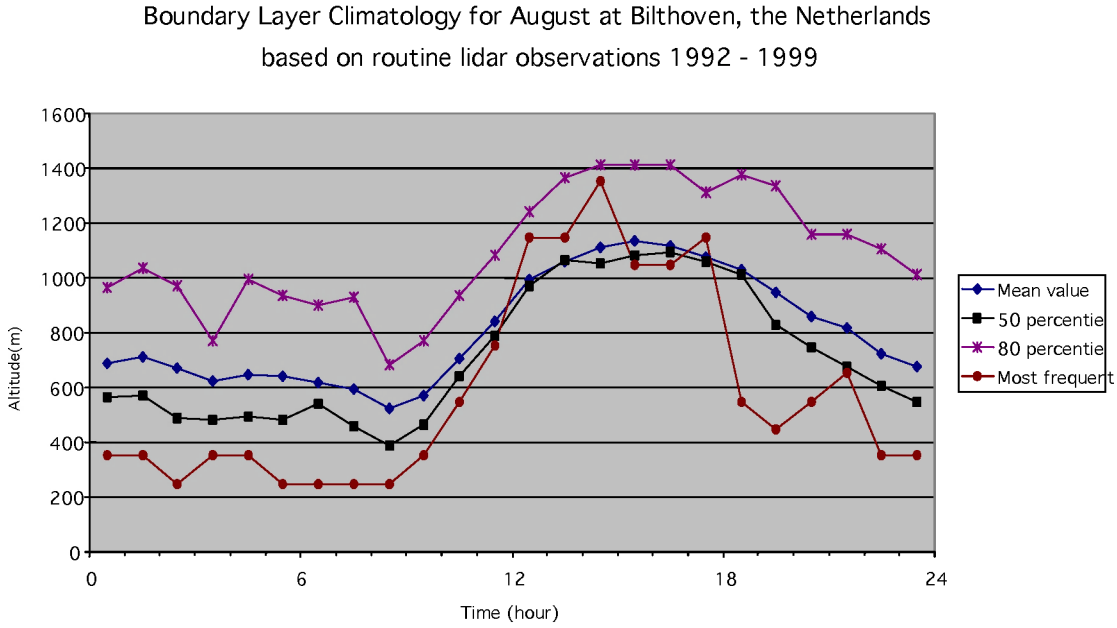

Figure 2.7: *Mixing height diurnal cycle. Climatology for August as derived from LIDAR measurements at Bilthoven. From Hans Bergwerff and Daan Swart (RIVM).*

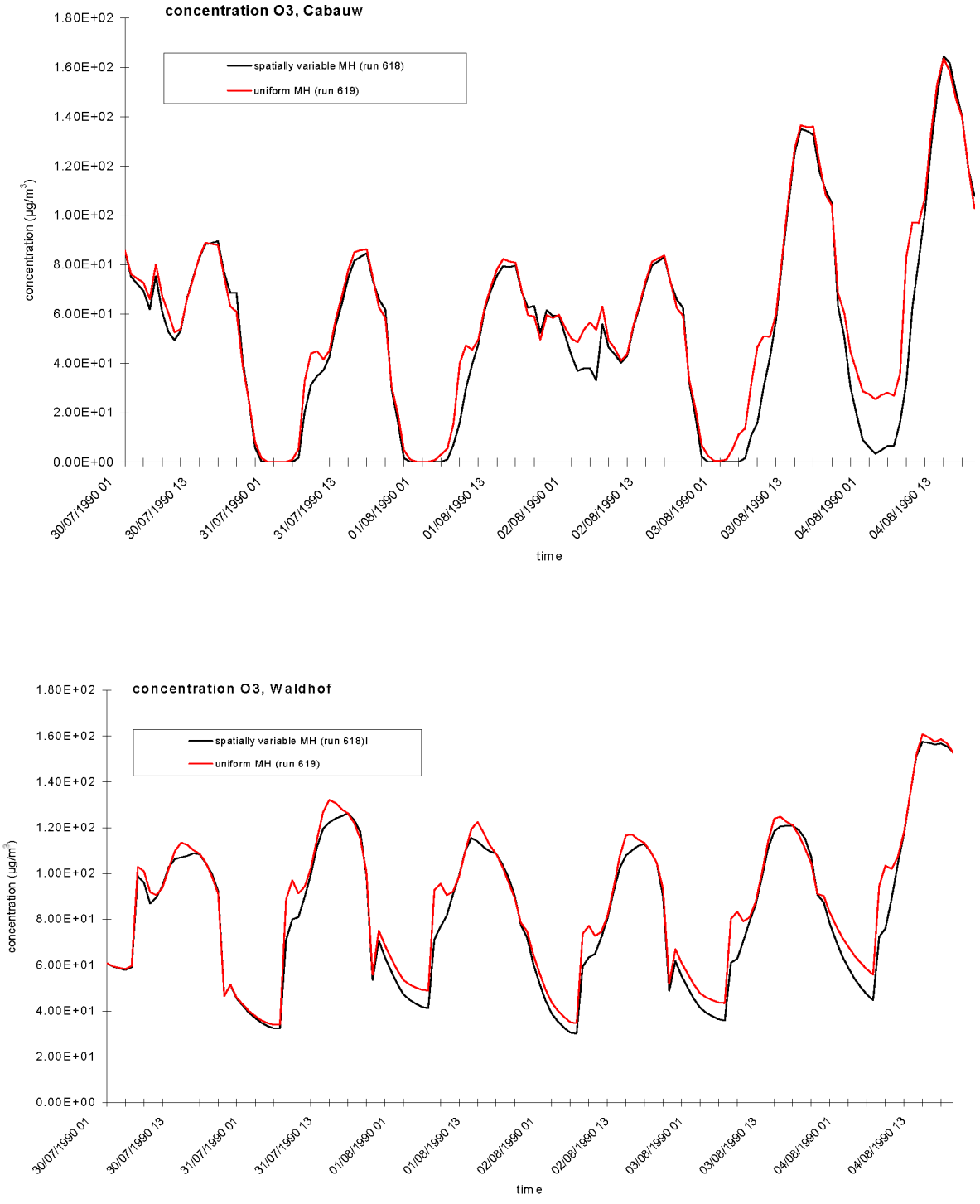

Figure 4.1: *Ground level ozone evolution as simulated by EUROS with a uniform mixing height over Europe, and with a spatially variable mixing height. No land/sea distinction is included. The reservoir layer top is set to 600m.*

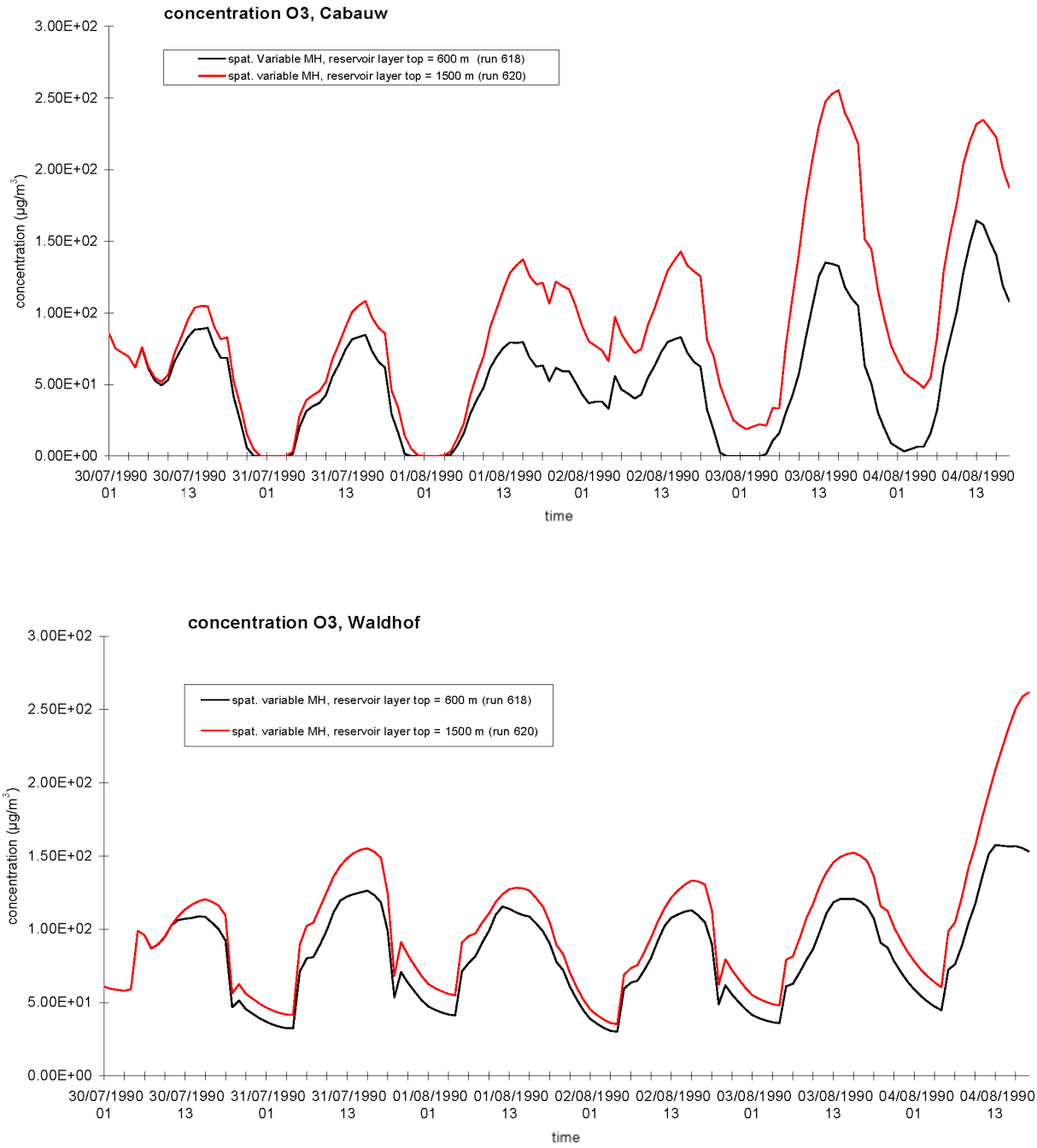

Figure 4.2: *Impact of the reservoir layer top on the ozone evolution as simulated by EUROS. The mixing height is spatially variable No land/sea distinction for the calculation of the mixing height.*

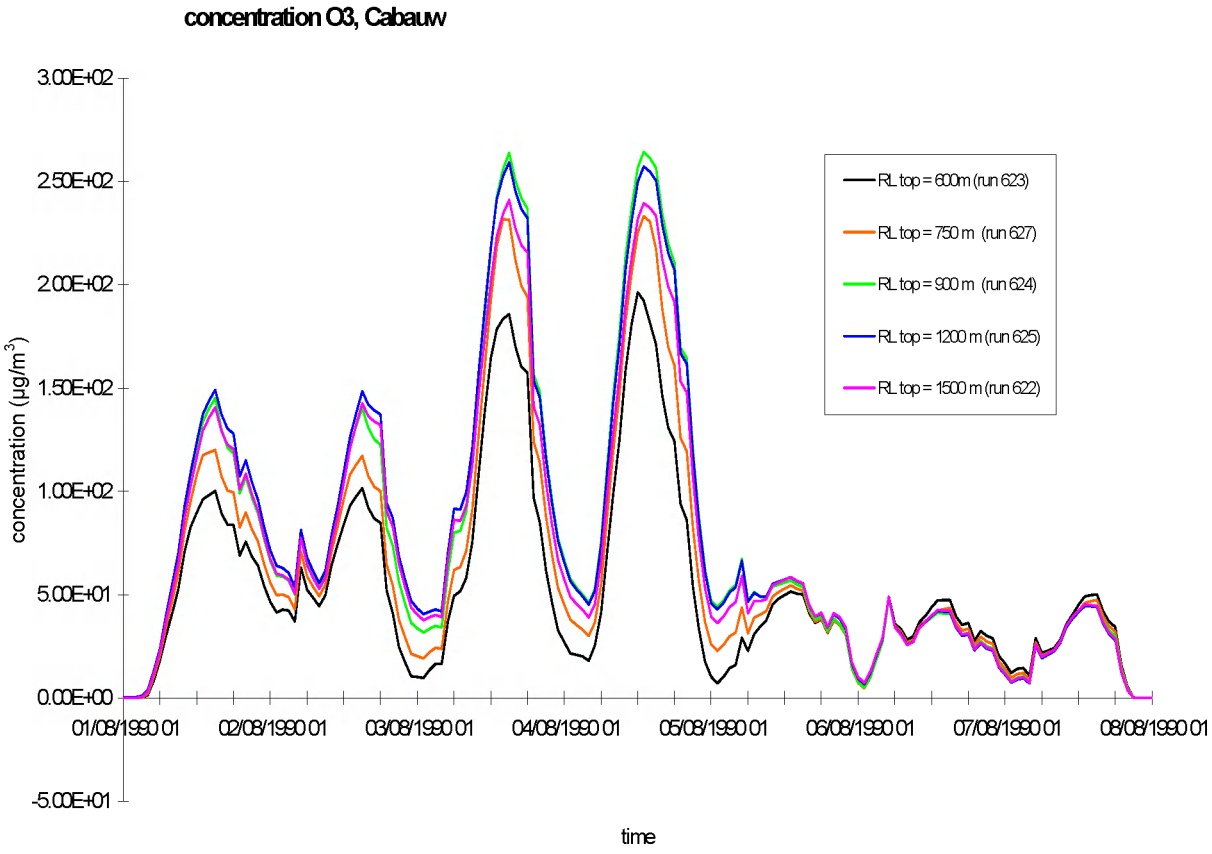

Figure 4.3: *Impact of the reservoir layer top on the simulated ozone concentrations. A uniform mixing height is used in all simulations.*

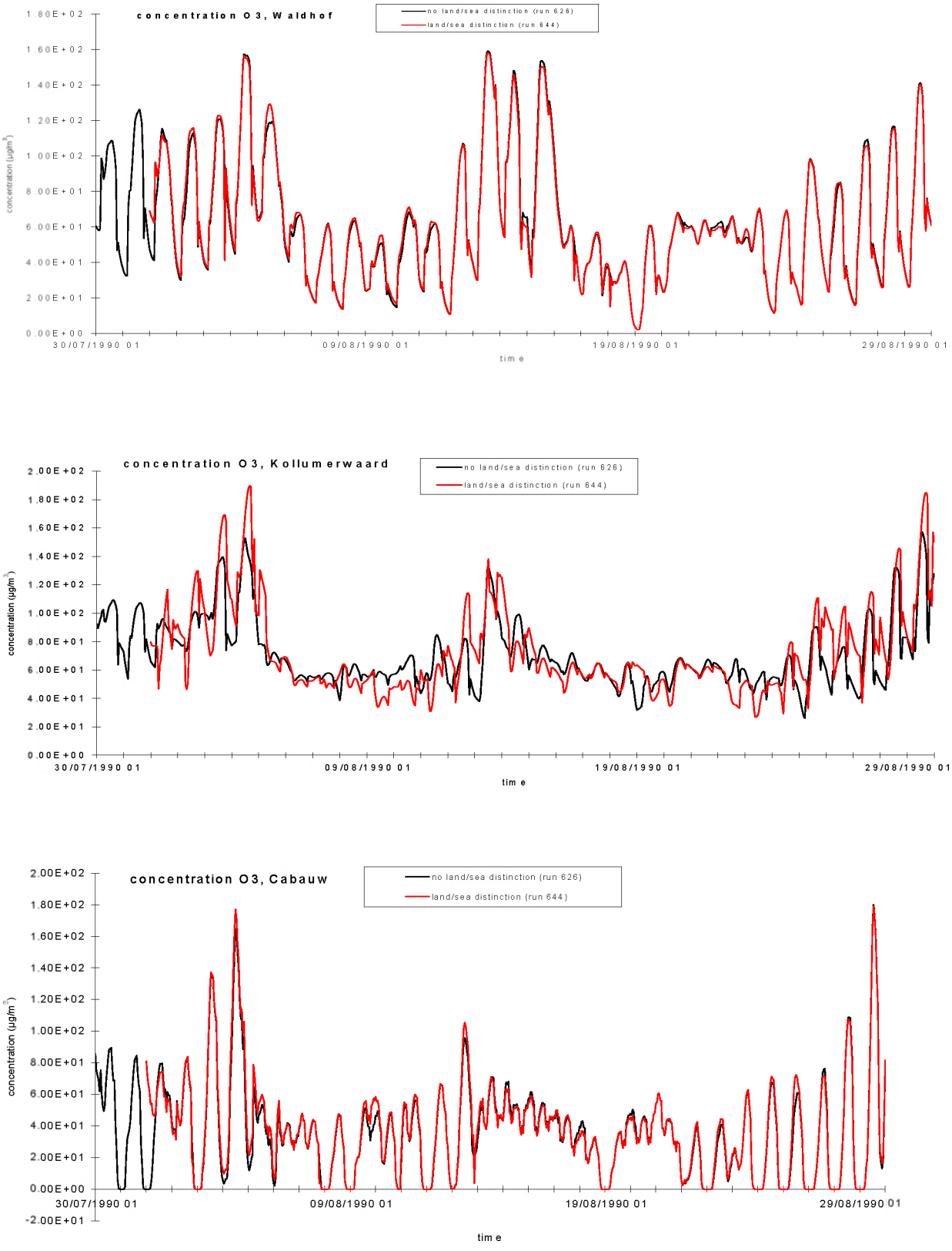

Figure 4.4: *Ozone evolution as simulated by EUROS. Impact of the land/sea distinction in the calculation of the mixing height.*

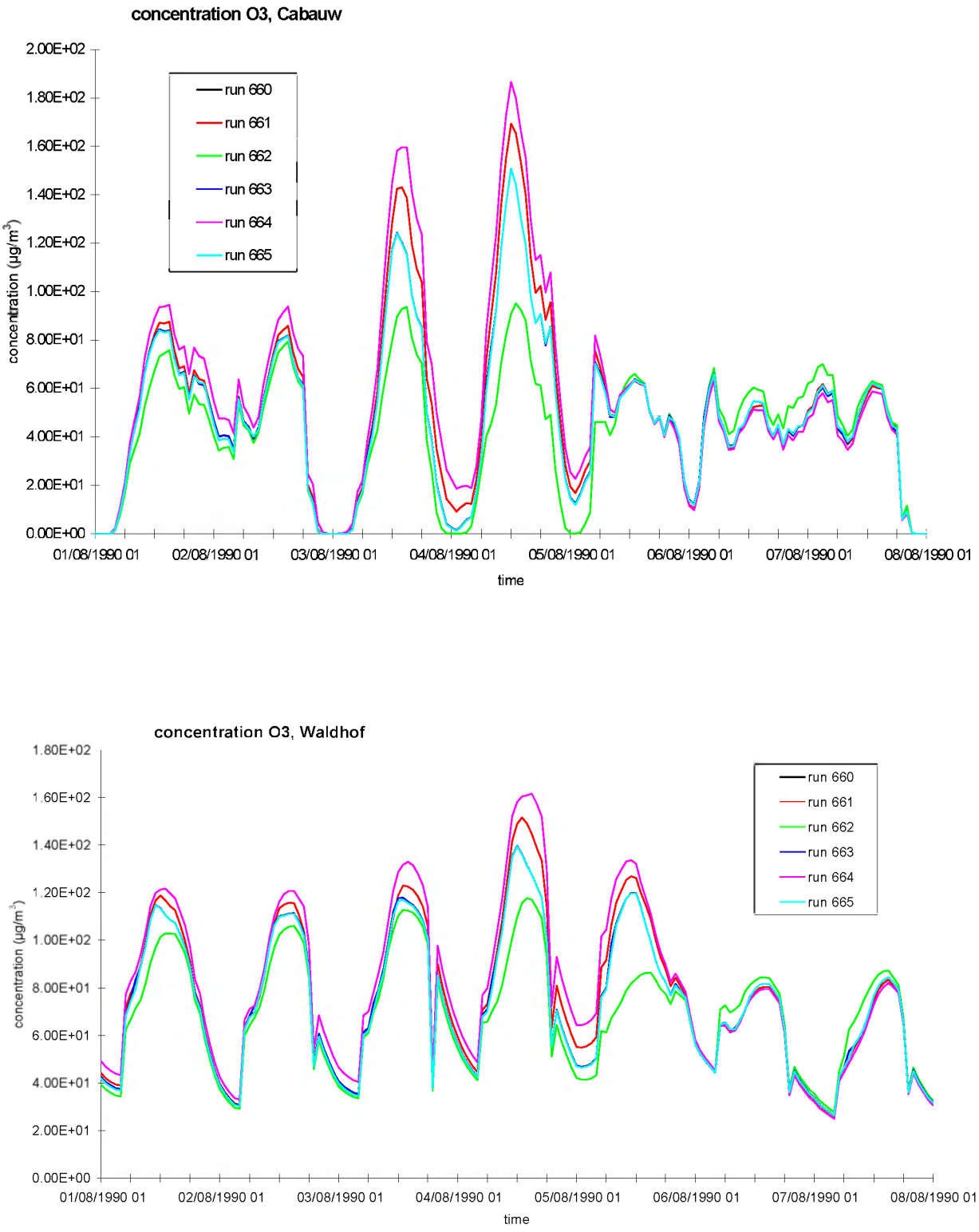

Figure 4.5: *Euros simulations with various vertical discretisations for the calculation of the advection. The various discretisations are described in table 1 of section 4.3.*

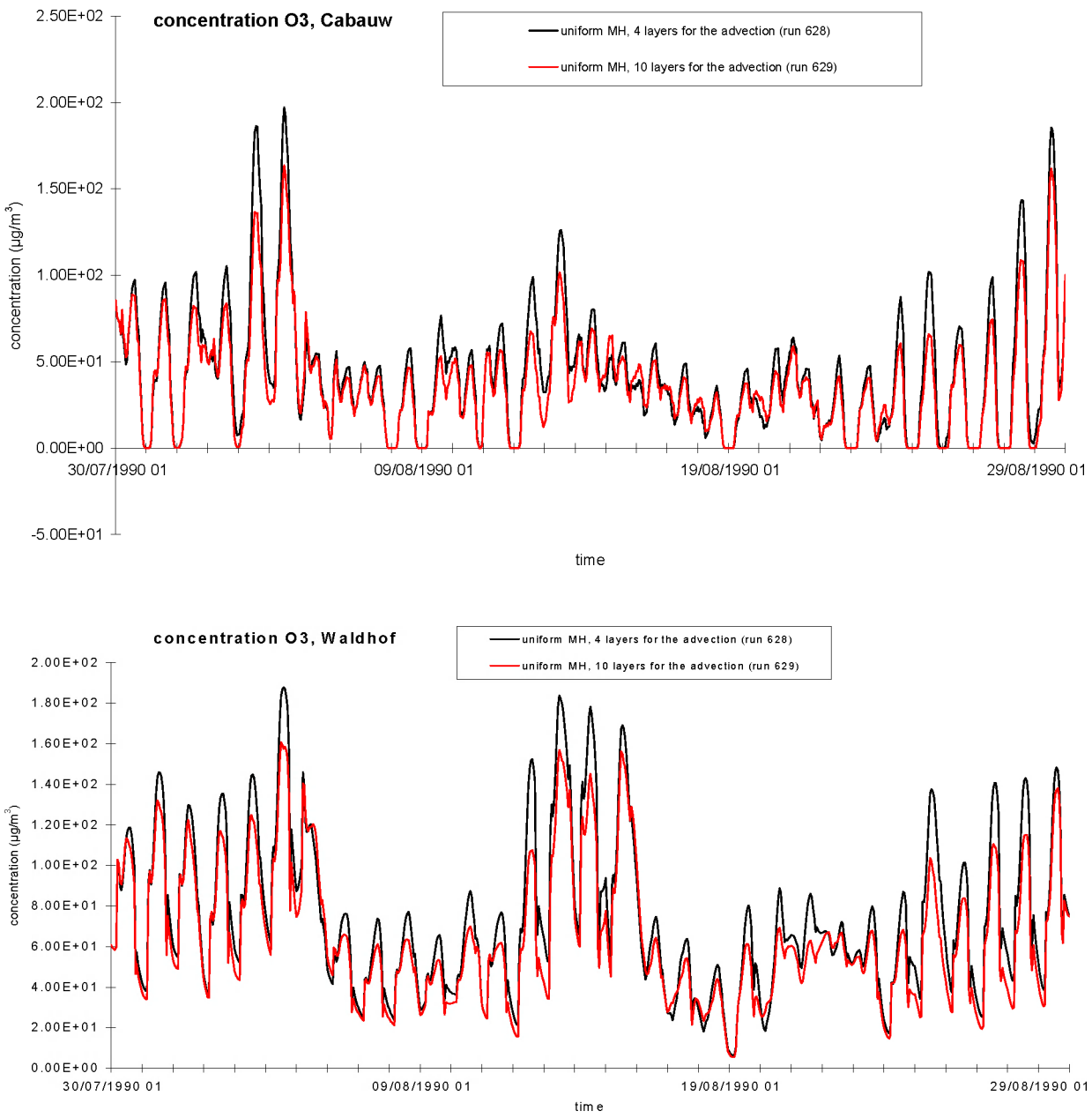

Figure 4.6: *Ozone evolution simulated by EUROS using 4 layers for the advection and using 10 layers for the advection. The MH is uniform over the whole domain.*

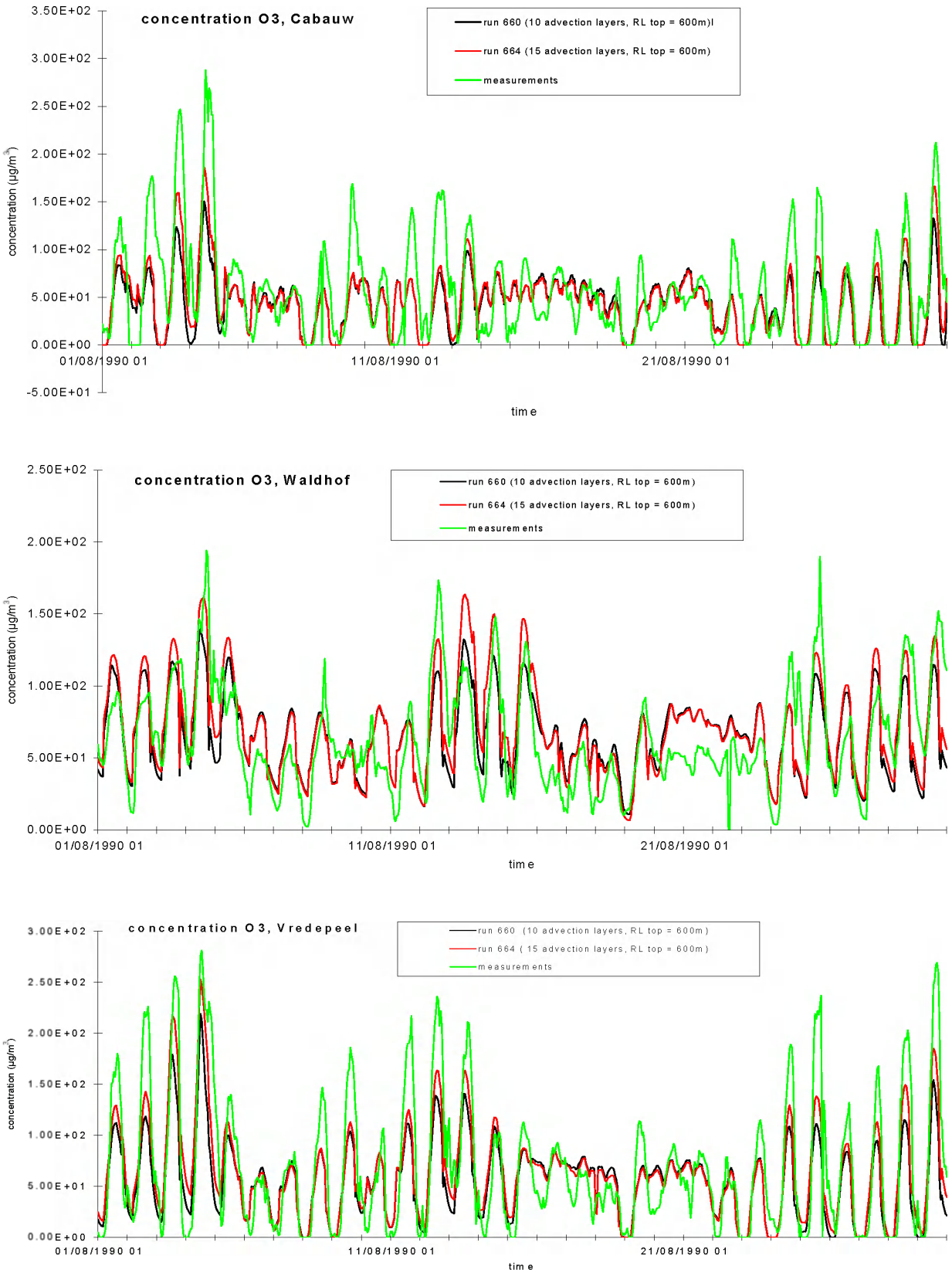

Figure 4.7: *Comparison between EUROS simulation results (run 660 and 664) and measurements.*

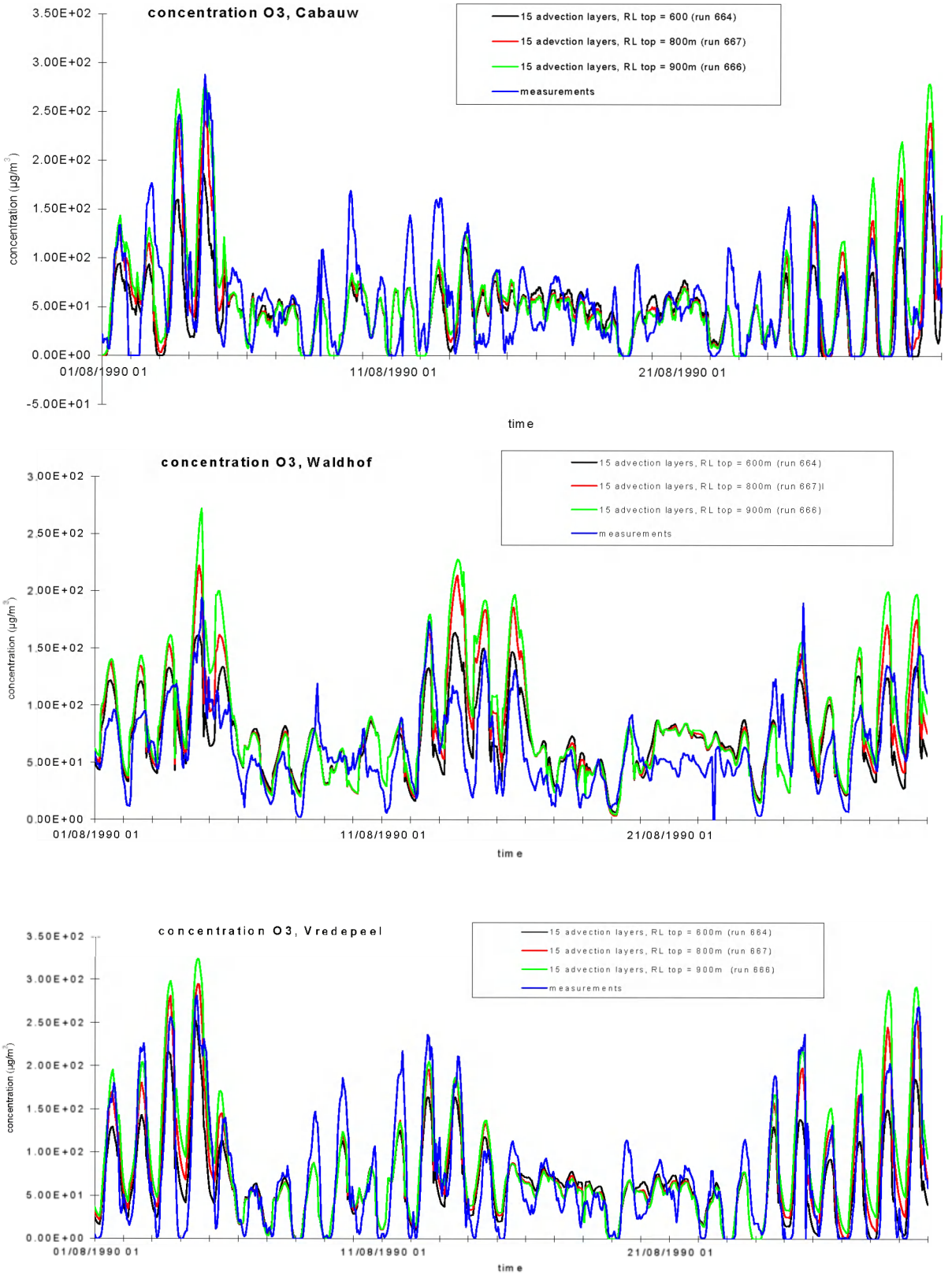

Figure 4.8: *Comparison between EUROS simulations (runs 664, 666, and 667) and measurements.*

5. USER INTERFACE [4]

SUMMARY

The first activity and longest is relative to the development of a data file for the EUROS model taking in detail the components of the simulation wanted by the user. The analysis and the modification of these components must remain in the domain of conviviality. The second activity requires an adaptation of the model EUROS, developed in FORTRAN in an environment UNIX, to the Windows environment on material of PC type. The third activity consists in giving the accessibility to the model and to its environment via a «network». It must allow a distant user to analyse the data, to ask for the execution of the simulation and to get to assure the legible returned result return through him «network».

In the present computer context the object-oriented programming imposes itself as the only solution to create a user-friendly interface. The flexibility and power of such a language allowed to solve a very big number of difficulties. The generalised usage of the Windows platforms and the significant growth of their power (CPU velocity and capacity memory) made that the retained programming language was Visual C++ of Microsoft. The complete project is constructed in Visual C++ except the EUROS model that has only been adapted to “run” under NT.

The result is simple and powerful. The software has been designed typically like a product «Windows», as Excel, Word,… It forms a complete set that allows all authorised user to access the system and to carry out specific impact studies. The simplicity results from the usage of dialog windows. The power comes from the object-oriented programming and the facility that Visual C++ offers to integrate Internet and the communication network.

The software presents another important quality: its flexibility. In the setting of the specifications and in the running time of the project, all demands were more than achieved. Besides, the software can be adapted in the future to new data processing contained in the general files of the EUROS model or in the results of the model. The object programming allows a dynamics and a globality that cannot be met with the classical approaches (FORTRAN, C).

The nature of the software makes that it is transportable on all computer of PC type of the last generation. The access to big files, the data visualisation, the windows administration and the new file construction requires a sufficiently powerful processor to perform these tasks.

[4] This chapter is taken from the following intermediary report: Passelecq C, Demuth C and Passelecq

5.1 Introduction

Dans la couche limite atmosphérique, l'ozone (O_3) se crée et s'élimine en suivant le cycle solaire pour autant que le milieu atmosphérique soit chargé en oxydes d'azotes (NO_x) et en composants organiques volatils (COV). Des interactions complexes entre ces composants chimiques interviennent en période estivale. La dynamique atmosphérique est une composante essentielle dans le phénomène de dispersion de l'ozone et des composants associés. La prévision spatiale et temporelle de toute cette chimie atmosphérique nécessite de recourir à un modèle mathématique adéquat.

Plusieurs modélisations sont possibles pour décrire la complexité des interactions physiques et chimiques existant entre les composants chimiques et le milieu atmosphérique. Le modèle de dispersion EUROS (**EUR**opean **O**perational **S**mog model) développé par le RIVM (**R**ijks**I**nstituut voor **V**olksgezondheid en **M**ilieu) constitue une voie médiane entre les modèles simples et complexes. Ce modèle, de type déterministe avec des réactions chimiques, a été implanté sous forme d'un logiciel appelé « Euros v... ». Il s'agit d'un programme écrit en FORTRAN 77/90 qui gère l'ensemble des calculs de la dispersion de plusieurs composants chimiques à partir de fichiers décrivant les émissions, les paramètres de surface et la météorologie. Les grandeurs météorologiques, non calculées par ce modèle, proviennent des analyses d'un modèle global de prévision du temps. En sortie, le modèle EUROS génère des fichiers qui contiennent, entre autres, des champs de concentration et des évolutions temporelles localisées.

L'utilisation du logiciel EUROS sans interface spécifique est difficile tant en ce qui concerne les entrées que les sorties. Toute nouvelle simulation passe par l'adaptation d'une liste d'instructions codifiées et l'adaptation des fichiers d'entrée. Des programmes particuliers « non intégrés » peuvent gérer les résultats. Le but de ce travail est d'unifier ces diverses actions en vue de les rendre conviviales. Pour ce faire, une interface utilisateur de type « Windows » a été construite sur base d'une programmation orientée objet autour du modèle « EUROS ». Cette interface permet à l'utilisateur, dans un environnement **unique**, d'effectuer toutes les tâches possibles depuis la création de scénarios à imposer au modèle jusqu'à la visualisation et la mise en forme des résultats du calcul.

Ce chapitre donne à l'utilisateur, en recherche de moyens pour des études d'incidence, une description des actions à effectuer pour gérer le modèle EUROS par l'intermédiaire de l'interface utilisateur. Il est divisé en trois sections. Les deux premieres portent respectivement sur l'acquisition du logiciel d'interface et sur la

---

D, 2001. BelEUROS project: EUROS Interface, Faculté Polytechnique de Mons, 2001.

description des fonctionnalités affichées dans une série de fenêtres accessibles à partir d'une barre de menu. La troisième décrit les phases fondamentales d'une simulation à savoir l'analyse, le calcul et l'exploitation.

5.2 Procédure d'acquisition du logiciel

Le modèle EUROS, implanté à la cellule CELINE, est géré à l'aide d'un logiciel « interface utilisateur ». Conçue pour effectuer toutes les opérations de visualisation des données d'entrée et de sortie, cette interface permet de piloter le modèle à partir de fichiers que l'on peut adapter pour effectuer toute simulation jugée utile en cas d'étude de scénarios particuliers d'émissions. Ce logiciel peut être acquis, à partir du serveur, par Internet au moyen du protocole FTP et sous réserve de la connaissance de clefs d'accès. En effet, la mise à disposition du modèle repose sur une demande préalable d'autorisation à faire par chaque utilisateur auprès de la direction de la cellule CELINE.

Deux phases importantes doivent être envisagées pour accéder à toutes les opérations relatives à la gestion du modèle EUROS. La première, dite d'acquisition de l'interface, permet le transfert des outils de gestion du serveur vers le client ou l'utilisateur. La seconde phase revient à « remplir » les répertoires créés lors de la phase initiale avec des fichiers de base nécessaires pour toutes les visualisations.

a) Phase d'acquisition de l'interface utilisateur

Les étapes à faire se suivent de la manière suivante :

- Effectuer la connexion (ftp://193.190.211.63/ALL/) ?…… ?
- Activer **« InstallEuros2.exe »** dont la réponse consiste en une fenêtre dénommée « *Téléchargement de fichier* » présentant deux options : exécuter et enregistrer.
- Choisir l'option **« exécuter »** et activer ensuite le bouton « **OK** » lequel fait apparaître la fenêtre « *Avertissement de sécurité* ».
- L'activation du bouton « **OK** » ouvre une nouvelle fenêtre « *InstallEuros* » qui indique les fichiers à transférer strictement nécessaires à l'utilisation de l'interface.
- Dans cette fenêtre « *InstallEuros* », activer le bouton « **Start install** ». Une sous fenêtre « *Institute* » se présente et demande l'introduction du nom de l'institution délivrée lors de l'acceptation de l'exploitation du modèle EUROS. Dans cette présentation, c'est « Irceline ». Cette donnée permet de créer sur le disque « C » de l'ordinateur du client un répertoire « Institute » à partir duquel une arborescence va se développer pour recevoir tous les fichiers.

- Revenir dans la fenêtre « *InstallEuros* » et activer le bouton « **Continue** ». La fenêtre « *InstallEuros* » liste la création de l'environnement ainsi que les fichiers utiles au dernier fichier dénommé « model.exe », l'exécutable de l'interface d'interrogation de l'environnement relatif au modèle EUROS.
- Terminer cette phase de transfert en activant « **Quit** ». La suite de la procédure demande de se rendre dans le répertoire utilisateur « C:\(Institute)\ » et d'y activer « model.exe » et éventuellement de créer un raccourci « bureau » pour ce programme.

A la fin de cette procédure, quatre sous-répertoires doivent avoir été créés dans « Institute » :

« meteoecmwf » : répertoire de tous les fichiers météorologiques

« NewInput » répertoire générique comprenant

« inpalg »: répertoire de fichiers statiques

« inpsmog »: répertoires de fichiers dont certains sont modifiables

« OUTfiles » : répertoire des fichiers de type « calcul » créés par le modèle EUROS.

« wmf » : répertoire des fichiers avec une extension « wmf » relatifs aux images sauvées.

b) Phase de « remplissage »

A ce stade il est nécessaire de lancer l'exécutable « model.exe » et de se rendre à l'intitulé « **Internet** » de la barre de menu de l'interface. Son activation fait apparaître un menu déroulant dans lequel les trois options commençant par **« FTP Get….. »** sont à considérer successivement.

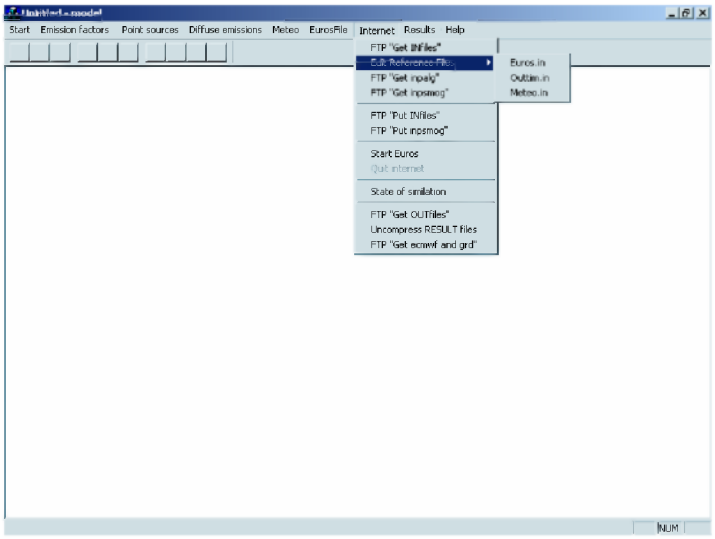

***Figure 1**: Ligne de menu « **Edit Reference Files** » de l'option « **Internet** » et son sous menu.*

1) L'action **« FTP GetINfiles »** transfère, du serveur à l'utilisateur, les trois fichiers modèles « euros46.in », « outtim.in » et « meteo.in » éditables par l'action **«Edit Reference Files »**.

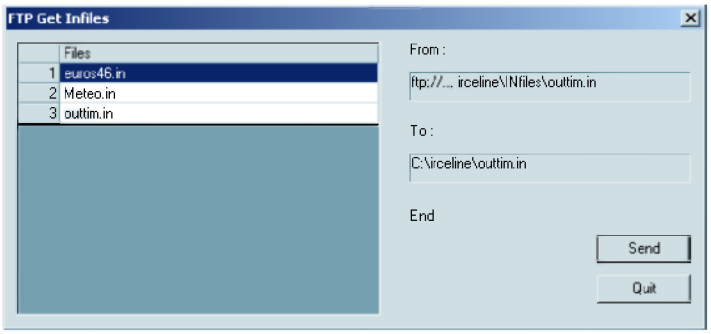

***Figure 2**: Boîte de dialogue de transfert des fichiers « Infiles ».*

2) L'action **« FTP Get inpalg »** transfère des fichiers qui resteront et doivent rester non modifiés tout au long des analyses et des visualisations.

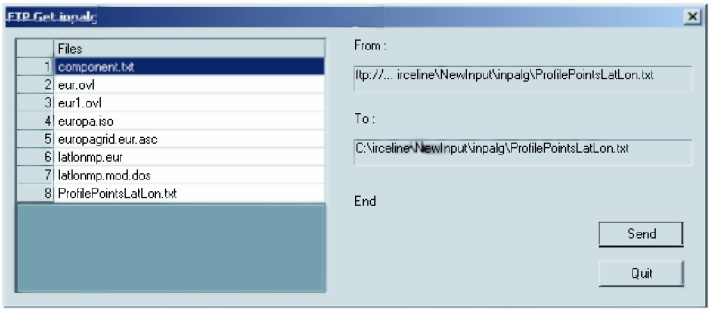

***Figure 3**: Boîte de dialogue de transfert des fichiers « inpalg ».*

3) L'action **« FTP Get inpsmog »** transfère les fichiers relatifs aux émissions dont certains sont modifiables.

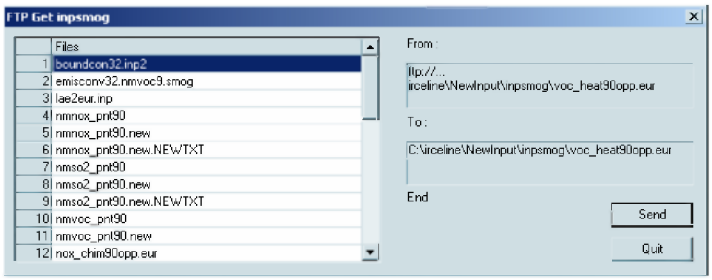

***Figure 4**: Boîte de dialogue de transfert des fichiers « inpsmog ».*

Dans les différentes boîtes, les noms des fichiers sont repris dans une liste que l'utilisateur peut consulter. Lorsqu'il clique sur le bouton **« Send »** de la boîte de dialogue, il voit défiler en dessous de l'intitulé « From », le nom du fichier situé sur le serveur. En dessous de l'intitulé « To », il voit le même nom de fichier transmis ainsi que son emplacement sur son ordinateur. Une fois le transfert de tous les fichiers terminé, le mot « End » apparaît dans la boîte de dialogue.

Les actions **« FTP Get… »** terminées, l'utilisateur ne peut accéder qu'aux options « **Start** » et « **Internet** » de la barre de menu de l'interface.

5.3 Présentation générale des fonctionnalités

La barre de menu de l'interface offre des options de base induisant l'affichage d'informations indispensables à la gestion du modèle. Les décrire constitue l'objet de cette section.

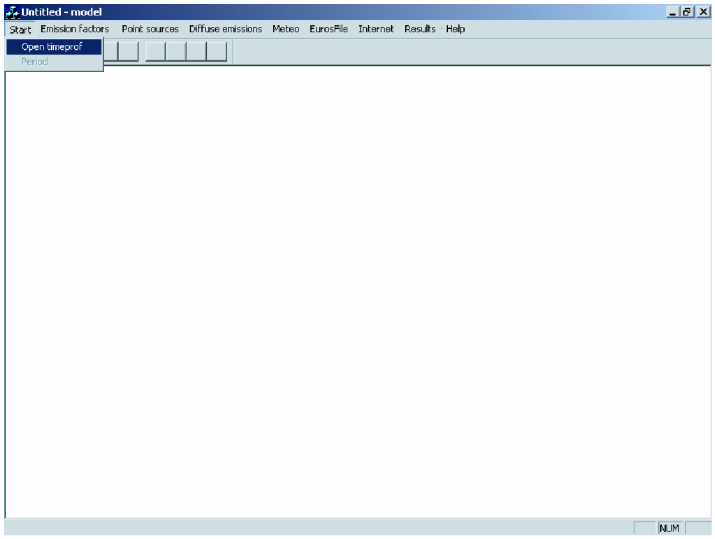

***Figure 5**: L'option « **Start** » et son menu.*

5.3.1 Option « Start »

En dehors de « **Start** » et « **Internet** », les autres options proposées par la barre de menu ne sont accessibles que pour autant que l'action « **Start** » ait été activée. L'activation de **« Start »** fait apparaître deux choix « **Open timeprof** » et « **Period** », seul « **Open timeprof** » est accessible au début des échanges.

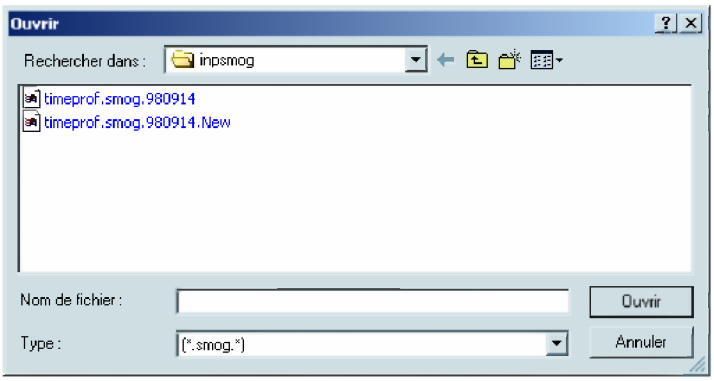

***Figure 6**: Boîte de dialogue permettant l'ouverture d'un fichier relatif aux facteurs d'émission.*

La ligne de menu **« Open timeprof »** permet à l'utilisateur de choisir le fichier définissant les facteurs d'émissions. Ces fichiers contiennent dans leur nom l'élément « .smog. ». Cette action obligatoire génère le chargement des fichiers nécessaires à la poursuite du processus. Une fois le fichier choisi, l'action **« Period »** permet, d'une part de déterminer la période de la simulation imposée au modèle EUROS et d'autre part d'ouvrir toutes les possibilités d'action autres que celles d'« **Internet** » comme le montrent les Figures suivantes:

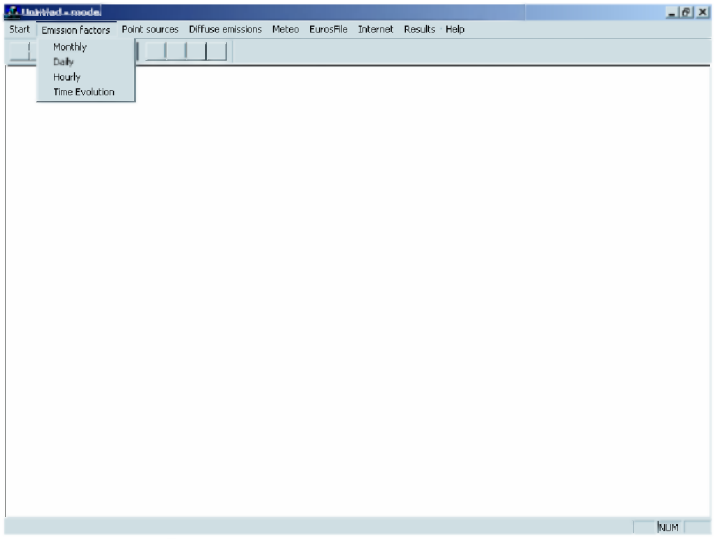

***Figure 7**: L'option « **Emisson factors** » avec son menu.*

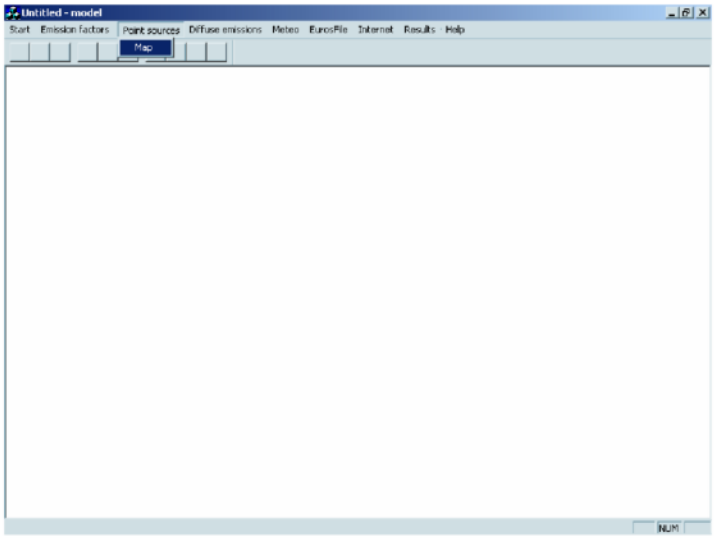

***Figure 8**: L'option « **Point sources** » avec son menu.*

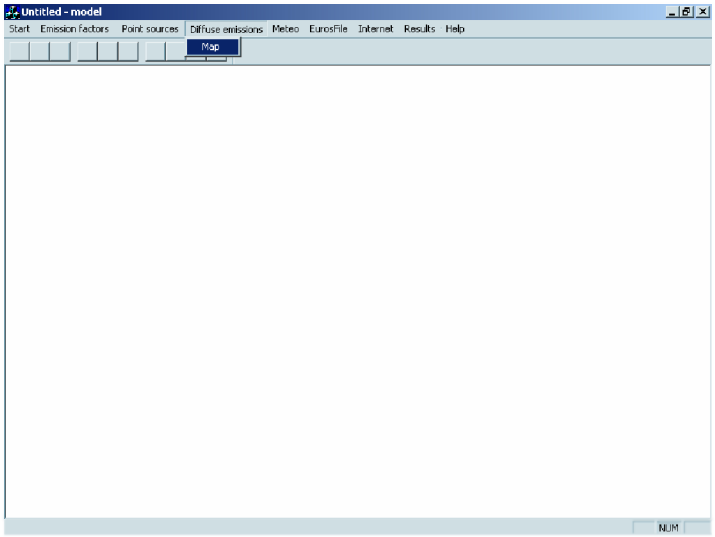

***Figure 9**: L'option « **Diffuse emissions** » avec son menu.*

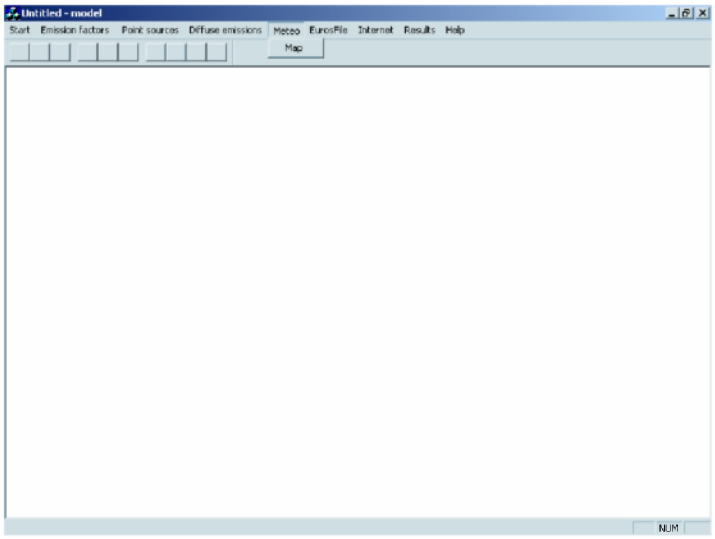

***Figure 10**: L'option « **Meteo** » avec son menu.*

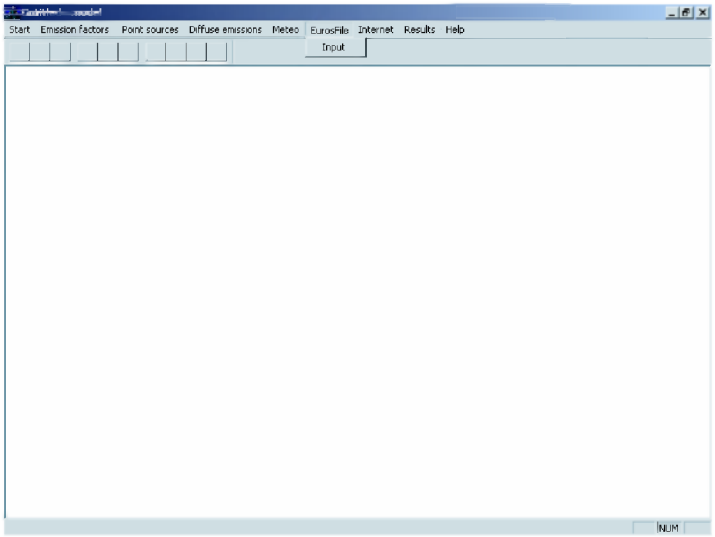

***Figure 11**: L'option « **EurosFile** » avec son menu.*

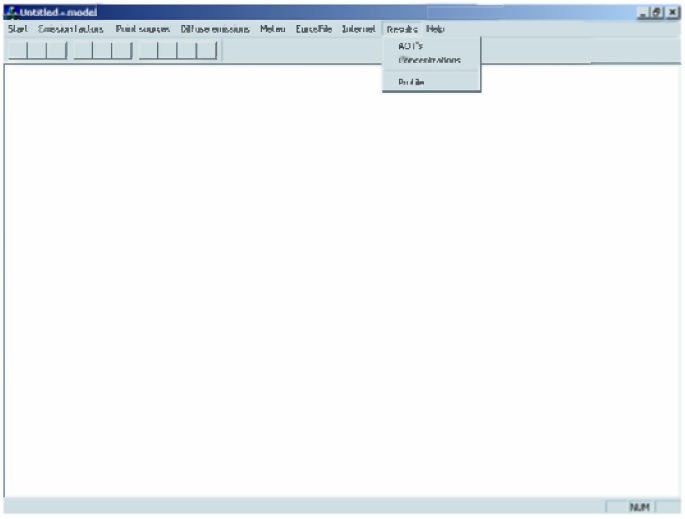

***Figure 12**: L'option « **Results** » avec son menu.*

La séquence initiale comprend donc les opérations suivantes:

1) Activation de l'option « **Start** ».

2) La ligne de menu **« Open timeprof »** ouvre une fenêtre permettant le choix d'un fichier contenant l'élément « .smog. » dans son nom.

3) Le choix d'un fichier avec « .smog. » induit directement la création d'une copie:

si le fichier choisi n'est pas terminé par une extension « New », une copie de ce fichier sera automatiquement créée avec le même nom mais complétée par l'extension « New ». Si cette copie existe déjà, il sera demandé à l'utilisateur de conserver le fichier avec l'extension « New » ou de le détruire de manière à le réinitialiser.

Pour tous les choix, le fichier terminé par l'extension « New » recevra toujours les modifications éventuelles attachées aux évolutions temporelles. Cette situation de choix implique à l'utilisateur qu'il est temps de sauver sous un nom qui lui est propre le fichier actuellement présent avec l'extension « New ». La gestion des fichiers sera appliquée à tous les fichiers modifiables situés dans le répertoire « inpsmog ».

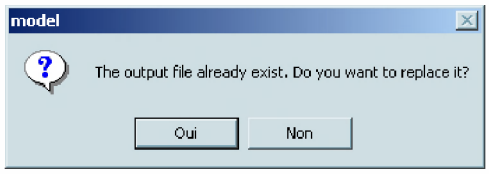

***Figure 13**: Boîte d'interrogation qui demande à l'utilisateur s'il désire remplacer le fichier existant.*

4) La confirmation du fichier choisi avec l'élément « .smog. » amène, si nécessaire, à une fenêtre indiquant la conservation ou non des anciennes modifications. A ce stade, les lignes de menu « **Point sources** », « **Diffuse emissions** » et « **Results** » de la barre de menu sont accessibles.

5) Vient ensuite une fenêtre indiquant le souhait de dessiner l'Europe avec des frontières finement ou largement décrites. La différence de taille est importante (50Ko/2.5Mo). Aussi pour accélérer l'interactivité il est conseillé lors de la génération des scénarios d'utiliser les frontières « larges » et de réserver les frontières « fines » pour les présentations finales, les publications...

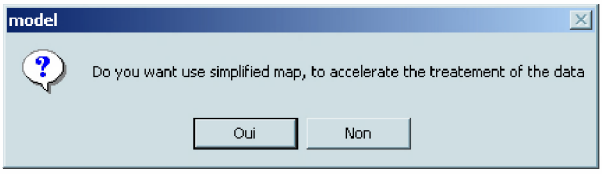

***Figure 14**: Boîte d'interrogation qui demande à l'utilisateur s'il travaille avec des frontières européennes «larges » ou « fines ».*

6) Enfin pour ouvrir les dernières possibilités de l'interface utilisateur, il faut activer la ligne de menu **« Period »** et inscrire dans une fenêtre les limites temporelles exprimées en jour. Ces limites sont importantes pour les évolutions temporelles (voir « Profile » situé dans l'intitulé « Results » de la barre de menu), la météorologie (voir « Meteo ») et la création dans «EurosFile » des fichiers « euros46.in » et « outtim.in » utiles au modèle EUROS.

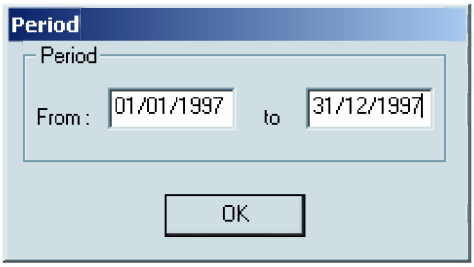

***Figure 15**: Boîte de dialogue permettant à l'utilisateur de définir la période de la simulation.*

5.3.2 Ligne de menu: « Emissions factors »

Cette option permet de modifier les trois fonctions temporelles relatives à la modulation globale des émissions sur toute la période retenue et pour chaque catégorie économique d'émission proposée (Source category). Lorsque la ligne de menu ***« Emissions factors »*** a été activée, un sous menu déroulant affiche les options suivantes:

1. Le choix de **« Monthly »** permet de distribuer une quantité annuelle totale entre les mois.

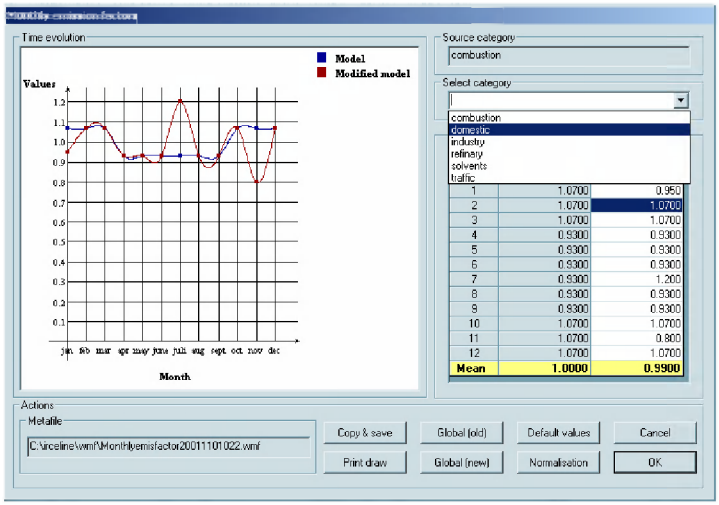

***Figure16**: Boîte de dialogue des facteurs d'émissions mensuels avec la liste des secteurs économiques.*

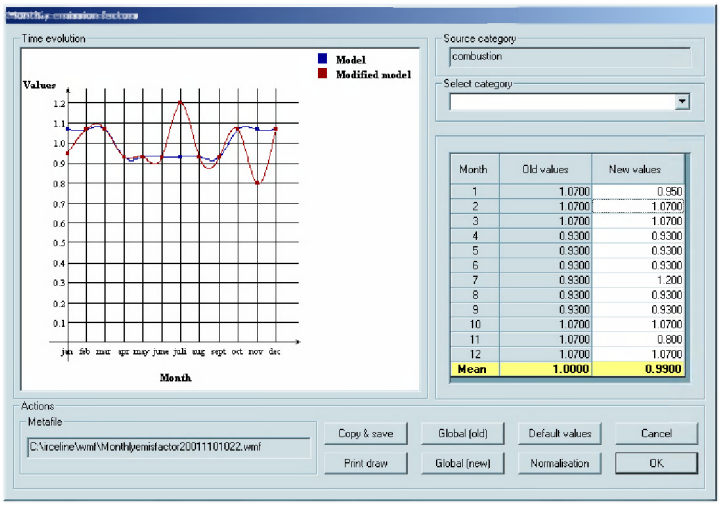

***Figure17**: Boîte de dialogue des facteurs d'émissions mensuels pour le secteur économique « combustion ».*

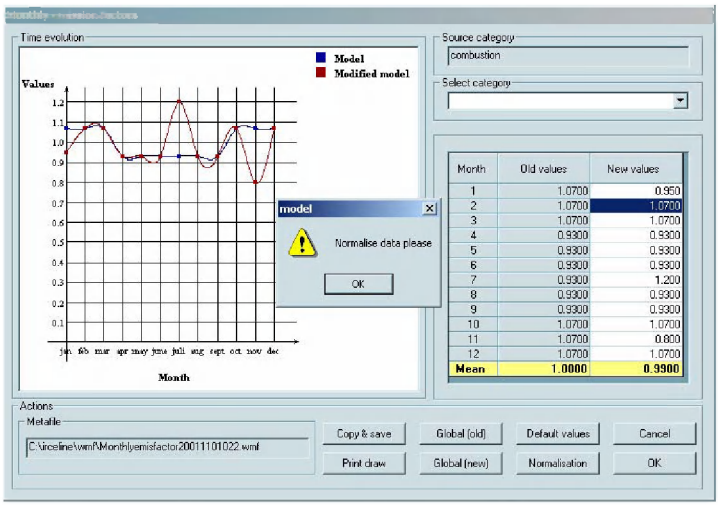

***Figure18**: La boîte de message, en avant plan, demande à l'utilisateur de normaliser les nouvelles données mensuelles.*

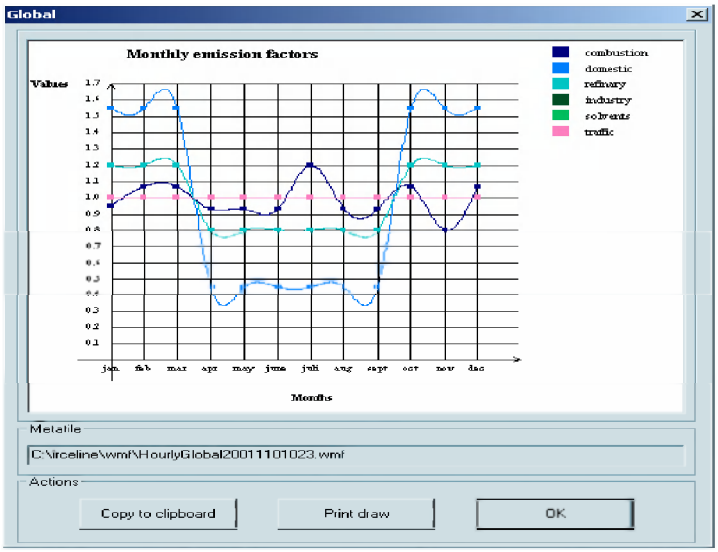

***Figure 19**: Boîte de dialogue qui affiche, pour tous les secteurs économiques, les facteurs d'émissions mensuels.*

2. Le choix **« Daily »** permet de distribuer une quantité hebdomadaire totale entre les jours de la semaine.

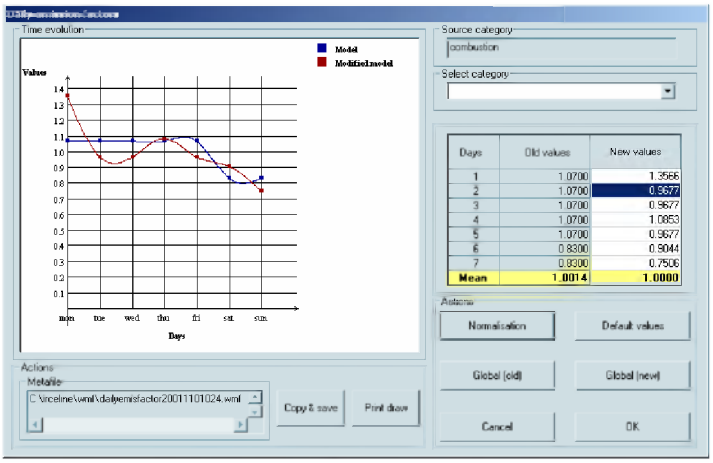

***Figure 20**: Boîte de dialogue des facteurs d'émissions journaliers pour le secteur économique « combustion ».*

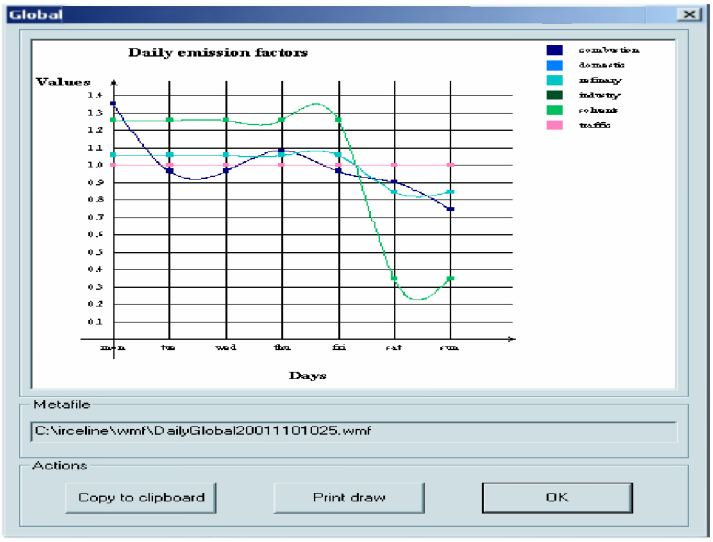

***Figure 21**: Boîte de dialogue qui affiche, pour tous les secteurs économiques, les courbes des facteurs d'émissions journaliers.*

3. Le choix de **« Hourly »** permet de distribuer une quantité journalière totale entre les heures de la journée.

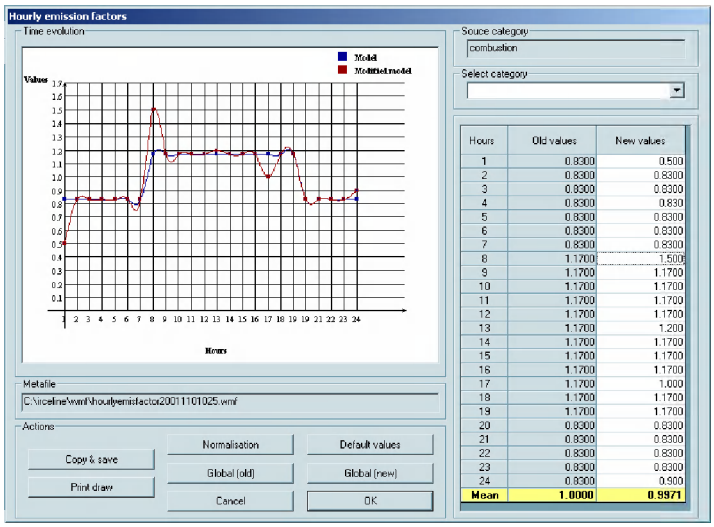

***Figure 22**: Boîte de dialogue des facteurs d'émissions horaires pour le secteur économique « combustion ».*

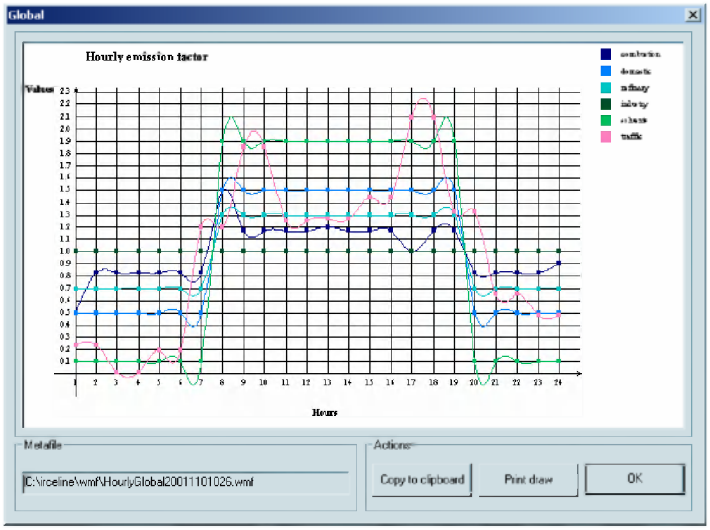

***Figure 23**: Boîte de dialogue qui affiche les courbes résultats des différents secteurs économiques pour les facteurs d'émissions horaires.*

Comme le montre les fenêtres présentées ci-dessus, pour les trois périodes temporelles définies, l'utilisateur

- peut choisir la catégorie d'émission dans la liste « Select category » ce qui entraîne l'affichage du tableau des valeurs des sources ponctuelles et l'affichage du graphe correspondant pour le secteur économique retenu (« Source category »).

- peut modifier les valeurs reprises dans la colonne intitulée « New values » et voir le résultat apparaître simultanément à l'écran. La ligne bleue représente la situation de référence, dénommée *Model,* dont les valeurs non modifiables sont reprises dans la colonne intitulée « Old values ». La ligne rouge, dénommée *Modified Model,* représente les valeurs situées dans la colonne intitulée « New values ».
- peut voir dans la dernière ligne « de couleur jaune » des différents tableaux, les moyennes respectives des colonnes « Old values » et « New values ».
- peut en cliquant sur le bouton **« Default values »** récupérer les valeurs de référence situées dans la colonne « Old values » et les mettre automatiquement dans la colonne « New values ».
- doit normaliser avec **« Normalisation »** les valeurs reprises dans la colonne « New values » afin que la moyenne arithmétique de cette colonne soit égale à 1.
- peut effectuer avec **« Copy & save »** une copie du graphique à la fois dans un méta fichier dont le nom est repris dans l'espace intitulé « Metafile » et dans le presse-papiers afin de pouvoir mettre cette dernière dans un logiciel qui admet le « copier-coller ». Dans l'intitulé « Metafile » le nom du fichier peut être modifié.
- peut imprimer avec **« Print draw »** le graphique sur l'imprimante choisie par défaut.
- peut afficher un récapitulatif des différentes courbes en cliquant sur les boutons **« Global (Old) »** ou **« Global (New) »** correspondant aux courbes des différentes catégories respectivement pour les anciennes et les nouvelles valeurs. Dans ce récapitulatif, l'utilisateur peut effectuer avec **« Copy to clipboard »** une copie du graphique à la fois dans un méta fichier dont le nom est repris dans l'espace intitulé « Metafile » et dans le presse-papiers afin de pouvoir mettre la copie dans un document « Word». Le graphique peut être imprimé sur l'imprimante choisie par défaut avec **« Print draw »**. Dans l'intitulé « Metafile » le nom du fichier peut être modifié.

Au terme d'une de ces actions sur les valeurs temporelles, l'utilisateur a la possibilité de:

- quitter par l'option **« Cancel »** de manière à revenir à l'état initial.
- quitter et enregistrer les nouvelles données dans le fichier comportant l'extension « New » en cliquant sur le bouton **« OK ».** La sortie et l'enregistrement de la nouvelle situation ne sont possibles que si les données sont préalablement normalisées.

4. « Time Evolution » présente, pour la période retenue, l'évolution temporelle le du produit des trois facteurs d'émission.

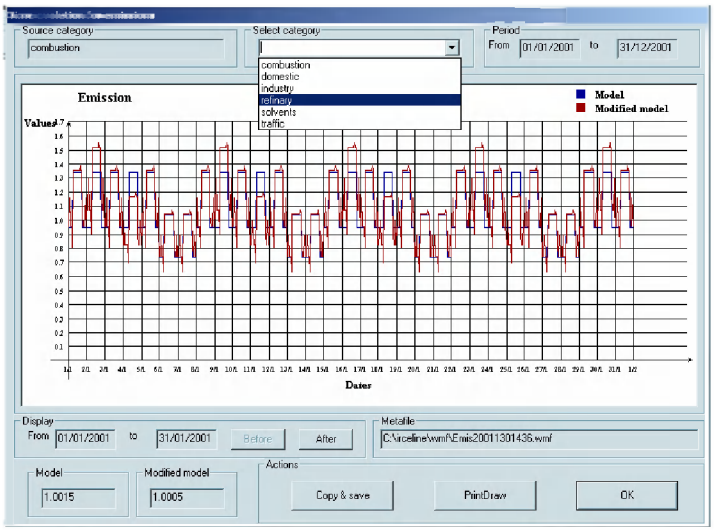

***Figure 24**: Boîte de dialogue de l'évolution temporelle du produit des trois facteurs d'émission avec l'affichage des secteurs économiques.*

***Figure 25**: Boîte de dialogue de l'évolution temporelle du produit des trois facteurs d'émission pour le mois de février après les actions « **After** » et « **Before** ».*

Grâce à cette fenêtre *« Time evolution for emission »*, l'utilisateur,

- peut, pour chaque catégorie d'émission, afficher le graphique de son évolution temporelle en se servant de la liste « Select category ».
- possède les informations relatives à la période globale retenue dans l'intitulé « Period » et du secteur économique retenu dans « Source category ».
- possède également des informations sur la période affichée dans l'intitulé « Display ». Les boutons **« Before »** et **« After »** permettent de voyager dans l'intervalle de temps par saut de trente et un jours au maximum. L'action d'un de ces boutons entraîne la mise à jour du graphique. La courbe bleue ou

Model représente la situation de référence. La courbe rouge ou *Modified model* représente la situation modifiée.

- peut effectuer avec "**Copy & Save**" une copie du graphique à la fois dans un méta fichier "Metafile" et dans le presse-papiers pour utilisation deans des rapports. Le nom du fichier peut être modifié dans l'intitulé "Metafile".
- peut imprimer par "**PrintDraw**" le graphique sur l'imprimane définie par défaut.

5.3.3 La ligne de menu « Point Sources »

De nature cartographie, cette option présente dans la grille du modèle EUROS les sources ponctuelles d'émission. Les débits, représentés par une moyenne annuelle (kg/an), sont groupés par secteurs économiques.

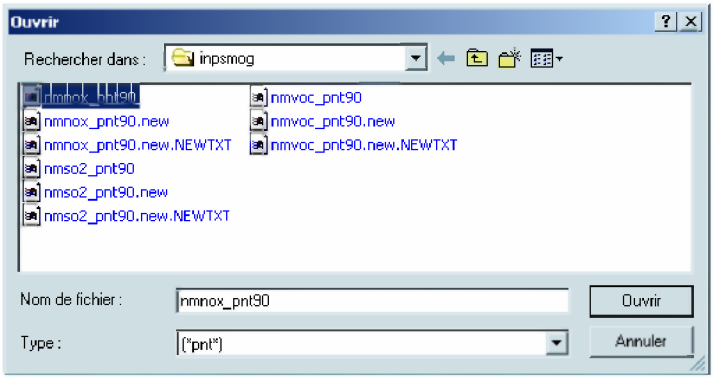

***Figure 26**: Boîte de dialogue permettant le choix d'un fichier de type « pnt ».*

L'action **« Ouvrir »** de cette fenêtre, générée par le système d'exploitation ici en français, permet à l'utilisateur de choisir le fichier définissant les points sources pour l'un des trois polluants suivants, NO_x, COV et SO_2. Les fichiers relatifs aux sources ponctuelles sont reconnus, pour traitement, par la présence de l'élément « pnt » dans leurs noms. L'intervention sur les données entraîne, en sortie normale, la création d'un fichier portant le même nom que l'initial mais terminé par l'extension « NEWTXT » si ce dernier n'existe pas encore. Dans le cas contraire, il sera demandé de le conserver momentanément ou de le réinitialiser au terme de modifications acceptées en sortie.

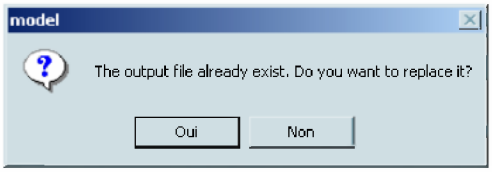

***Figure 27**: Boîte d'interrogation qui demande à l'utilisateur s'il désire remplacer le fichier existant avec l'extension « NEWTXT ».*

Une fois le fichier choisi, la carte de la distribution spatiale des sources s'affiche à l'écran.

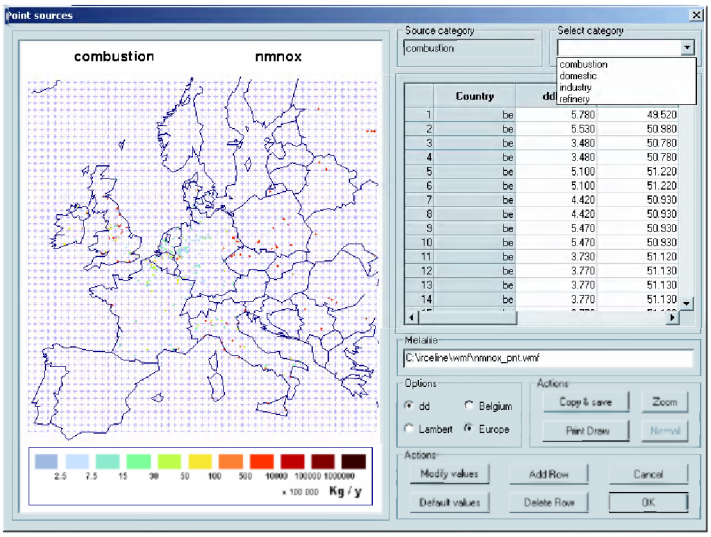

***Figure 28**: Boîte de dialogue des sources ponctuelles.*

A l'aide de cette fenêtre, l'utilisateur

- peut choisir la catégorie d'émission dans une liste prédéfinie « Select category » ce qui entraîne l'affichage du tableau des sources ponctuelles et l'affichage du graphe correspondant pour le secteur économique retenu («Source category »).
- peut modifier directement certains éléments d'une ligne dans le tableau, ajouter une ligne par « Add Row » ou supprimer une ligne par « Delete Row » dans le tableau des sources ponctuelles, les tableaux ainsi que la carte sont remis à jour après chaque modification.
- peut récupérer les valeurs initiales par le bouton « Default values »
- peut, à l'aide du bouton **« Modify values »,** changer globalement toutes les valeurs de la colonne « em (kg/y) » ou certains éléments de cette colonne pour un pays déterminé comme indiqué par la fenêtre suivante:

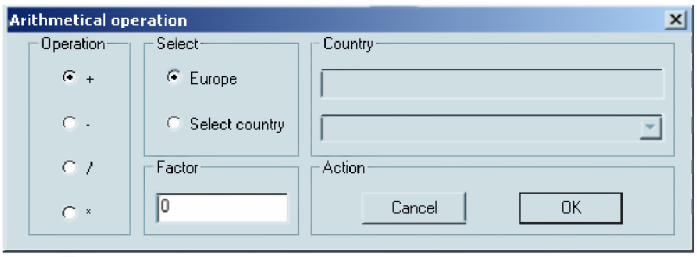

***Figure 29**: Boîte de dialogue des opérations arithmétiques.*

Dans cette boîte de dialogue, l'utilisateur peut choisir dans les rectangles portant les titres suivants:

- « Operation » le type d'opération qu'il désire effectuer (+, -, *, /). La division par zéro est automatiquement annulée.
- « Factor » le nombre qui va *, /, +, -, les émissions.
- « Selection » dans ce rectangle l'utilisateur peut choisir entre deux options (Europe ou Select country). Lorsque l'utilisateur clique sur le bouton radio situé en face de l'intitulé « Europe », l'opération arithmétique s'effectuera sur toutes les valeurs des pays après confirmation. Par contre, si l'utilisateur sélectionne l'option « Select country », la liste située dans le rectangle « Country » s'active et l'utilisateur choisit un pays. Le changement des émissions se limitera au pays retenu.

Les boutons « **OK** » et « **Cancel** » permettent de confirmer ou d'annuler les choix.

- peut choisir à l'aide des boutons radio situés devant les intitulés « dd » et « Lambert » d'afficher dans le tableau les coordonnées des sources ponctuelles en degrés décimaux ou en coordonnées Lambert dans le système Lambert belge.
- peut effectuer avec « Copy & save » une copie de la carte à la fois dans un méta fichier dont le nom est repris dans l'espace intitulé « Metafile » et dans le presse-papiers afin de pouvoir mettre cette carte dans un traitement de texte. Le nom du fichier peut être modifié dans l'intitulé « Metafile ».
- peut imprimer avec « Print Draw » la carte sur l'imprimante définie par défaut
- peut choisir, à l'aide des boutons radio situés devant les intitulés **« Europe »** et **« Belgium »**, d'afficher la carte de l'Europe ou d'afficher la carte du Benelux avec les régions voisines.

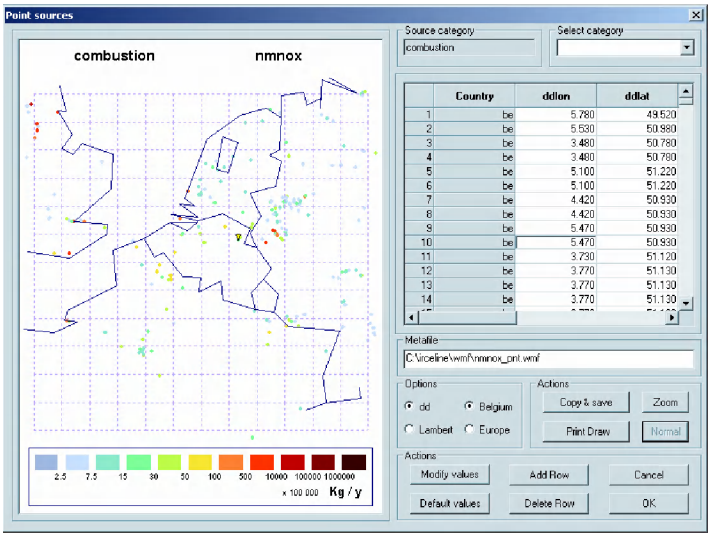

***Figure 30**: Boîte de dialogue des sources ponctuelles avec l'option « **Belgium** ».*

- peut également situer une source ponctuelle au départ d'une ligne du tableau, cette source sera localisée sur le graphique par une flèche jaune.

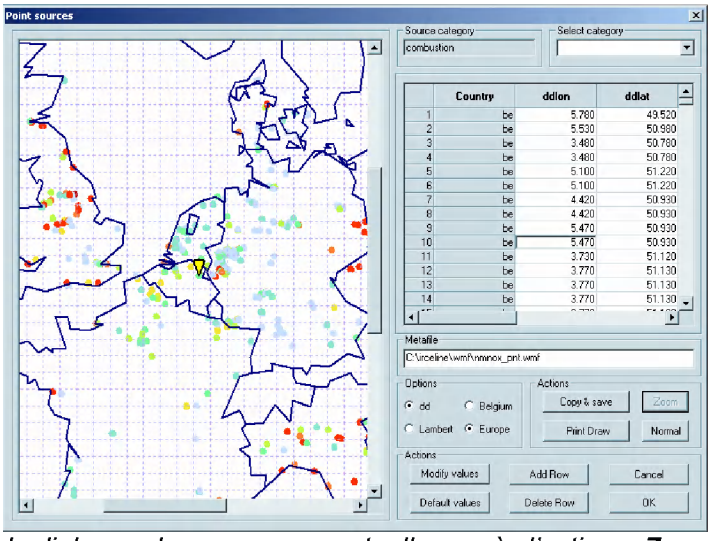

***Figure 31**: Boîte de dialogue des sources ponctuelles après l'action « **Zoom** ».*

- peut également effectuer un zoom de la carte en cliquant sur le bouton « Zoom » ou rétablir la carte dans le format initial en cliquant sur le bouton « Normal ».
- peut quitter la boîte de dialogue sans enregistrer les modifications avec le bouton « **Cancel** » ou en les enregistrant en poussant sur **« OK** ».

5) Ligne de menu « Diffuse emission »

Cette option présente dans la grille du modèle EUROS sous un aspect cartographique les sources de surface sur la base de leur intensité exprimée en moyenne annuelle (kg/an) et en fonction des secteurs économiques.

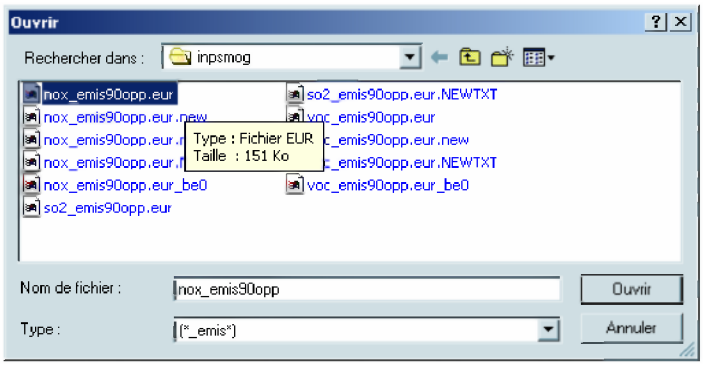

***Figure 32**: Boîte de dialogue permettant l'ouverture d'un fichier de type « _emis ».*

L'action **« Ouvrir »** de cette fenêtre, générée par le système d'exploitation, permet à l'utilisateur de choisir le fichier définissant les sources de surface définies en chaque maille du modèle EUROS et pour un des trois polluants suivants, NO_x, COV et SO_2. Les fichiers relatifs aux sources de surface sont reconnus, pour traitement, par la présence de l'élément « _emis » dans leurs noms. Toute modification des données entraîne la création d'un fichier portant le même nom que l'initial mais terminé par l'extension « NEWTXT » si ce dernier n'existe pas encore. Dans le cas contraire, il sera demandé de le conserver momentanément ou de le réinitialiser.

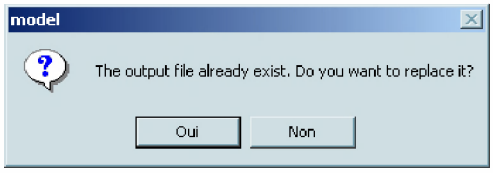

***Figure 33**: Boîte d'interrogation qui demande à l'utilisateur s'il désire remplacer le fichier existant avec l'extension « NEWTXT ».*

Une fois le fichier choisi, la carte des sources de surface s'affiche à l'écran.

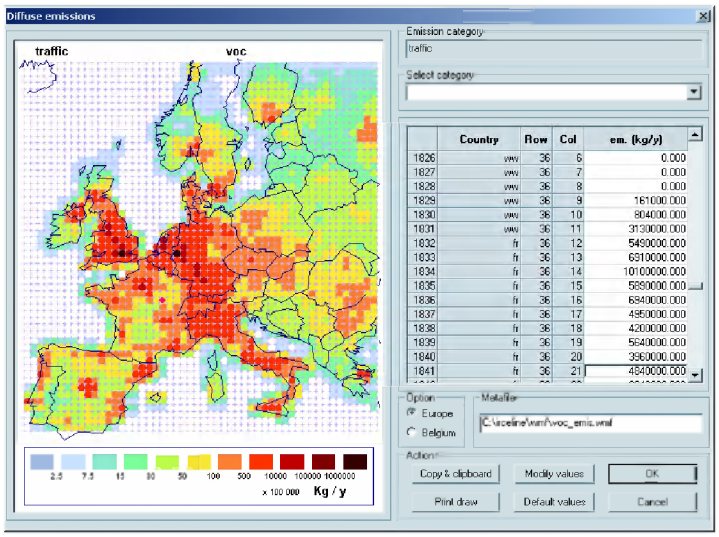

***Figure 34**: Boîte de dialogue des sources de surface pour le secteur économique « traffic ».*

A l'aide de cette fenêtre, l'utilisateur

- peut choisir la catégorie d'émission dans une liste prédéfinie « Select category » ce qui entraîne l'affichage du tableau des sources ponctuelles et l'affichage du graphe de leur répartition spatiale pour le secteur économique choisi dans « Emission category ».
- peut modifier une ligne dans le tableau des sources de surface, les tableaux ainsi que la carte sont remis à jour.
- peut à l'aide du bouton « Modify values » changer globalement toutes les valeurs de la colonne « em (kg/y) » ou certains éléments de cette colonne pour un pays déterminé comme indiqué par la fenêtre suivante:

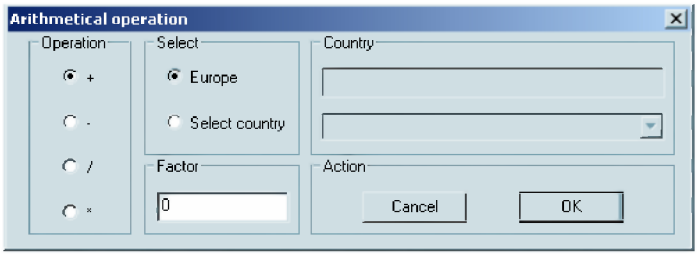

***Figure 35**: Boîte de dialogue des opérations arithmétiques.*

Dans cette boîte de dialogue, l'utilisateur peut choisir dans les rectangles portant les titres suivants:

- « Operation » le type d'opération qu'il désire effectuer (+, -, *, /). La division par zero est automatiquement annulée.
- « Factor » le nombre qui va *, /, +, -, les émissions.

- « Selection » dans ce rectangle l'utilisateur peut choisir entre deux options (Europe ou Select country). Lorsque l'utilisateur clique sur le bouton radio situé en face de l'intitulé « Europe », l'opération arithmétique s'effectuera sur toutes les valeurs des pays après confirmation. Par contre, si l'utilisateur sélectionne l'option « Select country », la liste située dans le rectangle « Country » s'active et l'utilisateur choisit un pays. Le changement des émissions se limitera au pays retenu.

Les boutons « **OK** » et « **Cancel** » permettent de confirmer ou d'annuler les choix.

- peut effectuer avec « Copy & clipboard » une copie de la carte à la fois dans un méta fichier dont le nom est repris dans l'espace intitulé « Metafile » et dans le presse-papiers afin de pouvoir mettre la copie dans un traitement de texte. Le nom du fichier peut être modifié dans l'intitulé « Metafile ».
- peut imprimer par « Print draw » la carte sur l'imprimante définie par défaut.
- peut choisir à l'aide des boutons « radio » situés devant les intitulés « Europe » et « Belgium **»** d'afficher la carte de l'Europe ou d'afficher la carte du Benelux avec les régions voisines.

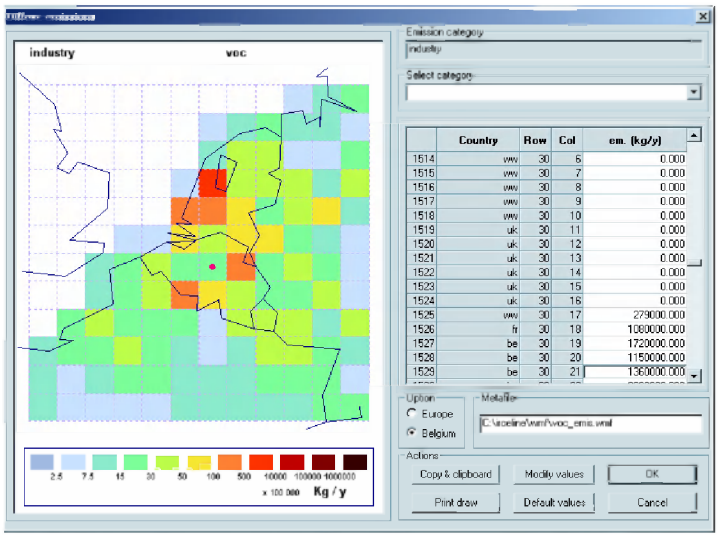

***Figure 36**: Boîte de dialogue des sources de surface avec l'option « **Belgium** ».*

- peut également établir une relation entre le graphique et le tableau: le choix d'une maille se marque par un disque rose sur la carte et par une mise en relief au niveau d'une ligne dans le tableau.
- peut récupérer les valeurs initiales en cliquant sur le bouton « **Default values** ».
- peut quitter la boîte de dialogue sans effectuer de modifications par le bouton **« Cancel »** ou les enregistrer en choisissant le bouton « **OK** ».

5.3.4 La ligne de menu « Meteo »

L'interface d'interrogation offre sous certaines conditions la possibilité de visualiser sans modifications les données météorologiques nécessaires aux simulations demandées. Le but est de pouvoir « situer » les résultats dans la dynamique atmosphérique retenue. Deux groupes de données météorologiques existent.

- Le premier groupe, dénommé « Ground », donne au niveau de l'observation les champs de la température (T), des précipitations (PR), de la norme de la vitesse horizontale du vent (WV), de l'humidité relative (rH) et de la couverture nuageuse (CC).

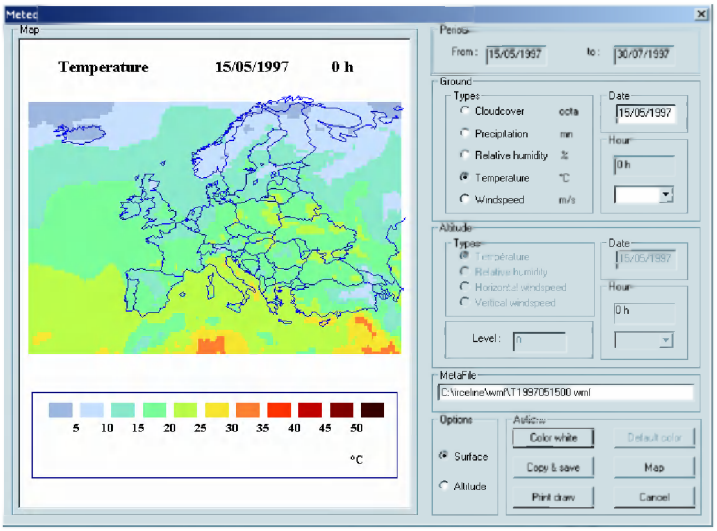

***Figure 37**: Boîte de dialogue permettant d'afficher les cartes météorologiques connues au niveau d'observation.*

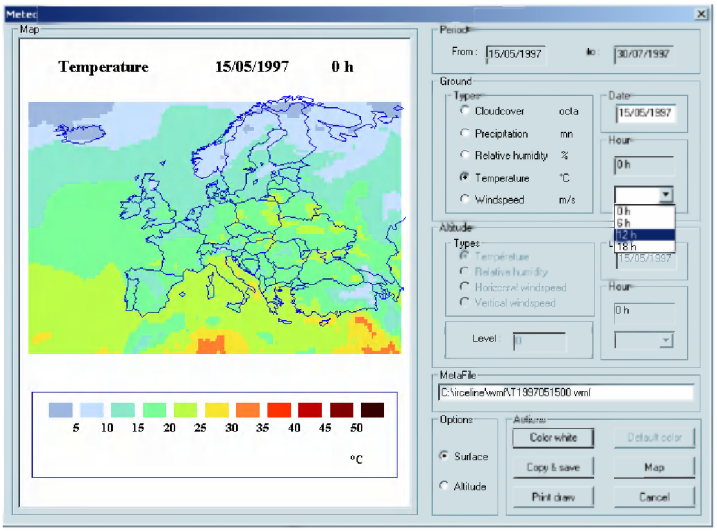

***Figure 38**: Affichage du champ de température niveau d'observation avec la présentation de l'option sur les heures.*

➧ Le second groupe dénommé « Altitude » donne accès à une visualisation des champs météorologiques définis à cinq niveaux en altitude. Ces champs traitent la température, l'humidité relative, la vitesse verticale et les composantes horizontales du vent. Toutes ces grandeurs physiques, connues aux cinq niveaux 1000hPa, 925hPa, 850hPa, 700hPa et 500hPa, résultent des calculs et analyses effectués au ECMWF (**E**uropean **C**enter for **M**edium-Range **W**eather **F**orecasts) pour un domaine recouvrant l'Europe maillée.

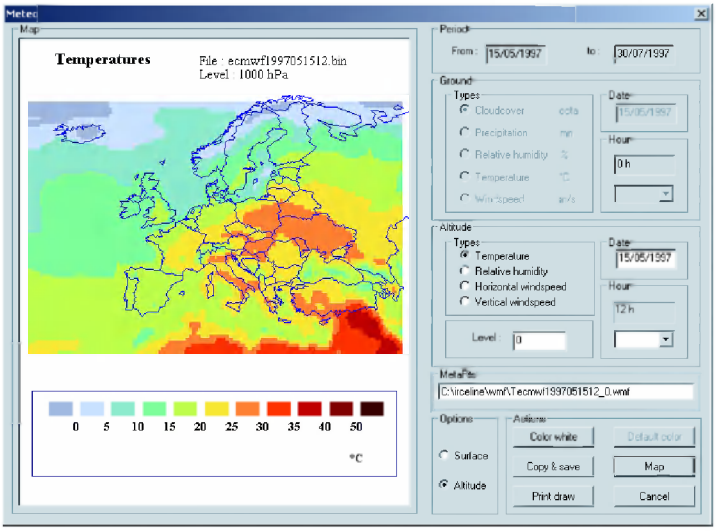

***Figure 39**: Boîte de dialogue des champs météorologiques en fonction de la pression. Affichage du champ de température à la hauteur de 1000hPa.*

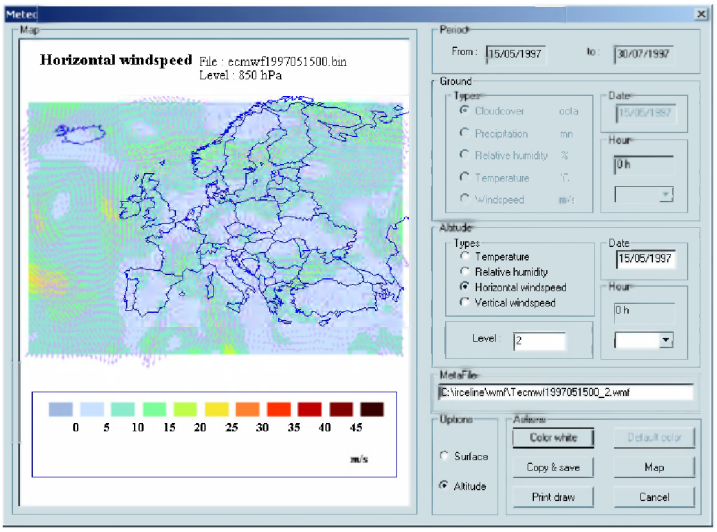

***Figure 40**: Affichage du champ vectoriel horizontal du vent à la hauteur de 850hPa.*

Pour rappel dans le modèle EUROS, la couche limite atmosphérique est composée de la couche de surface d'une épaisseur d'environ 50m (surface layer), de la couche mélangée variable au cours de la journée (mixing layer), de la couche réservoir (reservoir layer) et de la couche dite supérieure limitée en altitude (upper layer).

Comme le montre les fenêtres précédentes, l'utilisateur

- peut choisir un des deux groupes de données météo en allant dans le groupe « Options » et choisir « **Ground** » ou « **Altitude** ».
- peut, une fois le groupe météo choisi, représenter un des champs météorologiques proposés à une date choisie, dans l'intervalle temporel donné par « Period » et une heure choisie parmi 0h, 6h, 12h et 18h de la liste prédéfinie « Hour ». Une fois ces choix effectués, l'utilisateur doit cliquer sur le bouton « **Map** » pour afficher la carte demandée. Cette opération construit le nom du fichier et ouvre le fichier s'il existe (voir la restriction du début du paragraphe). Si le fichier n'existe pas, l'utilisateur en est informé. Pour l'option météo « **Altitude** », il est nécessaire de choisir le niveau (Level). Pour cela, il suffit d'introduire un des chiffres 0, 1, 2, 3, 4 derrière l'intitulé « Level ».
- peut choisir la couleur des frontières de l'Europe. S'il clique sur le bouton intitulé « **Color white** » les frontières sont dessinées en blanc. Dans le cas contraire, la couleur par défaut (noir) sera utilisée ou choisie à l'aide du bouton « **Default color** ».
- peut effectuer par « **Copy & save** » une copie de la carte dans un fichier dont le nom est repris dans l'espace intitulé « Metafile » et dans le presse-papiers. Dans l'intitulé « Metafile » le nom du fichier peut être modifié par l'utilisateur.
- peut imprimer avec « **Print draw** » la carte sur l'imprimante définie par défaut.
- quitte la fenêtre en activant le bouton « **Cancel** ».

5.3.5 La ligne de menu « EurosFile »

Cette option permet de constituer le « panel de fichiers » nécessaire au pilotage du modèle EUROS en tenant compte des modifications éventuelles effectuées dans les fichiers d'émissions. Quelques paramètres propres au modèle peuvent être adaptés, mais en général ils sont fixés par les concepteurs du modèle. L'ensemble des paramètres d'entrée du modèle proposé par cette option conduit à son terme à la création du fichier récapitulatif « euros46.in ».

Le fichier « outtim.in », également construit au terme de cette action, reprend toutes les informations que l'utilisateur souhaite vouloir extraire par le modèle EUROS comme, par exemple, la concentration d'un ou plusieurs composants chimiques dans les quatre couches atmosphériques du modèle ou encore les évolutions temporelles en des points d'observations connus.

Etant donné la quantité d'information à traiter, plusieurs formulations d'actions se sont révélées nécessaires. Les choix découlent des informations contenues dans la version 2000-06-29 du rapport « EUROS input and output. EUROS version 4.6 » de Liesbeth de Waal et Ferd Sauter du RIVM.

Le choix de **« EurosFile »** dans la barre de menu fait apparaître la fenêtre *« File input »* suivante:

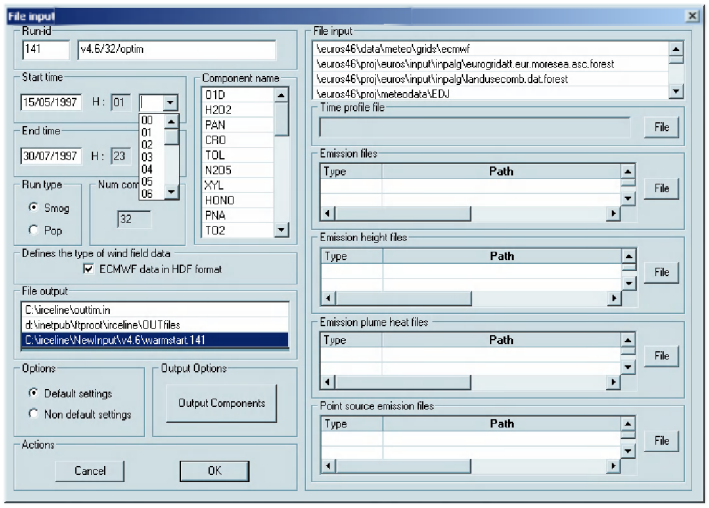

***Figure 41**: Boîte de dialogue permettant d'introduire des informations nécessaires pour la création du fichier « euros46.in ».*

L'analyse de cette boîte de dialogue se fait en fonction des compétences de l'utilisateur considéré comme un spécialiste ou un non-spécialiste du modèle EUROS. Avec cette distinction,

- l'utilisateur, **se considérant comme un non-spécialiste**, ne devrait agir que dans
  - « Run-id » pour caractériser la simulation.
  - « Start time » et « End time » pour définir la période de calcul.
  - « Time profile file » pour choisir un fichier relatif aux facteurs d'émissions.
  - « Emission files » pour choisir - obligatoirement dans l'ordre des polluants SO2, NOx et COV - les trois fichiers relatifs aux émissions des sources de surface.
  - « Emission height files » pour choisir - obligatoirement dans l'ordre des polluants SO2, NOx et COV -, les trois fichiers relatifs aux hauteurs des émissions des sources de surface.
  - « Emission plume heat files » pour choisir - obligatoirement dans l'ordre des polluants SO2, NOx et COV -, les trois fichiers relatifs aux émissions exprimées en MW des sources de surface.
  - « Point source emission » pour choisir - obligatoirement dans l'ordre des polluants SO2, NOx et COV -, les trois fichiers relatifs aux émissions des sources ponctuelles.

- « Options » et choisir obligatoirement « **Non default settings** » et ensuite sortir directement par le bouton « **OK** » de la fenêtre dénommée *« Options input file »* qui apparaîtra, tout ceci pour des raisons momentanées de calcul.

Le choix des fichiers est facilité par l'usage d'une fenêtre de dialogue. Pour « Time profile file » et sous l'action de « **File** » la boîte de dialogue *« Ouvrir »* apparaît qui ne comprend que les fichiers contenant dans leur nom l'élément « .smog. ».

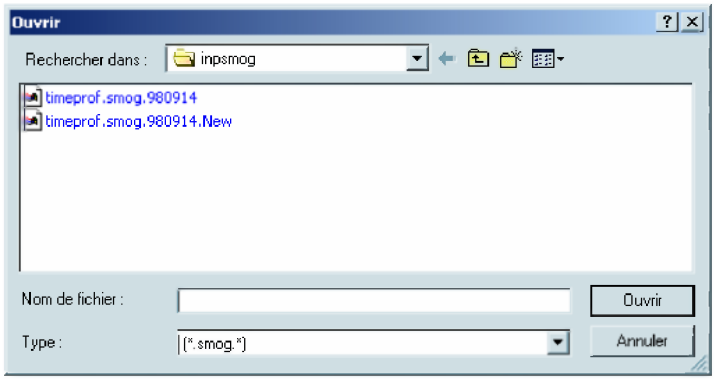

***Figure 42**: Boîte de dialogue permettant de choisir un fichier temporel.*

Pour les fichiers de type émission, une autre boîte de dialogue apparaît à l'écran:

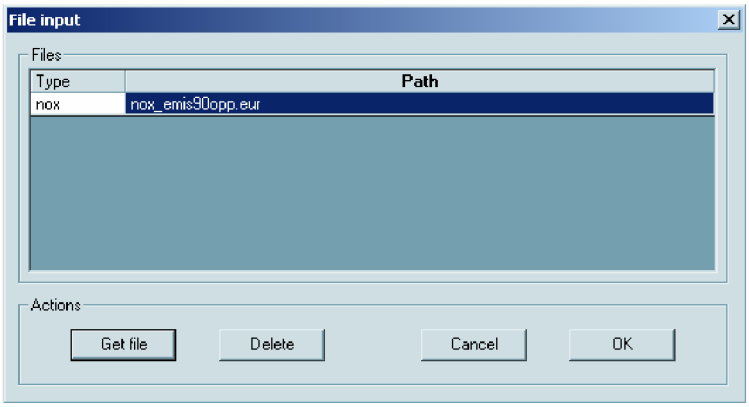

***Figure 43**: Boîte de dialogue reprenant la liste des fichiers relatifs aux émissions.*

Par cette fenêtre, l'utilisateur peut choisir un fichier proposé à la suite de l'action « **Get file** », les doublons et les fichiers découlant d'autres fichiers déjà repris dans la sélection ne peuvent être sélectionnés.

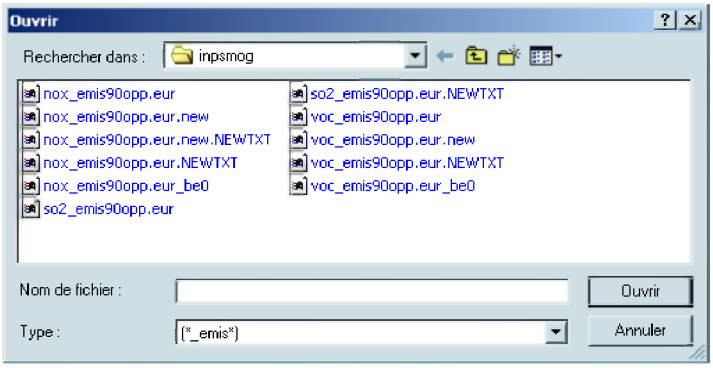

***Figure 44**: Boîte de dialogue permettant de choisir un fichier émission.*

L'utilisateur peut supprimer un fichier en se plaçant dessus et en cliquant sur le bouton « **Delete** ». Il confirme ses modifications en cliquant sur le bouton « **OK** » ou les infirme en cliquant sur le bouton « **Cancel** ». Par ces deux options, on revient à la boîte de dialogue *« File input »* précédente.

- l'utilisateur, **se considérant spécialiste**, aura la possibilité d'accéder à des informations complémentaires en cliquant sur le bouton radio situé devant l'intitulé « **Non default settings** ». La boîte de dialogue *« Options input file »* apparaît.

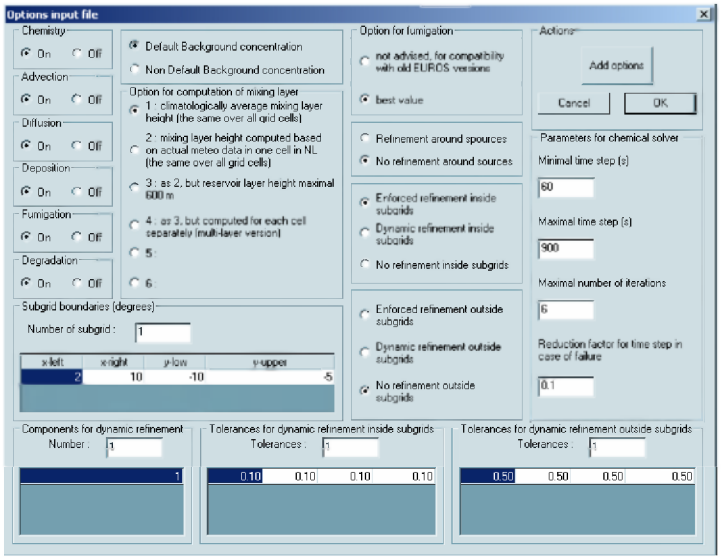

***Figure 45**: Boîte de dialogue permettant d'introduire des informations complémentaires pour la création du fichier « euros46.in ».*

- l'utilisateur peut une fois toutes les modifications effectuées dans *« Options input file »*, confirmer ses modifications en cliquant sur le bouton « **OK** » ou les annuler en cliquant sur le bouton « **Cancel** ». Dans les deux cas, on revient à la boîte de dialogue « *File Input »* précédente.

- l'utilisateur peut accéder, dans la fenêtre *« Options input file »*, à d'autres options en cliquant sur le bouton « **Add options** ». La boîte de dialogue suivante apparaît:

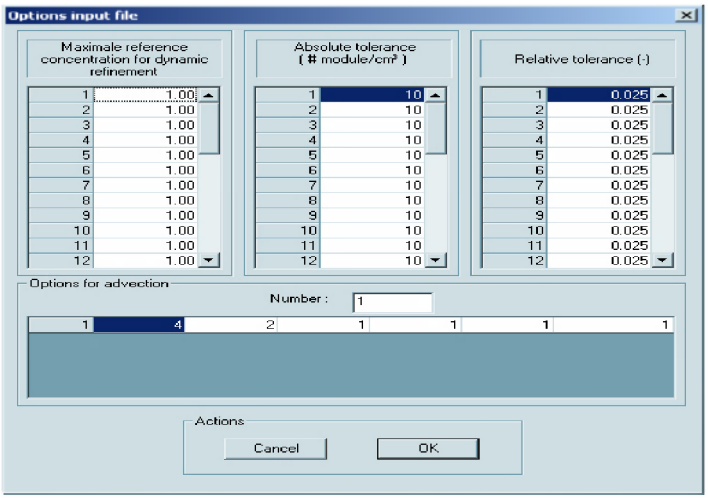

***Figure 46**: Boîte de dialogue permettant d'introduire des informations complémentaires pour la création du fichier « euros46.in ».*

- l'utilisateur, **spécialiste ou non-spécialiste**, une fois toutes les modifications effectuées et confirmées, a créé un fichier « euros46.in » temporaire. Il sera effectif en cliquant sur le bouton **« OK »** dans la fenêtre « *File Input* ». Le bouton **« Cancel »** permet de revenir au point de départ sans tenir compte des éventuelles modifications. Mais avant toute action de sortie, la rubrique « Output Options » peut être envisagées pour modifier le fichier de sortie gérant ce que l'on souhaite recevoir comme information au terme des calculs du modèle EUROS.

En cliquant sur le bouton **« Output Components »** de la boîte de dialogue *« File input »* l'utilisateur fait apparaître la boîte *« Output specification file »* présentant les informations relatives à la création du fichier de sortie « outtim.in ».

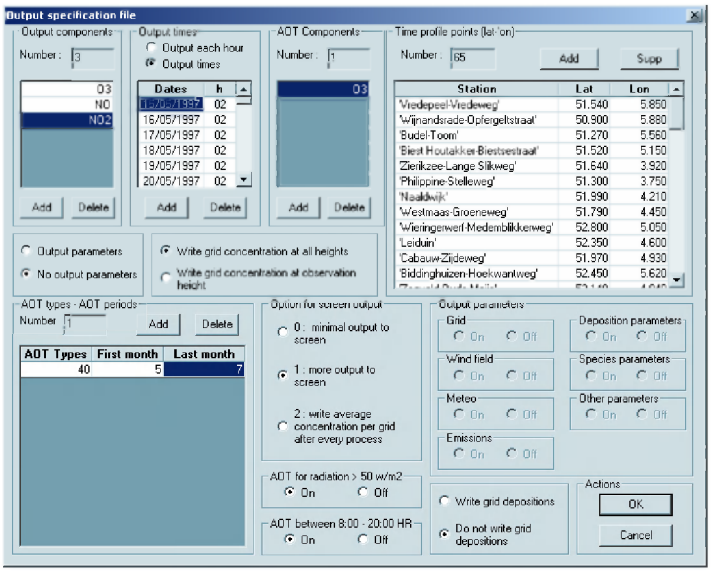

***Figure 47**: Boîte de dialogue permettant d'introduire des informations nécessaires pour la création du fichier « outtim.in ».*

L'utilisateur spécialiste peut modifier l'ensemble des informations présentées dans cette fenêtre. Pour le **non-spécialiste**, il est conseillé de ne considérer que les rubriques suivantes:

- « Output components » qui introduit les composants chimiques pour lesquels il y aura des valeurs calculées et mémorisées. Par défaut, les composants O3, NO et NO2 sont envisagés.
- « Time profile points (lat-lon) » présente les points de mesures où une évolution temporelle sera considérée en sortie. Les stations affichées par défaut proviennent du fichier « ProfilePointsLatLon » accessible par le chemin C:\(Institute)\NewInput\inpalg\.
- « Output times » permet de choisir les temps, dates et heures, où les valeurs à calculer sont mémorisées en vue de réaliser les cartes de concentartion.
- « AOT Components » fixe les composants chimiques pour lesquels un AOT (**A**ccumulated exposure **O**ver a **T**hreshold) est calculé.
- « AOT types – AOT periods » permet d'introduire avec « **Add** » ou de retirer avec « **Delete** » une valeur de référence (en ppb pour l'O3) avec la période suivant laquelle elle sert de référence. Les limites mensuelles sont sous la contrainte de la période de calcul fixée depuis le début des échanges.
- « AOT for radiation > 50 w/m2 » est un filtre sur les périodes temporelles pour lesquelles l'ensoleillement est supérieur à la limite de 50 W/m2. L'action « **On** » indique que le calcul se fait pour tous les composants chimiques retenus dans « AOT Components » et toutes les valeurs de référence choisies dans « AOT types – AOT periods ». Dans le cas contraire, il faut agir sur « **Off** ».

- « AOT between 8.00 – 20.00 HR » est un filtre sur les heures comprises entre 8h et 20h. L'action « **On** » indique que le calcul se fait pour tous les composants chimiques retenus dans « AOT Components » et toutes les valeurs de référence choisies dans « AOT types – AOT periods ». Dans le cas contraire, il faut agir sur « **Off** ».

Dans l'intitulé « Output times » l'utilisateur a le choix entre les deux options « Output each hour » et « Output times ». Lorsque l'utilisateur clique sur le bouton radio présent devant l'option « **Output times** », la boîte de dialogue *« Output times »* apparaît:

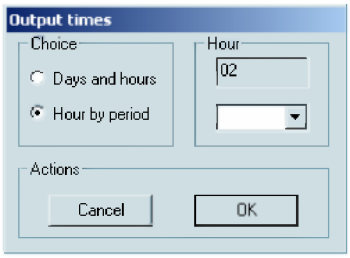

***Figure48**: Boîte de dialogue permettant à l'utilisateur de choisir l'heure pour tous les jours ou choisir ponctuellement les heures et les dates dans la période retenue.*

Dans cette boîte, l'utilisateur a le choix entre:

- l'option « **Days and hours** » qui lui permet de choisir les dates et les heures, à condition qu'elles soient comprises dans l'intervalle choisi dans l'option de menu « Period ».

- ii) l'option « **Hour by period** » qui lui permet de choisir l'heure.

- iii) Une fois l'heure choisie et la validation du choix effectuée en appuyant sur le bouton « **OK** » on fait apparaître, en dessous de l'intitulé « Output times », la liste de toutes les dates de l'intervalle à une heure préalablement choisie par l'action précédente.

Dans les boîtes de dialogue présentées ci-dessus apparaissent les boutons « **Add** » et « **Delete** ». Ces deux boutons permettent d'ajouter ou de supprimer des lignes dans les listes correspondantes.

5.3.6 La ligne de menu « Internet »

Les premières lignes de cette option ont déjà été envisagées lors du transfert du logiciel d'interface. Bien que la lecture des deux fichiers « euros46.in » et « outtim.in » restent toujours possibles, les autres options permettent successivement le transfert des fichiers conditionnés au serveur par l'action « **FTP Put INfiles** » pour « euros46.in », « outtim.in » et « meteo.in » et pour les fichiers

des émissions modifiés par « **FTP Put inpsmog** »

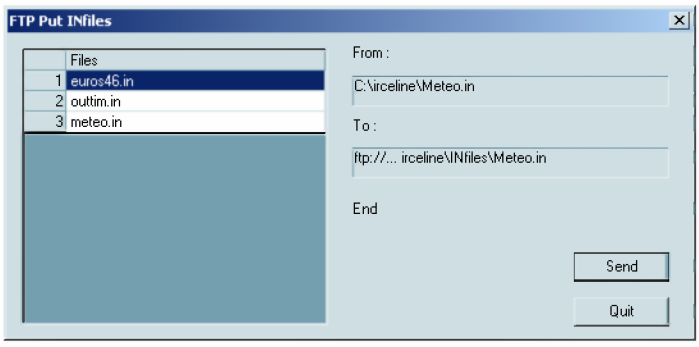

***Figure 49**: Boîte de dialogue de transfert des fichiers « Infiles ».*

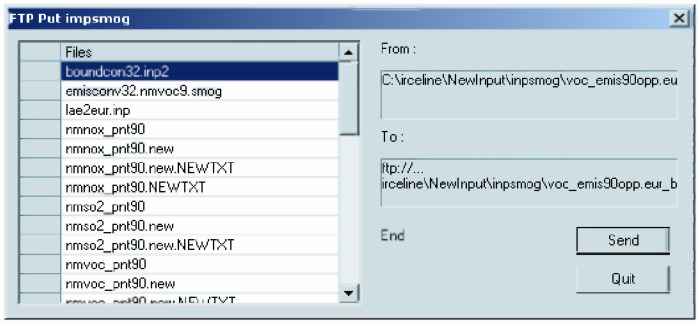

***Figure 50**: Boîte de dialogue de transfert des fichiers « impsmog ».*

de demander l'exécution du programme « EUROS », par l'action « **Start Euros** », pour la simulation choisie. Cette action est en relation avec « **Quit internet** » qui peut être considérée comme la seconde position d'un interrupteur. En poussant « **Start Euros** », une fenêtre de bienvenue apparaît. Elle permet de lancer la simulation en agissant sur le texte surligné à droite de l'intitulé « Start simulation ». Son action introduit la fenêtre bleue avec le texte « Login BelEUROS ». Pour continuer, trois champs doivent être obligatoirement complétés. Le champ « Login » prend le nom de l'utilisateur, « Organisation » celui de l'institution et « Password » le code réservé à l'utilisateur. L'écriture de ces champs doit obligatoirement respecter les « majuscules » et « minuscules ». En plus, l'utilisateur peut sous la rubrique « work » fixer la nature du travail demandé: « meteo » permet le transfert des seuls fichiers météo, « simulation » exécute le modèle EUROS, « meteo and simulation » cumule les deux choix précédents, les fichiers météo construits sont alors ceux qui correspondent aux dates de sorties de « outim.in ». Enfin « Outfiles compress » permet la compression des fichiers avant leur transfert.

L'action **« Quit internet »** maintenant disponible permet de mettre fin à la transaction de login.

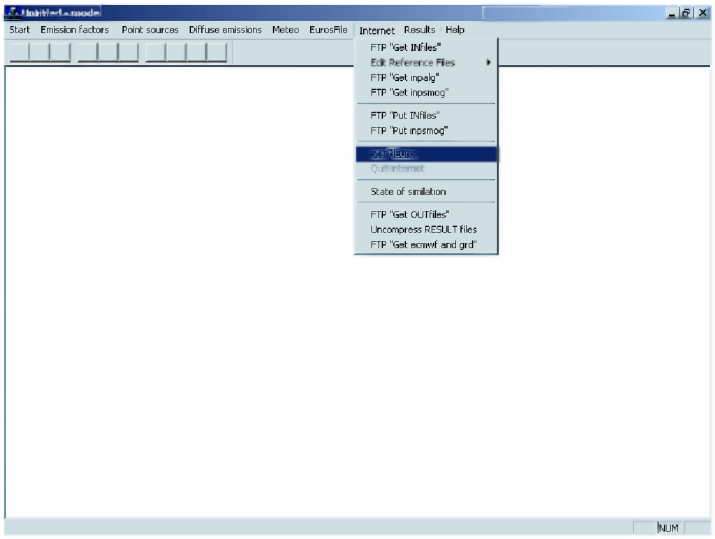

***Figure 51**: Line de menu « **Start Euros** » de l'option Internet.*

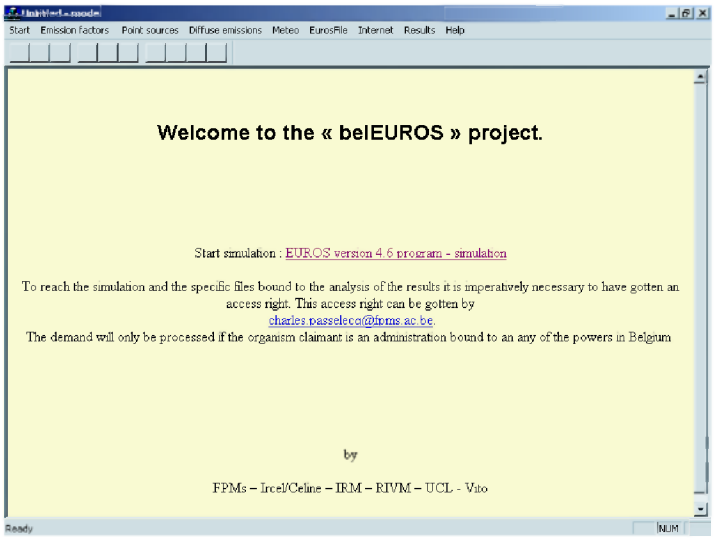

***Figure 52**: Fenêtre de bienvenue sur le site Internet de belEuros.*

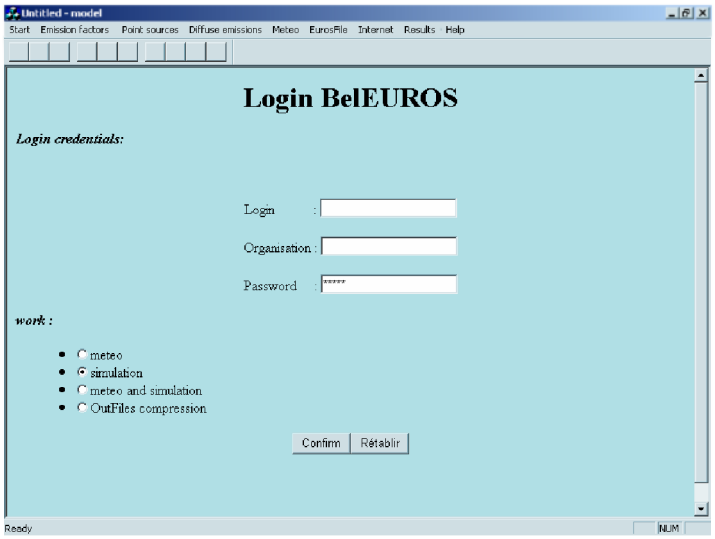

***Figure 53**: Fenêtre de login sur le site Internet de belEuros.*

a) de suivre le déroulement des calculs du modèle EUROS par l'action « **State of simulation** ».

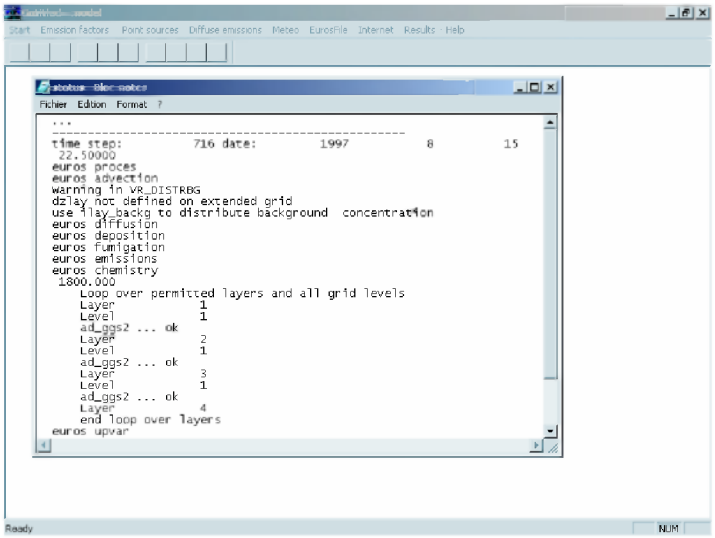

***Figure 54**: Fenêtre montrant l'état d'avancement de la simulation.*

b) de rapatrier chez l'utilisateur les fichiers demandés dans « outtim.in » par l'action de « **FTP Get OUTfiles** » et les fichiers météorologique relatifs à la simulation exécutée par l'intervention de « **FTP Get ecmwf and grd** ».

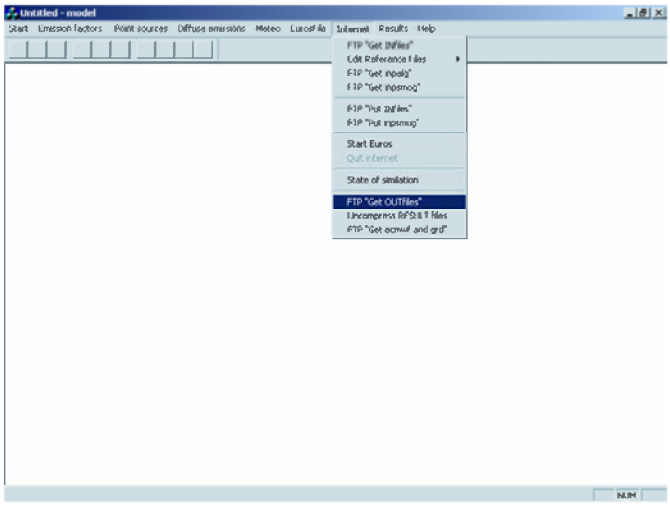

***Figure 55**: Ligne de menu « **FTP'Get OUTfiles** » de l'option Internet .*

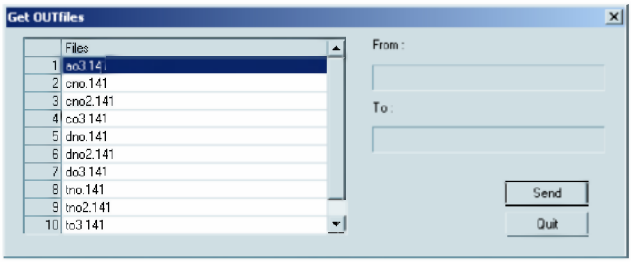

***Figure 56**: Boîte de dialogue de transfert des fichiers « **Get OUTfiles** ».*

Une fois les fichiers résultats rapatriés, il est nécessaire de les décompresser. L'action « **Uncompress RESULT files** » effectue automatiquement ce travail pour autant que le bouton « **Extract** » de la boîte de dialogue ci dessous soit poussé.

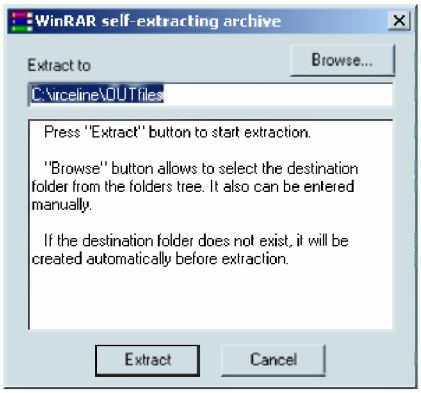

***Figure 57**: Boîte de dialogue qui permet de décompresser les fichiers résultats rapatriés.*

La liste des noms des fichiers décompressés s'affiche de la manière suivante:

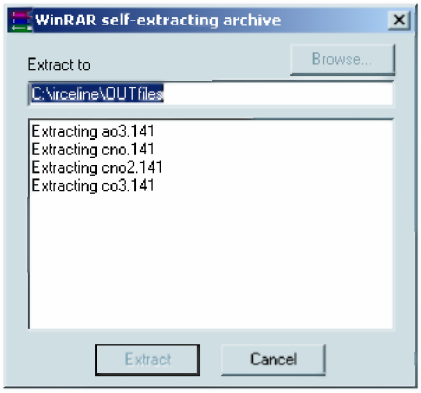

***Figure 58**: Boîte de dialogue qui permet de décompresser les fichiers résultats rapatriés.*

5.3.7 La ligne de menu « Results »

Cette option ne permet que d'afficher les résultats calculés. Pour rappels, les situations météorologiques étant éditables par l'action « **Meteo** ». Deux groupes d'actions sont disponibles:

a) Représentations spatiales

Cette première option permet de construire une cartographie des champs aux AOT (**A**ccumulated exposure **O**ver a **T**hreshold) et relatifs aux concentrations.

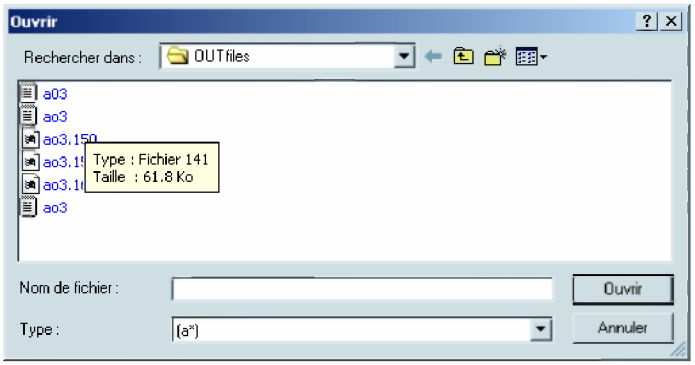

***Figure 59**: Boîte de dialogue permettant l'ouverture d'un fichier déterminé.*

L'utilisation de la ligne « AOTs » génère une Boîte de dialogue permettent de choisir le fichier à traiter. L'action « **Ouvrir** » de cette fenêtre, générée par le système d'exploitation, permet à l'utilisateur de choisir le fichier en fonction du composant chimique retenu, ici l'O_3. Chaque fichier AOT est reconnu par la présence de l'élément « a » dans son nom suivi du symbole chimique du composant analysé. Le chiffre correspond au numéro du « run » donné par l'utilisateur. Une fois un fichier

AOT choisi, la distribution spatiale suivante s'affiche à l'écran.

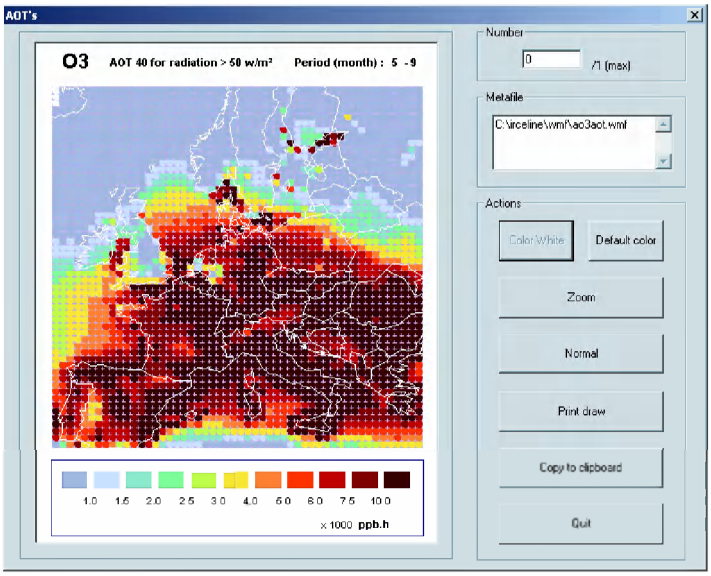

***Figure 60**: Boîte de dialogue des AOT's.*

Pour cette fenêtre l'utilisateur

- peut choisir dans l'encart « Number » le numéro de l'AOT calculé. Leur nombre maximum est indiqué à droite de l'ouverture. Il est à noter que la valeur affichée de l'AOT est exprimée dans l'unité de concentration affichée dans la légende (ppb.h).
- peut effectuer par « **Copy to clipboard** » une copie de la carte à la fois dans un fichier « Windows metafile » dont le nom est repris dans l'espace intitulé « Metafile » et dans le presse-papiers. Le nom du fichier peut être modifié dans l'intitulé « Metafile ».
- peut imprimer par « **Print draw** » la carte sur l'imprimante définie par défaut
- peut choisir la couleur des frontières de l'Europe. S'il clique sur le bouton « **Color White** » les frontières européennes sont dessinées en blanc. S'il désire la couleur par défaut (noir), il lui suffit de cliquer sur le bouton « **Default color** ».
- peut effectuer un zoom de la carte en cliquant sur le bouton « **Zoom** » ou la rétablir au format initial en cliquant sur le bouton « **Normal** ».

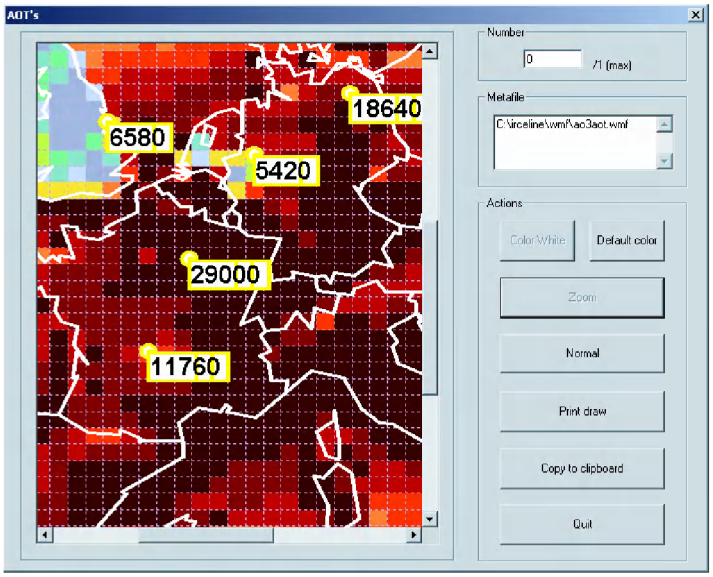

***Figure 61**: Boîte de dialogue des AOT's ou l'utilisateur à effectuer un zoom.*

- peut demander la valeur d'un AOT en une cellule déterminée de la carte en cliquant sur celui-ci avec le pointeur de la souris. La valeur locale exprimée par un entier s'affiche mais ne peut être effacée, sauf suite à une réinitialisation.

- quitte la boîte de dialogue par le bouton « **QUIT** ».

Pour afficher les résultats des concentrations, les actions sont les mêmes.

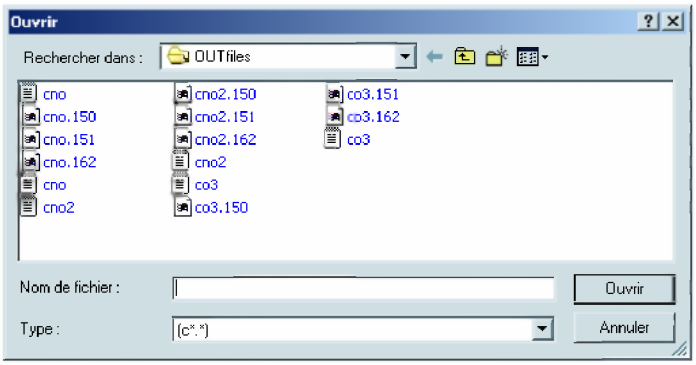

***Figure 62**: Boîte de dialogue permettant l'ouverture d'un fichier de son choix.*

L'action « **Ouvrir** » de cette fenêtre générée par le système d'exploitation, permet à l'utilisateur de choisir le fichier définissant les champs de concentrations en fonction des polluants retenus, NO, NO_2, O_3. Les fichiers relatifs aux concentrations sont

reconnus par la présence de l'élément « c » dans leurs noms. Une fois le fichier choisi, la distribution spatiale du composant chimique choisi s'affiche à l'écran en y reprenant la date, l'heure, le polluant et les valeurs extrêmes du champ de concentration.

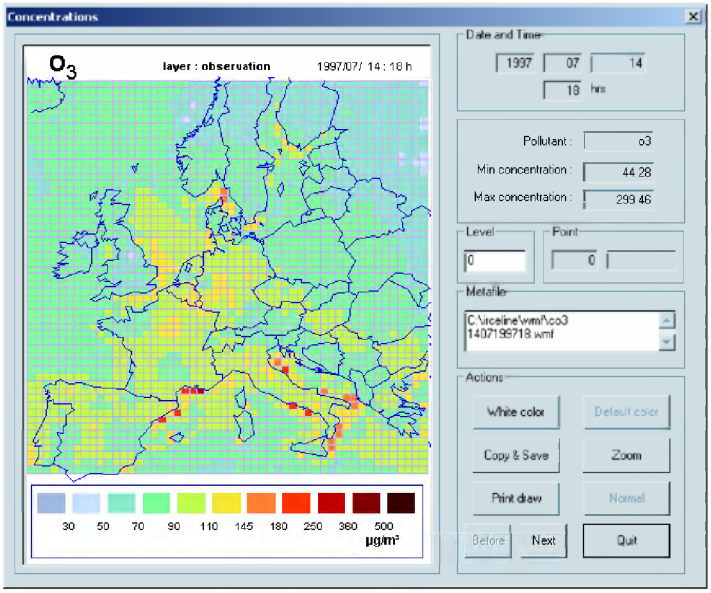

***Figure 63**: Boîte de dialogue des concentrations.*

Pour cette fenêtre, l'utilisateur

- peut introduire dans l'encart « Level » le numéro du champ de concentration relatif au niveau d'observation (0 - observation) ou à une des quatre couches formant la couche limite atmosphérique dans le modèle EUROS à savoir « 1 - surface », « 2 - mixing », « 3 - reservoir » et « 4 – upper ».
- peut effectuer par « **Copy & Save** » une copie de la carte à la fois dans un méta fichier dont le nom est repris dans l'espace intitulé « Metafile » et dans le presse-papiers. Le nom du fichier peut être modifié.
- peut imprimer par « **Print draw** » la carte sur l'imprimante définie par défaut
- peut choisir la couleur des frontières de l'Europe. Avec le bouton « **White color** », les frontières sont dessinées en blanc et avec la couleur par défaut, il suffit de cliquer sur « **Default color** ».
- peut passer à la carte suivante ou précédente, c'est-à-dire à la date et ou à l'heure suivante ou précédente, en cliquant respectivement sur les boutons « **Next** » ou « **Before** ».
- peut effectuer un zoom de la carte en cliquant sur le bouton « **Zoom** » ou la rétablir au format initial en cliquant sur le bouton « **Normal** ».

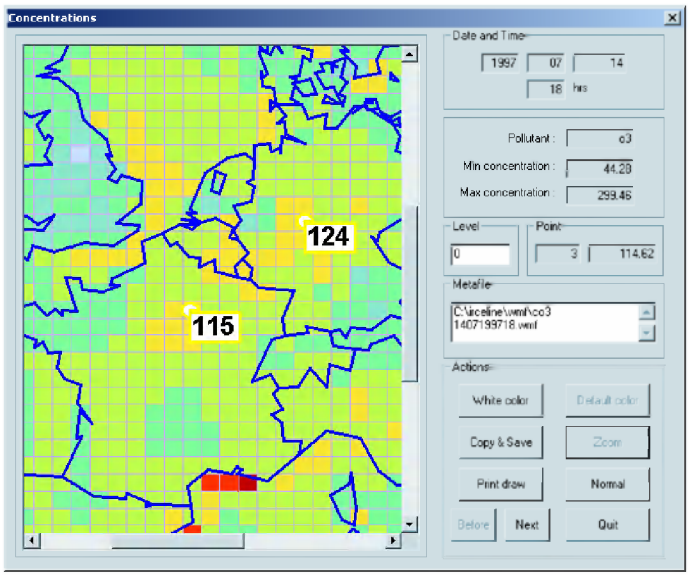

***Figure 64**: Boîte de dialogue des concentrations lorsque l'utilisateur a effectué un zoom.*

- peut demander la valeur de la concentration en une cellule déterminée de la carte en cliquant sur un point avec le pointeur de la souris. La valeur locale exprimée par un entier s'affiche sur le dessin mais sans une mise à jour complète de la carte. Le nombre de points affichés est indiqué sous la rubrique « Point » avec affichage de la dernière valeur choisie.
- quitte la boîte de dialogue par le bouton « **QUIT** ».

b) Evolutions temporelles

La seconde option donne une représentation graphique des évolutions temporelles horaires aux points d'observations retenus dans le fichier « outtim.in » pour la période de simulation considérée.

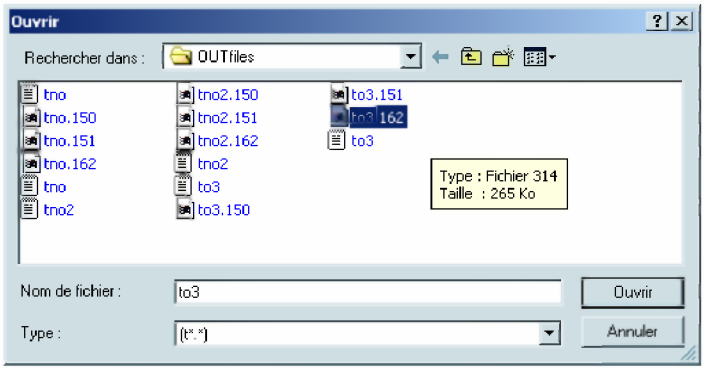

***Figure 65**: Boîte de dialogue permettant l'ouverture d'un fichier de son choix.*

L'action « **Ouvrir** » de cette fenêtre, générée par le système d'exploitation, permet à l'utilisateur de choisir le fichier définissant l'évolution temporelle en fonction des

polluants NO, NO_2 et O_3. Les fichiers relatifs aux évolutions temporelles sont reconnus par la présence de l'élément « t » dans leurs noms.

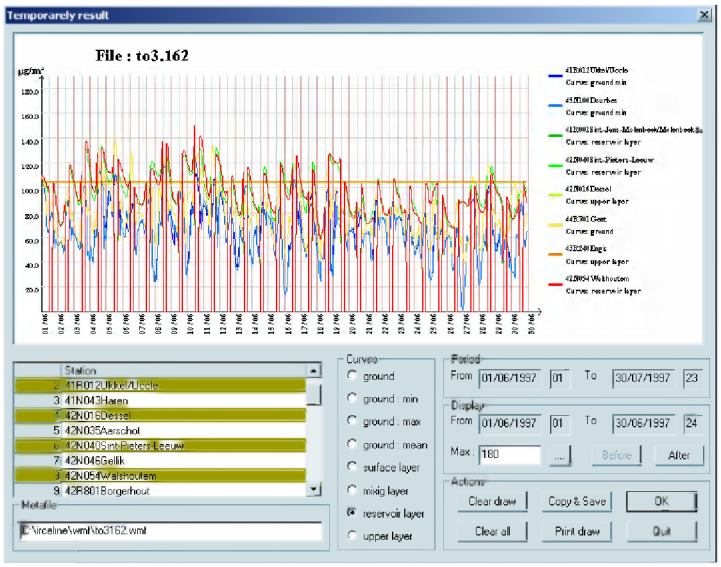

***Figure 66**: Boîte de dialogue des évolutions temporelles pour l'ozone.*

Grâce à cette fenêtre, l'utilisateur,

- peut afficher une ou plusieurs courbes en agissant à la fois dans la liste des stations « Station » et en fonction du type de courbes « Curves ». Le nombre de combinaison conduisant à une représentation graphique ne peut dépasser huit courbes à la fois, comme le montre le dessin de la fenêtre. Les choix retenus sont traduits explicitement à la droite du graphique. Pour changer seulement le graphique, il suffit d'agir sur le bouton « **Clear draw** ». Si on souhaite en plus remettre à zéro la sélection des stations, il suffit d'agir sur le bouton « **Clear all** ». Les courbes correspondent aux propositions suivantes:
  - « ground »: donne la concentration calculée au niveau du sol dans la maille du modèle EUROS contenant la station considérée.
  - « ground: min »: correspond à la valeur minimale des concentrations calculées dans la maille contenant la station et les huit mailles qui l'entourent.
  - « ground max »: correspond à la valeur maximale des concentrations calculées dans la maille contenant la station et les huit mailles qui l'entourent.
  - « ground mean »: correspond à la valeur moyenne des concentrations calculées dans les neuf mailles les plus proches de la station.

    - « surface layer »: donne la concentration dans la couche proche du sol (50m).
    - « mixing layer »: donne la concentration dans la couche mélangée.
    - « reservoir layer »: donne la concentration dans la couche réservoir.
    - « upper layer »: donne la concentration dans la couche sommet.
- possède les informations relatives à la période globale retenue dans l'intitulé « Period ».
- possède également des informations sur la période affichée dans l'intitulé « Display ». Les boutons « Before » et « After » permettent de voyager dans l'intervalle de temps par saut de trente et un jours au maximum. L'action d'un de ces boutons entraîne la mise à jour du graphique.
- peut changer l'échelle en introduisant la nouvelle valeur dans l'intitulé « Max ».
- peut effectuer avec « Copy & save » une copie du graphique à la fois dans un méta fichier dont le nom est repris dans l'espace intitulé « Metafile » et dans le presse-papiers. Le nom du fichier peut être modifié dans l'intitulé « Metafile ».
- peut imprimer avec « Print draw » le graphique sur l'imprimante définie par défaut.
- quitte la boîte de dialogue par le bouton « **QUIT** ».

5.4 Actions pour créer un scénario

1) Préparation de scénario

Les potentialités du logiciel ayant été présentées, ce chapitre décrit les objectifs d'une simulation, les données mises à disposition et finalement les étapes pour les mettre en œuvre.

a) Objectifs de la simulation

Il est intéressant de rappeler que l'objectif actuel n'est pas une utilisation en « temps réel » du modèle EUROS. Ce modèle doit surtout servir à déterminer sur la base de situations connues quel est l'impact d'une décision. Il est essentiellement conçu pour être une aide à la décision politique. La possession d'un tel modèle est devenu essentiel pour aider à initier une nouvelle politique de l'environnement.

b) Données mises à disposition

Pour effectuer les simulations en Europe, on dispose de fichiers de données d'émission relatives à plusieurs secteurs économiques. Ces fichiers donnent les moyennes annuelles d'émission. D'autres fichiers donnent un rapport d'intensité, par

rapport aux valeurs annuelles, en facteurs dépendant des mois, des jours et des heures, l'intégration sur la période d'un an devant restituer la valeur de l'émission annuelle. Cette condition est réalisée à l'aide d'une normalisation.

c) Etapes pour les mettre en oeuvres

Les étapes principales de la mise en œuvre d'un scénario sont reprises dans l'organigramme ci-après.

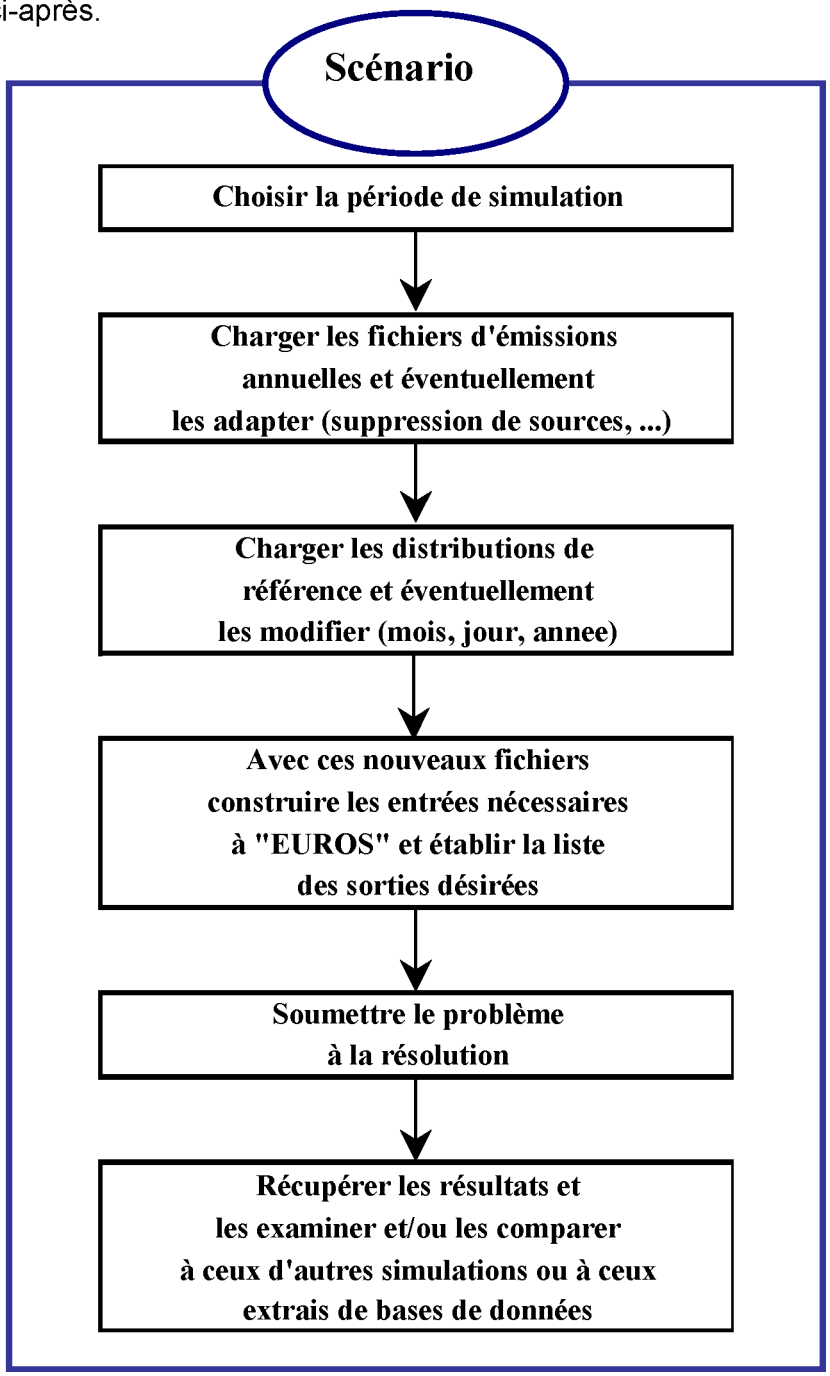

***Figure 52**: Organigramme résumé de la mise en œuvre d'un scénario.*

2) Activation de la simulation

L'activation de la simulation se fait sur le serveur situé à la cellule Celine par l'intermédiaire d'une connexion Internet sécurisée. Pour réaliser cette connexion aucun « navigateur » n'est nécessaire, ce dernier faisant partie intégrante de l'interface. Le sous menu « **Start Euros** » de l'option « **Internet** » génère une page html classique qui ouvre le dialogue avec l'extension serveur ISAPI. Celle-ci donne accès à un formulaire de demande de travail. Pour soumettre le travail, il est indispensable d'avoir une autorisation d'accès. Si cette dernière existe, il suffit de remplir les champs du formulaire et de proposer la requête. L'appui sur le bouton « **submit** » envoie la requête à l'extension serveur qui vérifie les permissions de l'utilisateur. Si elles sont correctes un nouveau formulaire de confirmation apparaît. L'acceptation conduit à lancer les opérations demandées sur le serveur. Il faut à ce moment quitter le Web. On peut alors à tout moment suivre l'état d'avancement du calcul.

En ce qui concerne la liaison Internet nous avons opté pour une connections non permanente avec possibilité d'interrogation ponctuelle puisque le calcul peut prendre jusqu'à une journée.

Les accès via le Net se résume donc à:

1°) transférer les fichiers d'entrée à modifier

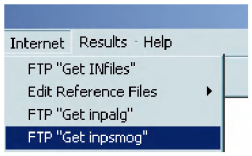

***Figure 53** : Option « Internet » de la barre des tâches.*

2°) transférer les fichiers modifiés et les fichiers « euros46.in », « outim.in » et « meteo.in »

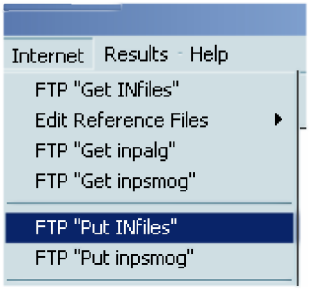

***Figure 56**: Option « Internet » de la barre des tâches.*

3°) soumettre les fichiers créés avec l'option « Start Euros »

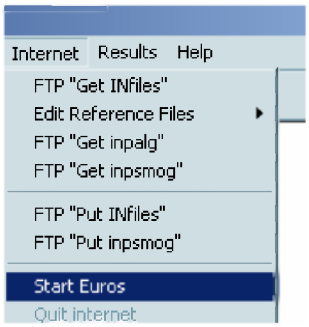

***Figure 57**: Ligne de menu « Start Euros » de l'option « Internet ».*

4°) suivre l'état d'avancement du calcul d'Euros

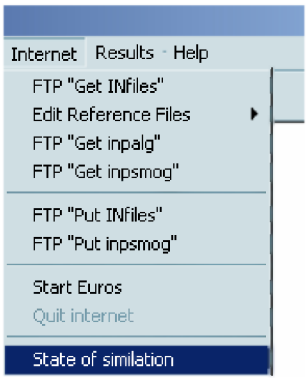

***Figure 58**: Ligne de menu « State of simulation » de l'option « Internet ».*

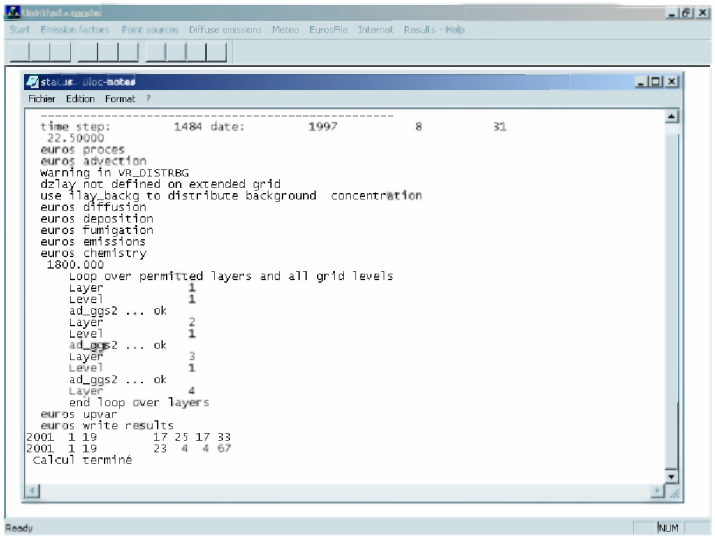

***Figure 59**: Fenêtre montrant l'état d'avancement de la simulation.*

5°) récupérer les résultats sous forme de fichiers compressés si la demande en a été faite explicitement. Cette récupération s'accompagne de l'effacement automatique des fichiers résultats sur le serveur. La responsabilité de la conservation des résultats est à charge exclusive du client.

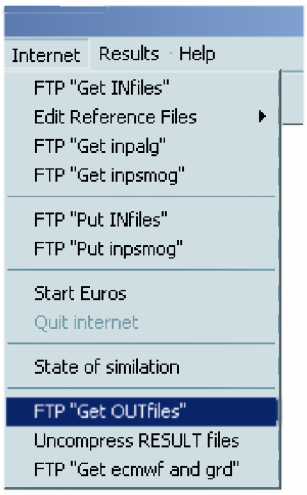

***Figure 60**: L'option « Internet » de la barre des tâches.*

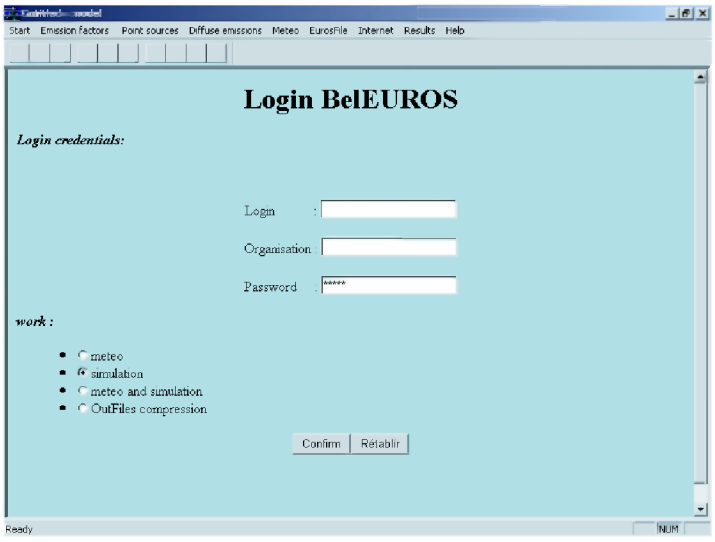

***Figure 61**: Fenêtre de login sur le site Internet de belEuros.*

3) Analyse des résultats

L'analyse des résultats se fait au départ de plusieurs fichiers construits par le logiciel EUROS. Ces fichiers appartiennent à trois catégories:

- les fichiers relatifs à la distribution spatiale des AOT.
- les fichiers relatifs à la distribution spatiale de la concentration des composants chimiques retenus.
- les fichiers relatifs aux évolutions temporelles des concentrations en des points géographiques choisis.

Ils sont stockés sous des formats divers et sont non modifiables ou d'évolution temporelle.

Pour faciliter l'interprétation physique des phénomènes, l'interface utilisateur donne, sans utilisation d'outils extérieurs, une représentation des résultats sous forme cartographique.

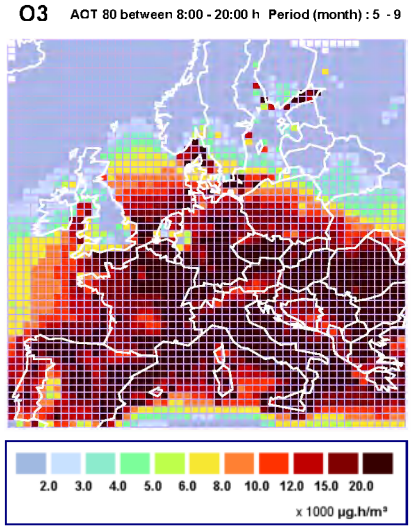

***Figure 62**: Distribution spatiale des AOT.*

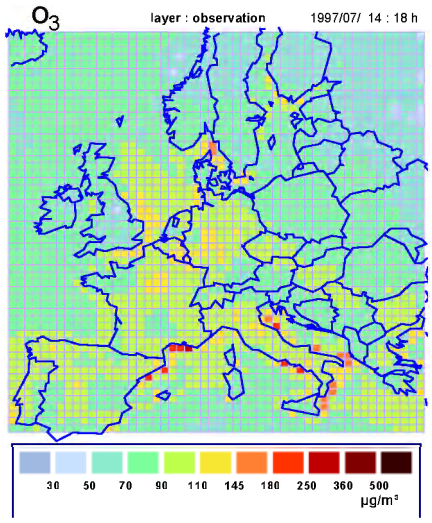

***Figure 63**: Distribution spatiale de la concentration en ozone.*

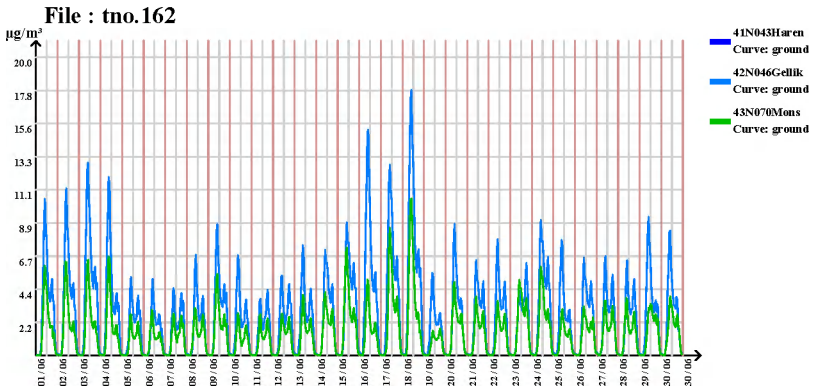

***Figure 64**: Evolutions temporelles des concentrations en NO pour trois récepteurs.*

Chaque résultat visualisé peut être stocké sous la forme d'un fichier « *.wmf » facilement importable dans un traitement de texte ou dans tout autre logiciel de présentation.

En plus, comme la connaissance des phénomènes météorologiques peut s'avérer indispensable à l'interprétation des résultats, une option « **météo** » a été introduite pour visualiser la météorologie ayant servi aux calculs dans le modèle EUROS. Cette option permet d'obtenir les champs météorologiques découlant du modèle de prévision du temps au ECMWF.

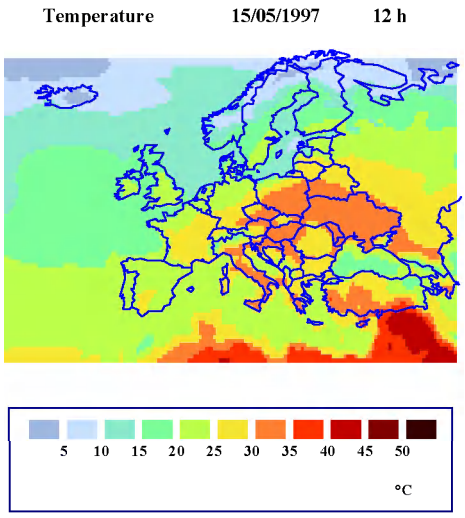

***Figure 65**: Exemple: champ de température au niveau d'observation.*

5.5 Conclusions

Dans le contexte actuel de prise de conscience de l'influence de l'activité humaine sur la qualité de la vie par l'intermédiaire de l'environnement, il apparaît nécessaire aux « décideurs » de posséder des outils de simulation pour faire des études d'impact.

Toutefois, pour que ces outils ne soient pas réservés aux seuls « spécialistes informatiques » ces outils doivent être accessibles et offrir une approche conviviale. Il faut que l'environnement de travail soit tel qu'il puisse permettre à l'utilisateur de se concentrer sur le problème à analyser sans être distrait par des problèmes « d'intendance ».

L'interface utilisateur développée autour du modèle EUROS répond à ce souhait d'autant plus qu'il donne accès via « Internet » à des moyens de calcul dont un utilisateur « occasionnel » ne pourrait peut être pas disposer personnellement.

6 IMPACT MODELLERING [5]

6.1 Inleiding

Dit hoofdstuk beschrijft het werkpakket 6 van BelEUROS betreffende de impact modellering. De bedoeling is de effecten van ozon op de gezondheid en de vegetatie in kaart te brengen met behulp van de resultaten van EUROS. De vergelijking met de Europese richtlijnen betreffende luchtverontreiniging door ozon is ook van groot belang.

In hoofdstuk 6.2 worden de effecten op de gezondheid en de vegetatie beschreven. Die effecten worden gemodelleerd aan de hand van blootstelling-effect relaties. Een kort overzicht van die relaties wordt gegeven. In hoofdstuk 6.3 wordt de huidige Europese wetgeving betreffende ozon beschreven alsook het nieuwe voorstel in voorbereiding. In hoofdstuk 6.4 wordt een samenvatting gegeven van alle indicatoren die voorlopig gebruikt worden. In het laatste hoofdstuk beschrijven we de manier waarop die indicatoren met behulp van EUROS kunnen worden berekend.

[5] The content of this chapter is taken from the intermediate report: Delobbe L., C. Mensink, R. Torfs and L. De Nocker, 2001. Implementatie en uitbreiding van het EUROS Model voor Beleidsondersteuning in België: Impact Modellering, scientific report, 2001/TAP/R/002, Vito, Mol.

6.2 Effect van ozon op gezondheid en vegetatie

6.2.1 Effect op gezondheid

Door zijn oxiderende capaciteit heeft ozon nadelige effecten op de gezondheid. De mogelijke effecten van hoge ozonconcentraties in de lucht zijn de volgende:

- Longfunctievermindering
- Luchtwegsymptomen als hoest, pijn op de borst, kortademigheid
- Mogelijke gevoelens van onbehagen, benauwdheid, hoofdpijn, misselijkheid, duizeligheid bij gevoelige personen
- Toename ernst en frequentie van symptomen bij personen met CARA (chronische aspecifieke respiratoire aandoeningen: ziekten van luchtwegen zoals astma en bronchitis)

Andere ongewenste stoffen maken deel uit van de zomersmog (o.a. peroxyacetylnitraat PAN, aromatische olefinene, butadieen, …). Die stoffen zijn verantwoordelijke voor prikkende ogen, hoest en irritatie van de slijmvliezen. Bij de huidige concentraties vormen de nadelige effecten van die stoffen blijkbaar geen belangrijk probleem voor de volksgezondheid.

Volgens de Wereld Gezondheidsorganisatie (WHO, 2000) doen acute kortetermijn effecten zich voor bij ozonconcentraties vanaf 160 $\mu g/m^3$. Bij kinderen treedt longfunctievermindering op als gevolg van kortetermijn blootstelling aan ozon in de range 120-240 $\mu g/m^3$. De "WHO Guidelines for Air Quality " (WHO, 2000) bevelen een doelstelling voor ozon aan van 120 $\mu g/m^3$ voor een maximale duur van 8 uur per dag. Desalniettemin kunnen gezondheidseffecten bij lagere concentraties niet worden uitgesloten.

6.3 Blootstellings-effect relaties voor gezondheid

Hierna geven we een kort overzicht van de blootstellings-effect relaties die voorlopig worden gebruikt. Voor meer details verwijzen we naar De Nocker en Torfs (2001) en Holland et al. (1999).

De concentratie van polluenten in omgevingslucht, waaraan een bevolking wordt blootgesteld, kan via een functie gekoppeld worden aan de mogelijke gezondseheidseffecten of eindpunten. Die functies worden bepaald op basis van epidemiologische en toxicologische studies. Het individuele blootstellingniveau hangt af van persoonlijke activiteiten, het aantal uren in de buitenlucht enz. De toename

van energiezuinige, maar slecht geventileerde woningen, kan het belang aan binnenhuisvervuiling doen toenemen. Hier wordt niet verder op ingegaan.

Grootschalige epidemiologische studies zoals APHEA ("Air Pollution and Health: a European Approach". Research project of the European Comission.) (APHEA2, 1998) hebben lineaire verbanden gelegd tussen ozon en acute sterfte en hospitaalopnames. In het algemeen wordt aangenomen dat de effecten van ozon kunnen gekwantificeerd worden en additief zijn aan deze van zwevend stof.

De manier waarop de effecten van ozon gekarakteriseerd worden verschillen van studie tot studie. Indicatoren als dagelijks uurlijks maximum (i.e. het maximum van de 24 1uur-gemiddelde waarden), dagelijks 5, 8, of 24 uur gemiddelde worden naast elkaar gebruikt. Verschillende blootstelling-effect relaties worden ontwikkeld in de loop van een aantal Externe projecten (ExterneE : Externalities of Energy. Research project of the European Comission[6]). De ExternE Methodologie wordt beschreven in Holland et al. (1999) (Hfstk. 8) en Holland et al. (1995) (Hfstk. 4). In die studies worden de blootstellings-effect relaties op dit ogenblik uitgedrukt aan de hand van het dagelijks 6 uur gemiddelde. Een korte beschrijving van de Externe Methodolgie wordt gegeven in bijlage. Het gebruik van deze blootstellings-effect relaties in een andere context dan deze waarbinnen ze afgeleid zijn, brengt onzekerheden met zich mee. Toch stelt men vast dat een groot aantal studies deze effecten beschrijven en kwantificeren, en dat de onzekerheid de laatste jaren afgenomen is.

De methodologische aanpak om de gezondheidseffecten te kwantificeren bestaat uit het vastellen:

a. Welke polluenten (in dit geval enkel ozon) in de lucht *geassocieerd* zijn met negatieve gezondheidseffecten (acuut of chronisch) en welke eindpunten ze beïnvloeden (sterfte, luchtwegaandoeningen,…);
b. Welke van deze associaties kan geïnterpreteerd worden als zijnde *causaal*, omdat de kwantificering van de effecten van een toegenomen luchtverontreiniging een causaal verband vereist;
c. Welke individuele studie of meta-analyse van epidemiologische studies een representatieve waarde geeft om effecten te kwantificeren, wanneer causaliteit voor een bepaalde impact van een polluent is aanvaard;
d. Hoe de blootstellings-effect relaties van deze studies kunnen aangepast worden om te gebruiken in het studiegebied (in casu Vlaanderen en Europa);
e. Welke combinatie of 'set' van kwantificeerbare blootstellings-effect relaties een geschikte basis vormen om de gezondheidseffecten van toegenomen luchtverontreiniging te bepalen.

[6] Zie ExternE website: http://externe.jrc.es

Wij verwijzen naar de volgende referenties voor een aantal effecten die werden bestudeerd.

- Acute mortaliteit (gekwantificeerd in termen van verloren levensjaren YOLL "Years of Life Lost"): Sunyer et al., 1996

- Respiratoire ziekenhuisopnames: Ponce de Leon et al., 1996

- Spoedopnames voor astma: Cody et al., 1992; Bates et al., 1992

- Dagen met beperkte activiteit (Restricted Activity Days): Ostro en Rothshild, 1989

- Acute effecten bij astmatici: Whittemore and Korn, 1980

De relaties die in die studies voorgesteld worden zijn meestal linaire relaties zonder drempel. Voor ozon bestaat er onenigheid over een drempelwaarde waaronder geen effecten voorkomen. De gehanteerde richtlijn van 120 µg/m³, die niet langer dan 8 uur mag overschreden worden, wordt door de WHO aanzien als een waarde waarbij de acute effecten op de volksgezondheid waarschijnlijk klein zijn. APHEA (Touloumi et al., 1997; Spix et al., 1998) heeft uitgewezen dat er ook een significant verband kan gelegd worden tussen uurlijkse en 8 uurlijkse maximale concentraties aan ozon, uitgemiddeld over een jaar of een seizoen (zoals GMD-max8u), en effecten op gezondheid bij gevoelige groepen in de maatschappij. Dit geeft aan dat mortaliteit en hospitaalopnames ook optreden bij langdurige blootstelling aan lagere concentraties. Of en waar een drempelwaarde ligt, wordt niet bepaald in deze studies.

Bij het begroten van effecten op gezondheid kan dus zowel een hoge inschatting (zonder drempel) als een lage (met drempel van 120 µg/m³, op basis van de indicator AOT60ppb-max8u) gemaakt worden. Deze vork geeft een indicatie van onzekerheden voor het beleid.

Door een 'set' van functies te gebruiken wordt de globale onzekerheid kleiner en zijn de uitkomsten van de kwantificering robuuster. Interpretatie in termen van welke impacts belangrijk zijn (beleidsconclusies), wordt eenvoudiger.

De Wereld Gezondheidsorganisatie (WHO, 2000) hanteert zijn eigen set van functies, deels afgeleid uit de meta-analyses van APHEA. Figuren 1 tot 4 in Delobbe et al. (2001) tonen blootstellings-effect relaties voor de volgende effecten:

- Verandering in FEV_1 = forced expiratory volume in first second of expiration (uitgeademd volume tijdens de eerste seconde van een geforceerde uitademing)
- Verandering in kans op ontstekingen van longen
- Verhoging in ziekenhuisopnames voor respiratoire problemen
- Verhoging in irritatiesymptomen

Twee indicatoren werden gebruikt, namelijk het maximale dagelijkse 1h-gemiddelde en het maximale 8h-gemiddelde per dag. De Figuren laten zien dat de gevoeligheid voor het 8h-gemiddelde groter is dan voor het 1h-gemiddelde. Dit verantwoordt de keuze voor de 8h-gemiddelde als nieuwe grenswaarde voor de bescherming van de gezondheid in het nieuwe voostel voor een europese richtlijn.

6.3.1 Effect op vegetatie

Ozon is een bijzondere toxische polluent, zowel voor bossen, natuurlijke planten als voor commerciële gewassen. O_3 is een zeer reactief gas dat bijgevolg vooral schade aanricht aan de celmembranen. Enige accumulatie of rechtstreekse interactie met het celmetabolisme lijkt daarom uitgesloten. Naast (of als gevolg van) een verstoring van de membranen is de beïnvloeding van de werking van de stomata een vrij algemeen mechanisme.

Bij hoge ozon concentraties zijn de voornaamste fysiologische processen aangetast en kan de productiviteit van de landbouwgewassen sterk verminderd zijn. De bosecosystemen kunnen eveneens worden aangetast. Een overzicht van de verschillende mechanismen waardoor ozon vegetatie beschadigt, wordt gegeven in De Temmerman en Vandermeiren (1999) (OZON DWTC).

Om de blootstelling van ecosystemen aan ozon te kwantificeren werd een normering uitgewerkt door de Wereld Gezondheidsorganisatie (WGO) en de Economische Commissie Europa van de Verenigde Naties (UN ECE) de WGO en de UNECE (United Nations, Economic Comission for Europe). Een waarde van 40 ppb (80 $\mu g/m^3$) wordt beschouwd als een goede drempelwaarde voor schade aan vegetatie. Deze drempel wordt regelmatig overschreden in Europa. De cumulatieve blootstelling boven 40 ppb heet de AOT40-waarde (Accumulated exposure Over a Treshold) en is gelijk aan de som over een bepaalde periode van alle positieve

verschillen tussen de waargenomen ozonconcentratie en 40 ppb voor elk uur tussen 8 en 20 MET (Midden-Europese Tijd). Soms wordt de AOT40 ook berekend voor alle daglichturen (lichtinval > 50W/m²). De cumulatieve blootstelling wordt uitgedrukt in ppb.uren.

Gewassen en semi-natuurlijke vegetatie

Uit experimentele studies bleek dat bij een AOT40 van 3000 ppb.uren landbouwgewassen een opbrengsverlies van 5 % vertonen. De AOT40 wordt berekend voor de 3 groeimaanden (mei, juni, juli) (Kärenlampi L. en Skärby L.L., 1996). Deze kritische blootstelling van 3000 ppb.uren werd opgesteld op basis van gegevens voor tarwe maar is vermoedelijk ook geldig voor andere gevoelige gewassen zoals katoen, tabak, raap, tomaat, aardappelen. Deze grenswaarde wordt naar voren geschoven als langetermijndoelstelling voor blootstelling van landbouwgewassen en van natuurlijke vegetatie aan ozon.

Bossen

Voor bossen wordt de AOT40 ook gebruikt maar wordt hier berekend als de som van de blootstelling boven 40 ppb over de periode april-september. Een grenswaarde van 10000 ppb.uren wordt voorgesteld door WGO en UNECE als langetermijndoelstelling.

6.3.2 Blootstelling-effect relaties voor vegetatie

De AOT40 laat toe de procentuele theoretische opbrengstvermindering door cumulatieve blootstelling boven de 40 ppb ozon (= 80 µg/m^3) te schatten. Deze opbrengstvermindering is gebaseerd op de nieuwe definitie door UNECE van het kritische niveau op lange termijn.

In de methode om milieuschadenkosten te bepalen (de ExternE methodologie) hanteert men dezelfde bron, om opbrengstverliezen en marginale opbrengstverliezen te bepalen. Hiervoor worden bomen en landbouwgewassen opgedeeld in 4 categorieën, met elk hun risicodrempel waarbij de opbrengst of groei afneemt met 10%. Een opbrengstverlies van 10% wordt bekomen bij onderstaande (zgn. kritische) concentraties.

- Tolerant : geen kritische dosis (bijv., Maïs, zacht fruit)
- Licht gevoelig: AOT40 = 10 ppm-h (bijv., Sojabonen)
- Gevoelig: AOT40 = 5.7 ppm-h (bijv., tarwe, aardappel, tomaat)
- Zeer gevoelig: AOT40 = 2.9 ppm-h (bijv., tabak)

Elke categorie omvat zowel groenten, bomen als wilde planten. De meeste bruikbare dosis-effect functies gebruiken de cumulatieve concentratie boven 40ppb als maat voor de dosis. Deze wordt uitgedrukt in ppm.h. De periode waarover wordt gesommeerd hangt af van de lengte van het groeiseizoen en verschilt van plant tot plant. Voor landbouwgewassen wordt meestal 3 maanden gerekend.

In eerste instantie (in *level I* studies, waar er geen onderscheid is tussen verschillende species) zijn deze waarden enkel te gebruiken als een indicator voor het potentiële risico op vermindering van groei of opbrengst (Kärenlampi L. en Skärby L.L., 1996). Nochtans kunnen deze risico's vertaald worden in functies die het verlies aan opbrengst kwantificeren. Jones et al. (1997) concludeerden na een doorlichting van de beschikbare studies dat een er evidentie is om de resultaten in functie van de AOT40 lineair te extrapoleren over een significant bereik. Mogelijke onzekerheden en problemen zijn hierbij:

- De gevoeligheid van verschillende gewassen;
- De veranderlijke gevoeligheid van planten over een levenscyclus;
- Interacties tussen ozon en andere polluenten;
- Adaptatiemechanismen aan ozon impacts;
- Vochtigheid en beschikbaarheid van water.

Dit is een potentieel belangrijke oorzaak voor fouten. Bij droog en warm weer sluiten de stomata zich zodat opname van ozon verhinderd wordt. Dit fenomeen speelt vooral een rol voor ozon impacts op planten in droge niet-geïrrigeerde gebieden. In onze streken, waar over de algemeen landbouwgebieden goed geïrrigeerd zijn, zal dit effect geen grote rol spelen.

Voor gevoelige species wordt de functie voor tarwe als voorbeeld genomen, nl.

$$y(\%) = 99.7 - 1.7 \times \mathrm{AOT40}_{(ppm.h, daglichturen)}$$

met $y(\%) = \text{relatieve opbrengst}$

zodat

$$Y = \left[0.997 - 0.017 \times \mathrm{AOT40}_{(ppm.h, daglichturen)}\right] \times Y0$$

met $Y = \text{werkelijke opbrengst}$

$Y0 = \text{opbrengst zonder ozon verontreiniging}$

Voor licht gevoelige species wordt de helling van deze functie gedeeld door 2, voor zeer gevoelige vermenigvuldigt met 2.

De aldus bepaalde opbrengstverliezen, uitgedrukt als percentage van de verwachte opbrengst in afwezigheid van een ozonverontreiniging, kunnen niet direct toegepast worden om de impacts van een marginale verhoging van luchtverontreiniging te bepalen. Er moet nog gecorrigeerd worden voor de achtergrondconcentraties die op zich al de te verwachte opbrengst beïnvloeden. De marginale relatieve opbrengstverliezen worden bepaald aan de hand van

$$\frac{Y(BG) - Y(BG + DC)}{Y(BG)} = \frac{0.017 \times \left(AOT40_{BG+DC} - AOT40_{BG}\right)}{0.997 - 0.017 \times AOT40_{BG}}$$

Y = opbrengst
BG= achtergrondconcentratie;
DC= incrementele of marginale concentratie.

Het volstaat de verhouding te bepalen om de opbrengstverliezen te kwantificeren m.b.v. de reële marktprijzen.

6.4 Wetgeving betreffende luchtverontreiniging door ozon

De wetgeving betreffende luchtverontreiniging door ozon wordt bepaald op het Europese niveau. De huidige wetgeving wordt omschreven in de Richtlijn 92/72/EEG van de Raad van de Europese Gemeenschappen. Een nieuwe richtlijn zal binnenkort verschijnen. Het voorstel voor die richtlijn wordt ook hierna beschreven.

Europese wetgeving

- **Richtlijn 92/72/EEG van de Raad van de Europese Gemeenschappen betreffende de verontreiniging van de lucht door ozon**

  - **Drempelwaarde voor de bescherming van de volksgezondheid**
    110 μg/m^3 voor de gemiddelde waarde over acht uur [7]

  - **Drempelwaarde voor de bescherming van de vegetatie.**
    200 μg/m^3 voor de gemiddelde waarde over één uur
    65 μg/m^3 voor de gemiddelde waarde over 24 uur

[7] Het gemiddelde over acht uur is een voortschrijdend gemiddelde zonder overlapping, het wordt viermaal per dag berekend op basis van de acht uurwaarden tussen 0 uur en 9 uur, 8 uur en 17 uur, 16 uur en 1 uur, 12 uur en 21 uur

- **Drempelwaarde voor het informeren van de bevolking**
  180 μg/m^3 voor de gemiddelde waarde over één uur

- **Drempelwaarde voor de alarmering van de bevolking**
  360 μg/m^3 voor de gemiddelde waarde over één uur

- **Voorstel voor een nieuwe richtlijn in het kader van de EU kaderrichtlijn 96/62/EC inzake de beoordeling en het beheer van de luchtkwaliteit.**

Streefwaarden voor 2010:

- **Streefwaarde voor de bescherming van de volksgezondheid**:
  120 μg/m^3 voor de hoogste 8-uursgemiddelde concentratie van de dag[8]. Die waarde mag niet overschreden worden gedurende meer dan 25 dagen per kalender jaar, uitgemiddeld over drie jaren.

- **Streefwaarde voor de bescherming van de vegetatie**.
  18000 μg/m^3.h voor de AOT40 [9] per jaar als gemiddelde over 5 jaren. De AOT wordt berekend uit 1h-waarden over de periode mei tot juli tussen 8 en 20 uur MET.

Langetermijndoelstellingen

- **Doelstelling voor de bescherming van de volksgezondheid**
  120 μg/m^3 voor de hoogste 8-uursgemiddelde concentratie van de dag binnen één kalender jaar.

- **Doelstelling voor de bescherming van de vegetatie**
  6000 μg/m^3.h voor de AOT40 berekend uit 1h-waarden over de periode mei tot juli tussen 8 en 20 u. MET.

[8] Het gemiddelde over acht uur moet hier om het uur berekend worden (het aangegeven tijdstip is het einde van de 8 uursperiode waarover werd gemiddeld.
[9] AOT = Accumulated exposure Over 40 ppb Threshold. Som van de verschillen tussen ozonconcentratie boven 40 ppb (80 μg/m^3) en 40 ppb van alle uurwaarden tussen 8 en 20 uur MET (Midden-Europese Tijd) over een bepaalde periode (mei tot juli voor de AOT40-vegetatie).

Informeren en alarmeren van de bevolking:

- **Drempelwaarde voor het informeren van de bevolking**
  180 $\mu g/m^3$ voor de gemiddelde waarde over één uur

- **Drempelwaarde voor de alarmering van de bevolking**
  240 $\mu g/m^3$ voor de gemiddelde waarde over één uur voor 3 uren achtereen

6.5 Samenvatting van alle indicatoren

In de vorige sectie werden een aantal indicatoren beschreven die worden gebruikt in de Europese wetgeving. Andere indicatoren werden voorgesteld als richtwaarden of doelstelling door verschillende instanties (WGO, UNECE United Nations Economic Comission for Europe, nationale en regionale instanties[10]). Hierna geven we een overzicht (inventaris) van alle indicatoren die voorlopig worden gebruikt.

- **NET60** (Number of Exceedances Threshold): aantal dagen per kalenderjaar waarop in minstens 1 meetplaats (in een bepaald land of regio) een overschrijding van 120 $\mu g/m^3$ door de hoogste 8-uursgemiddelde concentratie van een dag wordt geregistreerd.

- **AOT40-vegetatie**: Accumulated exposure Over 40 ppb Threshold. Som van de verschillen tussen ozonconcentratie boven 40 ppb (80 $\mu g/m^3$) en 40 ppb van alle uurwaarden tussen 8 en 20 uur MET (Midden-Europese Tijd) tijdens de 3 maanden mei, juni en juli.

- **AOT40-bossen**: Accumulated exposure Over 40 ppb Threshold. Som van de verschillen tussen ozonconcentratie boven 40 ppb (80 $\mu g/m^3$) en 40 ppb van alle uurwaarden tussen 8 en 20 uur MET (Midden-Europese Tijd) tijdens de 6 maanden april tot en met september.

- **AOT60-1h**: Accumulated exposure Over 60 ppb Threshold. Som van de verschillen tussen ozonconcentratie boven 60 ppb (120 $\mu g/m^3$) en 60 ppb van alle uurwaarden gedurende een kalender jaar.

- **AOT60-max8h**: Accumulated exposure Over 60 ppb Threshold. Som van de verschillen tussen ozonconcentratie boven 60 ppb (120 $\mu g/m^3$) en 60 ppb van alle dagelijkse grootste 8-uursgemiddelden gedurende een kalender jaar.

[10] Zie Dumont et al. (2000) in MIRA-S rapport voor Vlaanderen

- **GMD-max8h**: gemiddelde over een seizoen of jaar van de hoogste 8-uursgemidelde concentratie van de dag.

Voor een bepaalde periode en voor een bepaalde locatie kunnen nog de volgende indicatoren worden gebruikt:

- aantal dagen waarop de hoogste uurlijkse ozonconcentratie groter is dan de waarschuwingsdrempel (180 $\mu g/m^3$ volgens de huidige richtlijn 92/72/EEG, 240 $\mu g/m^3$ volgens het nieuwe voorstel)
- aantal dagen waarop de hoogste uurlijkse ozonconcentratie groter is dan de alarmdrempel (360 $\mu g/m^3$ volgens de huidige richtlijn 92/72/EEG)
- aantal dagen waarop de hoogste uurlijkse ozonconcentratie groter is dan de grenswaarde voor de bescherming van de vegetatie (200 $\mu g/m^3$ volgens 92/72/EEG)
- aantal 8-uursgemiddelden waarvoor de ozonconcentratie groter is dan de grenswaarde voor de bescherming van de gezondheid (110 $\mu g/m^3$ volgens 92/72/EEG; 120 $\mu g/m^3$ volgens het nieuwe voorstel)
- aantal dagen waarvoor het maximum van de 8-uur glijdende daggemiddelden groter is dan 110 $\mu g/m^3$ (of 120 $\mu g/m^3$ voor het nieuwe voorstel)
- aantal dagen waarop de gemiddelde ozonconcentratie groter is dan de daggrenswaarde voor de bescherming van de vegetatie (65 $\mu g/m^3$ in 92/72/EEG)
- gemiddelde van de dagelijkse maxima
- gemiddelde van de dagelijkse maxima van de 8-uur glijdende gemiddelden

6.6 Impact evaluatie met behulp van Euros

Het EUROS (EURopean Operational Smog) model is een Euleriaans luchtkwaliteit model dat oorspronkelijk ontwikkeld werd door RIVM (Nederland) (van Loon, 1996). De huidige versie van EUROS modelleert voor verschillende luchtverontreinigende stoffen (waardoor ozon) emissies, transport, chemische omzetting, droge en natte deposities naar water en bodem. Het domein beslaat heel Europa met een resolutie van 60 km x 60 km. Een speciale techniek kan worden aangewend om het rekenrooster te verfijnen in specifieke gebieden (bijvoorbeeld België) met een resolutie van 7.5 km x 7.5 km. Het model simuleert uur per uur de evolutie van ozonconcentraties in Europa. Door zijn beperkte rekentijd is het mogelijk om vrij lange simulaties (enkele maanden tot enkele jaren) uit te voeren.

In het kader van het BelEUROS project werd het model verder ontwikkeld (Delobbe et al., 2000a; Delobbe et al., 2000b). De nieuwe versie gekoppeld met een gebruiksvriendelijke input/output user interface (Passelecq et al., 2000) is nu geïnstalleerd bij IRCEL (Interregionale Cel voor het Leefmilieu). Momenteel wordt het

model operationeel gemaakt voor beleidsondersteuning in België om reductiestrategieën inzake troposferisch ozon te beoordelen.

In het kader van dit project werd ook een nieuwe emissie inventaris opgebouwd met verfijnde emissie data voor België (Mensink en Janssen, 2000). Het doel van de EUROS simulaties is om het effect van mogelijke emissiereductiemaatregelen te evalueren. De user interface laat toe om emissie gegevens te wijzigen per polluent (NOx, SO_2, VOS) en per economische sector (verbranding, raffinaderijen, industrie, solvent, gebouwverwarming, verkeer). De emissie gegevens kunnen veranderd worden per land maar ook voor specifieke grid cellen. Voor elke polluent en elke grid cel worden de emissiegegevens uitgedrukt in kg/jaar. De tijdsvariaties van de emissies worden in rekening gehouden door maandelijkse, dagelijkse en uurlijkse tijdsemissie factoren. Die factoren kunnen ook worden gewijzigd door de gebruiker om gevoeligheidstudies uit te voeren.

De analyse van de impact van emissiereductiescenario's moet gebaseerd worden op de verschillende indicatoren die werden beschreven in de vorige sectie. Vrij lange simulaties kunnen met EUROS uitgevoerd worden. Dit laat toe om alle statistische indicatoren die wij vermeld hebben (AOTs, NETs, …) te berekenen uit de uur per uur gesimuleerde ozon concentraties. Een interne berekening voor elke grid cel van de AOTS gebaseerd op de uurlijkse ozon waarden is voorzien in het EUROS model. De output user interface laat toe om die AOTs te visualiseren. Nochtans is het niet mogelijk om alle bestaande (en toekomstige) indicatoren te laten berekenen door het model. De evaluatie van sommige indicatoren moet dus gebeuren in een post-proceesing gebaseerd op de output van EUROS. Voor vrij korte simulaties is het mogelijk om de uurlijkse ozon waarden weg te schrijven voor alle grid cellen van het domein. Om de grootte van de output bestanden te beperken is dit niet mogelijk voor lange-termijn simulaties. In dit geval moet de gebruiker een aantal locaties selecteren (b.v. alle meetstations van Belgie) vaarvoor de uurlijkse waarden gewenst zijn.

6.7 Conclusies

In het kader van het BeleEUROS project werd het EUROS model verder ontwikkeld en gekoppeld aan een gebruiksvriendelijke user interface. De nieuwe versie van EUROS is nu geïnstalleerd bij IRCEL in Brussel en zal binnenkort beschikbaar zijn voor beleidsondersteuning in België.

Om mogelijke emissiereductiemaatregelen te kunnen evalueren met behulp van EUROS is het noodzakelijk om de resultaten van EUROS te vertalen in termen van indicatoren. Deze indicatoren laten toe de schadelijke effecten van ozon op de vegetatie en de gezondheid te kwantificeren. In dit rapport werd een inventaris opgesteld van alle indicatoren die tegenwoordig gebruikt worden en werd tevens beschreven hoe deze indicatoren met EUROS kunnen worden berekend.

Zo bevat de inventaris ook indicatoren die worden gebruikt in de huidige en de toekomstige Europese wetgeving of die als richtwaarden of doelstellingen worden aangewend door verschillende instanties (WGO, UNECE, nationale en regionale instanties zoals IRCEL of VMM). De belangrijkste indicatoren zijn de AOT40 (Accumulated exposure Over the Threshold of 40 ppb) voor de effecten op de vegetatie en het dagelijkse maximale 8-uur gemiddelde voor de effecten op de gezondheid. De nieuwe Europese wetgeving voorziet als streefwaarde voor de bescherming van de vegetatie een maximum van 18000 $\mu g/m^3$ voor de AOT40 per jaar als gemiddelde over 5 jaren. Voor de bescherming van de volksgezondheid is de streefwaarde voor 2010 een maximum van 25 dagen per kalenderjaar waarvoor het maximale 8-uursgemiddelde per dag de waarde van 120 $\mu g/m^3$ overschrijdt. De langetermijndoelstelling voorziet geen overschrijding van deze drempelwaarde.

Zowel deze twee belangrijke indicatoren als andere statistische indicatoren (aantal dagen per jaar met een bepaalde overschrijding, b.v.) kunnen gemakkelijk worden berekend uit de resultaten van EUROS omdat het model voor elke gridcel de uur per uur evolutie van de ozonconcentraties berekent. Door de beperkte rekentijd kan men met EUROS vrij lange simulaties uitvoeren (enkele maanden tot enkele jaren). Dit maakt het mogelijk om langetermijn indicatoren te evalueren.

6.8 References

APHEA2, 1998. Short-Term Effects of Air Pollution on Health: A European Approach to Methodology, Dose-Response Assessment and Evaluation of Public Health Significance, 1998.

Bates DV, Baker-Anderson M. Sizto R (1990). Asthma attack periodicity: A study of hospital emergency visits in Vancouver. Environ Res 51, 51-70.

Cody RP, Weisel CL, Birnbaum G, Lioy PJ. (1992). The effect of ozone associated with summertime photo-chemical smog on the frequency of asthma visits to hospital emergency departments. Environ Res 58, 184-194.

Delobbe,L., C. Mensink, O. Brasseur, G. Schayes, and A. Melikechi, 2000. Implementation of meteological data in EUROS. Scientific report 2000/TAP/R/001, VITO, Mol.

Delobbe, L., L. Kinnaer, C. Mensink, 2000. Optimization of chemical and advection modules in EUROS. Scientific report 2000/TAP/R/063, VITO, Mol.

De Nocker, L., Torfs, R., 2001. Externe kosten van energiegebonden polluenten in Vlaanderen. VITO rapport, Mol. (in press)

De Temmerman en K. Vandermeiren, 1999. Effecten van ozonverontreiniging op vegetatie. In Proceedings van Ozon in de Troposfeer: Onderzoek en Beleid. Brussel, 26 juni 1998. DWTC, Brussel.

Dumont, G., Mensink, C., en Brouwers, J., 2000: fotochemische luchtverontreiniging. In MIRA-S 2000. Milieu en- natuurrapport Vlaanderen: scenario's. Vlaamse Milieumaatschappij. Garant. Leuven.

Holgate S.T., Samet J.M, Koren H.S., Maynard R.L. (1999) Air pollution and health, Academic Press, Londen.

Holland et al. 1995 Externalities of Energy (ExternE). Volume 2: Methodology. European Commission, Directorate-General XII. Science, Research and Development. Brussels.

Holland et al. 1999 Externalities of Energy (ExternE). Volume 8: Methodology update. European Commission, Directorate-General XII. Science, Research and Development. Brussels.

Hornung et al. 1995. Impacts of air pollution on agriculture in ExternE, Externalities of Energy, Vol. 2. Methodology. EUR 16521 EN, 1995.

Jones et al. 1997. Impacts on terrestrial ecosystems in ExternE, Externalities of Energy, Vol. 7. Methodology 1998 update. EUR 19083, 1999.

Kärenlampi L. en Skärby L.L, 1996, eds.. Critical Levels for ozone in Europe: testing and finalising the concepts. UN-ECE Workshop Report 15-17 April 1996. University of Kuopio, Finland.

Loon, M. van, 1996: Numerical methods in smog prediction, PhD thesis, University of Amsterdam.

Mensink, C. en L. Janssen, 2000. A dynamic emission inventory for the EUROS model. Scientific report, 2000/TAP/R/6, Vito, Mol.

Ostro BD and Rothschild S. (1989). Air pollution and acute respiratory morbidity: An observational study of multiple pollutants. Environ Res 50, 238-247.

Passelecq et al., 2000. Développement d'un interface utilisateur pour le modèle EUROS. Rapport Faculté Polytechnique de Mons. Mons (en préparation).

Ponce de Leon A, Anderson HR, Bland JM, Strachan DP, Bower J. (1996). Effects of air pollution on daily hospital admissions for respiratory disease in London between 1987-88 and 1991-92. J Epidem Comm Health 50 (suppl 1): S63-70.

Spix C, et al. (1998) Short-term effects of air pollution on hospital admissions of respiratory diseases in Europe: a quantitative summary of APHEA study results. Air Pollution and Health: a European Approach. Arch Environ Health Jan-Feb;53(1):54-64.

Sunyer J, Castellsague J, Saez M, Tobias A, Anto JM. (1996). Air pollution and mortality in Barcelona. J Epidem Comm Health 50 (suppl 1): S76-S80.

Touloumi G. et al. (1997). Short-term effects of ambient oxidant exposure on mortality: a combined analysis within the APHEA project. American Journal of Epidemiology, vol. 146, No. 2, pp. 177-185.

Whittemore AS, Korn EL. (1980). Asthma and air pollution in the Los Angeles area. Am J Public Health 70, 687-696.

WHO (2000). Guidelines for Air Quality, World Health Organisation, Geneva, Switzerland.

van Ypersele, J.P., 1999. Ozon in de troposfeer: onderzoek, integratie en beleid. In Proceedings van Ozon in de Troposfeer: Onderzoek en Beleid. Brussel, 26 juni 1998. DWTC, Brussel.

7. GENERAL CONCLUSIONS

In the framework of the BelEUROS project, a new version of the EUROS model coupled with a state of the art user interface has been installed at the Interregional Cell for the Environment (IRCEL/CELINE, Brussels) as a tool for policy support with respect to tropospheric ozone. Hereafter, we summarise the main stages of the project and the most significant results. We also propose some suggestions for future work.

Generation of new input data for EUROS

For implementing the EUROS model in Belgium, some input data has been adapted. It concerned the emission data and the meteorological data. A dynamic emission inventory has been compiled for the European countries that are covered by the EUROS domain. The inventory provides the spatial and temporal variations in anthropogenic emissions for six economical sectors and the distribution of biogenic emissions varying with temperature. This inventory was implemented in a GIS (Arcview) which proved to be very helpful in this context.

As far as the meteorology is concerned, a new three-dimensional input data set for EUROS has been generated from the ECMWF meteorological data (European Centre for Medium-Range Weather Forecasts, Reading, UK). Moreover, an important atmospheric parameter in EUROS is the mixing height. Several methods have been explored to estimate the mixing height from the meteorological data set. The results have been compared with observational data and with the results of detailed model simulations. Based on these results, a new method has been proposed for the determination of the mixing height in air quality models.

Development of a new version of EUROS

The EUROS model has been further developed in close collaboration with the RIVM (Rijksinstituut voor Volksgezondheid en Milieu, Bilthoven, The Netherlands). A new version has been set up. It includes a spatially variable mixing height and a multi layer representation of the horizontal transport. This allows a much more realistic representation of the atmospheric boundary layer processes. The model is now provided with a three-dimensional grid structure, which constitutes a first step towards a fully three-dimensional representation of the advection and diffusion processes. The new version has been extensively tested by comparing the simulated ozone concentrations with observational data.

Development of a user interface

A user friendly interface has been developed. It allows the user to define his emission scenario, to start the simulation from his own computer and to visualise the output results. The user has the possibility to modify the emission rates of a given pollutant (NOx or VOC) for a given emission sector (traffic, space heating, refinery, solvents use, combustion, industry) and for a given geographical area. Monthly, daily and hourly emission factors can also be modified for each sector. These factors account for the influence of the hour in the day, the day in the week, and the hour of the day. The user interface consists of a Windows platform written in VISUAL-C++.

Installation at IRCEL/CELINE

The new version of the EUROS coupled with the user interface is now installed at IRCEL/CELINE and can be used by policy makers and researchers in the three Belgian regions for evaluating the impact of possible emission reduction strategies on ozone concentrations. The output results of EUROS allow estimating the indicators currently used for estimating the impact of ozone on vegetation and human health. Some of these indicators are also used in the current European legislation relating to ozone in ambient air.

Future work

Most of the objectives of the BelEUROS project have been achieved. Nevertheless, further work must be considered in order to consolidate EUROS as an efficient and valuable tool for policy support in Belgium. The following items can be mentioned.

Extensive testing of the EUROS model and its user interface. The performances of the EUROS model in simulating ozone episodes in Belgium must be assessed. An uncertainty analysis must be carried out. Possible shortcomings of the user interface must be identified and corrected.

Acquisition of new meteorological data. The current meteorological input data set of EUROS covers the period May -September 1997. In the future, it is desirable to extend this period to several years in order to take into account the interannual meteorological variability.

Refinement of the dynamic emission inventory

Grid refinement. The potentialities of the grid refinement over Belgium must be further explored in order to improve the representation of local scale processes. In the same perspective, the coupling with urban scale models would allow a better representation of important processes affecting ozone concentrations in and around the cities, such as titration effect.

New developments on the EUROS model have to be carried out in collaboration with the RIVM. It concerns mainly the introduction of a fully three-dimensional representation of the transport and diffusion processes.

Exploitation of the results for socio-economic studies or cost-benefit analyses like in the current OSTC project “economic impact modules for the EUROS model”.

To achieve these goals, new projects will be proposed in the framework of current and coming Belgian and International scientific programs.

ANNEX

A1: Scientific publications related to the project

Publications

Mensink, C. and Colles, A.: Modelling long-term effects of emission reductions on ozone for policy support in Belgium, in: Longhurst, J.W.S., Brebbia, C.A. and Power, H. (eds): Air Pollution IX, p. xxx-xxx, WITpress / Southampton, 2001 (to appear).

Mensink, C., 2000. Validation of urban emission inventories. Int. Journal Environmental Monitoring and Assessment, Kluwer academic publishers (to appear)

Mensink, C. and Duerinck, J.: Integrated Assessment of European Air Pollution Emission Control Strategies and their impact on the Flanders region, in: Gryning, S.E. and Schiermeier F.A. (eds.) Air Pollution Modelling and its Applications XIV, Kluwer Academic/Plenum Publishers, Boston, 2000 (to appear).

Mensink, C., L. Janssen and B. Bomans, 2000. An assessment of urban VOC emissions and concentrations by comparing model results and measurements, Int. J. Environment and Pollution (accepted).

Mensink, C. Debruyn, W, Janssen, L. and Ruts, M.: Transboundary flux measurements for the validation of emission inventories and regional atmospheric models, in: Barone, G., Builtjes P. and Giunta G. (eds.) Global and regional Atmospheric Modelling, Annali of the Naval University of Napels, University of Napels, Napoli, 2000.

Matthijsen, J. ,L. Delobbe, F.J Sauter, D.P.J. Swart, 2001. Long-term evaluation of two mixing height parameterizations with LIDAR observations. Abstract to appear in the Proceedings of the 2nd International Conference on Air Pollution Modelling and Simulation, APMS'2001, April 9-13, 2001, Paris , France.

Publications in the framework of the EUROTRAC program:

Mensink, C. and Delobbe, L.: Development and implementation of the EUROS model for policy support in Belgium, in: Munzenberg, A. and Builtjes P. (eds.) EUROTRAC

Annual Report 1999 (subproject GLOREAM), GSF-Forschungszentrum für Umwelt und Gesundheit, München.

Delobbe, L. and Mensink, C: Development and implementation of the EUROS model for policy support in Belgium, in: Munzenberg, A. and Builtjes P. (eds.) EUROTRAC Annual Report 2000 (subproject GLOREAM), GSF-Forschungszentrum für Umwelt und Gesundheit, München (to appear).

Mensink, C., L. Janssen, B. Bomans, N. Lewyckyj, N. and J. Nys, An assessment of the uncertainties in urban transport emission modelling, extended abstract to appear in the Proceedings of the EUROTRAC-2 Symposium 2000.

Delobbe, L., O. Brasseur, and C. Mensink, 2000. Determination of the Mixing Height from ECMWF data for Use in the Regional Photo-Chemical Smog Model EUROS. Extended abstract to appear in the Proceedings of the Eurotrac 2000 symposium.

Delobbe, L., J. Matthijsen, C. Mensink, F.J. Sauter, D.P.J. Swart, 2000. A comparison of mixing heights derived from meteo data and inferred from LIDAR measurements, extended abstract to appear in the Proceedings of the Eurotrac-Gloream workshop, September 2000, Cottbus, Germany.

Matthijsen, J., L. Delobbe, F.J. Sauter, L. de Waal, Changes of Surface Ozone over Europe upon the Gothenburg Protocol Abatement of 1990 Reference Emissions, extended abstract to appear in the Proceedings of the Eurotrac 2000 symposium.

Mensink, C., Van Rensbergen, J., Viaene, P., De Vlieger, I. and Beirens, F.: Temporal and spatial emission modelling for urban environments using emission measurement data, in: Borell, P.M. and Borell P. (eds.) Proceedings of EUROTRAC Symposium '98, Vol 2, p. 710-714, WIT Press, Southampton, 1999.

Viaene, P., Debruyn, W., Mensink, C. and Van Rensbergen, J.: Evaluation of a compact chemical mechanism for photochemical smog modeling, in: Borell, P.M. and Borell P. (eds.) Proceedings of EUROTRAC Symposium '98, Vol 2, p. 456-459, WIT Press, Southampton, 1999.

A2: List of the contributors to the project

Vlaamse Instelling voor Technologish Onderzoek (VITO)

- Laurent Delobbe
- Clemens Mensink
- Koen De Ridder
- Luc Kinnaer
- Liliane Janssen
- Marcel Ruts
- Rudi Torfs
- Léo De Nocker
- Hilde Caeyers

Faculté Polytechnique de Mons (FPMs)

- Charles Passelecq
- Dominique Passelecq

Université catholique de Louvain (UCL)

- Guy Schayes
- Olivier Brasseur
- Abdenour Melikechi

InterRegional Cell for the Environment (IRCEL/CELINE)

- Gerwin Dumont
- Claude Demuth
- Frans Fierens

A3: Annexe au chapitre 5: “User interface”

L’interface utilisateur a été conçue pour interagir de façon étroite avec le modèle « EUROS ». Toutefois pour des raisons de sécurité il a été convenu de protéger le modèle et certaines des données. Nous avons donc conçu un ensemble qui répond aux caractéristiques de la programmation dite Client/ Serveur. Les données protégées étant localisées sur le serveur qui doit en assurer la protection. Cette façon d’agir à aussi l’avantage de mettre à disposition du « Client » des moyens de calcul qu’autrement il ne pourrait peut être pas disposer. L’annexe A3.1, « Gestion du serveur », décrit ces aspects de liaison et de sécurité. Il a également été nécessaire, compte tenu des impositions dues à la protection, de faciliter la gestion des utilisateurs. Ceci est présenté dans l’annexe A3.2, « Gestion des utilisateurs ».

A3.1 Gestion du serveur

Le serveur est accessible par Internet sous conditions. Malgré cet accès conditionnel, le programme EUROS et certaines données associées ont été protégées plus efficacement.

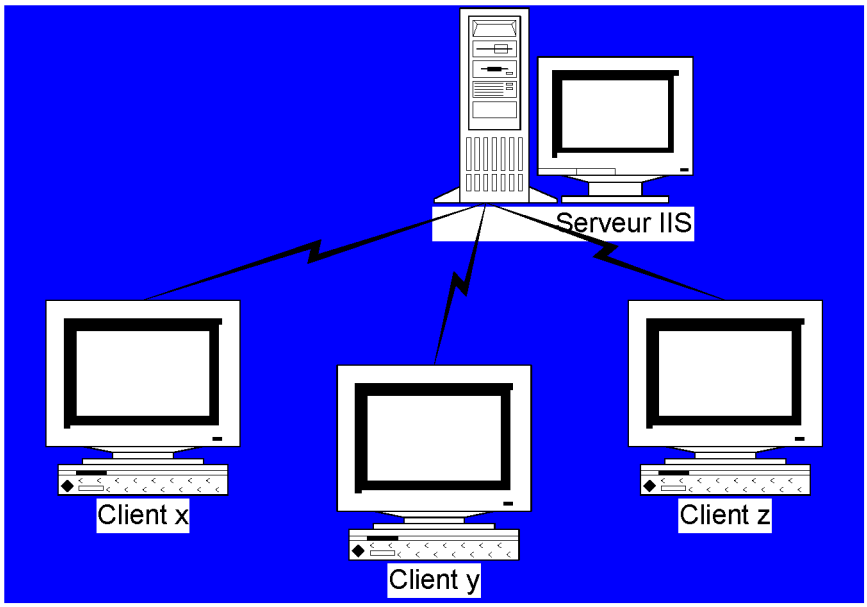

***Figure 66**: Schéma de connexion.*

Pour ce faire, une zone accessible par Internet (http et ftp) a été définie sur le serveur. Elle est gérée par « Internet Information Serveur » qui fait partie intégrante du système d’exploitation « Windows 2000 ». La gestion automatisée de l’accessibilité a été réalisée en y insérant une dll « dynamic link library » spécifique qui agit comme une extension ISAPI du serveur.

Cette extension contrôle l'accès au programme EUROS situé dans une zone protégée et permet son utilisation par plusieurs utilisateurs simultanément. Chaque utilisateur ou client n'a toutefois l'autorisation que d'exécuter une seule session à la fois.

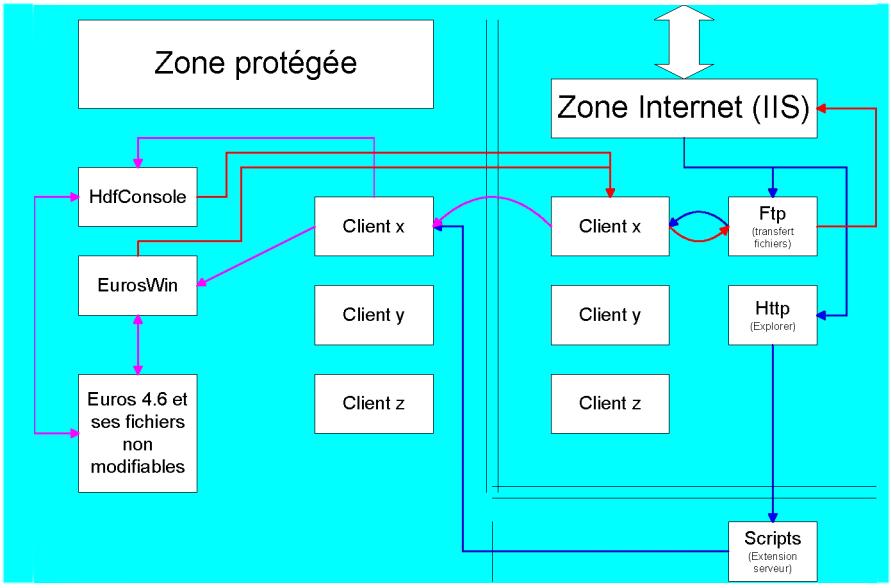

***Figure 67**: Distribution des zones.*

Chaque client peut accéder à la zone « IIS » du serveur par l'intermédiaire de l'interface utilisateur. Dans cette zone, un site « FTP » lui est réservé qui reçoit les données d'entrées utiles à sa simulation mais aussi tous les fichiers résultats correspondant à cette même simulation.

Lors de la soumission de la simulation proposée par le client, les données nécessaires à l'exécution du programme seront copiées dans une zone protégée où une image de son site « FTP » existe. Une session du programme « EUROS », située dans la zone protégée, sera alors activée par l'extension serveur.

Le programme « EUROS », au cours de son exécution, transmettra directement dans le site « FTP » du client soumissionnaire les résultats ainsi qu'un état d'avancement du calcul que le client pourra consulter à tout moment par l'intermédiaire de son interface utilisateur (voir sous l'intitulé « **Internet** » de la barre de menu, la ligne « **State of simulation** »). La fin des calculs est indiquée dans le fichier relatif à l'état de la simulation.

La simulation terminée, le client peut rapatrier les fichiers résultats en demandant par l'interface utilisateur une compression des fichiers résultats et un transfert vers son

ordinateur. Pour réaliser ceci, il faut dans l'option « **Internet** » activer « **Start Euros** » et choisir l'option « **OutFiles compression** » Le transfert terminé les fichiers résultats seront automatiquement effacés du serveur.

Sous conditions particulières, le client peut avoir besoin de certains fichiers non-modifiables pour une analyse des résultats des simulations. Les plus importants sont relatifs aux conditions météorologiques qui contraignent naturellement le problème de la dispersion. Ces informations sont contenues dans les fichiers météorologiques du ECMWF distribués par l'**I**nstitut **R**oyal **M**étéorologie (IRM).

Les originaux de ces fichiers, écrit dans le format **H**ierarchical **D**ata **F**iles (HDF), ne peuvent être distribués dans leur état natif aux utilisateurs. Ces fichiers originaux sont non transmissibles et existent sur le serveur dans la zone protégée. Toutefois, pour aider à la compréhension, ils peuvent à la demande être rendus disponibles sous la contrainte d'une modification profonde de leur nature et de leur structure. Une forme binaire temporaire et ponctuelle des fichiers est à la disposition du client dans son site « FTP ». Ils ne sont lisibles qu'à travers l'interface utilisateur (voir l'intitulé « **Meteo** » dans la barre de menu). Cette double contrainte de transformation des données originales et de lecture conditionnée ne doit pas faire oublier au client qu'il s'engage implicitement à n'utiliser toutes les données que dans le cadre de l'exploitation de belEUROS. Il ne peut en aucun cas les divulguer sans autorisations préalables.

A3.2 Gestion des utilisateurs

Un programme a aussi été développé pour assurer la gestion des utilisateurs. Par ce programme le responsable « Serveur » construit de façon automatique le fichier d'autorisations et les arborescences nécessaires (en zone protégée et site FTP) pour que le client puisse avoir accès aux fonctionnalités.

Un fichier « journal » est automatiquement géré par « IIS » et permet au responsable de la gestion du serveur de suivre quotidiennement les activités sur belEUROS. Le fichier d'autorisation, situé dans une zone protégée, conditionne de façon stricte l'accès par les clients.

Localisations et arborescences

Fichier d'autorisation:

« d:\inetpub\Scripts\Webclient.txt »

Programme de gestion des utilisateurs:

« d:\inetpub\Scripts\EurosSvrInstall.exe »

Programme de décodage/ codage des fichiers HDF:

« HDFfiles.exe » dans le dossier réservé au client de la zone protégée.

Programme extension serveur:

« d:\inetpub\Scrips\Euros46.dll »

Programme Eurosv4.6 pour Windows:

« EurosWin.exe » dans le dossier réservé au client de la zone protégée.

Programme d'installation chez le client via le « net »:

« d:\inetput\ftproot\All\InstallEuros2.exe »

Sur le serveur on trouve:

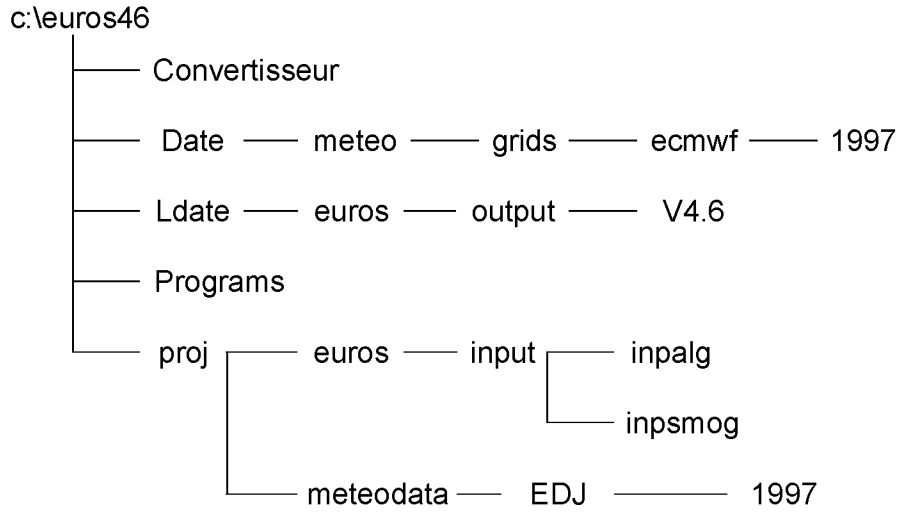

Par Client

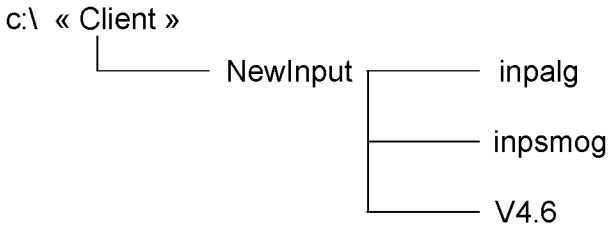

Liste de programmes développés dans le cadre du projet

a) Développé par le RIVM et le Vito et compilé par la FPMs

« EurosWin.exe » correspond à l'exécutable du modèle EUROS développé par le RIVM et le VITO en FORTRAN 77/90. La compilation est réalisée pour Windows

b) Développés par la FPMs en Visual C++

« Model.exe » correspond à l'exécutable de l'interface utilisateur que l'utilisateur doit télécharger

« InstallEuros2.exe » correspond au programme d'installation du modèle chez le client via « Internet »

« Euros46.dll » est une extension serveur ISAPI

« EurosSvrInstall.exe » gère les clients sur le serveur

AS/18/009

DEVELOPMENT OF A SPECIFIC INTERPOLATION METHOD FOR AIR POLLUTANTS MEASURED IN AUTOMATIC NETWORKS (SMOGSTOP)

FACULTÉ POLYTECHNIQUE DE MONS (FPMs)
Service Fluides - Machines
Rue du Joncquois
B-7000 MONS
C. PASSELECQ (coordinator AS/18/009)

CELLULE INTERRÉGIONALE POUR L'ENVIRONNEMENT (CELINE /IRCEL)
Avenue des Arts 10-11
B-1210 BRUXELLES
C. DEMUTH (partner)

TABLE OF CONTENTS

FOREWORD 1

1. INTRODUCTION 1

2. OBJECTIVE 1

3. INTERPOLATION METHOD 2

a) **Inverse distance method** 3
Definition 3
Mathematical formulation 3
Mathematical properties 4
b) **Interpolation based on the Delaunay triangulation** 5
Mathematical formulation 5
1) Two-dimensional linear interpolation *6*
2) Quadratic interpolation or method of Cendes-Wong *6*
3) Cubic interpolation or Akima method *6*
Extrapolation 7
c) **Spline function type thin plate** 7
Mathematical formulation 7
d) **Kriging method** 8
Spatial variability 8
Model 9
Ordinary kriging 12

4. COMPARITIVE STEPS AND STUDIES 14

a) **Phase 1** 14
b) **Phase 2** 20
Application of N.U.R.B.S. functions with the inverse-distance methods 20
Choice of the stations for the inverse-distance methods 25
1) Effect of the division for the total network *25*
2) Comparative study *35*
Improvement of the Akima method 37
1) Borders points and negative concentration values *37*
Linear interpolation based on the Delaunay triangulation 43

c) Phase 3 **51**
Quadratic interpolation based on the Delaunay triangulation 52
Spline function type thin plate 56
Kriging method 59
1) Ozone concentration *60*
2) SO_2 concentration *66*
Methods to estimate the parameters of a distance function 70
1) Exponent *70*
2) Radius of influence *74*

5. APPLICATION DESCRIPTION **76**

6. CONCLUSION **84**

APPENDIX **87**

REFERENCES **90**

FOREWORD

This final report makes the synthesis of a search for methods of interpolation necessary to the exploitation of pollutant concentration data which are generally dispersed on a given space field. Four great methods were adopted and applied to concrete pollution data and visualized in a very convivial data-processing environment. It appears that a great rigour in measurements, prudence in the interpretation and the choice of the methods are necessary so that the adopted methods of interpolation have objective results. It is usually the case, as this study will show it, that measurements concerning pollution force most of the interpolation methods to overcome their theoretical limits. The spatial distribution of the measuring sites is often far from the assumptions of a homogeneous distribution. The critical zones characterized by a superabundance or a poverty of information must be treated carefully. It is necessary to emphasize just the useful one when they are located in an environment either too overloaded in information or too few in measurements like it is currently the borders zones of the field of study. It is also to bear in mind that pollution measurements record, without distinguishing them, the internal and external contributions to the field of study.

1. INTRODUCTION

By the awakening growing on the need for acting to improve air quality, CELINE built starting from her creation in 1994 a database relating to the data of air pollution and the atmospheric data measured in sites close to those of pollution. All the data are collected starting from three regional networks of measure. With this current information, data former to 1994 were also introduced into the database. Practically, for the most important pollutants, it is possible to treat measurements since 1978 until today. All this quantified information, subjected to statistical processing, gives only one individual sight, but important, of the situation of the air pollution in Belgium. The total effects are gathered in sizes where space dimension is not directly visible. The recourse to space methods of interpolation coupled to maps is a need to seize the effects as well qualitative as quantitative space-time modifications made by pollution to the level of the Belgian territory.

2. OBJECTIVE

The objective of this study consists in developing a data-processing module fast and easy to use making it possible to build, starting from measurements with the receivers, a continuous space representation of pollution present on the studied area. It must allow cross analyses and cartographic visualizations, both necessary to the

exploitation as well of the bank of data as of models (such as model SMOGSTOP of forecast of the ozone peaks).

3. INTERPOLATION METHODS

Several space interpolation methods of a scalar variable exist since simplest, like the inverse distance method, until that related to geostatistic, worked out for the treatment of variable spatially correlated. The adopted methods belong to the following classes:

- Inverse distance method: this analytical method calculates the value in a point of the area like the weighted average of the measured values, the weights being decreasing functions of the distances. Weighting can extend, either on all the area, or in vicinity delimited by a limit of influence.

- Methods based on the Delaunay triangulation: from the single construction of a triangles network based on the existing stations, the interpolation on this network is carried out either by plane surfaces in the linear interpolation method, or by continuous surfaces until the derived first in the quadratic interpolation method or method of Cendes and Wong (1987), or by continuous surfaces until the derived seconds in the Akima interpolation method (1970 and 1978).

- Analytical method of approximation by overall defined functions, like the thin plate functions splines. The interpolating function resulting minimizes the curve of surface passing by the points of measurement. This type of method was retained like tool of analysis of the results of network AIRPARIF (Ionescu *et al.*., 1996).

- Statistical methods of which most traditional is the "Kriging". This geostatistic method, based on the space variability concepts and structure, is defined as an optimisation method of the estimate of a size known in the measurement network points.

The interpolation methods indicated above are presented and applied to data all extracted the CELINE database so as to return the application data-processing developed directly applicable to the context in which it must be established. The representations will be done starting from a rectangular grid covering at the same time the territory and the networks with measurement selected. The comparison of the methods will be done on a visual basis made starting from the result maps.

a) Inverse distance method

Definition

The inverse distance method is a local method which predicts the value Z_0 size analysed in an unspecified point $\mathbf{R}_0$ of a dimensional space, on the basis of result of the weighted average, in this point, of the measured values Z_I with N measurement points $\mathbf{R}_I$. These measurement points are generally dispersed in the study field. Weight W_{0i}, bond between each measurement point $\mathbf{R}_0$ and the calculation point $\mathbf{R}_I$, must hold account of the physical bonds existing on the geometrical fabric built by the distances between stations

$$h_{0i} = |\mathbf{r}_i - \mathbf{r}_0|$$

separating the calculation point of N measurement points. The way in which one defines the weights particularizes the method of balanced interpolation. Three traditional formulations utilizing explicitly the distance H_{0i} are retained, namely:

- an interpolation based on a whole negative power of H_{0i} who in the case of an exponent equal to 2 takes as a starting point the law of Newton of interaction between two solid bodies

- an interpolation utilizing a radius of influence R beyond whose the weight takes a zero value. Cressman (1959) in gave a simple linear expression which thereafter was slightly adapted by Thiébaux and Pedder (1987)

- an interpolation based on the relationship between the distance H_{0i} and the radius of influence R is proposed by Sasaki (1960) and Barnes (1964) like size intervening in an exponential function

All these formulations utilize physical parameters which must in one way or another being fixed by rigorous mathematical constraints. This approach by the weighted average which privileges each point of measurement individually consists of a passage obliged for better understanding than other methods of more total application will bring to the interpolated values.

Mathematical formulation

The weighted average in a point of calculation $\mathbf{R}_0$ is given by the following general expression:

$$z_0 = \sum_{i=1}^{n} w_i z_i \quad \text{with} \quad w_i = \frac{p(h_{0i})}{\sum_{i=1}^{n} p(h_{0i})} \quad \text{while} \quad \sum_{i=1}^{n} w_i = 1$$

The distance function p(H_{0i}) admits several forms. The most used are as follows:

a) Model of the reverse of a law in power

$$p(h_{0i}) = \frac{1}{h_{0i}^{\alpha}} \quad \text{with } \alpha = 2, 4$$

b) Sasaki and Barnes model

$$p_{0i} = \exp\left[-4\left(\frac{h_{0i}}{R}\right)^2\right]$$

c) Cressman (α = 1), Thiébaux and Pedder (α > 1) model

$$p_{0i} = \begin{cases} \left(\dfrac{R^2 - h_{0i}^2}{R^2 + h_{0i}^2}\right)^{\alpha} & \text{for } h_{0i} < R \\ 0 & \text{for } h_{0i} \geq R \end{cases}$$

According to the studies undertaken by Thiébaux and Pedder (1987), the exponent α is selected among the even values 2 and 4. The use recommended in the scientific literature is to employ value 2 for the extension of the method of Cressman and value 4 for the method of the reverse of a law in power. In what relates to the distance *R*, a lower limit R_{min} is proposed only in the case of a relatively homogeneous space distribution of the measuring sites in the field of analysis. This distance is fixed by the square root of the quotient of the surface of the field covering the points with measurement (here Belgium) at the number of stations selected. A higher limit can be associated and to be defined like doubles it at more this minimal distance $R_{min.}$.

Mathematical properties

- Any computed value by the inverse distance method cannot exceed the measured values or in other words the extremes will be always among the measured values. This property, which is not very physical, does not arise any more with the total methods which hold account the continuity of surface interpolating in all the points of the field of study.

- With a long distance of all the points of measurement, the interpolation balanced compared to the distances returns to a simple arithmetic mean. Indeed, it is enough to notice that in this particular case, the distances H_{0i} becoming of the same order of magnitude, the general expression does not depend practically any more a this distance so that the numerator is reduced to the measured values and the denominator is reduced to the number *N* points of measurement.

- Very often in the studies on the effects of the air pollution, the space interpolation is coupled with a temporal interpolation so as to know the effects of time on the space retained without being concerned with intermediate stages. If such is the case and if measurements are taken with intervals of regular times, the method of the weighted average admits a useful simplification for temporal calculations since the weights selected do not depend on time in this method. Time *T* affect only the measured values *z(t)* but not the function of distance $p(h_{0i})$ who depends only on the space variables built-in in the distance H_{0i}. If the temporal period *T* subdivides itself in *m* intervals, it is shown that the temporal average calculated in a point $\mathbf{R}_0$ result from the weighted average of the temporal averages of the measured values:

$$\overline{z}_0^{t} = \frac{1}{m}\sum_{t=1}^{m}\left(\frac{\sum_{i=1}^{n} p(h_{0i})z(h_{0i},t)}{\sum_{i=1}^{n} p(h_{0i})}\right) = \frac{\sum_{i=1}^{n} p(h_{0i})\overline{z}_{0i}^{t}}{\sum_{i=1}^{n} p(h_{0i})}$$

b) Interpolation based on the Delaunay triangulation

Mathematical formulation

To transfer information from the measuring sites towards the points of a fixed geographical area is generally done by regarding each measuring site as an individual source of information (inverse distance method) or by taking the whole of all the information known at the stations which one subjects to a particular total constraint (splines functions method). An intermediate situation amounts defining information on each piece of the space parcelled out on the elementary surfaces limited by the stations then to connect by continuity compartmental information to the entire zone of study. This kind of method calls upon a two-dimensional triangulation of the whole of the measuring sites to which one adds a linear interpolation, quadratic or cubic.

The most used triangulation is that known as of Delaunay. The method which is associated for him (Watson, 1981) makes it possible to build a whole of triangles satisfying the following properties:

- the interiors of the triangles are disjoined two to two,
- the union of the triangles covers the polygonal envelope exactly containing all the stations,

- the interior of the circle circumscribed with each triangle does not contain stations. This property implies the unicity of the triangulation.

1) Two-dimensional linear interpolation (2d)

On the basis of creation of a triangular network, the method makes pass to the right of each triangle of Delaunay a plan by the three values attached to the three measuring sites defining each triangle. One creates this way a whole of facets similar to surface cut of an invaluable stone. Just like for the inverse distance method, the interpolated values are always between the measured extremes. The very angular graphic result can be softened by the application of a N.U.R.B.S method of smoothing. This method, in addition to which it makes it possible to obtain a faithful interpolation, gives the possibility of extracting, from surface interpolating, information on the derivative first and secondary from the interpolated size.

2) Quadratic interpolation or method of Cendes-Wong

The method developed by Cendes and Wong (1987) is based on the Delaunay triangulation of the stations present in the studied area. They supplemented it by subdividing each triangle in six new triangles on which they make pass a quadratic surface of Bézier. This cutting, follow-up of a smoothing extended to the whole of the triangles, makes it possible to know the interpolating function and its two derived first in all the points contained in the perimeter delimited by the measuring sites. As indicated by the definition of the method, the use of this interpolation does not make it possible to give information on the curve of interpolating surface. If this information is necessary, it is necessary to choose the Akima method which approaches surface interpolating by continuous cubic surfaces and makes it possible to easily reach the values of the derived seconds in each point of surface.

3) Cubic interpolation or Akima method

The Akima method (1970 and 1978) made use of the concept of the splines applied to an irregular distribution of measure points to an area covered with a regular two-dimensional grid. It includes several phases:

- first consists in mathematically connecting the points of measurement by a triangulation of Delaunay characterizing each triangle by a mathematical form of polynomial type with good conditions of differentiability.

- second makes it possible to bind between them these polynomials by constraints of continuity between the triangles. In this manner, the area of study is described by a total mathematical formula dependent at the same time on the space configuration of the sources and measured values.

- the last phase amounts particularizing this function in each point of the regular grid selected.

Extrapolation

Even in the absence of an explicit triangulation, the interpolation suggested by the preceding methods exists only in the polygonal envelope of the measuring sites. In outside, it is not possible to extrapolate the information built at the interior of the envelope with all the risks that that comprises. If an extrapolation is necessary it is necessary to introduce fictitious additional stations to which have must attach "realistic" concentration values.

c) Spline function type thin plate

Mathematical formulation

A manner to distribute the concentration information $z(\mathbf{R}_l)$ known only at the measuring sites $\mathbf{R}_l = (X_l, y_l)^T$ dispersed in a fixed geographical surface amounts building a function $f(x, y)$ whose graph passes by the stations while minimizing the following functional calculus

$$\iint [\left(\frac{\partial^2 f}{\partial x^2}\right)^2 + 2\left(\frac{\partial^2 f}{\partial x \partial y}\right)^2 + \left(\frac{\partial^2 f}{\partial y^2}\right)^2] dx dy$$

The interpretation of this functional calculus is immediate if it is called upon the mathematical theory relative to a particular space of the functions with derivative of order 2 continuous. In this space, the functional calculus corresponds to a standard or a distance similar to the Euclidian norm of the traditional vector space. Of one physical point of view, it is in elasticity that an interpretation is possible and more particularly if the theory of the thin sections is considered (Pram and Lifchitz, 1967). A plate is known as thin if its thickness is low compared to two other space dimensions. For this kind of plate subjected to loads and consisted a material having a very small Poisson's ratio, the functional calculus represents, except for a coefficient, the free energy of deformation of the plate for small deformations. This amount assimilating the plate to a geometrical surface whose form is given by the effect of the external forces. With balance, the function $f(x, y)$, solution of the biharmonic equation $\Delta^2 f=0$ subjected to a force Z_l, to some extent principal the function admits

$$f(x, y) = \left(\frac{z_i}{8\pi}\right) r^2 \ln(r^2)$$

On the basis of this particular result, the function to be sought *f(x, y)* for a whole of specific requests or points of measurement presents itself as the sum of a linear combination of radial functions attached to the points of measurement in a number *N* and of a linear polynomial, the unit being written in the form

$$f(x,y)=\sum_{i=1}^{n} a_i r_i^2 \ln\left(r_i^2\right)+b_0+b_1 x+b_2 y$$

where R_I is the distance between the point of measurement *I* and the point of calculation *(x,y)*. Coefficients *has*$_I$ and B_0, B_1, and B_2 are given by imposing the exact interpolation on the point of measurement.

$$z_i=f(x_i,y_i)=\sum_{j=1}^{n} E_{ij}a_j+b_0+b_1 x_i+b_2 y_i \quad \text{avec} \quad E_{ij}=r_{ij}^2\ln(r_{ij}^2) \quad \text{si} \quad i\neq j$$

In the matrix form, minimization is written

$$z=Ea+T^T b$$

where *E* is a matrix of dimension *n*n* and *T* a matrix of 3 **N* of which them *N* columns are form $(1,x_I,y_I)^T$. By adding the following mathematical condition to it

$$Ta=0$$

coefficients of the function spline *f(x, y)* of thin section type are determined by the solution of the following matrix equation

$$\begin{pmatrix} E & T^T \\ T & 0 \end{pmatrix}\begin{pmatrix} a \\ b \end{pmatrix}=\begin{pmatrix} z \\ 0 \end{pmatrix}$$

d) Kriging method

Spatial variability

The field of concentration existing on a given area varies from one place to another according to the emitted pollutants and from the weather fields which request the analysed zone. The study of this space diversity can be done by a method holding account of the space correlation of the observations. This method, called kriging method, is based on the variability of a field of concentration known in sites of measurement dispersed on an area selected. The basic element to measure this

space heterogeneity of the studied regionalized variable rests on the difference of the values measured between two distinct stations $z(\mathbf{R}_I)$ and $z(\mathbf{R}_J)$ data by

$$\frac{1}{2}\left(z(\mathbf{r}_i)-z(\mathbf{r}_j)\right)^2=\frac{1}{2}\left(z(\mathbf{r}_i)-z(\mathbf{r}_i+\mathbf{h})\right)^2$$

where $\mathbf{H} = \mathbf{R}_J - \mathbf{R}_I$ represent the distance between stations. Matherton (1963) extends to the area the variability of the concentration by introducing the experimental variogram $\Gamma(h)$ who is defined as the average of the concentration variations between distant couples of stations between them of **H,** in a number N_H**,** that is to say

$$2\gamma(h)=\frac{1}{N_h}\sum_{i=1,n}^{N_h}\left(z(\mathbf{r}_i)-z(\mathbf{r}_i+\mathbf{h})\right)^2$$

The number of couple is to the maximum of *n*(n-1)/2* when the network of measurement contains *N* stations. The variogram is a positive size which is cancelled with the distance between stations ***H***. Associated the function $\Gamma(h)$ and in so far as *m* represent the space average of the values of the concentration on the network considered, the covariogram *C(h)* is defined by

$$C(h)=\frac{1}{N_h}\sum_{i=1,n}^{N_h}\left(z(\mathbf{r}_i)-m\right)\left(z(\mathbf{r}_i+\mathbf{h})-m\right)$$

The space variance is found *C(0)* when the distance between stations ***H*** is null. Moreover, sizes *C(h)* and $\Gamma(h)$ are connected between them by

$$\gamma(h)=C(0)-C(h)=\sigma^2-C(h)$$

Model

The variogram, considered as a discrete function of *H*, presents itself by a group of dots which often structure not in recognizable forms good useful for a visual determination of the space correlations between the stations. To improve legibility of it, with the place to introduce all the distances between the stations, one gathers the data by classes. Each classify the same length is characterized by a distance equal to the average distance from the couples of stations falling into the class and by a variogram equal to the average variogram from this class. Such a process allows a smoothed representation of the experimental variogram using a variograph which should highlight structuring properties following:

- to the long distances, the smoothed experimental variograph tends towards a stage (sill) starting from a distance *has* named the range (arranges). range translates the distance beyond which concentration at the point **R** do not bring any more information on the value of the concentration to the point **R + H**. There is no more space correlation for distant stations of more than range *has*.

- at the short distances, the smoothed experimental variograph can have a discontinuity at the origin. It is a bus possibility by definition the experimental variogram is null in the beginning. The behaviour at the origin of the smoothed experimental variogram specifies the degree of regularity of the analysed variable. The existence of a non null value in the beginning indicates an effect of nugget (nugget effect). This nugget effect translates an absence of space correlation which can be explained, either by the errors to the measure, or by space variability lower than the distance sampled between stations.

It is possible to go further in the analysis of the behaviour of the variogram while passing from the experimental variogram smoothed to that of model, quite useful to carry out estimates as that will be presented later on. The model is defined as an adjustment of the experimental variogram smoothed by a linear combination of elementary analytical functions depending on only one parameter *has*, generally the range. Basic models *g(h)* the most used in the literature are as follows:

- the nugget model

$$g(h) = \begin{cases} 1 & si\ h > 0 \\ 0 & si\ h = 0 \end{cases}$$

- the linear model

$$g(h) = h$$

- the spherical model

$$g(h) = \begin{cases} 0 & \text{si} \quad \text{h} \geq \text{a} \\ \frac{3}{2}\frac{h}{a} - \frac{1}{2}\left(\frac{h}{a}\right)^3 & \text{si} \quad 0 \leq \text{h} \leq \text{a} \end{cases}$$

- the Gaussian model is used when the behaviour in the beginning is parabolic for the analysed variable

$$g(h) = 1 - \exp\left(-3\left(\frac{h}{a}\right)^3\right)$$

- the model power utilizes an exhibitor has strictly positive but lower than 2

$$g(h) = h^a$$

- the exponential model

$$g(h) = 1 - \exp\left(-3\frac{h}{a}\right)$$

- the Holesin model is the complementary one to the unit of the cardinal sine of period has. This model is considered when the phenomenon has such a behaviour

$$g(h) = \begin{cases} 1 - \sin\left(2\pi\frac{h}{a}\right) \Big/ \left(2\pi\frac{h}{a}\right) & \text{if } h > 0 \\ 0 & \text{if } h = 0 \end{cases}$$

The successive modification of the experimental variogram, if it facilitates the analysis of the interactions, is not done without the introduction of additional difficulties related to the subjacent assumptions present into the stages of synthesis. First comes from the sampling of the distances between the stations and the number of couples to be observed by classes. The criterion of a sufficient continuity of the variograph is a condition necessary but name sufficient. Bogaert and *Al*. (1995) suggest in first analysis considering more than one ten classes equal amplitudes covering the interval of the distances active with distance zero to the distance corresponding to half of the smallest dimension of the studied area, this by supposing that the number of couple of stations by class is important, at least 50 in their analyses. If this number cannot be held, the stabilization of the variographs compared to the width of the classes is to be considered like one of the possible criteria of definition of the classes.

The second problem relates to the choice of the model of variogram. Although it is depending partly on the preceding criteria, the model to be retained can made only of one limited number of simple form if one refers to the "Razor of Occam", principle according to which "One should not multiply the entities more than it is necessary". In practice two to three basic models are to be retained. All the basic models can be combined by noting however that the use of the nugget model can be made only in so far as the selected combination explains the studied variable or that the use of the other continuous basic functions in the beginning cannot correctly adjust the smoothed experimental variograph.

It remains to describe the method whereby the model selected will marry the variograph as well as possible. Let us represent by *?(h)* the smoothed curve established starting from the experimental variogram for classes of equal amplitudes

in a number *nc* and by *g(h)* the model connected to *NS* basic models $G_K(H)$ by the linear relation

$$g(h) = \sum_{k=1}^{ns} b_k g_k(h)$$

with coefficients B_K to define. Adjustment of *g(h)* by report with *?(h)* is realized by the use of the method of least squares. This way of proceeding comes down to minimize the variable

$$\sum_{l=1}^{nc} p(h_l)(\gamma(h_l) - g(h_l))^2$$

under the constraint to preserve the positive character at the coefficients B_K (Bogaert and *Al*. (1995)) the introduction of the weights $p(h_L)$ allows to hold account of the contribution of information for each class *L*. The value of each weight corresponds to the relative frequency of the number of couples belonging to each class *L*.

Ordinary kriging (OK)

A manner simple to present this method is to return to the general formulation of the method of weighting. Let us consider on a given area them N measuring sites with their value of the concentration ZI measured at the point RI , catch at a time given or regarded as the average over a given period, as well as the value to be sought Z0 in an unspecified point of the area. In General, this point corresponds to a node of a rectangular grid covering the area of study. Instead of simply identifying the value sought with the weighted average of the concentrations (estimator) by using analytical functions adapted to fix the weights, it is more interesting to consider the existence of an error between the value to be sought and its estimator and to be useful of this error to fix the weights. To carry out that, one will seek to minimize the variance of this error while preserving the natural constraint that the sum of the weights W_I that is to say equalizes with the unit.

Mathematically, the problem leaves the expression of the variance of the error defined by

$$\sigma_e^2 = \left(z_0 - \sum_{i=1}^{n} w_i \, z(\mathbf{r}_i) \right)^2 \quad \text{with} \quad \sum_{i=1}^{n} w_i = 1$$

One develops then this expression while being useful oneself of the constraint on the weights to arrive at the expression

$$\sigma_e^2 = 2\sum_{i=1}^{n} w_i \frac{1}{2}\left(z_0 - z(\mathbf{r}_i)\right)^2 - \sum_{i=1}^{n} \sum_{j=1}^{n} w_i w_j \frac{1}{2}\left(z(\mathbf{r}_i) - z(\mathbf{r}_j)\right)^2$$

The minimization of this variance calls upon the function of Lagrange and its multiplier of the same name μ. i.e. with the function

$$L = \sigma_e^2 - 2\mu\left(\sum_{i=1}^{n} w_i z(\mathbf{r}_i) - 1\right)$$

The minimum is reached when that one cancels the derivative partial compared to the weight W_I and with the multiplier μ. This led to *(n+1)* linear equations called of the ordinary kriging

$$\begin{cases} \sum_{j=1}^{n} w_j \frac{1}{2}\left(z(\mathbf{r}_i) - z(\mathbf{r}_j)\right)^2 + \mu = \frac{1}{2}\left(z_0 - z(\mathbf{r}_i)\right)^2 \quad \text{for i} = 1,\ldots,\text{n} \\ \sum_{i=1}^{n} w_i - 1 = 0 \end{cases}$$

To be complete, it is still necessary to establish the minimal value of the variance of the error. One proceeds in two times while starting by multiplying first equation OK by the weight of kriging W_I , that one summons then on all the stations. The result, simplified by the constraint, is introduced into the developed expression of the variance, which leads to the following result

$$\sigma_e^2 = \sum_{i=1}^{n} w_i \frac{1}{2}\left(z_0 - z(\mathbf{r}_i)\right)^2 + \mu$$

Posed just as it is, the problem of the kriging cannot be solved strictly since the value of the variable to be sought is present in the whole of the equations. The only means, to circumvent this difficulty and to close the problem, is to introduce the model selected to explain the variability of the size studied and to replace each difference of the values of the variable between stations by the value of the model for the distance corresponding between stations. This way of proceeding led, if the location of the measuring sites is made each time starting from the point of interpolation, to the interpolated value Z_0 and with the variance of the error σ^2_E data by

$$\begin{cases} z_0 = \sum_{i=1}^{n} w_i z(h_i) \\ \sigma_e^2 = \sum_{i=1}^{n} g(h_i) + \mu \end{cases}$$

when weights of kriging W_i and the multiplier of Lagrange ? result from the linear equations

$$\begin{cases} \sum_{j=1}^{n} w_j g(h_{ij}) + \mu = g(h_i) \text{ pour } i = 1,...,n \\ \sum_{i=1}^{n} w_i - 1 = 0 \end{cases}$$

The analysis of equations OK show that the weights of kriging W_i depend

- variable to be analysed,
- relative localization of the stations between them,
- space structure of the variable known through the model of variogram.

4. COMPARATIVE STEPS AND STUDIES

a) Phase 1

In a first step, we adopted two methods of interpolation to know the method of weighting compared to the distances and the method of Akima. These methods were applied to two data files of air pollution which were extracted from the bank of data of CELINE. The first data file relates to the averages over 8 hours of measurements of ozone on all Belgium since the January beginning until the end September 1998. The second play considers pollution day labourer due to the sulphur dioxide SO_2 for the winter period of 1997-1998. Each data file includes/understands two files: the first giving the co-ordinates Lambert of the stations and the other values of the pollution measured to the stations over all the period of study selected. For ozone, there are 27 stations considered and 819 temporal steps (273 days) while there are 62 stations for the SO_2 and 182 temporal steps.

Figures OZONE and SO_2, presented below, the graphic results of the two methods of interpolation chosen by holding account of the variation of some their parameters give. The interpolated values are calculated with the nodes of a formed grid of squares covering all the Belgian territory in the frame of reference Lambert. The selected mesh *a priori* has a side of 1 km.

To facilitate the visual comparison between the various methods, all the charts relative to the same pollutant are presented with a scale of values (of colors) identical.

A first conclusion arises clearly from the results: the tendencies relative to the same pollutant are found in each of the two methods of interpolation. For recall, with the methods relating to the method of weighting compared to the distances, which occurs between the stations cannot exceed the values in these stations. The file of the data input indicates a maximum of 66?g/m^3 for ozone at the stations N113 and N121 and a maximum of 45?g/m^3 for the SO_2 at the R240 station. The results based on the method of Akima agree with the first method but while connecting, as it should be, overall the values measured at the stations. The second conclusion relates to the maximum values resulting from calculation on the grid of 1km on side. If one finds similar maximum values for each alternative of the weighted average for ozone with a maximum value of 65,7?g/m^3, one observes different maximum values according to the methods for the SO_2. the method of Akima based on the continuity of local cubic surfaces posts a more important maximum value naturally (90,4?g/m^3 for ozone and 47?g/m^3 for the SO_2), value which is not in a station. With this, one can add that the minimal values vary more slightly if account is not held, on the one hand, of the results out of ozone given by the method of Thiébaux and Pedder with a selected ray of influence of 40km (since the stations, although dispersed, are in a number lower than for the stations measuring the SO_2) and, in addition, of the negative values of the concentration obtained by the method of Akima with the SO_2 as we will see it later on.

The various figures emphasize the zones industrialized as well as the zones with great traffic attached to the towns of Brussels, Antwerp, Ghent and Charleroi. For the SO_2, to the south of the furrow Hatred, Sambre and Meuse, the dominant colour dark blue indicates that the concentration in SO_2 y is very weak. It is the reverse for ozone where one notices ozone peaks in the south of the furrow Haine, Sambre and Meuse but of the wells of ozone in the industrialized zones and traffic.

Let us consider maintaining the behaviour individual of the various methods of interpolation.

For the interpolation balanced by the distances with α = 2, the identical concentration curves are brought closer on the level of the points measurement than for the same curves calculated with α = 4.

For is the method of Thiébaux and Pedder, it interesting to remember that more? is large, more the weight given to the observations is small if the distance between the point of measurement and the point of calculation is while remaining lower than the ray of influence. Conversely, more this distance is small, more the observation takes weight. Variations of the exposant α influence the results slightly.

For does the method of Sasaki and Barnes with a ray of influence equalize with 40km, the behavior is practically identical to that of the method of Thiébaux and Pedder with one α = 2. More one moves away from the point of measurement plus the effect of measured pollution to a station decreases without never brutally falling to zero like in the method of Thiébaux and Pedder. There is no zone with zero values (blue harms).

The Akima method is very sensitive to the density of the initial points and their space distribution. More information is rich and distributed well, better is the result. A lack of data can give place to a non realistic result which does not return within the limits of the measured values. The Akima method individually does not consider more the points as the interpolation by the method of weighting compared to the distances can do it in the absence of a good density of points of measurement (absence of zone ' pâtés' or ' trous' goshawks of the points of measurement). Being given that the Akima method is a total method, it gives place to not very reliable results *apart from the closed traverse containing all the sources*. Indeed outside this polygon, the Akima method must extrapolate the values whereas it interpolates them inside. This phenomenon realizes easily at the border between France and Belgium along the line connecting the N100 stations to N029 and also in the North of Belgium according to the N016 line to R831. It is in the areas of extrapolation that one finds values negative of concentration as shows it the chart relating to the SO_2. With the interior of the polygon, of the adverse effects can also occur in areas located between urban zones at strong density of measuring site since the space stations distribution there is much dispersed. That is marked especially for the results relating to the SO_2, for example in the triangle Brussels, Ghent and Antwerp.

OZONE

Interpolation with Inverse-distance method, alpha = 2

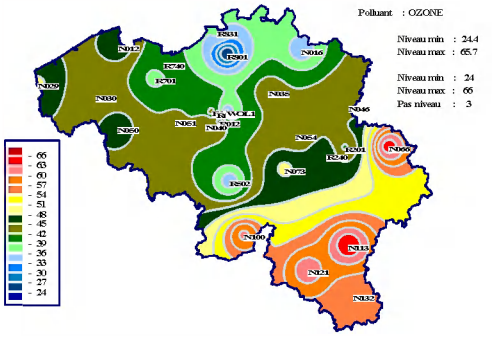

Interpolation with Inverse-distance method, alpha = 4

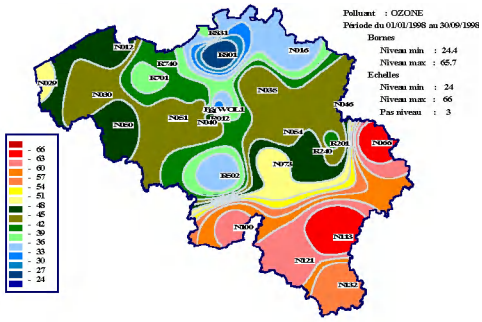

Thiébaux and Pedder model, alpha = 2, R = 40km

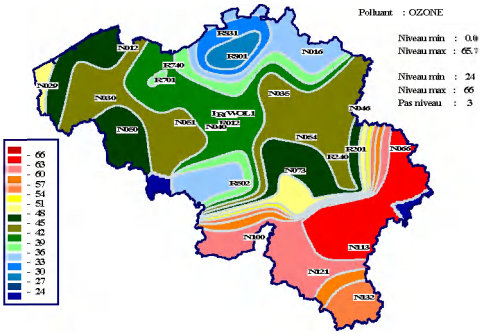

Thiébaux and Pedder model, alpha = 4, R = 40km

Sasaki and Barnes R = 40km

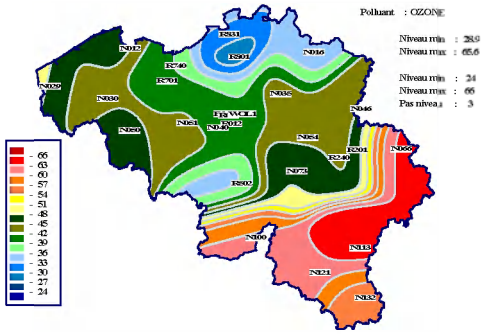

Akima method

SO_2

Interpolation with Inverse-distance method, alpha = 2

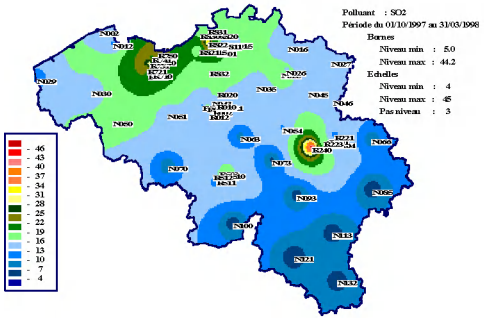

Interpolation with Inverse-distance method, alpha = 4

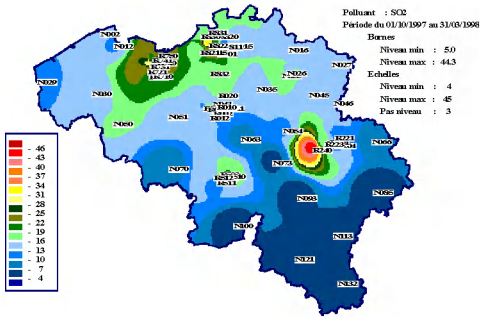

Thiébaux and Pedder model, alpha = 2, R = 40km

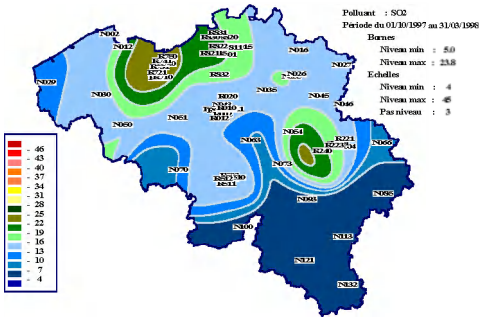

Thiébaux and Pedder model, alpha = 4, R = 40km

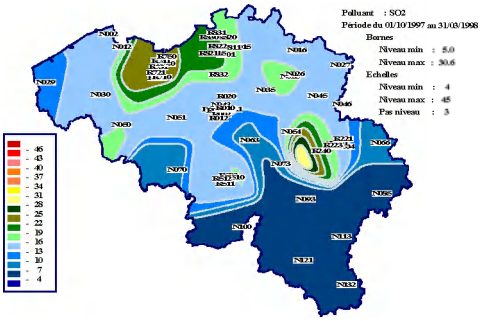

Sasaki and Barnes R = 40km

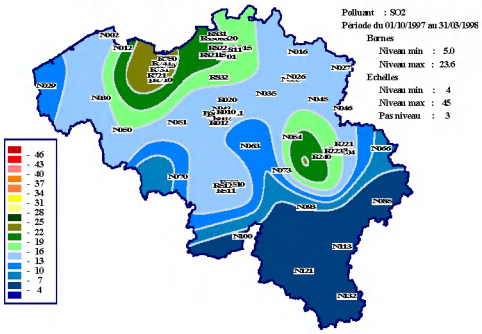

Akima method

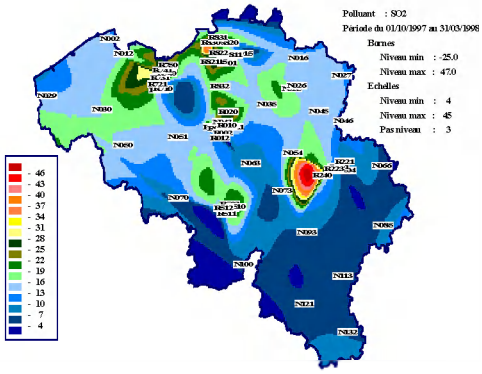

This first confrontation made it possible to highlight the advantages and the weaknesses of the first two adopted interpolation methods.

The inverse-distance method is a local method where each point of measurement is considered individually. Conversely, the Akima method (which is a total method), is more sensitive to the distribution of the measuring sites on the area of study. Difficulties exist dice that there are few measuring sites or that these stations are distributed in an irregular way. In these very current cases in pollution, it is necessary, on the one hand, to find compromises and, on the other hand, to seek an either definite method on the basis of a triangulation but by a minimization of a size extending on all the grid from calculation. A first solution is to locally use the method of the weighted average for better initialising the Akima method in the vicinity of the aberrant values.

To show the interest of it, a way simple to reduce the harmful effects is proposed on a purely example basis by the figures presented below where one associated the two types of methods of interpolation so as to hold account of their specificity, local or total. One represented there for ozone and the SO_2 does the average enter the results achieved by the method of Akima and the results of the method of interpolation balanced by the distances with an exhibitor α = 4, charts appearing very similar. In both cases, the effects edge are mitigated and a softer dispersion is felt around the wells of pollution in and around the cities while preserving the peaks of pollution. The maximum values reached remain very close to the maximum values calculated at the points of measurement.

Average between Akima method and Inverse-distance α = 4 for OZON

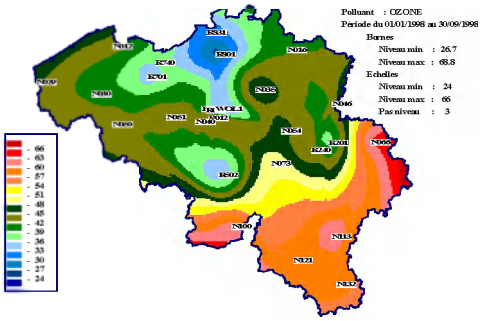

Average between Akima method and Inverse-distance α = 4 for SO2

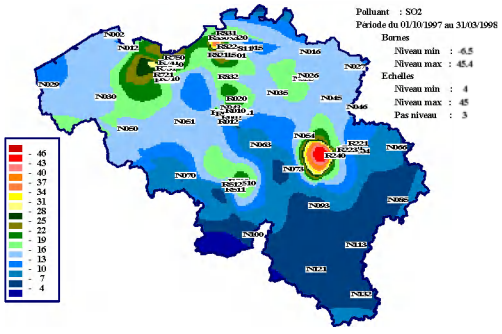

b) Phase 2

This second step wishes to make improvements to the former results by introducing a smoothing method, the separation of the stations according to their establishment close or remote of the sources of emission and a method of elimination of the aberrant values. More particularly, it considers:

- the application of the method of smoothing by N.U.R.B.S. with the results obtained by the inverse-distance methods.
- the influence of the separation of the stations between the national stations and the regional stations.
- improvement of the application of the method of Akima by suppression of the negative values of concentration resulting from the strong gradients and by the introduction of fictitious stations charged each one with relevant information to carry out extrapolations beyond closed polygonal contour containing all the triangles of Delaunay.

At this stage, the linear interpolation method based on the triangulation of Delaunay is applied. It constitutes the initial version of any interpolation based on a triangulation.

Application of N.U.R.B.S. functions with the inverse-distance methods

Method of smoothing by N.U.R.B.S. whose definition is proposed in appendix 1 is imposed on the three methods of weighting compared to the selected distances: the interpolation balanced by the opposite of the distances, the method of Sasaki - Barnes and the method of Thiébaux - Pedder. In the first calculation, the methods of weighting compared to the distances were used with a mesh of 1 km. The second calculation, carried out with an aim of reduction of the times computing and sensitivity to the choice of the mesh of the network of interpolation, cumulates an interpolation balanced compared to the distances for a mesh of 10 km with the method of N.U.R.B.S. so as to bring back the results to the level of a mesh of 1 km.

The two sets of figures have the results of the various methods of weighting compared to the distances retained without and with complementary application of the method of N.U.R.B.S.

The application of the N.U.R.B.S method show that one obtains a smoothing of the data interpolated without total assignment of the minimal and maximum values both for ozone and SO_2. Space representations without and with N.U.R.B.S. are similar, on the left figures, with a fine interpolation for a mesh of 1 km and, on the right of the

figures, with a 10 km mesh broader but reduced by N.U.R.B.S. with a mesh of 1 km. One can conclude that N.U.R.B.S. smooth the results obtained without weakening the extrema.

	OZONE		**SO_2**	
	Interpolation Inverse-distance method	**Interpolation Inverse-distance method with N.U.R.B.S.**	**Interpolation Inverse-distance method**	**Interpolation Inverse-distance method with N.U.R.B.S.**
α = 2	Min. : 24.4 Max. : 65.7	Min. : 29.1 Max. : 63.7	Min. : 5.0 Max. : 44.2	Min. : 6.4 Max. : 29.1
α = 4	Min. : 24.4 Max. : 65.7	Min. : 25.4 Max. : 65.6	Min. : 5.0 Max. : 44.3	Min. : 5.0 Max. : 36.8
	Sasaki and Barnes	**Sasaki and Barnes with N.U.R.B.S**	**Sasaki and Barnes**	**Sasaki and Barnes with N.U.R.B.S**
R=40km	Min. : 28.9 Max. : 65.6	Min. : 29.7 Max. : 65.7	Min. : 5.0 Max. : 23.6	Min. : 5.0 Max. : 23.4
	Thiébaux and Pedder model	**Thiébaux and Pedder model with N.U.R.B.S.**	**Thiébaux and Pedder model**	**Thiébaux and Pedder model with N.U.R.B.S.**
α = 2 R=40km	Min. : 0 Max. : 65.7	Min. : 0.9 Max. : 65.7	Min. : 5.0 Max. : 23.8	Min. : 4.8 Max. : 23.6
α = 4 R=40km	Min. : 0 Max. : 65.7	Min. : 0.9 Max. : 65.7	Min. : 5.0 Max. : 30.6	Min. : 4.7 Max. : 26.3

The results analysis presented in this table shows that the maximum values calculated by the various methods of interpolation supplemented by a smoothing using N.U.R.B.S. are always lower or equal to the maximum calculated by these same methods without the application of N.U.R.B.S. On the other hand, the minima remain relatively the same ones compared to the minima of the methods of interpolation without the use of N.U.R.B.S.

A disadvantage related to the application of N.U.R.B.S. is its computing time: three times are needed more time to carry out association balanced interpolation and N.U.R.B.S. that to make the only interpolation balanced with a fine grid.

OZONE

Interpolation Inverse-distance method alpha = 2

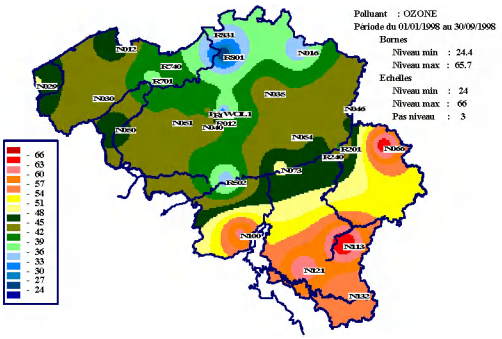

Interpolation Inverse-distance method alpha = 2 with N.U.R.B.S.

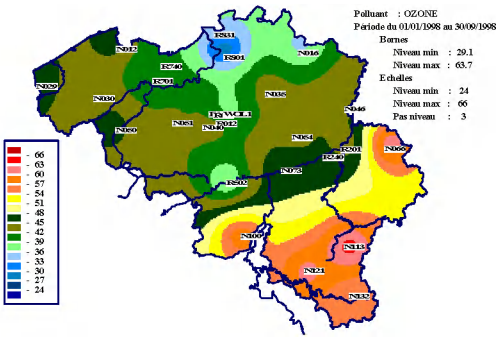

Interpolation Inverse-distance method alpha = 4

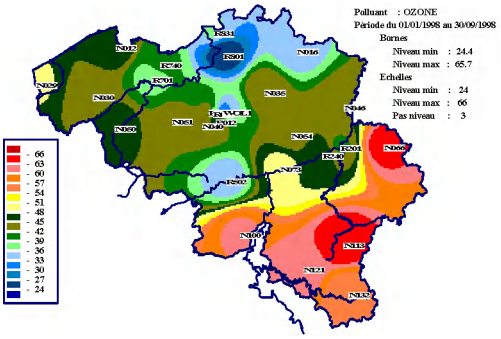

Interpolation Inverse-distance method alpha = 4 with N.U.R.B.S.

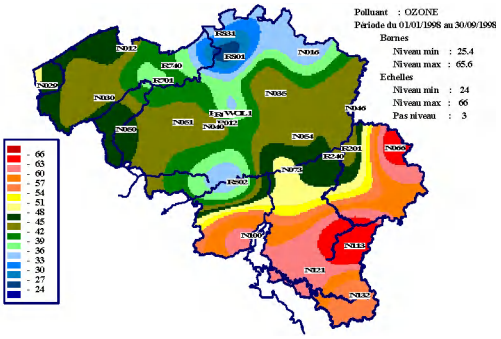

The application functions N.U.R.B.S. takes 8 minutes for the case above.

Sasaki and Barnes, R = 40Km

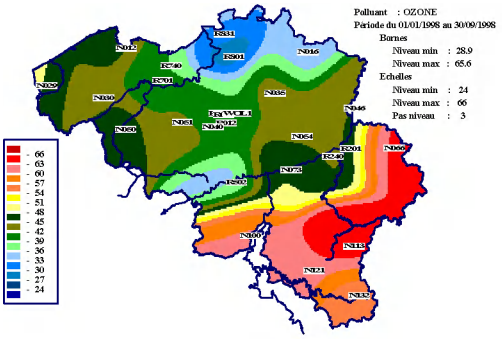

Sasaki and Barnes, R = 40Km, + N.U.R.B.S.

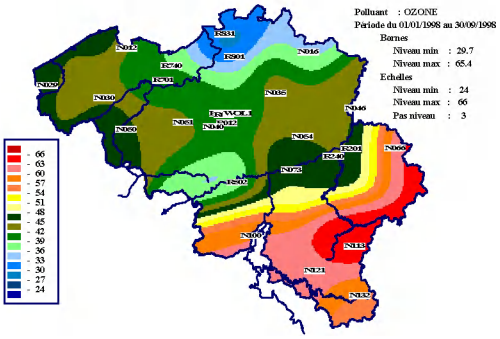

The application functions N.U.R.B.S. takes 15 minutes for the case above.

Thiébaux and Pedder model, alpha = 2 et R = 40Km

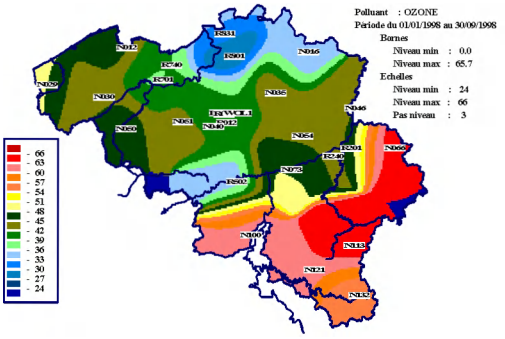

Thiébaux and Pedder model, alpha = 2 et R = 40Km + N.U.R.B.S.

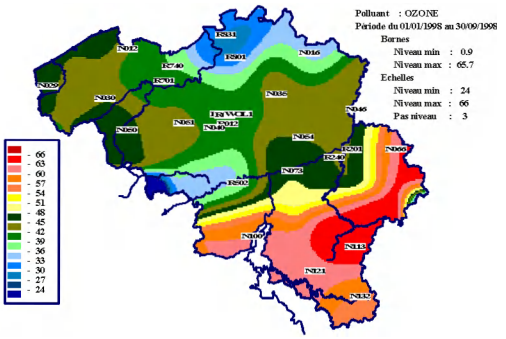

Thiébaux and Pedder model, alpha = 4 et R = 40Km

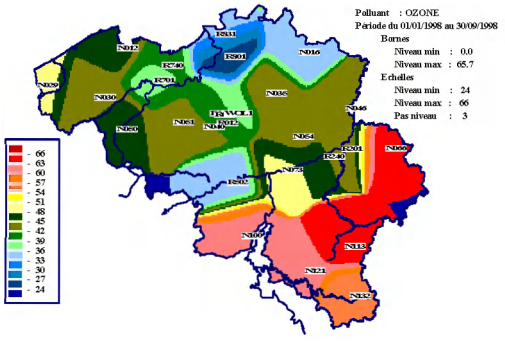

Thiébaux and Pedder model, alpha = 4 et R = 40Km + N.U.R.B.S.

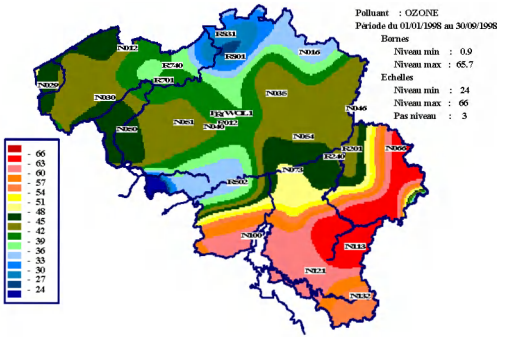

The application functions N.U.R.B.S. takes 15 minutes for the case above.

SO_2

Interpolation Inverse distance method alpha = 2

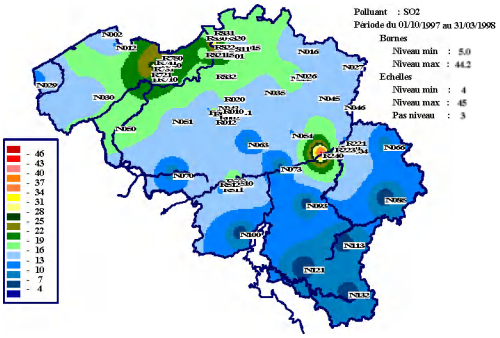

Interpolation Inverse distance method alpha = 2 with N.U.R.B.S.

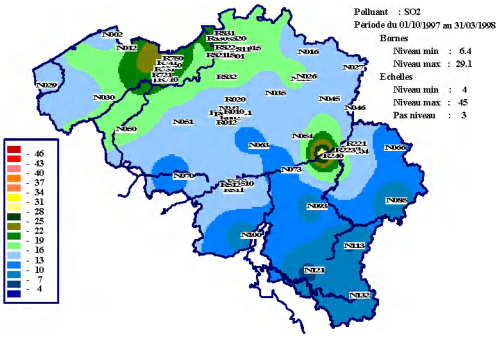

Interpolation Inverse-distance method alpha = 4

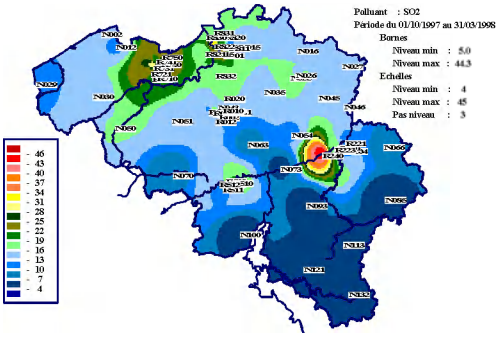

Interpolation Inverse-distance method alpha = 4 with N.U.R.B.S.

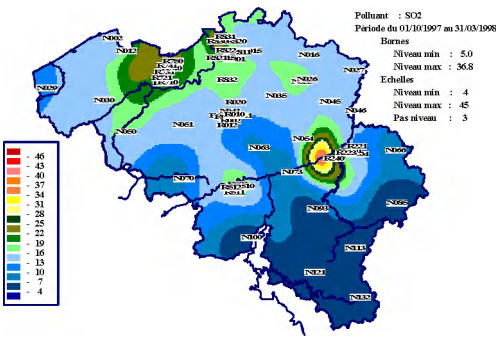

The application of N.U.R.B.S. takes 8 minutes for the case above.

Sasaki and Barnes, R = 40Km

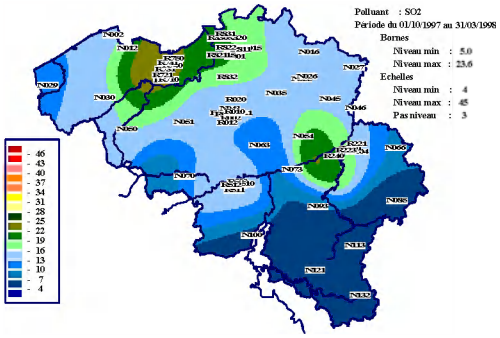

Sasaki and Barnes, R = 40Km, + N.U.R.B.S.

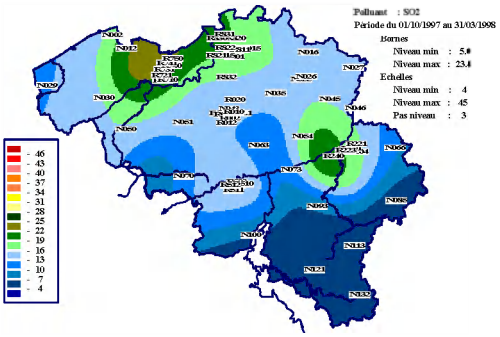

The application of N.U.R.B.S. takes 15 minutes for the case above.

Thiébaux and Pedder model
alpha = 2 and R = 40Km

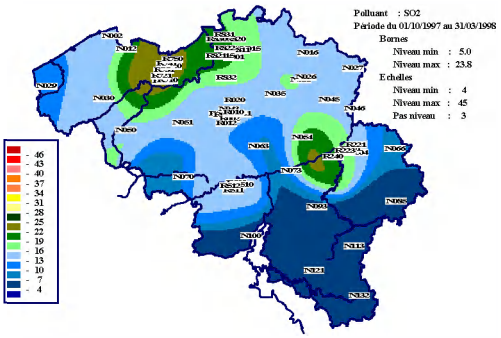

Thiébaux and Pedder model
alpha = 2 and R = 40Km, + N.U.R.B.S.

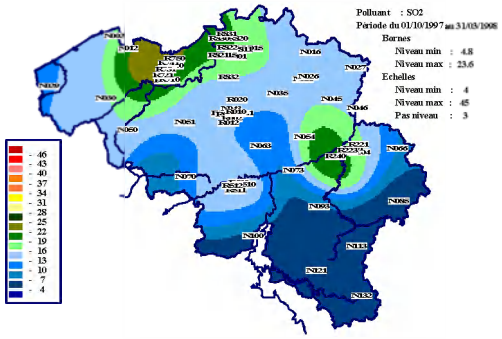

Thiébaux and Pedder model
alpha = 4 and R = 40Km

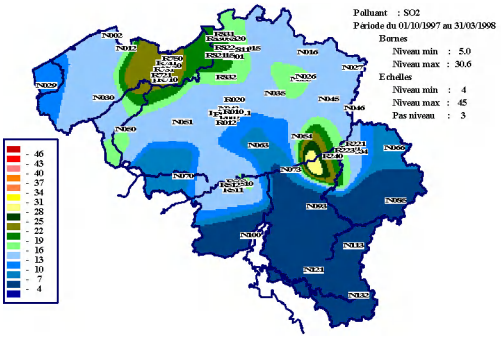

Thiébaux and Pedder model
alpha = 4 and R = 40Km, + N.U.R.B.S.

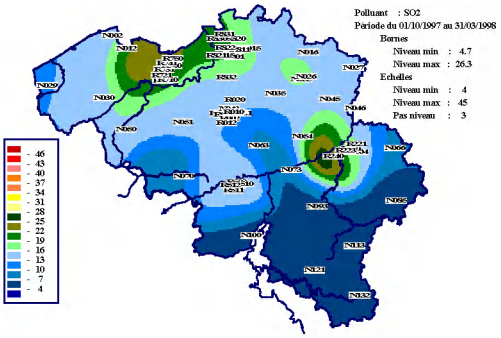

The application of N.U.R.B.S. takes 15 minutes for the case above.

Choice of the stations for the inverse-distance methods

1) Effect of the division for the total network

Since the creation of the measurements networks of pollution in Belgium, the name of the station carries information relative to its positioning compared to the sources. The measurement network can be separate in two networks called 'national' network and 'regional' network (cities). The measuring sites known as national are those which are supposed to be influenced little by point sources and/or surface sources. The other stations belonging to the regional network are established in the great agglomerations with their neighbouring factories site represented by Brussels, Charleroi, Liege, Ghent and Antwerp.

One easily locates the type of station thanks to the first letter of their name: letter N is used to determine a national station while the letter R (except for the station in Brussels WOL1), is reserved for the regional stations.

OZONE

SO2

As noted by the maps presented above, the stations relating to ozone are more or less well distributed on the safe territory in the Brussels area where the stations of the two types mix. The reverse arises for stations SO_2 where one especially notices much more zones with stations of the two types in the five great agglomerations.

What become now the results of the inverse-distance method coupled or not with N.U.R.B.S? The figures below illustrate the preceding applications by holding account of the nature of the stations distributed between the national and regional stations.

In these figures, one notes indeed that the national stations reflect well the situations of pollution relating to the entirety of the territory whereas the regional stations highlight the more local influences. It is to be noticed that while proceeding in this way one loses some stations located well for ozone what is not the case for the SO_2 for which the distribution remains very satisfactory, this being due to the greatest number of measuring sites for the SO_2 that for ozone.

It is to be noticed that the balanced interpolation gives a result more uniform and thus less tributary of the regrouping of the stations in the case where the selection is limited to the national stations. On the other hand, if the selection holds account only regional stations, it is noticed that the interpolation emphasized clearly the presence of these stations.

National stations for ozone

Inverse distance interpolation
alpha = 2, national stations

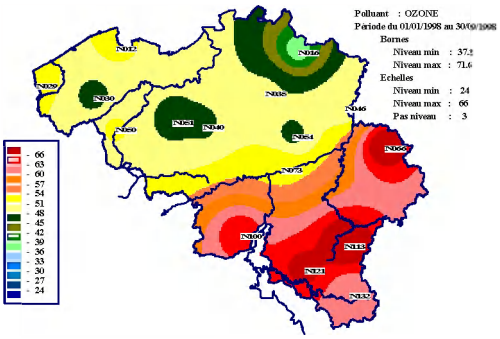

Inverse distance interpolation
alpha = 2, national stations,
+ N.U.R.B.S.

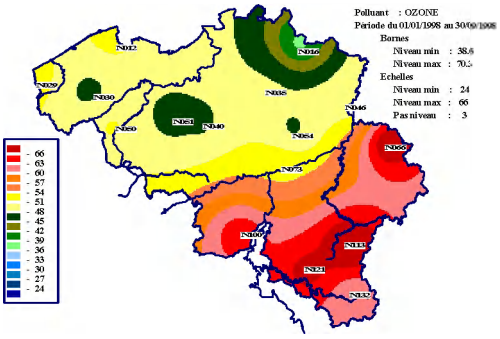

Inverse istance interpolation
alpha = 4 national stations

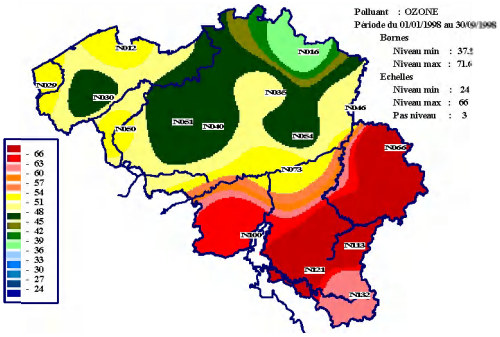

Inverse istance interpolation
alpha = 4 national stations,
+ N.U.R.B.S.

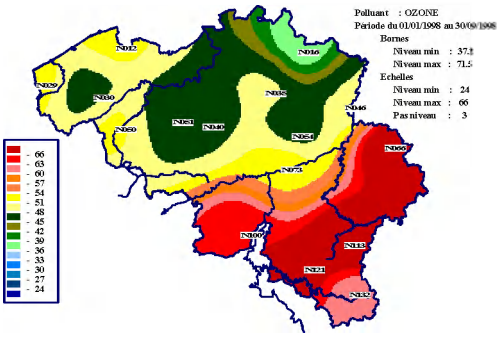

Sasaki and Barnes
national stations

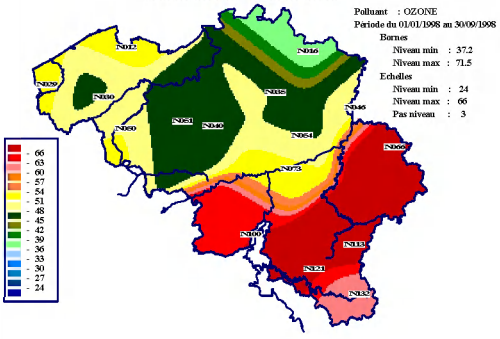

Sasaki and Barnes
+ N.U.R.B.S., national stations

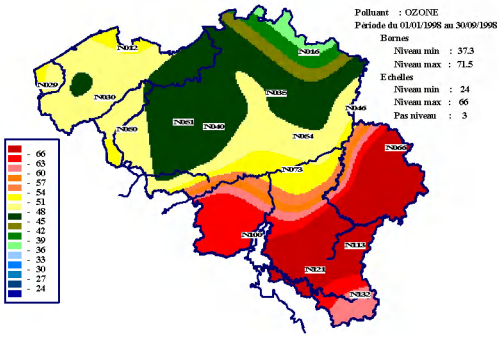

Thiébaux and Pedder model, alpha = 2,
R = 40km, national stations

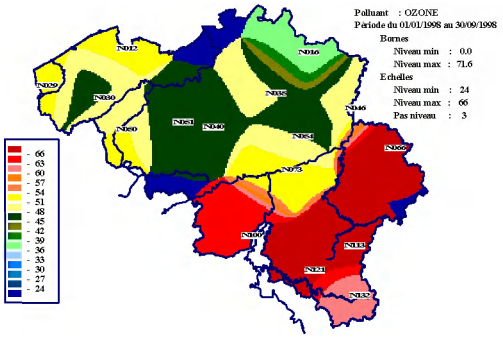

Thiébaux and Pedder model, alpha = 2,
R = 40km, + N.U.R.B.S., national stations

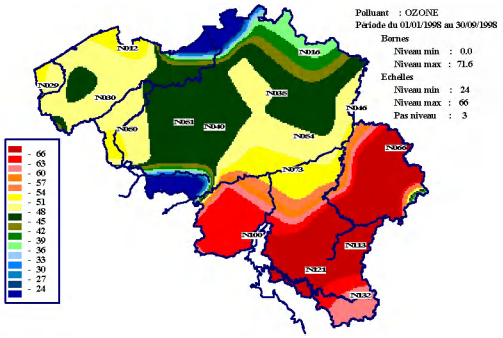

Modèle de Thiébaux et Pedder, alpha = 4,
R = 40km, stations nationales

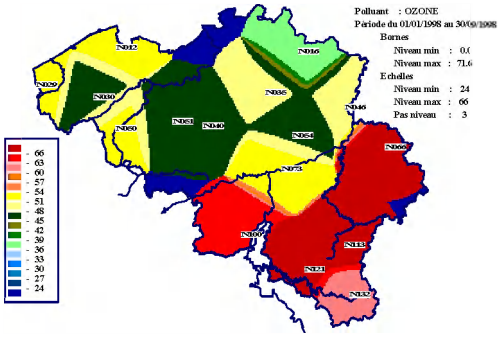

Modèle de Thiébaux et Pedder, alpha = 4,
R = 40km, + N.U.R.B.S., stations nationales

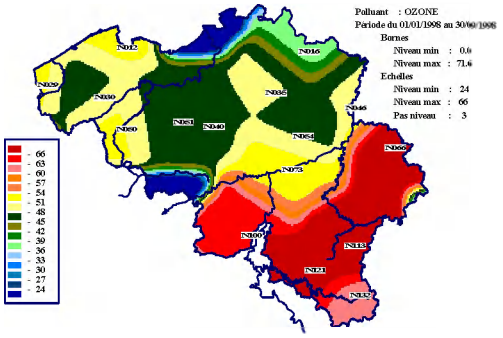

Regional stations for ozone

Interpolation inverse distance method, alpha = 2, regional stations

Interpolation inverse distance method, alpha = 2, regional stations, + N.U.R.B.S.

Interpolation inverse distance method, alpha = 4, regional stations

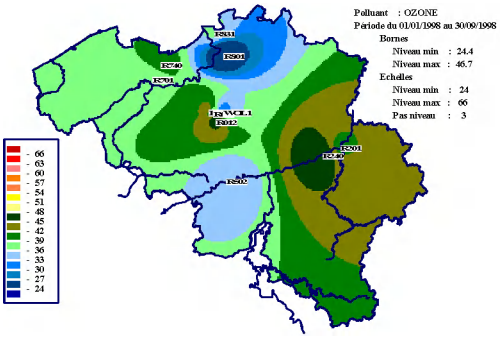

Interpolation inverse distance method, alpha = 4, regional stations, + N.U.R.B.S.

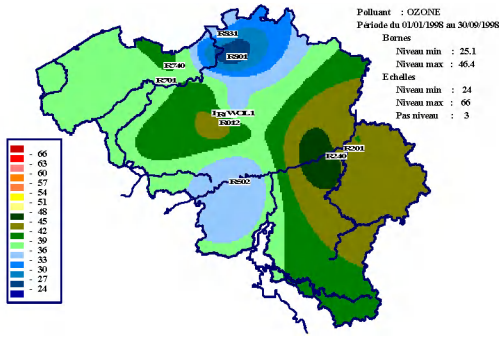

Sasaki and Barnes Regional stations

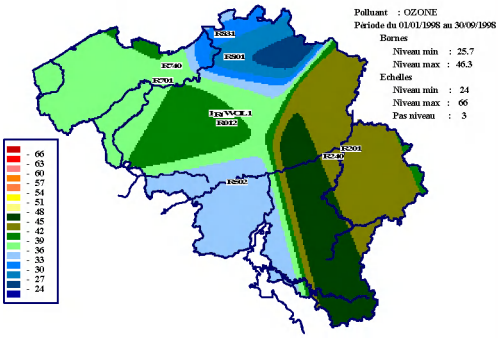

Sasaki and Barnes + N.U.R.B.S., regional stations

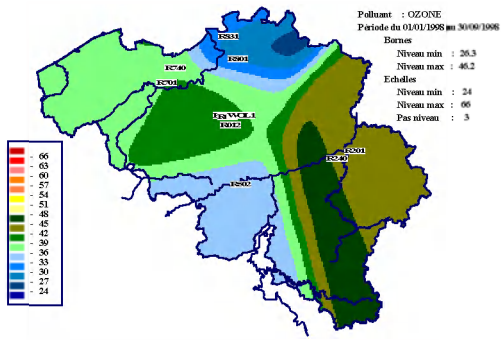

Thiébaux and Pedder model, alpha = 2,
R = 40km, regional stations

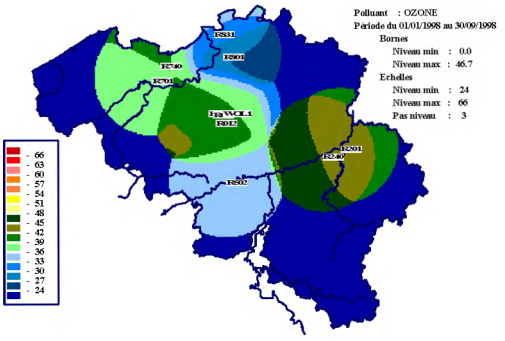

Thiébaux and Pedder model, alpha = 2,
R = 40km, + N.U.R.B.S., regional stations

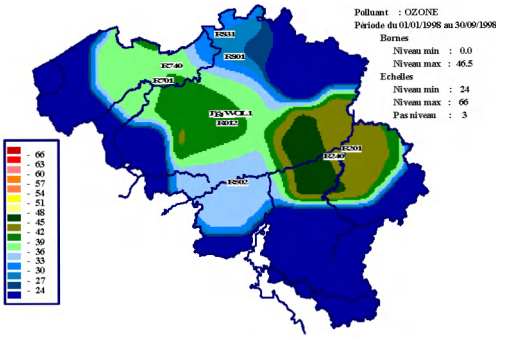

Thiébaux and Pedder model, alpha = 4,
R = 40km, regional stations

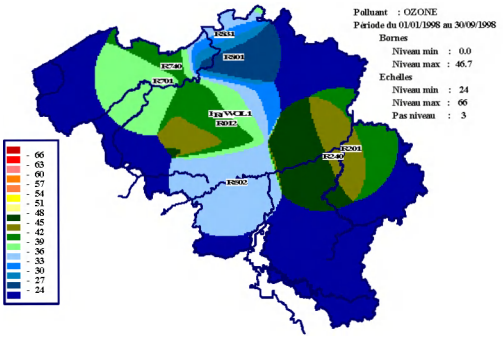

Thiébaux and Pedder model, alpha = 4,
R = 40km, + N.U.R.B.S, regional stations

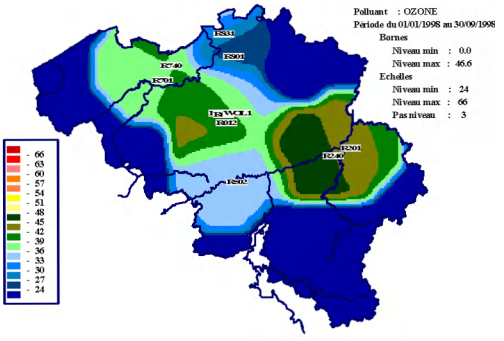

SO_2 national stations

Interpolation inverse distance method, alpha = 2, national stations

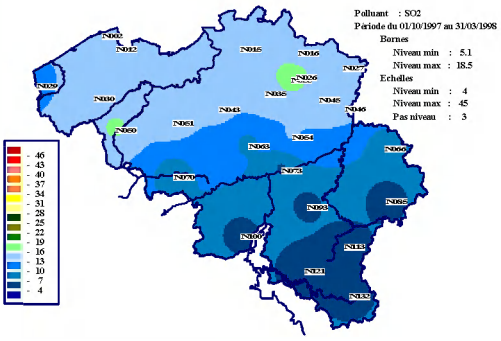

Interpolation inverse distance method, alpha = 2, national stations, + N.U.R.B.S.

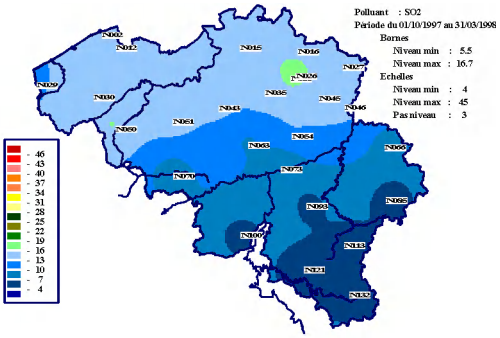

Interpolation inverse distance method, alpha = 4, national stations

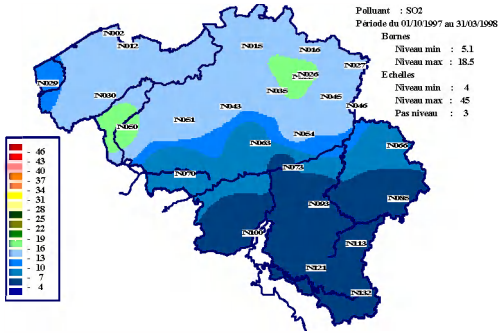

Interpolation inverse distance method, alpha = 4, national stations, + N.U.R.B.S.

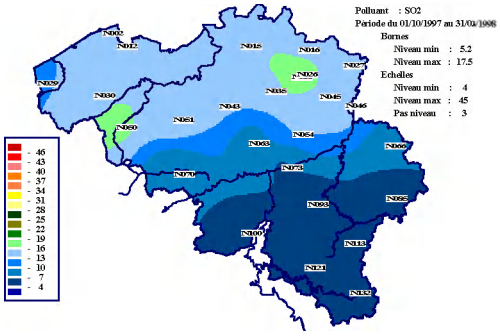

Sasaki and Barnes national stations

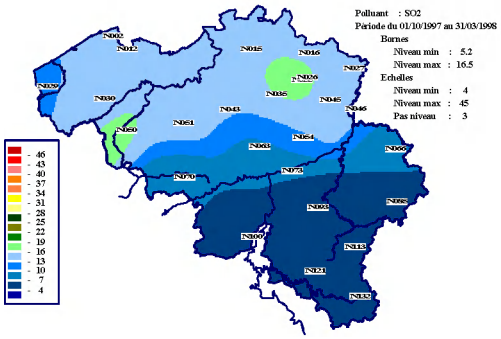

Sasaki and Barnes + N.U.R.B.S., national stations

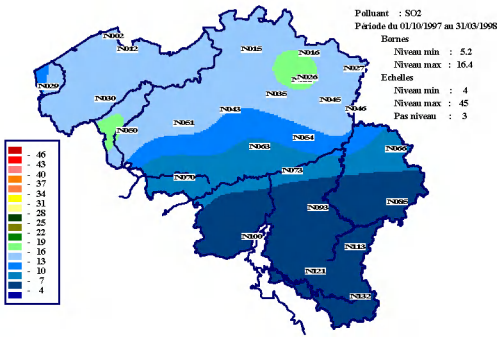

Thiébaux and Pedder method, alpha = 2,
R = 40km, national stations

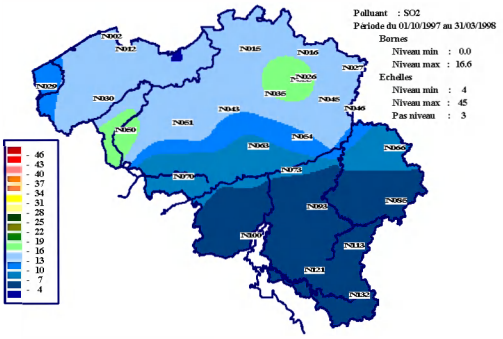

Thiébaux and Pedder method, alpha = 2,
R = 40km, + N.U.R.B.S., national stations

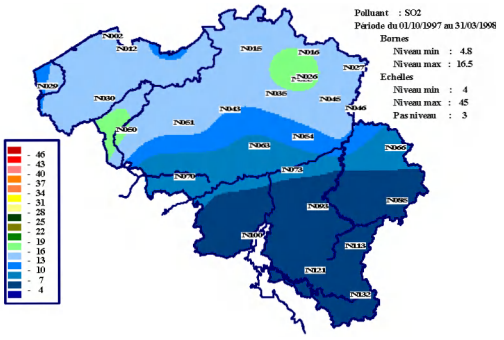

Thiébaux and Pedder model, alpha = 4,
R = 40km, national stations

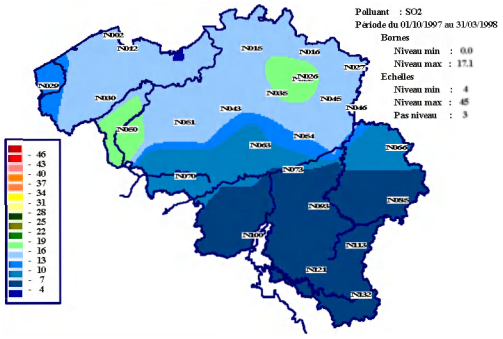

Thiébaux and Pedder model, alpha = 4,
R = 40km, + N.U.R.B.S., national stations

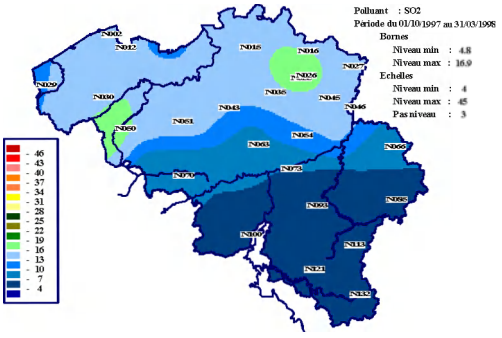

SO_2 regional stations

Interpolation inverse distance method
alpha = 2, regional stations

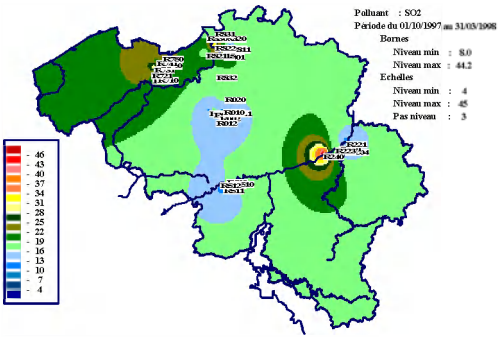

Interpolation inverse distance method,
alpha = 2, regional stations, + N.U.R.B.S.

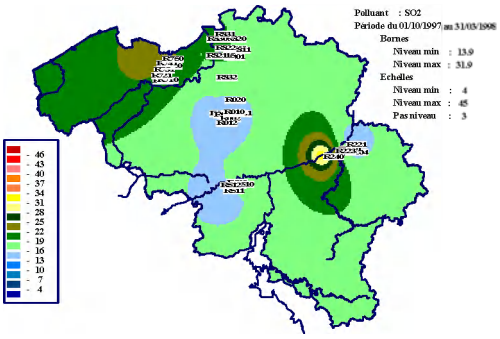

Interpolation inverse distance method,
alpha = 4, regional stations

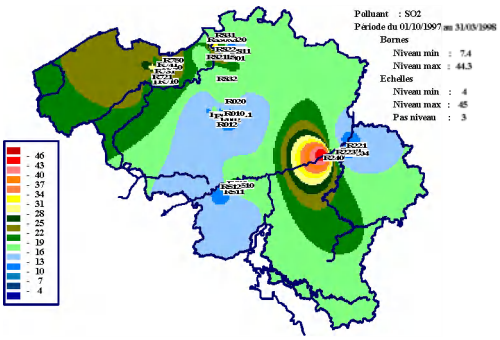

Interpolation inverse distance method,
alpha = 4, regional stations, + N.U.R.B.S.

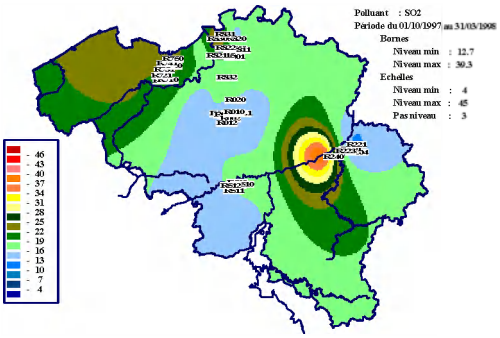

Sasaki and Barnes
regional stations

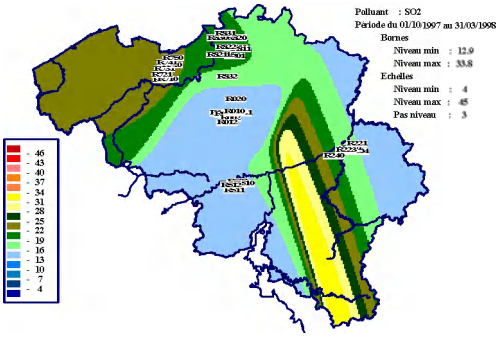

Sasaki and Barnes
+ N.U.R.B.S., regional stations

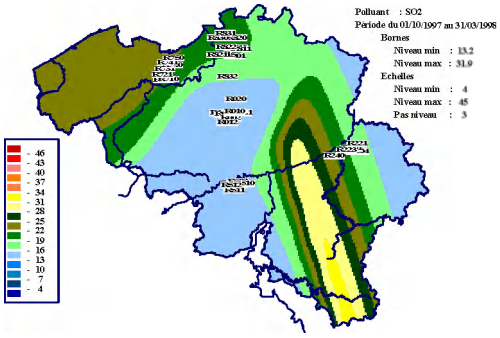

Thiébaux and Pedder model, alpha = 2,
R = 40km, regional stations

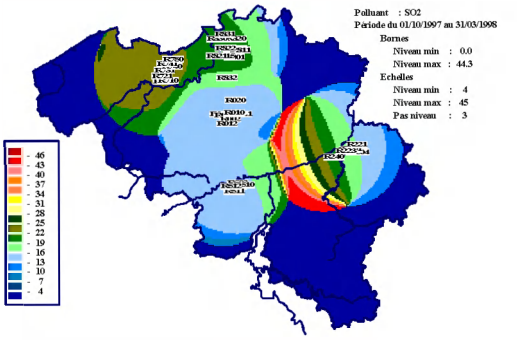

Thiébaux and Pedder model, alpha = 2,
R = 40km, + N.U.R.B.S., regional stations

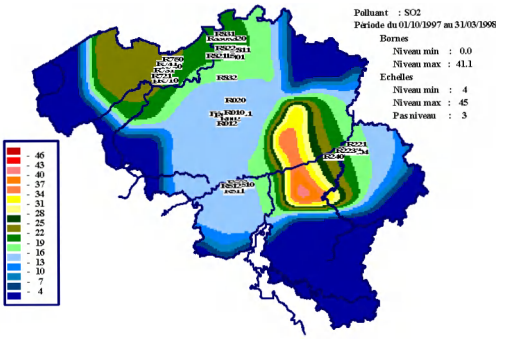

Thiébaux and Pedder model, alpha = 4,
R = 40km, regional stations

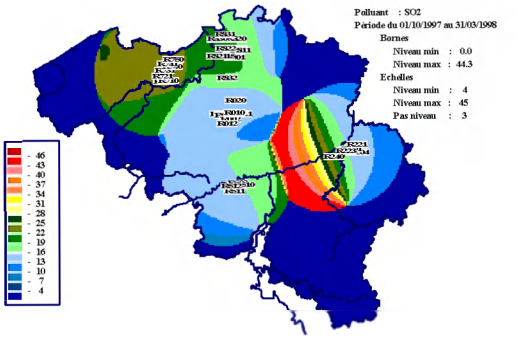

Thiébaux and Pedder model, alpha = 4,
R = 40km, + N.U.R.B.S., regional stations

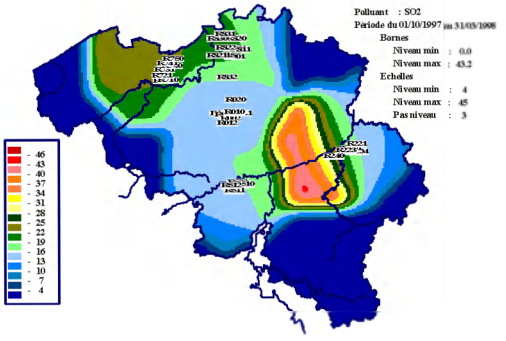

2) Comparative study

One now proposes to compare the results of the interpolation methods considered at this stage by holding account of all the stations with the results of these same methods but by separately considering the national stations and the regional stations.

	OZONE		**SO_2**	
	Interpolation inverse distance method	**Interpolation inverse distance method +N.U.R.B.S.**	**Interpolation inverse distance method**	**Interpolation inverse distance method +N.U.R.B.S.**
α = 2	Min. : 24.4 Max. : 65.7	Min. : 29.1 Max. : 63.7	Min. : 5.0 Max. : 44.2	Min. : 6.4 Max. : 29.1
α = 4	Min. : 24.4 Max. : 65.7	Min. : 25.4 Max. : 65.6	Min. : 5.0 Max. : 44.3	Min. : 5.0 Max. : 36.8
National stations				
α = 2	Min. : 32.7 Max. : 71.6	Min. : 38.6 Max. : 70.3	Min. : 5.1 Max. : 18.5	Min. : 5.5 Max. : 16.7
α = 4	Min. : 37.2 Max. : 71.6	Min. : 37.2 Max. : 71.5	Min. : 5.1 Max. : 18.5	Min. : 5.2 Max. : 17.5
Regional stations				
α = 2	Min. : 24.4 Max. : 46.7	Min. : 27.7 Max. : 45.5	Min. : 8.0 Max. : 44.2	Min. : 13.9 Max. : 31.9
α = 4	Min. : 24.4 Max. : 46.7	Min. : 25.1 Max. : 46.4	Min. : 7.4 Max. : 44.3	Min. : 12.7 Max. : 39.3
	Sasaki and Barnes	**Sasaki and Barnes + N.U.R.B.S**	**Sasaki and Barnes**	**Sasaki and Barnes + N.U.R.B.S**
R=40km	Min. : 28.9 Max. : 65.6	Min. : 29.7 Max. : 65.7	Min. : 5.0 Max. : 23.6	Min. : 5.0 Max. : 23.4
National stations				
R=40km	Min. : 37.2 Max. : 71.5	Min. : 37.3 Max. : 71.5	Min. : 5.2 Max. : 16.5	Min. : 5.2 Max. : 16.4

		Regional stations		
R=40km	Min. : 25.7 Max. : 46.3	Min. : 26.3 Max. : 46.2	Min. : 12.9 Max. : 33.8	Min. : 13.2 Max. : 31.9
	Thiébaux and Pedder	**Thiébaux and Pedder + N.U.R.B.S.**	**Thiébaux and Pedder**	**Thiébaux and Pedder + N.U.R.B.S.**
α = 2 R=40km	Min. : 0.0 Max. : 65.7	Min. : 0.9 Max. : 65.7	Min. : 5.0 Max. : 23.8	Min. : 4.8 Max. : 23.6
α = 4 R=40km	Min. : 0.0 Max. : 65.7	Min. : 0.9 Max. : 65.7	Min. : 5.0 Max. : 30.6	Min. : 4.7 Max. : 26.3
		National stations		
α = 2 R=40km	Min. : 0.0 Max. : 71.6	Min. : 0.0 Max. : 71.6	Min. : 0.0 Max. : 16.6	Min. : 4.8 Max. : 16.5
α = 4 R=40km	Min. : 0.0 Max. : 71.6	Min. : 0.0 Max. : 71.6	Min. : 0.0 Max. : 17.1	Min. : 4.8 Max. : 16.9
		Regional stations		
α = 2 R=40km	Min. : 0.0 Max. : 46.7	Min. : 0.0 Max. : 46.5	Min. : 0.0 Max. : 44.3	Min. : 0.0 Max. : 41.1
α = 4 R=40km	Min. : 0.0 Max. : 46.7	Min. : 0.0 Max. : 46.6	Min. : 0.0 Max. : 44.3	Min. : 0.0 Max. : 43.2

Comparison for ozone

The preceding results show that the lower and higher limits increased except for the method of Thiébaux and Pedder without the application of N.U.R.B.S. where the lower limit remains with zero value. For the regional stations, the lower limits remain relatively the same ones while the high delimiters decrease. It is also observed that the restricted parking zones and the green prevalence were primarily due to the regional stations. One realizes that the selection of the national stations gives a more homogeneous result on the whole of Belgium while the regional stations give a result which reveals the local influences.

Comparison for SO_2

The analysis shows that the high delimiters increase while the lower limits remain relatively the same ones except at the time of the application of the Thiébaux and Pedder method without N.U.R.B.S. where the lower limit falls to zero. For the regional

stations the lower limits increase while the high delimiters remain relatively the same ones. It is observed that the peaks and the green prevalence were primarily due to the regional stations. Here as one can see as the selection of the national stations gives a result less contrasted on the whole of Belgium while the regional stations give a posting result of the marked local influences.

Improvement of the Akima method

1) Borders points and negative concentration values

Let us return to the Akima method while trying on the one hand to remove the aberrant values of concentration and on the other hand to extrapolate the results judiciously by introducing fictitious stations in charge of relevant concentration information.

To this end a first test was tried by adding some fictitious points of measurement distributed on the Belgian border. A concentration was allotted by calculating it by the method of inverse distance method is defined by the reverse of the square of the distance (α = 2). Calculation is carried out by considering all measurements relative to the various stations in a selected temporal interval. The same approach reserved for the national measuring sites leads to more realistic results. This induces that the value of the borders points can be calculated by taking into account the values measured at the various national stations.

Another approach consists in seeking borders points making it possible the triangles of Delaunay to cover the unit with the Belgian territory. The tops of the triangles are distributed between the various measuring sites and the borders points. With to leave the triangles of Delaunay, we could determine the borders points which a computed value will be associated to them on the basis of preceding approach. These points are thirteen and their values are calculated starting from the values measured at the various national stations in the selected temporal interval.

Below the figures are presented representing the fields of concentration calculated by the method of Akima without and with borders points, as well as the representation of the triangles of Delaunay corresponding to each space situation selected.

These figures show that the distribution of interpolated pollution is relatively the same one for the Method of Akima and the method of Akima calculated with the borders points and this for each type of pollutant. One also notices, a disappearance of the effects edge in the method of Akima calculated with the borders points and a similarity in the tendencies relative to the two methods. Being given that the methods

of interpolations as that of Akima are very sensitive to the density of the initial points and with their space distribution, the interpolation quality is in direct relation with that of information injected. This remains valid of course for all the interpolation methods. It is also known that a lack of data can lead to unrealistic values to see aberrant which do not return within the measured values limits. The Akima method does not consider the points individually. Being given that it is a total method, it gives place to doubtful results apart from the closed traverse containing all the sources. Indeed outside this polygon, the Akima method must extrapolate the values. A way simple to improve the values in the border areas is to introduce borders points to completely cover the Belgian territory by a formed fabric of the Delaunay triangles.

By looking at the figures relating to the triangles, one notices that with the new borders points the improved Akima method imposes a triangulation entirely covering the territory. It is also noticed that the effects edge are gummed entirely without changing basically the result of the interpolation as well for ozone as the SO_2.

In the case of the SO_2, negative concentrations appear in areas located between zones at strong density of measuring site. To eliminate them, a simple procedure can be considered: initially the smallest negative value is sought and one raises the co-ordinates of this value. One time this value recorded, one applies the Akima method by adding to the positive data the new co-ordinate with a zero value of concentration. This repeated process if necessary does not modify of anything the final result, it gums only the negative wells by forcing them with zero value.

Ozone

Akima method

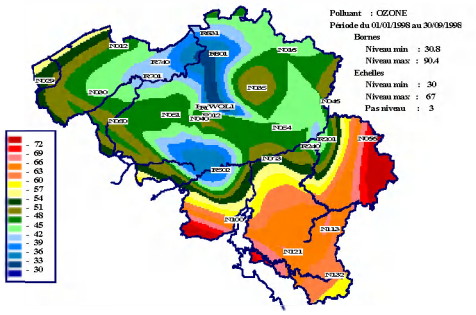

Akima method with borders points

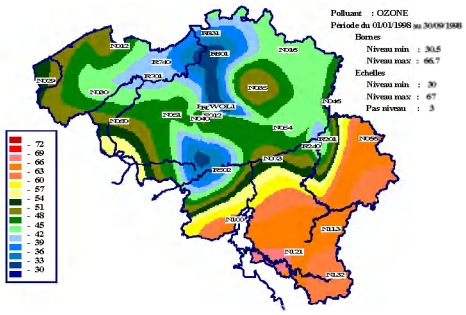

Corresponding Delaunay Triangles

Akima method

Akima method with borders points

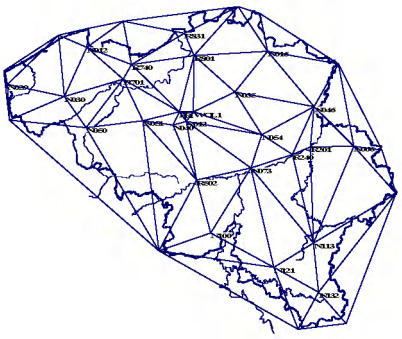

SO_2

Akima method

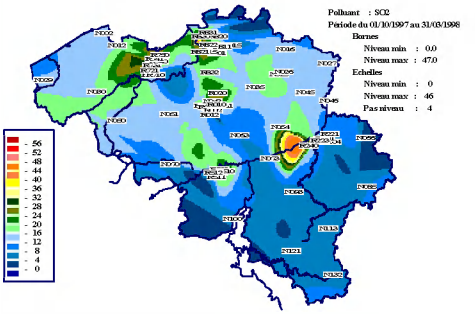

Akima method with borders points

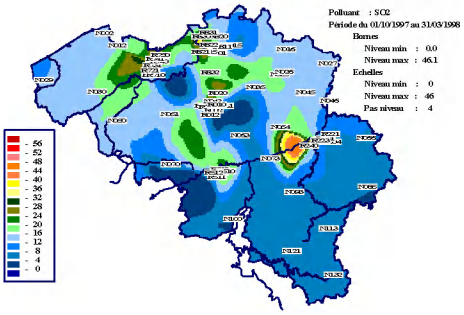

Corresponding Delaunay Triangles

Akima method

Akima method with borders points

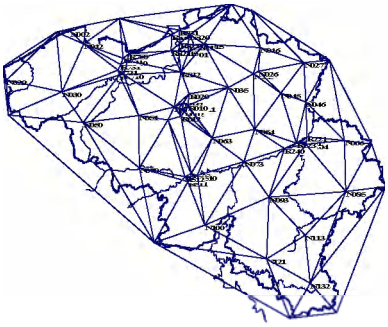

Extremely improvements made to the use of the Akima method, it is possible maintaining to apply this method by holding account of the distinction between the stations grouped in national or regional network. The results are presented in the figures and the extreme values table presented below.

It quickly arises for the national stations that the peaks and the wells of pollution are gummed and that the result is definitely homogeneous, this being valid both for ozone the SO_2. On the other hand, when the regional stations exclusively are selected, it is noticed well that pollution is concentrated in the polygon formed by these stations for ozone and that the result explodes out of the limits of the polygon for the SO_2.

Ozone

Akima method, national stations

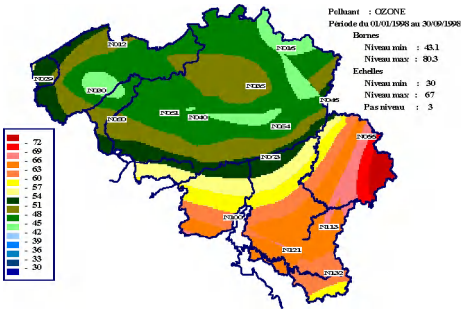

Akima method, regional stations

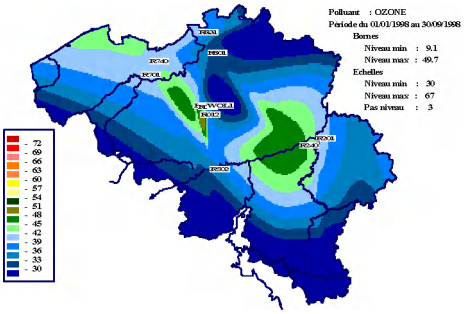

Akima method with borders points, national stations

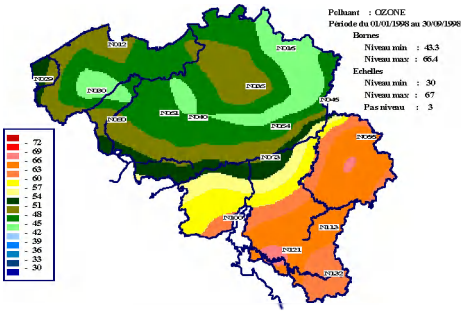

Akima method with borders points, regional stations

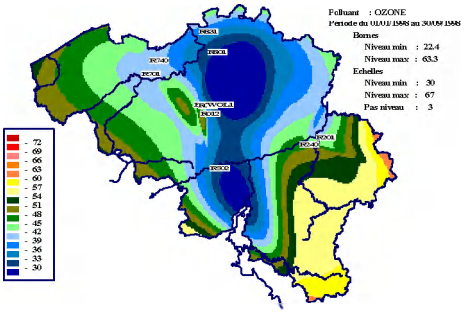

SO_2

Akima method, national stations

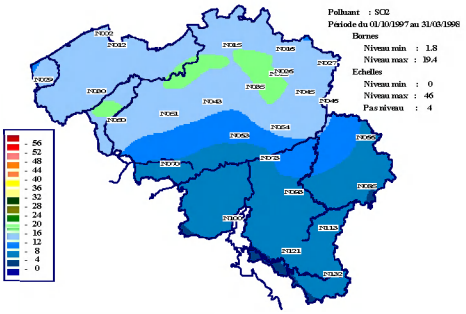

Akima method, regional stations

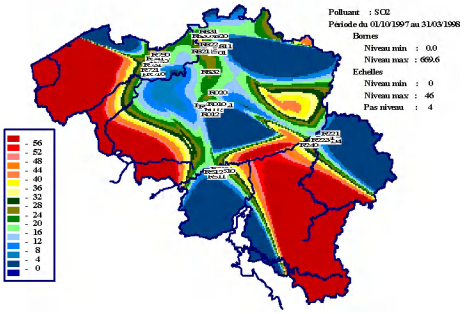

Akima method with borders points, national stations

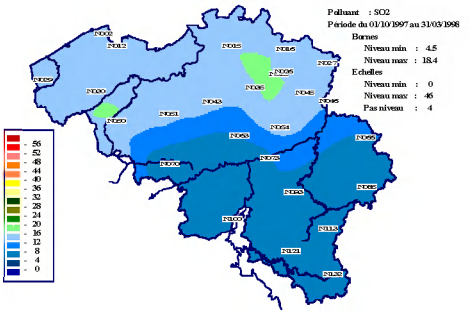

Akima method with borders points, regional stations

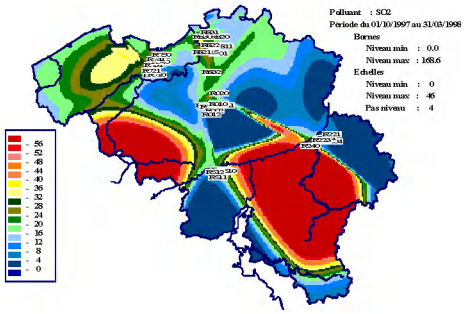

OZONE		SO_2	
Akima method	**Akima method with border points**	**Akima method**	**Akima method with border points**
Min. : 30.8 Max. : 90.4	Min. : 30.5 Max. : 66.7	Min. : 0.0 Max. : 47.0	Min. : 0.0 Max. : 46.1
Akima method National stations	**Akima method with border points National stations**	**Akima method National stations**	**Akima method with border points National stations**
Min. : 43.1 Max. : 80.3	Min. : 43.3 Max. : 66.4	Min. : 1.8 Max. : 19.4	Min. : 4.5 Max. : 18.4
Akima method Regional stations	**Akima method with border points Regional stations**	**Akima method Regional stations**	**Akima method with border points Regional stations**
Min. : 9.1 Max. : 49.7	Min. : 22.4 Max. : 63.3	Min. : 0.0 Max. : 669.6	Min. : 0.0 Max. : 168.6

When for all the stations one compares the Akima method applied to the only measurement points of with the Akima method with additional borders points, one notices a clear reduction in the maximum towards the values obtained by the method of weighting for ozone while for the SO_2 this reduction is much weaker. The minimal values remain relatively the same ones. The effects of the borders points, as one expected it, are made feel in all the field.

If the national stations are considered, it is noticed that the minimum increases for ozone and the SO_2. For the SO_2, the minimum takes off of zero value. This is simply due to a better distribution of the stations. One also notices for ozone that the maximum decreases slightly while for the SO_2 it strongly decreases, this being also due to a better distribution of the stations on the whole of the territory.

If the regional stations are considered, it is noticed that the minimum for ozone decreases while for the SO_2 it explodes completely this is the result of extrapolation.

Linear interpolation based on the Delaunay triangulation

Two calculations are necessary to manage to carry out this two-dimensional linear interpolation. If first relates to the construction of the Delaunay triangles, the second come down to make pass a plan by the three values of concentration to the right of the three tops of the triangle. The construction of the triangles known as of Delaunay rests on the principle which no station can belong to the circumscribed circle of a selected triangle. These definite triangles in a univocal way are then used by holding account of the Lambert co-ordinates of the tops by adding like value 'vertical' to it the value of the measured concentration with each top of the triangle. Each top of a triangle corresponds to a station.

Being given that the results are confined in the polygon wrapping all the triangles, the 'border' approach is adopted. The values in these points are calculated starting from the inverse distance method with a function of distance expressed by the reverse of the square of the distance when the national stations are only considered.

N.U.R.B.S. method was also added to this straight-line method. The linear interpolation is initially considered on a rectangular grid side of 10 km and then brought back by a smoothing N.U.R.B.S. with a grid of 1 km on side. The linear interpolation method associated N.U.R.B.S. allows to obtain a softer result, i.e. a result not emphasizing the sides of the triangles. Nevertheless the fields of concentration are similar in both cases.

Various maps of the simple linear interpolation with and without borders points, of the linear interpolation with a smoothing by N.U.R.B.S with and without borders points, as well as the maps of the results of this method with the selection of the national or regional stations are presented below.

Ozone

Linear interpolation

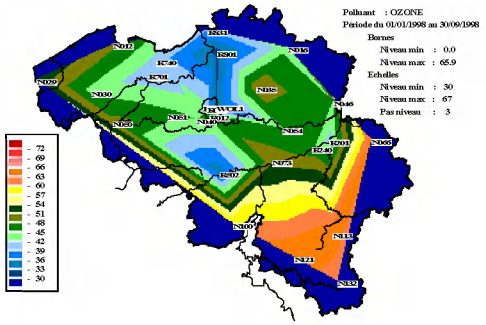

Linear interpolation + N.U.R.B.S.

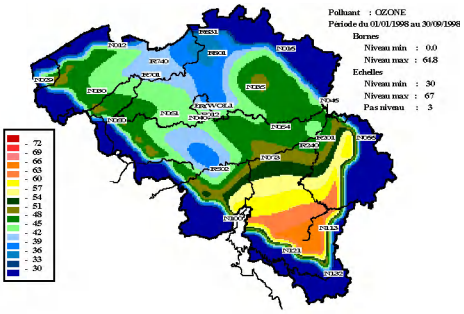

Linear interpolation with borders points

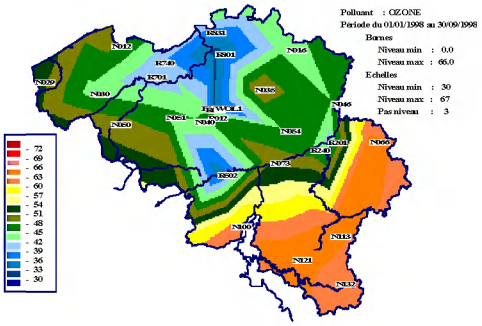

Linear interpolation with borders points + N.U.R.B.S.

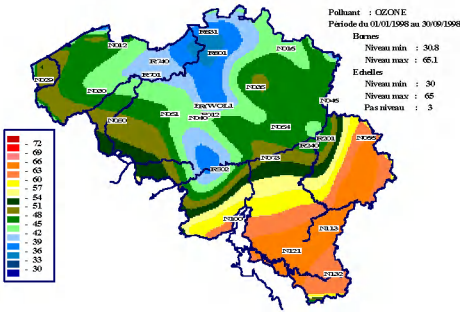

Linear interpolation, national stations

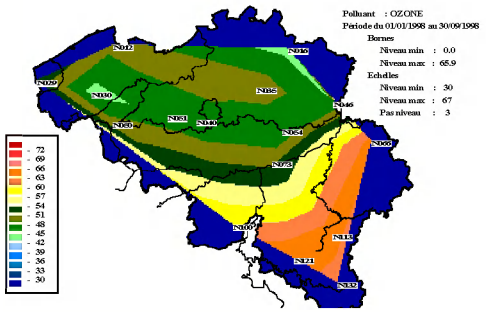

Linear interpolation national stations + N.U.R.B.S.

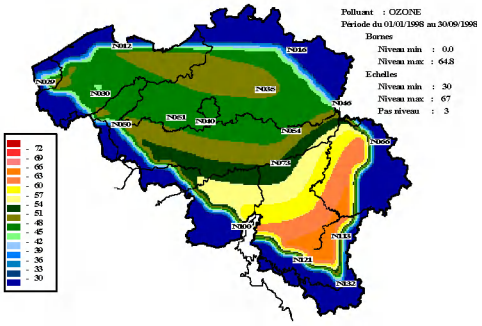

Linear interpolation
national stations with borders points

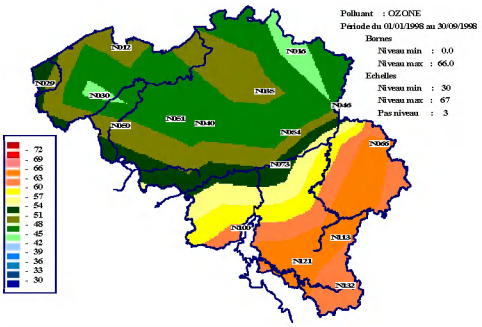

Linear interpolation
national stations with borders points
+ N.U.R.B.S.

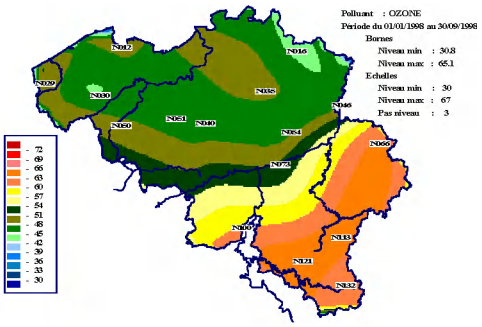

Linear interpolation

regional stations

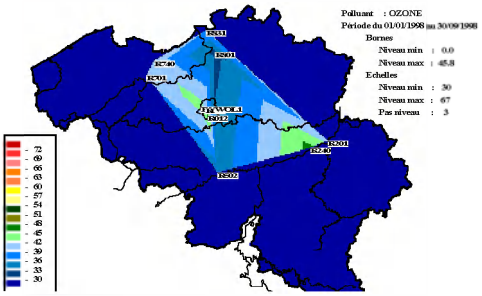

Linear interpolation

regional stations + N.U.R.B.S.

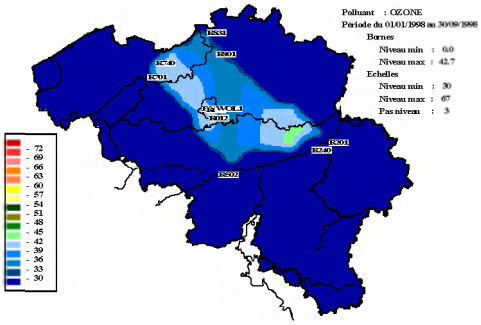

Linear interpolation
regional stationswith borders points

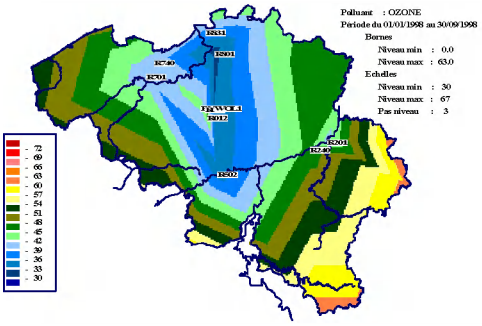

Linear interpolation
regional stations with borders points
+ N.U.R.B.S.

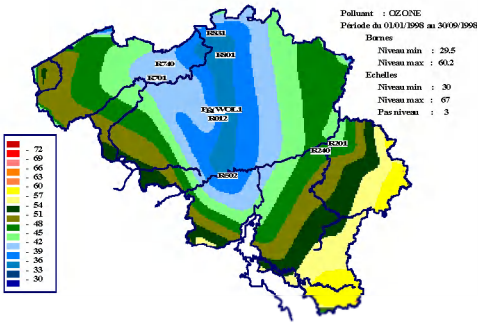

SO_2

Linear interpolation

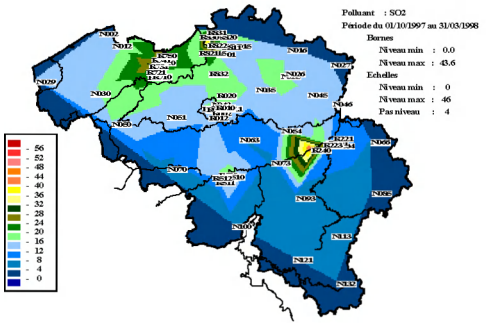

Linear interpolation + N.U.R.B.S.

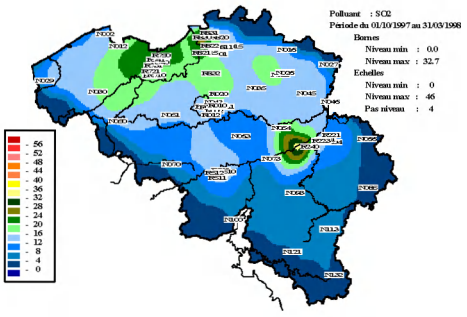

Linear interpolation with borders points

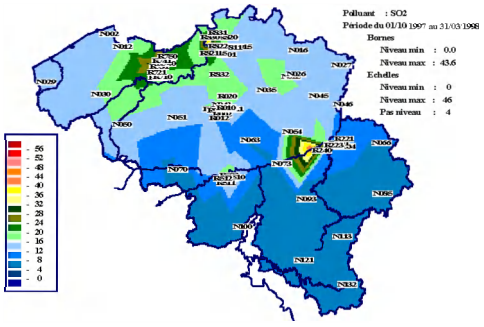

Linear interpolation with borders points + N.U.R.B.S.

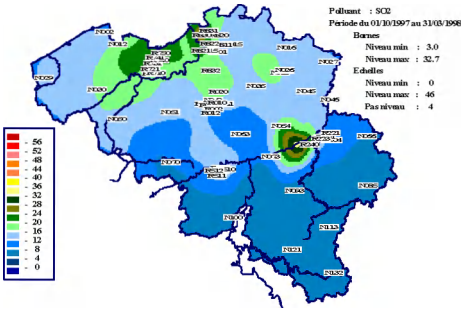

Linear interpolation national stations

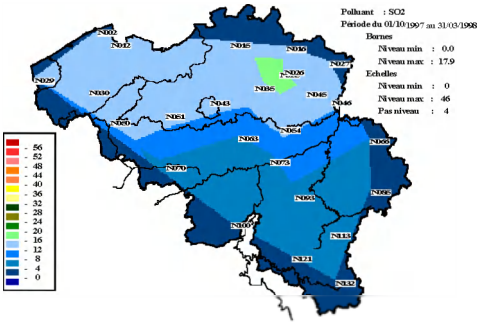

Linear interpolation national stations + N.U.R.B.S.

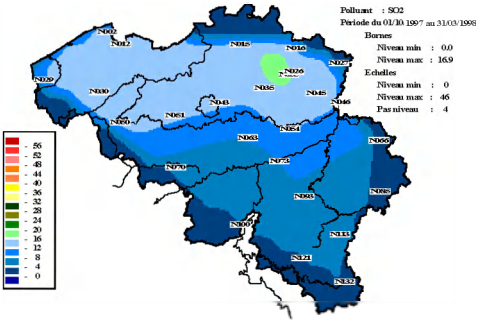

Linear interpolation
national stations with borders points

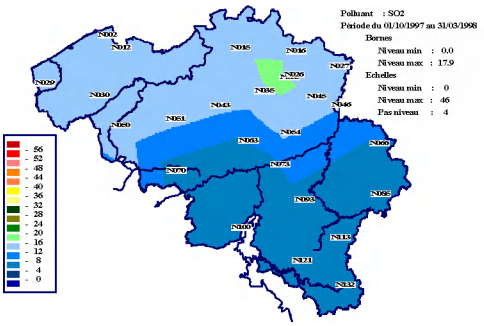

Linear interpolation, national stations
with borders points + N.U.R.B.S.

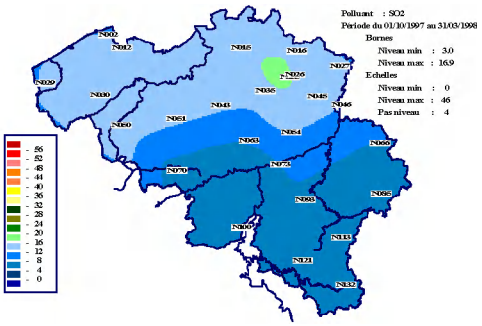

Linear interpolation
regional stations

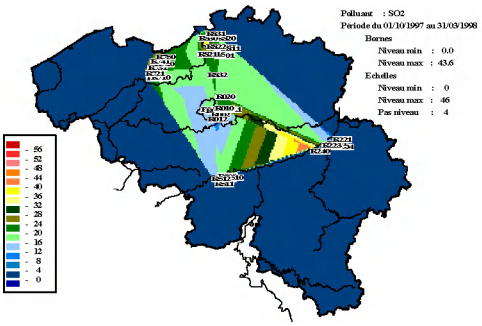

Linear interpolation , regional stations
+ N.U.R.B.S.

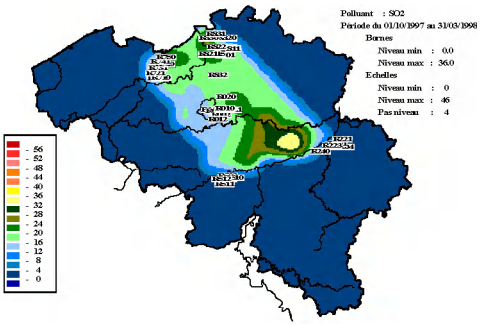

Linear interpolation, regional stations
with borders points

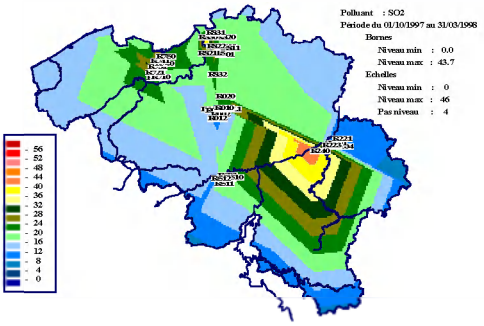

Linear interpolation, regional stations
with borders points + N.U.R.B.S.

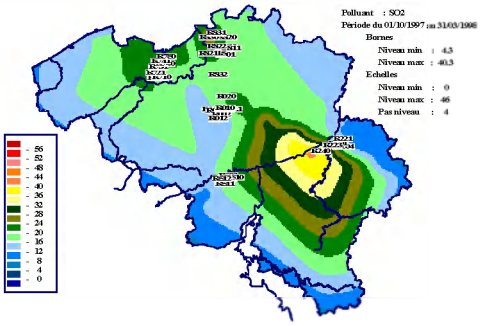

Comparison between the Akima method and the linear interpolation

OZONE			**SO_2**		
Akima method with borders points	**Linear interpolation with borders points**	**Linear interpolation with borders points + N.U.R.B.S.**	**Akima method with borders points**	**Linear interpolation with borders points**	**Linear interpolation with borders points + N.U.R.B.S.**
Min. : 30.5 Max. : 66.7	Min. : 0.0 Max. : 66.0	Min. : 30.8 Max. : 65.1	Min. : 0.0 Max. : 46.1	Min. : 0.0 Max. : 43.6	Min. : 3.0 Max. : 32.7
Akima method with borders points and national stations	**Linear interpolation with borders points and national stations**	**Linear interpolation + N.U.R.B.S. with borders points and national stations s**	**Akima method with borders points and national stations**	**Interpolation linéaire avec points frontière stations nationales**	**Interpolation linéaire + N.U.R.B.S. avec points frontière stations nationales**
Min. : 43.3 Max. : 66.4	Min. : 0.0 Max. : 66.0	Min. : 30.8 Max. : 65.1	Min. : 4.5 Max. : 18.4	Min. : 0.0 Max. : 17.9	Min. : 3.0 Max. : 16.9
Akima method with borders points and regional stations	**Interpolation linéaire avec points frontière stations régionales**	**Interpolation linéaire + N.U.R.B.S. avec points frontière stations régionales**	**Akima method with borders points and regional stations**	**Interpolation linéaire avec points frontière stations régionales**	**Interpolation linéaire + N.U.R.B.S. avec points frontière stations régionales**
Min. : 22.4 Max. : 63.3	Min. : 0.0 Max. : 63.0	Min. : 29.5 Max. : 60.2	Min. : 0.0 Max. : 168.6	Min. : 0.0 Max. : 43.7	Min. : 4.3 Max. : 40.3

It is noticed directly that the result obtained by the straight-line method with borders points is close to the result obtained by Akima method with borders points. This is not surprising. These two methods work on the same guiding principle to know the Delaunay triangulation. Once the determined triangles, the Akima method works out an interpolation by employing a surface cubic definite on a whole of close points what

allows a continuity of surfaces and plans tangent the right of the tops of the Delaunay triangles. This continuity involves however, according to the values of concentration, the possibility of extreme values apart from the limits measured as well as the possibility of negative values in certain areas with strong gradients of concentration.

OZONE			**SO_2**		
Akima method	**Linear interpolation**	**Linear interpolation + N.U.R.B.S.**	**Akima method**	**Linear interpolation**	**Linear interpolation + N.U.R.B.S.**
Min. : 30.8 Max. : 90.4	Min. : 0.0 Max. : 65.9	Min. : 0.0 Max. : 64.8	Min. : 0.0 Max. : 47.0	Min. : 0.0 Max. : 43.6	Min. : 3.0 Max. : 32.7
Akima method and national stations	**Linear interpolation and national stations**	**Linear interpolation + N.U.R.B.S and national stations**	**Akima method and national stations**	**Linear interpolation and national stations**	**Linear interpolation + N.U.R.B.S. and national stations**
Min. : 43.3 Max. : 80.3	Min. : 0.0 Max. : 65.9	Min. : 0.0 Max. : 64.8	Min. : 1.8 Max. : 19.4	Min. : 0.0 Max. : 17.9	Min. : 0.0 Max. : 16.9
Akima method and regional stations	**Linear interpolation and regional stations**	**Linear interpolation + N.U.R.B.S and regional stations**	**Akima method and regional stations**	**Linear interpolation and regional stations**	**Linear interpolation + N.U.R.B.S. and regional stations**
Min. : 9.1 Max. : 49.7	Min. : 0.0 Max. : 45.8	Min. : 0.0 Max. : 42.7	Min. : 0.0 Max. : 669.6	Min. : 0.0 Max. : 43.6	Min. : 0.0 Max. : 36.0

One notes for linear interpolation in the absence of borders points with and without N.U.R.B.S. that the lower limits are null since calculations are carried out in the polygon formed starting from the only stations. No calculation is carried out apart from polygon what explains the restricted parking zones on the various figures. Moreover values obtained in both cases are close the ones to the others. If one compares these same values with the Akima method without points borders one notes as, for the ozone calculated with all the stations and the ozone calculated with the only national stations, the lower and higher limits are different but that for the SO_2

the terminals are relatively close. On the other hand, if one selects only the regional stations one notices that for ozone the terminals are relatively identical while for the SO_2 the terminals are different.

The two-dimensional linear interpolation is valid only on the plane facets. This fact and contrary to the Akima method, negative values cannot appear with the straight-line method.

It is noticed that all the lower limits for the linear interpolation with and without borders points and with and without N.U.R.B.S., the minimal values are equal to zero for all the choices of the stations.

One can also notice that all the terminals between the Akima method with the borders points and the linear interpolation plus a smoothing by N.U.R.B.S. are virtually identical. Nevertheless, for the borders method with the borders points while taking into account only the regional stations one notes that the upper limit is definitely larger than the others.

It is also noticed that the result obtained by the linear interpolation with N.U.R.B.S. give a result more uniform than the linear interpolation or the Akima method. For the SO_2, the wells (dark restricted parking zones) given by the Akima method are completely gummed with the interpolations linear simple and smoothed by N.U.R.B.S. One observes the same phenomenon in the green zones where spots found by the Akima method are gummed by the linear interpolation. The peak of orange colour is also gummed. These results are appreciably the same ones for ozone. That it is for ozone or SO2, one finds the same visual representation for the unit of the applications.

Ultimately, the linear interpolation with N.U.R.B.S. give a graphic result similar to the Akima method. Nevertheless Akima method is faster in time of execution. It is necessary to count 7 minutes for the linear interpolation with a smoothing by N.U.R.B.S. and surroundings 1 to 2 minutes for the Akima method. Obviously, the two-dimensional straight-line method alone is close rapid.

From this second step, one can conclude that in the new applications, a solution by N.U.R.B.S. was proposed to free itself from too small meshes. The application of this double method, passage of a broad interpolation with a mesh of 10 km to a mesh of 1 km via N.U.R.B.S., led to results comparable with those acquired directly by a fine grid of 1 km with knowing a good smoothing of the data interpolated with a weak attenuation of the peaks and wells. The price to be paid is a significant increase in the computing time.

The use of the Delaunay triangulation makes it possible, if one wants to make significant extrapolations, to find the points borders which, with the stations, as well as possible cover the unit with Belgium. For the Akima method, the use of these pseudo-stations borders charged while polluting by the use with the inverse-distance method allowed the elimination of the effects edge due to the lack of points apart from the polygon including all the stations (necessarily internal polygon with the Belgian territory). The negative values sometimes present in the results given by the Akima method were the subject of a very satisfactory particular treatment. For the method of the two-dimensional linear interpolation, since the results are also confined in the polygon wrapping all the triangles, the borders points were added with values corresponding to those calculated starting from the interpolation balanced by the distances and that for the national stations.

For the various methods used, the measuring sites were separate between national stations and regional stations. This distinction makes it possible to highlight local influences at the time of the interpolation. In the case or one considers only the national stations, the result obtained is more homogeneous as one expected it. On the other hand, when only the regional stations are considered, the effect of these stations on the final result is important. For the Akima method, this working manner makes it possible to eliminate them adverse effects due to the bad distribution of the stations.

c) Phase 3

In this last phase, the inverse distance method is compared with the distance function of Thiébaux and Pedder, to calculate the exponent and to choose the radius of influence R. Three techniques of interpolation are considered:

- The quadratic interpolation of Cendes - Wong
- The spline function standard thin section
- Kriging method

These methods are applied to the data of ozone and SO_2. Calculations are carried out with a mesh of 1 km and to facilitate the visual comparison, the maps relative to the same pollutant are presented with the same scale of value (colour). One time these methods applied, particular determinations of the parameters intervening in the distance function of Thiébaux and Pedder are presented.

Quadratic interpolation based on the Delaunay triangulation

Ozone

Quadratic interpolation with borders points

Quadratic interpolation

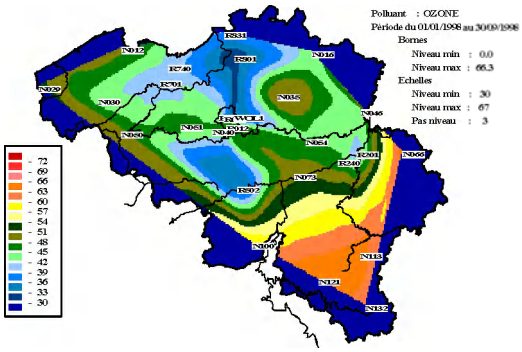

Quadratic interpolation with borders points

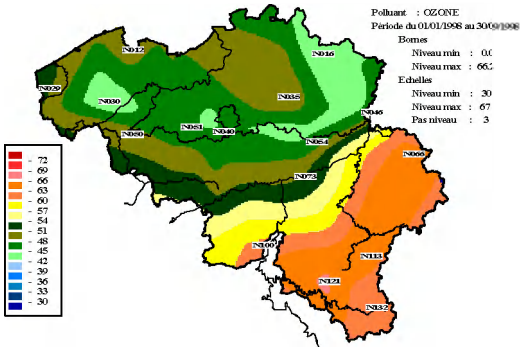

Quadratic interpolation

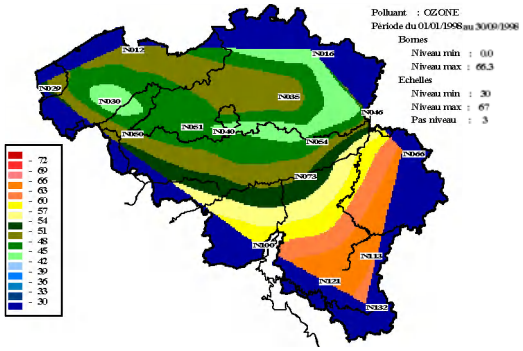

Quadratic interpolation with borders points

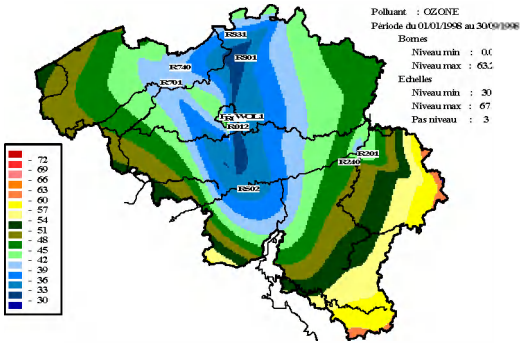

Quadratic interpolation

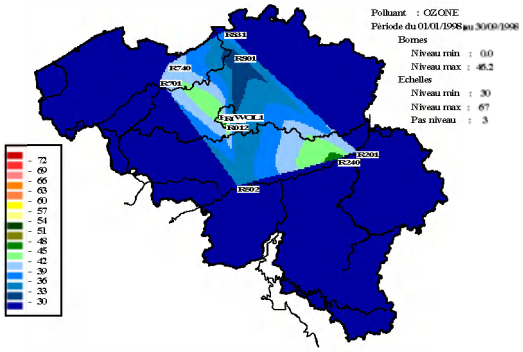

SO_2

Quadratic interpolation with borders points

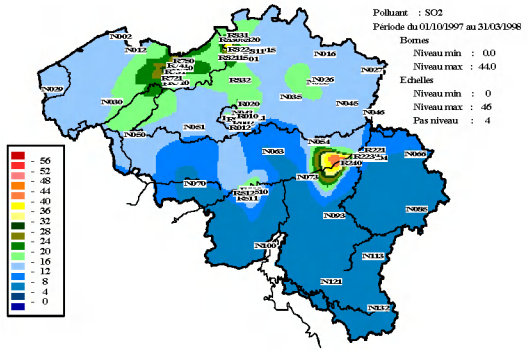

Quadratic interpolation

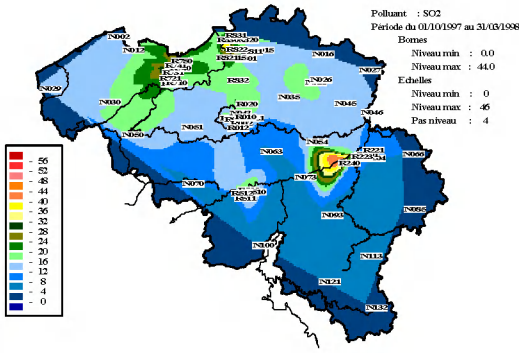

Quadratic interpolation with borders points

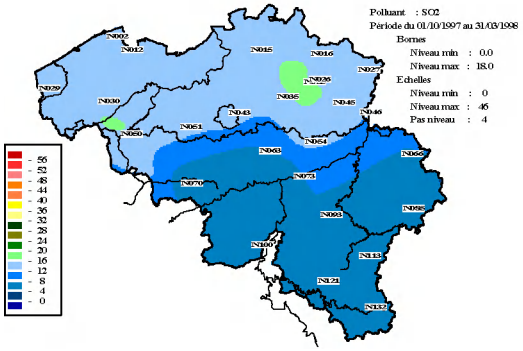

Quadratic interpolation

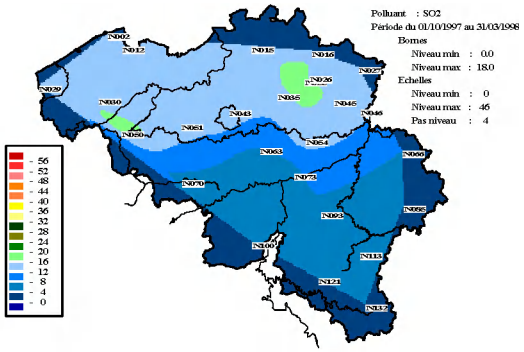

Quadratic interpolation with borders points

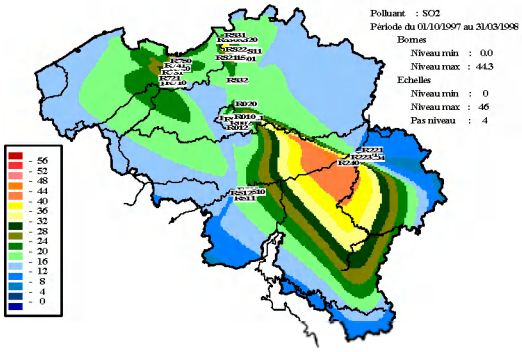

Quadratic interpolation

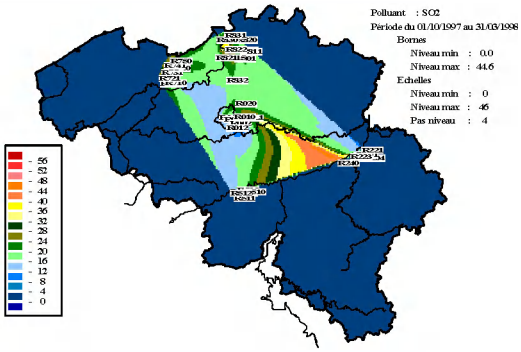

OZONE		SO_2	
Quadratic interpolation with borders points	**Quadratic interpolation**	**Quadratic interpolation with borders points**	**Quadratic interpolation**
Min. : 0.0 Max. : 66.2	Min. : 0.0 Max. : 66.3	Min. : 0.0 Max. : 44.0	Min. : 0.0 Max. : 44.0
Quadratic interpolation with borders points and national stations	**Quadratic interpolation and national stations**	**Quadratic interpolation with borders points and national stations**	**Quadratic interpolation and national stations**
Min. : 0.0 Max. : 66.2	Min. : 0.0 Max. : 66.3	Min. : 0.0 Max. : 18.0	Min. : 0.0 Max. : 18.0
Quadratic interpolation with borders points and regional stations	**Quadratic interpolation and regional stations**	**Quadratic interpolation with borders points and regional stations**	**Quadratic interpolation and regional stations**
Min. : 0.0 Max. : 63.2	Min. : 0.0 Max. : 46.2	Min. : 0.0 Max. : 44.3	Min. : 0.0 Max. : 44.6

The bounds comparison of the quadratic interpolation with and without the borders points shows practically identical values for the three combinations of stations. One exception however with ozone when the regional stations are or are not supplemented borders: it is noticed that the upper limit obtained without the borders points is definitely lower than that obtained with the borders points.

Now, if one compares this quadratic interpolation with the linear interpolation, both based on the network of Delaunay triangles, one notices that the maps for ozone and the SO_2 are practically similar with all the stations. On the other hand, with the regional stations and for the SO_2, the quadratic interpolation gives a map of the pollution more extended for the whole of all the colours and more particularly for the orange zone. As for the lower and upper limits they are practically identical.

If one considers the comparison between the quadratic method and the Akima method, both with borders points, the maps obtained appear overall similar both for

ozone the SO2 with however differences around the minima considering the presence of gradients more marked with the Akima method.

Without taking into account of the borders points, the quadratic interpolation gives zero values apart from polygonal contour locking up the Delaunay triangles. By against, with the Akima method without the borders points, if the result obtained in the polygonal envelope is very close to the result obtained by the method of the quadratic interpolation, the Akima method introduces a non judicious automatic extrapolation.

For ozone, the lower limits are null with the quadratic interpolation. By against, with the Akima method, the lower limits are definitely higher than zero while the upper delimiters are practically identical to the upper delimiters of the quadratic interpolation.

For the SO_2, if one compares the maps of the quadratic interpolation taking into account all the national stations and stations with the maps of the Akima method for the same selection of stations, one notices that the lower and upper limits are practically identical. On the other hand, if one holds account only regional stations, one note that the lower limits are similar and the upper delimiters are limited what is not the case with the Akima method.

Spline function type thin plate

Ozone

Spline function type thin plate with borders points

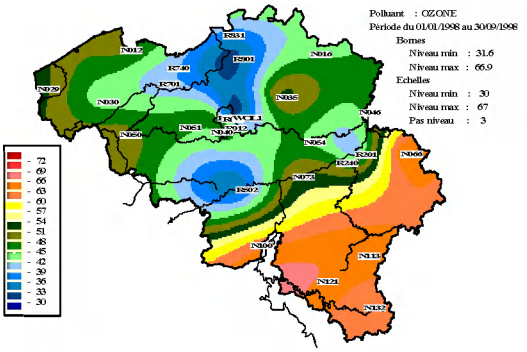

Spline function type thin plate

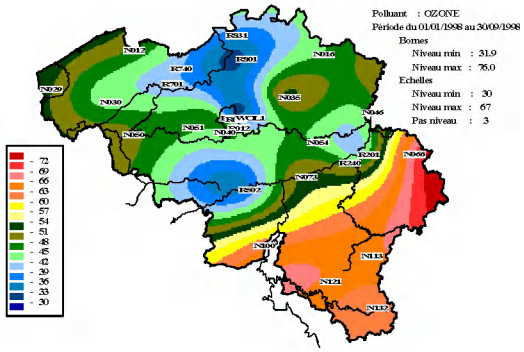

Spline function type thin plate with borders points, national stations

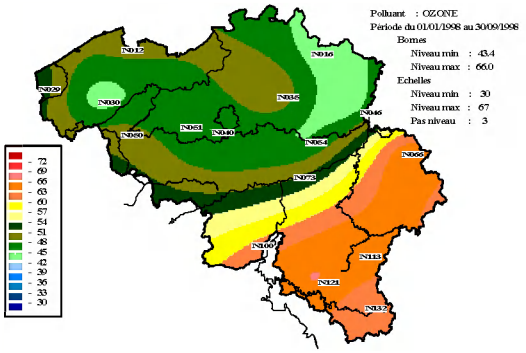

Spline function type thin plate national stations

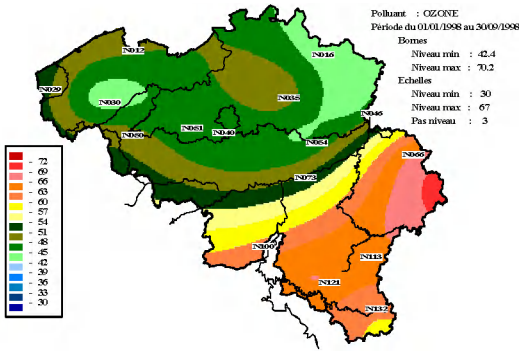

Spline function type thin plate with borders points, regional stations

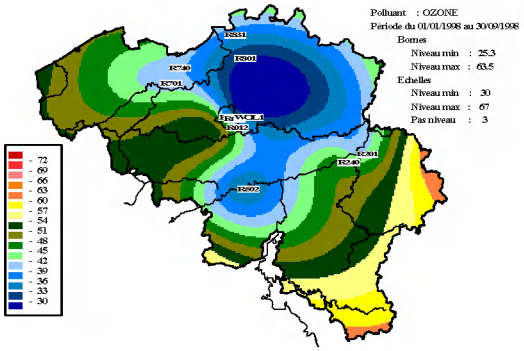

Spline function type thin plate regional stations

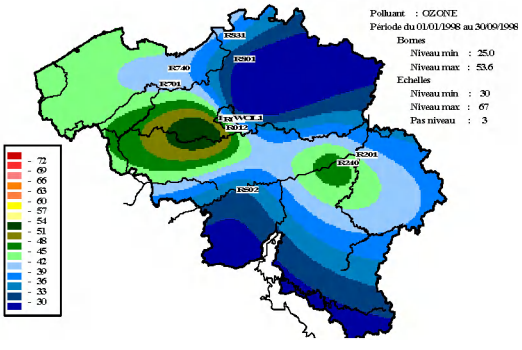

SO_2

Spline function type thin plate with borders points

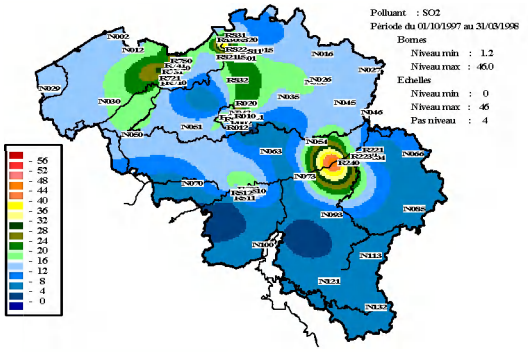

Spline function type thin plate

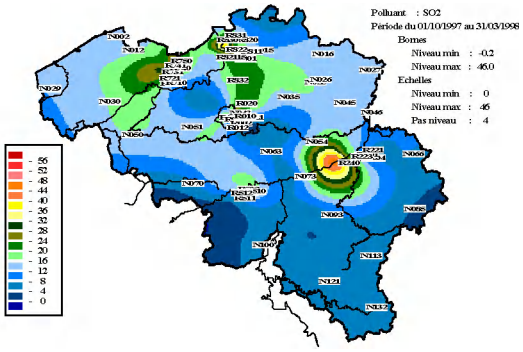

Spline function type thin plate with borders points, national stations

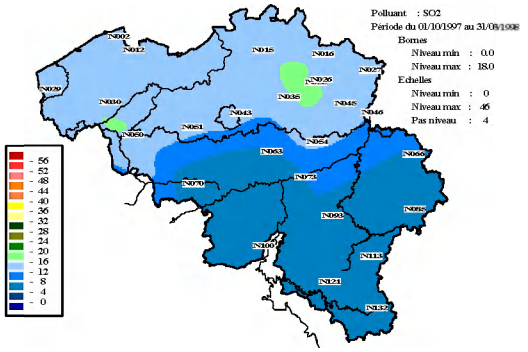

Spline function type thin plate national stations

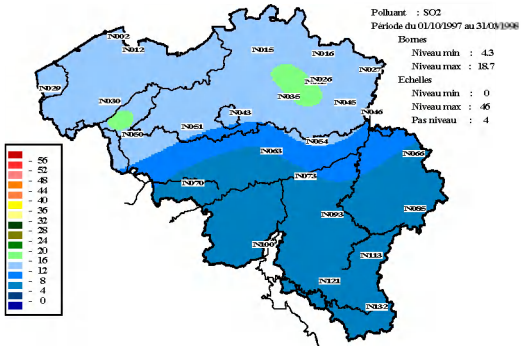

Spline function type thin plate with borders points, regional stations

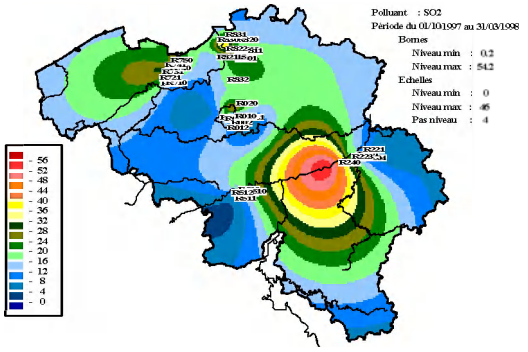

Spline function type thin plate regional stations

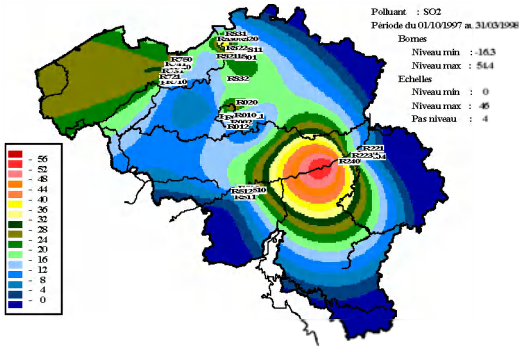

OZONE		SO_2	
Spline function type thin plate with borders points	**Spline function type thin plate**	**Spline function type thin plate with borders points**	**Spline function type thin plate**
Min. : 31.6 Max. : 66.9	Min. : 31.9 Max. : 76.0	Min. : 1.2 Max. : 46.	Min. : 1.2 Max. : 46.0
Spline function type thin plate with borders points and national stations	**Spline function type thin plate and national stations**	**Spline function type thin plate with borders points and national stations**	**Spline function type thin plate and national stations**
Min. : 43.4 Max. : 66.0	Min. : 42.4 Max. : 70.2	Min. : 0.0 Max. : 18.0	Min. : 0.0 Max. : 18.7
Spline function type thin plate with borders points and regional stations	**Spline function type thin plate and regional stations**	**Spline function type thin plate with borders points and regional stations**	**Spline function type thin plate and regional stations**
Min. : 25.3 Max. : 63.5	Min. : 25.0 Max. : 53.6	Min. : 0.2 Max. : 54.2	Min. : -16.3 Max. : 54.4

The maps resulting from the application of the thin plate function without and with the borders points show structures similar only inside polygonal contour locking up the Delaunay triangles but not outside where differences quite naturally appear of share the nature of the method. The obligation to take into account the values at the borders points changes the behaviour of the phenomenon reproduced in extreme cases of Belgium.

For ozone, the lower limits are practically identical. The upper delimiters take larger values with the thin plate function without borders points if one compares the map obtained with all the stations and the map obtained with the national stations. On the other hand, for the maps obtained with the regional stations one notices that the upper limit obtained with the borders points is higher than that obtained without the borders points.

For the SO_2, the lower and higher limits are practically identical for the applications obtained with all the national stations and stations. Differences appear however with the regional stations. It is noticed that the upper delimiters are identical while the lower limit is negative when the borders points are not taken into account. In this case, if one reveals on the map the Delaunay triangles without the borders points, one notices that the negative values are located apart from the limiting polygonal envelope.

If one compares the lower and higher limits of this method with those obtained by the Akima method, one can easily notice that the two methods lead to the same values by considering all the national stations or only stations. At the time of the taking into account of the regional stations, the method spline led, just like with the quadratic method, with an unacceptable value but however less than that obtained with the Akima method.

Generally, the various maps post very similar space information. This allows concluding that the thin plate function coherent with the Akima method to this difference close the method of Akima extrapolates the results apart from the circumscribed polygon which includes all the measurement points in an incorrect way. These extrapolated values are often likely to be inappropriate especially when the stations are badly distributed.

Kriging method

This method, contrary to all the other methods of interpolation, requires a comprehension of the stages leading to its application. It cannot be applied "the closed eyes" if one wants to benefit from the space structure contained in measurements. There have three stages to achieve:

- establishment of the experimental variogram smoothed by determining the number of classes of equal amplitudes on the basis of higher limit to allot to the whole of the distances between the stations.

- choice of a model as well as possible marrying the smoothed experimental variogram. The model is built starting from preset base forms.

- to carry out the minimization of the variance of the error.

The applications of Kriging are especially so as to make "feel" the dependence of the model on the interpolation. A particular model by pollutant is proposed.

1) Ozone concentration

For this measured pollutant in all the stations, the basic models selected are considered separately. Each figure below presents the smoothed experimental variogram (curve experimental) and the model (theoretical curve) with the value of the minimum of the adjustment between the two curves. The application of the first two phases of Kriging emphasizes mathematically the linear function like model interesting for ozone. For the interpolation, this model east cannot be the best but the application must be carried out until the end if one wants to ensure oneself some. Theoretical considerations relating to the studied phenomenon can as bring to choose a function of a particular form rather as another.

Improvement adjustment passes by a linear combination of the basic models. On the basis of adjustment carried out with only one function, the regrouping of the Gaussian function with a range of 120 km and the linear function allows obtaining a better adjustment than the linear function taken only.

Nugget effect

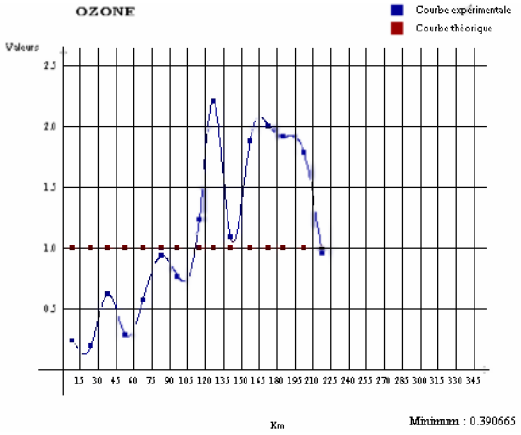

Linear function

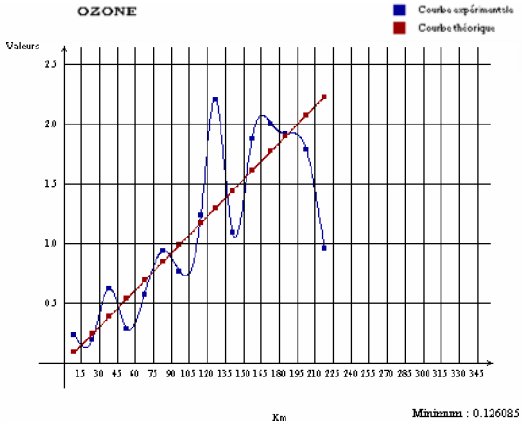

Spherical function, range 120 km

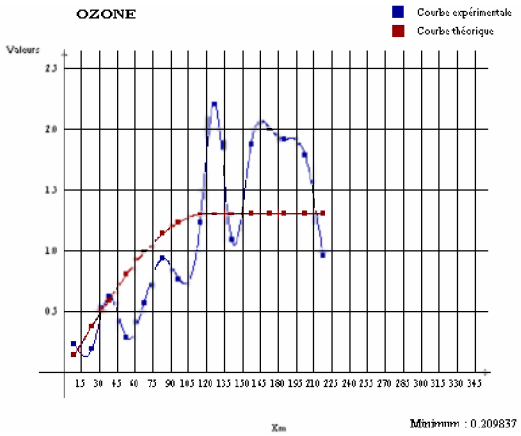

Gaussian function, range 120 km

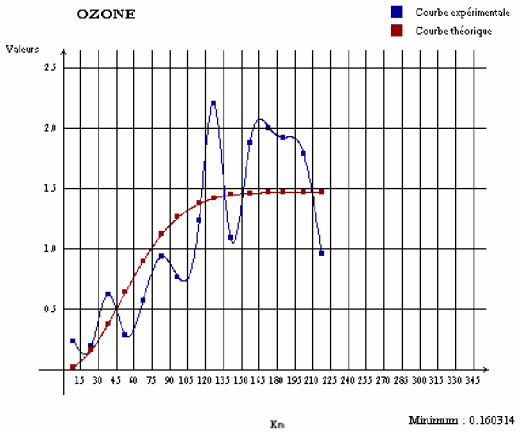

Exponential function , range 500 km

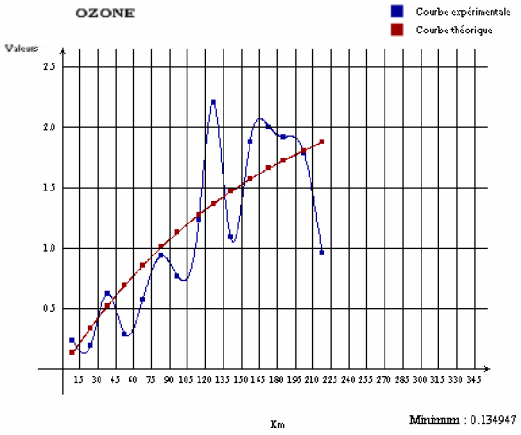

Law in power, exposing 1,1

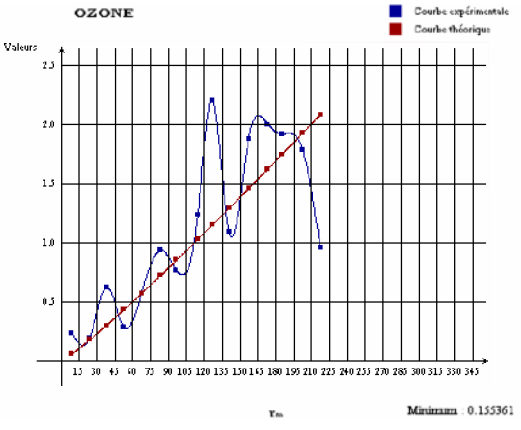

‘Holesin’, period 120 km

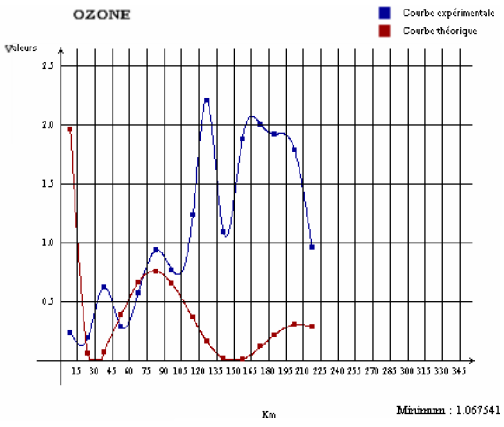

Holesin, period 30 km

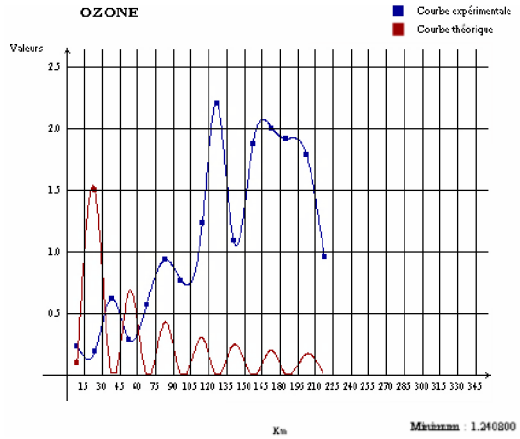

Gaussian function (range 120 km) + linear function

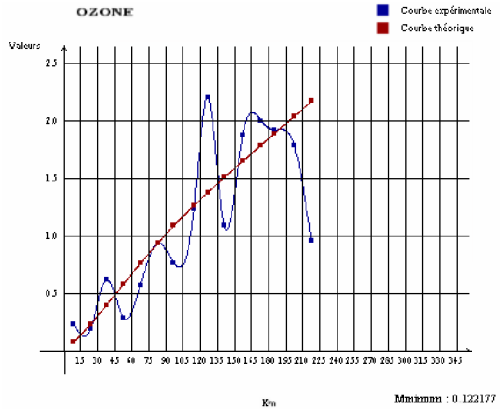

Estimated concentration (Kriging)

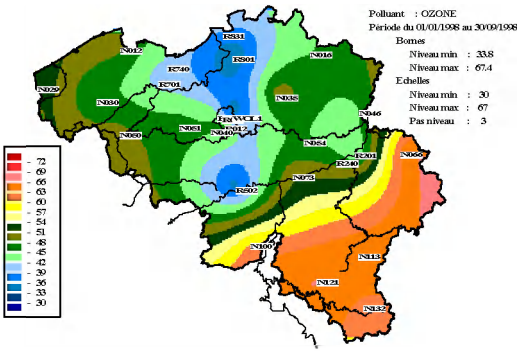

Estimated variance (Kriging)

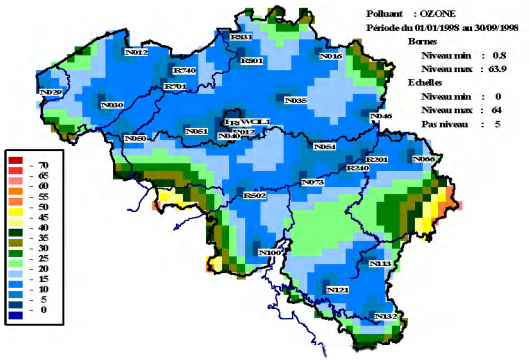

If it is admitted that this combination of model is satisfactory for ozone, the ordinary Kriging makes it possible to define at the same time the map of the estimated values and the map of the errors in estimation (variance). The map of the kriged values reveals the great structures obtained by the other methods when all the measuring sites are considered. The role of ozone put played by the cities and its industrial parks takes less importance in intensity by this method. The effects on the border areas are also apparent. It is enough to refer to the chart posting the errors in estimation. Without it being explicitly called upon the triangulation of Delaunay in the method of Kriging, it is obvious that the errors in estimation are important in the zones of extrapolation i.e. those which do not develop out of the network of triangles. It is interesting to notice (property of Kriging) that the error in estimation is minimal with the sites of measurement.

Now, if one limits the stations to the national stations, the application of Kriging with the same model as that under consideration with all the stations led i) to a better adjustment between the curves theoretical and experimental that in the case with all the stations and ii) with a good correspondence of the values kriged with the values estimated by the other methods of interpolation. The most significant differences appear in the zones of extrapolation as the map of the estimated variance confirms it.

The analysis of the model retained for ozone by holding account of all the stations and the national stations practically does not show an effect of nugget, absence of white vibration.

Gaussian function (range 120 km)
+ Linear function and national stations

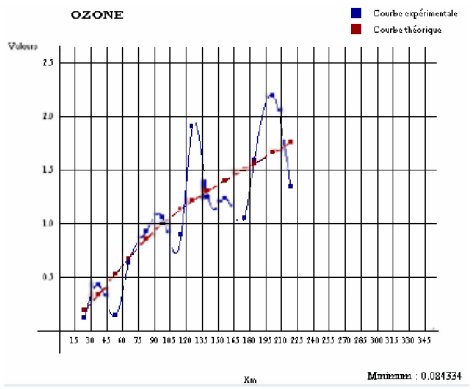

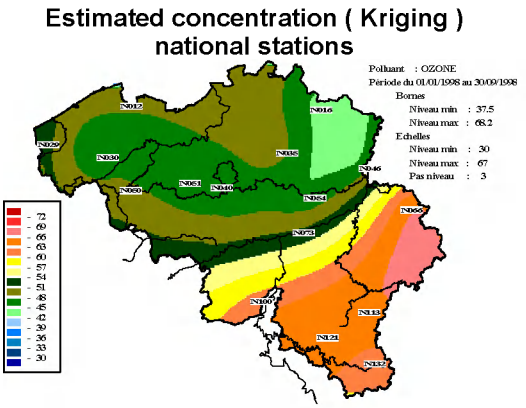

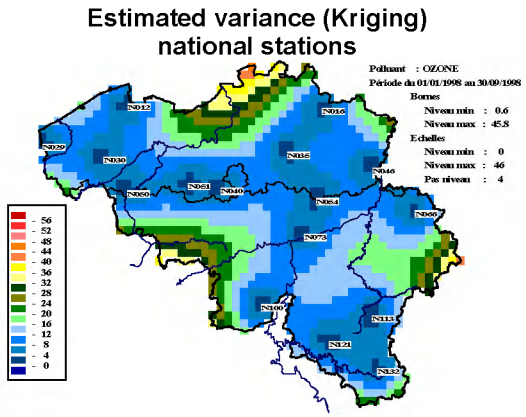

The problem of the interpolation with the regional stations is more complex as lets it suppose the use of the same model for the two other configurations of stations. The experimental variogram smoothed for the regional stations, presented below, very posts a behaviour oscillating related to the dispersion of the groupings of the stations by city. The model approaching this graph as well as possible should start with a stage to decrease then at the long distances what corresponds to the opposite tendency of the majority of the basic models presented in the literature relating to Kriging and mentioned again in this study. The absence of a model having behaviour is certainly due to theoretical considerations. If one remains with the models selected, the only one which can approach it, by excluding the model from nugget which does not seem adequate in our case because of the model established with all the national stations and stations, is the model "holesin". Two applications of Kriging were carried out with this model, one with one period of 20km and the other with one period of 30km. From both, on the basis of the value minimum of the adjustment (0,153 for 20km against 0,230 for 30km), the period of 20km seems the most justified. The map of the concentrations estimated out of ozone underlines, as it should be, the groupings of stations but also of the zones related to the periodicity introduced into the model. The map of the estimated errors indicates an important error outside the urban and industrial zones.

‘ Holesin’, period 20 km,
regional stations

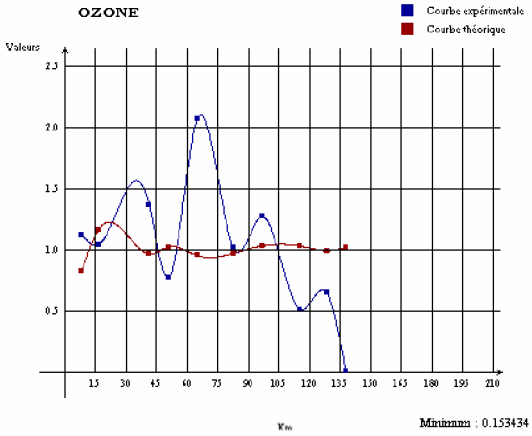

Estimated concentration (Kriging)
Regional stations

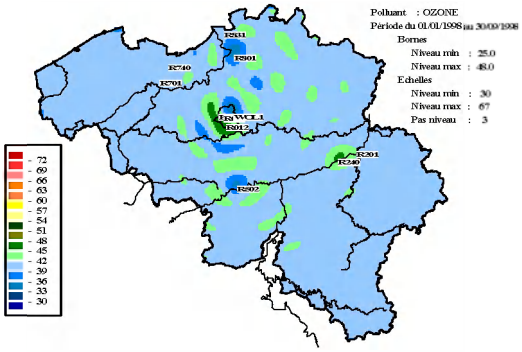

Estimated variance (Kriging)
Regional stations

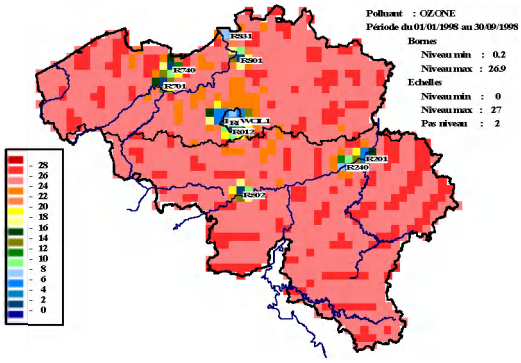

2) SO_2 concentration

The procedure planned to estimate ozone is taken again for this pollutant SO_2. When one consider all the stations, the adjustments between the smoothed experimental variogram and the simple models show that the combination of the effect of nugget and the linear model marries the experimental variogram as well as possible. The map of the estimated concentrations presents same alternations of colours as the other methods with however a maximum value very different from the computed values by these other methods. Within sight of the map of the errors in estimation, the method is "correct" only in the zones surrounding the cities.

Linear function

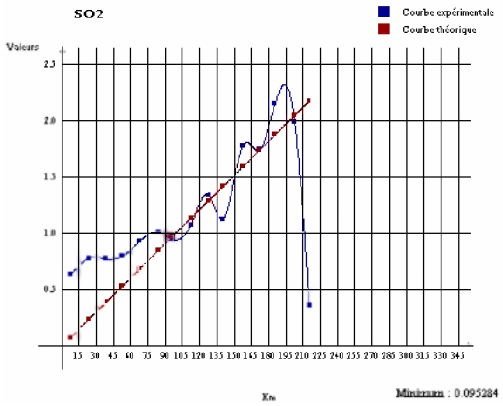

Spherical function (range 180 km)

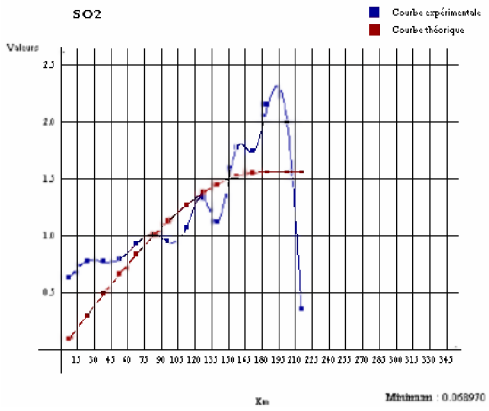

Gaussian function (range 90 km)

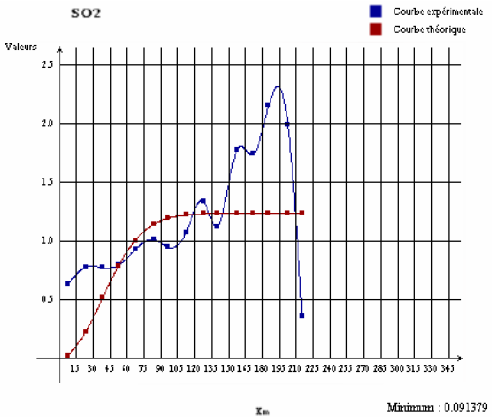

Effect of nugget and Gaussian function (range 120 km)

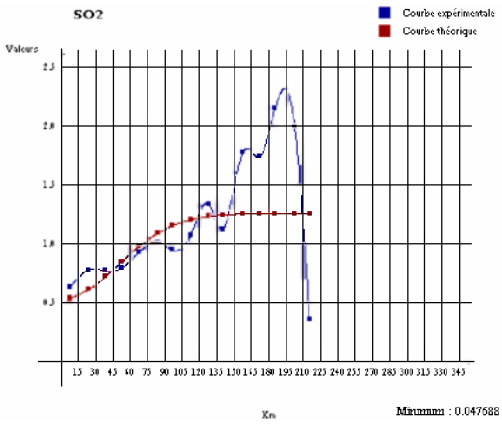

Law of power, exposing 1.2

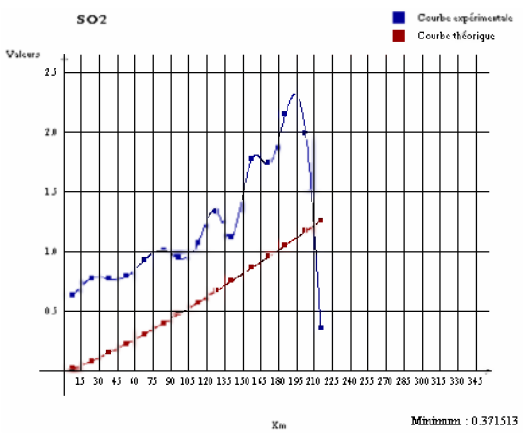

Effect of nugget and linear function

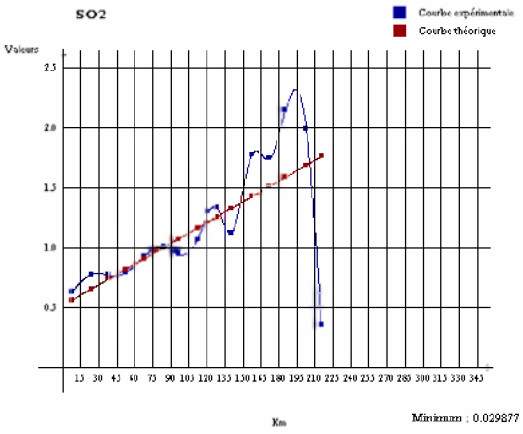

Exponential function (range 300 km)

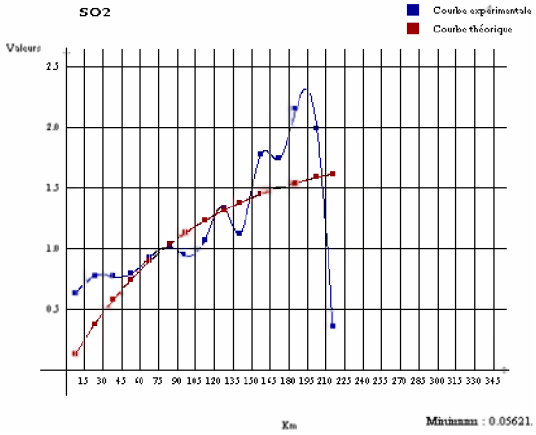

'Holesin', periodicity 60 km

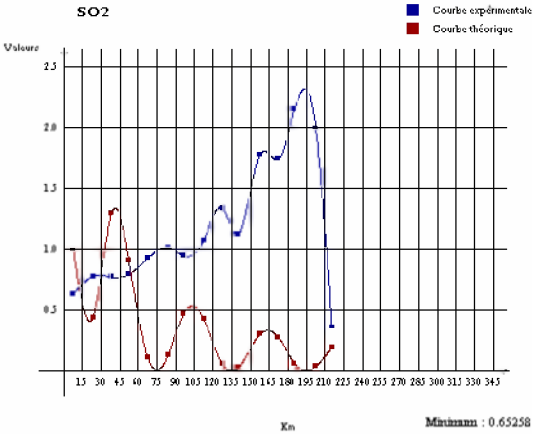

Effect of nugget, linear function

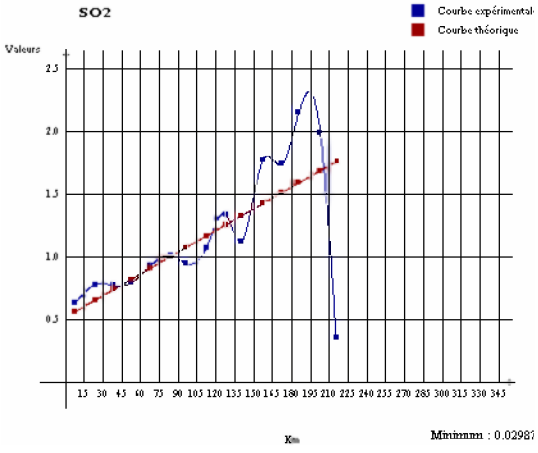

Estimated concentration (Kriging)

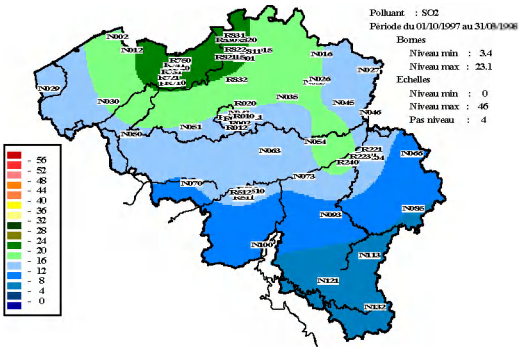

Estimated variance (Kriging)

The explanation of the kriged concentration with all the stations lights a little if only the national stations are considered. The model which adjusts the smoothed experimental variogram presents the same combination of simple models as for ozone namely an increased linear model of a Gaussian model of a range of 120km. Let us note that the experimental variogram smoothed SO_2 is very different from that obtained with all the stations what was not the case for ozone. The effect of nugget practically disappears and the map of the estimated concentrations resembles extremely the maps established with the other methods of interpolation.

Linear function and Gaussian function (range 120 km) national stations

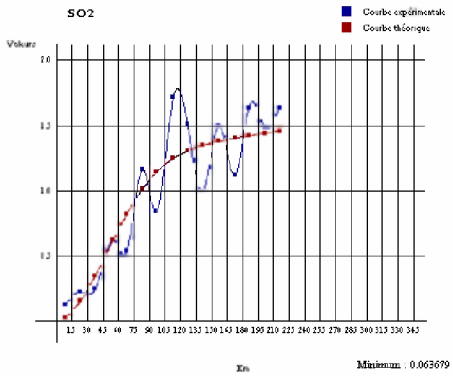

Estimated concentration (Kriging)
National stations

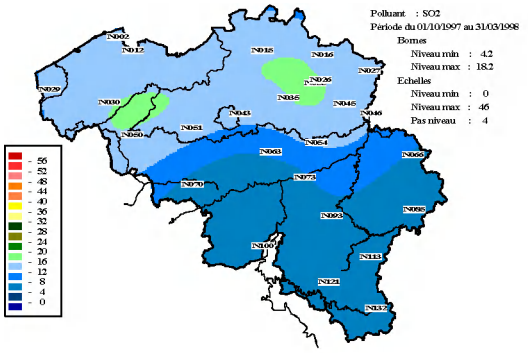

Estimated variance (Kriging)
National stations

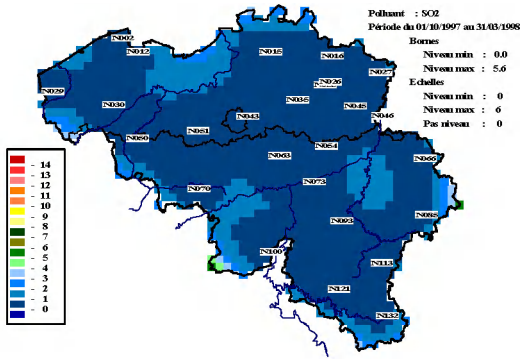

The variogram analysis with the regional stations is more delicate following the very dissymmetrical behaviour of its graph as the figure shows it below. An important maximum appears for a distance between the stations of 65km. It expresses the existence of important values measured in the industrial park inhabitant of Liège. This source of information conditions the adjustment so that it is difficult to find a good model. A combination is proposed which leads to kriged values which do not appear better than those calculated by the other methods. These space differences between the behaviours of the two studied pollutants is partly related to the difference in nature of these pollutants: SO2 is produced more locally contrary to the ozone which, while being to him under the dependence of the primary education pollutants, is transported outside the transmitting zones which are inter the cities.

Nugget effect, linear function and Gaussian function (range 120 km) regional stations

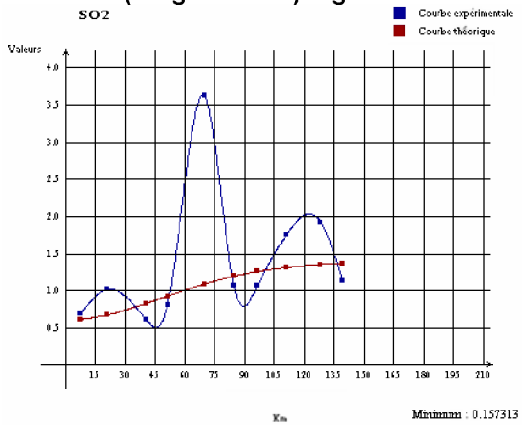

Estimated concentration (Kriging) regional stations

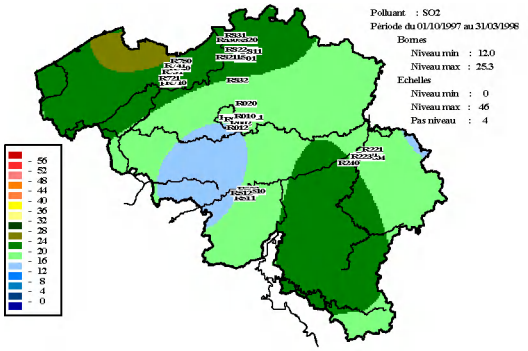

Estimated variance (Kriging) regional stations

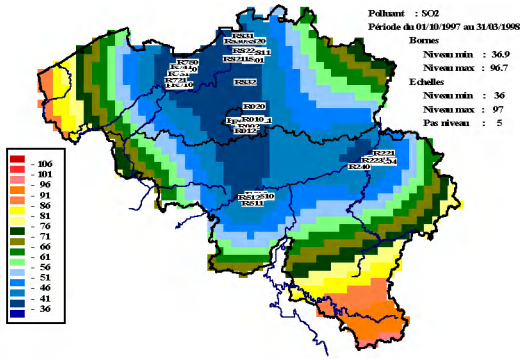

At the end of these analyses, it is to notice that both for ozone and SO_2, the method of Kriging is one of the method most complete since instead of imposing a policy *a priori* as the other methods do it allows initially a description of the space correlations by the construction of the variogram by distributing the data in classes of equal amplitudes. It subjects then the variograph to an adjustment so as to "drop" the not very significant structures. model, result of successive limitation, contains just useful information to carry out the spatial distribution of the basis values. Determination of the error related to the estimate adds an important complement to the analysis of the interpolation.

Methods to estimate the parameters of a distance function

For the methods of interpolation other than Kriging the method of the weighted average intervenes either directly or like a prolongation with more elaborate methods so as to allow those extrapolations by holding account of the behaviour of the fields of concentration in areas unfulfilled by their techniques. This part played by the method of the weighted average request its re-examination for better choosing the function of distance like its parameters like the radius of influence and/or the exponent.

1) Exponent

The work of Sen (1997) goes in this direction. This author seeks a manner of defining the experimental radius of influence starting from the variogram. For recall, the experimental variogram is a measurement of the space variability of a size compared to the distance existing between the points where it is measured. It is often presented as a group of dots of which it is necessary to withdraw the tendencies from them so as to fix the space structure of the studied size.

Rather than work in this direction Sen works out its method from cumulated experimental variogram. To manage to define this size, one leaves the experimental variogram which associates the distance for each couple of station the value corresponding to half of the square of the difference of the values measured to the two stations intervening in calculation of this distance. The variogram thus defined for a given period can be extended to all the period of study when one takes the temporal average of the variograms over all the period to be analysed. Cumulated variogram defines the CV (cumulative variogram). This amounts making, starting from ascending sort distances between stations, the successive sum of the values of the variogram associated the distances increasing between stations selected. The construction of function CV relating to the data of ozone and SO_2 conduit, after standardization of the distance and cumulated by their respective maximum value, with the following figures:

Cumulated results for Ozone

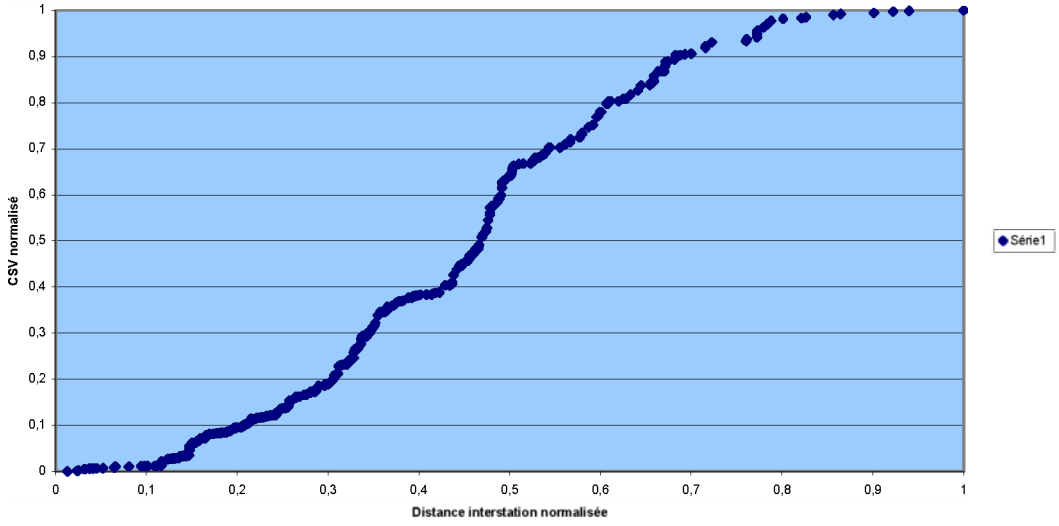

Cumulated results for SO2

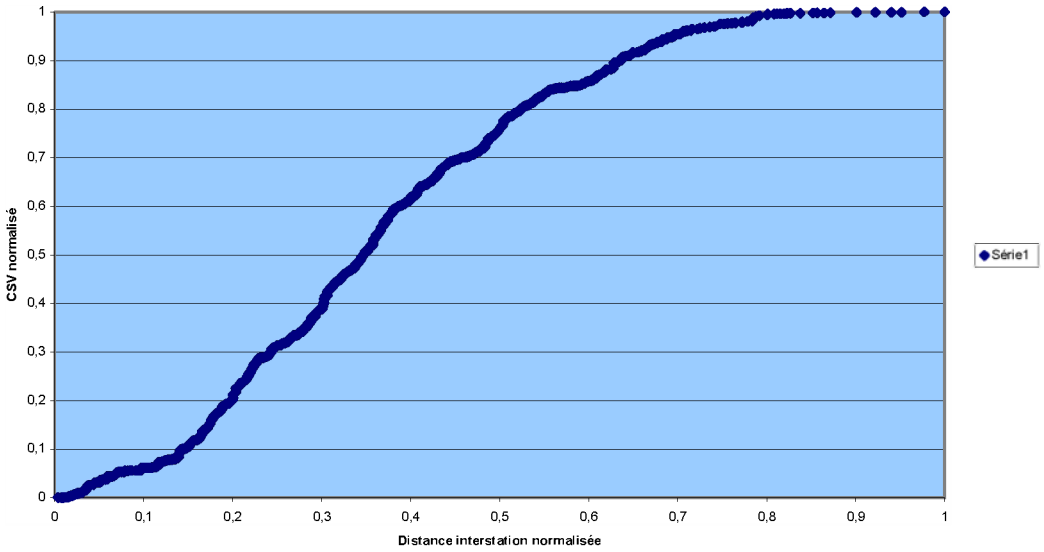

The normalisation of the distances retained in these representations does not correspond completely to that proposed by α . This author does not take the distance maximum between stations but a lower value established by traversing the CV in the direction of the increasing distances until the moment when the relative error of the CV becomes lower than a certain percentage. The distance corresponding to this percentage defines the radius of influence. It is this value used in the inverse-distance method of Cressman, of Thiébaux and Pedder (generalized form of Cressman) or of Sasaki and Barnes.

A little different approach from that of α in is considered, not for the research of the radius of influence, but rather for that of the exponent. Apart from the model of the reverse of the power of the distance between the station and the points of calculation, the distance functions of Thiébaux and Pedder and of Sasaki - Barnes, are written directly in an adimensional form. Using this property, it is easy to compare the CV with complementary to the unit of the functions of distance made adimensional. α in the fact for its standardization by comparing the CV with the functions of distance in their traditional formulation. It is possible to be further seeking the exhibitor, for example function of Thiébaux and Pedder, while asking to make minimum the average quadratic error between the CV and the complementary function. The following stage will be to minimize this error at the same time on the exhibitor and the ray of influence. In our approach, instead of carrying out this minimization on two parameters, the ray of influence will be estimated in another manner as that will be shown further. For the moment, if the CV are standardized by

the maximum value of the distance between stations, the exponent α intervening in the formulation of Thiébaux and Pedder takes the value of 1,67 for ozone and 2,88 for the SO_2. These two exponents move away from the whole value 2 already under consideration in the interpolations. Same approach carried out for a generalization of the function weight of Sasaki and Barnes, this generalization consisting in replacing by $\eta\alpha\sigma$ value 2 presents at the same time like multiplicative factor and exponent, conduit with a value of 1,91 for ozone and 2,43 for the SO_2, maybe of the values closer to the whole value 2 suggested by Sasaki and Barnes. The total behaviour of this minimization is given to the following figures

Ozone

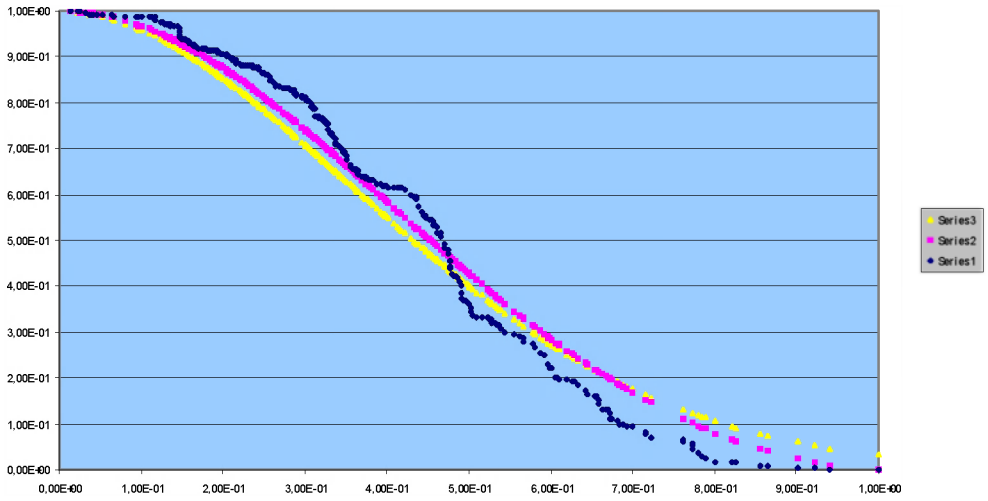

SO_2

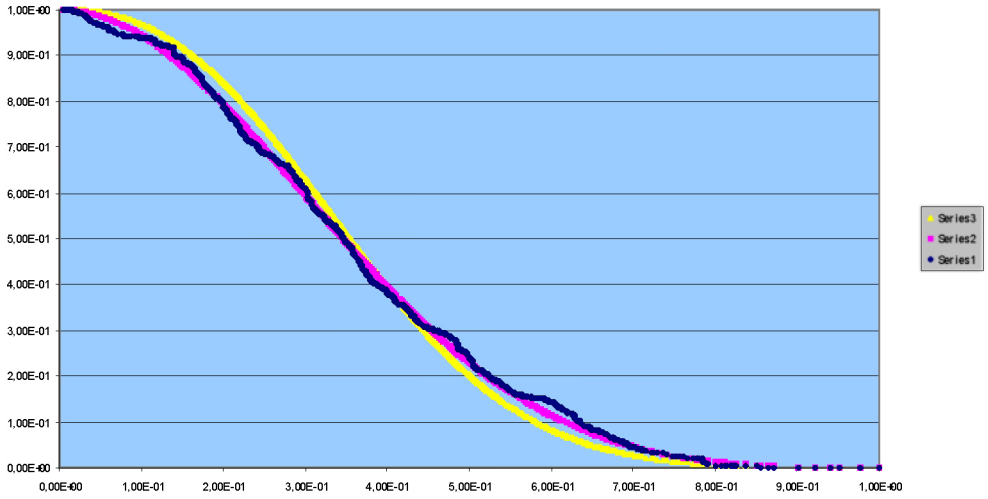

Series 1: experimental points

Series 2: Thiébaux and Pedder

Series 3: Sasaki and Barnes

2) Radius of influence

A method can be established starting from the treatment of the residues at the measurement points. By residue in a point of measurement $\mathbf{R}_I$, one hears the difference between the value interpolated in $\mathbf{R}_I$ by considering all the points except the value in this point. The result is noted Z_{-I} when Z_I represent the eliminated measured value. *N* calculated residues form a unit to which any statistical processing can apply. An interesting size is the quadratic average given by

$$\mathrm{LSCV} = \frac{1}{n}\sum_{i=1}^{n}(z_{-i} - z_i)^2 = \frac{1}{n}\sum_{i=1}^{n}\left(\sum_{j=1\neq i}^{n} w_j z_j - z_i\right)^2$$

and particularized with the inverse-distance method. The presence of the weight W_J in this formula allows regarding this average as a continuous function of the parameters defining the function of distance chosen to characterize the weight W_J. It is dice at the time possible while making evolve/move the only ray of influence to seek the "most interesting" minimum of this function, so minimum there is apart from the vicinity of the origin. This procedure bears the name of **L**east **S**quare **C**ross **V**alidation (Hardle, 1989).

Method LSCV was applied to the two data files by taking for the function of distance that of Thiébaux and Pedder treated beforehand to fix the value of its exponent. Results below show, according to the ray defined by increases in 5km, the existence for the SO_2 minima sufficiently marked to make the choice of a ray of influence. With all the stations, the ray of influence is of 15km. It passes to 30km for the national stations and the regional station since, in this last case, the beach around the minimum is marked very little. The results for ozone present, apart from peaks however absent for the SO_2, more beaches quasi constant than of well drawn minima. A value of 60km seems indicated to fix the ray of influence for all the national stations and stations. With the regional stations, a ray of influence of 95km appears to be appropriate. In all the cases, the chart of interpolation is one of the recourse to ensure itself of the "visual" quality of the interpolation.

Ozone, all stations

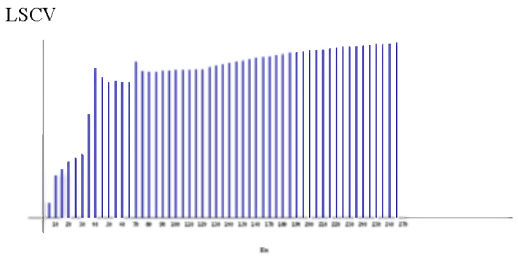

SO2, all stations

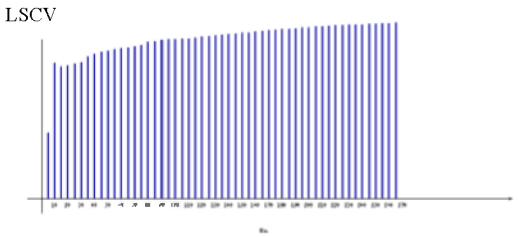

Ozone, national stations

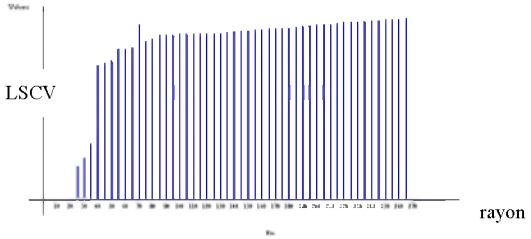

SO2, national stations

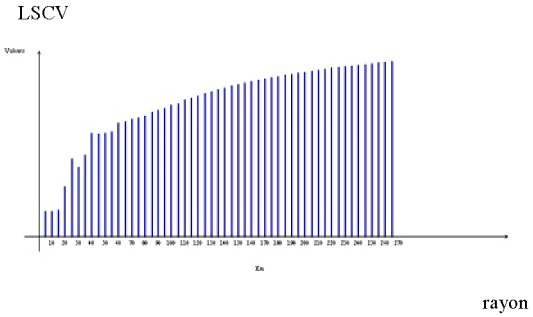

Ozone, regional **stations**

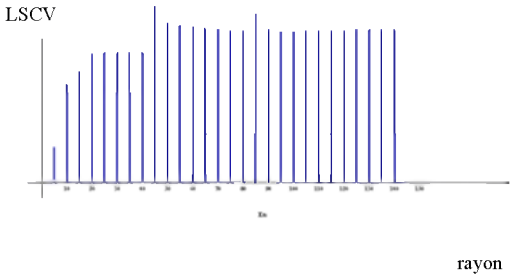

SO_2, regional stations

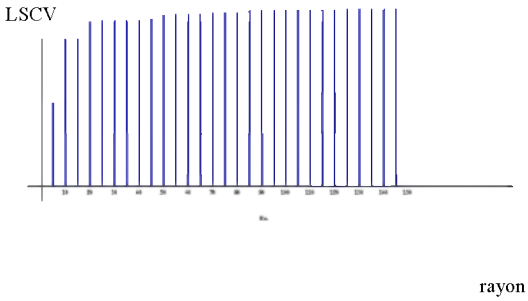

5. APPLICATION DESCRIPTION

The adopted methods of interpolation were implemented in an interactive data-processing module built with Microsoft Visual C++. The various possible actions are presented in a window including five menus called:

- ***File:*** This heading activates a drop-down menu with an target, either to open the data file (Open) to treat or to close the application (Exit).
- ***View:*** This heading activates a drop-down menu posting the toolbar or status bar. The selection of "Pollution map" activates one limps of dialogue which makes it possible to reduce to only one of the three Belgian areas the visualization of the result obtained. By defect, Belgium is taken overall in all calculations and representations.
- ***Interpolation:*** The drop-down menu activated by this selection reveals three pennies groups. First relates to the methods of interpolation. The second is worried only construction of the network of triangles according to the method of Delaunay. As for the third, it allows the opening of a file result for visualization or the creation of a useful metafile possibly for a treatment in the Word software.
- ***Ordinary Kriging:*** This heading allows to post the result of the variance considered obtained by the method of ordinary Kriging.
- ***Graphic:*** This heading activates a drop-down menu posting the parameters of visualization to be modified if necessary

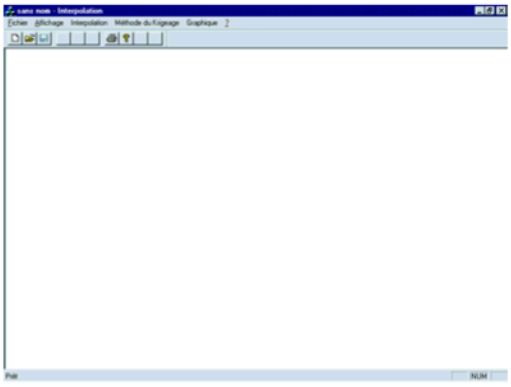

As the figures below show it, as long as a data file is not open it is impossible to reach the orders represented colour clear. However, at the time of the opening of a file result, the orders, making it possible to change the parameters of visualization and making it possible to create a metafile, are activated.

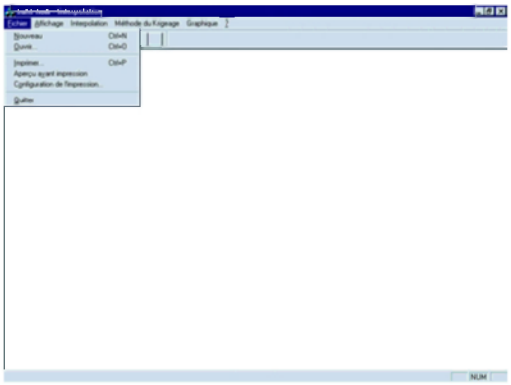

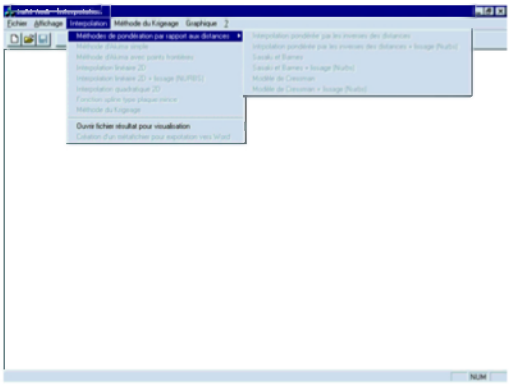

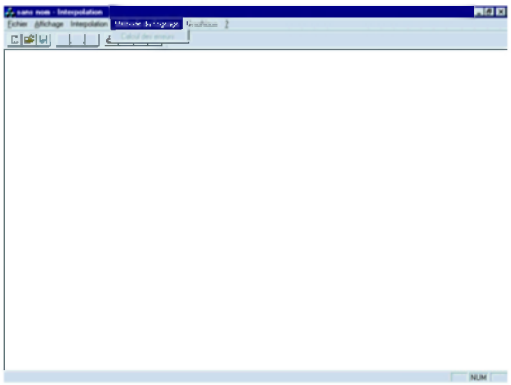

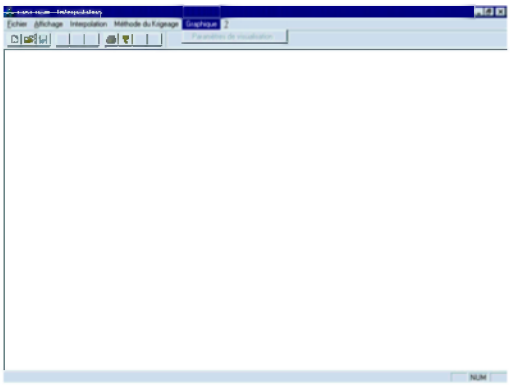

From the window opening the files, the application can be launched to activate the opening of two files, one defining the stations with their Lambert co-ordinates and the other describing the space-time evolution of the size to be interpolated. Once launched, the contour of Belgium as well as the names of the various stations takes shape with the screen. The various orders requiring the opening of a file are activated.

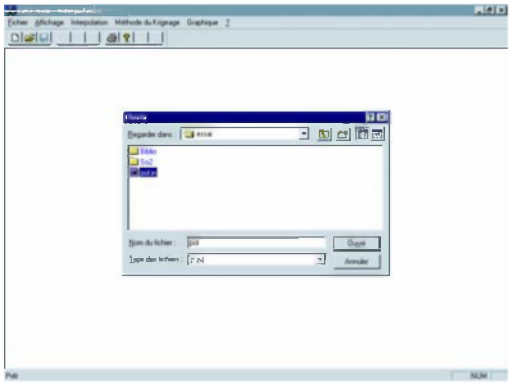

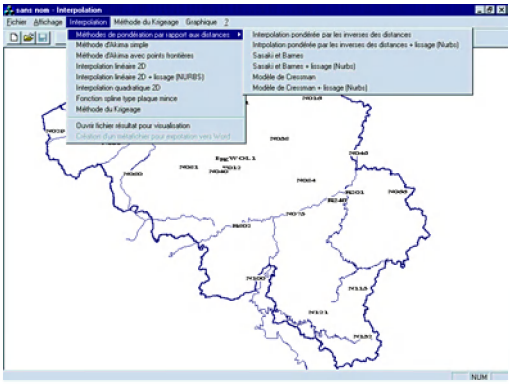

At the time of the choice of one of the interpolation methods, the user can select the type of station wished by the intermediary of the radio buttons. Once the selection carried out and the confirmed choice, the user can also choose the desired temporal period.

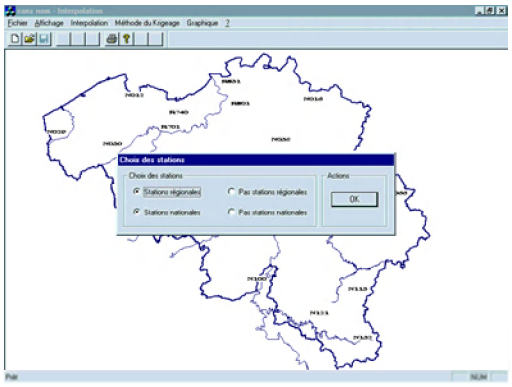

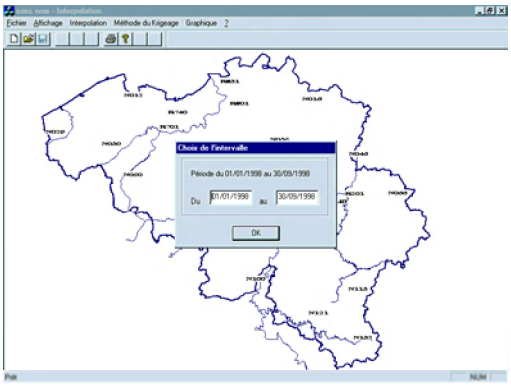

The application prepares the adequate tables according to the criteria of selection entered beforehand by the user.

In the case of the inverse distance method, the application can, for certain function of distance, to calculate an exponent. If such a value exists, the button "Value Calculated" will be activated. In the contrary case, this button is deactivated and the user can always choose another value that proposed by default and validate his choice.

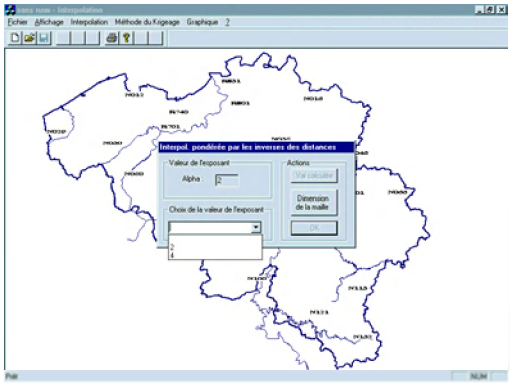

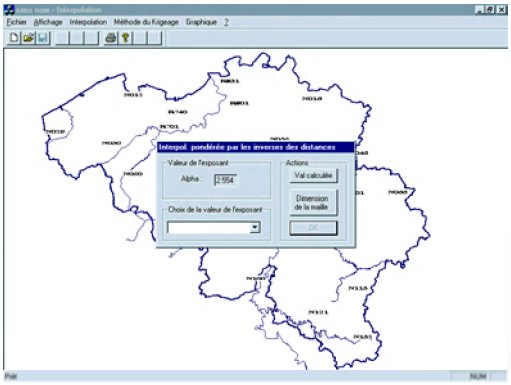

If the balanced interpolation uses a function of distance due to Sasaki-Barnes, a histogram is represented on screen. The user can select the influence radius starting from this graph or choose one of the values mentioned again in the list defined by default.

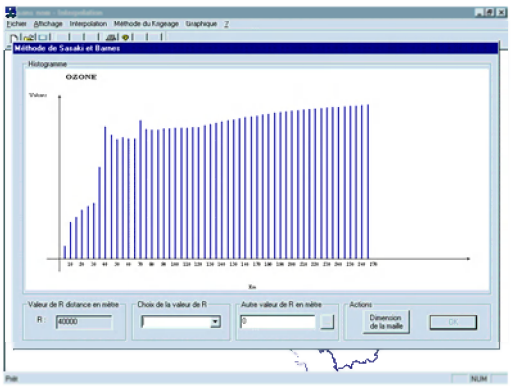

If the balanced interpolation uses a function of distance due to Thiébaux-Pedder (generalization of the Cressman function), a histogram is also represented on screen. The user can select the radius of influence starting from this graph or choose one of the values mentioned again in the list defined by default. The application also calculates the value of the exponent alpha. If calculation leads to a value, the button "Value calculated" is activated. In the contrary case, the button is de activated and the user can always choose another value, suggested either by default or introduced by itself. It is then necessary to validate this choice of the exponent.

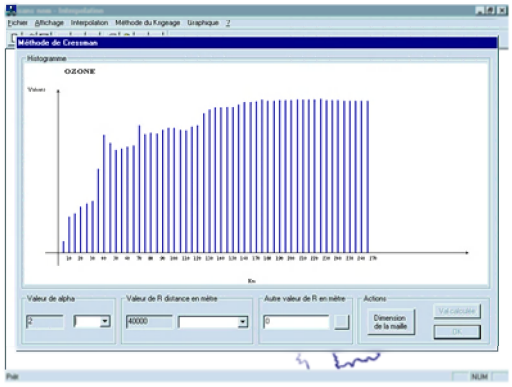

As soon as the parameters intervening in the inverse-distance were defined, it is requested from the user to choose the mesh of the calculation grid. By default, a mesh of 5 km is taken into account. After confirmation of the choice, calculation is carried out. Once finished, it is to ask the user to introduce a path as well as a file name. If the name exists the user will be able however to record the data under this name after confirmation.

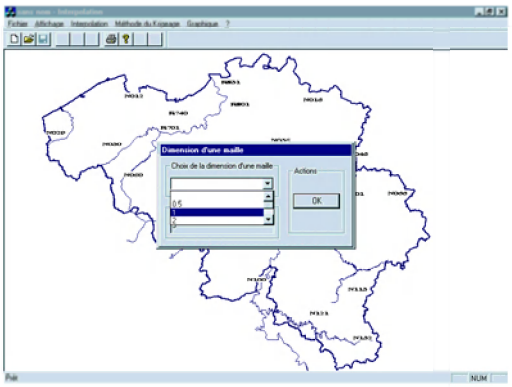

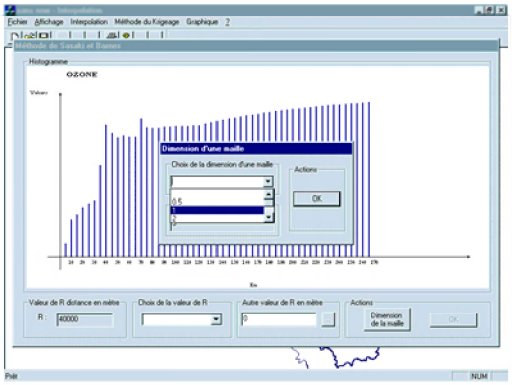

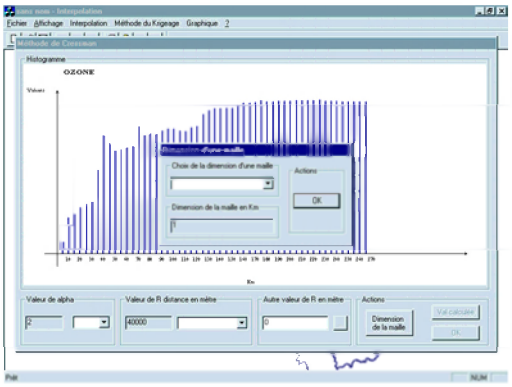

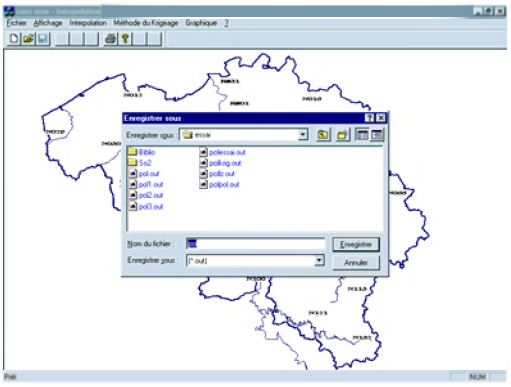

As soon as, the file result is recorded, the user sees appearing on the screen the map of the supplemented interpolation of following information:

- The type of pollutant
- The period of calculation as well as the lower and upper limits of pollution
- The scale chosen for the representation

At this stage, the user has the possibility of choice of the representation scale if it wishes to compare between them the results achieved with other methods. One time the choice of the scale of validated representation, the representation with the desired scale is posted on the screen.

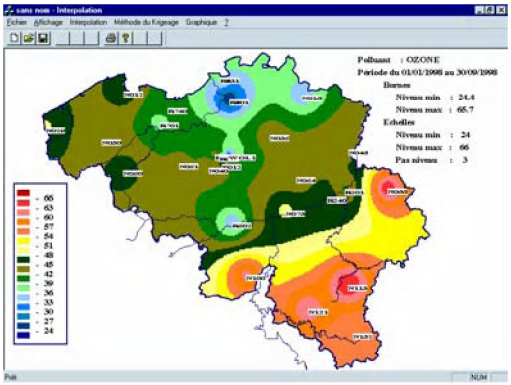

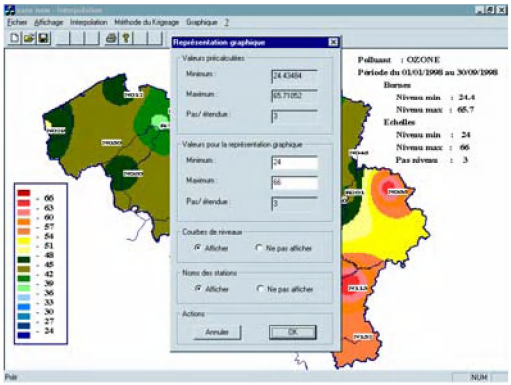

It can also record the map under the form of a metafile directly usable by Word and display the results of a calculation without having to remake it.

At the time of the selection of the interpolation method balanced by the opposite of the distances with a smoothing by the NURBS, as well as method of Cressman and its generalization with a smoothing by the NURBS and of the model of Sasaki and Barnes with a smoothing by the NURBS, the principle of operation is basically the same. With the only difference that the selected user a mesh in departure to which the selected method will be applied, smoothing enabling him to bring back the result on a lower mesh or equalizes with 5 km.

For the Kriging method the principle is different. At the time of the choice, it is also possible to select the types of stations wished by the intermediary of the radio buttons. Once the selection carried out and the choice to confirm, the application makes it possible to choose the desired temporal period. The application prepares the tables according to the criteria of selection introduced beforehand by the user.

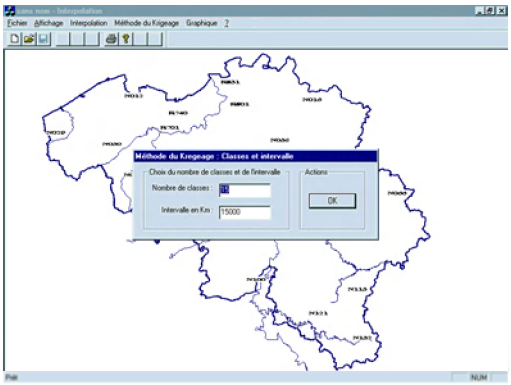

Then, the user sees appearing a dialog box asking him to introduce the number of classes like his dimension. A test is carried out in order to check that the number of classes is quite higher than 2 and that dimension belongs to the going interval of 1 km at 260 km. Thereafter, the user sees appearing the dialog box represented below. It can by the selection of radio buttons activate the use of the selected functions and introduce data into the "flexgrid". Calculation is carried out once that the user activates the button "Calculation". One graph appears on the screen. The user can compare the experimental curve (represented in blue) with the theoretical curve (represented in red). It can remake calculation and choose thereafter the theoretical curve which adjusts best the experimental curve without having to reintroduce the data. The quality of the adjustment is given by the numerical value indicated below the graph. The smaller this number is, the more the adjustment is "better". It can also carry out a zoom of the graph and change the scale of the squaring.

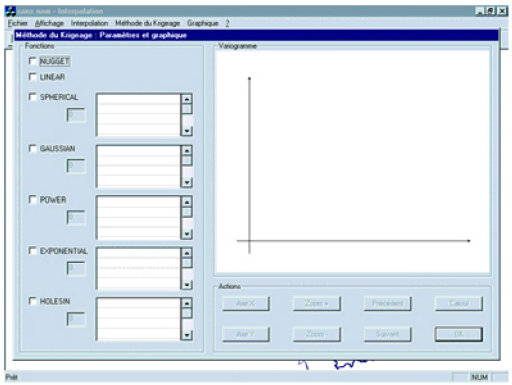

The user can also choose the mesh of the grid by knowing that by defect the mesh is of 5 km. Once the choice confirmed, calculation is carried out. Let us note that for the meshes lower than 3 km, the calculation of Kriging is realized with a mesh of 5 km and the results deferred by the use of function N.U.R.B.S. on the desired grid. This procedure allows a saving of time of calculation without loss of information.

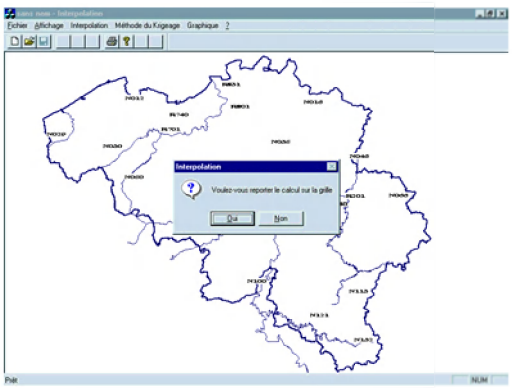

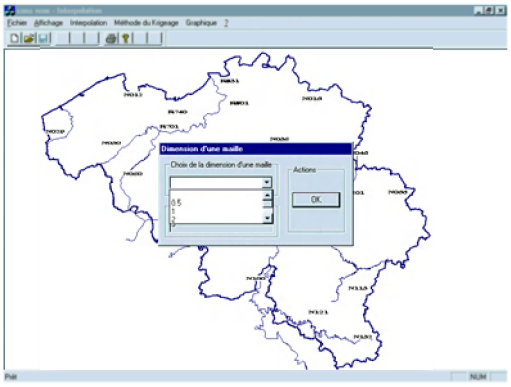

As soon as calculation is finished, it is of course requested from the user to record the data at a particular place on the disc. Two files are created: one including the

estimated concentration and the other the estimated variance. When calculation requires a mesh lower than 3 km, the variance estimated is given according to the mesh of calculation at knowing a mesh of 5 km.

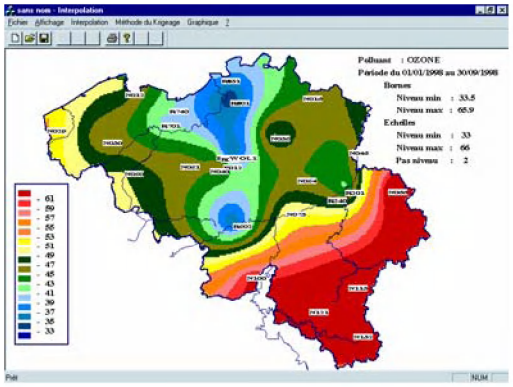

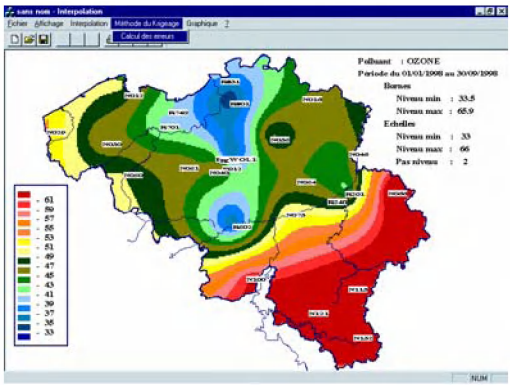

The estimated variance is to be visualized from dialog box corresponding. The parameters of visualization are also accessible in this case just like the possibility of creating a metafile.

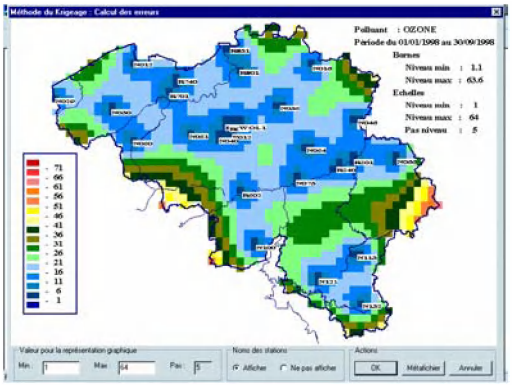

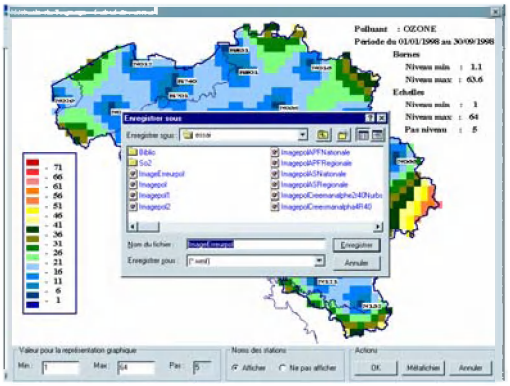

For the various methods, the possibility is offered to the user to display the result of the interpolation for a given area. The user activates the heading "Posting of the menu". A drop-down menu appears and the heading "Map of pollution" can be selected. A news dialog box appears. The user can then selects the area of his choice, modify the upper limit for the representation and create a metafile of the result.

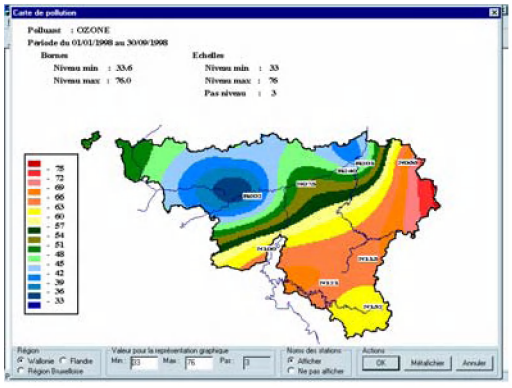

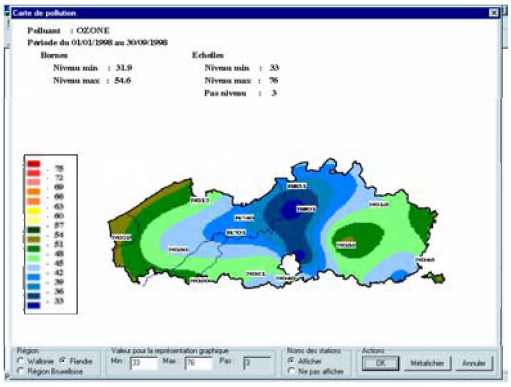

6. CONCLUSION

The examined methods of interpolation preserved in this study for a scalar variable turn around four great methods:

- **Inverse distance method.** This analytical formulation individually exploits the idea that each measured value contains some information which is degraded while moving away from the measurement point. The additive or linear effect of these various "sources" of information leads, by a weighted average, to an estimate of the measured size in each point of the studied geographical area. For a choice of a function defining the decrease of information an alternative of this type of method of interpolation corresponds (Model in the reverse of a distance power, models of Cressman, Thiébaux-Pedder and Sasaki-Barnes).
- **Methods based on the Delaunay triangulation.** These methods are of "patchwork" type i.e. that they build, starting from inter-connected elementary surfaces, a total surface passing by all the measurement points. As it is not possible to build a rectangular grid, elementary surfaces are triangles, with for tops three sites measuring, having good properties: their interiors must be disjoined two to two and each one cannot contain stations. The triangulation of Delaunay enable to build a single network of triangles having these properties. This parcelling out carried out, the quality of connectivity (continuity) defines the type of method: the interpolation on this network can be carried out by ensuring either a simple continuity in the method of interpolation linear, or a continuity until the first derivative in the method of interpolation quadratic or method of Cendes-Wong, or a continuity until the second derivative in the method of cubic interpolation known as method of Akima.
- **The thin plate method**. This method contrary to the preceding one does not require one cutting in triangles of the studied zone any more. It directly seeks a function which always passes by the measurement points (condition which can be softened) and which is subjected to a general constraint instead of satisfying local conditions of continuity. Total surface obtained resembles that given by a low thickness material (thin section) subjected to a whole of local forces (points of measurement) with boundary conditions particular.
- **Kriging method**. The individual characteristic which is used as a basis for the first method owes, actually, to be limited by the taking into account of the interactions existing between the measured values if one is willing to obtain a good interpolation. Some parameters of this method are defined by revealing these structuring interactions. The first method returns thus to a whole of separate actions which try to correct the individual nature of this method. On the contrary, the Kriging method is based on spatially correlated character of

the measured information of which it does not know *a priori* the structure. A great part of the method consists in explicitly defining this structure by using the variogram concept. Once this spacial structurality is modelled, the Kriging method itself consists in seeking the minimum of the error variance existing in each point of estimate. The various stages intervening in the Kriging method make this method more technical and thus less usable " eyes closed " as allows it the three other methods of interpolation.

For three of the four adopted methods, the interpolation results established on a rectangular grid covering the studied area can undergo a smoothing (face lift) using functions N.U.R.B.S. If this method enables, in some case, to free itself from a too small mesh to avoid of long computing time, it has the advantage of building an interpolation having of very good continuity conditions. All the methods of interpolation were developed in a data-processing application written in Visual C++.

The interpolations were applied to two pollutants having contrary behaviours namely ozone O_3 and the sulphur dioxide. SO_2. This primary education pollutant is mainly emitted in the cities and their periurban area. Ozone, secondary pollutant, is the result, under the action of solar energy, of chemical reactions mainly involving oxides of nitrogen and the volatile organic compounds (COV). If the SO_2 finds is mainly located to the periurban zone, ozone really starts beyond this area.

With these data files, the whole of the applications at the Belgian level highlights the following principal fact: straightly speaking, outside the polygon which contains all the triangles of Delaunay, "no salvation". In other words, even if certain methods not use it, the interpolation is only effective inside of the envelope which contains the measuring sites. Outside this envelope, the interpolation becomes an extrapolation which is difficult to control as long as information are unavailable outside Belgium. As long as there are no data exchanges at the European level, fictitious points were introduced. Values were attributed to these from an interpolation method based from basic values. This behaviour out of the triangular network clearly appears with the method of Kriging which is the only one to determine the error related to the estimate. It is always important in the vicinity of Belgian borders (outside triangular network) in the absence of the fictitious points of course when all the stations are considered. For the other methods of interpolation, it can be noticed by abnormal behaviours at the Belgian boundaries.

A second interesting result arises not only when all the stations are considered but when the stations are gathered in a class of national station and a class of regional station (city). This dichotomy was made possible thanks to the stations classification. Each name of station carries information enables to know if this station is urban (letter R) or not-urban (letter N) to hold account of the influence or not multi-

transmitters (transport, heating, industry). The results based on the national stations are, for all the methods, practically similar both for ozone the SO_2. This behaviour tends to confirm the objective of these stations which is to follow the air pollution known as of "bottom". The method does not matter; the structure of the pollution field seems well returned. Differences appear if the regional stations are only considered. The coherence of the interpolations obtained with these stations is difficult to show both for ozone and the SO_2. The reasons can be multiple, for example, a low number of regional stations for ozone or very concentrated groupings for the SO_2. If all the stations are considered, the results are also similar with all the methods. However, for the SO_2, the Kriging method clearly limits the extensions of some stations with strong values of concentration.

For a complete analysis, the Kriging method is a method which must be considered in first analysis since it enables on the one hand to decode the structures or spatial correlations of the analysed phenomenon and on the other hand to establish the estimated values as well as the errors related to the estimate. The results, if they lead to an internal coherence near to a reality in conformity with the practice, must be subjected to a confrontation with the obtained results by at least another method of interpolation. This one is to be sought among the total methods of type "patchwork" or thin section type. For these methods, negative values can appear. A procedure was elaborated to avoid the presence of important gradients no existing in reality.

If, a new case is considered from which few data are acknowledge, a first fast and effective analysis is to be made using a interpolation method based on the triangles of Delaunay (straight-line method with NURBS, the method of Cendes-Wong, Akima method) or the thin plate method. The particular choice of one of these methods will result from the continuity properties required by the secondary treatments applied to the data of the interpolation.

Appendix 1

Definition of N.U.R.B.S. method

N.U.R.B.S. are the initial ones of Not Uniform Rational B-Splines. The implementation of

B-Splines surface can take several directions. However the simplest and most current put down the same principle as the Bézier squares.

$$\vec{S}(u,v)=\sum_{i=0}^{n}\sum_{j=0}^{m}\vec{P}_{i,j}.N_{i,k}(u).N_{i,l}(v)$$

if $N_{i,k}$ et $N_{j,l}$ are two recursive functions with $N_{i,k}(t)$ as B-Splines function of order k associated with the point with control i, the parameter t varying from 0 to t_{max} with 2 ≤k ≤n+1

The B-Splines function is defined in a recursive way

$$N_{i,1}(t)=1 \quad \text{si } v_i \le t \le v_i+1$$

$$N_{i,1}(t)=0 \quad \text{ailleurs}$$

and

$$N_{i,k}(t)=\frac{(t-v_i).N_{i,k-1}(t)}{v_{i+1-k}-v_i}+\frac{(v_{i+k}-t).N_{i+1,k-1}(t)}{v_{i+1}-v_{i+1}}$$

where v_i is the $i^{ème}$ component of the nodal vector.

The B-splines function of order k is defined from that of order k-1.

The concept of nodal vector **[v_i]** bring a very great flexibility with the curves B-Splines, it makes it possible to manage the degree of the B-Splines function independently of the number of control points. This nodal vector appears as an additional degree of freedom which one can exploit. It is composed of ascending value v_I thus such $v_i \le v_{i+1}$ for all v_I

$\vec{P}_{i,j}$ is the element of a matrix [$\vec{P}$] containing the whole of the positions of the control points. The nodal vectors with degrees and different multiplicities can be defined according to the directions u and v. The formulation above imposes however that the polygons defined in a given direction have all the same number of points and the same multiplicity.

REFERENCES

Akima, H., 1970, A new method of interpolation and smooth curve fitting based on local procedures: Journal of the ACM, 17, 589-602.

Akima, H., 1978, A method of bivariate interpolation and smooth surface fitting for irregulary distributed data points: ACM Transactions on Mathematical Software, 4, 148-159.

Barnes, S. L., 1964, A technique for maximizing details in numerical weather map analysis: J. Appl. Meteor., 3, 396-409.

Bogaert, P., Mahau, P., and Beckers, F., 1995, The spatial interpolation of agro-climatic data: Agrometeorology Series Working Paper, n. 12, FAO Rome, Italy.

Cendes, Z. J., and Wong, S. H.,1987, C^1 Quadratic Interpolation Over Arbitrary Point Sets: IEEE Computer Graphics & Application, pp. 8-16.

Cressman, G. P., 1959, An operational objective analysis system: Mon. Wea. Rev., n. 87, pp.367-374.

Hardle, W., 1989, Applied Nonparametric Regression: Cambridge University Press, Cambridge.

Ionescu, A., Mayer, E., et Colda, I., 1996, Méthodes mathématiques pour estimer le champ de concentration d'un polluant gazeux à partir des valeurs mesurées aux points dispersés : Pollution Atmosphérique, n. 149, pp 78-89.

Landau, L. et Lifchitz, E., 1967, Théorie de l'élasticité : Editions MIR, 206 pp.

Pedder, M. A., 1993, Interpolation and filtering of spatial observations using successive correlations and Gaussian filters: Mon. Wea. Rev., 121, 2889-2902.

Sasaki, Y., 1960, An objective analysis for determining initial conditions for the primitive equations: Tech. Rep. 60-16T.

Şen, Z., 1997, Objective Analysis by Cumulative Semivariogram Technique and Its Application in Turkey: Journal of Applied Meteorology, v. 36, pp. 1712-1724.

Thiebaux, H. J., and Pedder, M. A., 1987, Spacial Objective Analysis with Applications in Atmospheric Science: Academic Press, 299 pp.

Watson, D. F.,1981, Computing the n-dimensional Delaunay tessellation with application to Voronoi polytopes: The Computer Journal, v. 24, n. 2, pp 167-172.